UNIVERSITY OF CALIFORNIA, SAN DIEGO

Experimental and Computational Investigation of the Seismic Performance of Stair Systems in Buildings

A dissertation submitted in partial satisfaction of the
requirements for the degree
Doctor of Philosophy

in

Structural Engineering

by

Xiang Wang

Committee in charge:

Professor Tara C. Hutchinson, Chair
Professor Joel P. Conte
Professor Jose I. Restrepo
Professor David T. Sandwell
Professor Peter M. Shearer

2015

The dissertation of Xiang Wang is approved, and it is acceptable in quality and form for publication on microfilm:

_____

_____

_____

_____

_____

Chair

University of California, San Diego

2015

DEDICATION

To my parents, who have gone far beyond the call of duty in supporting my pursuit of higher education.

EPIGRAPH

Now this is not the end.
It is not even the beginning of the end.
But it is, perhaps, the end of the beginning.
—Winston Churchill

TABLE OF CONTENTS

Signature Page . . . iii

Dedication . . . iv

Epigraph . . . v

Table of Contents . . . vi

List of Figures . . . x

List of Tables . . . xxii

List of Nomenclature . . . xxiv

Acknowledgements . . . xxvi

Vita and Publications . . . xxix

Abstract of the Dissertation . . . xxx

Chapter 1 Introduction . . . 1
- 1.1 Background . . . 1
- 1.2 Performance of Stair Systems in Past Earthquakes . . . 3
- 1.3 Previous Research on Seismic Behavior of Stair Systems . . . 5
  - 1.3.1 Experimental Studies . . . 5
  - 1.3.2 Numerical Studies . . . 9
- 1.4 Research Scope . . . 9
  - 1.4.1 Experimental Study . . . 10
  - 1.4.2 Numerical Study . . . 11
- 1.5 Dissertation Organization . . . 11

Chapter 2 Full-scale Building Shake Table Test Program . . . 15
- 2.1 Introduction . . . 15
- 2.2 Shake Table Test Facility, Test Building and its NCSs . . . 16
  - 2.2.1 Shake Table Test Facility . . . 16
  - 2.2.2 Test Building . . . 18
  - 2.2.3 Nonstructural Components and Systems . . . 20
  - 2.2.4 Estimated Weight of the Building and its NCSs . . . 22
- 2.3 Monitoring Systems . . . 23
- 2.4 Dynamic Test Protocol . . . 27
  - 2.4.1 White Noise and Pulse Base Excitations . . . 27
  - 2.4.2 Earthquake Input Motions . . . 30

2.4.2.1 Base Isolated Test Phase 31
2.4.2.2 Fixed Base Test Phase 34
2.5 Building Response 37
2.5.1 Building Response in the Base Isolated Test Phase 37
2.5.2 Building Response in the Fixed Base Test Phase . 41
2.6 Summary Remarks 44

Chapter 3 Shake Table Test Results of Prefabricated Steel Stairs 46
3.1 Introduction 46
3.2 Description of Stair System 47
3.2.1 Flights and Landing 47
3.2.2 Flight-to-Building Connections 49
3.2.3 Instrumentation 49
3.3 System Identification of Stairs 52
3.3.1 Deterministic-Stochastic Identification Method . . 52
3.3.2 White Noise Test Sequence 55
3.3.3 System Identification Results 58
3.4 Earthquake Test Results 62
3.4.1 Physical observations 62
3.4.2 Identification of Time Instance of Damage Occurrence 70
3.4.3 Measured Response 72
3.5 Summary and Conclusions 82

Chapter 4 Computational Assessment of the Seismic Behavior of Prefabricated Steel Stairs 84
4.1 Introduction 84
4.2 Model Description 85
4.2.1 Flight and Handrail 88
4.2.2 Landing 89
4.2.3 Connections 90
4.2.4 Material Models 93
4.2.5 Boundary Conditions 95
4.2.6 Modeling Limitations and Mesh Sensitivity Study . 95
4.3 Model Validation Studies 97
4.3.1 *OSU tests* (Higgins, 2009) 99
4.3.2 *UCSD tests* 100
4.4 Parametric Studies 106
4.4.1 Results: Baseline Model 108
4.4.2 Results: Modal Characteristics of Variable Design Models 112
4.4.3 Results: Lateral Force-Displacement Response of Variable Design Models 114

4.5 Summary and Conclusions 122

Chapter 5 Numerical Study of the Seismic Behavior of Building-Stair Systems 124
5.1 Introduction 124
5.2 Prototype Building Inventory 125
5.2.1 Steel Buildings 125
5.2.2 Reinforced Concrete Buildings 129
5.2.3 Prototype Building Design Summary 133
5.3 Modeling of Building-Stair Systems 134
5.3.1 Modeling of Structural Systems 134
5.3.2 Modeling of Prototype Buildings 136
5.3.2.1 Steel buildings 138
5.3.2.2 Reinforced Concrete Buildings 141
5.3.3 Modeling of Stair Systems within a Building – Coupled Building-Stair Models 144
5.4 Numerical Simulation Results 150
5.4.1 Eigenvalue Analysis 150
5.4.2 Nonlinear Static Analysis 155
5.4.3 Nonlinear Dynamic Analysis 168
5.5 Concluding Remarks 178

Chapter 6 Probabilistic Seismic Response Analysis of Building-Stair Systems and Loss Estimation of Stair Systems 180
6.1 Introduction 180
6.2 Probabilistic Seismic Analysis Methodology 181
6.2.1 General Framework 181
6.2.2 Probabilistic Seismic Analysis of Building-Stair Systems 183
6.3 Seismic Hazard Analysis 186
6.3.1 Site-specific Seismic Hazard Analysis 186
6.3.2 Ground Motion Set 190
6.4 Seismic Demand Analysis and Collapse Assessment . . . 194
6.4.1 Collapse Fragility Assessment 195
6.4.2 Statistics of Structural Demands 201
6.4.3 Probabilistic Structural Response 205
6.5 Probabilistic Seismic Damage and Loss Analysis 210
6.5.1 Seismic Fragility and Damage Analysis of Stairs . 210
6.5.2 Seismic Loss Analysis of Stair Systems 211
6.5.3 Stair Loss Results 217
6.6 Concluding Remarks 235

Chapter 7 Conclusions and Future Work 238
7.1 Motivation and Scope 238
7.2 Research Uniqueness 239
7.3 Major Findings 240
7.3.1 Full-scale Building Shake Table Testing 240
7.3.2 Detailed Finite Element Modeling 241
7.3.3 Probabilistic Seismic Analysis of Coupled Building-Stair Systems 242
7.4 Recommendations for Future Work 243

Bibliography 246

Appendix A Construction Drawings of the Stair System 255

Appendix B Measured Stair Acceleration Response 266

Appendix C Shake Table Test Results of Elevator System 306
C.1 Introduction 306
C.2 Description of Elevator System 307
C.2.1 Elevator Design 309
C.2.2 Instrumentation 309
C.2.3 Test Configurations 311
C.3 White Noise Test Results 313
C.4 Earthquake Test Results 315
C.4.1 Physical Observation 315
C.4.2 Measured Response 317
C.5 Summary and Conclusions 326

Appendix D Pre-test Simulation – OpenSees Model 329
D.1 Introduction 329
D.2 Model Description 329
D.3 Estimated Pre-test Weight of the Building 333
D.4 Pre-test Simulation Results 334
D.4.1 Eigen Analysis 334
D.4.2 Nonlinear Dynamic Analysis 334
D.5 Summary 337

LIST OF FIGURES

Figure 1.1 Typical geometric configurations of stairs (a) scissor configuration, and (b) straight-run configuration (source: FEMA, 2012). 2

Figure 1.2 Examples of stair damage in recent earthquakes: (a) damaged exterior reinforced concrete stairs in the 2010 Maule earthquake in Chile (photo courtesy of J. Restrepo), (b) damaged exterior wood stairs in the 2014 South Napa earthquake (photo courtesy of T. Hutchinson), and (c) partial collapse of interior precast concrete stairs in the 2011 Christchurch earthquake in New Zealand (photo courtesy of J. Restrepo). 4

Figure 1.3 Experimental study of precast concrete straight-run stairs: (a) test specimen and test setup, and (b) test loading protocol, and (c) damage to specimen Unit-I at the completion of the lateral displacement loading (figures courtesy of Simmons and Bull, 2000). 6

Figure 1.4 Experimental study of prefabricated steel stairs : (a) test specimen and test setup, (b) flight-to-landing connection yielding, and (c) initial weld cracking and connection plate buckling (photos courtesy of Higgins, 2009). 8

Figure 2.1 UCSD Large High-Performance Outdoor Shake Table (source: NEES, 2014). 17

Figure 2.2 Test building: (a) structural skeleton of the building, (b) test building at completion, (c) typical floor plan layout (note that interior partition wall layout varies from floor to floor), and (d) elevation. 19

Figure 2.3 Monitoring systems deployed on the test building (photo courtesy of Pantoli et al., 2013b). 24

Figure 2.4 Input acceleration of a complete white noise and pulse-like base excitation sequence. 30

Figure 2.5 Acceleration time histories of the achieved earthquake motions in the base isolated test phase. 32

Figure 2.6 Elastic response spectra of the achieved earthquake input motions in the base isolated test phase (damping ratio $\xi = 12\%$): (a) psuedo-acceleration spectra, (b) psudeo-velocity spectra, and (c) displacement spectra. 33

Figure 2.7 Acceleration time histories of the achieved earthquake input motions in the fixed base test phase. 35

Figure 2.8 Elastic response spectra of the achieved earthquake input motions in the fixed base test phase (damping ratio $\xi = 5\%$): (a) psuedo-acceleration spectra, (b) psudeo-velocity spectra, and (c) displacement spectra. 36

Figure 2.9 Floor acceleration time histories of the test building during test BI-7. 38

Figure 2.10 Interstory drift ratio time histories of the test building during test BI-7. 39
Figure 2.11 Building peak responses in the base isolated test phase: (a) peak floor accelerations, and (b) peak interstory drift response. 40
Figure 2.12 Peak isolator longitudinal shear strains (averaged) in the base isolated test phase. 41
Figure 2.13 Floor acceleration time histories of the test building during test FB-5. 42
Figure 2.14 Interstory drift ratio time histories of the test building during test FB-5. 43
Figure 2.15 Building peak responses in the FB test phase: (a) peak floor accelerations, and (b) peak interstory drift response. 44

Figure 3.1 Stair layout: (a) three-dimensional schematic of the stair (handrail not shown for clarity), (b) photograph of the stair installed in place during structural skeleton completion, and (c) photograph of the stairwell at building completion (note: double-headed arrow denotes the direction of input motion applied at the base of the test building). 48
Figure 3.2 Flight-to-building connection details: (a) lower flight to slab connection, (b) upper flight to slab connection, and (c) upper flight connection angle. 50
Figure 3.3 Instrumentation of the stair at level 2: (a) accelerometers, and (b) displacement transducers. Sensor orientations shown are consistent with the global coordinate system used for the building. Note that level 2 represents the most densely instrumented level of stairs. . 51
Figure 3.4 Selected (a) input and (b) output acceleration histories and corresponding Fourier amplitude spectra during the reference state (1.5% g RMS WN test S0). 57
Figure 3.5 Polar plot representations of the complex-valued mode shapes identified at the reference state (1.5% g RMS WN test S0). 58
Figure 3.6 Identified mode shapes: (a) 1st mode, (b) 2nd mode, and (c) 3rd mode. 59
Figure 3.7 Examples of observed stair damage: (a) closure plate detachment (DS-1; photograph taken at the landing between level 1 and 2 after test FB-4), (b) handrail fracture (DS-1; photograph taken at level 3 after test FB-5), (c) upper flight connection angle weld fracture (DS-3; photograph taken at level 3 following test FB-4), (d) plastic yielding of the connection plate between the landing and lower flight (DS-2; photograph showing the bottom view of the landing at level 2 following test FB-5), and (e) lower flight detachment and complete loss of vertical support (DS-3; photograph taken at level 3 after test FB-6). 63

Figure 3.8 Stair repair actions: (a) R-I (b) R-II, and (c) R-III (only the welds that require repair are shown in the figure). 63
Figure 3.9 Stair damage progression during the last three FB tests (notes: damage types are differentiated by color and marker shape, i.e, red for DS-3, yellow for DS-2, and green for DS-1; boxed values represent PIDRs during the specified seismic tests and are shown in black, and red values in parenthesis represent the actual IDR at damage instance). 65
Figure 3.10 Observed stair damage following test FB-4: (a) closure plate detachment (DS-1; photograph taken at the landing between level 1 and 2), (b) connection plate weld fracture (DS-3; photograph taken at level 3), (c) repaired connection plate on the northern side of the upper flight, and (d) repaired condition on the southern side of the upper flight). 66
Figure 3.11 Observed stair damage following test FB-5: (a) handrail (DS-1; photograph taken at the landing between level 1 and 2), (b) connection plate weld fracture (DS-3; photograph taken at level 3), and (c) repaired connection plate on the northern side of the upper flight. 67
Figure 3.12 Detected stair damage following test FB-6: (a) plastic yielding of the washer plate at the lower flight to landing connection at floor 1 (DS-2), and (b) lower flight detachment (DS-3; photograph taken at level 3). 68
Figure 3.13 Interstory drift response and the accumulated IDR cycle distribution for the two instances of upper flight connection angle vertical weld fracture: (a) FB-4, and (b) FB-5. 73
Figure 3.14 Absolute acceleration time histories and the associated Fourier amplitude spectra of the stair landing at level 2: (a) test FB-1, and (b) test FB-3. 74
Figure 3.15 Comparison of longitudinal and transverse PCAs of the stair landing at level 2: (a) BI test phase, and (b) the first three FB tests. 76
Figure 3.16 Displacement responses of the stair landing at level 2 relative to the lower floor during test FB-1 (note: red dot denotes the positive interstory drift peak and blue dot denotes the negative peak). . . . 77
Figure 3.17 Longitudinal connection deformation time histories of the stair at level 2 during test FB-1 (note: red dot denotes the positive interstory drift peak and blue dot denotes the negative peak). 79
Figure 3.18 Longitudinal connection deformation time histories of the stair at level 2 during test FB-3 (note: red dot denotes the positive interstory drift peak and blue dot denotes the negative peak). 80
Figure 3.19 Peak interstory drift at level 2 vs. peak landing displacement relative to the lower floor of the stair (a) in the longitudinal direction, and (b) in the transverse direction. 81

Figure 4.1 Finite element model of a generic prefabricated steel stair. 86
Figure 4.2 Finite element model of a stair flight with handrail. 88
Figure 4.3 Finite element model of a stair landing. 90
Figure 4.4 Finite element modeling of stair flight-to-building connections (Type-I connections): (a) upper flight, and (b) lower flight. 91
Figure 4.5 Finite element modeling of stair flight-to-building connections (Type-II connections): (a) upper flight, and (b) lower flight. 92
Figure 4.6 Modeling of bolted connections. 93
Figure 4.7 Uniaxial stress-strain response of the steel models: (a) monotonic response, and (b) cyclic response. 94
Figure 4.8 Force-displacement response of Type-I upper-flight-to-floor connection under monotonic paralell-to-stair-run loading. 96
Figure 4.9 Local response of Type-I upper-flight-to-floor connection under monotonic paralell-to-stair-run loading: (a) connection longitudinal displacement vs. effective plastic strain, and (b) connection longitudinal displacement vs. von-Mises stress. 97
Figure 4.10 Finite element models of the stairs used in the validation studies: (a) OSU tests, and (b) UCSD test. 98
Figure 4.11 Comparison of the force-displacement response of the *OSU test* specimen in: (a) parallel-to-stair-run loading, and (b) transverse-to-stair-run loading (double-headed arrow denotes the direction of loading). 101
Figure 4.12 Mode shapes of the UCSD test specimen (top view): (a) first mode, (b) second mode and (c) third mode. 103
Figure 4.13 Comparison of the landing displacements of the UCSD test specimen in test FB-1: (a) lower flight corner, and (b) upper flight corner. 105
Figure 4.14 Mode shapes of two predominant horizontal vibration modes – *Baseline Model* (top view): (a) transverse-to-stair-run direction (7.7 Hz), and (b) parallel-to-stair-run direction (19.3 Hz). 109
Figure 4.15 Illustration of the numerically predicted performance parameters of *Baseline Model* under positive parallel-to-stair-run loading: (a) lateral force-displacement response, and the von-Mises stress distribution of upper flight-to-building connection under (b) yield state and (c) ultimate state. 110
Figure 4.16 (a) Force-displacement response, and (b) landing displacements of the baseline model under monotonic displacement loading under the two horizontal directions (positive and negative). 111
Figure 4.17 Normalized modal frequencies of the stair models relative to *Baseline Model*: (a) transverse-to-stair-run modes, and (b) parallel-to-stair-run modes (cases denoted as BL and C1-8; see Table 4.6). . . 113
Figure 4.18 Normalized performance parameters of the force-displacement behavior of the stair models relative to *Baseline Model* (cases denoted as BL and C1-8; see Table 4.6). 117

Figure 4.19 Deformed shape and von-Mises stress distribution of the upper flight-to-building connections when the stairs reach the ultimate state (2.5% interstory drift) under positive parallel-to-stair-run loading: (a) Type-I connection – *baseline model*, (b) Type-II connection – *Case 6*, and (c) Type-III connection – *Case 7*. 120
Figure 4.20 Landing displacement trajectory of stair models with varying geometric configuration: (a) parallel-to-stair-run loading, and (b) transverse-to-stair-run loading. 121

Figure 5.1 Plan layout of the steel prototype buildings. 126
Figure 5.2 Elevation of building S-4 and the beam and column member sizes. 127
Figure 5.3 Elevation of building S-8 and the beam and column member sizes. 127
Figure 5.4 Elevation of building S-20 and the beam and column member sizes. 128
Figure 5.5 Plan layout of the reinforced concrete prototype buildings for: (a) RC-8 and RC-20, and (b) RC-4. 130
Figure 5.6 Elevation of building RC-4 as well as the member size and reinforcement ratio of the beams and columns. 131
Figure 5.7 Elevation of building RC-8 as well as the member size and reinforcement ratio of the beams and columns. 131
Figure 5.8 Elevation of building RC-8 as well as the member size and reinforcement ratio of the beams and columns. 132
Figure 5.9 Different modeling strategies of frame-type structural components. 135
Figure 5.10 Two-dimensional structural analysis model of the prototype building. 136
Figure 5.11 Nonlinear analysis model of steel SMF: (a) beam-column subassembly, and (b) joint panel zone model. 138
Figure 5.12 Modified Ibarra-Krawinkler model of $M-\theta$ response: (a) monotonic response, and (b) cyclic response. 139
Figure 5.13 V_y and γ_y response for rigid parallelogram model: (a) monotonic response, and (b) cyclic response (Gupta and Krawinkler, 1999). . 140
Figure 5.14 Nonlinear analysis model of reinforced concrete beam-column subassembly. 141
Figure 5.15 (a) Reinforced concrete fiber section discretization, and material stress-strain response (b) concrete in compression, and (b) concrete in tension, and (d) steel reinforcement. 142
Figure 5.16 Moment-bond slip rotation ($M-\theta_{sl}$) response (a) monotonic response, and (b) cyclic response. 143
Figure 5.17 Coupled building-stair model implemented in *OpenSees*. 145
Figure 5.18 Hysteretic force-displacement responses of the calibrated lumped springs: (a) parallel-to-stair-run direction, and (b) transverse-to-stair-run direction. 147
Figure 5.19 Variables considered in the idealized lumped springs of the stairs. 149
Figure 5.20 Normalized modal periods of the first three modes. 152

Figure 5.21 Normalized effective modal mass of the first three modes. 153
Figure 5.22 Modal shapes of the prototype buildings: (a) S-4, (b) S-8, (c) S-20, (d) RC-4, (e) RC-8, and (f) RC-20,. 154
Figure 5.23 Generic pushover curve and the associated performance parameters. 156
Figure 5.24 Pushover analysis results for S-4: (a) global pushover curve, and (b) floor displacement profile. 158
Figure 5.25 Pushover analysis results for S-8: (a) global pushover curve, and (b) floor displacement profile. 158
Figure 5.26 Pushover analysis results for S-20: (a) global pushover curve, and (b) floor displacement profile. 159
Figure 5.27 Pushover analysis results for RC-4: (a) global pushover curve, and (b) floor displacement profile. 161
Figure 5.28 Pushover analysis results for RC-8: (a) global pushover curve, and (b) floor displacement profile. 161
Figure 5.29 Pushover analysis results for RC-20: (a) global pushover curve, and (b) floor displacement profile. 162
Figure 5.30 Effects of stair response modification factor Ω_{stair} on building initial stiffness: (a) steel buildings, and (b) reinforced concrete buildings. 163
Figure 5.31 Building pushover response due to the effects of the stair system: (a) stair response modification factor Ω_{stair} and (b) stair ultimate deformation capacity IDR_{damage}. 164
Figure 5.32 Effects of the stair response modification factor Ω_{stair} and ultimate deformation IDR_{damage} on the overstrength factor Ω of the coupled building-stair systems. 166
Figure 5.33 Effects of the stair response modification factor Ω_{stair} and ultimate deformation IDR_{damage} on the ultimate roof drift ratio $\delta_{r,u}$ of the coupled building-stair systems. 167
Figure 5.34 Earthquake input motion: (a) acceleration history, and (b) 5% damped elastic pseudo-acceleration spectrum and ASCE 7-10 spectrum. . 169
Figure 5.35 Effects of stair stair response modification factor Ω_{stair} on the peak responses of building S-4: (a) PFA – SLE-43 motion, (b) PFA – DE motion, (c) PFA – MCE motion, (d) PIDR – SLE-43 motion, (e) PIDR – DE motion, and (f) PIDR – MCE motion. 171
Figure 5.36 Effects of stair response amplification factor Ω_{stair} on time history responses of building S-4: (a) acceleration at the roof – DE motion, (b) acceleration at the 2nd floor – MCE motion, (c) interstory drift ratio at the 2nd level – SLE-43 motion, (d) interstory drift ratio at the 2nd level – MCE motion. 172
Figure 5.37 Effects of stair ultimate deformability IDR_{damage} on the peak responses of building S-4: (a) PFA – SLE-43 motion, (b) PFA – DE motion, (c) PFA – MCE motion, (d) PIDR – SLE-43 motion, (e) PIDR – DE motion, and (f) PIDR – MCE motion. 174

Figure 5.38 Normalized PFA responses of the prototype buildings with stairs incorporated (Ω_{stair}=4, IDR_{damage}=5%): (a) building S-4, (b) building S-8, (c) building S-20, (d) building RC-4, (e) building RC-8, and (f) building RC-20. 176
Figure 5.39 Normalized PIDR responses of the prototype buildings with stairs incorporated (Ω_{stair}=4, IDR_{damage}=5%): (a) building S-4, (b) building S-8, (c) building S-20, (d) building RC-4, (e) building RC-8, and (f) building RC-20. 177

Figure 6.1 Probabilistic analysis procedure of coupled building-stair systems. 185
Figure 6.2 Uniform hazard spectra for the site of the prototype buildings (33.996N, 118.162W). 187
Figure 6.3 Site-specific hazard curves for the three steel buildings (33.996N, 118.162W). 187
Figure 6.4 Lognormal fitting of seismic hazard exceeded in 50 years and corresponding seismic hazard curve of building S-4. 189
Figure 6.5 The fitted first-order derivative of the seismic hazard curves of building S-4. 189
Figure 6.6 Response spectra of the FEMA P695 normalized far-field ground motion records (5% damped): (a) pseudo-acceleration spectra, and (b) displacement spectra. 192
Figure 6.7 Pseudo acceleration spectra of ground motions scaled to different *IM* levels (5% damped): (a) S-4 – IM_{475}, (b) S-4 – IM_{2475}, (c) S-8 – IM_{475}, (d) S-8 – IM_{2475}, (e) S-20 – IM_{475}, and (f) S-20 – IM_{2475}. 193
Figure 6.8 PIDR distributions of building S-4 (bare structure) at the eleven *IM* levels: (a) first story, (b) second story, (c) third story, and (d) fourth story. 195
Figure 6.9 Collapse fragility curve for building S-4 (bare building). 197
Figure 6.10 MAQ algorithm for calculating collapse MAR of building S-4 (bare building): (a) $G(x)$ in x domain (building collapse fragility curve), (b) $f(x)$ in x domain (slope of seismic hazard curve), (c) resultant integrand in x domain, and (d) resultant integrand in t domain and distribution of integration points. 199
Figure 6.11 Effects of stairs on building collapse MAR: (a) effect of stair response modification factor Ω_{stair}, and (b) effect of stair ultimate deformation capacity IDR_{damage}. 200
Figure 6.12 The empirical and fitted CDFs of the PIDR responses of building S-4 (bare structure) at three representative *IM* levels. 202
Figure 6.13 Kolmogorov-Smirnov goodness-of-fit tests of the PIDR distributions of building S-4 (bare building). 203
Figure 6.14 (a) Median $\theta_{EDP|IM}$, and (b) dispersion $\beta_{EDP|IM}$ curves of the building S-4 PIDR response (bare building). 203

Figure 6.15 Correlation coefficients $\rho_{EDP_i,EDP_j|IM}$ of the PIDR responses of the three prototype buildings. 204
Figure 6.16 Probabilistic peak floor acceleration responses of the steel buildings at three presentative *IM* levels. 206
Figure 6.17 Probabilistic peak interstory drift responses of the steel building at three presentative *IM* levels. 207
Figure 6.18 Effect of stair response modification factor Ω_{stair} on median peak floor acceleration responses of the steel buildings at three presentative *IM* levels. 208
Figure 6.19 Effect of stair response modification factor Ω_{stair} on median peak interstory drift responses of the steel buildings at three presentative *IM* levels. 209
Figure 6.20 Fragility curves of stairs with three median $\theta_{DS|EDP}$ values. 212
Figure 6.21 Multi-layer Monte Carlo simulation procedure for seismic loss analysis of stair systems. 216
Figure 6.22 Conditional mean of the loss of stairs $E[L_i|IM]$ at each story of building S-4: (a) first story, (b) second story, (c) third story, and (d) fourth story. 217
Figure 6.23 Conditional mean of the total stair loss $E[L_T|IM]$ of building S-4. 219
Figure 6.24 Conditional standard deviation of the total stair loss $\sigma_{L_T|IM}$ of building S-4. 219
Figure 6.25 Conditional probability of the stair total loss achieving or exceeding a specific value for building S-4. 220
Figure 6.26 Deaggreation of conditional mean of the total stair loss $E[L_T|IM]$ into story contributions $E[L_i|IM]$ at the three representative *IM* levels. 222
Figure 6.27 Variation of stair variables Ω_{stair} and IDR_{damage} on conditional mean of the total stair loss $E[L_T|IM]$. 223
Figure 6.28 Variation of stair variables Ω_{stair} and IDR_{damage} on conditional standard deviation of the total stair loss $\sigma_{L_T|IM}$. 224
Figure 6.29 Comparison of conditional mean of the stair total loss $E[L_T|IM]$ of the three prototype buildings at the three representative *IM* levels. 226
Figure 6.30 Evaluation the stair total MAL using the MAQ algorithm: (a) $G(x)$ in x domain (conditional mean of total stair loss $\mathrm{E}[L_T|IM = im]$), (b) $f(x)$ in x domain (slope of seismic hazard curve), (c) resultant integrand in x domain (Equation 6.21), and (d) resultant integrand in t domain and the integration point distribution. 228
Figure 6.31 Deaggreation of stair MAL $E[L_T]$ into contributions at different stories $E[L_i]$. 229
Figure 6.32 Stair loss hazard curve $\lambda_{L_T}(z)$ of building S-4. 230

Figure 6.33 Deaggregation of MAR of stair total loss in building S-4 achieving or exceeding corresponding to the three specified values (25%, 50%, and 100%) into contributions associated with different *IM* levels: (a) original MAR of exceedance, and (b) normalized MAR of exceedance. 230
Figure 6.34 Effects of stair variables Ω_{stair} and IDR_{damage} on the total stair loss hazard curves $\lambda_{L_T}(z)$ 232
Figure 6.35 Effects of stairs on probability of exceedance of stair loss within a given exposure time of 50 years: (a) effect of Ω_{stair} on P($L_T \geq 1$), and (b) effect of IDR_{damage} on P($L_T \geq 1$), (c) effect of Ω_{stair} on P($\widehat{L}_T \geq 50\%$), and (d) effect of IDR_{damage} on P($\widehat{L}_T \geq 50\%$), (e) effect of Ω_{stair} on P($\widehat{L}_T \geq 100\%$), and (f) effect of IDR_{damage} on P($\widehat{L}_T \geq 100\%$). 233
Figure 6.36 Effects of stairs on total stair MAL $E[L_T]$: (a) effect of stair response modification factor Ω_{stair}, and (b) effect of stair ultimate deformation capacity IDR_{damage}. 234
Figure 6.37 Deaggregation of stair total mean annual loss $E[L_T]$ of building S-4 into different *IM* levels (a) effect of stair response modification factor Ω_{stair}, and (b) effect of stair ultimate deformation capacity IDR_{damage}. 235

Figure 7.1 Innovative stair design strategy – landing separation. 245

Figure B.1 Accelerometer layout of the steel stair at level 2. 266
Figure B.2 Acceleration time history responses of the lower flight at level 2 during test BI-1. 267
Figure B.3 Acceleration time history responses of the landing at level 2 during test BI-1. 268
Figure B.4 Acceleration time history responses of the upper flight at level 2 during test BI-1. 269
Figure B.5 Acceleration time history responses of the lower flight at level 2 during test BI-2. 270
Figure B.6 Acceleration time history responses of stair landing at level 2 during test BI-2. 271
Figure B.7 Acceleration time history responses of the stair upper flight at level 2 during test BI-2. 272
Figure B.8 Acceleration time history responses of the lower flight at level 2 during test BI-3. 273
Figure B.9 Acceleration time history responses of stair landing at level 2 during test BI-3. 274
Figure B.10 Acceleration time history responses of the stair upper flight at level 2 during test BI-3. 275

Figure B.11 Acceleration time history responses of the lower flight at level 2 during test BI-4. 276
Figure B.12 Acceleration time history responses of stair landing at level 2 during test BI-4. 277
Figure B.13 Acceleration time history responses of the stair upper flight at level 2 during test BI-4. 278
Figure B.14 Acceleration time history responses of the lower flight at level 2 during test BI-5. 279
Figure B.15 Acceleration time history responses of stair landing at level 2 during test BI-5. 280
Figure B.16 Acceleration time history responses of the stair upper flight at level 2 during test BI-5. 281
Figure B.17 Acceleration time history responses of the lower flight at level 2 during test BI-6. 282
Figure B.18 Acceleration time history responses of stair landing at level 2 during test BI-6. 283
Figure B.19 Acceleration time history responses of the stair upper flight at level 2 during test BI-6. 284
Figure B.20 Acceleration time history responses of the lower flight at level 2 during test BI-7. 285
Figure B.21 Acceleration time history responses of stair landing at level 2 during test BI-7. 286
Figure B.22 Acceleration time history responses of the stair upper flight at level 2 during test BI-7. 287
Figure B.23 Acceleration time history responses of the lower flight at level 2 during test FB-1. 288
Figure B.24 Acceleration time history responses of the landing at level 2 during test FB-1. 289
Figure B.25 Acceleration time history responses of the upper flight at level 2 during test FB-1. 290
Figure B.26 Acceleration time history responses of the lower flight at level 2 during test FB-2. 291
Figure B.27 Acceleration time history responses of stair landing at level 2 during test FB-2. 292
Figure B.28 Acceleration time history responses of the stair upper flight at level 2 during test FB-2. 293
Figure B.29 Acceleration time history responses of the lower flight at level 2 during test FB-3. 294
Figure B.30 Acceleration time history responses of stair landing at level 2 during test FB-3. 295
Figure B.31 Acceleration time history responses of the stair upper flight at level 2 during test FB-3. 296

Figure B.32 Acceleration time history responses of the lower flight at level 2 during test FB-4. 297
Figure B.33 Acceleration time history responses of stair landing at level 2 during test FB-4. 298
Figure B.34 Acceleration time history responses of the stair upper flight at level 2 during test FB-4. 299
Figure B.35 Acceleration time history responses of the lower flight at level 2 during test FB-5. 300
Figure B.36 Acceleration time history responses of stair landing at level 2 during test FB-5. 301
Figure B.37 Acceleration time history responses of the stair upper flight at level 2 during test FB-5. 302
Figure B.38 Acceleration time history responses of the lower flight at level 2 during test FB-6. 303
Figure B.39 Acceleration time history responses of stair landing at level 2 during test FB-6. 304
Figure B.40 Acceleration time history responses of the stair upper flight at level 2 during test FB-6. 305

Figure C.1 Elevator hoistway: (a) plan layout, (b) photograph (view down from level 3), (c) cabin with sand bags, and (d) counterweight. 308
Figure C.2 Elevator instrumentation: (a) accelerometers on the cabin, (b) accelerometers on the counterweight, and (c) strain gauges of the bracket anchors (SG-X-XS and SG-X-XN denote the anchors on the north and south sides attaching the same bracket). 310
Figure C.3 Test configurations for the elevator system (west bay of the building). 312
Figure C.4 The first three natural frequencies of the test building (in the fixed base configuration) with elevator components placed in configurations C-I to C-III (Figure C.3). 314
Figure C.5 Damage to the elevator: (a) incipient gapping of the door at level 3 following test FB-5, (b) door distortion at level 3 following test FB-6, and (c) corner crushing of the door at level 3 following test FB-6. 316
Figure C.6 Acceleration time histories and associated Fourier amplitude spectrum of: (a) cabin, and (b) counterweight during test FB-1. . . . 318
Figure C.7 Acceleration time histories and associated Fourier amplitude spectrum of: (a) cabin, and (b) counterweight during test FB-5. . . . 319

Figure C.8 Acceleration amplification ratios: (a) cabin in the BI tests, (b) counterweight in the BI tests, (c) cabin in the FB tests, and (d) counterweight in the FB tests (solid markers denote the high frequency cutoff of 100 Hz, while hollow markers denote the high frequency cutoff of 25 Hz; * denotes that the elevator was tested in configuration C-III, otherwise the test was conducted with the elevator placed in configuration C-I). 322
Figure C.9 Time histories of the bracket anchor forces at floor 5 during test FB-1. 324
Figure C.10 Time histories of the bracket anchor forces at floor 5 during test FB-5. 324

Figure D.1 Pre-test building model and modeling details of the shear walls and columns. 330
Figure D.2 Modeling details of beams and slabs of a typical floor. 332
Figure D.3 Estimated modal shapes and the associated modal periods: (a) first mode (T=0.71 sec), (b) second mode (T=0.68 sec), (c) third mode (T=0.47 sec), and (d) fourth mode (T=0.20 sec). 335
Figure D.4 Predicted and measured building responses during FB-1: (a) peak floor accelerations, and (b) peak interstory drift ratios. 336
Figure D.5 Predicted and measured building responses during FB-5: (a) peak floor accelerations, and (b) peak interstory drift ratios. 336

LIST OF TABLES

Table 2.1 Performance specifications of the UCSD Large High-Performance Outdoor Shake Table. 17
Table 2.2 Estimated weight distribution of the test building and its nonstructural components (units in kN). 23
Table 2.3 Distribution of the analog sensor channels in the test building. . . . 25
Table 2.4 Summary of dynamic tests in the base isolated (BI) test phase . . . 28
Table 2.5 Summary of dynamic tests in the fixed base (FB) test phase 29
Table 2.6 Summary of achieved earthquake input motions during the base isolated test phase. 33
Table 2.7 Summary of achieved earthquake motions during the fixed base test phase. 36

Table 3.1 WN base excitation tests selected for stair system identification. . . 56
Table 3.2 Identified modal parameters of the stair at different WN test states. 60
Table 3.3 Stair damage states and physical descriptions of the damage mechanisms. 62
Table 3.4 Summary of detected stair damage and the associated building PIDR during test FB-4. 64
Table 3.5 Summary of detected stair damage and the associated building PIDR during test FB-5. 68
Table 3.6 Summary of detected stair damage and the associated building PIDR during test FB-6. 69
Table 3.7 Identified damage instances. 71
Table 3.8 Damage instances for the two upper flight connection angle vertical weld fracture failures (DS-3). 72
Table 3.9 Peak acceleration responses of the stair landing at level 2. 75
Table 3.10 Peak responses of the landing displacement relative to the lower floor and the upper flight-to-slab connection deformation of the stair at level 2. 81

Table 4.1 Stair components implemented in the finite element models and the associated element formulations. 87
Table 4.2 Material strengths of ASTM steel products. 87
Table 4.3 Comparison of the experimental studies used for model validations. 99
Table 4.4 Modal characteristics of the *UCSD test* specimen. 102
Table 4.5 Comparison of peak acceleration and displacement response of the landing in the *UCSD tests*. 104
Table 4.6 Prefabricated steel stair parameter study variables 107
Table 4.7 Modal characteristics of two predominant horizontal vibration modes – *Baseline Model*. 109

Table 4.8 Modal frequencies and the associated effective modal mass of the stair models in the parametric study. 113
Table 4.9 Performance parameters of the stair design variants under parallel-to-stair-run-loading. 115
Table 4.10 Performance parameters of the stair design variants under transverse-to-stair-run-loading. 116
Table 4.11 flight-to-building connection behavior under parallel-to-stair-run loading at 2.5% interstory drift. 121

Table 5.1 Seismic design parameters of the prototype buildings 133
Table 5.2 Effective seismic gravity load and seismic mass at each story of the prototype buildings 137
Table 5.3 Stair quantities at each story associated with the prototype buildings 144
Table 5.4 Modal periods and effective modal masses of the prototype buildings 151
Table 5.5 Comparison of the pushover performance parameters of the steel prototype buildings 159
Table 5.6 Comparison of the pushover performance parameters of the reinforced concrete prototype buildings 162
Table 5.7 Spectral acceleration comparison of the input motion with ASCE 7-05 design spectrum (5% damped) 169

Table 6.1 Seismic hazard for the three prototype buildings at three representative Intensity Measures 188
Table 6.2 Earthquake source and site characteristics for the FEMA P695 far-field ground motion set (FEMA, 2009) 191
Table 6.3 Collapse hazard for the steel prototype mabuildings (bare structure) 199
Table 6.4 Mean stair loss in 50 years for the steel buildings 228

Table C.1 Comparison of the elevator component mass and floor mass in different test configurations. 312
Table C.2 Acceleration responses of the cabin and counterweight in the white noise tests. 313
Table C.3 Peak component acceleration responses of the cabin and counterweight during the seismic tests. 320
Table C.4 Peak anchor forces of the brackets from the mid-height of level 4 to the mid-height of level 5 during the FB tests. 325

Table D.1 Estimated pre-test weight of the building and its nonstructural components (units in kN). 333

LIST OF NOMENCLATURE

The following list summarizes the nomenclature used throughout this dissertation.

Notation	Definition
ACI	American Concrete Institute
AISC	American Institute of Steel Construction
ASCE	American Society of Civil Engineers
ASME	American Society of Mechanical Engineers
ASTM	American Society for Testing and Materials
ATC	Applied Technology Council
BI	base isolation
BNCS	Building Nonstructural Components and Systems project
CDF	cumulative distribution function
CFS	cold-formed steel
DAQ	data acquisition system
DE	design earthquake
DS	damage state
DSI	deterministic-stochastic identification
DM	damage measure
EDP	engineering demand parameter
EERI	Earthquake Engineering Research Institute
FB	fixed base
FAS	Fourier amplitude spectra
FEMA	Federal Emergency Management Agency
GPS	global positioning system
HSS	hollow structural steel
IBC	International Building Code
ICC	International Code Council
IDA	incremental dynamic analyses
IDR	interstory drift ratio
IM	intensity measure
LHPOST	Large High-Performance Outdoor Shake Table
MAC	modal assurance criterion
MAL	mean annual loss
MAR	mean annual rate
MAQ	Magnitude-oriented Adaptive Quadrature algorithm
MCE	maximum considered earthquake
MLE	maximum likelihood estimation
NCS	nonstructural components and systems
NEES	Network for Earthquake Engineering Simulation
NERHP	National Earthquake Hazards Reduction Program

NIST	National Institute of Standards and Technology
OSU	Oregon State University
PBEE	performance-based earthquake engineering
PCA	peak component acceleration
PDF	probability density function
PEER	Pacific Earthquake Engineering Research Center
PFA	peak floor acceleration
PIDR	peak interstory drift ratio
RBS	reduced beam sections
RMS	root mean square
SMF	special moment frame
UCSD	University of California, San Diego
UHS	uniform hazard spectrum
US	United States
USGS	United State Geologic Survey
WN	White Noise

ACKNOWLEDGEMENTS

I would like to gratefully acknowledge everyone involved in the success of the BNCS shake table test project as well as those who have been instrumental, both in academia and in life, to my completion of this dissertation.

First, I would like to express my gratitude to my Doctoral Committee Members: Professors Tara Hutchinson, Joel Conte, Jose Restrepo, Peter Shearer, and David Sandwell for their time, support, and excellent suggestions. I would particularly like to thank my advisor, Professor Tara Hutchinson, for granting me the opportunity to pursue my research interests as outlined in this dissertation. With her mentorship, I have transitioned from a graduate student to a diverse researcher within structural/earthquake engineering and its many explored areas, so far in my career.

Second, I would like to acknowledge each of my fellow graduate students working on the BNCS project: Consuelo Aranda, Rodrigo Astroza, Michelle Chen, Hamed Ebrahimian, Elias Espino, Giovanni De Francesco, Jin-Kyung Kim, Steven Mintz, Elide Pantoli, Hae-Jun Park, and Francesco Selva. Thank you for the countless hours of hard work and companionship during those long days and nights at the Englekirk Center. In addition, I would like to acknowledge the staff and students working at the Englekirk Structural Engineering Center. Thank you for your dedication to ensuring the successive execution of our experiments.

Third, I would like to acknowledge my fellow students and friends at UCSD. I have been lucky to be surrounded by many graduate students who have supported me in idea-sharing, critique of work, and general friendship and support. I would particularly like to thank: Dr. Barbara Chang, Dr. Yong Li, Dr. Weian Liu, Dr. Jinchi Lu, Dr. Zhu Mao, Dr. Saurabh Prasad, Dr. Hefu Pu, Mr. Lindong Sun, Mr. Christopher Trautner, Dr. Ning Wang, and Dr. Richard Wood. In addition, I would like to thank everyone on the Red Army soccer team. Enjoying soccer with you every weekend has been an indispensable ingredient during my PhD study.

Lastly, I would like to thank my family for their constant love and support. Although separated in distance, your encouragement and sacrifices have always been my motivations. None of my success is possible without you.

****

This dissertation research was supported by the National Science Foundation under Grant No. CMMI-0936505, "Full-Scale Structural and Nonstructural Building System Performance during Earthquakes". The experiments were conducted at the Large High-Performance Outdoor Shake Table test facility at the University of California, San Diego, which was supported by the Network for Earthquake Engineering Simulation (NEES) program during the testing. Specific to the stair system tested within the experiments, the dissertation author appreciates Pacific Stairs Company for their support for providing the stair manufacturing and site installation as well as Prof. Chris Higgins for constructive discussions in the early stage of the test program. This dissertation research also received partial support through a dissertation fellowship from the Department of Structural Engineering at the University of California, San Diego. The above support is gratefully acknowledged. Opinions and findings of this dissertation are those of the author and do not necessarily reflect those of the sponsors.

****

Portions of the following publication, for which the dissertation author was the primary investigator and author, are contained in Chapter 3:

- Wang, X., Astroza, R., Hutchinson, T., Conte, J., and Restrepo, J. (2015). "Dynamic Characteristics and Seismic Behavior of Prefabricated Steel Stairs in Full-Scale Five-Story Building Shake Table Tests." *Earthq. Eng. Struct. Dyn.*, 44(14), 1507–1527.

Portions of the following submitted publication, for which the dissertation author was the primary investigator and author, are contained in Chapter 4:

- Wang, X., Hutchinson, T., and Conte, J. "Computational Assessment of the Seismic Behavior of Prefabricated Steel Stairs." Submitted to *ASCE J. Struct. Eng.*

Portions of the following manuscript, for which the dissertation author was the primary investigator and author, are contained in Chapter 6:

- Wang, X., Hutchinson, T., and Conte, J. "Probabilistic Seismic Loss Assessment of Stair Systems in Buildings." In preparation for submission.

Portions of the following submitted publication, for which the dissertation author was the primary investigator and author, are contained in Appendix C:

- Wang, X., Hutchinson, T., Astroza, R., Conte, J., and Restrepo, J. "Shake Table Testing of an Elevator System in Full-Scale Five-Story Building Shake Table Tests." Submitted to *Earthq. Eng. Struct. Dyn.*

The dissertation author would like to thank all the co-authors for their contributions to the above publications. Permission to use material from these publications has been secured from each co-author and the appropriate copyright holders.

VITA

2004	B. S. in Civil Engineering, Hunan University, China
2009	M. S. in Structural Engineering, South China University of Technology, China
2015	Ph. D. in Structural Engineering, University of California, San Diego, USA

PUBLICATIONS

Chang, B., Hutchinson, T., **Wang, X.**, and Englekirk, R. (2013). "Experimental Seismic Performance of Beam-Column Subassemblies Using Ductile Embeds." *ASCE J. Struct. Eng.*, 139(9), 1555–1566.

Chang, B., Hutchinson, T., **Wang, X.**, and Englekirk, R. (2014). "Seismic Performance of Beam-Column Subassemblies with High Strength Steel Reinforcement." *ACI Struct.*, 111(6), 1329–1338.

Wang, X., Pantoli, E., Hutchinson, T., Restrepo, J., Wood, R., Hoehler, M., Grzesik, P., and Sesma, F. (2015). "Seismic Performance of Cold-Formed Steel Wall Systems in a Full-Scale Building." *ASCE J. Struct. Eng.*, 141(10), 04015013.

Wang, X., Astroza, R., Hutchinson, T., Conte, J., and Restrepo, J. (2015). "Dynamic Characteristics and Seismic Behavior of Prefabricated Steel Stairs in Full-Scale Five-Story Building Shake Table Tests." *Earthq. Eng. Struct. Dyn.*, 44(14), 1507–1527.

Chen, M., Pantoli, E., **Wang, X.**, Astroza, R., Ebrahimian, H., Hutchinson, T., Conte, J., Restrepo, J., Marin, C., Walsh, K., Bachman, R., Hoehler, M., Englekirk, R., and Faghihi M. (2015). "Full-Scale Structural and Nonstructural Building System Performance during Earthquakes: Part I – Specimen Description, Test Protocol and Structural Response" *Earthq. Spec.* In press.

Pantoli, E., Chen, M., **Wang, X.**, Astroza, R., Ebrahimian, H., Hutchinson, T., Conte, J., Restrepo, J., Marin, C., Walsh, K., Bachman, R., Hoehler, M., Englekirk, R., and Faghihi M. (2015). "Full-Scale Structural and Nonstructural Building System Performance during Earthquakes: Part II – Specimen Description, Test Protocol and Structural Response" *Earthq. Spec.* In press.

Pantoli, E., Chen, M., H., Hutchinson, T., Astroza, R., Conte, J., Ebrahimian, H., Restrepo, J., and **Wang, X.** (2015). "Landmark Dataset from the Building Nonstructural Components and Systems (BNCS) Project." *Earthq. Spec.* In press.

ABSTRACT OF THE DISSERTATION

Experimental and Computational Investigation of the Seismic Performance of Stair Systems in Buildings

by

Xiang Wang

Doctor of Philosophy in Structural Engineering

University of California San Diego, 2015

Professor Tara C. Hutchinson, Chair

Stairs serve as an essential nonstructural system within buildings, providing a safe means of egress as well as much needed access for emergency responders following an earthquake. Unfortunately, the state of knowledge regarding the seismic behavior of these critical systems is limited, despite the fact that past earthquakes repeatedly reveal that stair systems are highly vulnerable to damage even in low- or moderate-intensity earthquakes. As a result, disruptions to building functionality, delayed rescue operations, and life safety hazards ensue.

To this end, this dissertation presents a first-of-its-kind experimental investigation of the seismic behavior of a prefabricated steel stair system incorporated in a full-scale five-story building shake table test program. These system-level tests allowed investi-

gation of the seismic behavior of these systems under realistic installation and dynamic loading conditions. In this work, the modal characteristics of the stair system identified using white noise base excitation test data as well as the physical observations of the stair system during earthquake tests of increasing intensities are presented. Analysis of the earthquake response of the stair system particularly focuses on associating their behavior with the seismic demands of the test building and the associated implications on seismic design. These shake table tests highlight the seismic vulnerability of modern designed stair systems and in particular the importance of improving the deformability of flight-to-building connections.

The second part of this work involves a comprehensive computational study to capture at first the salient seismic response characteristics of prefabricated steel stairs in isolated configurations and subsequently the key response characteristics of building-stair systems. Detailed three-dimensional finite element models of a pair of prefabricated steel stairs are developed and their efficacy evaluated through extensive comparison with experimental data. The validated modeling approach is then used in a parametric assessment of the seismic behavior of stair systems using a broader range of design variables commonly found in practice. Subsequently, a system-level numerical study is conducted to investigate the interaction between buildings and stair systems and the associated impacts on building response characteristics as well as estimated stair loss using a probabilistic seismic analysis framework. Simulation results indicate that although the presence of stairs does not significantly modify the seismic response of buildings, enhancing the stair deformability can effectively mitigate the severity of seismic damage and loss of these critical nonstructural systems.

Chapter 1

Introduction

1.1 Background

Stair systems are a common vertical transportation system and an essential nonstructural system within buildings, providing a safe means of building evacuation as well as much needed access for emergency responders in the event of an emergency. While elevators are the customary vertical transport for multi-story buildings, they may not be functional following an earthquake due to counterweight derailment, damage to the electrical or mechanical components, or loss of power in the building (Suárez and Singh, 2000). As a result, current design guidelines require that stair systems remain operable following even a rare earthquake and the ensuing post-earthquake disasters to support immediate building functionality and accessibility (FEMA, 2014; ICC, 2012).

The structural behavior of stairs is complex due to the variability in spatial geometry (e.g., straight-run, scissor, and spiral) (Figure 1.1), material (e.g., reinforced concrete, steel, and wood), and construction methods (e.g., cast-in-place, site-assembled, precast, or prefabricated). Each of these aspects significantly affect the structural behavior and consequently the integrity of stairs. For example, stairs in a scissor configuration are susceptible to twist as their structural form rises in elevation, whereas straight-run stairs are significantly weaker orthogonal to the run direction. Steel stairs tend to be more deformable and lighter than those constructed with reinforced concrete. In addition, some stairs (e.g., cast-in-place reinforced concrete stairs) may even detrimentally interact with

the supporting structure by acting as diagonal braces during lateral loading. These stiffer and heavier stairs may shift the centers of mass and stiffness of a building, and therefore induce significant torsion to the building.

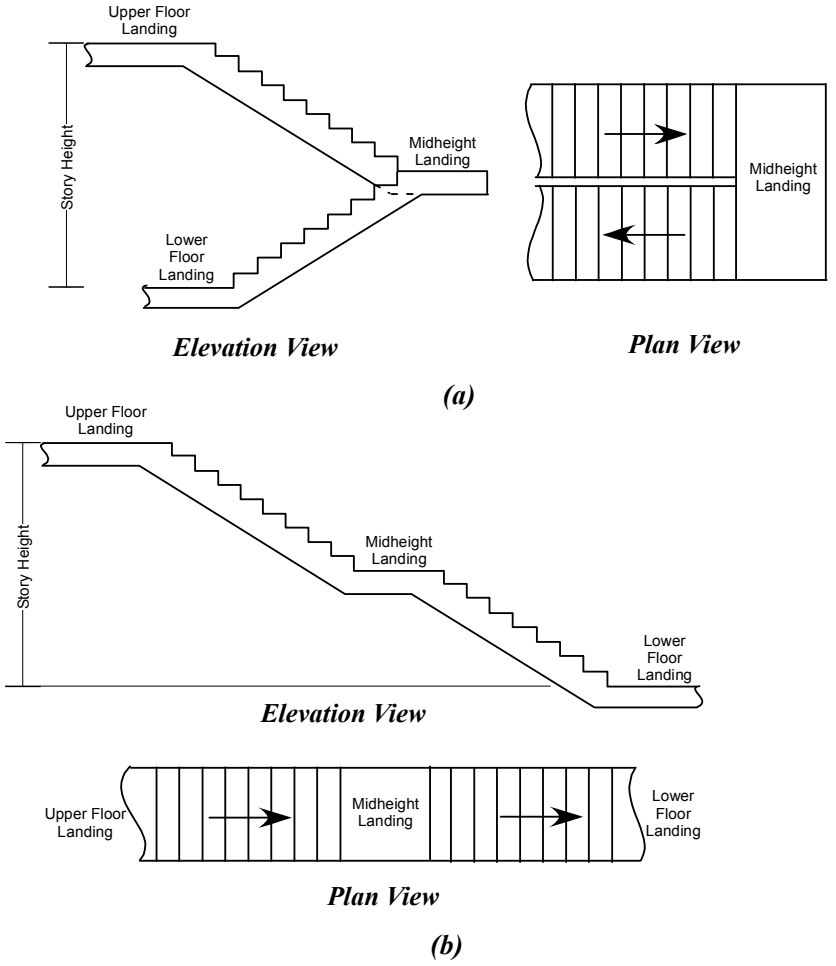

Figure 1.1. Typical geometric configurations of stairs (a) scissor configuration, and (b) straight-run configuration (source: FEMA, 2012).

In United States (US) design practice, stairs are typically attached to their primary structure and span as a floor-to-floor system. Therefore, they are subjected to dynamic excitations at multiple support locations during an earthquake. Depending on structural system and construction material, the design of stair systems may require compliance with the American Institute of Steel Construction provisions (AISC, 2010) or American

Concrete Institute requirements (ACI, 2014) for proportioning stair components and connections. The seismic design forces for stairs can be readily determined from ASCE-7 code provisions (ASCE, 2010). However, detailing these floor-to-floor systems to remain damage-free during relative deformation between their upper and lower floors is difficult. The current state of practice often imposes specific deformable mechanisms to one end of the stair (e.g., ductile or slotted connections, seismic gaps) and fixed boundary on the other end to accommodate the anticipated floor-to-floor (interstory) relative displacements. In contrast, earlier design practice more commonly fixes both the top and bottom of a stair system to the upper and lower floors of the supporting structure. This practice has demonstrated catastrophic results, as the stair as a system cannot accommodate the large differential displacements, and are therefore unprotected during an earthquake.

1.2 Performance of Stair Systems in Past Earthquakes

Despite their significance related to occupant evacuation and post-event recovery operations, past earthquakes have repeatedly demonstrated the seismic vulnerability of stair systems. Damage to stairs have been reported since the 1964 Alaska and the 1971 San Fernando earthquakes as well as earthquakes outside of the United States (e.g., Ayres and Sun, 1973; Roha et al., 1982). In early design practice, stairs were often attached to the primary structural system as heavy and rigid elements, and therefore resulted in undesirable interactions with the primary structure during an earthquake. These unintended interactions significantly modified the overall structural response, causing extensive damage not only to stair systems but as well to the adjacent structural elements.

Although design of stair systems has improved primarily via the introduction of damage mitigation strategies in the form of separation gaps or slotted connections, extensive damage to stair systems continues to be observed in recent earthquakes (e.g., Bull, 2011; Kam and Pampanin, 2011; Li and Mosalam, 2013). For example, cast-in-place reinforced concrete or precast concrete stairs sustained severe damage or even

(a)

(b)

(c)

Figure 1.2. Examples of stair damage in recent earthquakes: (a) damaged exterior reinforced concrete stairs in the 2010 Maule earthquake in Chile (photo courtesy of J. Restrepo), (b) damaged exterior wood stairs in the 2014 South Napa earthquake (photo courtesy of T. Hutchinson), and (c) partial collapse of interior precast concrete stairs in the 2011 Christchurch earthquake in New Zealand (photo courtesy of J. Restrepo).

collapse during the 2008 Wenchuan earthquake in China (e.g., Li and Mosalam, 2013). Similar damage to stairs has repeated in the 2010 Maule earthquake in Chile (Figure 1.2a) (Miranda et al., 2012). In the 2010 Darfield and the 2011 Christchurch earthquakes in New Zealand, both concrete and steel stairs suffered severe damage or collapse in at least four multi-story buildings (Figure 1.2c)(Bull, 2011; Kam and Pampanin, 2011). In addition, damage to stairs has occasionally occurred in even low- or moderate-intensity earthquakes (Figure 1.2b) (EERI, 2014). These and other evidence emphasize that stair systems remain highly vulnerable to damage in recent earthquakes. It is noted that the overarching issue causing such unfortunate results continues to be related to the large differential displacements the stair system must absorb.

1.3 Previous Research on Seismic Behavior of Stair Systems

Lessons learned from past earthquakes highlight the seismic vulnerability of stair systems. To complement previous earthquake reconnaissance observations, a limited number of research studies have been conducted in the past few decades to advance understanding of their seismic behavior. A brief literature review of recent experimental and numerical studies on stair systems is summarized in this section.

1.3.1 Experimental Studies

To date, to the author's knowledge, only two detailed experimental studies have been conducted specifically aimed at understanding the response of stair systems when subjected to earthquake loading. Each of these studies are described below.

Simmons and Bull (2000)

Simmons and Bull (2000) conducted quasi-static cyclic tests of three full-height precast concrete straight-run stairs conforming to the New Zealand design code. The three specimens had similar overall geometry, however the specimens incorporated different reinforcing plans and details as the test variables. The specimens each consisted of two

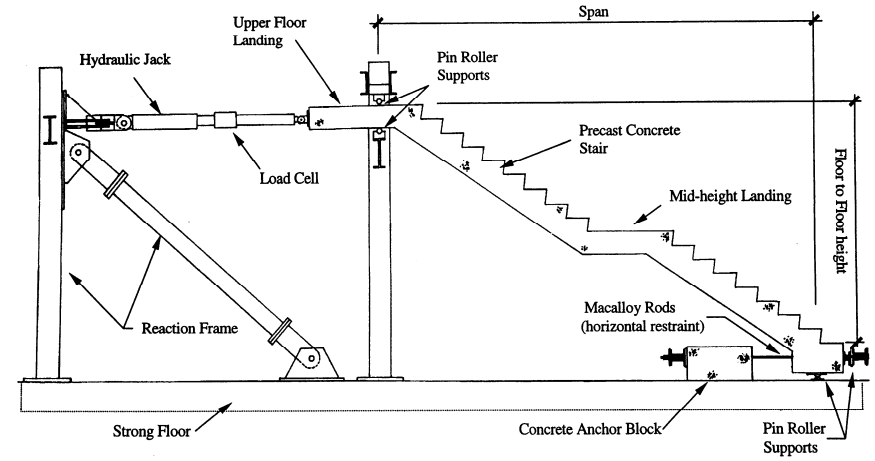

(a)

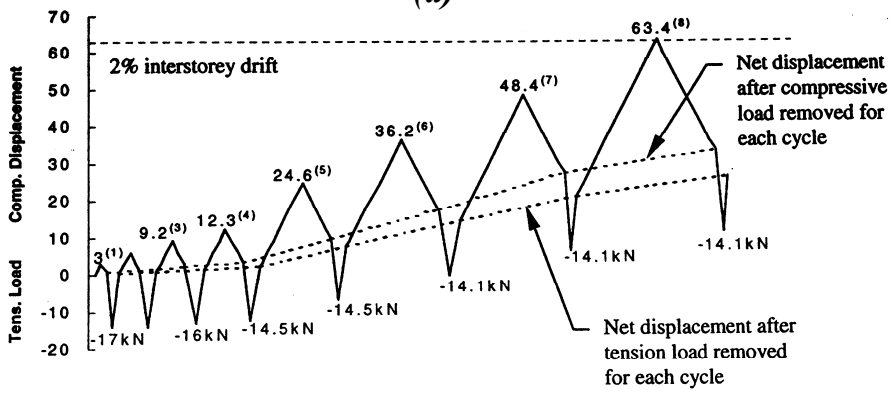

(b)

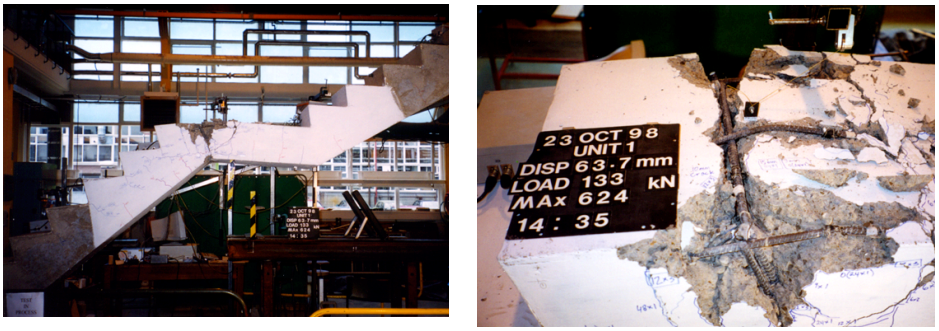

(c)

Figure 1.3. Experimental study of precast concrete straight-run stairs: (a) test specimen and test setup, and (b) test loading protocol, and (c) damage to specimen Unit-I at the completion of the lateral displacement loading (figures courtesy of Simmons and Bull, 2000).

stair flights and an intermediate landing located mid-height between the upper and lower flights (Figure 1.3a). The stair had a story height of 3.1 m and a landing width of 1.2 m. Lateral displacements were applied at the top landing in the parallel-to-stair-run direction, while the bottom landing was pinned to simulate the effects of seismic gaps. Rollers were used to constrain the vertical displacements at the top of the stair flight.

The specimens were subjected to asymmetric cyclic displacement-controlled loading, with each cycle starting with a compressive reversal followed by unloading and subsequently a smaller tensile reversal (Figure 1.3b). Each specimen attained a maximum interstory drift of approximately 2% during the tests. Additional mass representing a service-level live load of 5.7 kPa was applied to the specimen following the completion of the lateral displacement loading test phase to assess the vertical load capacity of the stair units. Although the stairs sustained significant damage during the lateral displacement loading test phase (Figure 1.3c), each stair withstood the expected service-level live load in the presence of structural damage (Simmons and Bull, 2000).

Higgins (2009)

Higgins (2009) tested two full-size prefabricated steel stair assemblies using cyclic pseudo-static displacement loading protocol. The two specimens employed similar structural system and details but different stair treads. The specimens were configured as scissors stairs, each consisting of two flights and an intermediate landing located mid-height (Figure 1.4a). The story height of each specimen was 3.6 m, and the landing dimension was about 1.2×2.4 m. Lateral displacements were successively applied at the top landing in the two horizontal directions, while the lower flight and the base of the landing were bolted to the base frame.

The imposed lateral displacement cycles were symmetrically applied with progressively increasing amplitudes up to the attainment of maximum target displacement corresponding to an interstory drift ratio of 2.5%, which is representative of the seismic design demands of moment frame buildings in the US. Following the completion of the lateral loading tests, extra mass was applied on the stair to represent the full factored

(a)

(b)

(c)

Figure 1.4. Experimental study of prefabricated steel stairs : (a) test specimen and test setup, (b) flight-to-landing connection yielding, and (c) initial weld cracking and connection plate buckling (photos courtesy of Higgins, 2009).

design live load of 7.7 kN. To simulate the earthquake aftershock effect, each specimen was further subjected to displacement loading with an amplitude of 50% the maximum target displacement. The two stair specimens sustained the lateral displacement loading and extra lateral displacement tests under full-factored vertical loads. At the completion of the tests, the two specimens remained operable with only moderate damage in the form of connection yielding and initial cracking (Figure 1.4b–c) (Higgins, 2009).

1.3.2 Numerical Studies

Recent experimental studies advance the state of understanding regarding the seismic behavior of stair systems. Numerical studies have also attempted to quantify the influence of stair systems on the overall building response (e.g., Cosenza et al., 2008; Tegos et al., 2013). These coupled analysis efforts primarily focus on studying the effect of stairs on the global response of a building with and without stairs incorporated. However, the stair systems are often assumed to respond elastically in these simulations. Therefore, the capability of the models to capture the seismic response of the stairs in a system-level simulation, in particular when the stairs are subjected to significant inelastic deformation during high-intensity earthquake excitations, needs to be further verified.

1.4 Research Scope

Despite the repeated evidence from past earthquakes of the vulnerability of stair systems, the state of knowledge regarding their seismic behavior remains largely unknown. To this end, a comprehensive experimental and numerical research is undertaken in this dissertation in an effort to advance the understanding of the seismic performance of stair systems and provide design recommendations for these critical nonstructural systems. The first portion of this dissertation describes a first-of-its-kind experimental study of prefabricated steel stairs tested in a full-scale five-story building shake table test program. The second portion of this dissertation consists of a comprehensive computational research effort using detailed finite element modeling of prefabricated steel stairs (component-level simulations) as well as coupled numerical analysis of buildings in-

corporated with stair systems (system-level simulations). The scope of each part of the dissertation is presented in the following sections.

1.4.1 Experimental Study

The experimental work presented herein is part of a landmark experimental program – the Building Nonstructural Components and Systems (BNCS) project (Chen et al., 2013; Pantoli et al., 2013a). This research project is a collaboration between four academic institutions (University of California, San Diego, San Diego State University, Howard University, and Worcester Polytechnic Institute), four governmental or granting agencies, and over 40 industry partners, and two oversight committees. Within its broader scope of shake table testing of a full-scale five-story reinforced concrete building outfitted with a broad variety of NCSs, for the first time, a fully operable prefabricated steel stair system was incorporated at full-scale, allowing investigation of system-level interactions between the building and the stair systems as well as between the stair system and its surrounding nonstructural components under realistic loading and installation conditions.

Within the shake table test program, the test building comprised two test phases, namely: (i) the building isolated at its base, and (ii) the building fixed at its base. In addition, low-amplitude white noise base excitation tests were conducted at various stages during the test program for the purposes of identifying the dynamic characteristics of the test building and its NCSs. Herein, the dynamic characteristics and the seismic behavior of the stair system are thoroughly studied. Of particular interest are the modal characteristics of the stair system identified using white noise base excitation test data as well as the physical observations of the stair system during the earthquake tests. The observed damage to the stairs is categorized into three damage states and correlated with the peak interstory drift demands experienced by the test building.

1.4.2 Numerical Study

The numerical portion of this dissertation focuses on evaluation of the seismic behavior of prefabricated steel stairs as well as the effects of stairs on buildings using coupled building-stair models. First, detailed finite element models of prefabricated steel stairs are developed using a general finite element program *LS-DYNA* (LSTC, 2013a; LSTC, 2013b). The capability of the modeling approach for simulating seismic behavior of the stairs under static and dynamic loading is validated using test data measured from recent experimental studies, namely, those conducted by Higgins (2009) and the shake table testing as presented in Chapters 2 and 3 of the dissertation. Parametric investigations are subsequently conducted using a broader range of stair configurations and details. The emphasis of the parametric study is to characterize the modal characteristics and the force-displacement response of the stairs due to the effects of different design variables. In addition, these results provide a useful basis for system-level simulation of coupled building-stair systems.

In the system-level numerical simulations, a broad variety of coupled building-stair systems are modeled using an open-source structural analysis platform *OpenSees* (Mazzoni et al., 2014). Prototype buildings include two sets of special moment frame structures with varying structural systems and number of stories. Prefabricated steel stairs with varying force-displacement behavior are incorporated into the prototype buildings. The system-level numerical study evaluates the effects of building systems and stair systems on the overall structural response of the coupled systems. In addition, the coupled building-stair systems are employed to assess the seismic loss of stairs using a probabilistic seismic assessment methodology. The system-level simulation study provides insights into the seismic performance of the buildings-stair systems as well as the cost-efficiency of stair systems due to the variations of their behavior.

1.5 Dissertation Organization

This dissertation is organized into seven chapters, as follows:

- **Chapter 2**: Full-Scale Building Shake Table Test Program

This chapter provides a general overview of a landmark full-scale building shake table program. The full-scale five-story reinforced concrete test building, outfitted with a broad variety of nonstructural components and systems (NCSs), was subjected to a suite of earthquake motions as well as low-amplitude white noise base excitations. The building design, monitoring systems, and the dynamic test protocol are described in this chapter. This chapter concludes with the presentation of the measured responses of the test building. The pertinent background information of the overall experimental program is crucial for understanding the seismic performance of the prefabricated systems discussed in Chapter 3.

- **Chapter 3**: Shake Table Test Results of Prefabricated Steel Stairs
  This chapter presents the test results of a fully functional stair system in the full-scale shake table test program. This chapter studies the modal characteristics of the stairs identified using the data recorded from white noise base excitation tests as well as the physical and measured responses of the stairs from the earthquake tests. In particular, the observed damage to the stairs is categorized into three damage states and correlated with the peak interstory drift demands experienced by the test building.

- **Chapter 4**: Computational Assessment of the Seismic Behavior of Prefabricated Steel Stairs
  This chapter presents a finite element modeling study of the seismic behavior of prefabricated steel stairs. The proposed modeling approach implemented in a general-purpose finite element program *LS-DYNA* is validated through extensive comparison with experimental data. The validated modeling approach is subsequently used in a parametric study to assess the modal characteristics and lateral force-displacement behavior of a broader range of stair configurations and design details. The parametric study assesses the effects of the selected design variables on the seismic behavior of prefabricated steel stairs and provide useful basis for the system-level simulation of coupled building-stair systems as discussed in the following chapter.

- **Chapter 5**: Numerical Modeling of Coupled Building-Stair Systems

This chapter presents a comprehensive numerical study of coupled building-stair systems. The prototype buildings include two sets of special moment frame structures with variation in structural system and number of stories. The stair systems incorporated into the buildings are simplified as lumped springs using the force-displacement responses reflecting those the prefabricated steel stairs. Coupled building-stair systems are implemented into a structural analysis platform *OpenSees* using design-oriented numerical models. The system-level numerical simulations evaluate the interacting effects of building systems and stair on the structural response characteristics of the coupled systems.

- **Chapter 6**: Probabilistic Seismic Response Analysis of Building-Stair Systems and Loss Estimation of Stair Systems
  This chapter investigates the seismic response of coupled building-stair systems and seismic loss of stairs in buildings using a probabilistic seismic performance assessment methodology. The emphasis of the study is to characterize the probabilistic structural response of the building systems and loss assessment of stair systems in buildings due to the interaction between the building and stair systems. This study provides insights into the seismic performance of the buildings-stair systems as well as the cost-efficiency of stair systems due to the variations of their behavior.

- **Chapter 7**: Conclusions and Future Work
  This chapter contains a summary of the key findings from Chapters 3 through 6. In addition, recommendations for future work are provided for researchers aiming to conduct further study regarding the seismic behavior of stair systems.

Supplemental materials are included in four appendices, as follows:

- **Appendix A**: Construction Drawings of the Stair System
  This appendix provides a complete set of construction shop drawings of the prefabricated steel stairs incorporated into the test building.

- **Appendix B**: Measured Stair Acceleration Response
  This appendix provides the measured acceleration time histories of the prefab-

ricated steel stair system obtained during the earthquake tests of the full-scale building shake table test program.

- **Appendix C**: Shake Table Test Results of Elevator System
  Within the shake table test program, two operable egress systems were installed and tested with the full-scale building. While the test results of the stair system are discussed in Chapter 3, this appendix presents important findings regarding the seismic behavior of the fully functional passenger elevator. It is important to note that this study represents the first-of-its kind system-level experimental research on the seismic behavior of elevator systems.

- **Appendix D**: Pre-test Simulation – OpenSees Model
  This appendix summarizes a pre-test numerical study of the full-scale test building using a design-oriented model implemented in *OpenSees*. This appendix first summarizes the modeling techniques of the building and subsequently presents the pre-test simulation results of the test building. It is noted that the pre-test simulation effort was essential for the development of the earthquake test protocol and design of the nonstructural systems for the test program.

Chapter 2

Full-scale Building Shake Table Test Program

2.1 Introduction

A landmark experimental program of a full-scale five-story building was conducted on the Large High-Performance Outdoor Shake Table (LHPOST) (Van Den Einde et al., 2004) at the University of California, San Diego (UCSD) in 2012.[1] The building, designed as a "total" system, was incorporated with complete functionality (service)

[1]This research project, coined Building Nonstructural Components and Systems (BNCS), is discussed in detail within a series of four technical reports:

BNCS Report #1: Full-scale structural and nonstructural building system performance during earthquakes and post-earthquake fire – specimen design, construction, and test protocol. *SSRP-2013/09*, Department of Structural Engineering, University of California, San Diego, La Jolla, CA.

BNCS Report #2: Full-scale structural and nonstructural building system performance during earthquakes and post-earthquake fire – test results. *SSRP-2013/10*, Department of Structural Engineering, University of California, San Diego, La Jolla, CA.

BNCS Report #3: Full-scale structural and nonstructural building system performance during earthquakes and post-earthquake fire – camera and analog sensor details. Structural *SSRP-2013/11*, Department of Structural Engineering, University of California, San Diego, La Jolla, CA.

BNCS Report #4: Full-scale structural and nonstructural building system performance during earthquakes and post-earthquake fire – construction details and technical specifications of specific subsystems. *SSRP-2013/12*, Department of Structural Engineering, University of California, San Diego, La Jolla, CA.

In addition, a complete set of high-quality test data from this research project is archived and publicly available in the NEES data repository (DOI: 10.4231/D38W38349).

and architectural layouts. As such, it was outfitted with a broad array of nonstructural components and systems, including a complete façade, two operational egress systems, mechanical-electrical-plumbing (MEP) systems on all floors. Architectural spaces were detailed as residential, office, laboratory and hospital occupancies. The test building was subjected to earthquake motions, low-amplitude white noise and pulse excitations first while base isolated (BI) and subsequently in a fixed-base (FB) configuration. These tests generated a broad variety of unique datasets that considerably improve the understanding of the seismic behavior of nonstructural components and systems (NCSs). This chapter provides the pertinent background information of this unique experimental program. These information are essential to understand the seismic performance of the stair system discussed in Chapter 3.

This chapter is organized into six sections. Section 2.2 provides an overall description of the shake table test facility as well as the test building and its NCSs. Section 2.3 discusses the monitoring systems deployed on the test building and its NCSs. Subsequently, the dynamic test protocol including the earthquake input motions and the low-amplitude white noises in the base-isolated and fixed-base test phases are presented in Section 2.4. Section 2.5 presents the measured building floor responses during these two test phases as well as the physical observations of the building structure at the completion of the test program. Section 2.6 concludes the chapter with a brief summary of the shake table test program and the building test results. It is noted that a concise summary of the test program and key test results are available in Chen et al. (2015) and Pantoli et al. (2015b).

2.2 Shake Table Test Facility, Test Building and its NCSs

2.2.1 Shake Table Test Facility

The UCSD LHPOST is the largest outdoor shake table in the world and largest shake table of its kind in the US (Figure 2.1). This experimental facility was operated (during the test program) within the Network for Earthquake Engineering Simulation (NEES) equipment inventory. Uniquely, it enables seismic testing of large scale and/or

Figure 2.1. UCSD Large High-Performance Outdoor Shake Table (source: NEES, 2014).

full-scale structural or geotechnical systems with realistic earthquake loading, extensive instrumentation and data archiving. This testing site is essential for capturing system responses of the full-scale tests that cannot be achieved at smaller scales.

The LHPOST consists of a steel platen (12.2×7.6 m); a reinforced concrete reaction block; two servo-controlled dynamic actuators with a force capacity in tension/compression of 2.6 and 4.2 MN, respectively; a platen sliding system (six pressure-balanced vertical bearings with a force capacity of 9.4 MN each); an overturning moment restraint system (a pre-stressing system consisting of two nitrogen-filled hold-down struts

Table 2.1. Performance specifications of the UCSD Large High-Performance Outdoor Shake Table.

Variable	Specification
Size	7.6 × 12.2 m
Peak acceleration (bare table)	4.2 g
Peak acceleration (400 ton payload)	1.2 g
Peak velocity	1.8 m/s
Stroke	0.75 m
Maximum vertical payload	20 MN
Force capacity of actuators	6.8 MN
Maximum overturning moment (bare table)	35 MN-m
Maximum overturning moment (400 ton payload)	50 MN-m
Frequency bandwidth	0 – 33 Hz

with a stroke of 2m and a hold-down force capacity of 3.1 MN each); a yaw restraint system (two pairs of slaved pressure balanced bearings along the length of the platen); a real-time multi-variable controller, and a hydraulic power supply system. The major performance specifications of the LHPOST are summarized in Table 2.1. Additional information regarding the LHPOST test facility can be found in Van Den Einde et al. (2004) and Ozcelik et al. (2008).

2.2.2 Test Building

The test building consisted of a cast-in-place five-story reinforced concrete structure with moment resisting frames providing lateral resistance in the direction of shaking (east-west direction) (Figure 2.2a). The building design utilized ground motions developed for a site in Southern California, with the maximum considered earthquake (MCE) ground motion spectrum for a Site Class D (stiff) soil conditions, a short-period spectral acceleration S_{MS} = 2.1 g and a one-second spectral acceleration S_{M1} = 1.4 g. Performance targets of 2.5% peak interstory drift ratio and a maximum peak floor acceleration between 0.7 – 0.8 g were selected during the conceptual design phase.

The building consisted of two bays in the longitudinal direction and one bay in the transverse direction, with a plan dimension of 11.0×6.6 m (Figure 2.2c). Two moment resisting frames were placed in the east bays in the longitudinal (shaking) direction, while two shear walls were placed within the interior the building to resist transverse lateral and partial torsional loads. As shown in Figure 2.2d, the floor diaphragm provided two major openings: one on the northwest to facilitate a full-height elevator shaft (from the first floor to the fifth floor) and the other on the southeast to accommodate the stairs (from the second floor to the roof). Consequently, the building provided two useful architectural spaces on each floor (the northeast and southwest rooms) to accommodate a broad variety of NCSs. Occupancies designated for these spaces are briefly discussed later. The building floor-to-floor height was 4.3 m at each level, resulting in a total building height of 21.3 m above the foundation . The building (excluding the foundation) had an estimated weight of 3009 kN for the structural skeleton and a total estimated weight of 4492 kN including all nonstructural components and systems, and

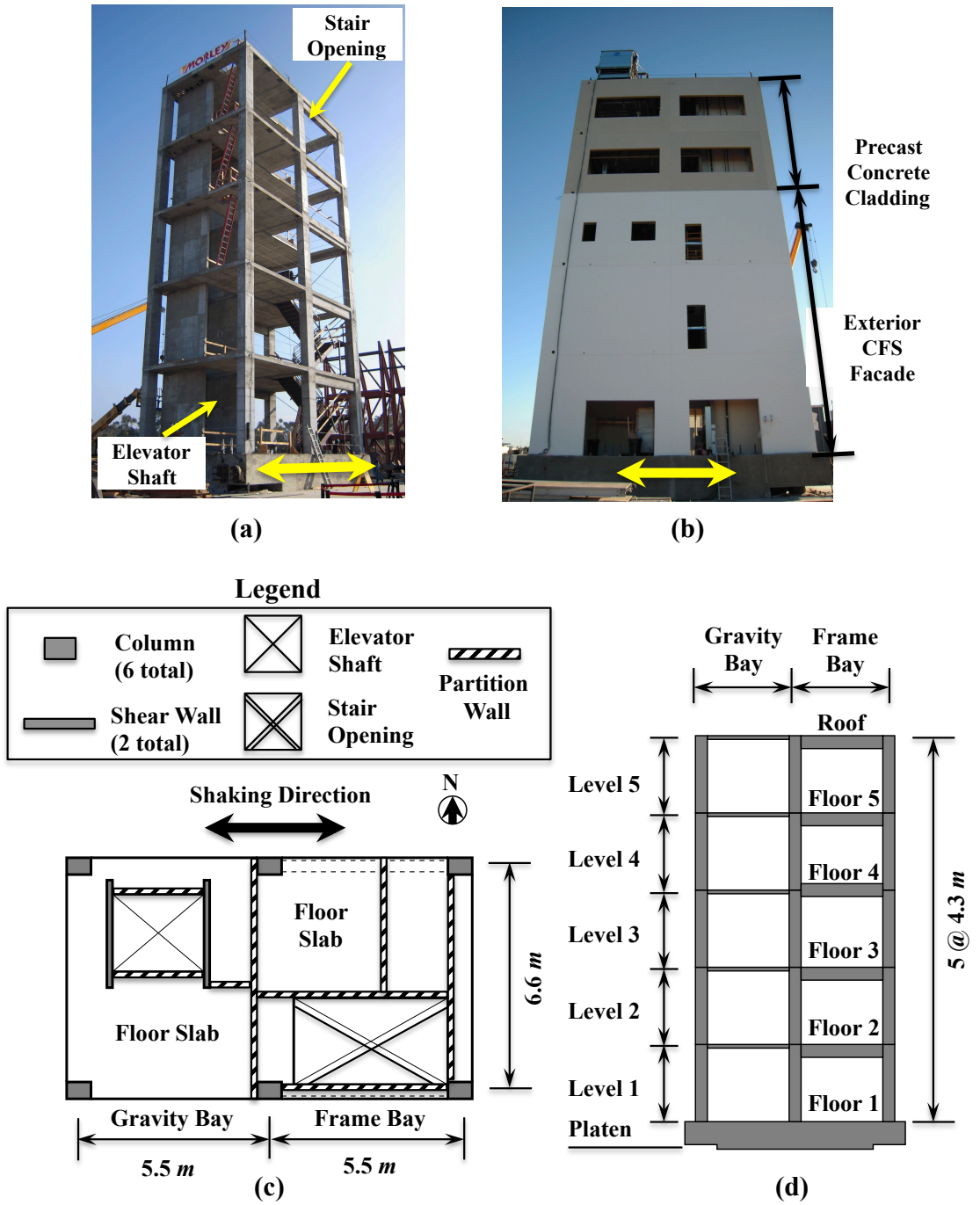

Figure 2.2. Test building: (a) structural skeleton of the building, (b) test building at completion, (c) typical floor plan layout (note that interior partition wall layout varies from floor to floor), and (d) elevation.

the foundation had an estimated weight of 1868 kN.

All beams of the moment resisting frames were 300 mm wide by 700 mm deep and were designed with equivalent beam moment capacities, however different types of details were adopted at each floor level of the building. The second and third floor beams utilized high strength reinforcement to achieve the desired moment capacity. The fourth and fifth floor beams both used ductile rods at beam-column joints. In addition, the fourth floor beams incorporated hybrid frame details. Frame beam and column joint details adopted on floors two through five exhibited stable ductile performance in previous component test programs and have since been used in practice (Chang et al., 2013, 2014). In contrast, at the roof, where the lowest interstory drift demands were anticipated, special moment frame detailing followed the ACI code requirements (ACI, 2008) . Although the longitudinal reinforcing varied within the beams, confining reinforcement within the frame beams was consistently provided by #4 ties at 102 mm on center at the column faces and 152 mm along the remaining beam.

All six columns were 460 $\times$ 660 mm and were detailed with transverse reinforcing steel prefabricated into grids and spaced at 102 mm on center, with a longitudinal reinforcement ratio ρ = 1.42%. The axial load due to self-weight of the building and its NCSs at the base of the columns varied between 1.8% and 5.3%. Transverse shear walls, with a thickness of 150 mm, were placed on both the east and west sides of the elevator opening. These walls were detailed with #3 rebar spaced at 152 mm on center in both directions with two #9 longitudinal bars at each end. In addition, the building diaphragm was a cast-in-place concrete slab with a thickness of 0.2 m at each floor. All structural components of the building and foundation were constructed using cast-in-place concrete, with a specified 28-day concrete strength of 40 MPa for the columns and shear walls but 35 MPa for the beams and slabs.

2.2.3 Nonstructural Components and Systems

The test building was outfitted with a broad variety of NCSs following completion of the construction of its structural skeleton. With the exception of the stairs, all NCSs

were installed between September 2011 and April 2012. The major NCSs installed on the test building included:

- *Egress Systems*:
  The test building was equipped with two full-height egress systems, namely, (1) a prefabricated steel stair system on the northwest side and (2) a functioning passenger elevator on the southeast. The stairs provided access to all floors including the roof, whereas the elevator provided access to all floors except the roof (Figure 2.2a).

- *Facades*:
  Two different types of architectural façades were installed on the building, namely, (1) balloon framed cold-formed steel (CFS) studs overlaid with a synthetic stucco at the lower three levels, and (2) precast architectural concrete cladding at the upper two levels (Figure 2.2b);

- *Interior Architectural Components*:
  Occupancy largely dictated the details and types of NCSs installed in the building. Level one was designated as a utility floor allowing sufficient space for placement of electrical services and installation of four large access doors (two steel rolling doors and two sectional garage doors) placed on the longitudinal faces of the building. Level two was detailed as both a laboratory and residential space, while level three was planned for live fire tests and therefore provided with the most complete detailing of partition walls, ceilings, plenum space and associated finish work. In addition, two large computer servers were anchored to the slab at level three. Levels four and five were detailed as hospital floors.

- *Services*:
  Services common to a building were installed to varying degrees of detail at each floor of the building. fire protection piping; gas piping; heating, ventilation and air-conditioning; and electrical systems.

- *Equipment*:
  Pending the occupancy, various types of equipment were installed on each level

of the test building. Occupancies were selected as: level 1 – utilities, level 2 – laboratory and residential, level 3 – computer server space, level 4 – intensive care unit, level 5– surgery suite. In addition, a cooling tower, penthouse and air-handling unit were installed on the roof.

2.2.4 Estimated Weight of the Building and its NCSs

Due to the weight uncertainties associated with a variety of NCSs (e.g., partition walls, exterior CFS facade, piping, and etc.), a total of four different strategies, namely, 1) least squares estimate using motion data, 2) lifting building with actuators (prior to seismic tests), 3) lifting building with hydraulic jacks (during the installation and removal of isolators), and 4) hand calculation, were conducted to estimate the total weight of the test building including its NCSs. The results determined using the different methods range between 6170 kN and 6361 kN with a maximum discrepancy of less than 200 kN, indicating small method-to-method variabilities relative to the total weight of the test building including its NCSs (about 3% of the total weight). Among the four different methods, the results obtained during the installation and removal of the base isolators are believed to contained the least possible error sources, therefore the measured weight of 6361 kN was taken as final weight estimate of the test building including its NCSs. Subsequently, individual floor weights were determined by adjusting the discrepancy between the individually added component weights (hand calculation) and the final estimated values. Lastly, a difference of 122 kN was distributed evenly to each floor in account for the weight of miscellaneous NCSs on each floor (e.g., piping, sprinklers, smaller components, etc.).

Table 2.2 provides the total weight of the test building and its NCSs and the floor distribution of the total weight. The total vertical (gravity) and inertial (seismic) weight of the test building including its NCSs were 6360 kN and 6305 kN, respectively. It is noted that while the vertical weight considers the gravity effects of the test building and all the NCSs installed on the building, the inertial weight is slightly less, as not all the NCSs were attached to the building (e.g., movable medical equipment, elevator cabin and counterweight). Detailed information regarding the weight calculation of the test

building including its NCSs can be found in Appendix G of Chen et al. (2013).

Table 2.2. Estimated weight distribution of the test building and its nonstructural components (units in kN).

Floor	Vertical weight			Inertial weight		
	Building	NCSs	Total	Building	NCSs	Total
Roof	527.5	65.8	593.3	527.5	167.2	694.7
Floor 5	593.6	484.5	1078.1	593.6	469.8	1063.4
Floor 4	593.8	442.5	1036.3	593.8	395.3	989.1
Floor 3	581.0	122.8	703.8	581.0	175.7	765.7
Floor 2	581.0	93.0	674.0	581.0	145.5	726.5
Floor 1	132.4	274.2	406.6	132.4	73.8	206.2
Foundation	1868.5	/	/	1865.5	/	/
Total (w/o Foundation)	3009.2	1482.9	4492.1	3009.2	1427.4	4436.6
Total (w/ Foundation)	4877.7	/	6360.6	4877.7	/	6305.1

2.3 Monitoring Systems

The test building was monitored with four types of monitoring systems in a effort to document the performance of the test building and its NCSs during the shake table tests (Figure 2.3). These monitoring systems included still cameras, video cameras, analog sensors, and a global positioning system (GPS). This section provides a succinct description of the important aspects of each of these systems. Detailed information regarding the monitoring systems including video camera and analog sensor instrumentation can be found in Pantoli et al. (2013b).

Still Cameras

Photographs were taken in the construction and test phases by a number of individuals involved in the project, including researchers and industry partners. The photographs taken in the construction phase were used to document the construction details of the building and its NCSs as well as the construction progress, while the photographs taken in the post-shaking inspection were used to characterize physical damage of the test

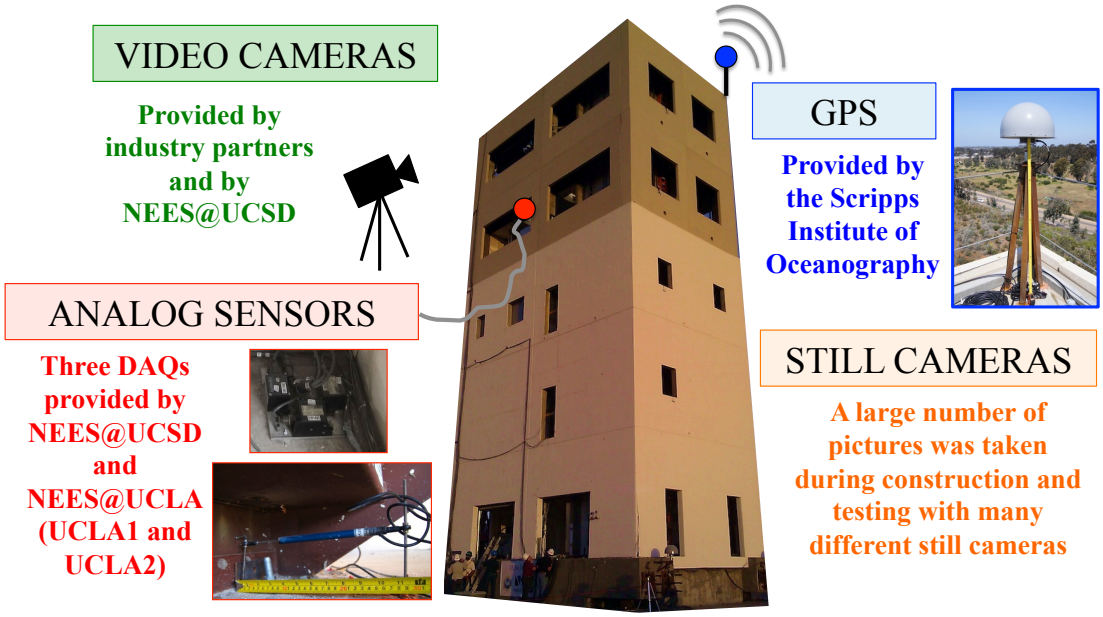

Figure 2.3. Monitoring systems deployed on the test building (photo courtesy of Pantoli et al., 2013b).

building and individual NCSs.

Video Cameras

A dense video camera system was employed throughout the seismic test phase, which included over 85 video cameras simultaneously documenting the interior and exterior of the test building. During the 13 earthquake tests, nearly an abundance of video data was captured to document the behavior of the test building and its NCSs. The videos captured during this project complemented the analogue data.

Analog sensors

A total of 516 analog sensor channels from three different data acquisition systems (DAQs) – UCSD, UCLA1, and UCLA2 system – were deployed on the test building and its NCSs during the seismic tests. While the UCLA systems comprised entirely of accelerometers, the sensors in the UCSD systems included accelerometers, displacement transducers (string potentiometers and linear potentiometers), strain gauges, and load cells. Table 2.3 summarizes the distribution of sensors from the three DAQs used

to monitor the test building (i.e., structural skeleton and isolators), the NCSs, and the shake table platen. Approximately two thirds of the analogue sensors were installed on the NCSs while the remaining one third were installed on the test building and the shake table platen. It is also noted that not all analogue sensors were installed prior to the beginning of the seismic test phase. The sensors were modified as needed during the test phase.

Table 2.3. Distribution of the analog sensor channels in the test building.

Location	number of sensors						Sum
	UCLA1	UCLA2	UCSD				
	A[1]	A[1]	A[1]	DT[2]	SG[3]	LC[4]	
Test buidling	4	72	17	57	23	/	173
NCSs	8	/	124	108	23	62	325
Shake Table	/	9	9	/	/	/	18
Total	12	81	150	165	46	62	516

[1]A – accelerometer; [2]DT – displacement transducer; [3]SG – strain gage; [4]LC – load cell

- *UCSD System*: The UCSD system was composed of ten chassis (also known as nodes), of which eight nodes were used for the test program. Each node recorded data using a maximum of 64 sensor channels. In addition, the UCSD system also recorded data from the controller system of the shake table. While the controller sampled data at a frequency of 256 Hz, data recorded using the nodes were sampled at a frequency of 240 Hz.

  The sensors from the UCSD system were primarily deployed on the NCSs, although a small amount of accelerometers were installed on the test building and the shake table platen. In particular, the prefabricated steel stairs were instrumented with accelerometers and displacement transducers to directly measure the absolute acceleration of the stairs and their relative movement with respect to partition walls, slabs, and between flights and landings. Detailed instrumentation plan of the stair system are discussed in Chapter 3.

- *UCLA1 System*: The UCLA1 system consisted of 12 channels of accelerometers

collecting data at a sampling frequency of 500 Hz. These included four channels measuring the roof acceleration response and the remaining eight measuring the acceleration response of the equipment installed on the roof (e.g., cooling tower and penthouse).

- *UCLA2 System*: The UCLA2 system was composed of 81 channels of accelerometers with a sampling frequency of 200 Hz. The accelerometers in this system were primarily deployed for measuring the response of the test building and the shake table platen. It is noted that triaxial accelerometers were installed at every corner of the foundation and floor slabs. The measured building floor responses presented later in this chapter were processed using the data recorded in the UCLA2 system.

Since different sampling frequencies were used in the three DAQ systems, time series data recorded from different DAQ systems need to be time synchronized to correlate the responses of the test building and the NCSs. The time series data from different systems were first resampled to the same sampling frequency and subsequently shifted in the time domain to account for the time lag between two DAQ systems. The time lag were determined using the acceleration data from different systems measuring response at the same location. For example, the accelerometers at the southwest corner of the foundation were used to synchronize the UCSD and UCLA2 systems and the accelerometers on the shake table platen for the controller and the nodes of the UCSD system.

Global Positioning System

Displacement data obtained from double integration of acceleration measurements can be unreliable at low frequencies, whereas GPS data is unreliable at high frequencies because of low sampling rates. By collocating GPS and accelerometer sensors, an optimal combination can be achieved to produce accurate and broadband velocity and displacement waveforms (Bock et al., 2011). In this test program, a total of five GPS stations were deployed at different location within the test building. Three stations were installed on the roof at the southwest, northwest and northeast corners, and two stations

were installed on the foundation at the southwest and northwest corners. Furthermore, one static reference station was placed within 50 m to the west of the building (off the shake table).

2.4 Dynamic Test Protocol

The test program consisted of two seismic test phases, namely: (i) the building isolated at its base (BI), and (ii) the building fixed at its base (FB). A sequence of dynamic tests including white noise (WN) and pulse-like excitations as well as earthquake motions were conducted using the LHPOST. These included a total of 13 earthquake tests, 31 low-amplitude WN base excitation tests, and 45 pulse-like base excitation tests. Each of the input motions were applied in the east-west direction using the single-axis shake table, whose axis coincided with the longitudinal axis of the building.

Tables 2.4 and 2.5 summarize the dynamic tests performed in the two test phases, respectively. The input motions in each test phase were ordered chronologically in the tables. For each earthquake input motion, the table summarizes earthquake motion details of the source earthquake motion, scale factor, and a short name associated with each motion. These short names are employed to facilitate result presentation in this and the following chapter. It is noted that with the exception of motion BI-4, the first four motions within the BI test phase (BI-1, BI-2/3, BI-5 and BI-6) were repeated on the test building in a similar sequence during the FB test phase (FB-1 through FB-4). In addition, low-amplitude WN base excitation tests were conducted on three different dates (i.e., September 12, 2011, February 23, 2012, and March 9, 2012) during the construction stage with the purposes of studying the dynamic characteristics of the test building.

2.4.1 White Noise and Pulse Base Excitations

A sequence of white noise and pulse excitations was applied to the test building prior to and following each of the seismic tests for the purposes of system identification. A complete white noise and pulse-like base excitation sequence consisted of two pulses

Table 2.4. Summary of dynamic tests in the base isolated (BI) test phase

Date	Description	Name	Scaling method[1]
April 16, 2012	1.5%g RMS + 3.0%g RMS + 3.5%g RMS	WN-1	
	1994 Northridge — Canoga Park — 100%	**BI-1:CNP100**	SM
	1.5%g RMS + 3.0%g RMS + 3.5%g RMS	WN-2	
	1994 Northridge — LA City Terrace — 100%	**BI-2:LAC100**	SM
	1.5%g RMS+3.0%g RMS + 3.5%g RMS	WN-3	
April 17, 2012	1.5%g RMS+3.0%g RMS + 3.5%g RMS	WN-4	
	1994 Northridge — LA City Terrace — 100%	**BI-3:LAC100**	SM
	1.5%g RMS+3.0%g RMS + 3.5%g RMS	WN-5	
	2010 Maule (Chile) — San Pedro — 100%	**BI-4:SP100**	AM
	1.5%g RMS+3.0%g RMS + 3.5%g RMS	WN-6	
April 25, 2012	1.5%g RMS+3.0%g RMS + 3.5%g RMS	WN-7	
April 26, 2012	**2007 Pisco (Peru) — Ica — 50%**	**BI-5:ICA50**	AM
	1.5%g RMS+3.0%g RMS + 3.5%g RMS	WN-8	
April 27, 2012	**2007 Pisco (Peru) — Ica — 100%**	**BI-6:ICA100**	AM
	1.5%g RMS+3.0%g RMS + 3.5%g RMS	WN-9	
	2007 Pisco (Peru) — Ica — 140%	**BI-7:ICA140**	AM
	1.5%g RMS+3.0%g RMS + 3.5%g RMS	WN-10	

[1]White noise test: amplitude; earthquake test (bold face): event – location – scale factor.
[2]AM – motion with amplitude scaling only; SM – motion scaled using spectral matching.

Table 2.5. Summary of dynamic tests in the fixed base (FB) test phase

Date	Description[2]	Name	Scaling method[2]
May 7, 2012	1.5%g RMS + 3.0%g RMS + 3.5%g RMS	WN-11	
	1994 Northridge — Canoga Park — 100%	**FB-1:CNP100**	SM
	Double pulse		
May 9, 2012	Double pulse		
	1994 Northridge — LA City Terrace — 100%	**FB-2:LAC100**	SM
	Double pulse		
	Double pulse		
	2007 Pisco (Peru) — Ica — 50%	FB-3:ICA50	AM
	Double pulse		
May 11, 2012	Double pulse		
	2007 Pisco (Peru) — Ica — 100%	**FB-4:ICA100**	AM
	1.5%g RMS	WN-12	
May 15, 2012	3.0%g RMS	WN-13	
	2002 Denali — TAPS pumps station#9 — 67%	**FB-5:DEN67**	SM
	1.5%g RMS	WN-14	
	3.5%g RMS	WN-15	
	2002 Denali — TAPS pumps station#9 — 100%	**FB-6:DEN100**	SM

[1]White noise test: amplitude; earthquake test (bold face): event – location – scale factor.
[2]AM – motion with amplitude scaling only; SM – motion scaled using spectral matching.

followed by broad-band white noise (0.25-25 Hz) at three distinct amplitude levels, namely, with root-mean-square (RMS) acceleration of 1.5, 3.0 and 3.5% g, respectively (Figure 2.4). These excitations were consistently applied to the test building prior to and following the seismic tests in the BI test phase. In the FB test phase, however, low amplitude white noise base excitation tests were conducted only prior to the first (FB-1) and the last two (FB-5 and FB-6) earthquake tests. With the exception of the WN test conducted prior to FB-1 that included a complete sequence with three amplitude levels, the other two WN tests in the FB test phase contained the input excitation at a single amplitude level. Instead, double pulse base excitations were applied to the test building prior to and following the seismic tests throughout the FB test phase.

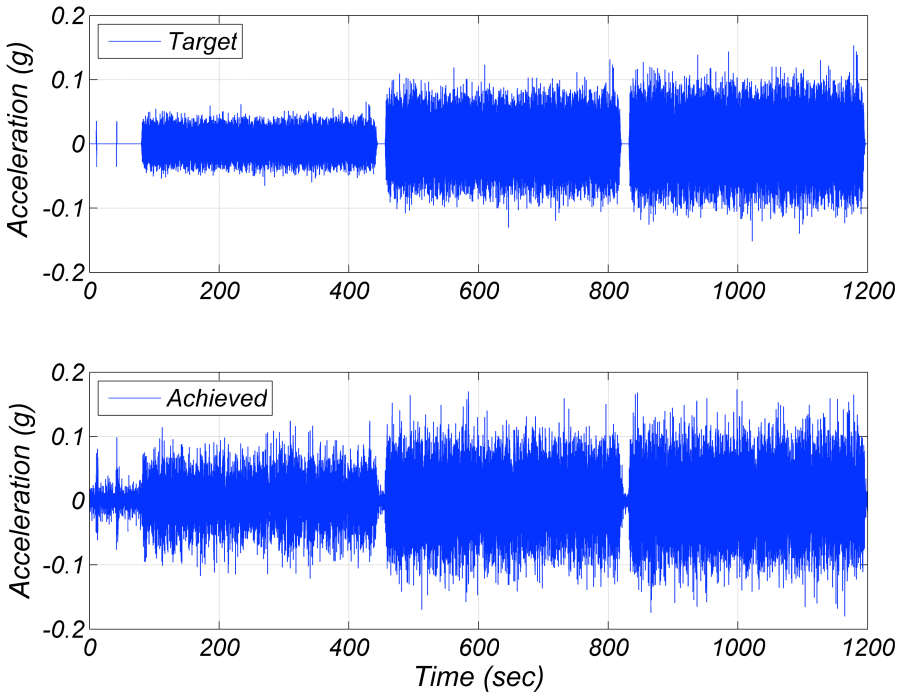

Figure 2.4. Input acceleration of a complete white noise and pulse-like base excitation sequence.

2.4.2 Earthquake Input Motions

The earthquake input motions selected in the test program encompassed a broad range of characteristics including different frequency contents as well as varied strong

motion durations and amplitudes. Recorded motions consisted of those from the subduction zone of South America, the coast of California, and the central area of Alaska, representing the ground motion characteristics with varied seismicity. The motions recorded from the earthquakes in Chile and Peru were actual recordings that were scaled only in amplitude, while the Denali test motion was scaled in both frequency and amplitude (scaled using spectral matching) to a targeted response spectrum with Site Class D soil conditions for the selected site. A 100% scale factor of the Denali motion implies that the test motion's response spectra matches a maximum target response spectrum with spectral acceleration values of S_{MS} = 2.1 g and S_{M1} = 1.4 g, whereas 67% scale of the motion indicates that the test motion has a response spectrum that was intended to match the design event response spectrum and impose the performance targets set for the building. All the Northridge earthquake input motions were spectrally matched to achieve a seismic hazard level with a return period of 43 years (approximately 20% of the maximum target response spectrum). The seismic motions were designed and applied to the building and its NCSs with the intent to progressively increase the seismic demands on the building and NCSs in both the BI and FB test phases, while minimizing the impact of the lower intensity motions on the failure response mechanisms developed in the specimen under the highest intensity motion. Details of the input earthquake motions in the two test phase are discussed in the following sections.

2.4.2.1 Base Isolated Test Phase

While the test building was in the base isolated configuration, two spectrally matched motions (Canoga Park and LA City Terrace, both from the 1994 M_w = 6.7 Northridge earthquake) and four actual earthquake motions (San Pedro from the 2010 M_w = 8.8 Maule earthquake in Chile and Ica amplitude scaled to 50%, 100% and 140% from the 2007 M_w = 8.0 Pisco earthquake in Peru) were applied to the test building. These motions were intended to impose minimal damage to the structural systems prior to FB test phase. For this reason, scale factors were selected with the guidance of pre-test numerical simulations such that the maximum interstory drift ratio remained less than about 0.5% while the building was base isolated (Ebrahimian et al., 2013; Wang et al., 2013).

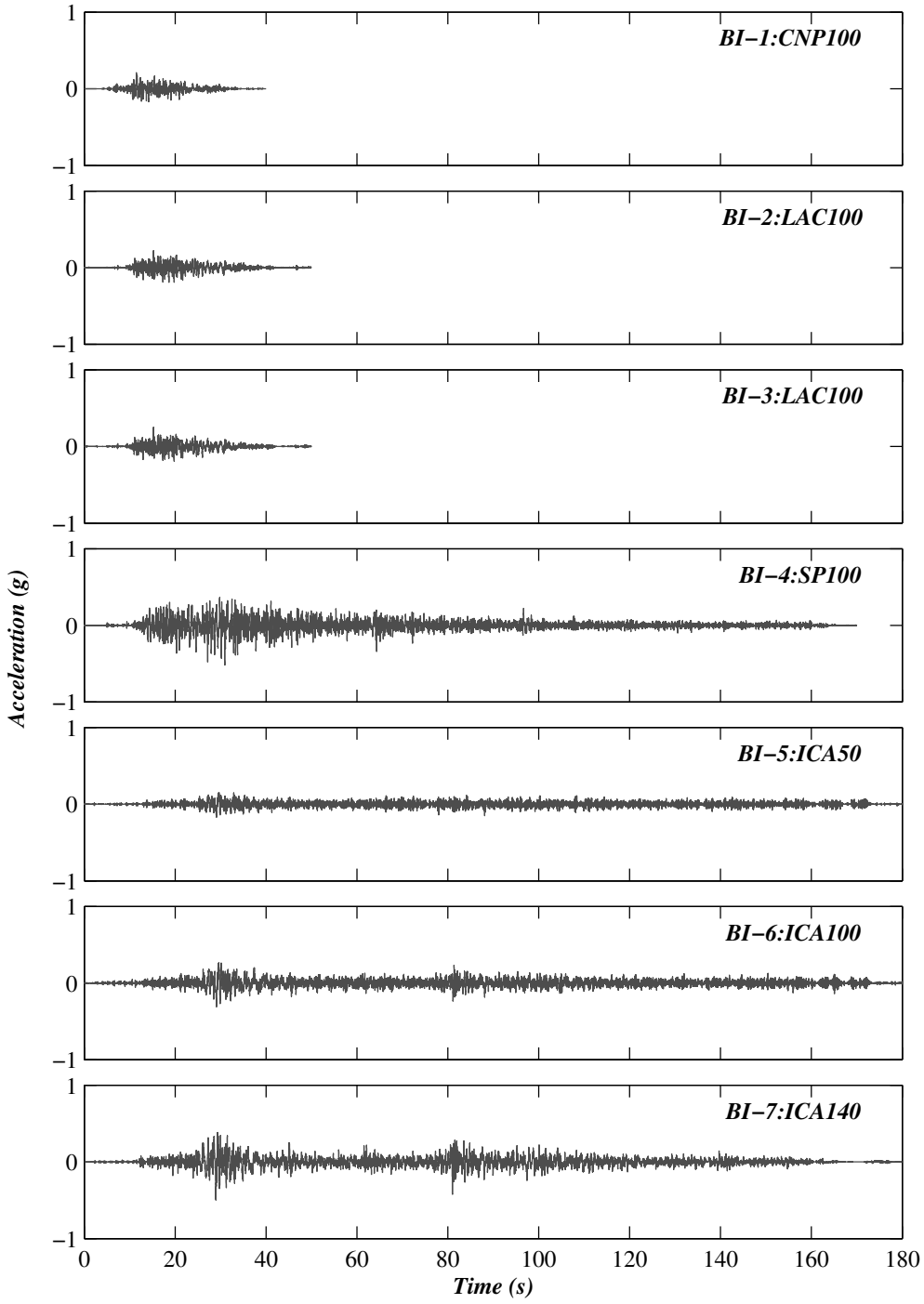

Figure 2.5. Acceleration time histories of the achieved earthquake motions in the base isolated test phase.

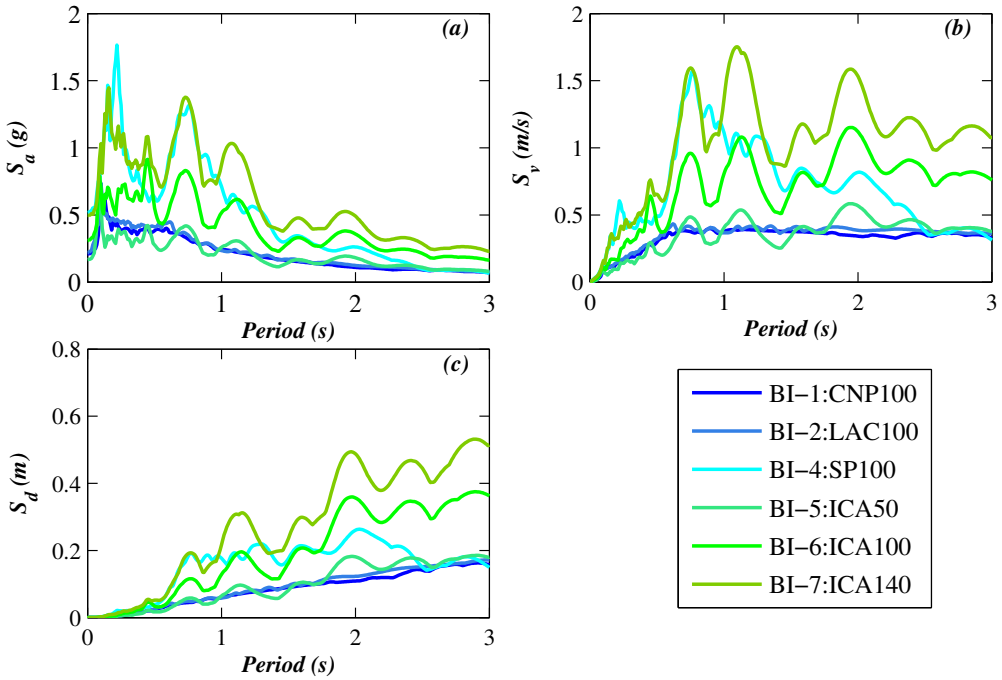

Figure 2.6. Elastic response spectra of the achieved earthquake input motions in the base isolated test phase (damping ratio $\xi = 12\%$): (a) psuedo-acceleration spectra, (b) psudeo-velocity spectra, and (c) displacement spectra.

Table 2.6. Summary of achieved earthquake input motions during the base isolated test phase.

Motion name	PIA[1] (g)	PIV[2] (m/sec)	PID[3] (m)	T_d[4] (sec)	$S_a(T_1,\xi)$[5] (g)
BI-1:CNP100	0.21	0.23	0.08	15	0.09
BI-2:LAC100	0.22	0.24	0.09	20	0.06
BI-3:LAC100	0.25	0.24	0.09	20	0.08
BI-4:SP100	0.52	0.35	0.08	80	0.08
BI-5:ICA50	0.17	0.22	0.04	130	0.08
BI-6:ICA100	0.31	0.43	0.09	128	0.15
BI-7:ICA140	0.50	0.63	0.13	97	0.23

[1] PIA – peak input acceleration; [2] PIV – peak input velocity; [3] PID – peak input displacement; [4] T_d – strong motion duration; [5] $S_a(T_1,\xi)$ – elastic spectral accelerations of the input motion ($T_1 = 2.5$ s and $\xi = 12\%$ for the BI test phase.

Figure 2.5 shows the acceleration time histories of the earthquake input motions achieved on the shake table platen during the BI test phase. The peak acceleration, velocity, displacement, and strong motion duration of each achieved input motion are summarized in Table 2.6. The strong motion duration is defined by the time interval between 5% and 95% of the Arias intensity (Arias, 1970) of an earthquake motion. It is noted that the motions from the 2010 Maule earthquake in Chile and the 2007 Pisco earthquake in Peru were of substantially long duration, with their 5%–95% duration of strong shaking estimated at about 4-5 times that of the Northridge earthquake motions. Figure 2.6 shows the 12% damped elastic displacement, pseudo-velocity, and pseudo-acceleration response spectra for the achieved earthquake motions. Considering a predominant period of 2.5 s (although the period varies for different values of shear strain) for the combined structure-isolator system, the elastic response spectra indicate that displacement demands ranging from 0.08 m – 0.13 m and acceleration demands ranging from 0.06 g – 0.23 g were estimated to occur during the motion sequence.

2.4.2.2 Fixed Base Test Phase

While fixed to the shake table platen, four spectrally matched motions (Canoga Park and LA City Terrace, both originating from the 1994 M_w = 6.7 Northridge earthquake and Denali 67% and 100%, each from the 2002 M_w = 7.9 Denali-Alaska earthquake) and two amplitude-scaled motions (Ica 50% and 100% from the 2007 M_w = 8.0 Pisco-Peru earthquake) were applied to the test building. Figure 2.7 shows the acceleration time histories of each input motion achieved on the shake table platen during the FB test phase, and the elastic response spectra (damping ratio of 5%) for the corresponding motions are presented in Figure 2.8. The peak acceleration, velocity, displacement, and strong motion duration of each achieved input motion are summarized in Table 2.7. It is also noted that although the building fundamental period T_1 varied during the testing as a result of accumulated structural damage, a reference value of 1.0 s for the building in the FB test phase is used for evaluating the elastic spectral accelerations

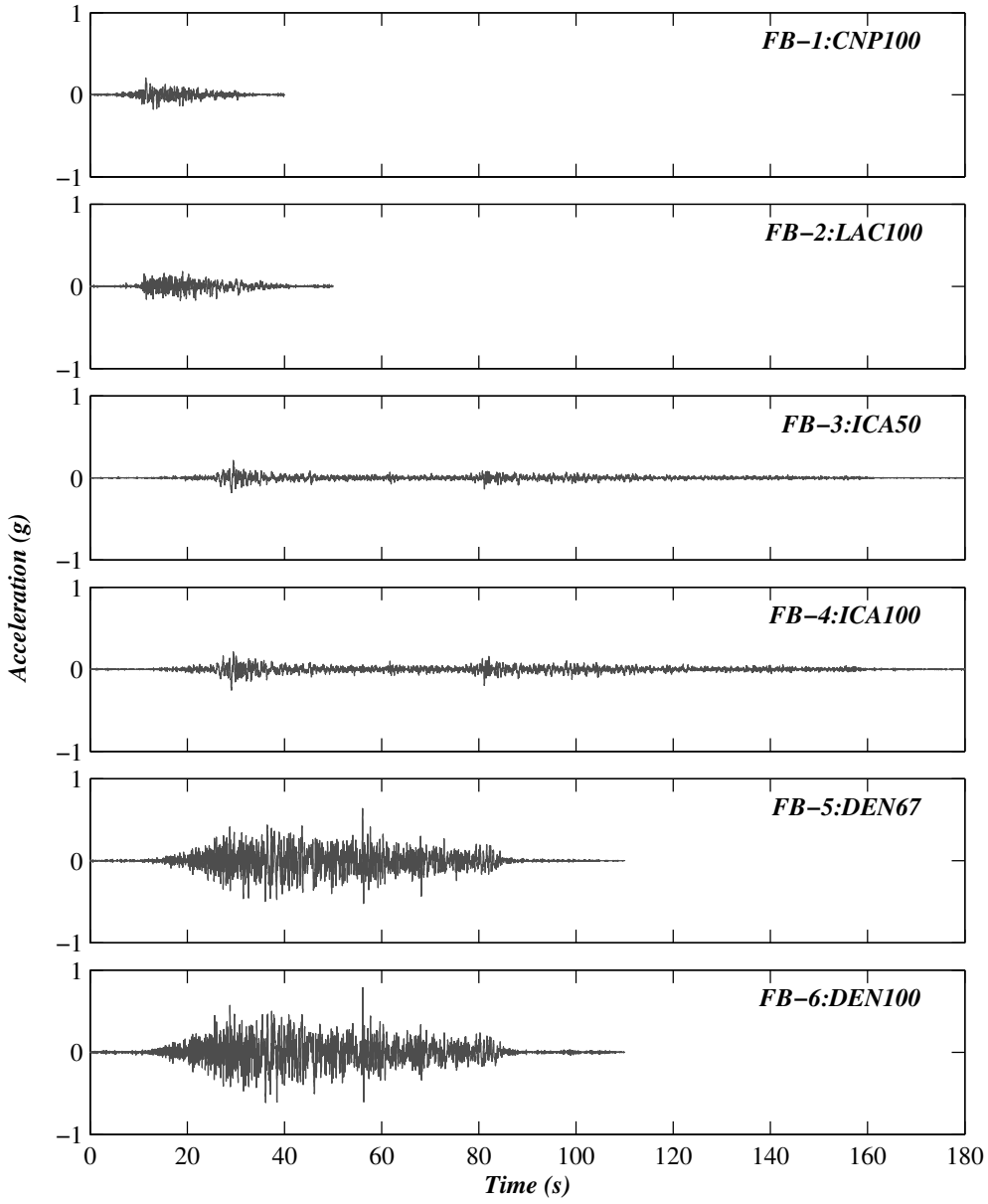

Figure 2.7. Acceleration time histories of the achieved earthquake input motions in the fixed base test phase.

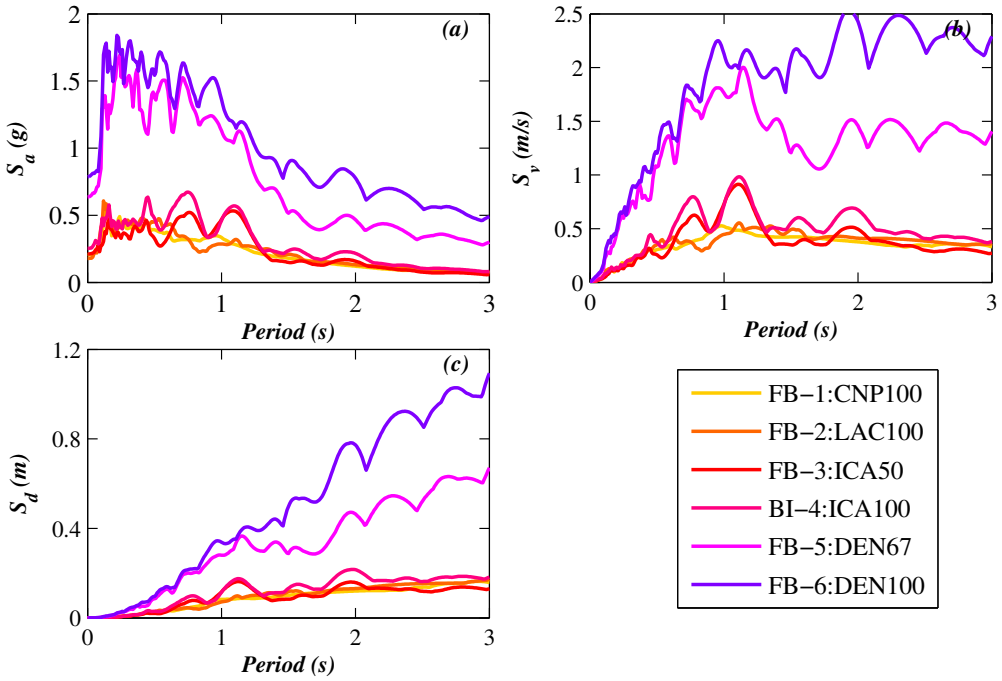

Figure 2.8. Elastic response spectra of the achieved earthquake input motions in the fixed base test phase (damping ratio ξ = 5%): (a) psuedo-acceleration spectra, (b) psudeo-velocity spectra, and (c) displacement spectra.

Table 2.7. Summary of achieved earthquake motions during the fixed base test phase.

Motion name	PIA[1] (g)	PIV[2] (m/sec)	PID[3] (m)	T_d (sec)	$S_a(T_1,\xi)$ (g)
FB-1:CNP100	0.21	0.24	0.09	15	0.33
FB-2:LAC100	0.18	0.23	0.09	20	0.29
FB-3:ICA50	0.21	0.26	0.06	91	0.47
FB-4:ICA100	0.26	0.28	0.07	96	0.46
FB-5:DEN67	0.64	0.64	0.20	49	1.13
FB-6:DEN100	0.80	0.84	0.34	49	1.36

[1]PIA – peak input acceleration; [2]PIV – peak input velocity; [3]PID – peak input displacement; [4]T_d – strong motion duration; [5]$S_a(T_1,\xi)$ – elastic spectral accelerations of the input motion (T_1 = 1.0 s and ξ = 5% for the FB test phase).

2.5 Building Response

This section presents the measured building floor acceleration and interstory drift responses during the seismic tests. These responses are critical not only for understanding the structural behavior of the building itself, but also because the structural responses are the input excitation to the NCSs installed on the building. As previously discussed, the earthquake motions applied to the building in all of the shake table tests were unidirectional, and therefore the building responses in the transverse direction were much smaller than their longitudinal counterparts (the peak floor accelerations and peak interstory drift response in the transverse direction were less than 10% of their counterparts in the longitudinal direction). As a result, only the longitudinal responses of the test building are presented in this section. Interested readers are referred to Pantoli et al. (2013a) for additional details regarding the building response during the seismic tests.

The building responses were obtained using data recorded by the UCLA2 data acquisition system, namely, with a triaxial accelerometer installed at each of the four corners of each floor. Raw acceleration measurements were filtered using a fourth order bandpass Butterworth filter with corner frequencies of 0.08 and 25 Hz. Accelerations measured at the four corners of the building were double integrated to obtain floor level displacement histories and subsequently interstory drift was calculated as the difference of two displacement histories between sequential floors. Interstory drift ratio was then calculated by normalizing these values by the floor heights. Detailed information regarding the data processing of the measured building response can be found in Appendix A of Pantoli et al. (2013a).

2.5.1 Building Response in the Base Isolated Test Phase

Figures 2.9 and 2.10 show the measured floor acceleration and interstory drift ratio (IDR) time histories, respectively, during test BI-7. The time histories presented in these figures are taken as the average response of the four corners of the building. It is clearly indicated that the building longitudinal accelerations were relatively constant up the height of the building, while the interstory drift responses at the lower levels were

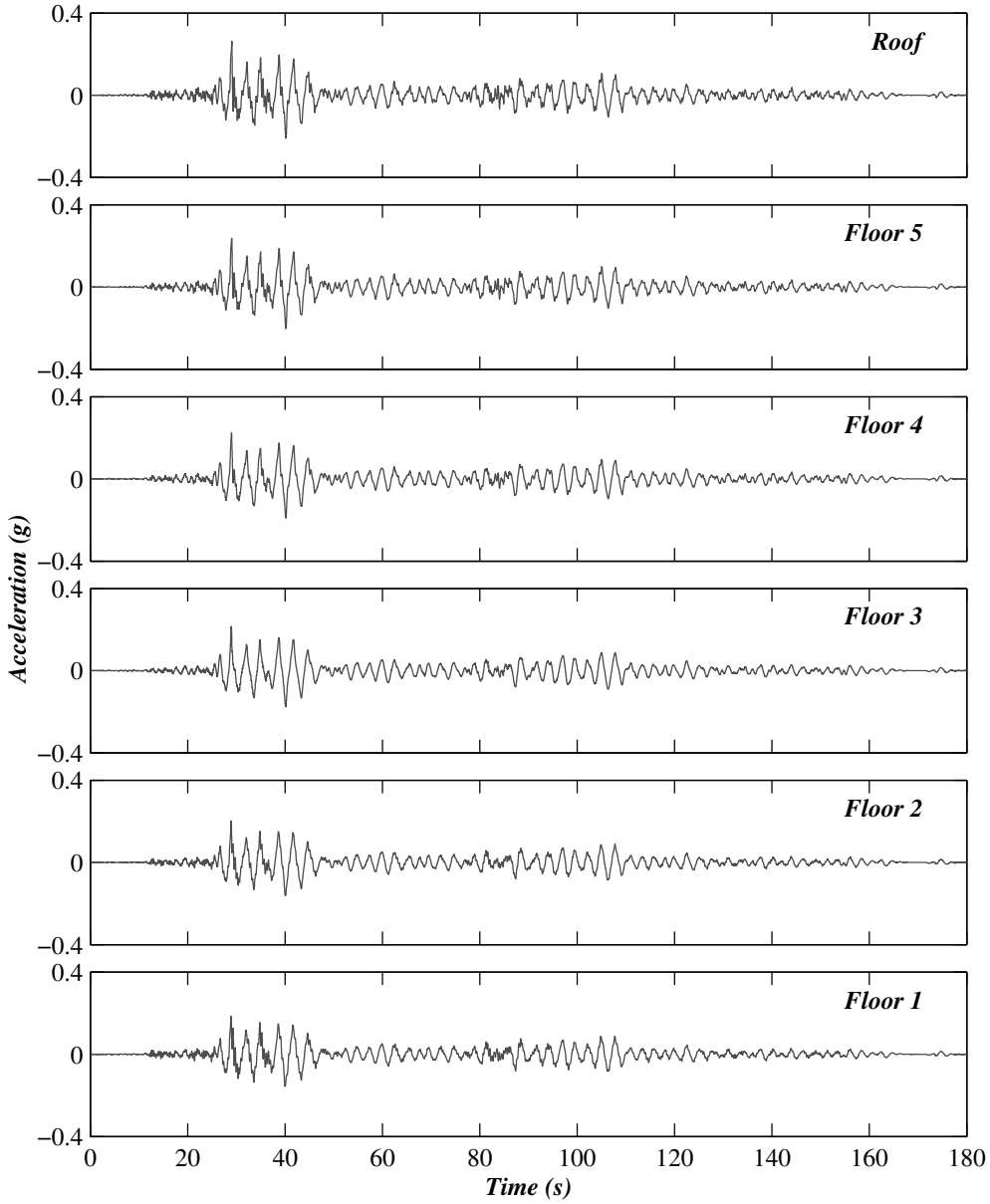

Figure 2.9. Floor acceleration time histories of the test building during test BI-7.

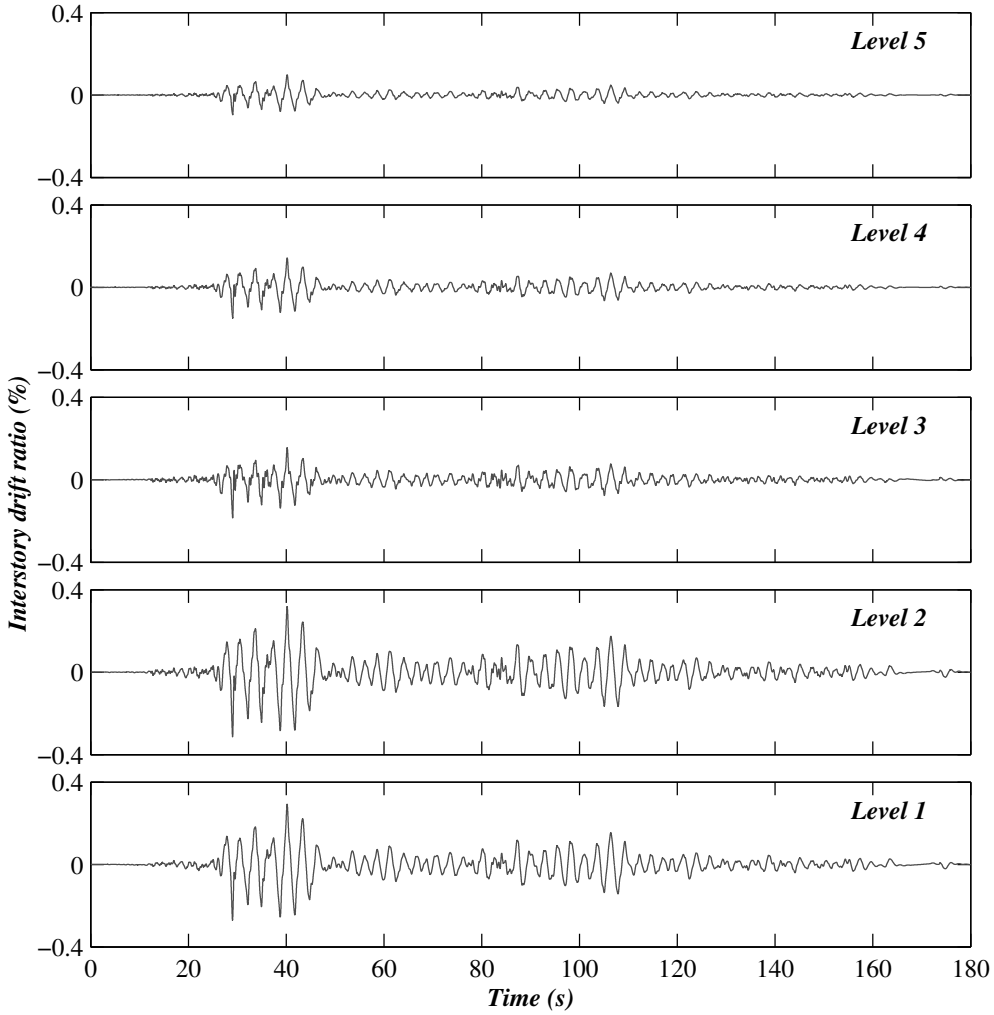

Figure 2.10. Interstory drift ratio time histories of the test building during test BI-7.

appreciably larger than those in the upper levels.

Figure 2.11 shows the measured peak interstory drift ratios (PIDRs) and peak floor accelerations (PFAs) in the BI test phase. Both positive and negative values are presented to demonstrate the asymmetric demands imposed on the test building. Simultaneously, input accelerations were dramatically attenuated by more than 50% (Figure 2.11a). Moreover, the building observed less than 0.4% interstory drift ratio (Figure 2.11b) along its shaking direction.

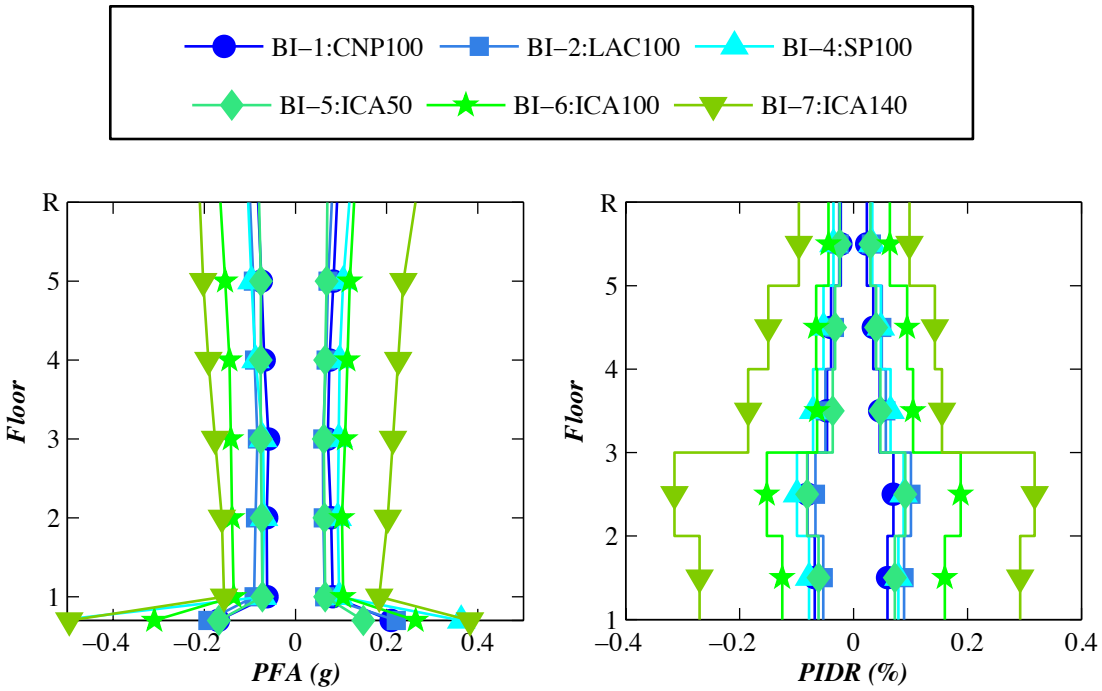

Figure 2.11. Building peak responses in the base isolated test phase: (a) peak floor accelerations, and (b) peak interstory drift response.

Figure 2.12 presents the average peak longitudinal shear strains of the four isolators in the BI test phase. The longitudinal shear strain of the isolators is measured as the ratio of the relative horizontal displacement across the total height of the isolators to the height of the rubber in the base isolators. During each BI test, the four isolators responded with almost identical maximum longitudinal shear strains. The averaged strain were observed as much as 160% during test BI-7 (final test in the BI test phase),

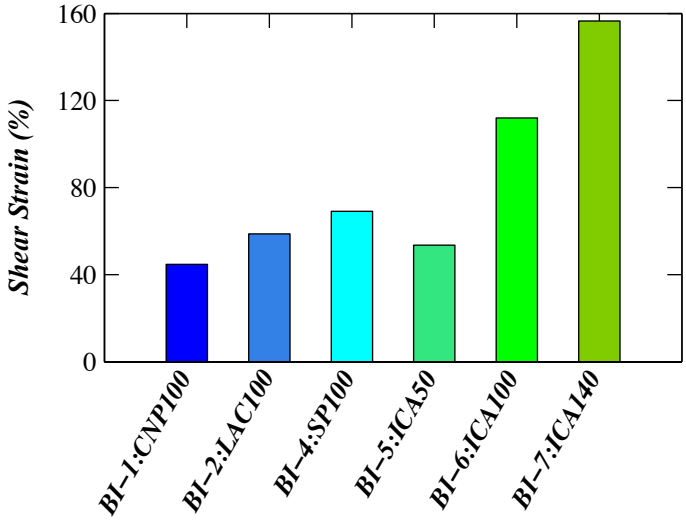

Figure 2.12. Peak isolator longitudinal shear strains (averaged) in the base isolated test phase.

which corresponds a longitudinal displacement of 325 mm. Furthermore, it is noted that approximately 90% of the total roof displacement relative to the shake table platen was concentrated in the isolators during all BI tests (Chen et al., 2015).

2.5.2 Building Response in the Fixed Base Test Phase

In contrast to the PFAs measured while the building was base isolated, the PFAs increased with increasing height from the base of the building and with each subsequent motion imposed during the test protocol while the building was fixed at its base. During the FB testing phase, the largest floor level accelerations were consistently observed at the roof of the structure, with a maximum value of about 1.0 g achieved during the targeted design event (test FB-5). The intense structural demands resulted in softening of the test building at lower stories and consequently very large PIDRs approaching 6% during FB-6:DEN100 (Figure 2.15b). With deformations concentrated predominantly within the lower stories, the PIDRs above level four remained below 2%.

During the design event earthquake (test FB-5), the largest PIDR values were concentrated at the lower levels (about 2.8% between levels 2-3), while the upper levels (above level 4) measured PIDRs less than about 2%. In contrast, test FB-6 resulted in

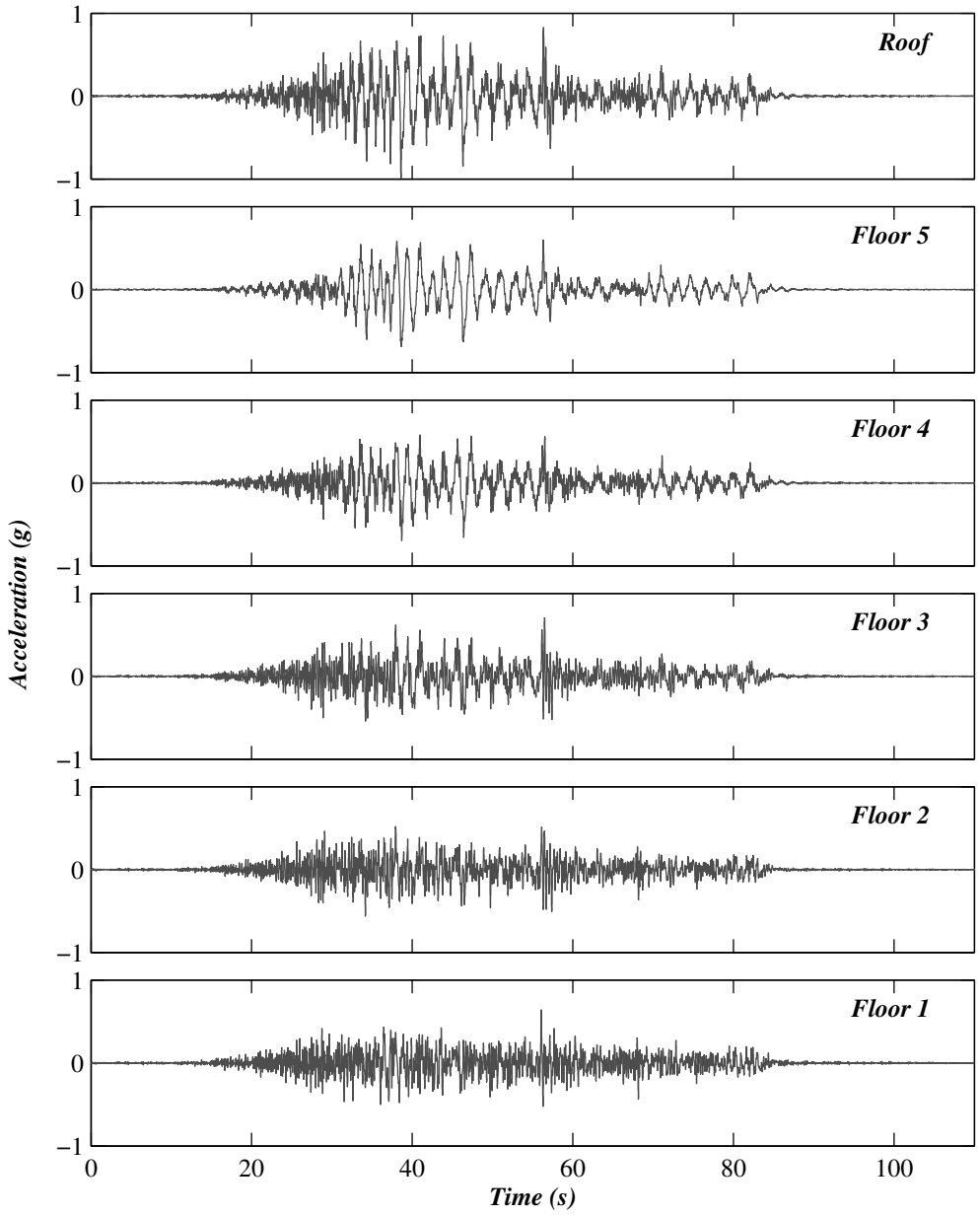

Figure 2.13. Floor acceleration time histories of the test building during test FB-5.

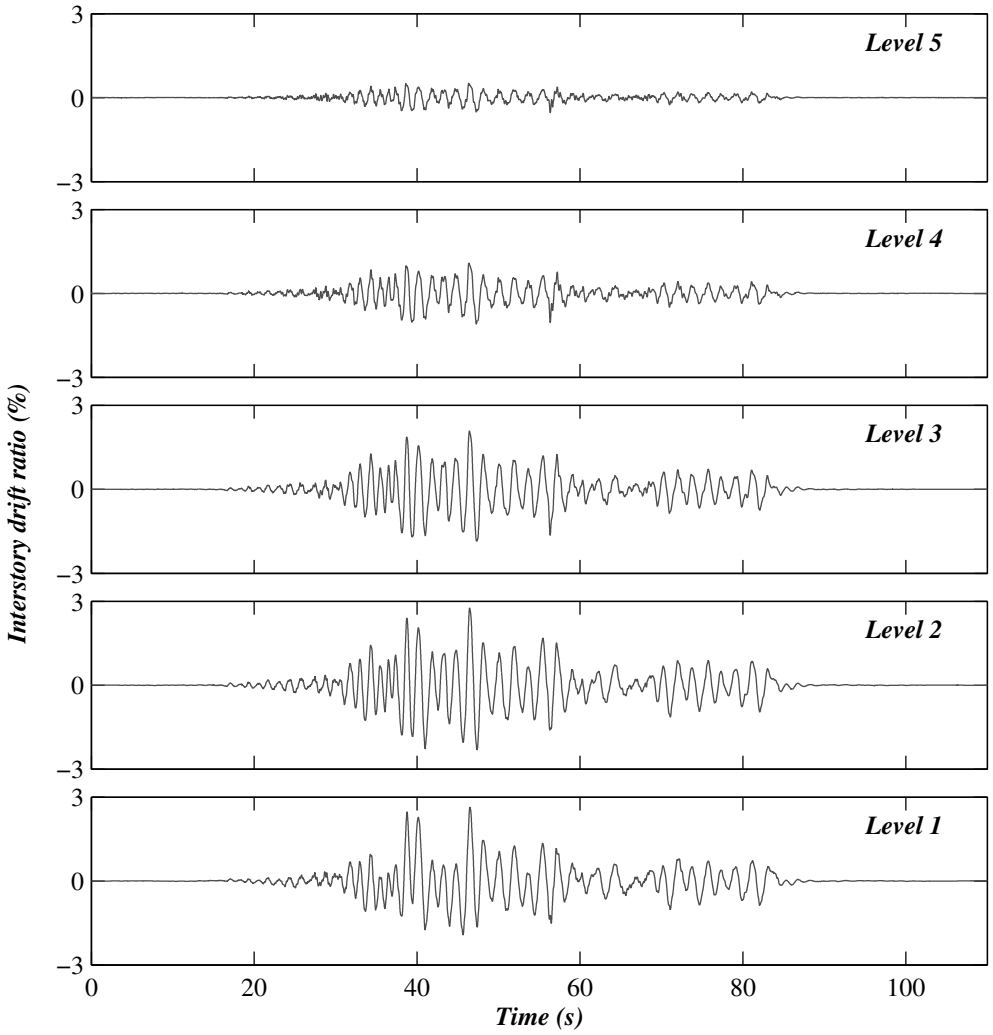

Figure 2.14. Interstory drift ratio time histories of the test building during test FB-5.

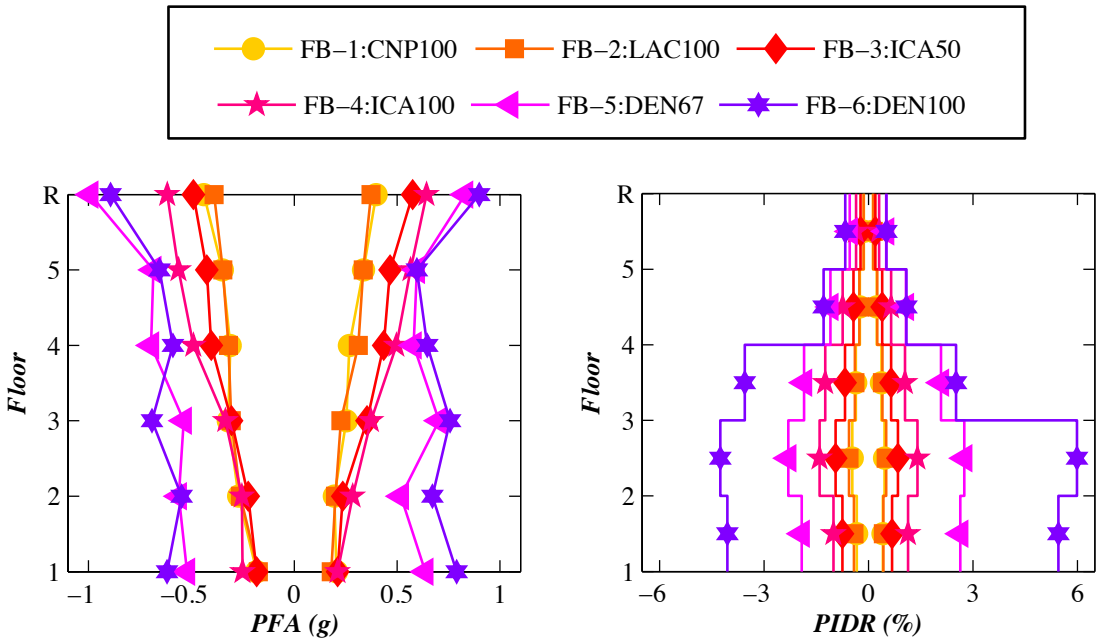

Figure 2.15. Building peak responses in the FB test phase: (a) peak floor accelerations, and (b) peak interstory drift response.

the yielding and fracture of longitudinal bars in the frame beams at the column faces on the north and south sides of the building. In addition, punching shear failure at the slab-column connections developed along with extensive cracking in the slabs on both floors two and three of the building, with cracking densely concentrated at the frame columns and extending outward. Closely spaced flexural and shear cracks were observed along the lengths of the beams and concentrated at the ends of the beams, with the most severe beam cracking at the lower levels. Interested readers are referred to Pantoli et al. (2013a) for detailed damage observations the primary structure of the test building during the FB test phase.

2.6 Summary Remarks

A landmark full-scale five-story shake table test program was conducted at the UCSD LHPOST in 2012. Unlike prior full-scale building shake table test programs, these experiments focused on investigating the interaction between structural and non-structural systems during earthquakes. Therefore, the building was designed as a "total" system, intended to be fully functional and architecturally complete. As such, it was

outfitted with a variety of essential nonstructural components and systems, including a complete façade, two operational egress systems, mechanical-electrical-plumping systems on all floors, and incorporated architectural spaces detailed as residential, office, laboratory and hospital occupancies, to support the operability of modern buildings with a range of occupancies. Within this chapter, a brief overview of the shake table test program, including the design and construction of the building, the NCSs incorporated into the building, the seismic test protocol, and specific observations regarding the response of the primary structure during the earthquake motion suite, is presented.

The test building was subjected to a series of earthquake motions, low-amplitude white noise and pulse excitations, first while base isolated and subsequently in a fixed base configuration. As the seismic demands on the building (superstructure) were relatively low (with PIDR < 0.4% and PFA < 0.3 g) in the BI test phase, the building sustained only minor damage to its most brittle nonstructural components such as partition walls (Wang et al., 2015) and very little damage to its structural components. In the FB test phase, the earthquake motions were applied with increasing intensity to progressively damage the structure. It is notable that test FB-5 is considered as design event for the test building since the design target PIDR of about 2.5% was achieved during this test, while test FB-6 represents a well above design event scenario as the the achieved PIDR was as much as 6%. The building sustained extensive damage during the last two FB tests as a result of the large seismic drift demands. Physical damage during test FB-6 included fracture of the longitudinal reinforcement at the ends of the frame beams and punching shear mechanisms at the slab–column interfaces of the second and third floors. This resulted in the development of a soft story mechanism at the lower levels of the test building (also known as an intermediate failure mechanism).

Chapter 3

Shake Table Test Results of Prefabricated Steel Stairs

3.1 Introduction

Within the test building as discussed in Chapter 2, two operable egress systems were incorporated at full-scale, allowing investigation of the system-level interactions of the egress systems within the test building. While the test results of the elevator are discussed in Appendix C, this chapter presents the dynamic characteristics of the stairs identified using data recorded from white noise base excitation tests as well as the physical observation and measured response of the stair system during the earthquake tests. The observed damage to the stairs is categorized into three damage states and correlated with the peak interstory drift demands experienced by the test building.

This chapter is organized into five sections. Section 3.2 provides a description of the prefabricated steel stairs installed in the test building as well as the associated instrumentation plan. In Section 3.3, the experimentally determined dynamic characteristics of the stairs from the white noise base excitation tests are presented. Section 3.4 discusses the physical and measured responses of the stairs during the seismic tests. Lastly, Section 3.5 summarizes the important findings regarding the dynamic characteristics and seismic behavior of the stairs in these shake table tests as well as their implications

related to design practice.

3.2 Description of Stair System

The prefabricated steel stairs were located on the southeast side of the building (Figure 2.2a) and provided access to all floors including the roof. As shown in Figure 3.1, the stair assembly at each level was installed in a scissor configuration, consisting of a mid-level landing and two parallel straight flights running in opposite directions from the landing. The flights, landings, and handrails were factory fabricated and installed in place by the stair manufacturer in conjunction with construction of the building. The in-place installation consisted of welding of the flights and landing posts to steel embeds cast within the beams and slabs of the test building. Bolted connections were only utilized at connections between the flights and the landings. The total weight of the stair was approximately 10.1 kN, with 3.3 kN from the landing and 3.4 kN from each of the flights (including handrails). The stairs were enclosed within cold-form steel framed gypsum partition walls framed from floor to floor on all sides of the openings (Figures 2.2a and 3.1c). A nominal gap between the stairs and the partition wall enclosure was provided and ranged between 30 and 40 mm.

3.2.1 Flights and Landing

The flight stringers utilized ASTM A36 25.4 mm thick plates, and the treads and risers were constructed with 14 gage checkered plates welded to the stringers. Each flight consisted of eleven steps, with a horizontal projected length of 3.07 m and a vertical projected height of 2.13 m. The 1.07×2.24 m landing deck was supported on two ASTM A36 C200×17.1 joists placed in the transverse-to-stair-run direction. Four ASTM A36 76.2×76.2×6.4 mm hollow structural steel (HSS) landing posts provided vertical support to the landing joists at the corners at each level. These landing posts were each connected to the landing joists using two 16mm diameter ASTM A325 bolts and were fillet welded to steel embeds cast with the building at their base. In addition, the connections between the (upper and lower) flights and the landing joists utilized two 16 mm diameter ASTM A325 tension control bolts per flight.

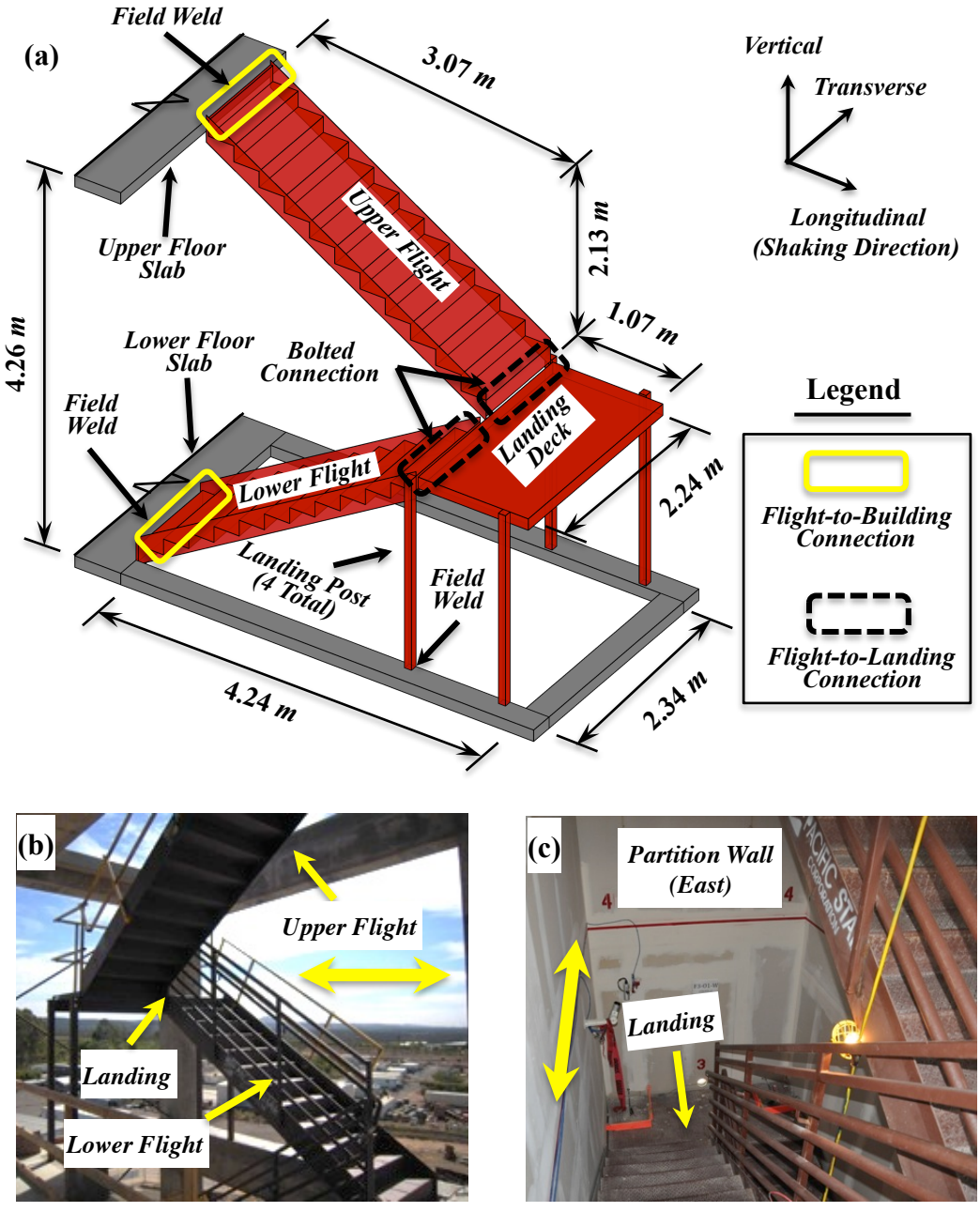

Figure 3.1. Stair layout: (a) three-dimensional schematic of the stair (handrail not shown for clarity), (b) photograph of the stair installed in place during structural skeleton completion, and (c) photograph of the stairwell at building completion (note: double-headed arrow denotes the direction of input motion applied at the base of the test building).

3.2.2 Flight-to-Building Connections

With the exception of the lower flight at level 1, which was connected to the slab at the first floor (foundation) using post-installed wedge anchors, the lower flights at level 2 through level 5 were each connected to the building using an ASTM A36 L102×76×6.4 mm angle (Figure 3.2a). Likewise, the upper flights at all levels were each connected to the building using an ASTM A36 L76×51×6.4 mm angle (Figure 3.2b). All these connection angles were shop welded to the stair stringers at each end and field welded to the steel embed cast with the building using 51 mm long stitch welds spaced at 305 mm on center. It is noteworthy that while the lower flight to building connections were designed to provide limited deformability, the upper flight connection angles differed from those at the lower flight due to the presence of a pair of notches at the ends of the vertical legs of the connection angles (Figure 3.2c). These notches were intended to yield during design interstory drift demands, and thus accommandate floor-to-floor relative motions at or beyond the design level earthquakes.

3.2.3 Instrumentation

The stairs were instrumented with an array of 20 uni-axial accelerometers and 30 displacement transducers, accounting for about 10% of the total sensors deployed within the test specimen. These sensors were connected to the UCSD data acquisition system, which collected data simultaneously at a sampling frequency of 240 Hz. It is noted that while the accelerometers on the stairs were all installed prior to the tests, the displacement transducers were modified as needed during the test program. Figure 3.3 presents the instrumentation of the stair at level 2 during test FB-6. It is noted that each sensor channel is assigned with a unique name, and these names are used in the discussion of the measured stair response later in this chapter. As shown in the figure, the stair at level 2 was densely instrumented and included eighteen accelerometers, six each on the flights and the landing, and eight displacement transducers (D-L-1 through D-L-8) measuring relative deformations of the stair connections as well as three between the landing and surrounding partition walls (D-L-9, D-L-10, and D-T-1). Four networked video cameras were also deployed at the stairwell to monitor the physical behavior of

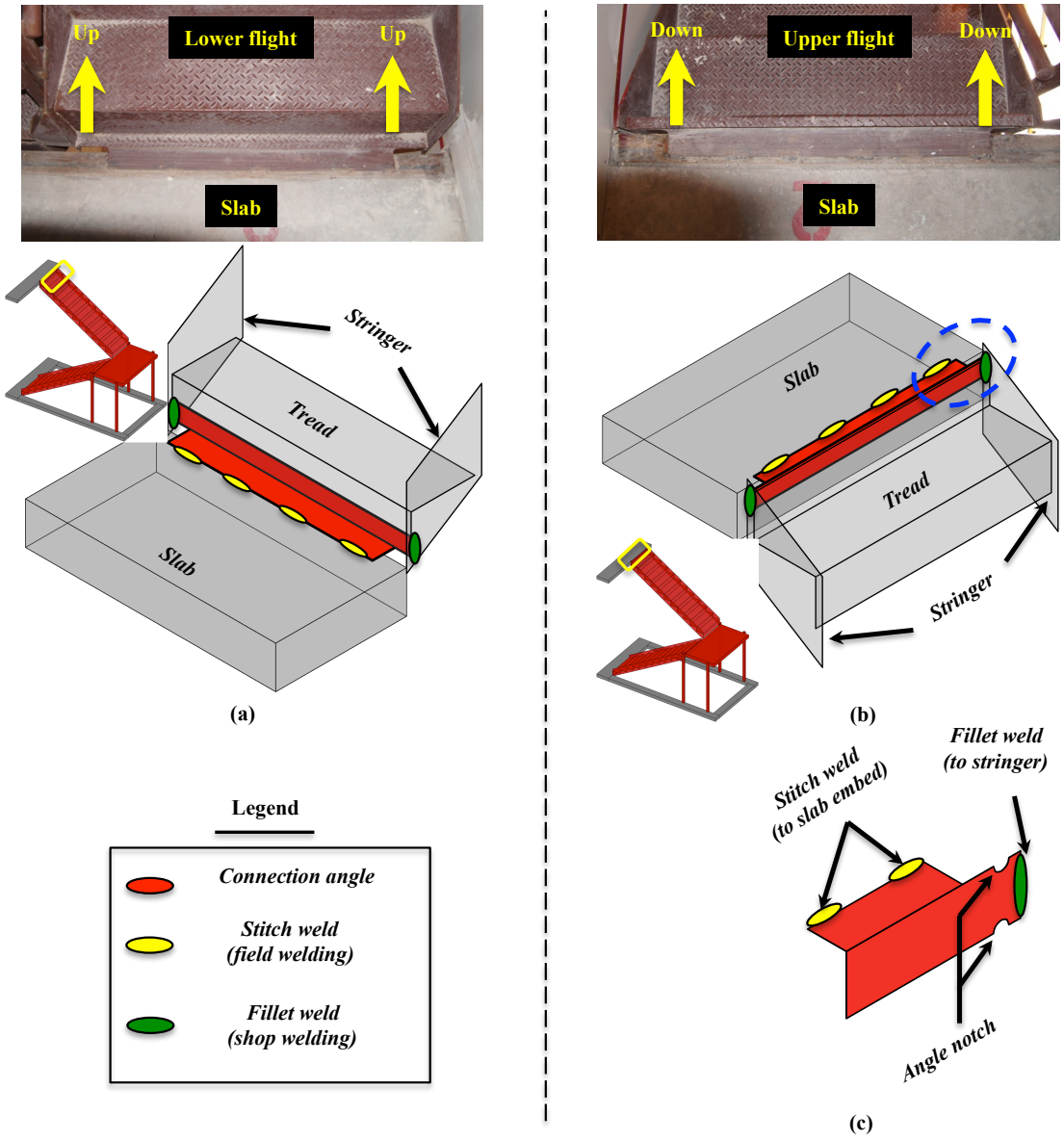

Figure 3.2. Flight-to-building connection details: (a) lower flight to slab connection, (b) upper flight to slab connection, and (c) upper flight connection angle.

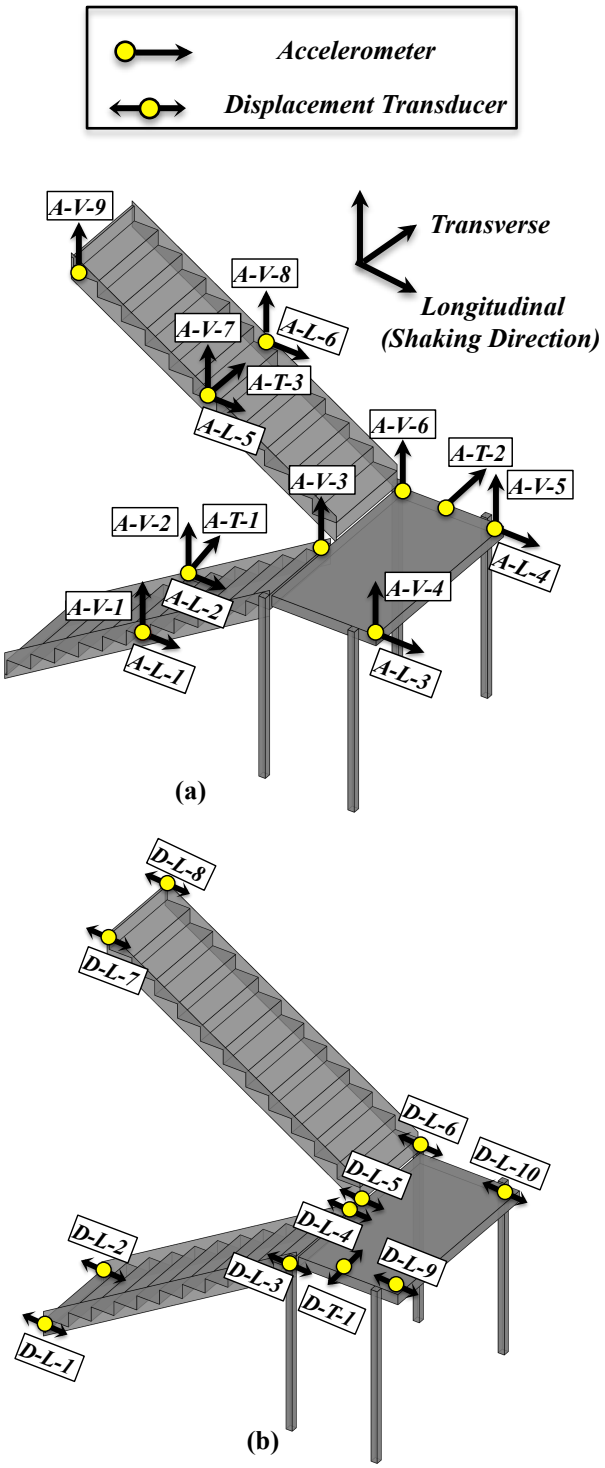

Figure 3.3. Instrumentation of the stair at level 2: (a) accelerometers, and (b) displacement transducers. Sensor orientations shown are consistent with the global coordinate system used for the building. Note that level 2 represents the most densely instrumented level of stairs.

the stairs. The response of the building structure was measured with the UCLA2 data acquisition system sampling data at a frequency of 200 Hz. Additional details of the instrumentation of the stairs and the test building can be found in Pantoli et al. (2013b).

3.3 System Identification of Stairs

Low-amplitude white noise (WN) base excitations were applied to the building using the shake table at various stages during the test program. Although low amplitude, the modal parameters derived from these tests provide a unique understanding of the initial dynamic characteristics of the stairs and are useful for numerical model calibration. Using measurements from these WN tests, the deterministic-stochastic identification (DSI) method (Van Overschee and De Moor, 1996) is used to estimate the modal parameters (natural frequencies, damping ratios, and mode shapes) of the stairs. The DSI method is a time-domain system identification method that realizes a linear state-space model using input-output data. It is robust to both process noise and measurement noise because both terms are explicitly considered in its formulation. Furthermore, it is suitable for dynamic systems with multiple inputs (multiple-support excitations). This method has been applied successfully to identify the modal parameters of the full-scale test building (Astroza et al., 2015) as well as other large-scale structures in previous shake table tests (Belleri et al., 2014; Moaveni et al., 2010). However, unlike the building that considered base excitation as the single input for the system, the system identification of stairs requires consideration of multiple inputs since the stairs were subjected to excitations from both the upper and lower floors of the building in the WN tests.

3.3.1 Deterministic-Stochastic Identification Method

In the deterministic-stochastic identification (DSI) method, the dynamic response for a discrete-time linear time-invariant systems can be written as:

$$\begin{aligned} x(k+1) &= Ax(k) + Bu(k) + w(k) \\ y(k) &= Cx(k) + Du(k) + v(k) \end{aligned} \tag{3.1}$$

with

$$\mathbf{E}\left[\begin{pmatrix} w_k^T \\ v_k^T \end{pmatrix}\begin{pmatrix} w_l^T & v_l^T \end{pmatrix}\right] = \begin{bmatrix} Q & S \\ S^T & R \end{bmatrix}\delta_{kl} \tag{3.2}$$

where A, B, C, and D denote the discrete-time state-space matrices, $u(k)$, $y(k)$, and $x(k)$ denote the input, output and state vectors, respectively. In this model, the process noise $w(k)$ corresponds to unmeasured disturbances and modeling inaccuracies while the measurement noise $v(k)$ models the sensor inaccuracies. However, in the stochastic system, both noise terms implicitly include the input information since it is difficult to distinguish the input from the noise.

Considering the following two assumptions: (1) the deterministic input $u(k)$ is uncorrelated with the process noise $w(k)$ and the measurement noise $v(k)$, and (2) both noise terms are not identically zero, a robust system identification algorithm was developed by Van Overschee and De Moor (1996) in order to identify the state-space matrices in the combined deterministic-stochastic system. Numerical techniques such as QR factorization, singular value decomposition, and least square fitting are incorporated into this method to identify state-space matrices A, B, C, and D using measured input and output dynamic testing data.

The identified state-space matrices are then used to extract the modal parameters of interest. The system matrix A can be decomposed as:

$$A = \Psi\Lambda_d\Psi^{-1} \tag{3.3}$$

where Ψ is the eigenvector matrix and Λ_d is a diagonal matrix that contains the discrete time eigenvalues μ_i. The eigen-frequencies are computed as:

$$\lambda_i = \frac{ln(\mu_i)}{\Delta t} \tag{3.4}$$

where λ_i denotes the continuous time eigenvalues and Δt is the sampling time. The damping ratio is then obtained as:

$$\xi_i = \frac{\lambda_i^R}{|\lambda_i|} \tag{3.5}$$

where $|\cdot|$ denotes the complex modulus. The mode shape matrix Φ is computed from:

$$\Phi = C\Psi \tag{3.6}$$

In DSI method, stability diagrams are widely used for correct selection of the model order (number of Hankel matrix block rows) for the modal parameter identification (Peeters and De Roeck, 2001). Stability diagrams show the poles of a system with varying model orders. To remove the spurious modes as shown in the stability diagram, the stabilization criteria are implemented to compute the differences in modal parameters between two consecutive model orders n and $n+1$:

$$\begin{aligned} \frac{f^n - f^{n+1}}{f^n} &< \epsilon_f \\ \frac{\xi^n - \xi^{n+1}}{\xi^n} &< \epsilon_\xi \\ \mathrm{MAC}(\phi^n, \phi^{n+1}) = \frac{|\widehat{\phi}^n \phi^{n+1}|^2}{(\widehat{\phi}^n \phi^n)(\widehat{\phi}^{n+1} \phi^{n+1})} &> \mathrm{MAC}_\phi \end{aligned} \tag{3.7}$$

where f is the natural frequency, ξ is the damping ratio, ϕ is the modal shape, and $\widehat{\phi}$ denotes the complex conjugate transpose of the modal shape ϕ. The user-specified tolerances for the frequency, damping ratio, and modal assurance criterion (MAC) value (Allemang and Brown, 1982) are denoted as ϵ_f, ϵ_ξ, and MAC_ϕ, respectively. Typical stabilization criteria values are selected as $\epsilon_f = 1\%$ for frequency convergence, $\epsilon_\xi = 5\%$ for damping ratio convergence, and $\mathrm{MAC}_\phi = 98\%$ for convergence of the modal assurance criterion (MAC) values.

3.3.2 White Noise Test Sequence

As shown in Table 3.1, four WN tests are selected for system identification of the stair, each associated with a representative state during the test program. Tests S0 and S2 correspond to the beginning and end states of the base-isolated test phase, respectively, while test S1 corresponds to an intermediate state during this test phase. Test S3 corresponds to the beginning state of the fixed-base test phase. It is noted that test S3 is the only WN test in the fixed-base test phase prior to the occurrence of severe damage of the stair at level 2. All subsequent WN tests in the fixed-base test phase were conducted after test FB-4. As the stair sustained severe damage during test FB-4 and the subsequent two fixed-base earthquake tests, this rendered the system identification results unstable.

Each of the selected WN tests consisted of input excitations of three distinct amplitude levels with root-mean-square (RMS) accelerations of: 1.5% g, 3.0% g, and 3.5% g . For result comparison purposes, the state of the stair during the 1.5% g RMS WN test S0 (at the beginning of the test program) is selected as the reference state. Table 3.1 also summarizes the PIDR and the cumulative number of interstory drift ratio (IDR) cycles of level 2 of the test building corresponding to each representative state. It is noted that both the PIDR and the IDR cycles consider the interstory drift response from the beginning of the test program to the beginning of each WN test. The cumulative number of IDR cycles are determined using the rainflow counting method Downing and Socie (1982), in which the IDR bins are centered at values starting from 0.1% to the maximum IDR at a constant width of 0.1% (e.g., the first bin represents a range between 0.05% and 0.15%). It is also noted that IDR cycles with amplitudes less than 0.05% are excluded from the cycle counting algorithm, as their effects on the damage to the stairs are considered insignificant. Provided the fact that the interstory drifts of the building were insignificantly small ($< 0.05\%$) during the WN tests in the base-isolated test phase, the cumulative IDR cycles as presented in Table 3.1 are the contributions of the seismic tests. This also explains the fact that the PIDR and the cumulative IDR cycles remained unchanged from state S2 to S3, since no seismic test was conducted between these two states.

Table 3.1. WN base excitation tests selected for stair system identification.

State	Test configuration	$PIDR_{L2}$[1] (%)	Cumulative number of IDR cycle
S0 (before BI-1)	BI	N/A	0
S1 (after BI-5)	BI	0.11	29
S2 (after BI-7)	BI	0.32	83
S3 (before FB-1)	FB	0.32	83

[1]peak interstory drift achieved at level 2

In the system identification procedure, the averaged absolute longitudinal accelerations measured on the second and third floors of the building are used as input data, while the accelerations measured on the stair at level 2 are used as output data. To illustrate the characteristics of the input and output data of the system, Figure 3.4 presents the acceleration responses measured on the second floor of the building and the stair at level 2 during the reference state (1.5% g RMS WN test S0). Since the base excitation applied to the building was only in the longitudinal direction, the amplitudes of the transverse floor accelerations were much smaller than (about 5%) their longitudinal counterparts in the WN tests (Figure 3.4a). In addition, the longitudinal floor accelerations measured at the four corners of the building were very similar to each other, as the relative RMS errors between the floor accelerations at the corners and the averaged floor accelerations were generally less than 5%. In this regard, only the averaged longitudinal accelerations at the lower (second) and upper (third) floors are considered as input data for the stair at level 2. Despite the predominant longitudinal floor excitations, the stair landing and flights observed acceleration responses of comparable amplitudes in all three directions (Figure 3.4b). In addition, the frequency contents of these acceleration responses differed considerably. The spectral peaks as observed in the frequency range different from those of the building (5–25Hz) are indications of modal frequencies of the stair. Therefore, the output data considers the stair accelerations measured in all three directions. This results in a multiple-input multiple-output system with two input and eighteen output channels. It is noted that the input and output data were filtered with a fourth-order Butterworth filter using band-pass frequency between 0.25 and 50 Hz. In addition, the input and output data were recorded using separate data acquisition systems sampling

data at different frequencies (i.e., 200 Hz for the building and 240 Hz for the stairs), and therefore the measured accelerations were resampled and synchronized before applying the system identification algorithm. The processed data were resampled to 100 Hz such that the Nyquist frequency (50 Hz) is much higher than the modal frequencies of interest in this study.

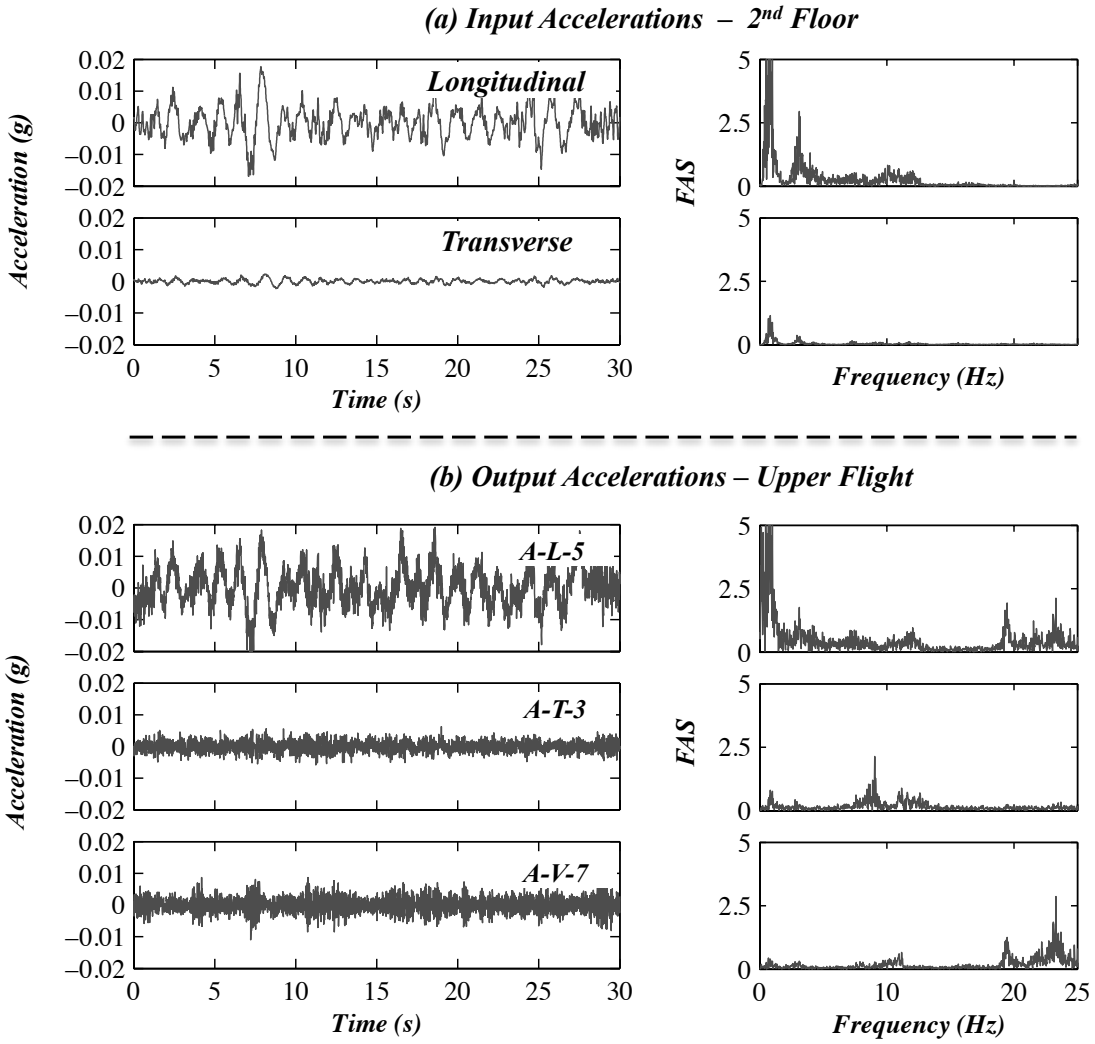

Figure 3.4. Selected (a) input and (b) output acceleration histories and corresponding Fourier amplitude spectra during the reference state (1.5% g RMS WN test S0).

3.3.3 System Identification Results

Stability diagrams indicate that three stable vibration modes are consistently present in the WN tests. Figure 3.5 presents the polar plot representations of the complex-valued mode shapes identified at the reference state (1.5% g RMS WN test S0). It is observed that the three identified modes are nearly classically damped since the mode shape components are nearly collinear. The real-valued mode shapes of the stair obtained using the method proposed by Imregun and Ewins (1993) are shown in Figure 3.6. The first and second modes both correspond to global torsional vibration modes of the stair and the third mode represents global vibration of the stair in its parallel-to-flight direction. Importantly, each of the three identified modes includes vertical vibration of the flights. It is noted that the first and second modes exhibit very similar mode shapes. This is due to the fact that the effects of the handrails are not considered in the identification in the absence of measurements on the handrails, while they accounted for about 30% of the total mass of the stair at each level. This is confirmed by eigen-value analysis using a detailed finite element model of the stair as discussed in Chapter 4, which indicates that the deformation of the handrails differs completely in these two modes, even though the deformation of the flights and landing appears similar.

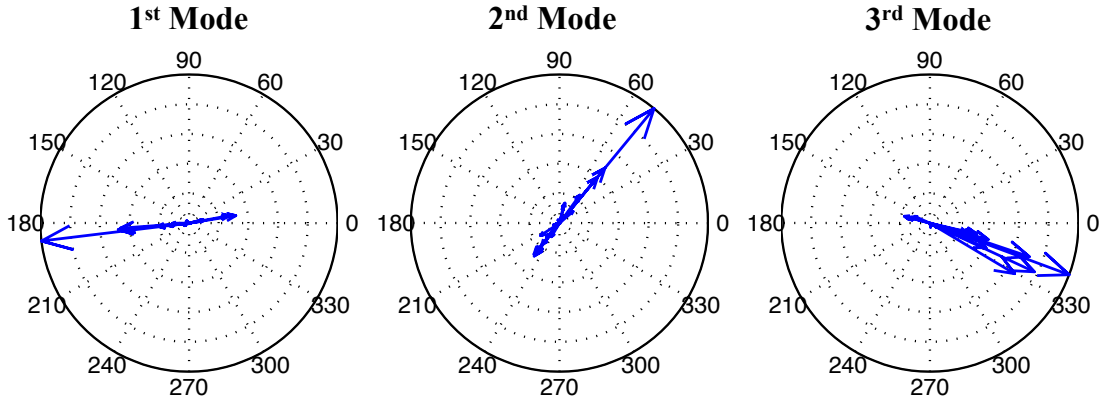

Figure 3.5. Polar plot representations of the complex-valued mode shapes identified at the reference state (1.5% g RMS WN test S0).

Table 3.2 summarizes the identified natural frequencies, damping ratios, and modal assurance criterion (MAC) values (Allemang and Brown, 1982) for the three identified

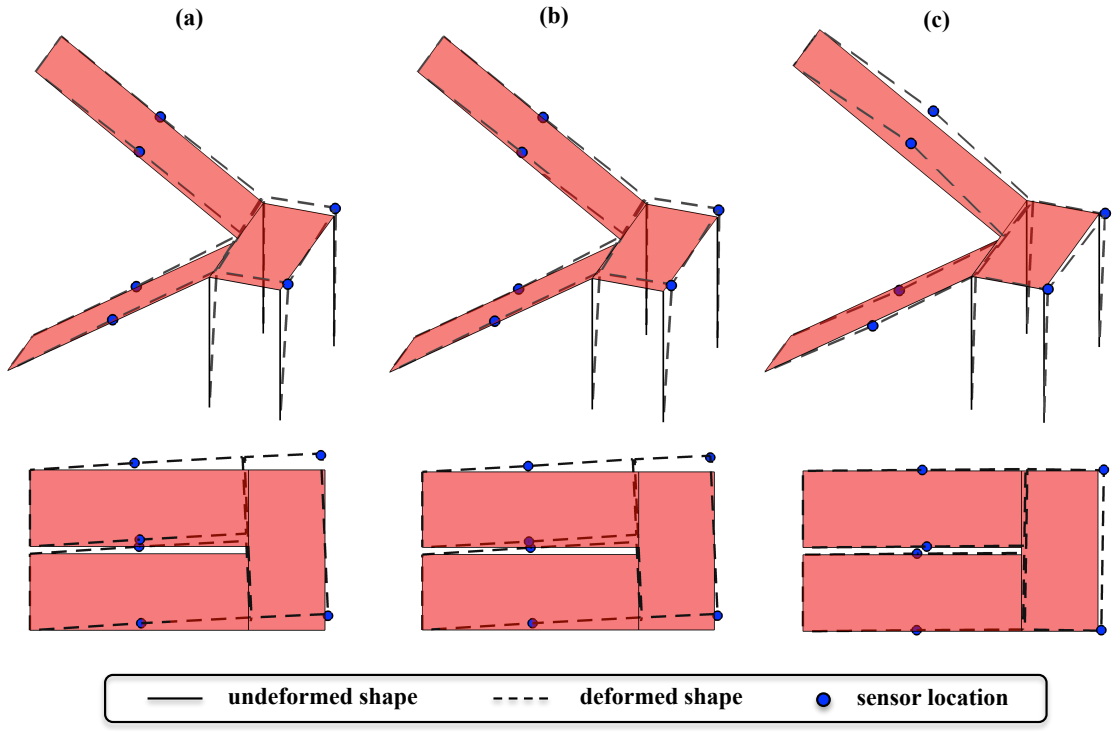

Figure 3.6. Identified mode shapes: (a) 1st mode, (b) 2nd mode, and (c) 3rd mode.

modes at different WN test states. The MAC values are computed between each identified mode shape and its counterpart identified at the reference state (1.5% g RMS WN test S0). Important observations from the modal identification results are:

1. The identified natural frequencies at state S1 remained nearly identical with those at state S0, as the building experienced very low PIDR demands (0.11%) prior to state S1 and accumulated IDR cycles (29). However, the natural frequencies slightly decrease in state S2 as the PIDR (0.32%) and the cumulative number of IDR cycles (83) increases. Although the PIDR and cumulative number of IDR cycles remained unchanged between state S2 and S3, the natural frequencies underwent further decrease at state S3. This is due to the larger amplitude of the interstory drifts during the WN test S3, since the building was fixed at its base at state S3. These observations suggest that the accumulation of IDR cycles as well as larger PIDR result in reduction of the identified natural frequencies for the system.

2. The identified damping ratios are primarily in the range of 1–5% during these WN

Table 3.2. Identified modal parameters of the stair at different WN test states.

WN Test		1st Mode			2nd Mode			3rd Mode		
State	RMS Amplitude	Frequency[1] (Hz)	ξ (%)	MAC	Frequency[1] (Hz)	ξ (%)	MAC	Frequency[1] (Hz)	ξ (%)	MAC
S0	1.5% g	8.88 [100]	4.17	1.00	11.14 [100]	4.52	1.00	19.75 [100]	1.01	1.00
	3.0% g	8.78 [98.9]	4.21	1.00	11.20 [100.5]	4.01	0.99	19.50 [98.7]	1.26	0.99
	3.5% g	8.76 [98.6]	4.10	0.99	11.10 [99.6]	3.68	0.99	19.47 [98.6]	0.72	0.99
S1	1.5% g	8.90 [100.2]	4.17	1.00	11.16 [100.2]	4.62	1.00	19.74 [99.9]	1.03	1.00
	3.0% g	8.79 [99.0]	4.21	0.99	11.21 [100.6]	4.07	0.98	19.51 [98.8]	1.27	0.99
	3.5% g	8.78 [98.9]	4.13	0.99	11.14 [100]	3.68	0.99	19.44 [98.4]	0.72	0.99
S2	1.5% g	8.53 [96.1]	5.64	0.99	11.07 [99.4]	2.32	0.96	19.02 [96.3]	1.46	0.97
	3.0% g	8.52 [95.9]	4.51	0.99	11.10 [99.6]	2.72	0.94	18.91 [95.7]	1.42	0.98
	3.5% g	8.50 [95.7]	4.71	0.98	11.03 [99.0]	2.83	0.94	18.85 [95.4]	1.29	0.94
S3	1.5% g	8.37 [94.2]	3.95	0.99	11.02 [98.9]	1.32	0.95	18.74 [94.9]	1.21	0.95
	3.0% g	8.29 [93.4]	4.85	0.99	10.90 [97.8]	2.68	0.93	18.57 [94.0]	1.63	0.94
	3.5% g	8.22 [92.6]	4.39	0.99	10.76 [96.6]	3.01	0.92	18.31 [92.7]	2.12	0.94

[1]value in the square bracket shows the frequency relative to that in the reference state (1.5% g RMS WN test S0); unit in percentage.

tests. The first two modes (torsional) present notably higher values of damping ratio than those of the third mode (longitudinal) in the reference state (1.5% g RMS WN test S0). In most cases, the identified damping ratios of the third mode slightly increased and the values of the first two modes decreased as IDR cycles accumulated. However, unlike the case of natural frequencies, the damping ratios do not consistently correlate with the increase of PIDR or the accumulation of IDR cycles.

3. The MAC values for the three identified modes are reasonably close to unity in the first two states (S0 and S1). During the last two states (S2 and S3), the calculated MAC values of the higher modes slightly deviate from unity as a result of the accumulated IDR cycles and the increased PIDR. However, all identified MAC values remain larger than 0.9, indicating that the identified mode shapes are consistent with those at the respective identified reference state (1.5% g RMS WN test S0).

4. The experimentally identified modal parameters (e.g., frequency, damping ratio, and mode shape) can be used for verification of numerical models of the stairs and therefore improving the predictive capacity of such models when used in time history analysis. However, it is noteworthy that the parameters identified using the DSI system identification method are developed based on linear system theory, and therefore the identified results represent those of an equivalent linear system at their specific states. The dynamic response of the stairs is nonlinear from the onset of loading even when subjected to low-amplitude excitations. The physical dissipative sources of nonlinearity (e.g., friction, yielding, and contact) are lumped into the identified equivalent viscous damping. Therefore, direct application of the identified damping ratios in structural modeling for nonlinear time history analysis may lead to erroneous results.

3.4 Earthquake Test Results

3.4.1 Physical observations

Damage Metrics and Repair Actions

Post-shaking inspection of the stairs were conducted at each inspection phase to characterize their physical damage. Damage documentation relied upon visual inspections as well as detailed photographs, videos, and notes. It is noted that inspections of the weld connections at the bottom of the landing posts were not possible since they were enclosed within the partition walls. As shown in Figure 3.7, five common types of damage mechanisms were observed during the tests. These are categorized into three distinct damage states (DSs) according to their implications on stair functionality and repair actions. The definitions of the damage states and the physical description of the observed damage are summarized in Table 3.3, and the repair actions implemented in these tests for the different damage mechanisms are illustrated in Figure 3.8. It is noted that, while no repair action was taken for minor and moderate damage during these tests, severe damage to the stairs was repaired immediately to restore safe access to the test building and to allow the execution of subsequent tests.

Table 3.3. Stair damage states and physical descriptions of the damage mechanisms.

Damage state	Damage implications and corresponding repair actions	Physical descriptions of the damage mechanisms
DS-1 (minor)	No immediate repair needed for continued service	Closure plate detachment (Figure 3.7a); handrail fracture (Figure 3.7b)
DS-2 (moderate)	Repair needed with minimal disruption to service, safe egress prior to repair is possible by occupants	Connection plate yielding (Figure 3.7d); anchor bolt washer plate yielding
DS-3 (severe)	Immediate repair needed with downtime required to assure service (this state may be unsafe for egress)	Connection weld fracture (Figure 3.7c); flight detachment (Figure 3.7e)

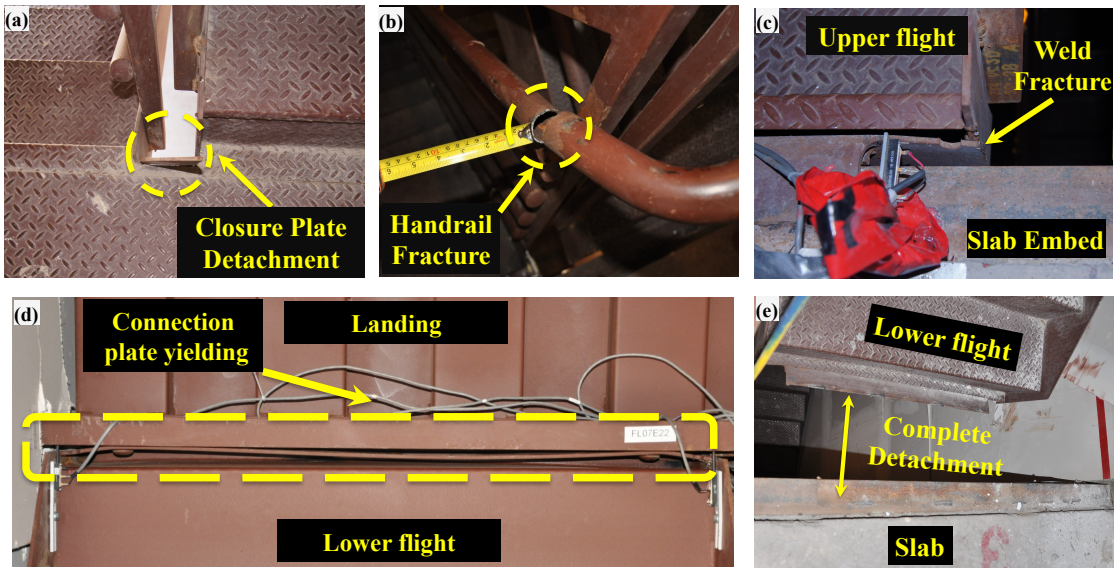

Figure 3.7. Examples of observed stair damage: (a) closure plate detachment (DS-1; photograph taken at the landing between level 1 and 2 after test FB-4), (b) handrail fracture (DS-1; photograph taken at level 3 after test FB-5), (c) upper flight connection angle weld fracture (DS-3; photograph taken at level 3 following test FB-4), (d) plastic yielding of the connection plate between the landing and lower flight (DS-2; photograph showing the bottom view of the landing at level 2 following test FB-5), and (e) lower flight detachment and complete loss of vertical support (DS-3; photograph taken at level 3 after test FB-6).

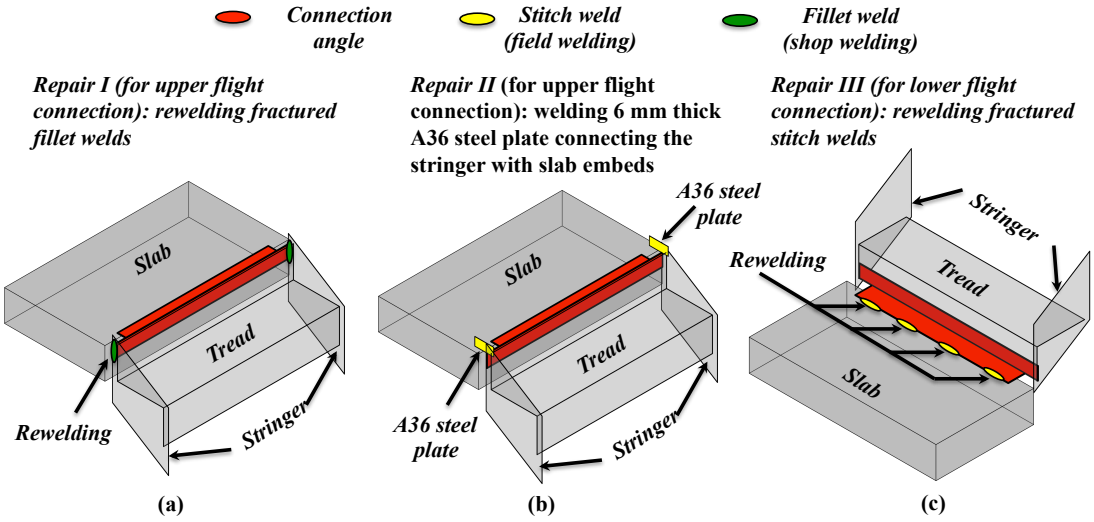

Figure 3.8. Stair repair actions: (a) R-I (b) R-II, and (c) R-III (only the welds that require repair are shown in the figure).

Damage Progression

No physical damage to the stairs was observed in the BI test phase and the first three FB tests, as the building drift demands remained relatively low (PIDR < 1%). Damage to the stairs initiated during test FB-4 and became extensive in the last two FB tests. Figure 3.9 illustrates the progression of stair damage as observed post-shake at each of the last three FB tests and the associated repair actions. The associated PIDRs during the specified seismic tests (as boxed and in black) and the interstory drift ratios (IDRs) related to the exact time of damage occurrence (in parenthesis and in red when available) are also presented in this figure.

FB-4:ICA100

Inspection following test FB-4 indicated a detached closure plate (DS-1) at the landing at level 1 (Figure 3.10a) as well as the upper connection vertical fillet weld fractures (DS-3) at levels 2 (Figure 3.10b) and 4. The details of the stair damage during test FB-4 are summarized in Table 3.4. It is noted that although complete detachment and subsequent loss of vertical support did not occur, the service capacity of the stair was compromised, as its lateral connectivity to the building was non-existent at these two levels. The two cases of weld fracture were repaired prior to test FB-5: i) welding steel plates between the upper flight stringer and the slab embed (R-II) at the level 2 (Figure 3.10c), and ii) re-welding of the upper connection to the upper flight stringer (R-I) at the level 4 (Figure 3.10d). The damage to the stairs and the associated building PIDR during test FB-4 are summarized in Table 3.4.

Table 3.4. Summary of detected stair damage and the associated building PIDR during test FB-4.

Location	Damage mode	Damage state	PIDR (%)	Repair action
Landing (Level 1)	Closure plate detachment	Minor	1.24	No repair
Upper flight (Level 2)	Flight-to-building connection plate weld fracture	Severe	1.41	R-III
Upper flight (Level 3)	Flight-to-building connection plate weld fracture	Severe	0.74	R-III

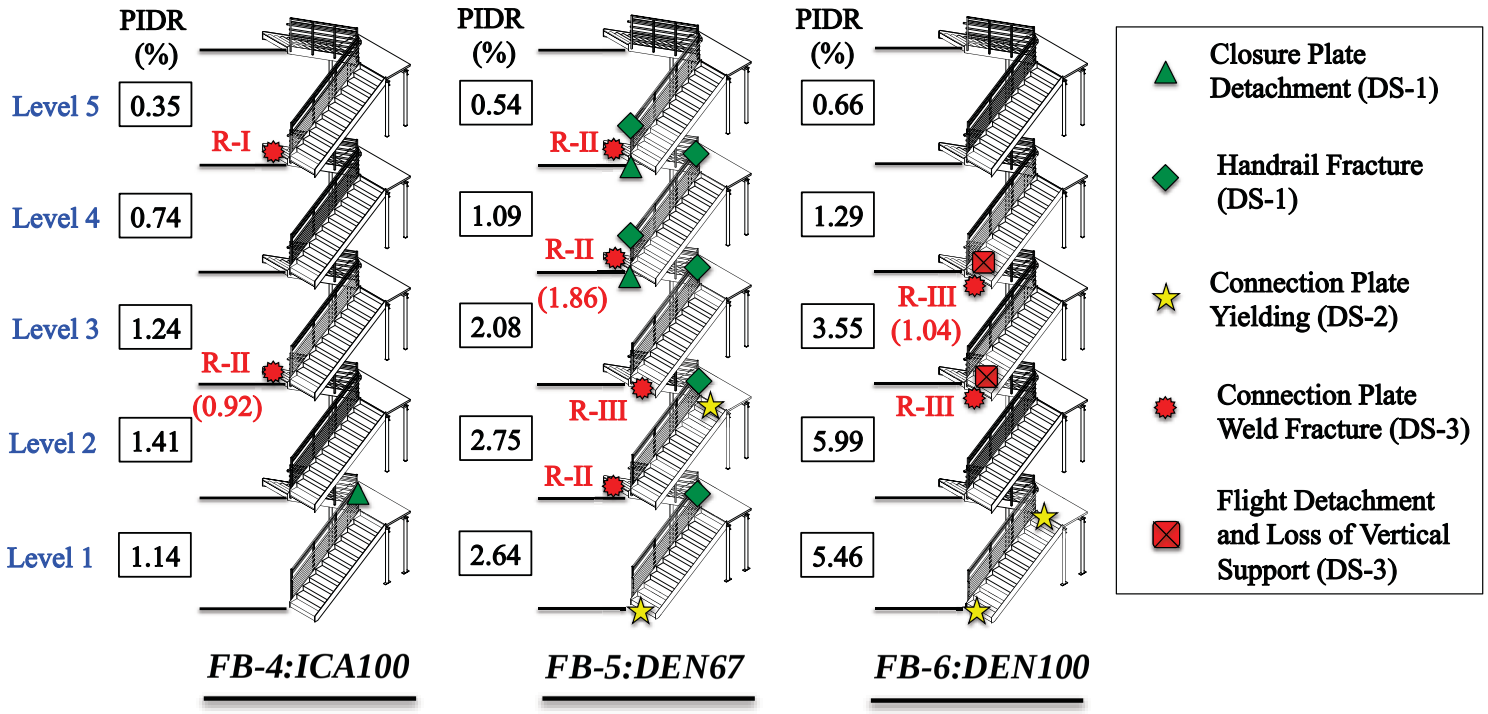

Figure 3.9. Stair damage progression during the last three FB tests (notes: damage types are differentiated by color and marker shape, i.e, red for DS-3, yellow for DS-2, and green for DS-1; boxed values represent PIDRs during the specified seismic tests and are shown in black, and red values in parenthesis represent the actual IDR at damage instance).

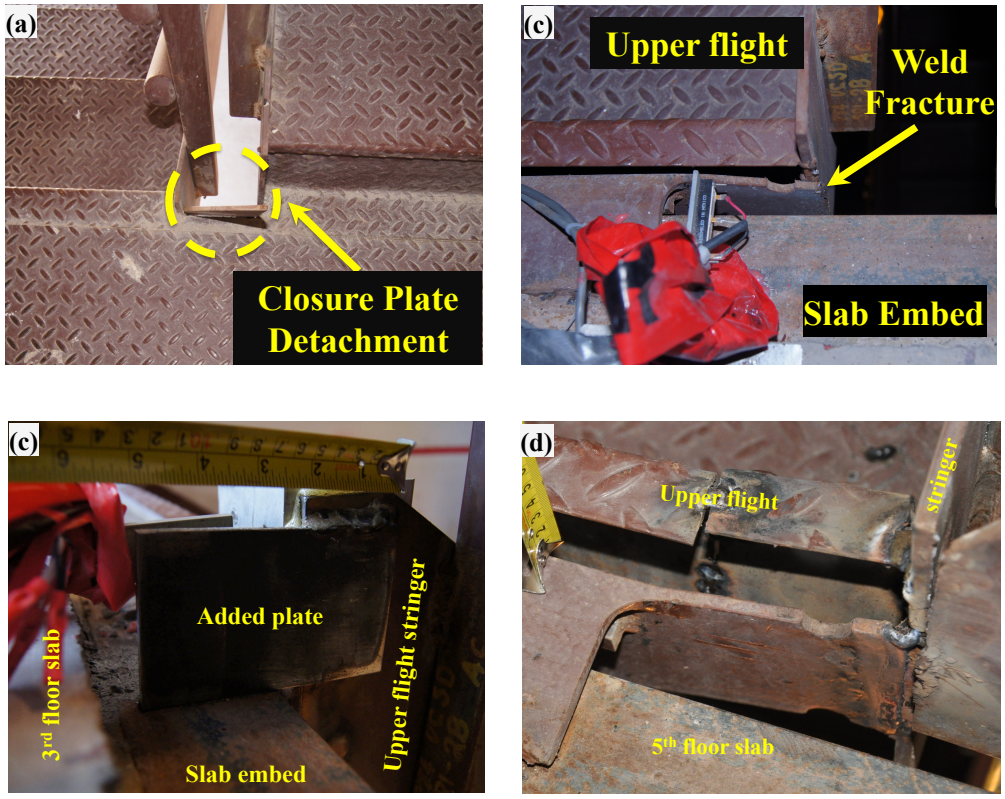

Figure 3.10. Observed stair damage following test FB-4: (a) closure plate detachment (DS-1; photograph taken at the landing between level 1 and 2), (b) connection plate weld fracture (DS-3; photograph taken at level 3), (c) repaired connection plate on the northern side of the upper flight, and (d) repaired condition on the southern side of the upper flight).

FB-5:DEN67

Damage to the stairs was distributed at various locations in the form of closure plate detachment (DS-1), handrail fracture (DS-1) (Figure 3.11a), connection plate yielding (DS-2) (Figure 3.11c), and connection weld fracture (DS-3). Table 3.5 summarizes the the stair damage as detected following test FB-5 and the associated repair actions. Severe damage that requires immediate repair included: i) the lower connection stitch weld fracture (albeit the lower flight did not detached from the slab embed) at level 3 (DS-3), and ii) the upper connection vertical fillet weld fractures (DS-3) at levels 1, 3, and 4. Repair of the lower connection stitch weld fracture was conducted by re-welding of the lower connection to the slab embed (R-III) (3.11b), and the three cases of the upper connection vertical weld fracture were repaired by R-II. In addition, plastic

yielding occurred at the connection plate (DS-2) between the landing and lower flight at level 2 as well as washer plates (DS-2) at the lower flight to landing connection at level 1. The damage to the stairs and the associated building PIDR during test FB-5 are summarized in Table 3.5.

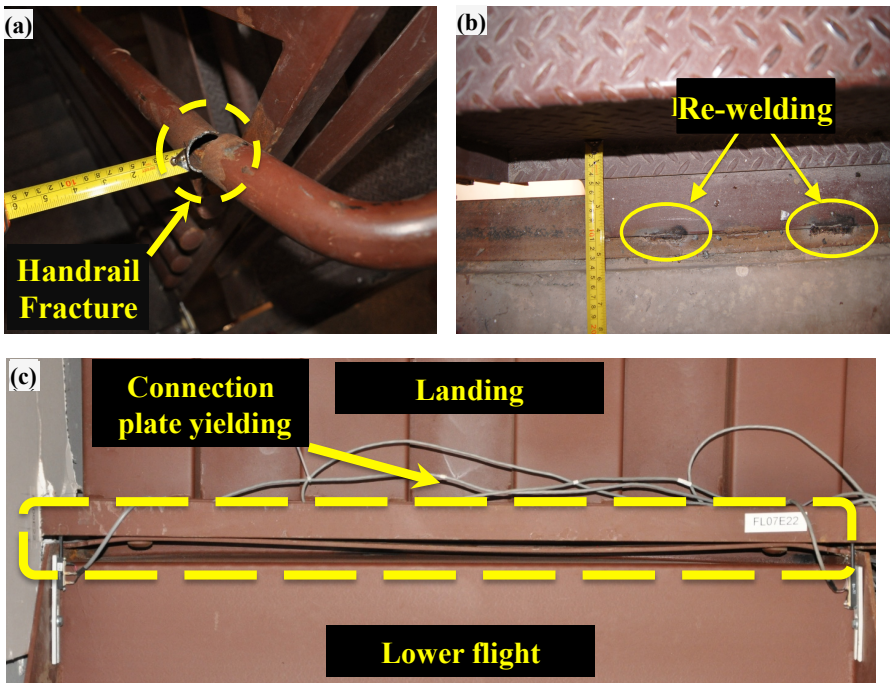

Figure 3.11. Observed stair damage following test FB-5: (a) handrail (DS-1; photograph taken at the landing between level 1 and 2), (b) connection plate weld fracture (DS-3; photograph taken at level 3), and (c) repaired connection plate on the northern side of the upper flight.

FB-6:DEN100

Table 3.6 summarizes the the stair damage as detected following test FB-6 and the associated repair actions. The lower flights at levels 3 and 4 completely detached from the slab embeds (DS-3) and were no longer vertically supported on the slab due to complete weld failure (Figure 3.12b). Repair of the detached flights involved re-positioning the flights in place and re-welding the flights to the slab embeds (R-III). Furthermore, plastic yielding of the connection plate (DS-2) between the landing and lower flight at level 1 was detected, and the washer plates at the lower flight to landing connection at level 1 suffered continued plastic deformation (DS-2) (Figure 3.12a).

Table 3.5. Summary of detected stair damage and the associated building PIDR during test FB-5.

Location	Damage mode	Damage state	PIDR (%)	Repair action
Floor 4	Closure plate detachment	Minor	1.09	No repair
Floor 5	Closure plate detachment	Minor	0.54	No repair
Mid-level 1	Handrail fracture	Minor	2.64	No repair
Mid-level 3	Handrail fracture	Minor	2.08	No repair
Floor 4	Handrail fracture	Minor	2.08	No repair
Mid-level 4	Handrail fracture	Minor	1.09	No repair
Floor 5	Handrail fracture	Minor	1.09	No repair
Lower flight (Level 1)	flight-to-building connection plate plastic yielding	Minor	2.64	No repair
Lower flight (Level 2)	flight-to-landing connection plate plastic yielding	Moderate	2.75	No repair
Upper flight Level 2	flight-to-building connection plate weld fracture	Severe	2.64	R-III
Upper flight Level 3	flight-to-building connection plate weld fracture	Severe	2.08	R-III

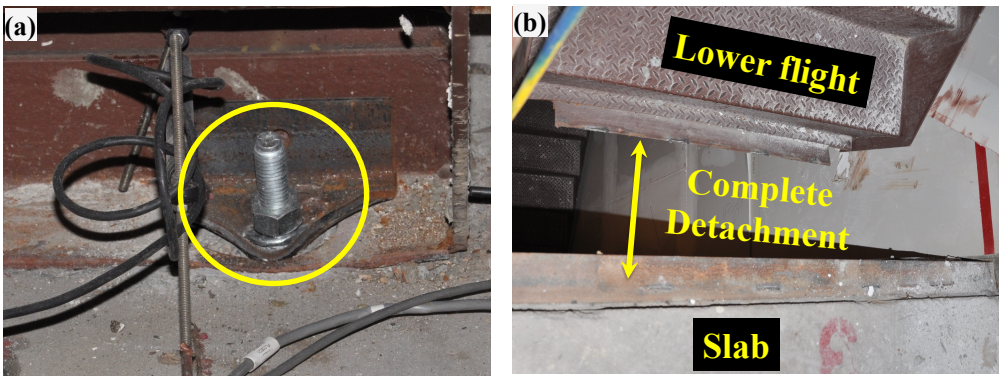

Figure 3.12. Detected stair damage following test FB-6: (a) plastic yielding of the washer plate at the lower flight to landing connection at floor 1 (DS-2), and (b) lower flight detachment (DS-3; photograph taken at level 3).

Table 3.6. Summary of detected stair damage and the associated building PIDR during test FB-6.

Location	Damage mode	Damage state	PIDR (%)	Repair action
Lower flight (Level 1)	flight-to-building connection plate plastic yielding	Moderate	5.99	No repair
Lower flight (Level 1)	flight-to-landing connection plate plastic yielding	Moderate	5.99	No repair
Lower flight Level 3	Lower flight detachment	Severe	3.55	R-III
Lower flight Level 3	Lower flight detachment	Severe	1.29	R-III

Summary of Physical Damage during the Earthquake Tests

These physical damage observations highlight that stair damage was sensitive to interstory drift demands of the building. It is noted that test FB-5 represents an earthquake scenario that achieved the design performance objectives of the building (PIDR of 2.5%), and that this design target PIDR is comparable with prescribed values in ASCE 7-10 (ASCE, 2010). This test (FB-5) coincidentally also caused four instances of severe damage to the stairs, including at levels of PIDR below the 2.5% performance target.

During all earthquake tests, eight instances of severe damage were detected at all levels except at level 5. Severe damage to the stairs at each level initiated consistently in the form of upper flight connection angle vertical fillet weld fracture, with associated PIDRs of: 2.64% at level 1 (test FB-5), 1.41% at level 2 (test FB-4), 2.08% at level 3 (test FB-5), and 0.74% at level 4 (test FB-4). Notably, even prior to attainment of the building design target PIDR, safe egress from the building was compromised during test FB-4 as a result of the two occurrences of upper flight connection angle vertical fillet weld fracture. The associated PIDRs which caused this severe damage (0.74% and 1.41%) were much lower than the design performance target (2.5%). During the last two FB tests, severe damage to the stairs continued to occur in the form of upper flight connection angle vertical fillet weld fracture, lower flight connection angle stitch weld fracture, and ultimately complete lower flight detachment that rendered the stairs

completely inoperable. It is noteworthy that ground motions as intense as those of the last two fixed-base tests can result in the development of a double-story mechanism, also known as an intermediate failure mechanism (Kuntz and Browning, 2003; Moehle et al., 2008), in reinforced concrete moment resisting frames designed according to the ACI-318 requirements (ACI, 2014). This aspect further complicates the seismic design of stairs and other vertically distributed nonstructural systems, since large drift demands tend to concentrate at only a few levels of a special moment frame building.

3.4.2 Identification of Time Instance of Damage Occurrence

The PIDR represents the absolute maximum of an interstory drift history and may not coincide with the IDR at which the most pronounced damage occurs. Fortunately, during these tests, additional time-synchronized measurement sources were available at select locations to allow identification of time instances of the stair damage. Table 3.7 summarizes five instances of moderate and severe damage to the stairs during the last three FB tests identified using the data measured by the displacement transducers and the video camera monitoring the stair connections.

As shown in Table 3.7, two instances of upper flight connection angle vertical weld fracture were identified using the data measured by the displacement transducers and the video camera monitoring the stair connection. The IDR cycles are determined using the rainflow counting method Downing and Socie (1982). These cycles account for the contribution of both the seismic tests and the low-amplitude WN base excitation tests from the beginning of the test program until the occurrence of the damage. Figure 3.13 provides the distributions of the IDR cycles as well as the associated IDR time histories of the two damage instances. In the rain flow counting, the IDR bins are centered at values starting from 0.1% to the maximum IDR at a constant width of 0.1% (e.g., the first bin represents a range between 0.05% and 0.15%). IDR cycles less than 0.05% are excluded from the cycle counting, since these cycles are considered insignificant to affect the stair behavior. In addition, cycles in the 0.4% or larger IDR bins are defined as high-amplitude IDR cycles as numerical simulation of the stair suggests that plastic yielding of the upper flight connection plate occurs at an IDR of about 0.3%–0.4%.

Table 3.7. Identified damage instances.

Test	Location	Damage mode	Damage state	Data source	$PIDR$ (%) [time (sec)]	IDR_{damage} (%) [time (sec)]	Δ^{conn}_{damage} (mm) [2] [time (sec)]
FB-4	Upper flight (Level 2)	Flight-to-building connection plate weld fracture	Severe	Linear pot	1.41 [29.34]	0.92 [27.56]	17.4 [27.56]
FB-5	Lower flight (Level 1)	Flight-to-building connection plate plastic yielding	Moderate	Linear pot	2.64 [46.42]	2.33 [38.78]	10.5 [38.78]
FB-5	Lower flight (Level 2)	Flight-to-landing connection plate plastic yielding	Moderate	Linear pot	2.75 [46.45]	2.39 [38.76]	16.5 [38.76]
FB-5	Upper flight (Level 3)	Flight-to-building connection plate weld fracture	Severe	Video camera	2.08 [46.42]	1.86 [38.72]	/ /
FB-6	Lower flight (Level 4)	Flight-to-building connection plate weld fracture	Severe	Video camera	1.29 [38.26]	1.04 [41.50]	/ /

[1]Data source refers to the measurement source to obtain the IDR_{damage} (the IDR at the time instance of damage); [2]Δ^{conn}_{damage} refers to the longitudinal connection deformation at the time instance of damage.

As shown in Figure 3.13, the majority of low-amplitude cycles (0.1%–0.3% bin) were contributed from either the WN tests or the BI tests, while high-amplitude cycles (0.4%-and-larger bin) were exclusively attributed to the FB tests. It is also shown in Figure 3.13 that the stair at level 3 experienced 66 high-amplitude IDR cycles prior to the weld fracture, as compared to 33.5 cycles for the identical damage instance at level 2. Although the two damage instances may not provide adequate information on the low-cycle fatigue behavior of the welds, these observations do not warrant a clear trend of loading histories on the weld fracture, since the stair that was damaged at a higher IDR value (1.86%) underwent twice as many high-amplitude cycles as the one damaged at a smaller value (0.92%).

Table 3.8. Damage instances for the two upper flight connection angle vertical weld fracture failures (DS-3).

Test	Location	Data source[1]	$PIDR$ (%) [time (sec)]	IDR_{damage} (%) [time (sec)]	IDR Cycles	
					Total	High-amplitude
FB-4	Level 2	LP	1.41 [29.34]	0.92 [27.56]	668	33.5
FB-5	Level 3	Cam.	2.08 [46.42]	1.86 [38.72]	960	66.0

[1]Data source refers to the measurement source to obtain the IDR_{damage} (the IDR at the time instance of damage); LP denotes linear potentiometer, Cam. denotes video camera.

3.4.3 Measured Response

Acceleration Response

The absolute acceleration time histories of the stair landing at level 2 during tests FB-1 and FB-3 and the corresponding Fourier amplitude spectra (FAS) are presented in Figure 3.14. The measured acceleration responses were filtered with a fourth-order Butterworth filter with band-pass frequencies between 0.25 and 25 Hz. The longitudinal accelerations at the two corners of the stair landing (A-L-3 and A-L-4, see Figure 3.3a) were comparable, and their amplitudes were both similar to those at the upper and lower floors Pantoli et al. (2013a). Despite the insignificantly small floor excitations in the transverse direction, the amplitude of the transverse landing acceleration (A-T-2) is even

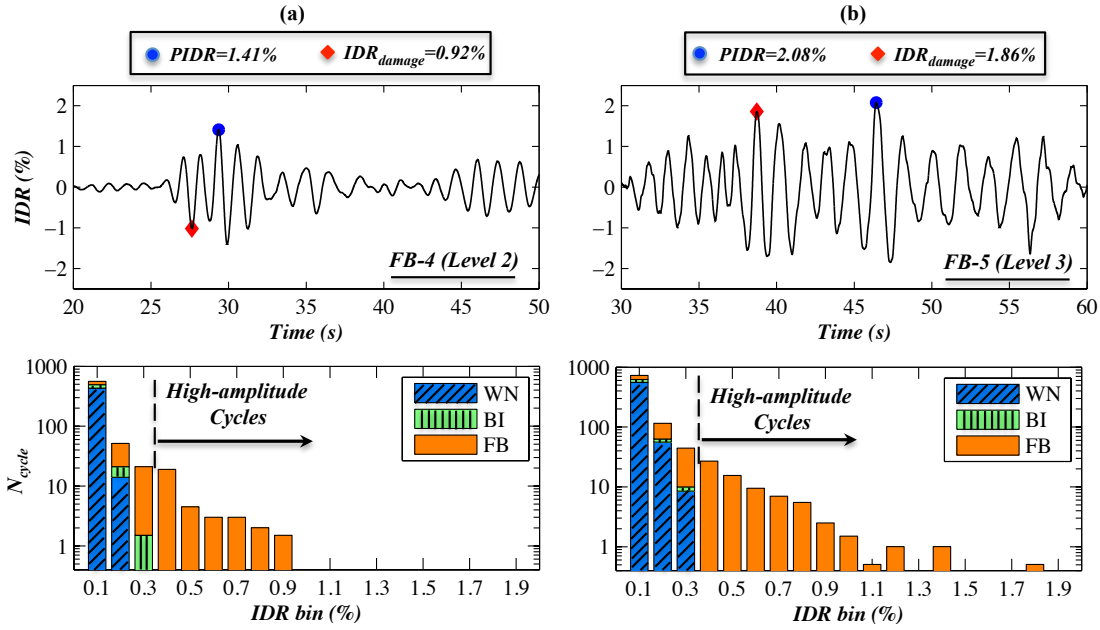

Figure 3.13. Interstory drift response and the accumulated IDR cycle distribution for the two instances of upper flight connection angle vertical weld fracture: (a) FB-4, and (b) FB-5.

larger than its longitudinal counterparts (A-L-3 and A-L-4). In addition, it is observed that the FAS peak of the landing longitudinal acceleration responses occur at around 1 Hz, which correspond to the first longitudinal vibration mode of the building at this damage state, while the landing transverse acceleration response was predominately attributed to the first torsional vibration mode of the stair at a higher frequency around 7.5 Hz. This frequency also corresponds to the higher modes of the building in its fixed-base configuration (Astroza et al., 2015).

Table 3.9 summarizes the peak component accelerations (PCAs) of the stair landing at level 2 and the PFAs at the corresponding floors for all base-isolated and the first three fixed-base seismic tests. In this case, the PCA is defined as the absolute maximum of the landing acceleration time history. It is noted, however, that the landing observed frequent high-frequency acceleration spikes during the last three FB tests as a result of pounding of the stair with its surrounding partition walls as well as abrupt connection weld fractures. These high frequency responses are not representative of the dynamic characteristics of the stairs and are instead a result of the practical configuration of the

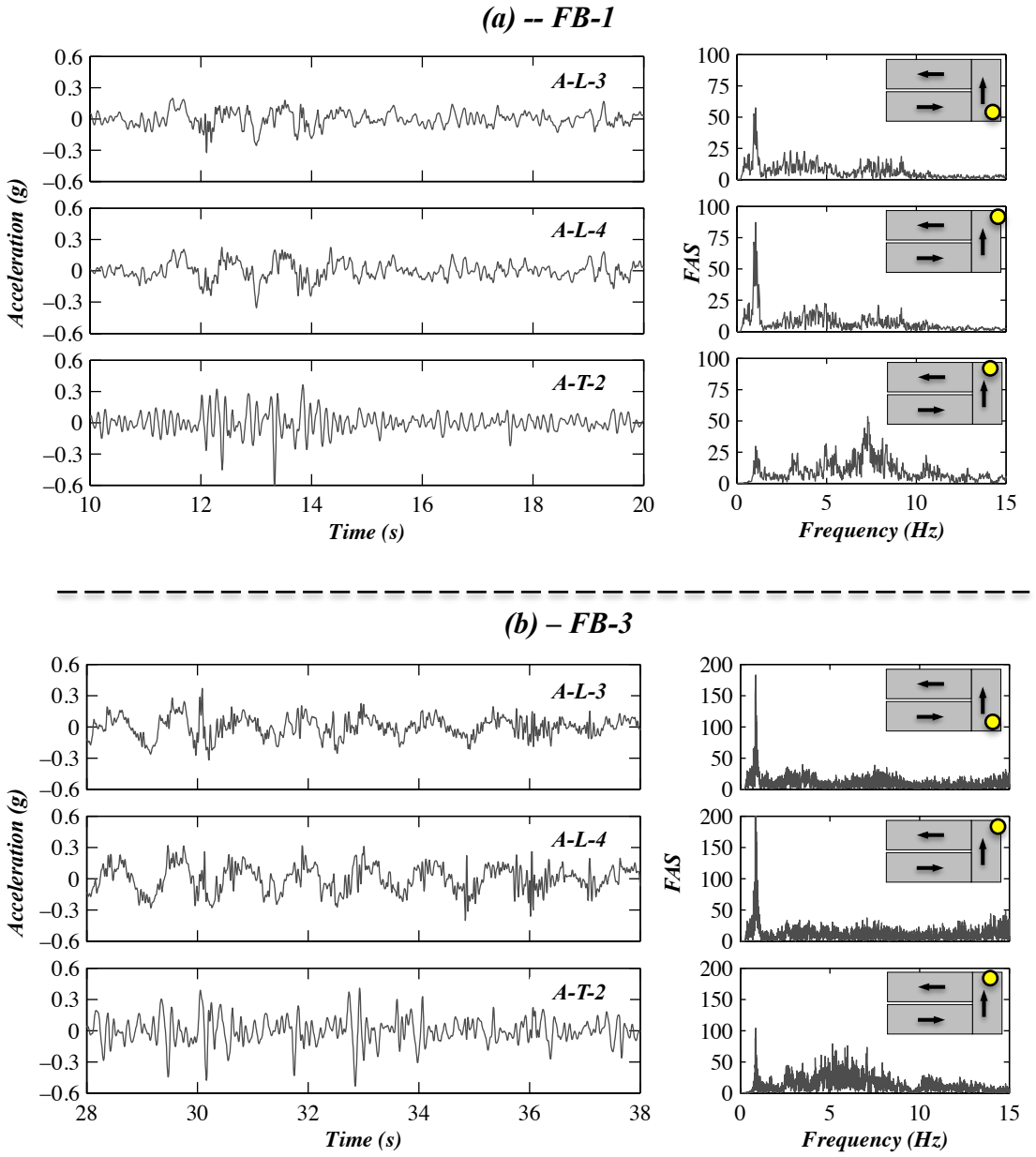

Figure 3.14. Absolute acceleration time histories and the associated Fourier amplitude spectra of the stair landing at level 2: (a) test FB-1, and (b) test FB-3.

Table 3.9. Peak acceleration responses of the stair landing at level 2.

Test name	PFA		$PCA_{long}^{landing}$	$PCA_{trans}^{landing}$	$\frac{PCA_{long}^{landing}}{PFA_{ave}}$	$\frac{PCA_{trans}^{landing}}{PCA_{long}^{landing}}$
	2nd floor (g)	3rd floor (g)	(g)	(g)	(%)	(%)
BI-1:CNP100	0.08	0.07	0.07	0.02	92	35
BI-2:LAC100	0.09	0.08	0.08	0.03	88	39
BI-3:LAC100	0.09	0.08	0.08	0.03	89	42
BI-4:SP100	0.08	0.09	0.09	0.04	99	42
BI-5:ICA50	0.07	0.08	0.08	0.02	98	22
BI-6:ICA100	0.14	0.14	0.14	0.03	97	22
BI-7:ICA140	0.20	0.21	0.20	0.08	97	41
FB-1:CNP100	0.27	0.32	0.36	0.59	115	179
FB-2:LAC100	0.28	0.31	0.28	0.44	98	164
FB-3:ICA50	0.24	0.35	0.40	0.53	131	138

Notes: PFA – peak floor acceleration; PFA_{ave} – peak floor acceleration as averaged between the floors above and below the landings of level 2; $PCA_{long}^{landing}$ – peak component acceleration of the stair landing in the longitudinal direction; $PCA_{trans}^{landing}$ – peak component acceleration of the stair landing in the transverse direction.

stairs with their adjacent systems. As a result, these values are excluded from the table. During the base-isolated tests, the acceleration response of the landing underwent no amplification in the longitudinal direction, as the ratios between the landing PCAs in this direction and the corresponding peak floor accelerations were all below 100%. In addition, the landing PCAs in the transverse direction were 20–40% of their longitudinal counterparts during the base-isolated tests (Figure 3.15a). In contrast, the landing accelerations were amplified notably while the building was fixed at its base, with amplifications as high as 30%. In addition, the PCAs in the transverse direction exceeded their longitudinal counterparts by about 40–80% (Figure 3.15b). The distinction of the acceleration responses between the base-isolated and fixed-base tests can be attributed to the period shift of the test building, since the predominant long period response of the BI building was less likely to excite the higher frequency stair torsional response than the response of the fixed-base building.

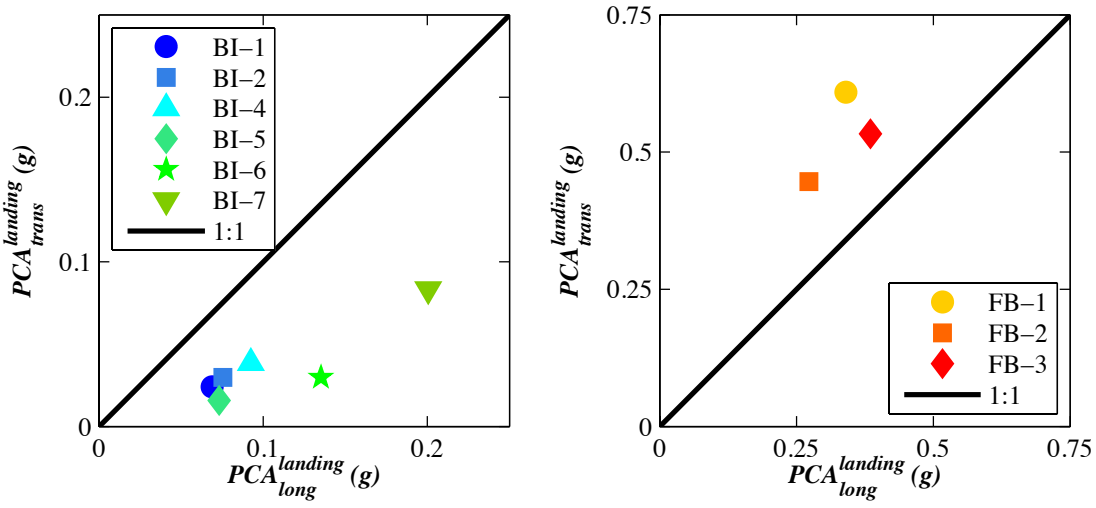

Figure 3.15. Comparison of longitudinal and transverse PCAs of the stair landing at level 2: (a) BI test phase, and (b) the first three FB tests.

Displacement Response

Figures 3.16 shows the displacement time histories of the stair landing at level 2 relative to the lower (second) floor of the building as well as the interstory drifts of level 2 during tests FB-1 and FB-3. The time instances of the positive (red dot) and

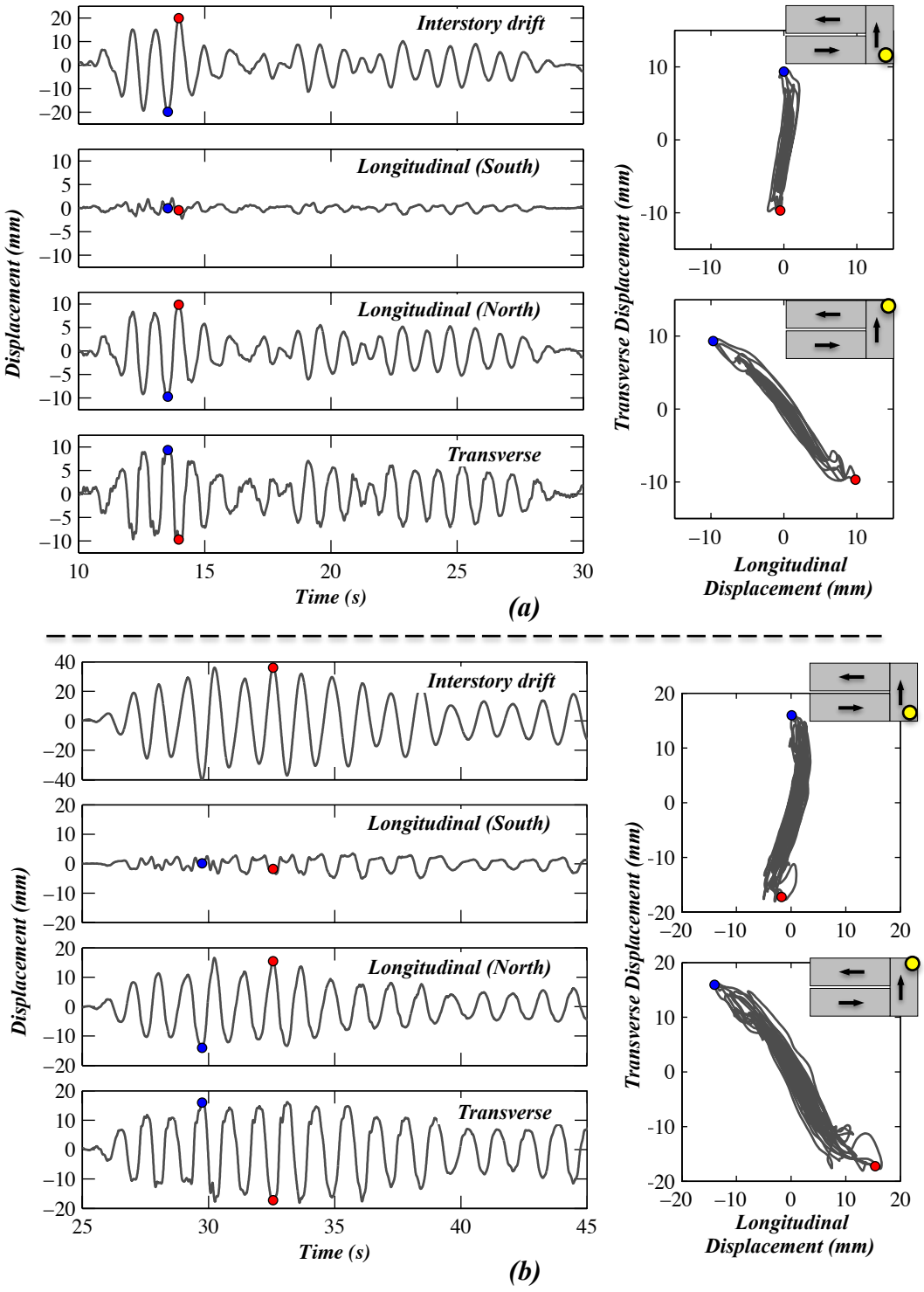

Figure 3.16. Displacement responses of the stair landing at level 2 relative to the lower floor during test FB-1 (note: red dot denotes the positive interstory drift peak and blue dot denotes the negative peak).

negative (blue dots) peak interstory drift response are correlated with the landing displacement responses. As shown in the figure, the longitudinal landing displacements at the two corners differed notably. While the peak relative displacements were about 10 mm (50% of the interstory drift) on the north corner, the response was much smaller at the south corner of the landing and the peaks did not occurred coincidently with those of the interstory drift response. In addition, the transverse landing displacement was as large as the longitudinal response at the north corner. Figure 3.16 also presents the bi-directional displacement responses at the two corners of the landing. It is clearly shown that the landing was subjected to considerable torsional response. While the relative displacement was primarily in the transverse direction at the south corner, the north corner of the landing moved diagonally as the relative displacements were similar in the two orthogonal directions. This can be attributed to the fact that the upper flight-to-building connection was much more deformable than the lower flight-to-building connection, and therefore lead to landing torsional movement against the landing-to-lower flight connection.

Connection Deformation Response

Figures 3.17 and 3.18 show the longitudinal connection deformation responses of the stair at level 2 during tests FB-1 and FB-3, respectively. These responses were measured directly using displacement transducers (D-L-1 to D-L-8), and they were filtered with a low-pass fourth-order Butterworth filter with a corner frequency at 25 Hz. As shown in the figure, the deformation of the upper flight-to-building connection was about 16 mm (about 30% of the interstory drift at level 2) and were much larger than that of the lower flight-to-building connection. It is noted, however, that D-L-1 failed to record the connection deformation shortly after the negative peak interstory drift occurred. In addition, comparison of the connection deformation responses to the peak interstory drifts suggests that the two flight-to-building connection deformation responses were in the complete reversed direction. The flight-to-landing connection deformations were also small compared to those of the upper flight-to-building connection. It is noteworthy that the repair action R-II (Figure 3.8b) of the upper flight-to-slab connection for the stair at level 2 immediately following test FB-4 modified the original deformation mechanism

of the stair system. Absent the intended yielding mechanism at the upper flight-to-building connection due to the repair, the relative deformation of the other connections increased significantly during the last two FB tests and led to plastic yielding of the connection plate between the lower flight and the landing during test FB-5 (Figure 3.7d).

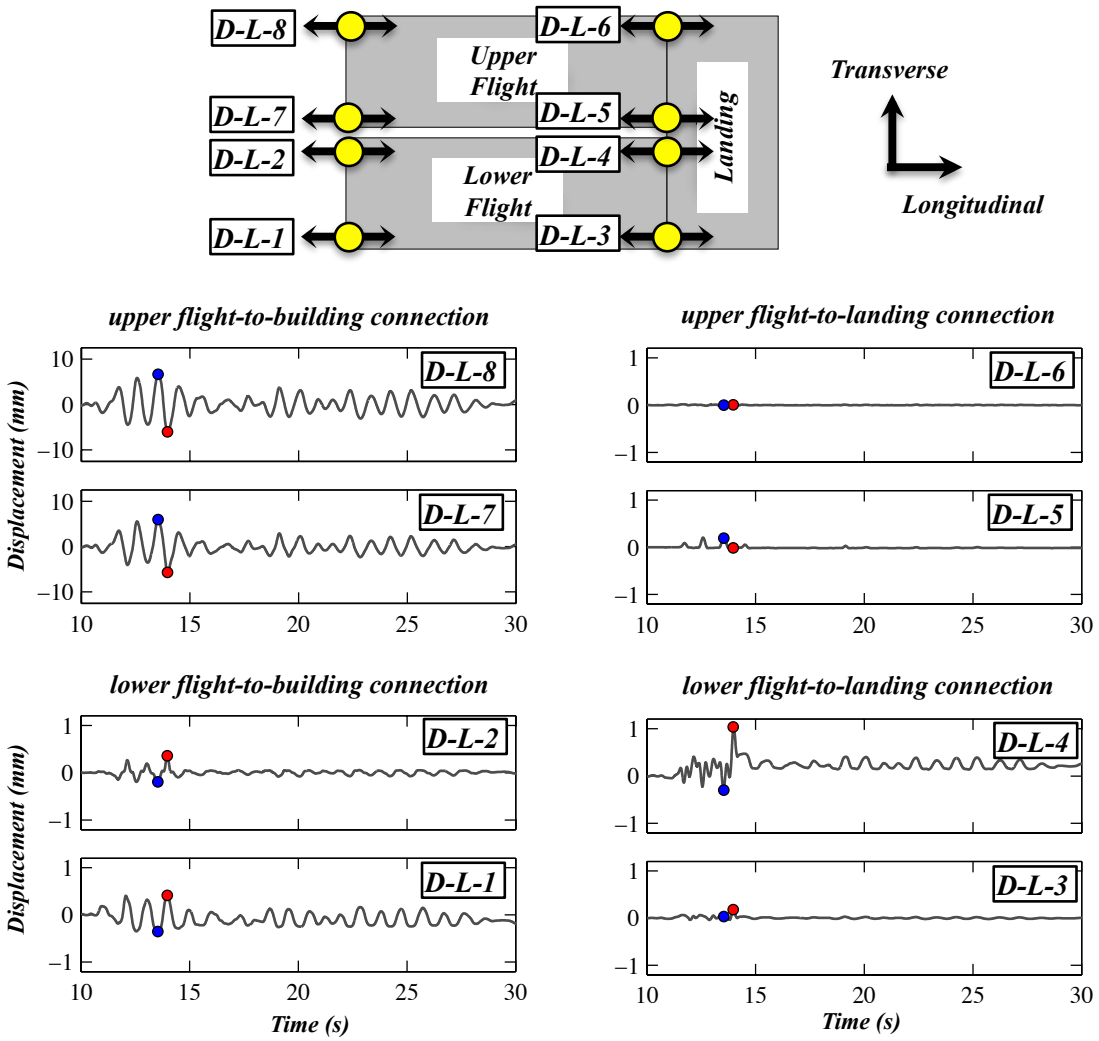

Figure 3.17. Longitudinal connection deformation time histories of the stair at level 2 during test FB-1 (note: red dot denotes the positive interstory drift peak and blue dot denotes the negative peak).

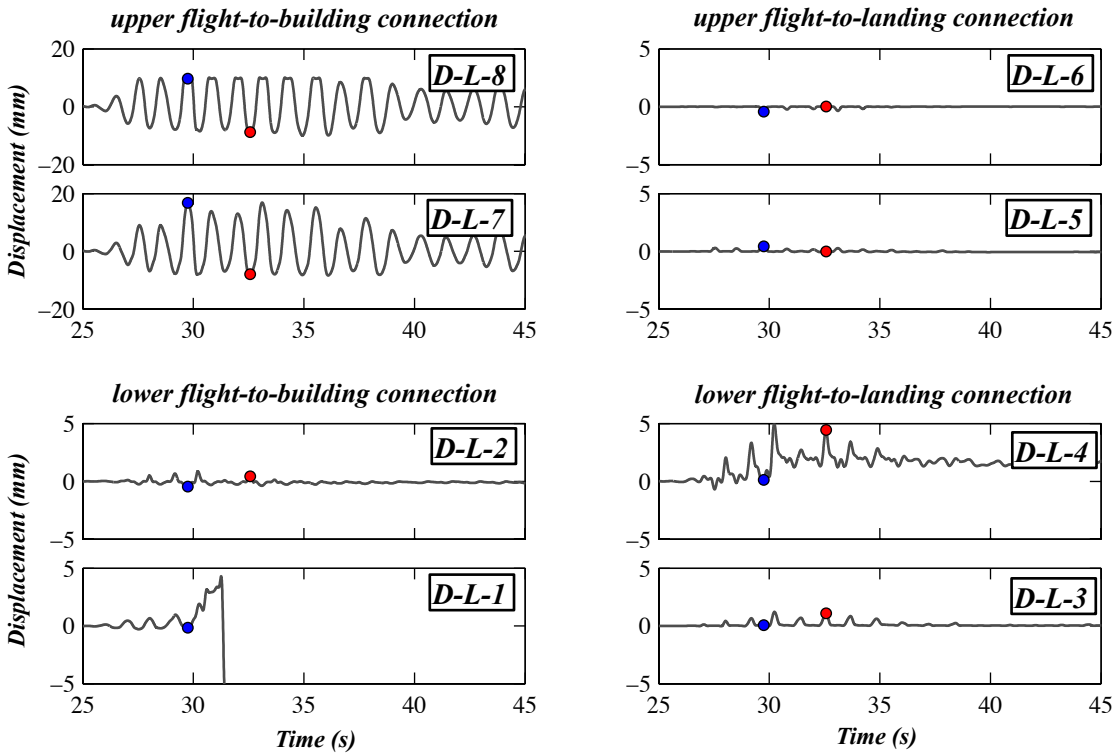

Figure 3.18. Longitudinal connection deformation time histories of the stair at level 2 during test FB-3 (note: red dot denotes the positive interstory drift peak and blue dot denotes the negative peak).

Discussion of the Displacement Responses of the Stair System

Prior to the onset of severe damage to the stair, the measured responses indicate that deformation of the stair at level 2 is characterized by the landing torsional movement as well as the upper flight-to-building connection deformation. Table 3.10 summarizes the peak landing displacements relative to the lower floor and the upper flight-to-building connection deformation at level 2 in all BI and the first three FB tests. These responses are compared with the associated peak interstory drifts (PIDs). It is observed that the peak landing displacements relative to the lower floor were very similar in the two orthogonal directions in all these tests. While these displacements were about 20–30% those of the interstory drifts in the BI tests, the ratio increased to 45–50% in the first three FB tests (Figure 3.19). In addition, the upper flight to building connection deformation consistently accounted for more than 30% of the interstory drift in each of the first three FB tests.

Table 3.10. Peak responses of the landing displacement relative to the lower floor and the upper flight-to-slab connection deformation of the stair at level 2.

Test name	$PIDR$ (%)	PID (mm)	$\Delta_{long}^{landing}$ (mm)	$\frac{\Delta_{long}^{landing}}{PID}$ (%)	$\Delta_{trans}^{landing}$ (mm)	$\frac{\Delta_{trans}^{landing}}{PID}$ (%)	Δ^{conn} (mm)	$\frac{\Delta^{conn}}{PID}$ (%)
BI-1	0.08	3.5	0.9	26	0.9	26	/	/
BI-2	0.10	4.3	1.0	22	0.8	18	/	/
BI-3	0.11	4.5	1.0	21	0.7	16	/	/
BI-4	0.10	4.2	1.4	33	1.4	32	/	/
BI-5	0.09	3.9	0.7	19	0.7	19	/	/
BI-6	0.19	8.0	1.5	18	1.4	17	/	/
BI-7	0.32	13.6	3.2	24	2.4	18	/	/
FB-1	0.47	19.8	9.9	50	9.9	50	6.3	32
FB-2	0.55	23.8	10.3	43	11.3	48	7.8	33
FB-3	0.94	40.2	16.6	41	18.1	45	13.3	33

Notes: $PIDR$ – peak interstory drift ratio; PID – peak interstory drift; $\Delta_{long}^{landing}$ – peak longitudinal landing displacement relative to the lower floor; $\Delta_{trans}^{landing}$ – peak transverse landing displacement relative to the lower floor; Δ^{conn} – peak deformation of the upper flight-to-building connection (data not available in the BI tests).

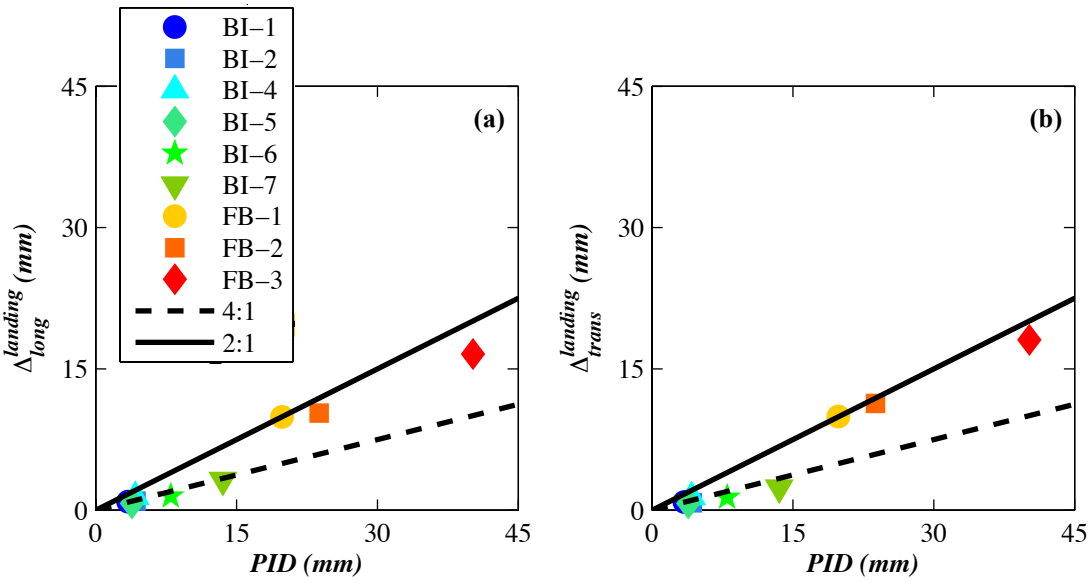

Figure 3.19. Peak interstory drift at level 2 vs. peak landing displacement relative to the lower floor of the stair (a) in the longitudinal direction, and (b) in the transverse direction.

3.5 Summary and Conclusions

A prefabricated steel stair system was installed within a full-scale five-story reinforced concrete building and was subsequently tested with the building in a shake table test program (see Chapter 2). The building was subjected to a suite of uni-directional earthquake motions and low-amplitude white noise base excitations, first while the building was isolated at its base and subsequently fixed to the shake table platen. These system-level tests, for the first time, allowed investigation of the seismic behavior of stair systems under realistic installation conditions and earthquake motions. Coincident with the seismic tests, low-amplitude white noise base excitations were applied to the test building. These data are used to perform modal identification of the stair system at various stages of the test program. Important findings regarding the dynamic characteristics and seismic response of the prefabricated steel stairs are summarized as follows:

1. The modal identification results indicate that the first and second vibrational modes of the stairs both correspond to the global torsional vibration of the stair systems with frequencies of 8.9 Hz and 11.1 Hz, respectively. As a result, the stairs observed considerable acceleration and displacement responses in the transverse-to-flight direction, even when loading was imposed entirely in the parallel-to-flight direction. The stair landing displacements were comparable in the two directions, and its accelerations in the transverse-to-flight direction was observed to be even larger than those in the parallel-to-flight (loading) direction.
2. During the seismic tests, severe damage to the stairs was detected at all levels except level 5. The most severe damage to the stairs consistently initiated in the form of vertical weld fracture of connection angles between the uppers flights and the slab embeds, with the associated PIDRs ranging from 0.74% to 2.64%. Safe egress from the building was compromised even when the associated drift demands (PIDRs of 0.74% and 1.41%) were much lower than the design performance target of the building (PIDR of 2.5%).
3. Consistent with the findings in previous studies, the seismic performance of stair systems is highly dependent on the deformability of their connections to the building, and in the case of scissor stairs, the torsional deformability of the system is

particularly important. Prior to severe damage to the stairs in the present tests, the deformation of the upper flight-to-building connection accommodated more than 30% of the interstory drift demands, while the torsional deformation of the landing was about 50% of that of the interstory drift demands.

4. As a result of predominantly torsional movement, the stair system observed considerable out-of-plane (transverse) forces and deformations of similar amplitudes to those imposed along the in-plane (longitudinal) direction, despite that the seismic floor excitations to the stairs were almost uni-directional.

The system-level experimental test data (building outfitted with stairs and other nonstructural components and systems) provide unique opportunities for calibrating numerical models and subsequent parametric studies to further investigate the seismic response of prefabricated steel stairs.

Acknowledgements

Portions of the following publication, for which the dissertation author was the primary investigator and author, are contained in this chapter:

- Wang, X., Astroza, R., Hutchinson, T., Conte, J., and Restrepo, J. (2015). "Dynamic Characteristics and Seismic Behavior of Prefabricated Steel Stairs in Full-Scale Five-Story Building Shake Table Tests." *Earthq. Eng. Struct. Dyn.*, 44(14), 1507–1527.

Chapter 4

Computational Assessment of the Seismic Behavior of Prefabricated Steel Stairs

4.1 Introduction

In this chapter, a comprehensive computational study is undertaken to advance understanding of the seismic behavior of prefabricated steel stairs. Detailed finite element models of prefabricated steel stairs are developed and validated through extensive comparison with experimental data. The validated modeling approach is subsequently used in a parametric study to assess the modal characteristics and lateral force-displacement behavior of a broader range of stair configurations and details. In particular, the effects of story height, connection detailing, landing posts, and geometry on the behavior of these the systems are studied. The objectives of the computational study are to: (1) develop detailed finite element models of prefabricated steel stairs that are capable of capturing the global response of the stairs as well as the physical behavior of the connections, (2) assess the accuracy of the developed models to simulate the seismic behavior of the stairs assemblies by comparing the analysis results with the experimental results, and (3) conduct a parametric study on the seismic behavior of prefabricated steel stairs considering a broad range of design parameters commonly found in practice.

This chapter is organized into five sections. Section 4.2 describes the detailed modeling approach of the prefabricated steel stairs implemented in *LS-DYNA*, including the Element and material properties, the connection details, and modeling assumptions. Subsequently, Section 4.3 conducts validation studies of the proposed modeling approach via comparison with experimental studies. The validated modeling approaches are then used in a parametric study by considering a broader range of stairs with various design variables, and their effects on the seismic behavior of stairs are investigated in Section 4.4. Lastly, Section 4.5 summarizes the major findings regarding the seismic behavior of the stairs in the parametric study.

4.2 Model Description

Although stairs vary in aspects such as geometric configuration and construction material, prefabricated steel stairs in a scissors configuration are considered as the prototype stairs in this study, since they are a common practice and are characterized by complex structural behavior, in particular torsional response. In addition, two recent well-documented experimental studies on this type of stairs, namely, the component-level tests conducted by Higgins (2009) and the shake table testing as presented in Chapter 3, facilitate the calibration of computational models. In this regard, the baseline configuration and other aspects of the stairs of this study follow those tested in these experimental studies.

As shown in Figure 4.1, the prototype prefabricated steel stair consists of a mid-height landing and two parallel flights running in opposite directions from the landing to the upper and lower floors of the building. These components are assembled on-site using bolted or welded connections. Presence of a handrail system on the stair is optional pending the position of the stairs relative to other architectural features. The finite element models implemented in *LS-DYNA* (LSTC, 2013a; LSTC, 2013b) explicitly consider all stair components and connections, resulting in a detailed representation of the stairs using 40,000–50,000 elements in each of the stair models. Components or

connections with distinctly different sectional or material properties are implemented in the models as different parts. Each part of the stair models is associated with a specific element formulation and material constitutive rule, as summarized in Table 4.1. The material properties of the different steel products used in the finite element models are summarized in Table 4.2.

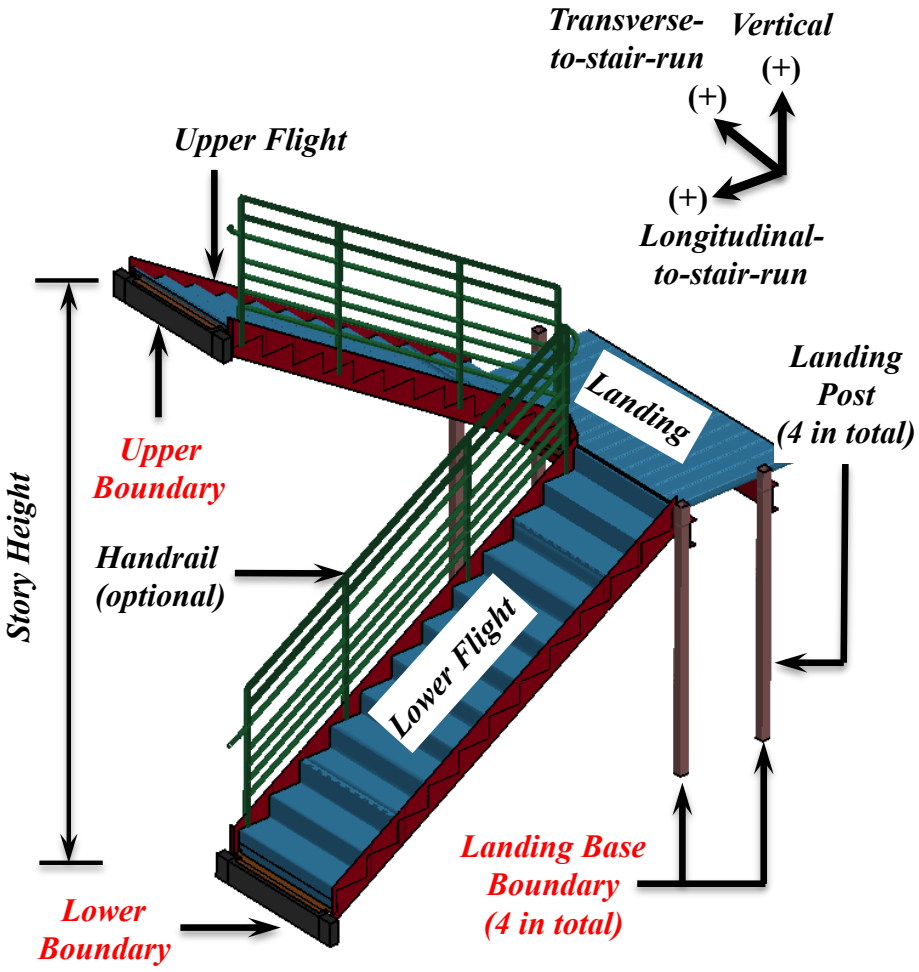

Figure 4.1. Finite element model of a generic prefabricated steel stair.

In the proposed models, material nonlinearity is considered assuming elasto-plastic behavior of steel material, and geometric nonlinearities are accounted for through small-strain large-displacement element formulations. In addition, contact between elements is implemented into the models to prevent unrealistic penetrations. Additional model-

Table 4.1. Stair components implemented in the finite element models and the associated element formulations.

Components and parts		ASME product	Element type
Flight	Stringers	A36 plate	Fully integrated shell element [1]
	Tread and riser	A786 checkered plate	
Landing	Post	A36 angle or A500 hollow structural section (HSS)	
	Joist	A36 channel	
	Deck	A786 checkered plate	
Handrail	Post	A53 pipe	Hughes-Liu beam element [2]
	Liner	A53 pipe or A500 HSS	
Connection plate		A36 plate	Fully integrated shell element
Connection angle		A36 angle	
Flight-to-landing connection bolts (or flight-to-building)		A325 tension control bolt	Spot weld beam element [3]
Landing post-to-joist connection bolts		A307 hex head bolt	

Notes: [1]shell element type 16 in *LS-DYNA*; [2]beam element type 1 in *LS-DYNA*; [3]beam element type 9 in *LS-DYNA*.

Table 4.2. Material strengths of ASTM steel products.

ASTM Designation	f_y (MPa)	f_u (MPa)
ASTM A36	248	397
ASTM A53	241	386
ASTM A500	317	507
ASTM A786	228	365
ASTM A325	/	827
ASTM A307	/	413

Notes: f_y denotes steel yield strength; f_u denotes steel ultimate strength.

ing details of individual components (e.g., flights, landings, handrails) and connections (e.g., flight-to-landing and flight-to-building connections), the material models, and the boundary conditions are discussed in subsequent sections.

4.2.1 Flight and Handrail

Figure 4.2 illustrates the finite element model of a flight subassembly with handrail. The flight stringers are fabricated of ASTM A36 steel plate, while the treads and risers are made of ASTM A786 checkered plate. All the parts of the flights are modeled using four-node fully integrated shell elements (element type 16 in *LS-DYNA*). A refined mesh

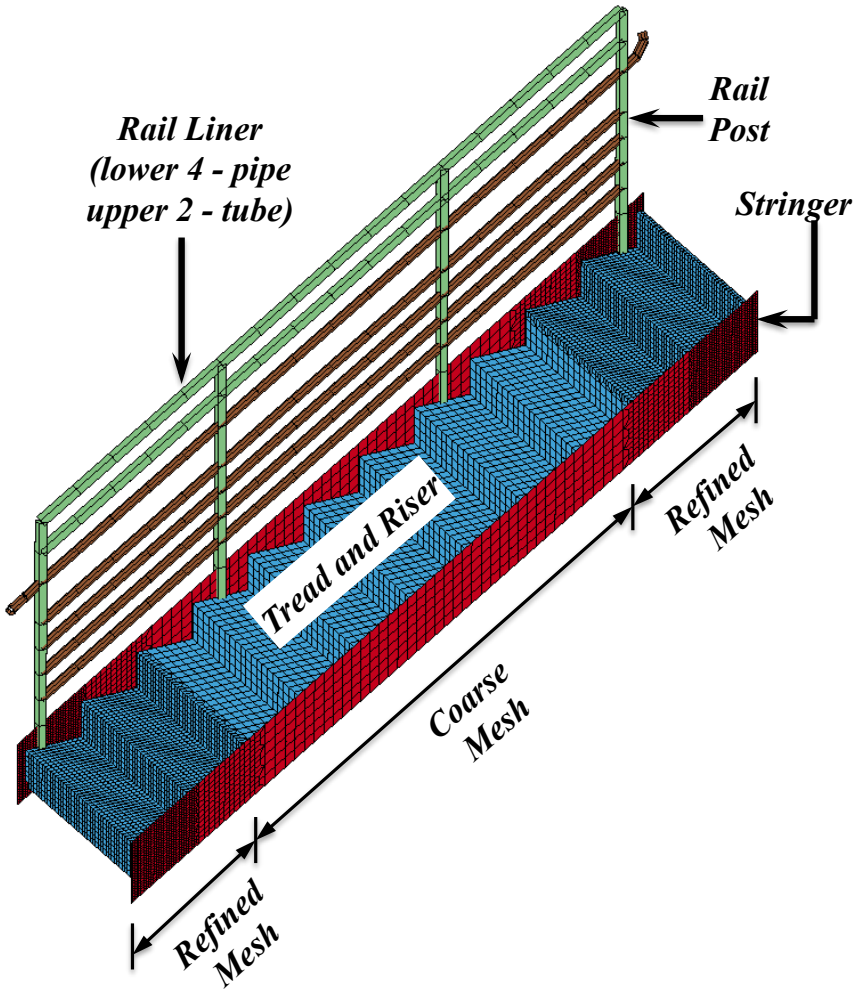

Figure 4.2. Finite element model of a stair flight with handrail.

ranging in element length from 13 mm to 25 mm is used at the both ends of the flight, since large strain and stress gradients are expected in such regions, and the remaining region of the flight employ a coarser mesh with an element length of ~50 mm to reduce the computational demand. Cyclic plasticity material models (material type 125 in *LS-DYNA*) are used to model the inelastic stress-strain response of steel in the refined-mesh regions (two ends of the flight), while elastic material is used in the coarse-mesh regions (flight mid-span). Simulation results confirmed that yield stress never exceeded at the coarse-mesh regions and therefore justified the use of elastic material in these regions.

As shown in Figure 4.2, the handrail consists of rail posts (vertical components) and liners running in parallel with stringers. The upper two liners are constructed using ASTM A500 hollow structural sections, while the remaining liners made of ASTM A53 pipes (Figure 4.2). The posts and liners are modeled using two-node Hughes-Liu beam elements (element type 1 in *LS-DYNA*) with a typical element length of approximately 100 mm. The nonlinear behavior of the beam elements is modeled using a user-defined section integration rule, in which each sectional integration point (a discretized fiber) is associated with a specific material model. Integration at the element level is performed at only one section, which is located at the midpoint of the element. As cyclic plasticity material models are not implemented for modeling beam elements with user-defined section integration rules, J2 plasticity models (material type 024 in *LS-DYNA*) are used for modeling these beam elements.

4.2.2 Landing

Figure 4.3 illustrates the finite element model of a landing subassembly. The four landing posts are fabricated using ASTM A500 hollow structural section (HSS), and the joists are made of ASTM A36 channels. In addition, the landing surface is constructed with ASTM A786 checkered plate. The landing posts at the four corners are each connected to the landing joist using two 16mm diameter ASTM A307 hex head bolts (f_u = 248 MPa) at the top and fillet welded to steel embeds of a reinforced concrete floor or bolted to steel framing members at the base. All landing parts are modeled using

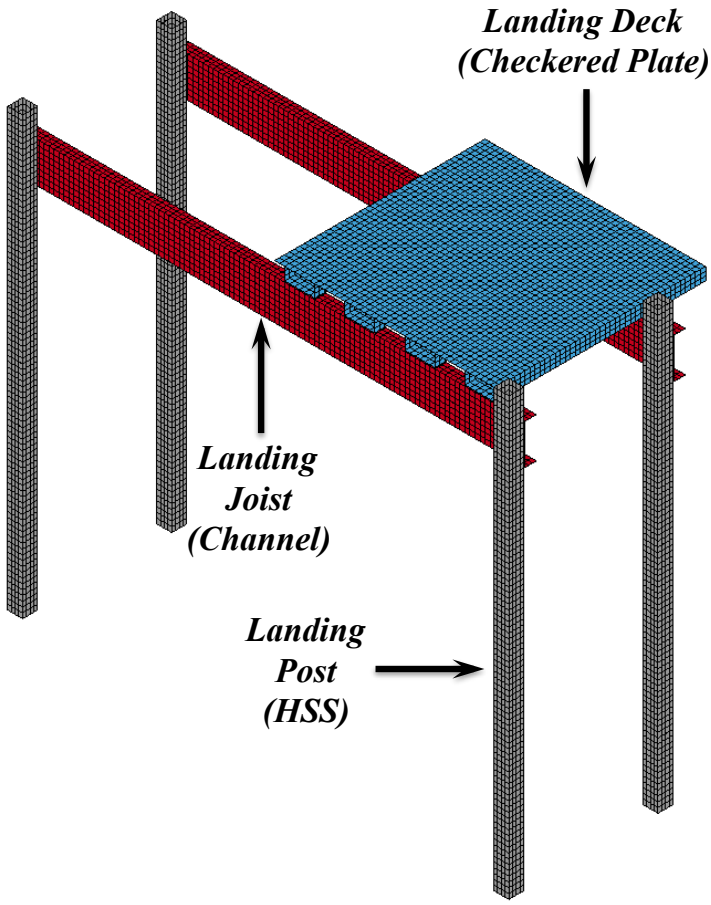

Figure 4.3. Finite element model of a stair landing.

four-node fully integrated shell elements and cyclic plasticity material models (Yoshida et al., 2002). Similar to those of the flight, the typical length of the landing shell element ranges between 25 mm and 50 mm.

4.2.3 Connections

The flights are attached to the building at one end and to the landing joist at the other end using connection members made of ASTM A36 plates or angles. Connection details differ significantly depending on their locations and the supporting structure. Figure 4.4 represents the flight-to-building connections used for steel buildings, in which the connection plate and the angle are both bolted to the steel members using two ASTM A325 tension control bolts (f_u = 248 MPa) per connection (hereafter referred to as Type-I

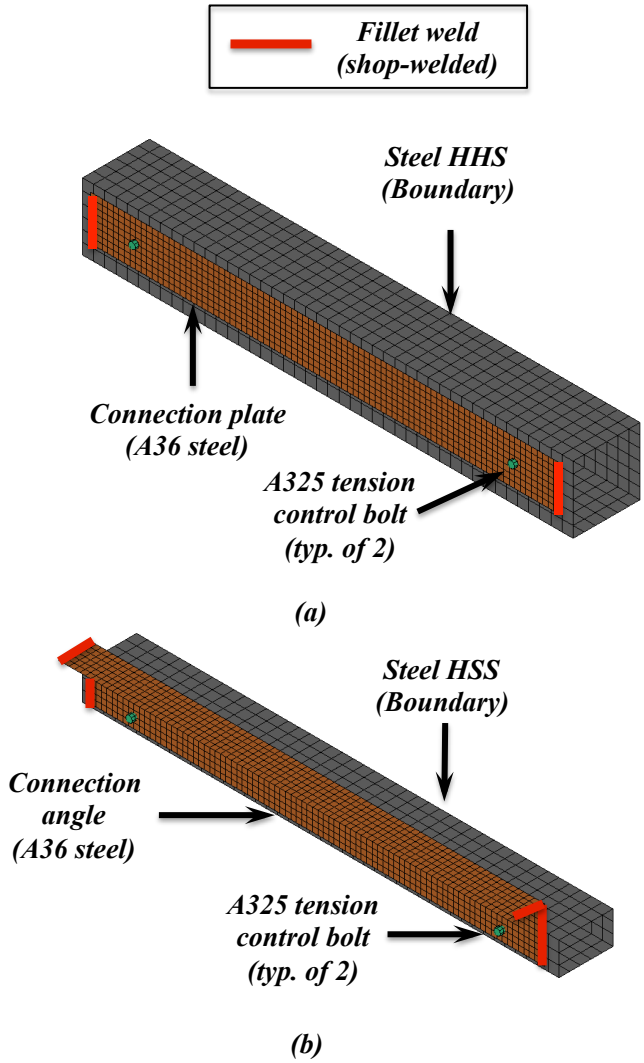

Figure 4.4. Finite element modeling of stair flight-to-building connections (Type-I connections): (a) upper flight, and (b) lower flight.

connections). Figure 4.5 represents the connections used to attach the flights to steel embeds cast within a concrete floor. These connection angles are field welded to the steel embeds using stitch welds along the edge of its horizontal leg (hereafter referred to as Type-II connections). It is noted that all the connection members (plates or angles) are shop-welded to the flight stringers using fillet welds at the two ends of the member (Figure 4.4–4.5). These connection members are all modeled using four-node fully integrated shell elements and cyclic plasticity material models (Yoshida et al., 2002). Since large inelastic deformations with complex stress-strain states are expected to concentrate on the connections during lateral loading, refined mesh with an element length of

13 mm is used for the connections.

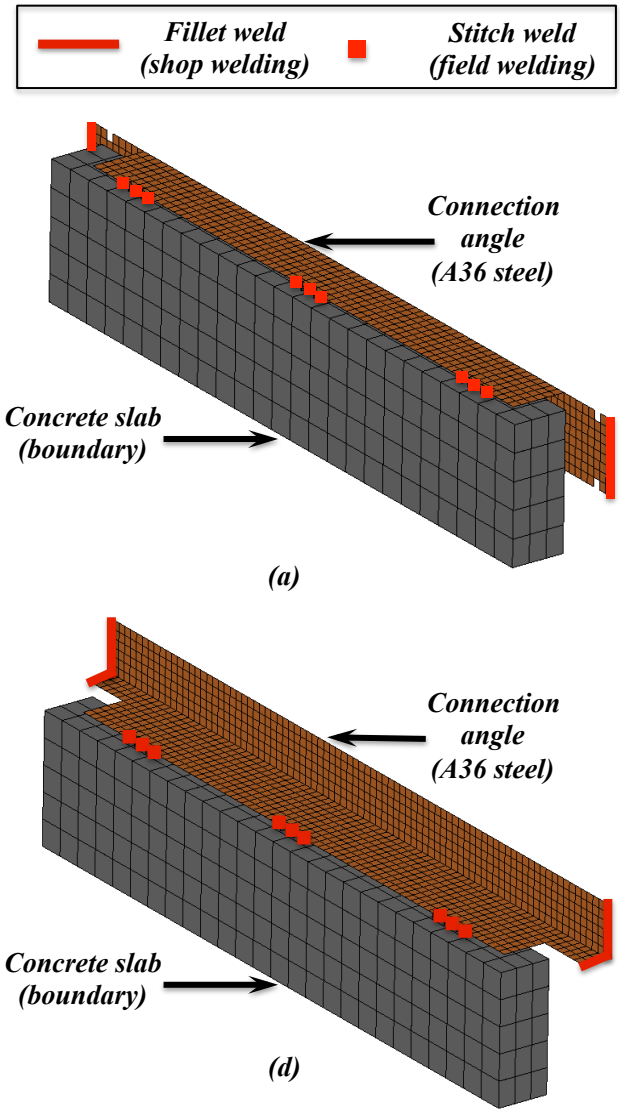

Figure 4.5. Finite element modeling of stair flight-to-building connections (Type-II connections): (a) upper flight, and (b) lower flight.

In these connections, the welds are modeled using penalty-based tie contact that rigidly constrains all translational and rotational degrees-of-freedom for the nodes on the two sides of the welds. The bolts are modeled using beam elements with a spot-weld material model (material type 100 in *LS-DYNA*). This material model is capable of applying an initial stress (bolt pretension) on the beam elements. It also allows the bolt

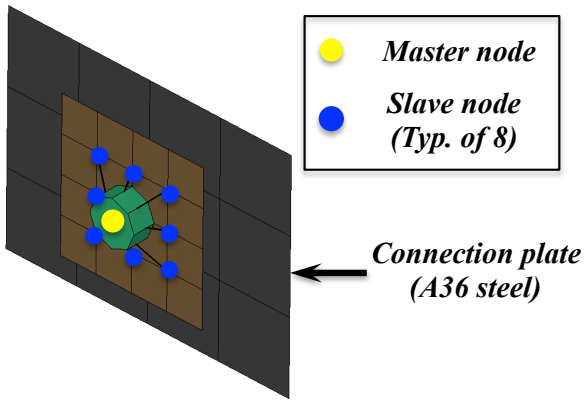

Figure 4.6. Modeling of bolted connections.

failure be considered by defining a specific damage rule. However, no damage criteria are implemented in this material since connection bolts were not severely damaged in the experimental studies. As shown in Figure 4.6, two rigidly constrained node sets are implemented on each end of the bolt, with the node on the bolt defined as the master node and the remaining nodes on the bearing member as slave nodes. These rigidly constrained node sets allow bolt pretension be transferred onto the bearing plates. Surface-to-surface contact is defined on the bearing plates to model the friction mechanism that provide resistance to gravity loads of the stairs.

4.2.4 Material Models

Two types of material models are used for modeling inelastic steel response: (1) a two-surface cyclic plasticity model (material type 125 in *LS-DYNA*) with combined isotropic-kinematic hardening rules (Yoshida et al., 2002), and (2) a J2 plasticity model (material type 024 in *LS-DYNA*) with the isotropic hardening rule defined using an arbitrary piecewise linear curve to represent the post-yield effective stress versus effective plastic-strain relationship. Figure 4.7 provides the monotonic and cyclic stress-strain responses of ASTM A36 steel (f_y = 248 MPa, f_u = 397 MPa). These results are obtained using a shell element under uniaxial displacement loading. Since material test data for the stair specimens were unavailable in this study, the strain corresponding to the ultimate steel strength is defined as 0.15, which is a reasonable estimate for similar steel materials based on the tensile test results reported in the literature (Jia and Kuwamura,

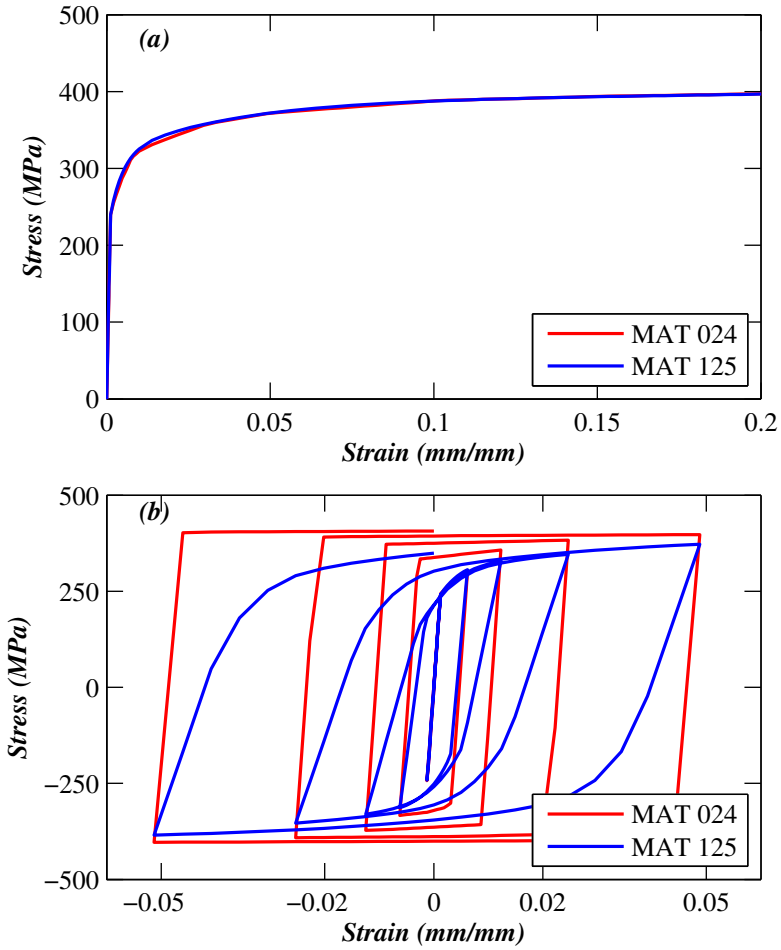

Figure 4.7. Uniaxial stress-strain response of the steel models: (a) monotonic response, and (b) cyclic response.

2013). Despite of varying hardening rules, the parameters of the two models are defined such that they provide consistent stress-strain response under monotonic loading (Figure 4.7a). Under cyclic loading, the cyclic plasticity model provides reasonable hysteretic response as a result of its capability of reproducing the Bauschinger effect and the progressive deterioration of unloading stiffness as a function of effective plastic strain (Figure 4.7b). However, these aspects are not well addressed by the J2 plasticity model due to the limitations related to its constitutive law such as isotropic hardening rule and elastic unloading stiffness. This leads to significant overestimation of the material strength as well as sharp transitions in the hysteretic stress-strain response, in particular when the material is subjected to large inelastic cyclic deformation. As such, cyclic

plasticity models are used for the fully integrated shell elements, while the J2 plasticity model is only used for the beam elements of the handrail systems (cyclic plasticity model is not applicable for the beam element). The fact that the handrails never achieved large plastic strains in the simulations justifies the use of this material model. Occasionally, an elastic material is used in the coarse-mesh regions of the flight stringers, risers, and treads to reduce computational demand.

4.2.5 Boundary Conditions

The stair is attached to the upper and lower floors of a building at multiple locations: (1) the upper flight attached to the upper floor, (2) the lower flight attached to the lower floor, (3) the four landing posts attached to the lower floor at their base (Figure 4.1). The boundaries are applied with either prescribed displacements or single point constraints (fixed boundaries) dependent on the analysis method. The handrail system, when present, introduces two additional nodal boundaries at the upper and lower ends of the handrail liners. Since the liners span continuously between adjacent floors, six degree-of-freedom discrete (zero-length spring) elements are used at the nodal boundaries to account for the stiffness contribution of the handrails. The stiffness coefficients of these discrete elements are determined by imposing a very small displacement at each degree of freedom.

4.2.6 Modeling Limitations and Mesh Sensitivity Study

As discussed in the previous chapter, occurrences of connection weld fracture of the prefabricated steel stairs are possible during seismic loading. Previous studies also indicate that low-cycle fatigue has important effects on the seismic behavior of steel components and connections (Jones et al., 2002; Kanvinde and Deierlein, 2007). Accurate modeling of these aspects relies on well-defined damage criteria calibrated with experimental data. Absent test data of the stair connection behavior in this study, the weld fracture and low-cycle fatigue effects are not explicitly modeled. Therefore, it is assumed in this study that the welds remain damage-free throughout the simulations. It is noted, however, that the proposed models can be readily extended to consider these

aspects via the introduction of element erosion (removal) techniques with specific damage criteria when experimental results on these connections become available.

Although connection weld fracture is not explicitly modeled, the stress-strain response of the connections is used to assess the plastic strain demands and the potential for fracture (El-Tawil et al., 2000; Mao et al., 2001). Since large inelastic deformations with complicated stress-strain states are expected to concentrate on the connections during lateral loading, mesh dependency issues are studied by modeling the response of Type-I (upper-flight-to-floor) connection (Figure 4.4a) under monotonic paralell-to-stair-run displacement loading. The connection is modeled using fully-integrated shell elements considering two different meshing with element sizes of 12.7 mm and 6.4 mm. The simulation results confirms that the models with different element sizes provide consistent global force-displacement results as well as element-level stress-strain response (Figures 4.8 and 4.9). This is likely due to the absence of softening behavior for the steel material used in the models. These studies substantiate the use of the stress-strain results for assessing the seismic performance of the connections.

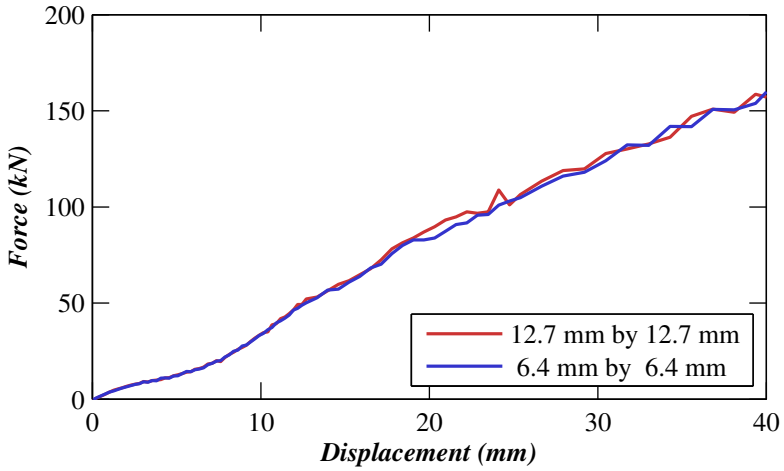

Figure 4.8. Force-displacement response of Type-I upper-flight-to-floor connection under monotonic paralell-to-stair-run loading.

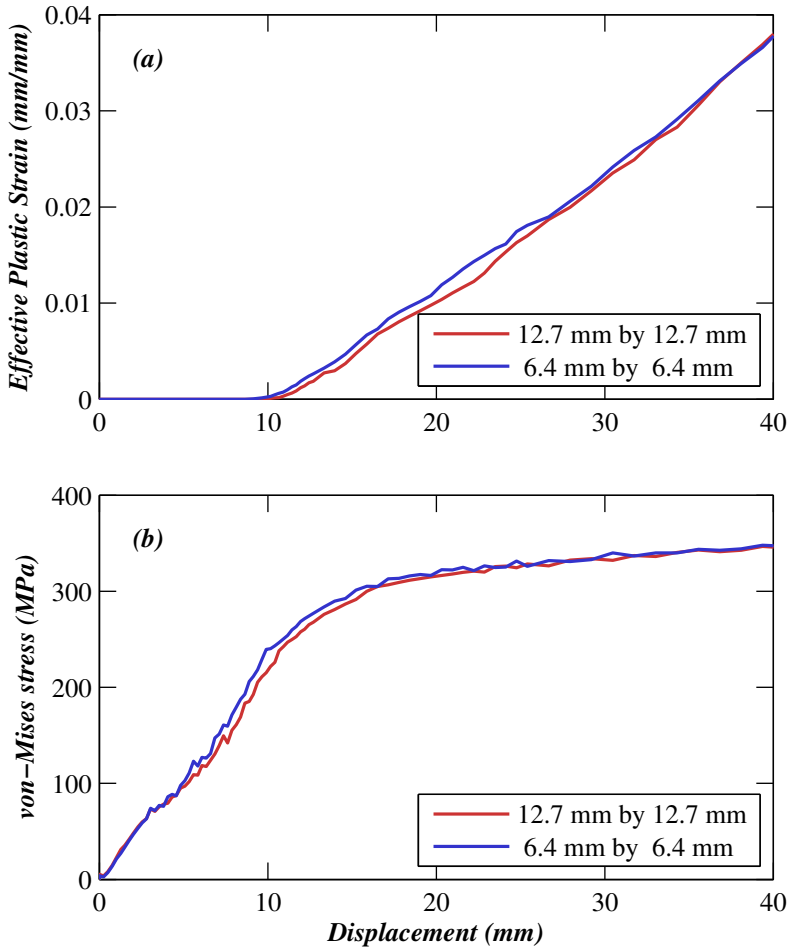

Figure 4.9. Local response of Type-I upper-flight-to-floor connection under monotonic paralell-to-stair-run loading: (a) connection longitudinal displacement vs. effective plastic strain, and (b) connection longitudinal displacement vs. von-Mises stress.

4.3 Model Validation Studies

The efficacy of the proposed modeling approaches in capturing the seismic behavior of the stairs are validated through comparisons with two prior experimental studies: (a) the component-level cyclic pseudo-static tests conducted at the Oregon State University (hereafter referred to as the *OSU tests*) (Higgins, 2009), and (b) the system-level shake table tests conducted at the University of California, San Diego (hereafter referred to as the *UCSD tests*, see Chapter 3). The stair specimens tested in these two experimental studies were designed and fabricated using similar strategies. However, as shown in Figure 4.10, the test specimens and protocols between these two studies differed in

several important aspects. The major differences of the model validation studies are summarized in Table 4.3.

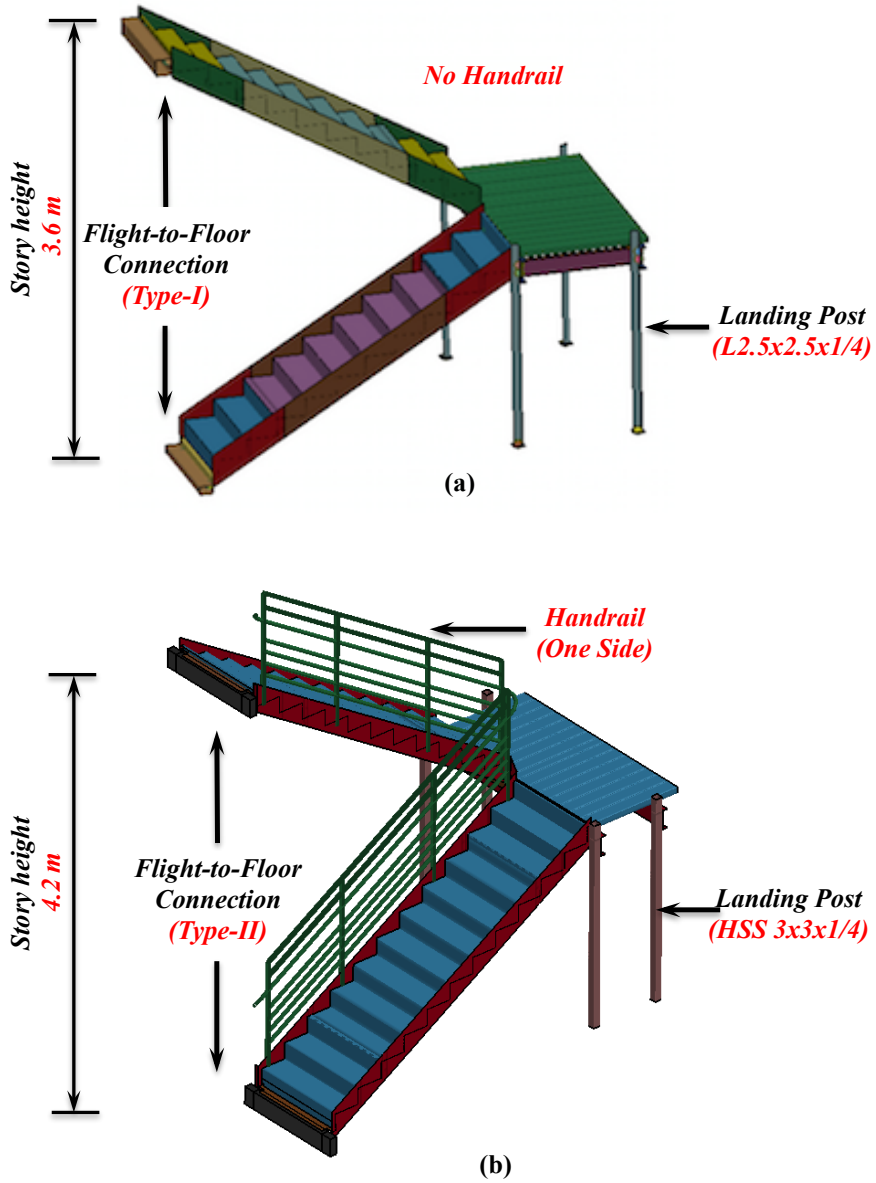

Figure 4.10. Finite element models of the stairs used in the validation studies: (a) OSU tests, and (b) UCSD test.

The validation study of the OSU tests is conducted using implicit nonlinear static analyses. Pseudo-static displacement is applied at the upper floor boundary, while the

Table 4.3. Comparison of the experimental studies used for model validations.

Variable	*OSU tests*	*UCSD tests*
Test protocol	Pseudo-static loading, component-level tests	Dynamic loading, system-level tests
Story height (m)	3.6	4.2
Landing post	L2.5×2.5×1/4 (ASTM A36)	HSS 3×3×1/4 (ASTM 500)
Handrail	None	One side
Weight	6.4 kN (self weight) + 25.4 kN (live load)	10.1 kN (self weight)
Flight-to-floor connection	Type-I (Figure 4.4)	Type-II (Figure 4.5)

lower floor boundary and the base of the four landing posts are fixed. In contrast, the analysis of the UCSD tests includes both eigen-value analyses and nonlinear dynamic analyses using a combined implicit-explicit time integration scheme. While all boundaries are fixed in the eigen-value analyses, the absolute floor displacement histories measured at the upper and lower floors of the test building during the tests are used as the input excitations when conducting the nonlinear dynamic time history analyses. It is also noted that the pre-tension of the connection bolts and the gravity load of the stair are applied prior to performing the eigen-value analyses, nonlinear static or dynamic analyses.

4.3.1 *OSU tests* (Higgins, 2009)

Higgins (2009) tested two full-size prefabricated steel stair assemblies using cyclic pseudo-static displacement loading protocol. As the two specimens demonstrated similar behavior during the tests, the validation study focuses only on the checkered plate specimen. The imposed lateral displacement cycles were applied with progressively increasing amplitudes up to the attainment of maximum target displacement selected as an interstory drift ratio (IDR) of 2.5%, which is representative of the seismic demands of moment frame buildings subjected to design earthquakes. Following the completion of the primary loading tests, extra mass was applied on the stair to represent the full

factored design live load, and the specimen was subjected to additional displacement loading with an amplitude of 50% the maximum target displacement. Interested readers are referred to Higgins (2009) for additional information about the stair specimens and the test program.

Figure 4.11 compares the numerical lateral force-displacement responses with the experimental results in the two horizontal loading directions. It is shown that the model produces force-displacement responses correlate reasonably well with the experimental results, and the salient characteristics in the hysteretic behavior such as stiffness degradation and pinching are also well captured. When the imposed displacements in the parallel-to-stair run direction become relatively high (>1% IDR), the lateral force is slightly overestimated, and the estimated hysteresis loops slightly deviate from those of the experimental results (Figure 4.11a). This is due to the fact that the simulations of the two loading directions are conducted independently, and therefore the stair damage accumulated at the end of the initial loading direction (transverse-to-stair-run) are not considered in the subsequent loading direction (parallel-to-stair-run). As discussed in Higgins (2009), damage accumulated in the initial loading direction resulted in reduction of stiffness and energy dissipation capacity of the stair in the subsequent loading direction.

4.3.2 *UCSD tests*

As described in the previous chapter, a prefabricated steel stair system was installed within a full-scale five-story reinforced concrete building and subsequently tested with the building. The test building was subjected to a suite of uni-directional earthquake motions and low-amplitude white noise base excitations while the building was first isolated at its base and subsequently fixed to the shake table platen. Analysis of the UCSD tests focuses on the stair unit at level 2 as it represented the most densely instrumented stair among those in the test building. In addition, level 2 attained the largest IDR demands during the earthquake tests (~2.5% for the design event FB-5). However, it is noted that the stair sustained severe damage in the form of connection weld fracture as well as frequent pounding with surrounding partition walls during the last three earthquake in

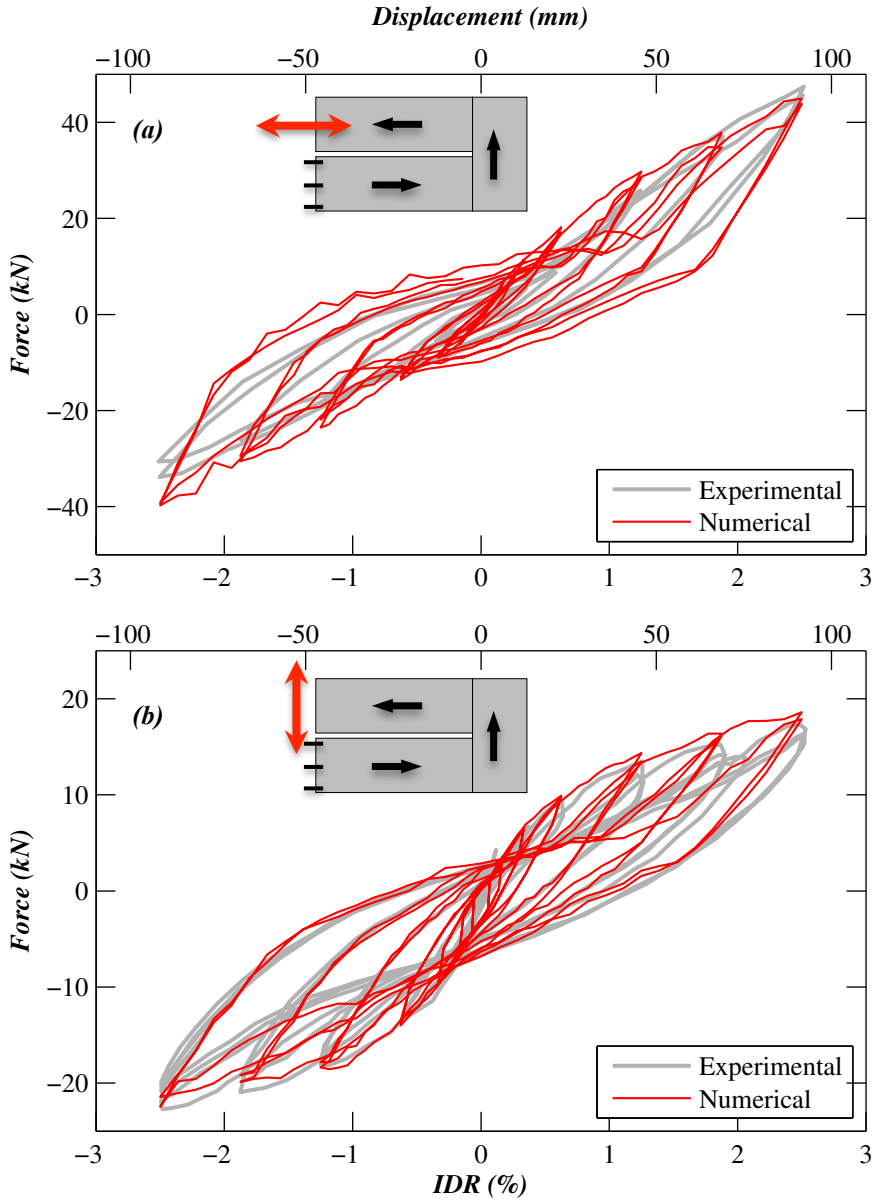

Figure 4.11. Comparison of the force-displacement response of the *OSU test* specimen in: (a) parallel-to-stair-run loading, and (b) transverse-to-stair-run loading (double-headed arrow denotes the direction of loading).

the fixed-base test phase and are therefore excluded from simulation. Additional details about the shake table test program and the test building and the experimental results of the stair are discussed in the previous two chapters.

Table 4.4 compares the modal parameters of the stair obtained from eigen-value

analyses with the system identification results using low-amplitude white noise base excitations. The mode shapes of these vibrational modes are illustrated in Figure 4.12. These modal characteristics represent those of the stair in its initial (undamaged) state. The modal assurance criteria (MAC) values (Allemang and Brown, 1982) provides as a measure of consistency between the experimentally and computationally identified mode shapes. As shown in the table, the model reasonably reflects the dynamic characteristics of the stair identified using the white noise test data. The differences related to the frequencies are all less than 5% for the three identified modes. In addition, the lowest MAC value corresponding to the three modes is observed as approximately 0.9, indicating good correspondence between the identified mode shapes. As shown in Figures 4.12a and c, the first and third vibrational modes represent the predominant vibration modes of the stair in the parallel-to-stair-run and the transverse-to-stair-run directions, respectively, as the effective modal mass exceeds two thirds of the total mass in the corresponding directions of vibration. In contrast, the second mode (Figure 4.12b) does not reflect a global vibrational mode due to the low contribution of the modal mass (< 5% in the two horizontal directions). As shown in the figure, although the flight and landing displacement pattern of the second mode resembles those of the first mode, the handrail system deforms at much larger amplitudes than the flights and and moves in a direction opposite to that of the flights. As the mass of the handrail system accounts for approximately 30% of the total mass of the stair and the displacements of the handrail are opposite to other stair components, this mode has a very small effective modal mass.

Table 4.4. Modal characteristics of the *UCSD test* specimen.

Mode	f_{num}	f_{exp}	$M_{eff,x}$	$M_{eff,y}$	$M_{eff,z}$	MAC
	(Hz)	(Hz)	(%)	(%)	(%)	value
1st Mode	9.2	8.9	0.6%	68.7%	0.2%	0.98
2nd Mode	11.7	11.1	0.6%	3.1%	0.1%	0.91
3rd Mode	19.5	19.8	66.3%	0.6%	0.2%	0.85

In the nonlinear dynamic analyses, the measured absolute displacement histories at the second and third floors of the test building are imposed at the lower and upper floor boundaries as the inputs excitations. Rayleigh damping is implemented in the model

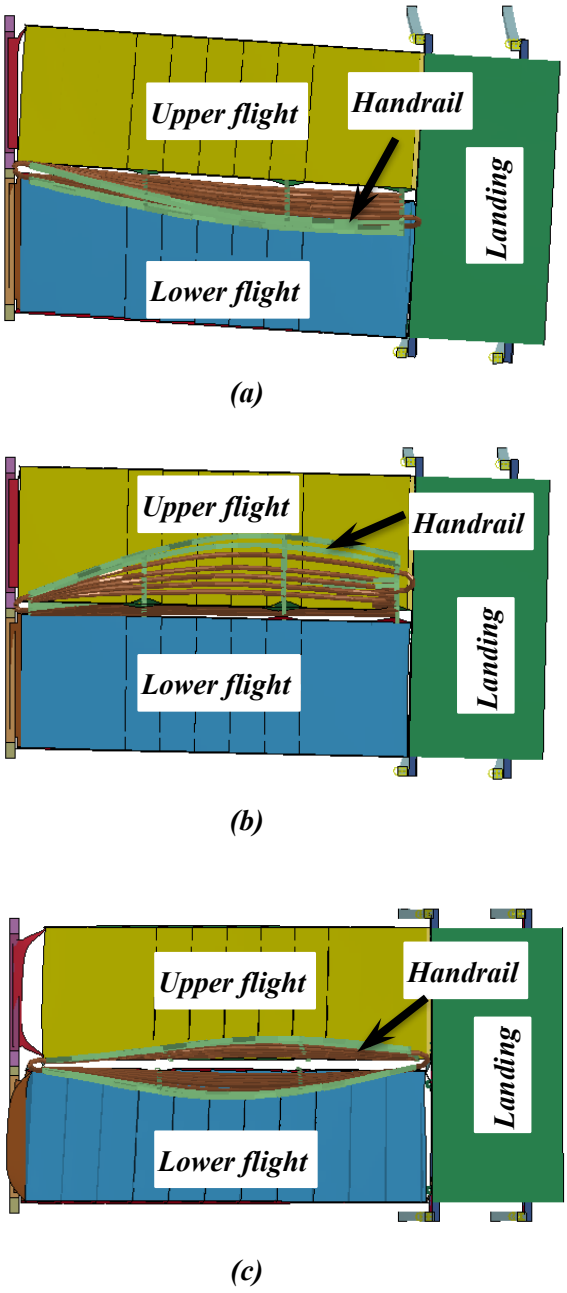

Figure 4.12. Mode shapes of the UCSD test specimen (top view): (a) first mode, (b) second mode and (c) third mode.

using a critical damping ratio of 2% at the two predominate modes in the two orthogonal directions. It is noted that the damping is intended to account for energy dissipative sources other than those dissipated through material nonlinearity, as this mechanism is directly considered with the elasto-plastic behavior of the steel material. Figure 4.13 compares of the numerical and experimental results of the landing displacement histories relative to lower floor of the stair at level 2 in the first fixed-base seismic test (FB-1). The simulation results reasonably capture the torsional deformation of the landing, showing a diagonal displacement trajectory at the upper flight corner with comparable amplitude in the two orthogonal directions and primarily transverse displacement at the lower flight corner. It is noted that the experimental results of the relative landing displacements did not capture the permanent displacements due to the plastic yielding of the connections, as the results were obtained using double integration of the acceleration measurements and thereby were not capable of capturing the permanent displacements of the landing.

Table 4.5 compares the peak landing accelerations and landing displacements relative to the lower floor for the stair at level 2 during the first two fixed-base tests (FB-1 and FB-2). These comparisons demonstrate that the simulation results reasonably capture the peak relative displacements and rotations of the landing as measured in the tests

Table 4.5. Comparison of peak acceleration and displacement response of the landing in the *UCSD tests*.

Test Motion		$PCA_{long}^{landing}$	$PCA_{trans}^{landing}$	$\Delta_{long}^{landing}$	$\Delta_{trans}^{landing}$	$\theta^{landing}$
		(g)	(g)	(mm)	(mm)	(rad)
FB-1	Experimental	0.36	0.59	9.9	9.9	0.046
	Modeling	0.53	0.65	9.0	8.7	0.041
FB-2	Experimental	0.28	0.44	10.3	11.3	0.049
	Modeling	0.44	0.62	10.7	10.2	0.043

Notes: $PCA_{long}^{landing}$ and $PCA_{long}^{landing}$ represent the peak component acceleration of the landing in the parallel-to-stair-run and transverse-to-stair-run directions, respectively; $\Delta_{long}^{landing}$ and $\Delta_{long}^{landing}$ represent the peak landing displacement relative to the lower floor in the parallel-to-stair-run and transverse-to-stair-run directions, respectively; $\theta^{landing}$ represents the landing rotation.

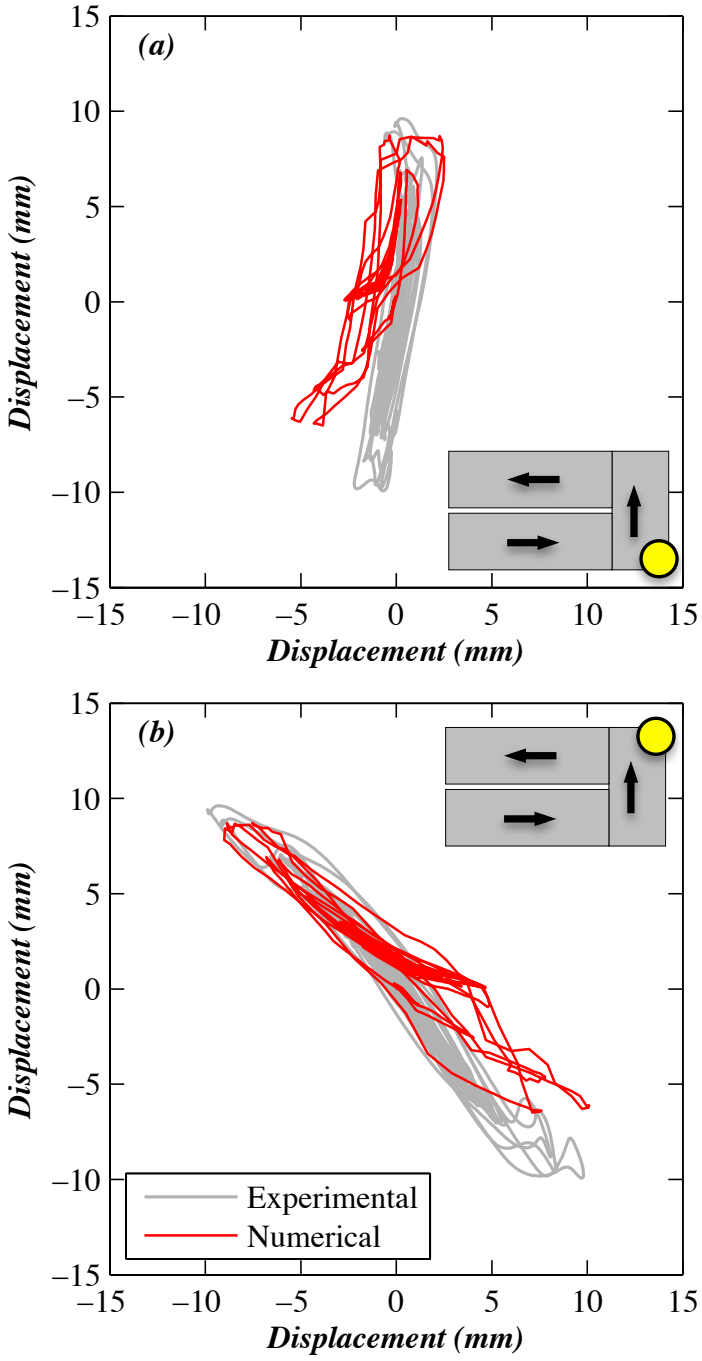

Figure 4.13. Comparison of the landing displacements of the UCSD test specimen in test FB-1: (a) lower flight corner, and (b) upper flight corner.

with about only 10% differences from the experimental results. Peak landing accelerations, however, are overestimated in the numerical analyses, with the largest difference of about 30%. This is likely due to the fact that the nonlinear dynamic analyses are conducted separately without accounting for progressive damage of the stairs accumulated during the test sequence. Since the stair in the analysis represents that at its initial condition, this leads to the larger stiffness than that of the stair in the tests.

4.4 Parametric Studies

Using the modeling approaches as validated previously, a parametric investigation is conducted to assess the seismic behavior of prefabricated steel stairs with design variables commonly found in practice. As shown in Table 4.6, the parametric study includes a total of eight stair variants with design variables in four categories: story height, landing post, connection details, and geometric configuration. Model *Case-1* is defined as *Baseline Model* in the parametric study, which represents the checkered plate specimen in the *OSU tests* (Higgins, 2009). The remaining seven models are derived from the *Baseline Model* by modifying one design variable at a time of the four sets of design variables: story height (*Cases 2 and 3*), landing post (*Cases 4 and 5*), connection details (*Cases 6 and 7*), and geometric configuration (*Case 8*). Regarding the different connection details, the *Baseline Model* (*Case-1*) is representative of those of the stair attached to steel members (Type-I connections as shown in Figure 4.4), while model Case 6 reflects typical connections for concrete floors (Type-II connections as shown in Figures 4.5). These two connection types both utilize a yielding mechanism on the upper flight-to building connection to accommodate the expected interstory drifts. In contrast, *Case 7* (Type-III connections) is intended to represent a stair with fixed-end flight-to-building connections at both the lower and upper floors. The details of Type-III connections (*Case 7*) differ from those of Type-II connections (*Case 6*) by lacking the cutoff areas on the upper flight-to-building connection angle.

The parametric study focuses on the modal characteristics of the stair variants as well as the lateral force-displacement behavior in the two horizontal loading directions.

Table 4.6. Prefabricated steel stair parameter study variables

Model [1]	Story height	Landing post	Connection details[2]	Geometric configuration
Case 1	**3.6 m**	**L2.5×2.5×1/4**	**Type-I**	**Scissors**
Case 2	**4.2 m**	L2.5×2.5×1/4	Type-I	Scissors
Case 3	**4.8 m**	L2.5×2.5×1/4	Type-I	Scissors
Case 4	3.6 m	**L3×3×1/4**	Type-I	Scissors
Case 5	3.6 m	**HSS3×3×1/4**	Type-I	Scissors
Case 6	3.6 m	L2.5×2.5×1/4	**Type-II**	Scissors
Case 7	3.6 m	L2.5×2.5×1/4	**Type-III**	Scissors
Case 8	3.6 m	L2.5×2.5×1/4	Type-I	**Straight**

[1]case 1 represents baseline model; [2]see Figures 4.4 and 4.5 for Type-I and Type-II connections; connection Type-III differs from Type-II by absence of cutoff on the upper flight-to-building connection angle.

Similar to the validation studies, the modal properties of the stairs are determined using eigen-value analyses, and the lateral force-displacement responses are obtained using nonlinear static analyses with the monotonic displacement loading imposed at the upper floor boundary of the stairs while the lower floor boundaries are fixed. Consistent with the OSU tests (Higgins, 2009), the maximum target displacement considered in the parametric studies is defined as 2.5% interstory drift. The suitability of numerical results with a larger target displacement requires further verifications due to the potential limitations on capturing the physical damage of the stair connections under extreme loading conditions.

It is assumed in the parametric study that dynamic excitations do not significantly affect the global force-displacement response of the stairs and thus the seismic behavior of the stairs can be adequately captured using pseudo-static loading. This assumption is considered reasonable for the prefabricated steel stairs discussed in this chapter, as the predominant frequencies of these systems are much higher than the fundamental frequency of the supporting structure, thus avoiding possible tuning effects. In addition, the inertial forces of these lightweight systems induced by dynamic excitations are far less significant than the pseudo-static force induced by differential displacements at multiple supports. However, further investigation is needed to better understand the

dynamic effects of these or other stairs when the above assumptions become not applicable, in particular when the mass of the stairs becomes substantially larger or the natural frequencies of the stairs are tuned with the fundamental frequency of the supporting structure.

4.4.1 Results: Baseline Model

Table 4.7 summarizes the modal frequencies and the effective modal mass of the baseline stair model. The associated modal shapes of *Baseline Model* is shown in Figure 4.14. Absent handrail systems in *Baseline Model*, the two predominant horizontal vibration modes correspond to the two lowest frequencies, each accounting for more than two thirds of the total mass in the corresponding direction of vibration. The vertical vibrational modes, also not shown herein, are characterized by high frequencies (>30 Hz) and less concentration of modal mass in a single vibrational mode (< 30% of the total mass). The frequencies of the predominant horizontal modes are more likely to coincide with the higher building modes rather than the fundamental mode. Vertical vibration modes are of less importance under earthquake excitations, as these frequencies are likely too high to be considered in seismic design.

Important performance parameters to characterize stair force-displacement response under pseudo-static displacement loading are illustrated in Figure 4.15. The yield state is determined as initial yielding of the critical stair components (e.g., the upper flight-to-floor connections) when the von-Mises stress exceeds the steel yield strength (Figure 4.15b). The initial stiffness K_e is then defined as the secant stiffness when the lateral force attains 50% the yield capacity. The ultimate loading state represents the attainment of the maximum target displacement corresponding to 2.5% interstory drift (Figure 4.15c). The overstrength factor Ω is then defined as the ratio between the ultimate capacity F_u and the yield capacity F_y. Furthermore, the peak landing displacements relative to the lower floor $\Delta_{long}^{landing}$ and $\Delta_{trans}^{landing}$ are considered as performance parameters, since they are useful for determining the gap size and prevent undesirable impacts between the stair and its surrounding enclosure.

Table 4.7. Modal characteristics of two predominant horizontal vibration modes – *Baseline Model*.

Mode	f	$M_{eff}^{long\,1}$	$M_{eff}^{trans\,2}$	$M_{eff}^{vert\,3}$
	(Hz)	(%)	(%)	(%)
Transverse-to-stair-run	7.7	0.1	66.9	0.0
Parallel-to-stair-run	19.3	73.9	0.7	0.1

[1]effective modal mass in the parallel-to-stair-run direction; [2]effective modal mass in the transverse-to-stair-run direction; [3]effective modal mass in the vertical direction.

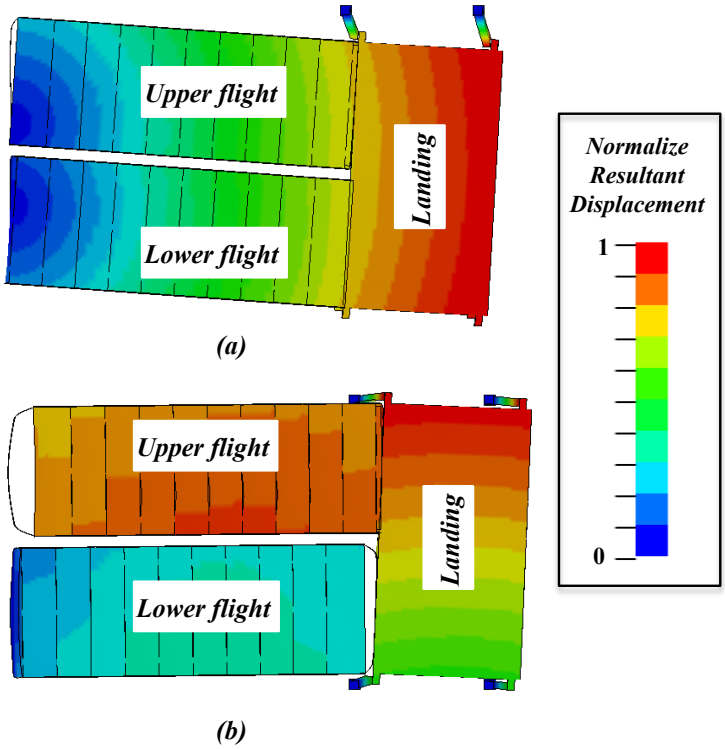

Figure 4.14. Mode shapes of two predominant horizontal vibration modes – *Baseline Model* (top view): (a) transverse-to-stair-run direction (7.7 Hz), and (b) parallel-to-stair-run direction (19.3 Hz).

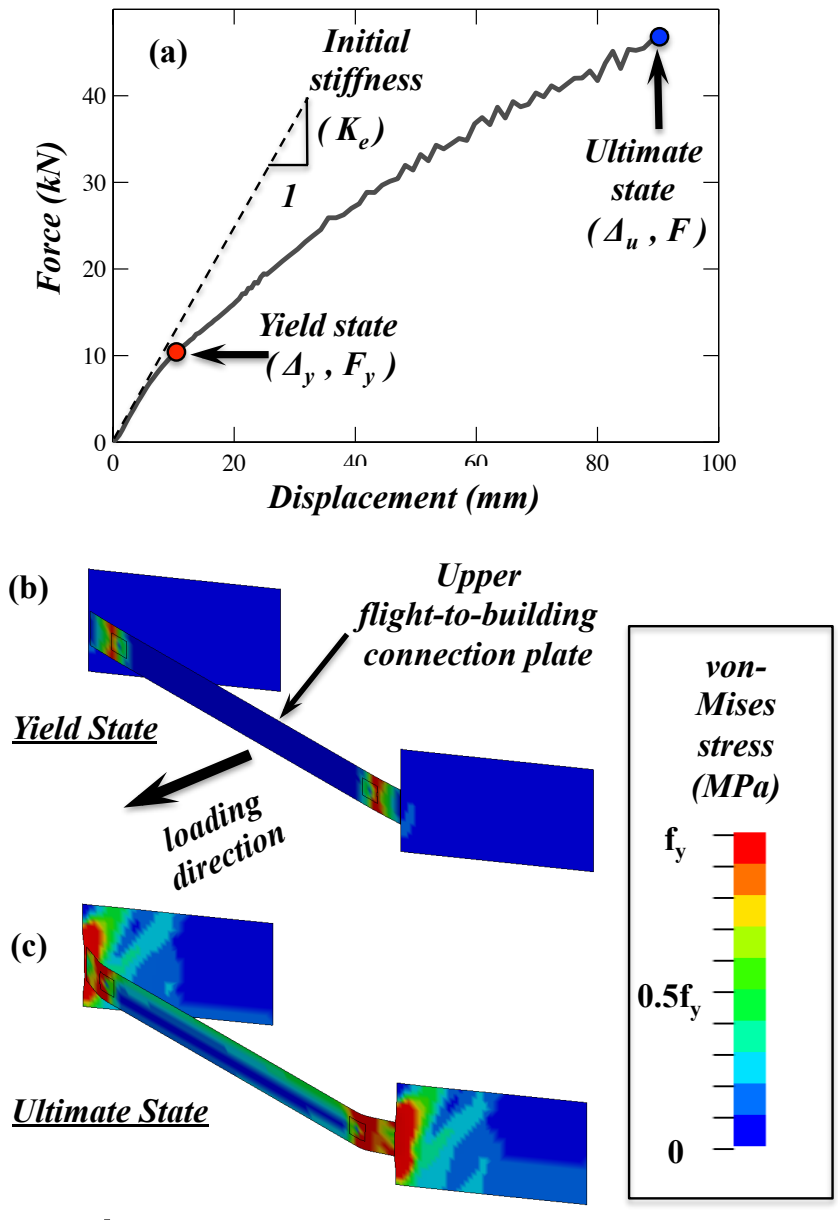

Figure 4.15. Illustration of the numerically predicted performance parameters of *Baseline Model* under positive parallel-to-stair-run loading: (a) lateral force-displacement response, and the von-Mises stress distribution of upper flight-to-building connection under (b) yield state and (c) ultimate state.

Figure 4.16 shows the force-displacement response and the landing displacement of *Baseline Model* under monotonic displacement loading in two horizontal directions. As clearly shown in Figure 4.16a, the stair force-displacement response varies significantly in the two horizontal loading directions. While the yield forces are comparable in the two loading directions, the initial stiffness and ultimate force under the parallel-to-stair-run loading direction (hereafter referred to as parallel direction) is about twice as large as that under the transverse-to-stair-run loading direction (hereafter referred to as transverse direction). In addition, the yield displacements are about 0.2% interstory drift under the parallel loading, as compared to 0.35–0.5% interstory drift under transverse loading. These values indicate that yielding of the stair connections may even occur during a low-amplitude earthquake when the building response remains elastic.

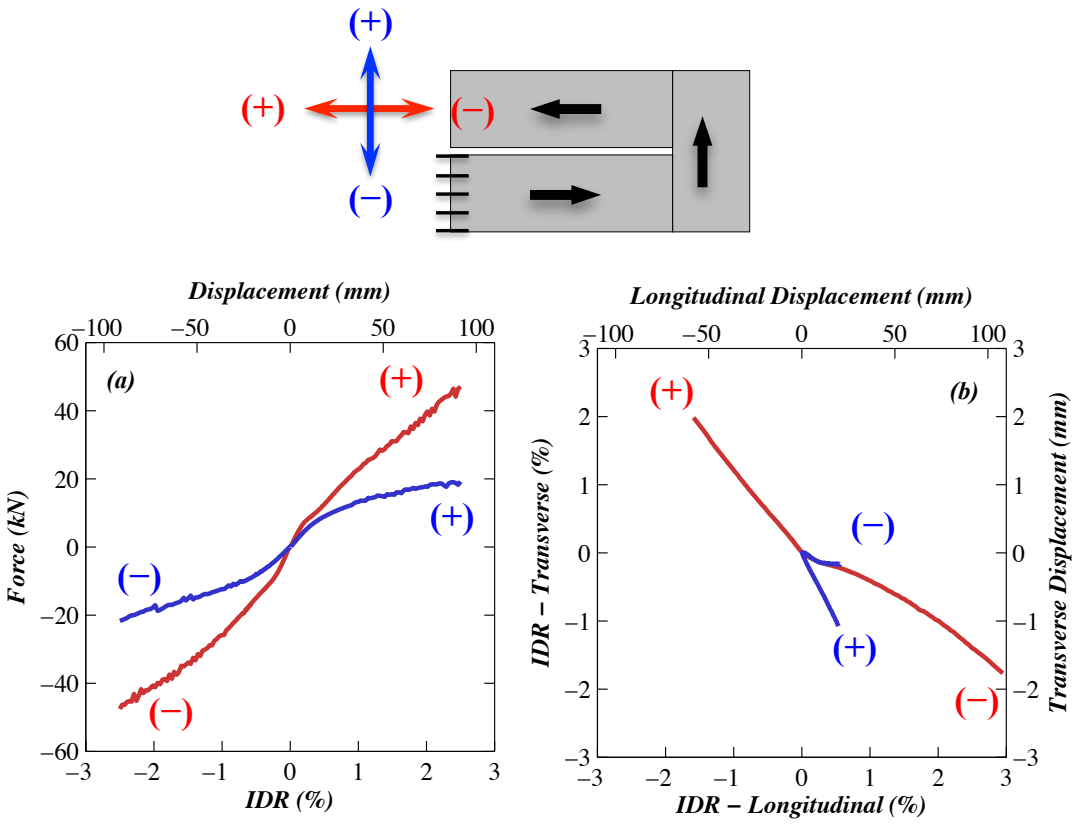

Figure 4.16. (a) Force-displacement response, and (b) landing displacements of the baseline model under monotonic displacement loading under the two horizontal directions (positive and negative).

As shown in Figure 4.16b, the landing displacement differs substantially in the two loading directions as a result of different deformation pattern. While upper flight deformation effectively improves the stair deformability and reduces landing displacements during transverse loading, differential displacements impose large deformation demands on the landing and connections when loading is applied on the parallel direction. For this reason, the landing displacements under parallel-to-stair-run loading appear significantly larger than those under transverse-to-stair-run loading. At the ultimate state (2.5% interstory drift), the relative landing displacements under parallel loading direction attain as much as 3% interstory drift but only about 1% interstory drift in transverse loading. In addition, the displacement trajectories of the landing differs significantly between positive and negative transverse displacement loading. This is due to the fact that the stair in a scissors configuration leads to different contact locations between the upper flight and landing for loading applied in positive and negative directions.

4.4.2 Results: Modal Characteristics of Variable Design Models

Table 4.8 summarizes the modal frequencies and the effective modal mass of the two horizontal predominate vibration modes of the eight stair models. The effects of design variables on modal characteristics of these stair systems are investigated by comparing the modal properties of the seven design variants with those of *Baseline Model*. These results are subsequently grouped according to design variable category, as shown in Figure 4.17.

As can be seen from Figure 4.17, geometric configuration and connection details exert the most significant effects on stair modal frequencies among the four sets of design variables. Model *Case 7*, which employes fixed-end connections on both the upper and lower flight-to-floor boundaries, observes a frequency increase by about 50% associated with the two horizontal vibration modes. The modal frequencies of the straight-run stair (*Case 8*) are also appreciably higher than those of the scissors stair (*Baseline Model*), with an increase of 100% for the transverse-to-stair-run mode and 50% for the parallel-to-stair-run mode. This is due to the fact that the deformation mechanism of a straight-run stair differs fundamentally from that of a scissors stair. Although the modal

Table 4.8. Modal frequencies and the associated effective modal mass of the stair models in the parametric study.

Model	Transverse-to-stair-run				Parallel-to-stair-run			
	f (Hz)	M_{eff}^{long} (%)	M_{eff}^{trans} (%)	M_{eff}^{z} (%)	f (Hz)	M_{eff}^{long} (%)	M_{eff}^{trans} (%)	M_{eff}^{z} (%)
Case-1	7.7	0.1	66.9	0.0	19.3	73.9	0.7	0.1
Case-2	6.2	0.1	68.1	0.0	17.9	73.1	0.5	0.0
Case-3	5.1	0.0	68.8	0.0	16.2	71.0	0.2	0.0
Case-4	8.4	0.1	66.9	0.0	19.3	74.0	0.7	0.1
Case-5	12.4	0.1	68.8	0.0	19.3	74.3	0.4	0.1
Case 6	6.9	2.1	63.4	0.0	14.3	59.3	4.7	0.0
Case 7	12.7	0.2	65.4	0.0	29.4	52.1	4.8	0.0
Case 8	14.8	0.0	68.5	0.0	30.5	56.7	0.0	4.4

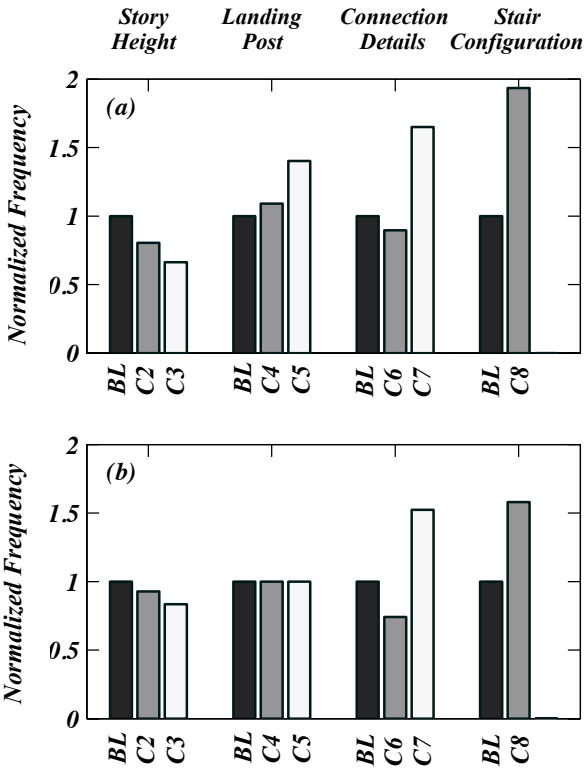

Figure 4.17. Normalized modal frequencies of the stair models relative to *Baseline Model*: (a) transverse-to-stair-run modes, and (b) parallel-to-stair-run modes (cases denoted as BL and C1-8; see Table 4.6).

characteristics appear less sensitive to the remaining two sets of design variable, increasing the building height reduces the frequencies of the two fundamental modes as a result of larger flight span and landing posts. In addition, stiffer landing posts (*Case 5*) effectively increase the frequency of the stair transverse-to-stair-run mode, however its influence on the parallel-to-stair-run mode is almost insignificant.

4.4.3 Results: Lateral Force-Displacement Response of Variable Design Models

To investigate the effects of design variables on the lateral force-displacement responses of the stair models, the numerically predicted performance parameters are summarized in Tables 4.9–4.10. The performance parameters of each model are normalized by their corresponding values of *Baseline Model*. These results are subsequently grouped by design variable category, as presented in Figures 4.18. The figure consists of four rows, each representing one of the four design categories considered in the parametric study. In addition, the figures on the left column show the force-displacement results of the stair models in the parallel loading direction, while those on the right show the results in the transverse loading direction.

Effect of Story Height and Landing Post

As shown in Figures 4.18a–d, the influence of story height and landing post on the performance parameters investigated in this study are limited. The largest observed differences of all performance parameters are no more than 50%. The most significant effect of increasing story height is the increase of landing relative displacement when loading applied in the parallel direction and the reduced stiffness when loading applied in the transverse direction. Since the stair behavior under transverse loading is highly dependent on the upper flight bending, a larger flight span due to increased story height effectively reduces the stair stiffness in the transverse loading direction. Similarly, larger transverse landing displacements during parallel loading is attributed to longer landing posts, since the stair response under parallel loading are largely dictated by landing torsional behavior. Therefore, stiffer landing posts (HSS in *Case 5*) effectively increase

Table 4.9. Performance parameters of the stair design variants under parallel-to-stair-run-loading.

Model	Loading direction	K_e (kN/mm)	Δ_y (mm [%])	F_y (kN)	F_u (kN)	Ω	$\Delta_{long}^{landing}$ (mm [%])	$\Delta_{trans}^{landing}$ (mm [%])
Case 1 (Baseline)	Positive	1.09	7.1 [0.20]	7.9	47.6	6.1	107.1 [2.98]	65.2 [1.81]
	Negative	1.05	7.6 [0.21]	7.2	47.0	6.5	58.0 [1.61]	71.1 [1.97]
Case 2	Positive	1.04	7.7 [0.18]	7.7	49.8	6.5	130.2 [3.10]	104.2 [2.48]
	Negative	1.01	7.7 [0.18]	7.1	52.1	7.3	73.1 [1.74]	97.9 [2.33]
Case 3	Positive	0.99	8.1 [0.17]	7.6	51.9	6.8	151.6 [3.16]	143.7 [2.99]
	Negative	0.98	8.8 [0.18]	7.6	57.2	7.5	89.9 [1.87]	128.8 [2.68]
Case 4	Positive	1.23	7.6 [0.21]	9.0	49.5	5.5	103.4 [2.87]	53.9 [1.50]
	Negative	1.10	7.6 [0.21]	7.5	49.8	6.7	53.1 [1.47]	63.8 [1.77]
Case 5	Positive	1.54	7.6 [0.21]	11.3	55.8	4.9	98.5 [2.74]	40.1 [1.11]
	Negative	1.26	7.1 [0.20]	7.7	54.6	7.1	40.3 [1.12]	45.3 [1.26]
Case 6	Positive	0.50	14.7 [0.41]	6.3	32.3	5.2	73.0 [2.03]	63.6 [1.77]
	Negative	0.64	12.2 [0.34]	6.9	41.2	6.0	56.2 [1.56]	75.8 [2.10]
Case 7	Positive	1.20	7.6 [0.21]	8.4	43.9	5.2	89.1 [2.48]	69.6 [1.93]
	Negative	1.99	8.6 [0.24]	15.2	67.1	4.4	83.2 [2.31]	88.5 [2.46]
Case 8	Positive	1.00	8.1 [0.23]	7.3	43.5	6.0	42.7 [1.19]	0.6 [0.02]
	Negative	7.92	8.1 [0.23]	52.7	152.5	2.9	69.6 [1.93]	0.3 [0.01]

Table 4.10. Performance parameters of the stair design variants under transverse-to-stair-run-loading.

Model	Loading direction	K_e (kN/mm)	Δ_y (mm [%])	F_y (kN)	F_u (kN)	Ω	$\Delta_{long}^{landing}$ (mm [%])	$\Delta_{trans}^{landing}$ (mm [%])
Case 1 (Baseline)	Positive	0.59	12.7 [0.35]	7.0	19.2	2.7	20.6 [0.57]	6.4 [0.18]
	Negative	0.51	17.8 [0.49]	8.1	21.7	2.7	19.7 [0.55]	39.2 [1.09]
Case 2	Positive	0.41	14.8 [0.35]	5.7	15.9	2.8	20.6 [0.49]	6.3 [0.15]
	Negative	0.34	21.3 [0.51]	6.7	17.4	2.6	19.8 [0.47]	45.0 [1.07]
Case 3	Positive	0.29	18.3 [0.38]	4.8	13.9	2.9	19.8 [0.41]	6.0 [0.13]
	Negative	0.24	25.7 [0.54]	5.6	14.0	2.5	19.4 [0.40]	49.8 [1.04]
Case 4	Positive	0.59	13.2 [0.37]	7.2	19.8	2.7	20.2 [0.56]	5.4 [0.15]
	Negative	0.53	17.3 [0.48]	8.3	20.8	2.5	19.6 [0.55]	38.9 [1.08]
Case 5	Positive	0.61	13.2 [0.37]	7.4	21.2	2.9	19.5 [0.54]	4.0 [0.11]
	Negative	0.59	15.7 [0.44]	8.8	22.9	2.6	18.0 [0.50]	33.9 [0.94]
Case 6	Positive	0.41	17.3 [0.48]	5.7	16.3	2.9	4.6 [0.13]	1.0 [0.03]
	Negative	0.40	17.3 [0.48]	5.7	16.6	2.9	2.4 [0.07]	8.4 [0.23]
Case 7	Positive	0.94	17.8 [0.49]	11.1	24.5	2.2	3.3 [0.09]	18.4 [0.51]
	Negative	0.92	16.8 [0.47]	10.9	24.6	2.3	0.6 [0.02]	8.2 [0.23]
Case 8	Positive	0.23	24.4 [0.68]	5.4	9.9	1.8	3.4 [0.10]	50.4 [1.40]
	Negative	0.23	24.4 [0.68]	5.5	10.0	1.8	3.4 [0.10]	50.3 [1.40]

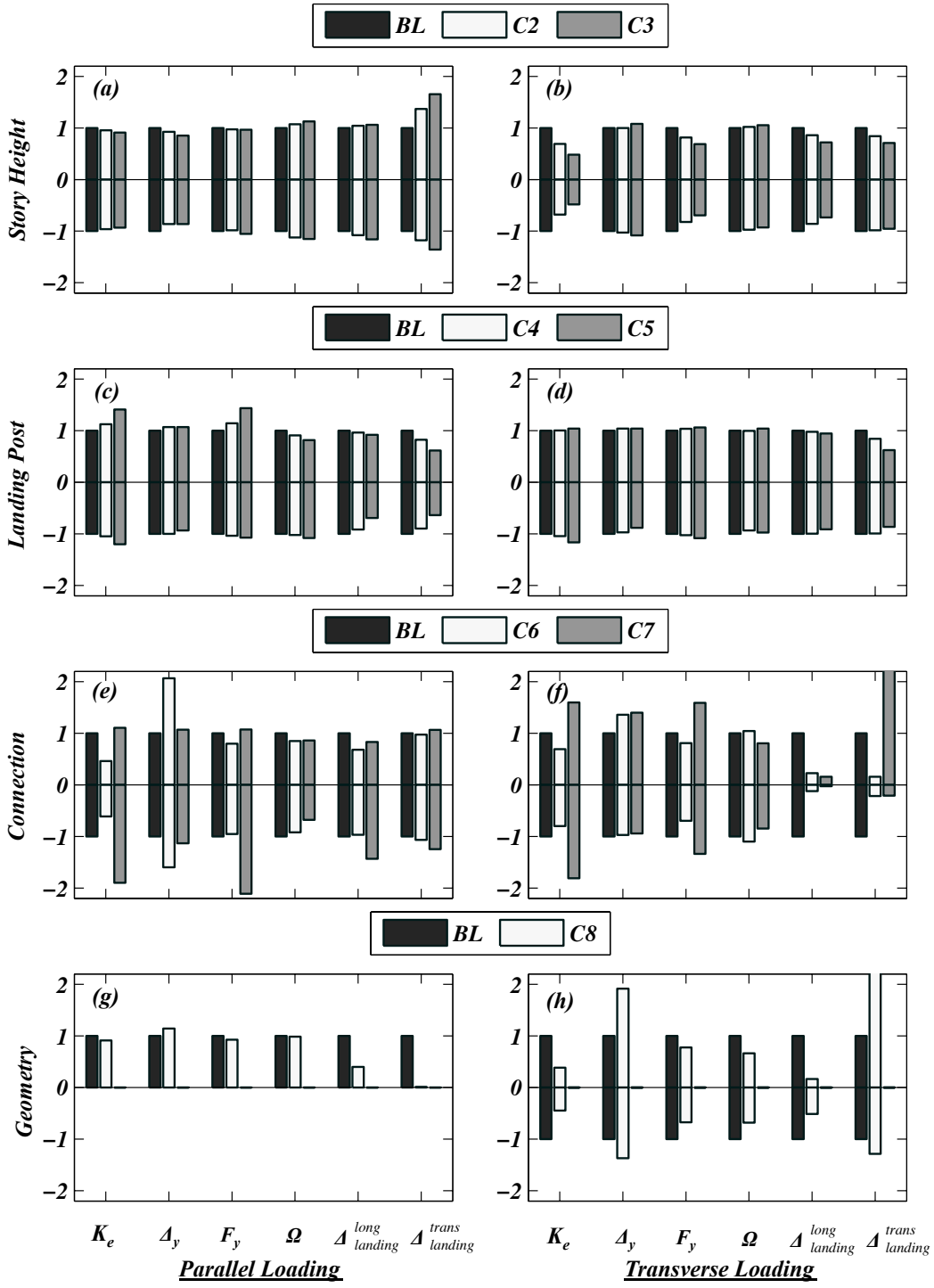

Figure 4.18. Normalized performance parameters of the force-displacement behavior of the stair models relative to *Baseline Model* (cases denoted as BL and C1-8; see Table 4.6).

the stiffness of the stair and thus reduces the landing deformation in the parallel loading case, however its influence on the stair behavior in transverse loading case is much less significant.

Effect of Connection Details

As shown in Figure 4.18e–f, connection details on the performance parameters appear much more sensitive to than the story height and the landing post configuration. It is noted that *Baseline Model* (Type-I connection) and *Case 6* (Type-II connection) are designed with a intended yielding mechanism on the upper flight-to-floor connections, while *Case 7* (Type-III connection) represents fixed-end connection design on both the upper and lower flight-to-floor connections (schematic illustrations of the upper connections are provided in Figure 4.19). As can be seen in the figures, The initial stiffness of the stair with Type-II connection are about 50% lower than that of Type-I connection *Baseline Model*, while the stair Type-III connection leads to an increase of stiffness and ultimate force by as much as twice compared to that with Type-I connection (*Baseline Model*). It is also observed in Figure 4.18f that the transverse landing displacements of the stair with Type-III connection are much larger than that of the *Baseline Model* during the transverse loading case. However, it is important to note that the landing displacements in the transverse loading case is much smaller than those in the parallel loading case (Figure 4.16b), and therefore the landing displacements remain very small despite of a large ratio of increase.

The stress and strain responses of the stair connections are used to investigate the local behavior for different types of connections. As discussed previously, the stairs sustain considerably larger forces and displacements when displacement loading is applied in the parallel direction. Therefore, comparison of the connection local behavior is focused on the parallel-to-stair-run loading case. The principal stresses of the shell elements along the welds are used as indicators of potential for brittle fracture. Previous research has revealed that weld fracture usually occurs abruptly and is not always accompanied with global plastic deformation (El-Tawil et al., 2000). Consequently, the PEEQ index (Lu et al., 2000; Mao et al., 2001), defined as the plastic equivalent strain

divided by the yield strain, is used as a measure of the ductile fracture potential. In addition, the connection deformation is used as an index for evaluating the global deformation demands of these connections.

Table 4.11 summarizes the stress and strain behavior of the flight-to-building connections as well as the connection deformations for stairs with different connection details (Type-I connection – *Baseline Model*, Type-II connection – *Case-6*, and Type-III connection – *Case-7*). Monotonic displacement loading is applied in the parallel direction until the stairs attain their ultimate state (2.5% interstory drift). The deformed shapes and von-Mises stress distribution of the upper flight-to-building connections of these stairs are illustrated in Figure 4.19. As shown in Table 4.11, *Baseline Model* and *Case-6* attain considerable large deformations (accounting for 30%-40% interstory drift) on the upper connection, since these connections are specifically designed with a intended yielding mechanism (Figure 4.19a–b). In contrast, the connection deformation of Type-III connection (*Case-7*) is much smaller (Figure 4.19c) due to lack of deformability at both the upper and lower connections. As a result, the differential displacement demands are accommodated primarily by the landing movement and flight-to-landing connection deformation. Although the maximum principal stresses of the upper connections are comparable for the three stair variants, the stress demands on the lower connections are slightly smaller than those of the upper connections for Type-II and Type-III connections. In addition, the PEEQ indices indicate that the fixed-end upper connection (*Case-7*) sustains much larger localized plastic strains than the other two connection types with intended yielding mechanism. While plastic yielding are fully developed on both ends of the flexible connections when the stairs reach the ultimate state of 2.5% interstory drift (Figures 4.19a and b), plastic deformation tends to concentrate at the tip of the vertical weld on one side of the fixed-end connection, while the other side of the connection remains essentially elastic (Figure 4.19c).

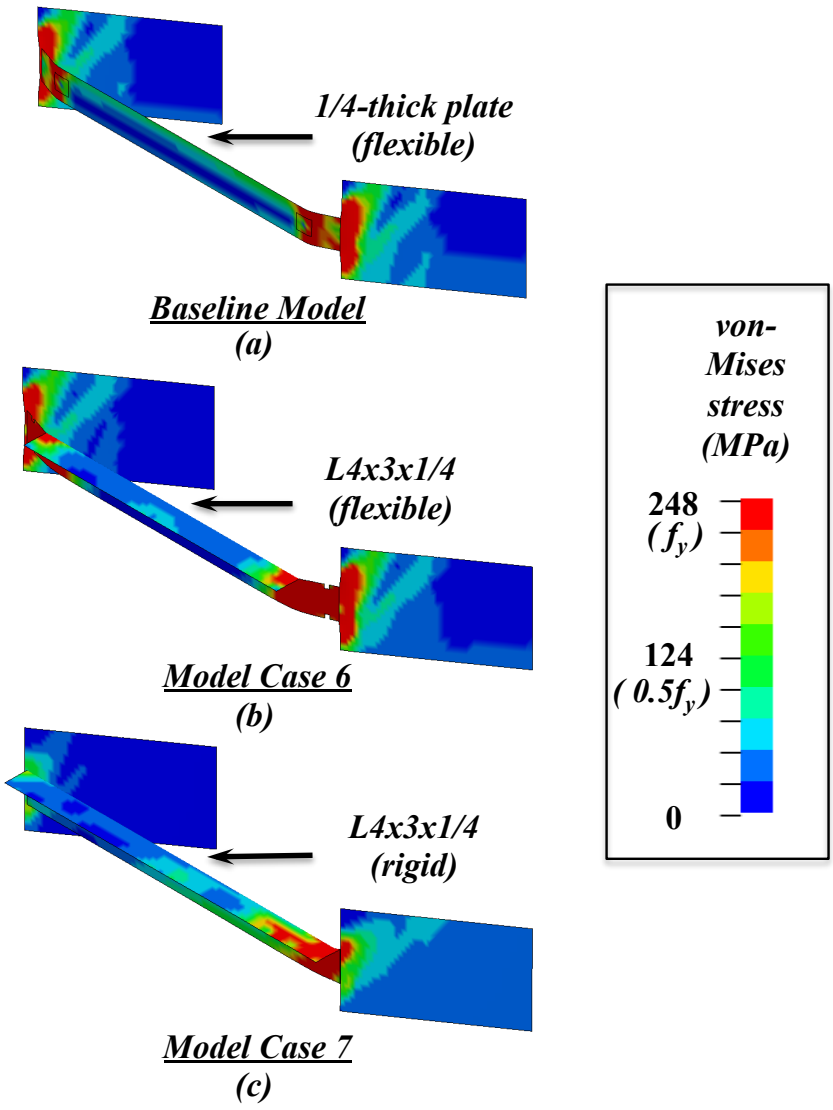

Figure 4.19. Deformed shape and von-Mises stress distribution of the upper flight-to-building connections when the stairs reach the ultimate state (2.5% interstory drift) under positive parallel-to-stair-run loading: (a) Type-I connection – *baseline model*, (b) Type-II connection – *Case 6*, and (c) Type-III connection – *Case 7*.

Table 4.11. flight-to-building connection behavior under parallel-to-stair-run loading at 2.5% interstory drift.

Connection type [1] (Model case)	Location	σ_1 [2] (MPa)	PEEQ index[3]	Δ^{conn} [4] (mm)
Type-I (Case 1 - Baseline)	Upper	366	90	36.0
	Lower	358	82	9.3
Type-II (Case 6)	Upper	357	76	42.3
	Lower	300	66	7.6
Type-III (Case 7)	Upper	365	242	2.4
	Lower	310	75	4.5

[1]see Table 4.6 for the stair models defined for the parametric study; [2]maximun principle stress of the connection plate or angel; [3]a measure of the connection ductile fracture potential, which is defined as plastic equivalent strain divided by the yield strain; [4]longitudinal deformation of the connection.

Effect of Geometric Configuration

As shown in Figure 4.18g–h, the performance parameters of the straight-run stair (*Case 8*) remain similar to those of *Baseline Model*, however its stiffness reduces more than 50% during transverse loading. As discussed previously, the stair behavior during

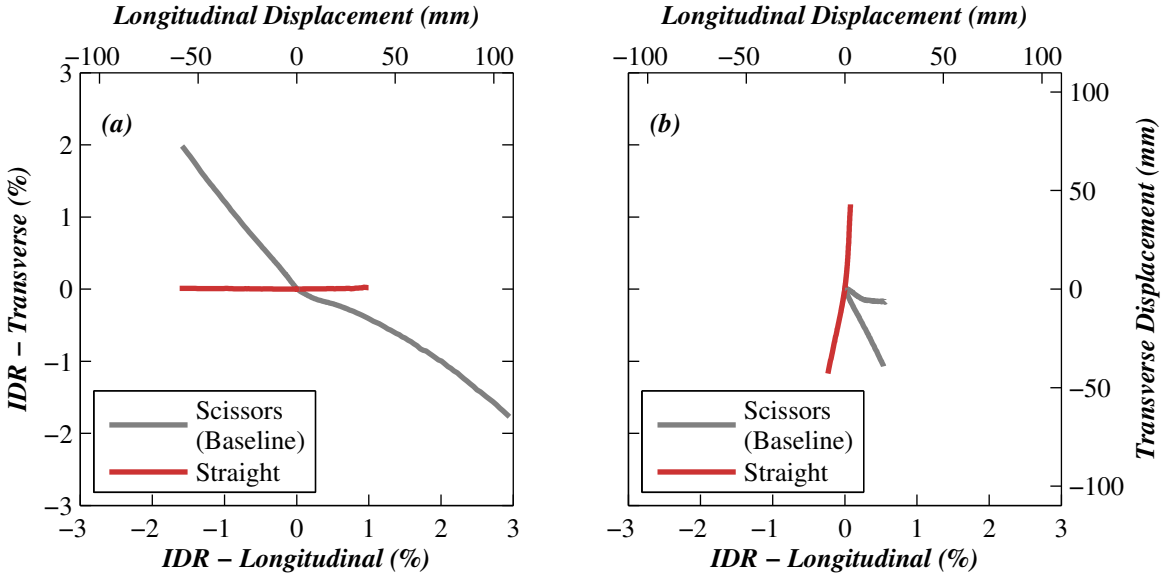

Figure 4.20. Landing displacement trajectory of stair models with varying geometric configuration: (a) parallel-to-stair-run loading, and (b) transverse-to-stair-run loading.

transverse loading is largely dependent on the flight behavior. A straight-run configuration effectively increases the stair flexibility when stairs deforms transversely, and therefore leads to significant stiffness reduction and slightly lower force demand. The most significant aspect due to the change of stair configuration, however, is related to the deformation pattern of the stair system. As shown in Figure 4.20, while the landing sustains substantial torsion in a scissor configuration, this effect becomes insignificant when a straight configuration is used, since the displacement trajectory of the landing remains essentially in parallel with the loading direction.

4.5 Summary and Conclusions

This chapter presents a computational study to assess the seismic behavior of prefabricated steel stairs using detailed three-dimensional finite element models. The accuracy of the models in capturing the seismic behavior of the stairs is validated through comparison with extensive experimental data. A parametric study is subsequently performed to explore the effect of critical design variables on the modal characteristics and the force-displacement responses of a broad range of stair design. Design variables studied in this chapter include story height, landing post configuration, connection details, and geometric configuration. Based on the parametric assessment of the eight stair models, key findings regarding the seismic behavior of the prefabricated steel stairs are summarized as follows:

1. The predominant frequencies of the stairs are 5–15 Hz for the transverse-to-stair-run and 15–30 Hz for the parallel-to-stair-run vibrational modes, respectively. The frequency range of the two horizontal modes is more likely to coincide with the higher modes of a typical multi-story frame building. The vertical vibration modes are less likely to be activated, as these vibrational frequencies are considered too high for buildings under earthquake excitations.

2. While the occurrences of plastic yielding of the prefabricated steel stairs vary for loading in the two horizontal directions, the yield displacements are smaller than 0.5% interstory drift, indicating that the yielding of the stairs may occur during a low-amplitude earthquake when the building response remains elastic.

3. The force-displacement responses of the stairs differ significantly for loading in the two horizontal directions. The stair is subjected to smaller force and relative landing displacement demands in the case of transverse-to-stair-run loading. This is due to the fact that upper flight deformation effectively improves the deformability of the stairs and reduces the force demands and the landing displacements in the case of transverse-to-stair-run loading, while interstory drift demands may impose large deformation demands on the landing and connections in the case of parallel-to-stair-run loading.

4. Among the four sets of design variables considered in this chapter, the modal characteristics and the seismic response of the stairs are most sensitive to the variation of connection details and geometric configurations, as these parameters significantly modify the deformation mechanisms of the stair systems. In particular, the connections are subjected to large stress and plastic strain demands under lateral loading. The capability of these connections to sustain the force and deformation demands is crucial for the seismic performance of the stair systems.

The computational study presented in this chapter provides insight into understanding the seismic behavior of prefabricated steel stairs in its isolated configuration. These results are used as a basis for system-level numerical simulation studies in the following chapter.

Acknowledgements

Portions of the following submitted publication, for which the dissertation author was the primary investigator and author, are contained in this chapter:

- Wang, X., Hutchinson, T., and Conte, J. "Computational Assessment of the Seismic Behavior of Prefabricated Steel Stairs." Submitted to *ASCE J. Struct. Eng.*

Chapter 5

Numerical Study of the Seismic Behavior of Building-Stair Systems

5.1 Introduction

Building upon the understanding gained from the experimental research and numerical parametric study of the stair components described in the previous chapters, the stairs are integrated into building models to investigate the interaction between buildings and stair systems. the coupled building-stair systems. The coupled building-stair systems, implemented as two-dimensional design-oriented models, are developed using the structural analysis platform *OpenSees* (Mazzoni et al., 2014). For the coupled systems, the prototype buildings include two sets of special moment frame structures with varied structural system and number of stories, and stair systems are represented by prefabricated steel stairs with parameterized force-displacement response characteristics.

This chapter is organized into five sections. Section 5.2 describes the seismic design criteria, structural systems, design loads, and other design aspects related to the prototype buildings. Section 5.3 presents the modeling techniques of the building structural systems and the stair systems implemented into the system-level models. Section 5.4 presents the system-level simulation results using different analysis procedures. In particular, the interacting effects between buildings and stair systems on the struc-

tural response of the coupled building-stair systems are investigated. Lastly, Section 5.5 summarizes the important findings regarding the system-level numerical study of the coupled building-stair systems.

5.2 Prototype Building Inventory

The building inventory includes two sets of special moment frame (SMF) buildings – steel buildings and reinforce concrete buildings. Each building set consists of three building variants with 4, 8, and 20 stories, representing typical low-, medium-, and high-rise building design. These buildings are designed as part of the FEMA P695 project (FEMA, 2009; NIST, 2010) for seismic performance and collapse safety evaluation (Haselton et al., 2010; Zareian et al., 2010). The hypothetical site of the prototype building design represents a high seismic region near downtown Los Angeles (33.996N, 118.162W), corresponding to a NERHP site class D (stiff soil) with a $V_{s,30}$ of 285 m/s (Haselton and Deierlein, 2007). According to the 2003 IBC seismic design hazard maps (ICC, 2003), the mapped spectral accelerations are S_s = 1.50 g and S_1 = 0.60 g. Therefore, the spectral accelerations S_{DS} = 1.0 g and S_{D1} = 0.60 g are used in the seismic design of the prototype buildings.

5.2.1 Steel Buildings

The steel prototype buildings were designed in accordance with the code-based requirements within AISC 341-05, *Seismic Provisions for Structural Steel Buildings* (AISC, 2005a), AISC 358-05, *Prequalified Connections for Special and Intermediate Steel Moment Frames for Seismic Applications* (AISC, 2005b), and ASCE 7-05, *Minimum Design Loads for Buildings and Other Structures* (ASCE, 2005). The response spectrum analysis procedures were employed to determine the minimum base shear and story drift limits of the steel SMF buildings. The seismic response modification factor R was taken as 8 and the deflection amplification factors C_d as 8 in the design.

The three steel buildings employed identical plan layout with a dimension of 42.7 × 30.5 m (140×100 ft), as shown in Figure 5.1. They are hereinafter referred to as build-

ing S-4, S-8, and S-20, respectively. The lateral load resisting system of each building consisted of two three-bay SMFs placed at the perimeter in each of the two horizontal directions, with equal spans of 6.1 m on center. The building height was 4.6 m for the first story and 4.0 m for all remaining stories. The design dead and life loads were 4.3 kN/m^2 and 2.4 kN/m^2, both of which were assumed uniformly distributed over each floor of the building. Furthermore, the cladding load of 1.2 kN/m^2 on the building perimeter was considered in the design.

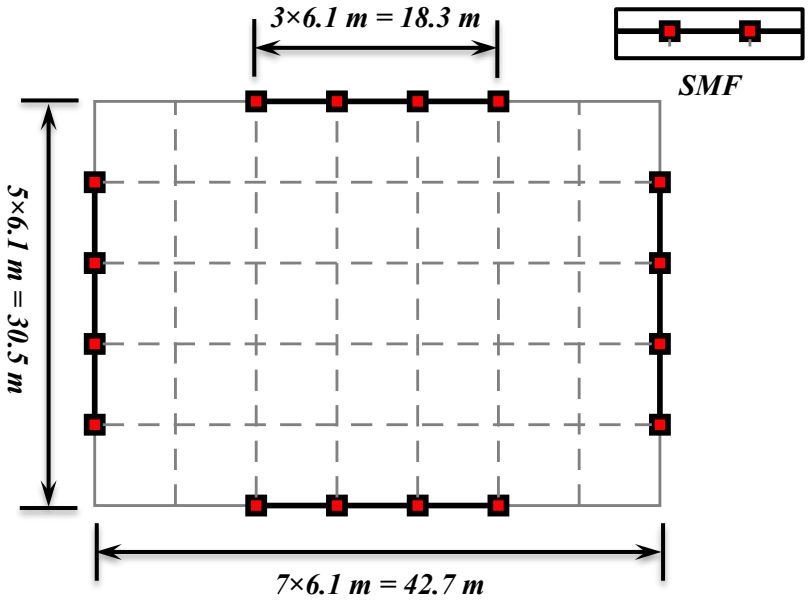

Figure 5.1. Plan layout of the steel prototype buildings.

Figures 5.2–5.4 show the elevation of the three steel prototype buildings and the sizes of wide-flange beams and columns. While an exterior column may differ from an interior column at the same story, the beams were all designed using an identical member. Beams and columns of the steel SMFs were designed using ASTM A992 steel (f_y=345 MPa). Reduced beam sections (RBSs) conforming to AISC 358-05 requirement (AISC, 2005b) were applied on the beams. In addition, doubler plates were provided in the joint panel zones according to the AISC-360 requirements (AISC, 2005c). Additional information of the design of the steel prototype buildings are documented in NIST GCR 10-917-8 (NIST, 2010).

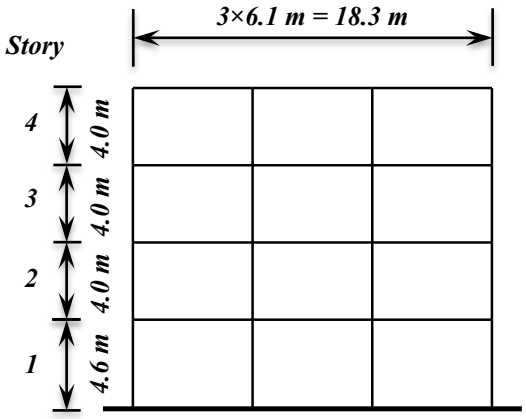

Member Size			
Story	*Beam*	*Exterior Column*	*Interior Column*
4	W21×57	W24×62	W24×62
3	W21×57	W24×62	W24×62
2	W21×73	W24×103	W24×103
1	W21×73	W24×103	W24×103

Figure 5.2. Elevation of building S-4 and the beam and column member sizes.

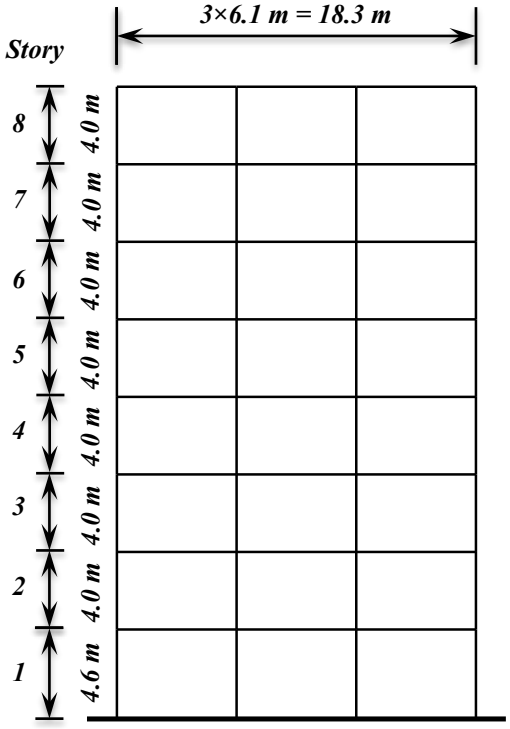

Member Size			
Story	*Beam*	*Exterior column*	*Interior column*
8	W21×68	W24×94	W24×94
7	W24×84	W24×94	W24×94
6	W24×84	W24×131	W24×131
5	W27×94	W24×131	W24×131
4	W27×94	W24×131	W24×162
3	W30×116	W24×131	W24×162
2	W30×116	W24×131	W24×162
1	W30×108	W24×131	W24×162

Figure 5.3. Elevation of building S-8 and the beam and column member sizes.

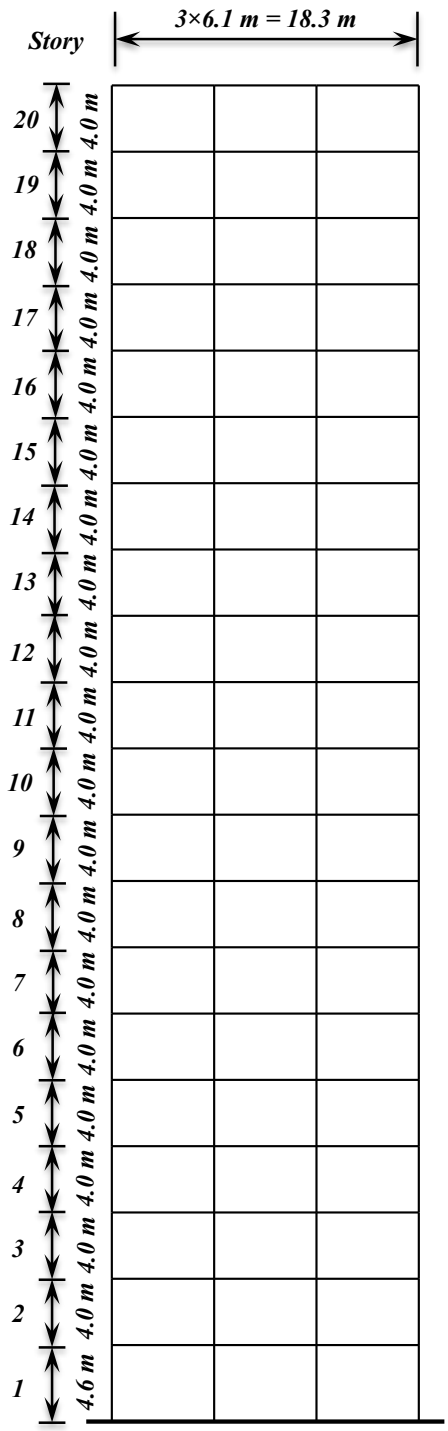

Member Size

Story	*Beam*	*Exterior column*	*Interior column*
20	W24×62	W14×132	W24×103
19	W24×62	W14×132	W24×103
18	W30×108	W14×132	W24×162
17	W30×108	W14×132	W24×162
16	W30×108	W14×159	W24×162
15	W30×108	W14×159	W24×162
14	W33×141	W14×233	W24×250
13	W33×141	W14×233	W24×250
12	W33×141	W14×283	W24×250
11	W33×141	W14×283	W24×250
10	W33×141	W14×311	W24×279
9	W33×141	W14×311	W24×279
8	W33×169	W14×370	W24×335
7	W33×169	W14×370	W24×335
6	W33×169	W14×398	W24×335
5	W33×169	W14×398	W24×335
4	W33×169	W14×426	W24×335
3	W33×169	W14×426	W24×335
2	W33×169	W14×426	W24×335
1	W33×169	W14×426	W24×335

Figure 5.4. Elevation of building S-20 and the beam and column member sizes.

5.2.2 Reinforced Concrete Buildings

The three reinforced concrete buildings were designed following the seismic design provisions of ACI 318-05 *Building Code Requirements for Structural Concrete* (ACI, 2005) and ASCE 7-05, *Minimum Design Loads for Buildings and Other Structures* (ASCE, 2005). The response spectrum analysis procedures were employed as the basis for the seismic design of these reinforced concrete SMFs. The seismic response modification factor R was taken as 8 and the deflection amplification factors C_d as 5.5 in the design.

Figure 5.5 shows the plan configuration of the three reinforced concrete buildings. They are hereinafter referred to as building RC-4, RC-8, and RC-20, respectively. It is noted that building RC-4 had a larger plan configuration of 36.6 × 54.9 m (Figure 5.5b), while buildings RC-8 and RC-20 had a square plan configuration of 36.6 × 36.6 m (Figure 5.5a). Similar to the steel buildings, the lateral load resisting system of each reinforced concrete building consisted of two three-bay perimeter SMFs spaced at 9.1 m on center in each of the two horizontal directions. The building height was 4.6 m for the first story and 4.0 m for all remaining stories. The uniformly distributed design dead and live loads were 3.8 kN/m^2 and and 2.4 kN/m^2, respectively.

Figures 5.6–5.8 shows the elevation of the three reinforced concrete prototype buildings as well as the associated reinforcement details of the beams and columns. It is noted that while the column reinforcement ratio denotes the total reinforcement ratio of the section, the beam reinforcement ratio differs between the top and the bottom of a beam section and therefore are specified separately. Concrete strength of the columns were determined by satisfying strong-column-weak-beam and joint shear requirements. The beam stirrups was controlled by shear capacity design, while the column transverse reinforcement was based on confinement requirements. Additional information of the design of the reinforced concrete buildings are documented in FEMA P-695 (FEMA, 2009).

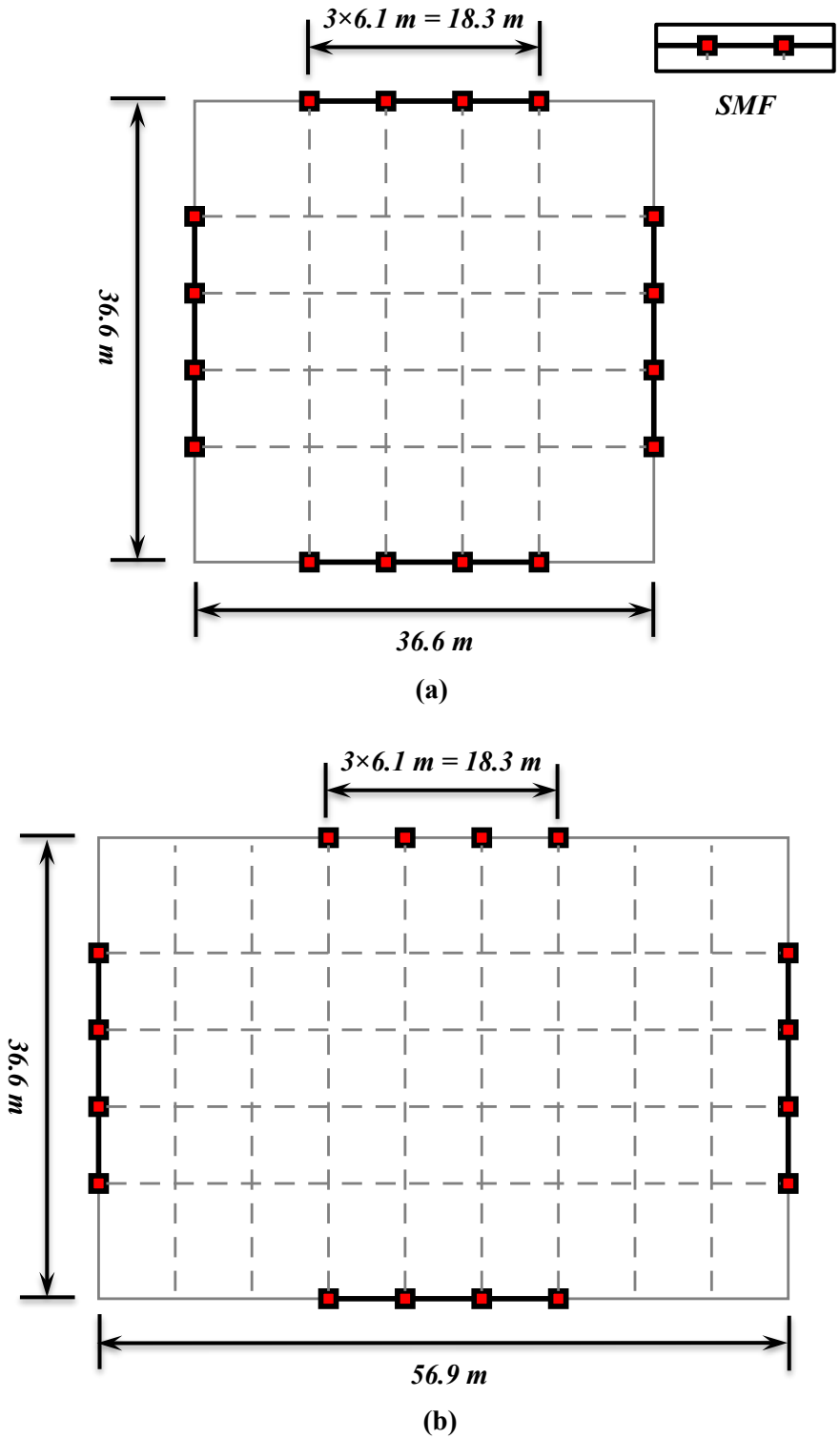

Figure 5.5. Plan layout of the reinforced concrete prototype buildings for: (a) RC-8 and RC-20, and (b) RC-4.

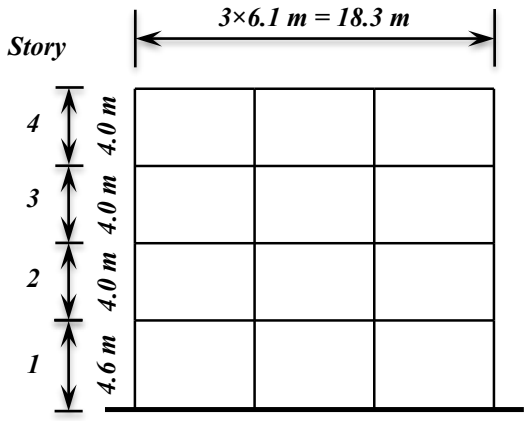

Story	Member Size (Longitudinal Reinforcement Ratio) Beam	Exterior Column	Interior Column
4	0.61×0.81 m (0.48%/0.60%)	0.76×0.81 m (1.00%)	0.96×0.81 m (1.00%)
3	0.61×0.81 m (0.93%/1.08%)	0.76×0.81 m (1.00%)	0.96×0.81 m (1.00%)
2	0.61×0.81 m (1.00%/1.15%)	0.76×0.81 m (1.00%)	0.96×0.81 m (1.00%)
1	0.61×0.81 m (1.08%/1.23%)	0.76×0.81 m (2.10%)	0.96×0.81 m (1.60%)

Figure 5.6. Elevation of building RC-4 as well as the member size and reinforcement ratio of the beams and columns.

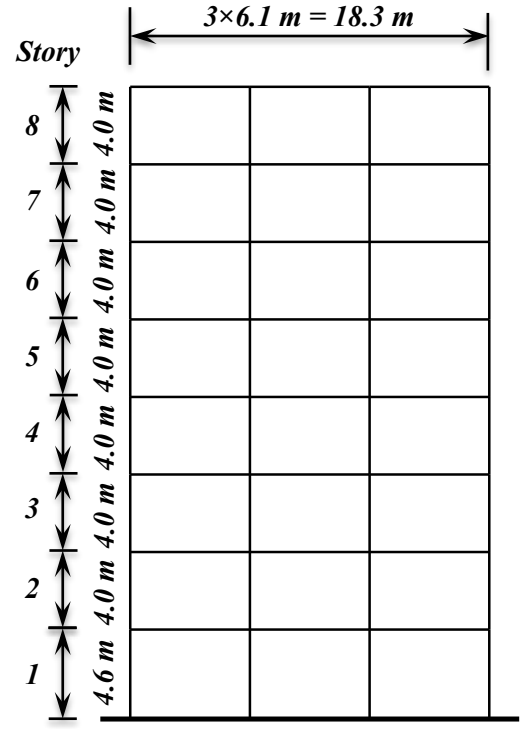

Story	*Member Sizes (Longitudinal Reinforcement Ratio)* Beam	Exterior column	Interior column
8	0.76×0.66 m (0.32%/0.32%)	0.71×0.66 (1.00%)	0.71×0.66 m (1.00%)
7	0.76×0.66 m (0.32%/0.40%)	0.71×0.66 m (1.00%)	0.71×0.66 m (1.40%)
6	0.76×0.66 m (0.40%/0.55%)	0.71×0.66 m (1.00%)	0.71×0.66 m (1.50%)
5	0.76×0.66 m (0.63%/0.75%)	0.71×0.66 m (1.30%)	0.71×0.66 m (2.20%)
4	0.76×0.66 m (0.68%/0.75%)	0.71×0.66 m (1.28%)	0.86×0.66 m (1.13%)
3	0.76×0.66 m (0.68%/0.80%)	0.71×0.66 m (1.48%)	0.86×0.66 m (1.30%)
2	0.76×0.66 m (0.73%/0.83%)	0.71×0.66 m (1.48%)	0.86×0.66 m (1.30%)
1	0.76×0.66 m (0.68%/0.75%)	0.71×0.66 m (2.00%)	0.86×0.66 m (1.80%)

Figure 5.7. Elevation of building RC-8 as well as the member size and reinforcement ratio of the beams and columns.

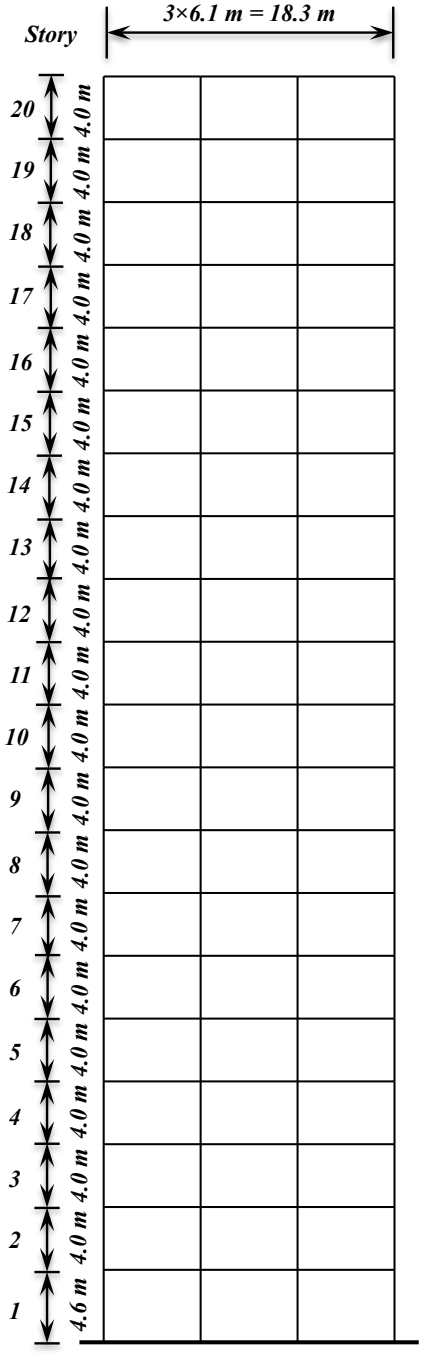

Story	Member Size (Longitudinal Reinforcement Ratio) Beam	Exterior column	Interior column
20	1.07×0.81 m (0.33%/0.33%)	0.91×0.81 (1.00%)	0.91×0.81 m (1.20%)
19	1.07×0.81 m (0.33%/0.33%)	0.91×0.81 (1.00%)	0.91×0.81 m (1.30%)
18	1.07×0.81 m (0.33%/0.33%)	0.91×0.81 (1.00%)	0.91×0.81 m (1.30%)
17	1.07×0.81 m (0.33%/0.33%)	0.91×0.81 (1.00%)	0.91×0.81 m (1.50%)
16	1.07×0.81 m (0.33%/0.33%)	0.91×0.81 (1.00%)	0.91×0.81 m (1.60%)
15	1.07×0.81 m (0.33%/0.33%)	0.91×0.81 (1.00%)	0.91×0.81 m (1.70%)
14	1.07×0.81 m (0.33%/0.33%)	0.91×0.81 (1.20%)	0.91×0.81 m (1.80%)
13	1.07×0.81 m (0.33%/0.33%)	0.91×0.81 (1.20%)	0.91×0.81 m (1.90%)
12	1.07×0.81 m (0.33%/0.33%)	1.07×0.81 m (1.10%)	1.07×0.81 m (1.60%)
11	1.07×0.81 m (0.33%/0.33%)	1.07×0.81 m (1.10%)	1.07×0.81 m (1.60%)
10	1.07×0.81 m (0.33%/0.33%)	1.07×0.81 m (1.20%)	1.07×0.81 m (1.60%)
9	1.07×0.81 m (0.33%/0.33%)	1.07×0.81 m (1.25%)	1.07×0.81 m (1.60%)
8	1.07×0.81 m (0.33%/0.33%)	1.07×0.81 m (1.30%)	1.07×0.81 m (1.65%)
7	1.07×0.81 m (0.33%/0.33%)	1.07×0.81 m (1.40%)	1.07×0.81 m (1.65%)
6	1.07×0.81 m (0.33%/0.33%)	1.07×0.81 m (1.45%)	1.07×0.81 m (1.70%)
5	1.07×0.81 m (0.33%/0.33%)	1.07×0.81 m (1.50%)	1.07×0.81 m (1.70%)
4	1.07×0.81 m (0.33%/0.33%)	1.07×0.81 m (1.60%)	1.07×0.81 m (1.70%)
3	1.07×0.81 m (0.33%/0.33%)	1.07×0.81 m (1.70%)	1.07×0.81 m (1.70%)
2	1.07×0.81 m (0.65%/0.70%)	1.07×0.81 m (1.80%)	1.07×0.81 m (1.70%)
1	1.07×0.81 m (0.60%/0.63%)	1.07×0.81 m (2.50%)	1.07×0.81 m (1.70%)

Figure 5.8. Elevation of building RC-8 as well as the member size and reinforcement ratio of the beams and columns.

5.2.3 Prototype Building Design Summary

According to ASCE 7-05 code requirements (ASCE, 2005), important seismic design parameters for the two sets of prototype buildings are summarized in Table 5.1. The table includes the design spectral accelerations S_{DS} and S_{D1}, the response modification factor R, the deflection amplification factor C_d, the code-based building fundamental period T, the numerically determined buildingfundamental period T_1, the seismic base shear coefficient C_s, and the design spectral acceleration associated with the code-based building period $S_a(T)$.

Table 5.1. Seismic design parameters of the prototype buildings

Building	S_{DS} (g)	S_{D1} (g)	R	C_d	T (sec)	T_1 (sec)	C_s	$S_a(T)$ (g)
S-4	1.0	0.6	8	8	0.95	1.50	0.067	0.95
S-8	1.0	0.6	8	8	1.64	2.00	0.039	0.55
S-20	1.0	0.6	8	8	3.37	3.60	0.037	0.27
RC-4	1.0	0.6	8	5.5	0.81	0.75	0.092	1.11
RC-8	1.0	0.6	8	5.5	1.49	1.25	0.050	0.60
RC-20	1.0	0.6	8	5.5	3.36	2.12	0.044	0.27

As prescribed in ASCE 7-05 (ASCE, 2005), the code-based building fundamental period T is calculated as $T = C_u T_a$ where C_u denotes the upper limit coefficient for period determination (Table 12.8-1 of ASCE 7-05) and T_a denotes the approximate fundamental period (Table 12.8-2 of ASCE 7-05). The base shear coefficient C_s is subsequently calculated as $C_s = S_{DS}/R$ for short-period buildings ($T < T_s$) and $C_s = S_{D1}/TR$ long-period buildings ($T_s < T < T_L$, where the transition periods $T_s = S_{D1}/S_{DS} = 0.6$ second and $T_L = 8$ second). It is noted that the calculated value of C_s are constrained by the minimum base shear requirement (ASCE, 2005). As shown in the Table 5.1, the design base shear coefficient C_s of the steel buildings are consistently smaller than those of their reinforced concrete building counterparts. This is due to the fact that the code-based fundamental periods T of steel buildings are slightly larger than those of reinforced concrete buildings.

5.3 Modeling of Building-Stair Systems

The coupled building-stair systems are developed in *OpenSees* (Mazzoni et al., 2014) as two-dimensional nonlinear analysis models. In these models, structural systems are modeled using phenomenological elements per ATC/PEER recommendations (ATC, 2010). Stair systems are modeled as idealized lumped springs to represent their force-displacement response under differential displacements. These models are a simplified design-oriented representation of the building-stair systems commonly used in practice. Detailed modeling techniques of the prototype buildings and the stairs of the system-level numerical models are discussed later in this section.

5.3.1 Modeling of Structural Systems

According to the idealization strategies of structural component modeling, various modeling techniques have been developed to analyze the seismic response of frame-type structural components. As shown in Figure 5.9, structural component models are often classified into three categories: concentrated plasticity models, distributed plasticity models, and continuum finite element models. A concentrated plasticity model consists of an elastic beam element with concentrated plastic hinges located at the two ends of the linear beam element to model the nonlinear response (Figure 5.9a), while a distributed plasticity model accounts for component nonlinear behavior using several fiber sections distributed along its longitudinal axis (Figure 5.9b). These two component models are also referred to as phenomenological models, since model calibration with test data are often required for accurately capture the component-level nonlinear behavior. On the other hand, continuum finite element models are the most sophisticated but computationally intensive models, which explicitly model the nonlinear component behavior using finely discretized continuum elements (Figure 5.9c). Although continuum models have the potential of accurately capturing the nonlinear behavior of structural components in the lack of test data, well-calibrated phenomenological models are capable of reflecting the overall response of the components at a much lower computational cost, and therefore they are the preferred modeling techniques for nonlinear structural analysis (ATC, 2010).

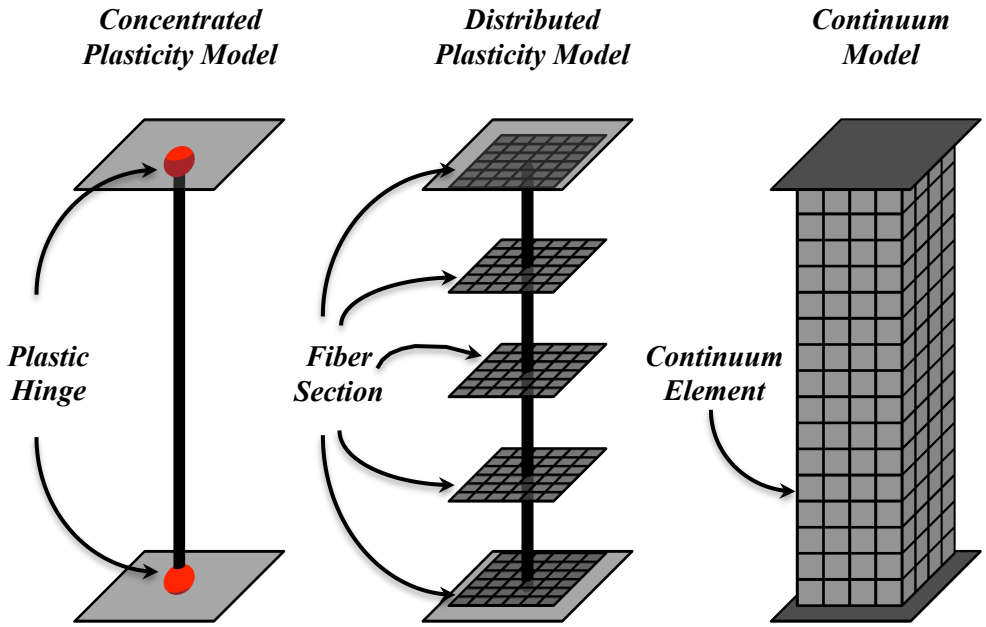

Figure 5.9. Different modeling strategies of frame-type structural components.

The structural components of the steel SMF buildings are modeled using concentrated plasticity models. The nonlinear moment-rotation response are modeled using a material model proposed by Ibarra et al. (2005) and later calibrated by Lignos and Krawinkler (2010) using extensive steel component cyclic test data. This model has been proved to be suitable for capturing steel component behavior under a wide range of deformation stages from the elastic loading stage to large inelastic deformation stage associated with significant stiffness and strength deterioration. In contrast, the response of a reinforced concrete component is nonlinear from the onset of loading, assuming a linear response prior to component yielding may not effectively reflect the response of reinforced concrete components under low- and moderate-intensity earthquakes (Haselton and Deierlein, 2007). Therefore, the structural components of reinforced concrete buildings are modeled using distributed plasticity models that explicitly considers the uniaxial stress-strain response of different materials in the section level.

5.3.2 Modeling of Prototype Buildings

Despite of different component modeling strategies for steel and reinforced concrete buildings, the general modeling assumptions of the two sets of the structural systems remain similar. Figure 5.10 illustrates a structural analysis model of the prototype buildings implemented in *OpenSees*. The model consists of a SMF system and "leaning columns" connected to the SMF, representing half of the prototype building. Since the lateral forces of each building are assumed to be resisted by the SMF, the interior gravity system are not explicitly considered in the structural model. Instead, the "leaning columns" are connected to the SMF using axially rigid truss elements with insignificant flexural stiffness at each floor to account for the $P-\Delta$ effects of the building systems. In addition, the buildings are assumed fixed at the column bases and therefore neglecting the foundation flexibility and soil-structure interaction effects.

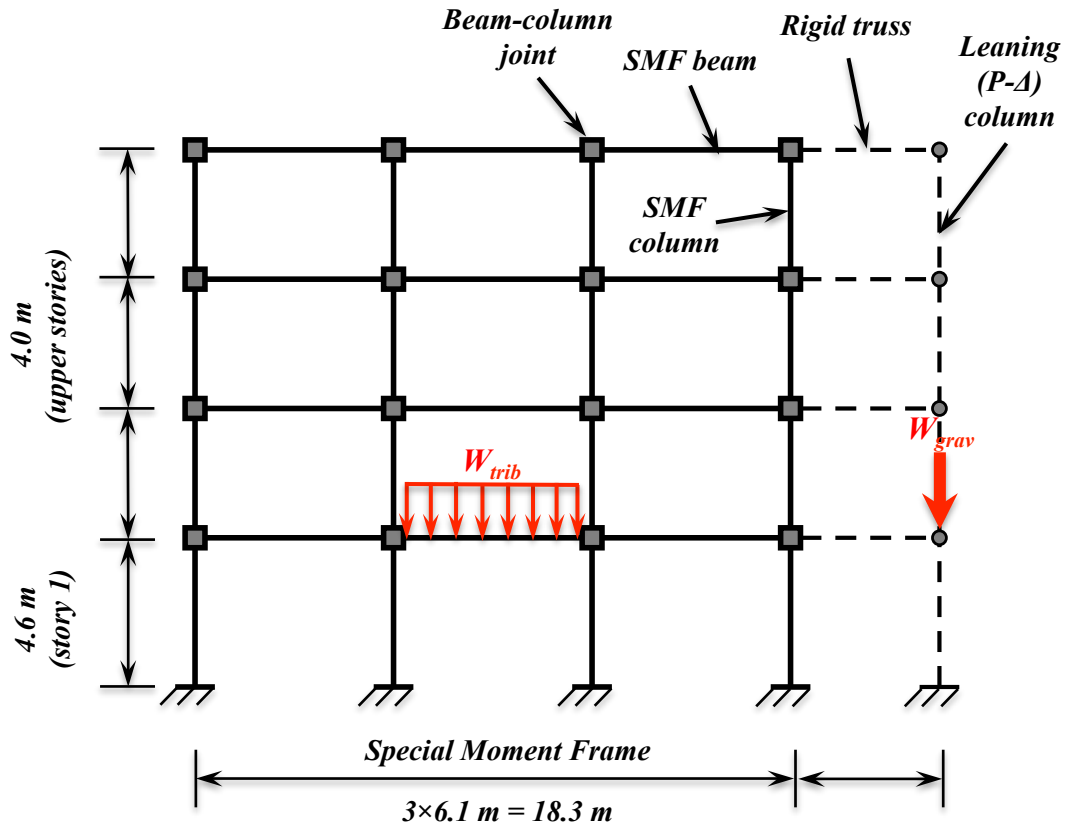

Figure 5.10. Two-dimensional structural analysis model of the prototype building.

The effective seismic gravity load of the structural systems are determined using the load combination $1.05D + 0.25L$, where D and L denote the nominal (unfactored) dead and live loads. These load factors intend to reflect a realistic gravity load condition of the buildings during earthquakes. The gravity loads and the corresponding seismic mass at each story of the prototype buildings are summarized in Table 5.2. Since the structural model represents only half of the prototype building, half of the total effective seismic gravity load and mass is assigned to the structural model. As shown in Figure 5.10, W_{trib} represents the gravity load directly tributary to the SMFs, while W_{grav} represents the gravity load tributary to the interior gravity system and are applied on the leaning columns. In addition, the structural models employ expected material strength instead of nominal strengths used in the design. Specifically, the expected strength is taken as 1.1 time the nominal strength for steel and 1.2 times the nominal strength for concrete.

Table 5.2. Effective seismic gravity load and seismic mass at each story of the prototype buildings

Prototype building	Plan dimension	W_{floor} (kN)	W_{trib} (kN)	W_{grav} (kN)
S-4	42.7×30.5 m	6187	681	5506
S-8	42.7×30.5 m	6187	681	5506
S-20	42.7×30.5 m	6187	681	5506
RC-4	54.9×36.6 m	9951	1095	8856
RC-8	36.6×36.6 m	6634	730	5904
RC-20	36.6×36.6 m	6634	730	5904

Rayleigh damping is incorporate into the structural analysis model with a damping ratio of $\xi = 2\%$ corresponding to the first and third vibration modes of each building. This is due to the fact that the first three modes of consist of more than 95% of total modal mass of the system. It is noted that the stiffness proportional damping is assigned only to the SMF beam and column elements excluding zero-length springs, while the mass proportional damping is assigned to all the nodes of the frame. This specific treatment of Rayleigh damping avoids unrealistic damping forces when the buildings are subjected to high-intensity earthquakes and provides more reasonable results in nonlinear dynamic analysis (Zareian and Medina, 2010).

5.3.2.1 Steel buildings

Beams and columns of the steel SMFs are modeled using concentrated plasticity models, with two zero-length rotational springs located at the ends of the elastic beam element (Figure 5.11a). Since all the frame beams in the steel buildings are design as RBS components, the concentrated plastic hinges (rotational springs) are placed at the center location of the RBS connections. In contrast, the frame columns are not, and therefore the column hinges are placed at the interfaces between the joint panel zones and the columns. In addition, the joint panel zones of the steel buildings are modeled using rigid parallelogram models (Gupta and Krawinkler, 2000) (Figure 5.11b).

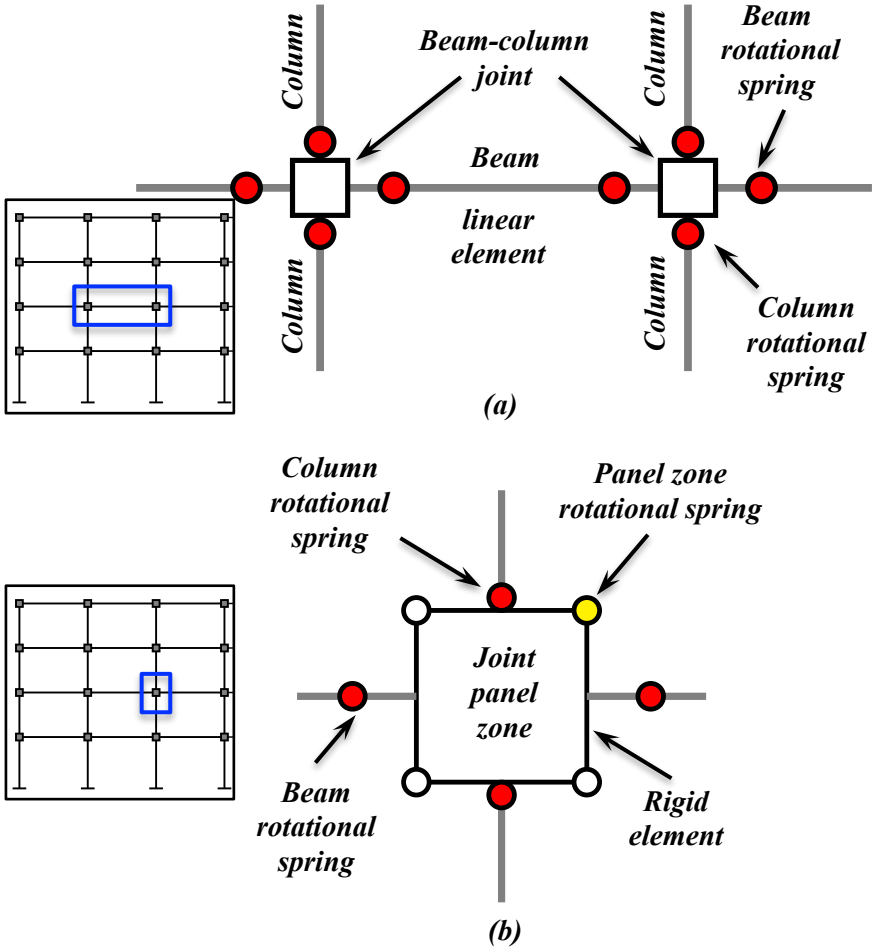

Figure 5.11. Nonlinear analysis model of steel SMF: (a) beam-column subassembly, and (b) joint panel zone model.

The moment–rotation behavior of the beam and column plastic hinges are modeled using *Bilin* uniaxial material (Lignos and Krawinkler, 2010). As shown in Figure 5.12a, the monotonic moment–rotation ($M-\theta$) response is defined in terms of: (1) yield strength and rotation (M_y and θ_y), (2) capping strength and associated rotation under monotonic loading (M_c and θ_c), (3) plastic rotation for monotonic loading (θ_p), (4) post-capping rotation (θ_{pc}), (5) residual strength (M_r), and (6) ultimate rotation (θ_u). The pre-yield moment-rotation response is determined based on the assumption of a double curvature deformation mechanism, which leads to an elastic stiffness of $K_e = 6EI/L$ and an yield moment $M_y = f_y Z_p$, where f_y is the steel yield strength, and Z_p is the section plastic modulus. The model parameters related to the post-yield behavior and the cyclic deterioration rules are calculated based on regression analysis using a large experimental dataset of cyclic test data (Figure 5.12b) (Lignos and Krawinkler, 2012).

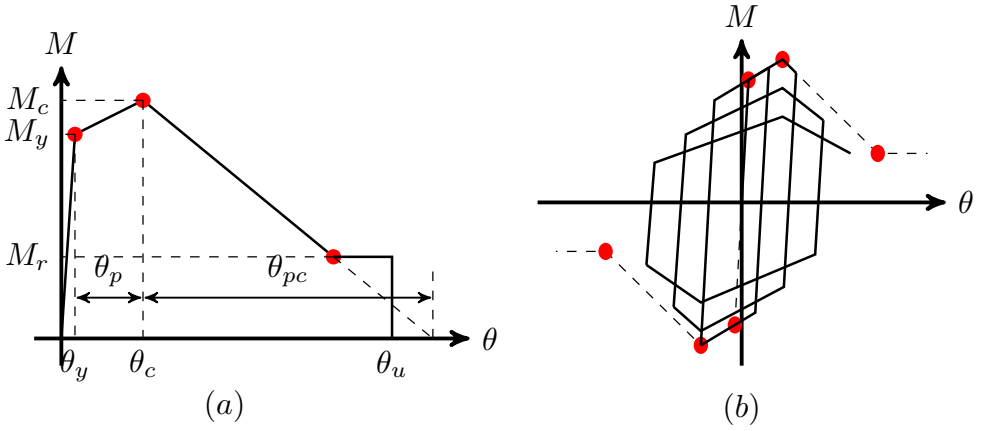

Figure 5.12. Modified Ibarra-Krawinkler model of $M-\theta$ response: (a) monotonic response, and (b) cyclic response.

As illustrated in Figure 5.11b, the rigid parallelogram model is modeled with four rigid links connected by three pinned hinges (with no rotational stiffness and denoted in white) and a rotational spring (denoted in yellow) at the fourth corner of the panel zone. As shown in Figure 5.13, a tri-linear backbone curve is employed to represent the monotonic shear force-shear deformation ($V-\gamma$) response of the panel zone, which is implemented using *Hysteretic* uniaixal material. The backbone curve consists of two

control points: (1) yield shear strength and the associated shear distortion (V_y and γ_y), and (2) full plastic strength and the associated shear distortion (V_p and γ_p). The yield shear strength V_y and the yield shear distortion γ_y are calculated as:

$$V_y = \frac{f_y}{\sqrt{3}} A_{eff} = \frac{f_y}{\sqrt{3}} (0.95 d_c t_p) = 0.55 f_y d_c t_p \tag{5.1}$$

$$\gamma_y = \frac{f_y}{\sqrt{3} G} \tag{5.2}$$

where f_y is the steel yield strength, A_{eff} is the effective shear area, d_c is the depth of the column, t_p is the thickness of the column web including doubler plates, and G is the G is the shear modulus of steel. The full plastic shear strength of the joint, V_p, which accounts for additional shear resistance provided by the panel zone after first yielding, is estimated as:

$$V_y = 0.55 f_y d_c t_p \left(1 + \frac{3 b_c t_{cf}^2}{d_b d_c t_p}\right) \tag{5.3}$$

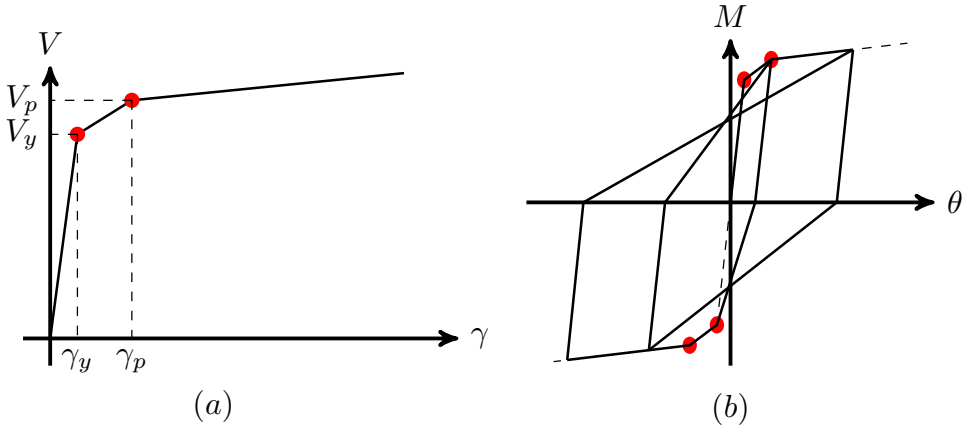

Figure 5.13. V_y and γ_y response for rigid parallelogram model: (a) monotonic response, and (b) cyclic response (Gupta and Krawinkler, 1999).

where b_c is the column flange width, and t_{cf} is the column flange thickness. The associated shear distortion γ_p is assumed as $4\gamma_y$ (ATC, 2010). In addition, a very small strain-hardening ration can be taken to define the shear force–shear distortion curve as the shear distortion exceeds γ_p.

5.3.2.2 Reinforced Concrete Buildings

Beams and columns of the reinforced concrete buildings are modeled using force-based nonlinear beam-column elements (Figure 5.14). Each beam element consists of five fiber sections (integration points), but four fiber sections for each column element. Previous research indicates that a considerable portion of inelastic response of reinforced concrete buildings are attributed to bond-slip and yield penetration of beam-column joints (Lowes et al., 2004; Panagiotakos and Fardis, 2001), lumped-plasticity rotational springs are placed at the two ends of each nonlinear beam and column elements to account these effects. Unlike the steel buildings, the beam-column joints of the reinforced concrete buildings are assumed rigid in the analysis.

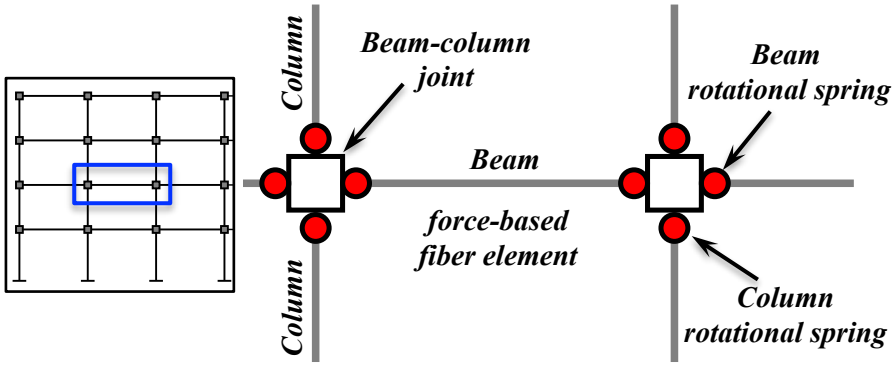

Figure 5.14. Nonlinear analysis model of reinforced concrete beam-column subassembly.

As shown in Figure 5.15a, a reinforced concrete fiber section consists of three distinct materials: unconfined concrete, confined concrete, and reinforcing steel. Uniaxial material *Concrete02* is utilized for unconfined and confined concrete. The modified Kent-Park model (Scott et al., 1982) is adopted as the compressive backbone curve, which consists of a parabolic ascending branch and a linear softening branch (Figure 5.15b). The tensile backbone curve is idealized using a bilinear curve with an ascending branch followed by a descending branch to consider tensile softening (see Figure 5.15c). The confining effect of transverse reinforcement on core concrete is considered using the confined concrete model proposed by Mander et al. (1988). Furthermore, uniaxial material *Steel02* (modified Menegotto-Pinto constitutive model proposed

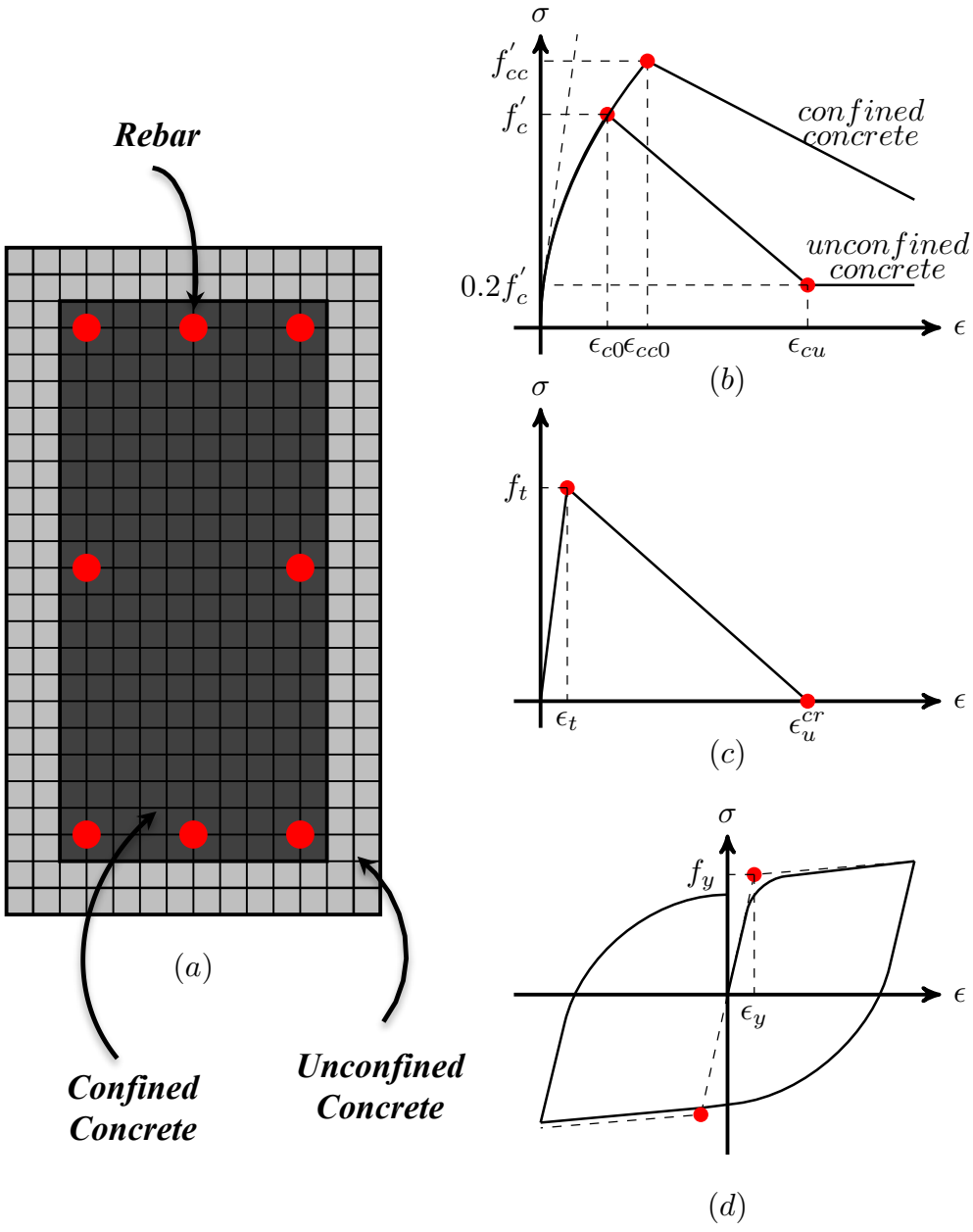

Figure 5.15. (a) Reinforced concrete fiber section discretization, and material stress-strain response (b) concrete in compression, and (b) concrete in tension, and (d) steel reinforcement.

by Filippou et al. (1983)), which is capable of capturing both kinematic and isotropic hardening as well as the Bauschinger effect, is employed for steel rebar (Figure 5.15d). To avoid fictitiously large stress on steel fibers when the components sustain extremely large inelastic deformation demands, a wrapper material *MinMax* is used in conjunction with uniaxial material *Steel02*, which assumes that ultimate failure of the reinforcement occurs at an ultimate strain of 0.15 either in tension or compression.

The monotonic response of moment-bond slip rotation ($M-\theta_{sl}$) is modeled using a simplified bilinear curve (Figure 5.16a). The bond slip rotation corresponding to the flexural yielding $\theta_{y,sl}$ is determined using an empirical equation established base on cyclic test results of over 1000 reinforced concrete components (Panagiotakos and Fardis, 2001):

$$\theta_{sl} = \frac{\epsilon_y}{d-d'}\frac{0.25 d_b f_y}{\sqrt{f_c'}} \tag{5.4}$$

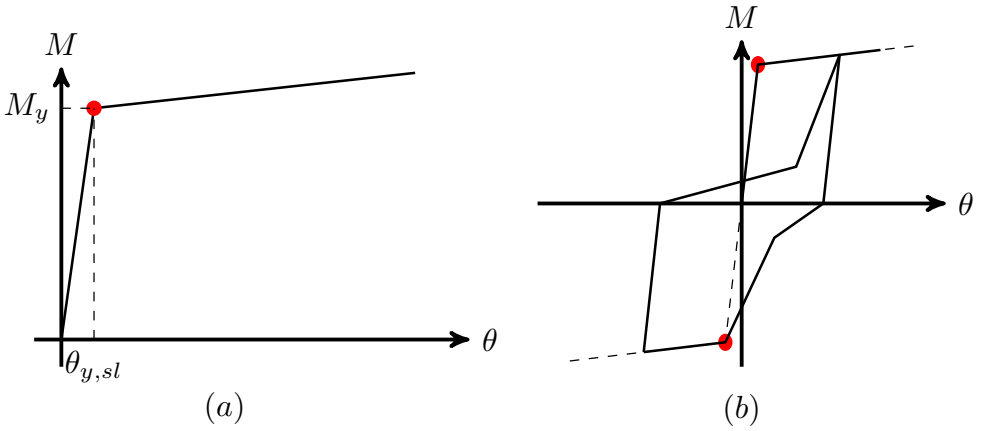

Figure 5.16. Moment-bond slip rotation ($M-\theta_{sl}$) response (a) monotonic response, and (b) cyclic response.

where ϵ_y is the yield strain of the rebar, $d-d'$ is the distance between the top and bottom rebars, d_b is the diameter of the rebar, f_y is the steel yield stress (unit in MPa), and f_c' is the concrete compressive strength (unit in MPa). The post-yield hardening ratio of the bond-slip spring is taken as 0.05 to avoid localization of the inelastic deformations on the spring. The cyclic response of the bond-slip spring employs the relationship as

recommended by Mitra and Lowes (2007), in which the initial unloading stiffness equals to the initial stiffness with subsequent pinching behavior (Figure 5.16b).

5.3.3 Modeling of Stair Systems within a Building – Coupled Building-Stair Models

Quantification of Stairs in a Building

Based on a survey of about 3,000 typical buildings with various occupancies, FEMA P-58 (FEMA, 2012) provides recommended normative quantities for a variety of common nonstructural components. For stair systems in specific, the normative quantities are estimated as 8.6×10^{-4}, 1.1×10^{-3}, and 1.3×10^{-3} per gross square meters (8.0×10^{-5}, 1.0×10^{-4}, and 1.2×10^{-4} per gross square foot) for the 10th-, 50th-, and 90th-percentile quantities, respectively. Table 5.3 summarizes the quantities of stairs per story of each prototype building. As the calculated stair quantities at each story does not vary substantially using different percentile numbers, three stairs at each story are used for building RC-4 due to its larger plan dimension and two stairs per story for the remaining buildings.

Table 5.3. Stair quantities at each story associated with the prototype buildings

Prototype building	Floor area (m^2)	10th percentile	50th percentile	90th percentile	Number of stairs per story
S-4	1300	1.1	1.4	1.7	2
S-8	1300	1.1	1.4	1.7	2
S-20	1300	1.1	1.4	1.7	2
RC-4	2007	1.7	2.1	2.6	3
RC-8	1338	1.1	1.4	1.7	2
RC-20	1338	1.1	1.4	1.7	2

Lumped Spring Modeling of Stairs

Although detailed three-dimensional finite element models presented in the previous chapter are capable of providing a thorough understanding of the seismic behavior of prefabricated steel stairs in their isolated configuration, these stairs are modeled us-

ing idealized lumped springs in the system-level numerical study. The motivations for such simplifications are due to considerations in the following two aspects: (1) stairs are vertically distributed throughout a building at each story, and therefore detailed modeling of stairs in a system-level model would significantly increase the computational demands, and (2) the use of lumped springs for modeling stairs is compatible with the phenomenological representation of structural analysis models in current practice, thus allowing analysts to incorporate stairs into their structural analysis models with minimal adjustment to structural models.

It is assumed that prefabricated steel stairs primarily contribute lateral strength and

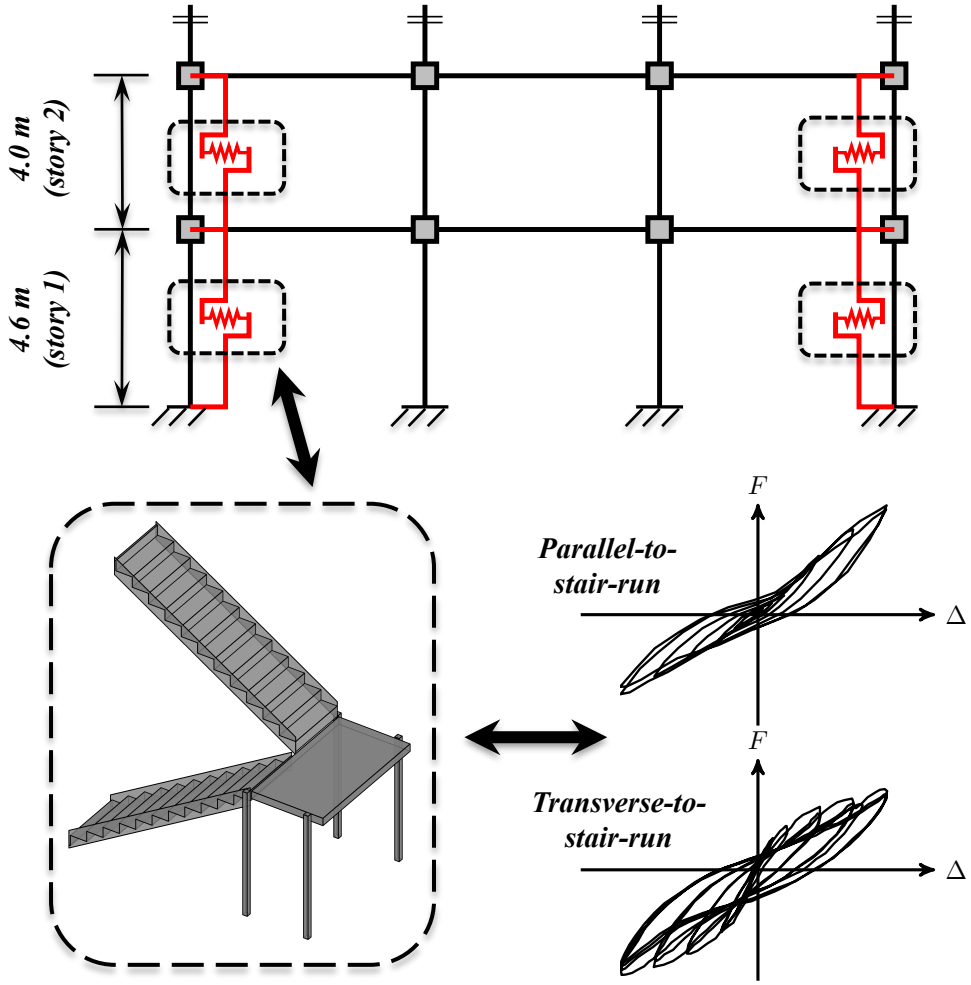

Figure 5.17. Coupled building-stair model implemented in *OpenSees*.

stiffness to the coupled systems during seismic excitations. Since the mass of these stairs are almost negligible compared with that of the building, their inertial effects are not considered in this study. As shown in Figure 5.17, each stair is modeled using a massless lumped spring connected to the beam-column joints at two adjacent floors. These springs are restrained only in the horizontal direction, thus representing the force-displacement response when the stairs are subjected to the differential displacements (interstory drifts) induced by the upper and lower floors. Except for building RC-4 that includes three stairs at each story, the remaining prototype buildings each consists of two stairs at each story. The two stairs are connected to the two edge beam-column joints. In the case of building RC-4, the third stair is connect to one of the center columns. It is noted, however, that stairs in practice are often connected to floor slabs or stairwell boundaries instead of beam-column joints, the placement of stairs in this study represents an idealized stair-building connectivity in the system-level simulations.

According to the pushover analysis, the axial deformations of the beam elements in the steel buildings are insignificantly small during lateral loading. Despite that the axial deformations of the reinforced concrete beam elements are slightly larger than those of the steel beams due to the axial-flexural interactions, the interstory drifts for different columns of the same story remain similar (less than 10% differences at a roof drift ratio of 3%) in the pushover analysis. In this regard, it is concluded that the analysis results of the coupled models do not appear sensitive to the placement of stairs.

Lumped Spring Model Calibration

As discussed in the previous chapter, the stair response during the parallel-to-stair-run loading is dictated by stair landing torsion and connection deformation, however its response is dominated by the upper flight deformation during the transverse-to-stair-run loading. The force-displacement response in the parallel-to-stair-run direction is modeled using *Steel02*, *Pinching4*, and *Multilinear* in a parallel configuration, while the response in transverse-to-stair-run direction is modeled using *Steel02* and *Pinching4* in a parallel configuration. Figure 5.18 compares the calibrated force-displacement response of the idealized lumped springs with the experimental data of the OSU tests (Higgins,

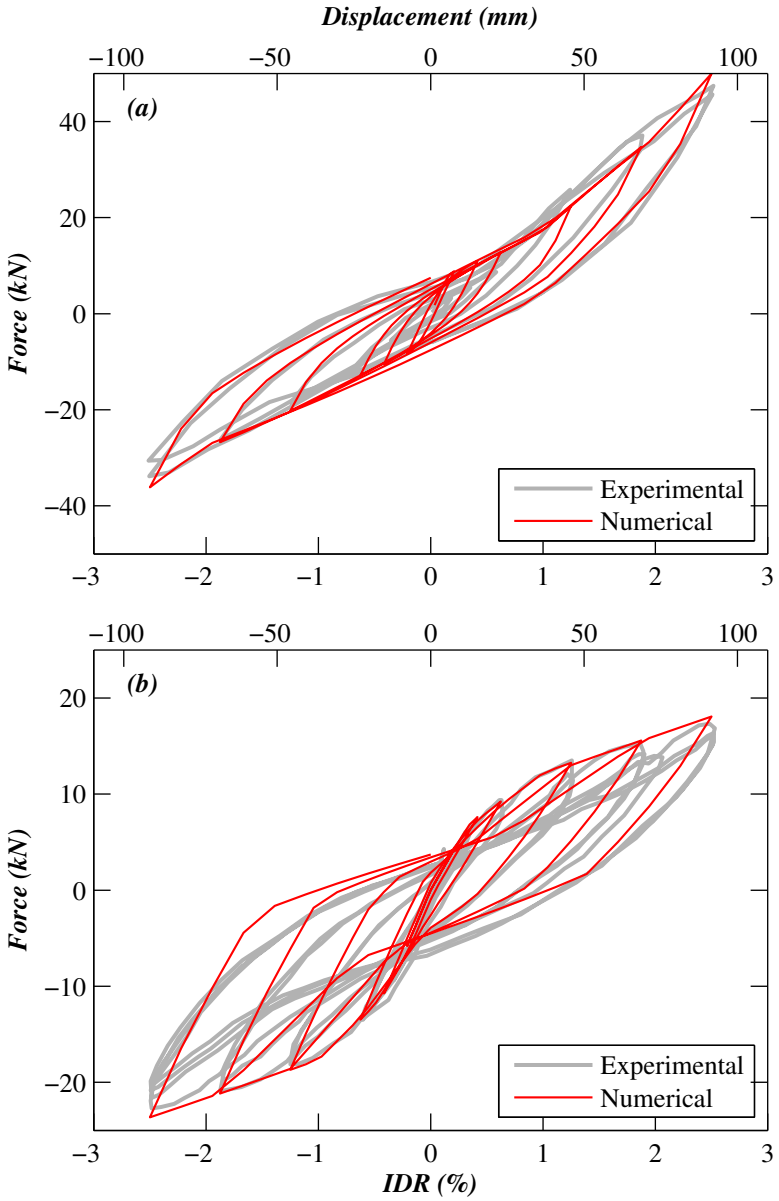

Figure 5.18. Hysteretic force-displacement responses of the calibrated lumped springs: (a) parallel-to-stair-run direction, and (b) transverse-to-stair-run direction.

2009). The comparison demonstrates that the lumped springs reasonably capture the overall force-displacement responses of the stair in both loading directions as well as the hardening and pinching effects related to cyclic loading. It is noted, however, that the stair force-displacement responses in the two loading directions are slightly non-symmetric due to the complicated structural behavior. The strength differences between the positive and negative loading appear as much as 20%. Stiffness hardening effect is also observed during the positive loading in the parallel direction. With careful calibration of the material parameters, these effects can also be captured by adjusting the monotonic backbone response of the lumped spring models.

Parameterization of Stair Force-Displacement Responses

According to previous experimental and computational studies, two important aspects are considered as variables in the stair force-displacement response: (1) the variation of stair force-displacement responses due to different configurations or construction details, and (2) the variation of ultimate deformation capacity of the stairs. The former aspect considers the effects of stair design parameters on modifying the stiffness and strength, while the latter aspect accounts for the scattering of the stair deformability associated with the ultimate damage state as observed in the shake table tests. Since the transverse-to-stair-run stair response has much less influence on the building responses due to the smaller strength and stiffness contributions, the system-level simulation considers only the stair response in the parallel-to-stair-run direction in the following sections.

To facilitate a parametrized representation of the stair force-displacement response, the backbone curve of the stair is determined by averaging the monotonic responses in the positive and negative directions obtained from detailed finite element modeling results, while the hysteretic response parameters remain identical to those calibrated using experimental data. Although the use of an averaged backbone curve modifies the original stair force-displacement behavior, this introduces very limited differences to the system-level simulation results. Furthermore, experimental data of the stair responses are available only up to a maximum interstory drift of 2.5%. However, its behavior dur-

ing very large displacement demands remain uncertain, the force is therefore assumed to remain constant when the interstory drift exceeds 2.5%. This assumption aims to avoid fictitiously large force demands of the stair lumped springs in the case of large interstory drift demands (> 5%).

As shown in Figure 5.19, two variables are considered in this study to account for different stair force-displacement responses: (a) stair response modification factor Ω_{stair}, and (b) stair ultimate deformation capacity IDR_{damage}. The stair response modification factor Ω_{stair} amplifies the stair force by a factor of Ω_{stair}, thereby leading to an increase the stair initial stiffness by a factor of Ω_{stair}. The stair ultimate deformation capacity IDR_{damage} represents a threshold value for triggering the ultimate stair damage (e.g., connection weld fracture). The stair is assume to lose its structural integrity when the associated interstory drift demand exceeds the prescribed IDR_{damage} value and thereafter does not provide stiffness or strength to the building system. This is accounted for by wrapping the stair lumped spring with a *MinMax* uniaxial material. In the parametric study, the stair response modification factor Ω_{stair} is selected as 1, 2, 4, and 8. Ω_{stair} value of 1 represents the baseline stair as tested by Higgins (2009). Ω_{stair} value of 2

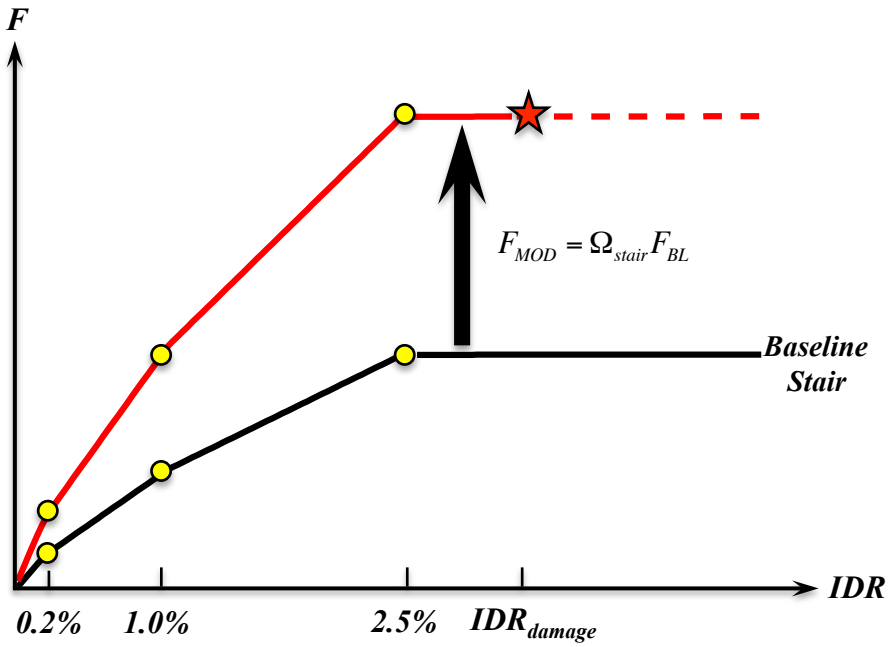

Figure 5.19. Variables considered in the idealized lumped springs of the stairs.

and 4 are intended to consider stair variants with rigid connections at both the upper and lower ends, and Ω_{stair} value of 8 is considered an extreme case in the parametric study. The stair ultimate deformation capacity IDR_{damage} considers three representative values of the 1.5%, 2.5%, 5%. IDR_{damage} value of 10% is used only in the pushover analysis with an intent to provide an upper bound limit for demonstrating the effects of stairs on the coupled building systems.

5.4 Numerical Simulation Results

A numerical parametric study of the coupled building-stair systems is conducted to assess the effects of stairs on the building response characteristics. Numerical simulations consists of three different analysis procedures: eigenvalue analyses, nonlinear static (pushover) analyses, and nonlinear dynamic (time-history) analyses. The accuracy of the bare building models (without stair incorporated) is validated against the results available in recent literature (Elkady and Lignos, 2014; Haselton et al., 2010). Different aspects related to the buildings and stair systems are considered as variables in the parametric study: (1) the building structural systems, (2) the story number of the buildings, and (3) the stair force-displacement responses.

5.4.1 Eigenvalue Analysis

Modal properties of interest include the modal periods of the first three vibrational modes T, the effective modal mass M^{eff}, and the model shapes ϕ of the prototype buildings. In addition, the modal assurance criteria (MAC) values are presented to provide a measure of consistency between the mode shapes of the coupled building-stair systems and their bare building counterparts. The effective modal mass M_i^{eff} and the $\text{MAC}_{i,j}$ value of two mode shape vectors are calculated as:

$$M_i^{eff} = \frac{\left(\sum_{j=1}^{n} \phi_i^j m_j\right)^2}{\sum_{j=1}^{n} \phi_i^{j^2} m_j} \tag{5.5}$$

$$\mathrm{MAC}_{i,j} = \frac{|\widehat{\phi_i}\phi_j|^2}{(\widehat{\phi_i}\phi_i)(\widehat{\phi_j}\phi_j)} \tag{5.6}$$

where ϕ_i^j denotes the jth component of the mode shape vector ϕ_i, m_j is the mass of the jth component (the jth floor), and $\widehat{\phi}$ denotes the complex conjugate transpose of a mode shape vector ϕ.

Table 5.4 summarizes the modal periods and effective modal masses corresponding to the first three vibrational modes of the bare buildings (without stairs incorporated). The effective modal mass is normalized by the total effective seismic mass of the building. As is shown in Table 5.4, the cumulative effective modal mass of the first three vibrational modes exceeds 95% of the total building mass for each building. This indicates that the first three modes is capable of capturing almost all the lateral dynamic response of the building. In addition, the first-mode effective modal mass the of prototype building reduces as the story number increases, indicating more significant participation of the higher modes for taller buildings. Regardless, the effective modal mass of the first-mode of each prototype building remains larger than 70% of the total mass of the building.

Table 5.4. Modal periods and effective modal masses of the prototype buildings

Prototype building	First Mode		Second Mode		Third Mode	
	T_1 (sec)	M_1^{eff} (%)	T_2 (sec)	M_2^{eff} (%)	T_3 (sec)	M_3^{eff} (%)
S-4	1.50	82.9	0.49	12.3	0.27	3.1
S-8	1.99	79.9	0.70	12.2	0.40	4.2
S-20	3.60	74.9	1.38	14.0	0.80	4.4
RC-4	0.75	82.2	0.22	11.8	0.11	4.4
RC-8	1.25	80.6	0.42	11.7	0.24	3.8
RC-20	2.05	73.1	0.68	17.1	0.36	4.3

Figure 5.20 presents the effects of stair response modification factor (Ω_{stair} = 1, 2, 4, and 8) on the modal periods of the first three modes of the coupled building-stair systems. The modal periods are normalized by the values of their bare building coun-

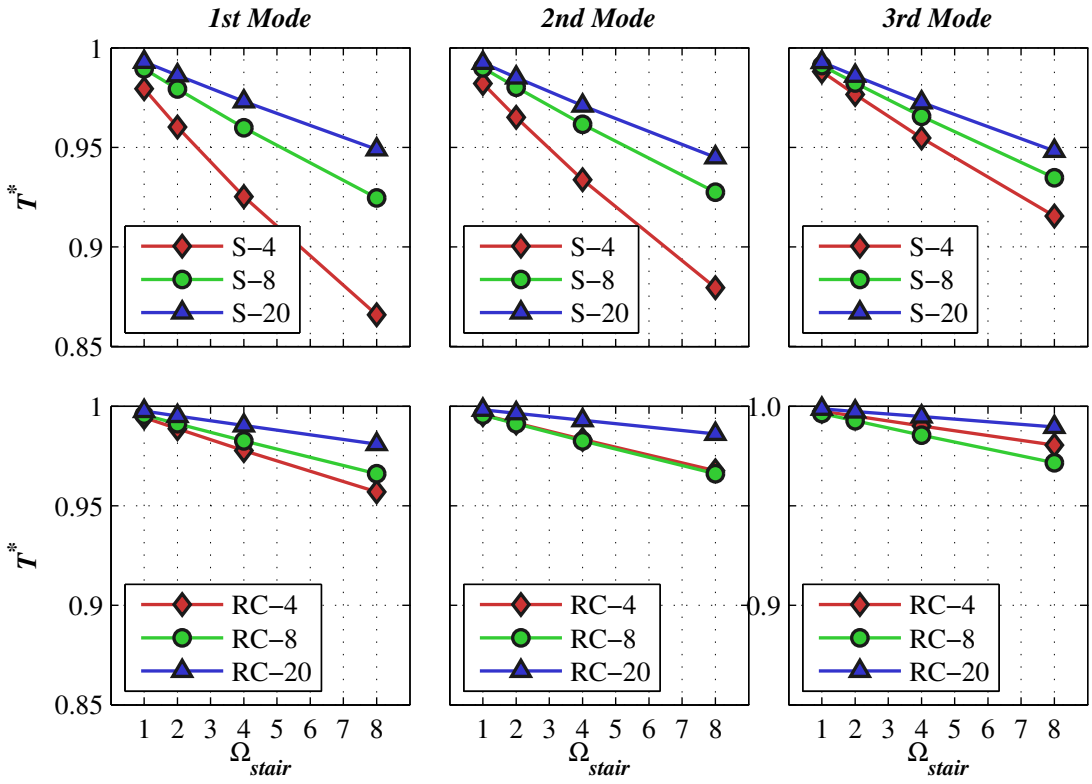

Figure 5.20. Normalized modal periods of the first three modes.

terparts (responses normalized by the corresponding response of bare building hereafter are denoted using superscript asterisks). In the case of baseline stair ($\Omega_{stair} = 1$), the largest period reduction is only 3% as observed for the case of building S-4. Increasing the stair response modification factor Ω_{stair} leads to larger stiffness of the stair systems, and therefore more significant period shortening of the coupled systems. Regardless, the variations of the first-mode periods appear more sensitive to the presence of stairs than those of the second and third modes. It is also observed that the building periods decreases as the story number increases, and that the periods of the steel buildings appear more significantly affected than the reinforced concrete buildings. Provided that the stiffness contribution of the stair systems remains identical among different prototype buildings, the effects of stairs attenuate as the overall stiffness of the structural system increases, which can be attributed to increasing the building story numbers or a stiffer structural system is used (reinforced concrete buildings).

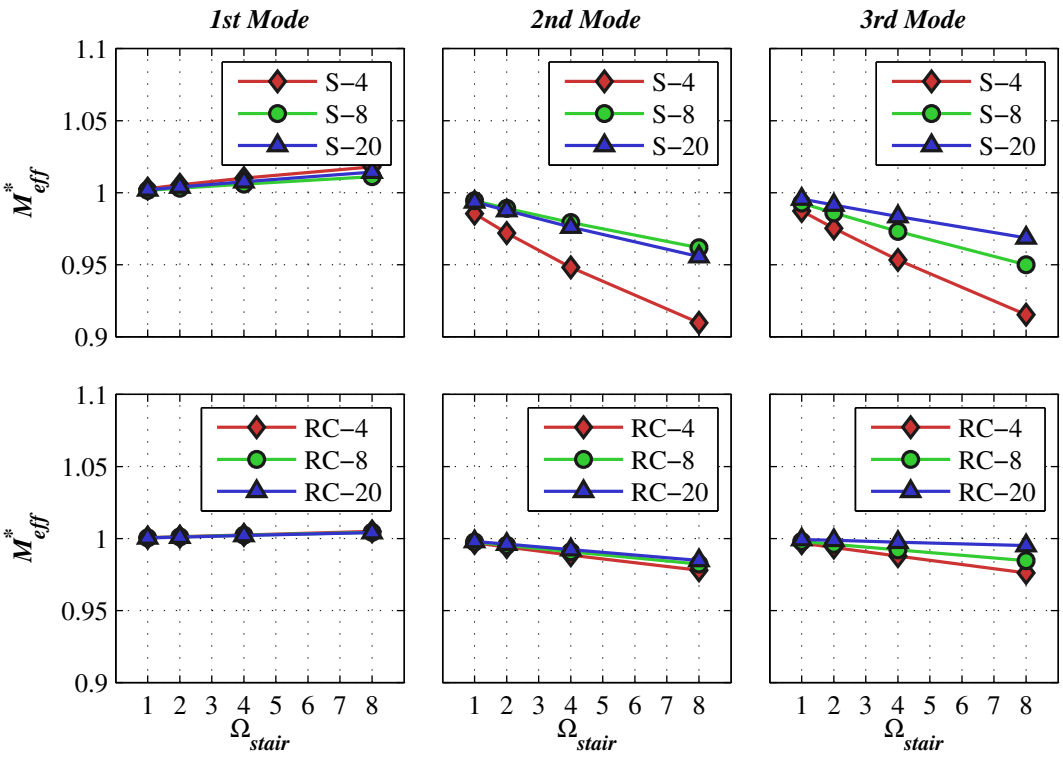

Figure 5.21. Normalized effective modal mass of the first three modes.

Figure 5.21 shows the effects of stair response modification factor (Ω_{stair} = 1, 2, 4, and 8) on the effective modal masses of the first three modes of the coupled building-stair systems. Unlike the modal periods, the modal masses of the higher modes appear more sensitive to the presence of stairs than those of the first mode. However, it is noted that the absolute values of the effective modal masses for the higher modes are much smaller than those of the first modes, and therefore larger variations relative to the bare building do not significantly modifies their absolute values. Increasing the building story number or use of a stiffer structural system attenuate the effects of stairs on the effective modal masses, as the contribution of the stair systems relative to the structural system tend to reduce as the building stiffness increases.

Figure 5.22 shows the mode shapes of the first three vibration modes for all the bare buildings. These mode shapes are normalized such that the modal coordinate at the roof of the building equal to unity. The mode shapes of the coupled building systems are nearly identical to those of their bare building counterparts. This is corroborated by the

fact that the MAC values between the coupled systems and their bare building counterparts are nearly unity. Even in the most extreme case (building S-4 with $\Omega_{stair} = 8$), the MAC values of the first three modes remain larger than 0.99. This further indicates the modal shapes are almost insensitive to the presence of stairs in the coupled systems.

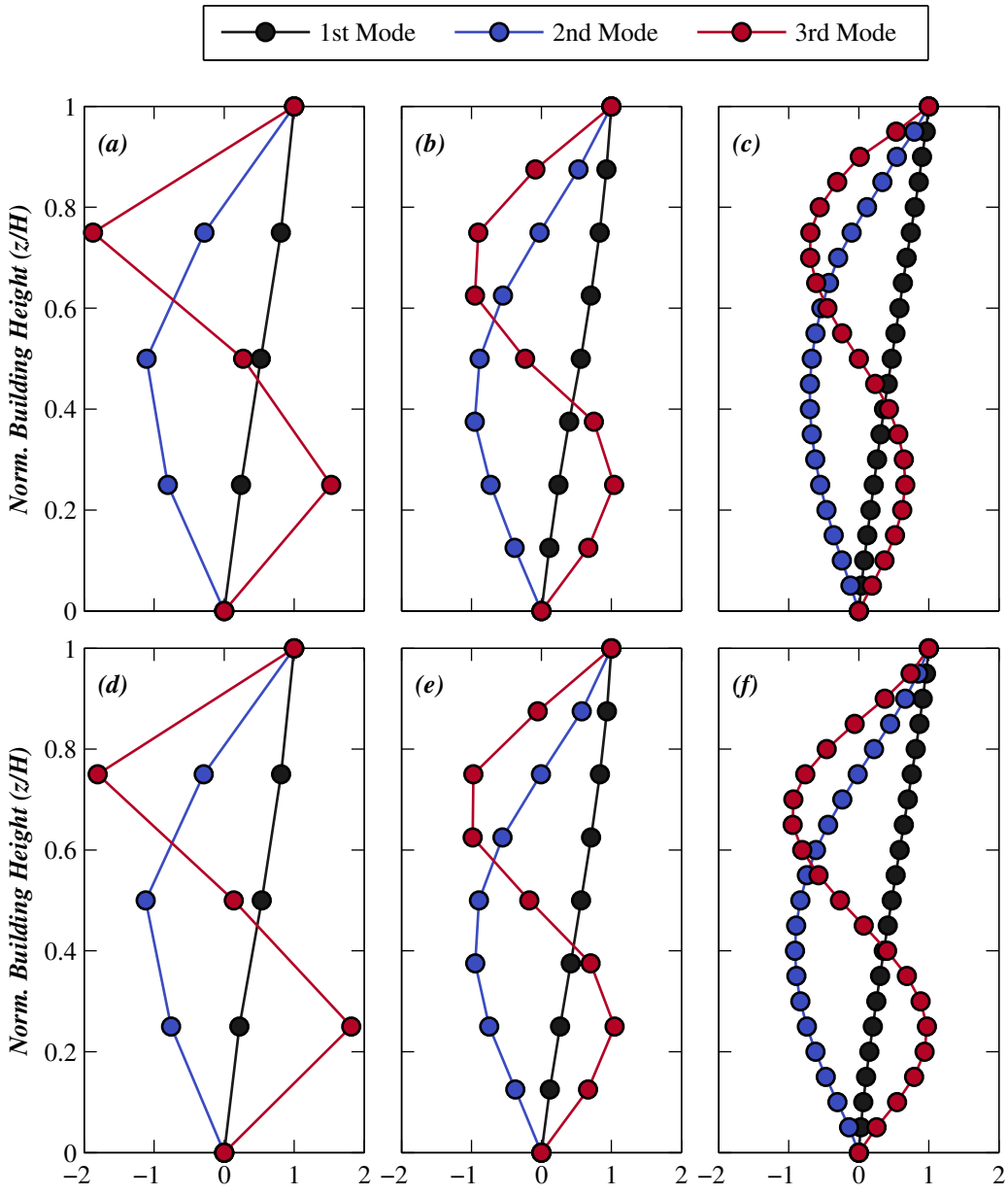

Figure 5.22. Modal shapes of the prototype buildings: (a) S-4, (b) S-8, (c) S-20, (d) RC-4, (e) RC-8, and (f) RC-20,.

5.4.2 Nonlinear Static Analysis

Nonlinear static (pushover) analyses are conducted using an invariant lateral load distribution proportional to the fundamental mode shape of the corresponding building. As the mode shapes are not sensitive to the presence of stairs, the lateral load distributions of the coupled systems remain almost identical to those of their bare building counterparts. These pushover analyses intend to provide a qualitative assessment of the response characteristics (e.g., stiffness, yield strength, overstrength, ductility) of the building systems under lateral loading. However, it is important to note that while the invariant lateral force distribution reasonably reflects the seismic response characteristics for first-mode dominated buildings, this assumption may not be sufficient when the building higher-mode effects can not be neglected or the dynamic characteristics of the building are modified by large inelastic deformation during an earthquake (Krawinkler and Seneviratna, 1998).

Pushover analyses are conducted using displacement control with equal increments applied on the roof of the building. Effective seismic gravity loads are applied on the building prior to the pushover analysis and thereafter remain constant during the pushover analysis. The analysis is terminated when the base shear force drops to zero or an excessively large interstory drift ratio (10%) is achieved. Figure 5.23 schematically illustrates a global pushover curve (base shear – roof displacement response) of the prototype building. It is noted that the force and displacement are presented using normalized units to facilitate consistency of the result comparisons between different buildings. The normalized base shear force V^* is obtained by dividing the base shear V with the effective seismic weight of the building W, and the roof drift ratio (δ_r) is calculated as the ratio of the roof displacement Δ_r and the total building height H.

Pushover Performance Parameters

As illustrated in Figure 5.23, performance parameters associated with the pushover analysis include building initial stiffness K^*_{init}, effective yield stiffness K^*_{eff}, maximum normalized base shear V^*_{max}, yield roof drift ratio $\delta_{r,y}$, ultimate roof drift ratio $\delta_{r,u}$, over-

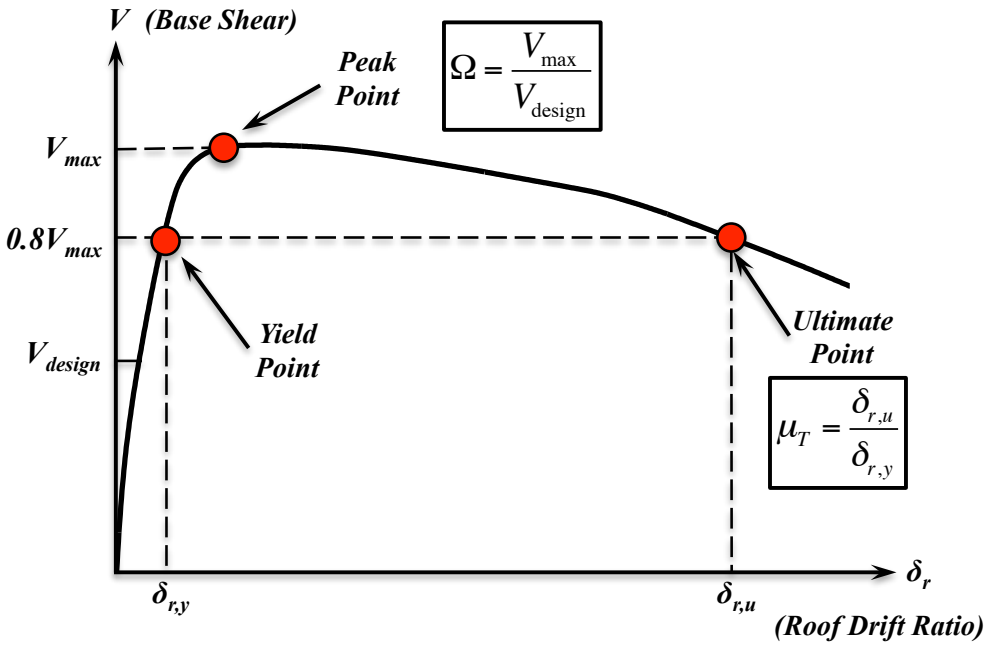

Figure 5.23. Generic pushover curve and the associated performance parameters.

strength factor Ω, and period-based ductility factor μ_T. The initial stiffness K^*_{init} of the building is calculated as the secant stiffness when the base shear V^* reaches 30% of the design base shear V^*_{design} (building response is expected to remain linear at this loading stage), while the effective stiffness K^*_{eff} is defined as the secant stiffness of the building when the normalized base shear force V^* achieves 80% of the maximum normalized base shear V^*_{max} (yield point). Since the force and displacement are both presented using normalized units, a K^*_{eff} value of 0.2 represents that the base shear equals 20% of the total building weight when the roof drift ratio attains 1.0% (provided that the pushover response remains linear). The ultimate roof drift ratio $\delta_{r,u}$ is defined as the roof drift ratio when the base shear drops to 80% of the normalized maximum base shear V^*_{max} in the post-peak region (ultimate point). In addition, the overstrength factor Ω is defined as the ratio between the maximum base shear strength V_{max} and the code-based design base shear V_{design} (values presented in Table 5.1), and the period-based ductility factor μ_T is calculated as the ratio of ultimate roof drift ratio $\delta_{r,u}$ and the yield roof drift ratio $\delta_{r,y}$.

Global Pushover Curves

Figures 5.24–5.26 present the pushover analysis results of the steel bare structures and coupled systems with baseline stairs (with $\Omega_{stair} = 1$ and $IDR_{damage} = 10\%$). The results presented in the figures include the global pushover curves (base shear – roof displacement response) as well as the building lateral displacement profiles at various target roof drift ratios. It is noted that the IDR_{damage} of the base stairs incorporate into the building are taken as 10%, which assumes that the no stair damage are triggered in these analysis and intends to provide an upper bound case for considering the effects of stairs. For example, as shown in Figure 5.24a, building S-4 (bare building) behaves linearly from the onset of lateral loading prior to achieving its yield roof drift ratio δ_r of 0.80%, and later attains the peak normalized base shear force V^*_{max} of 0.151 at a roof drift ratio δ_r of 1.20%. Subsequently, the building strength start to deteriorate and attains its ultimate state (20% drop of strength) at an ultimate roof drift ratio $\delta_{r,u}$ of 4.46. As the design base shear coefficient is given as 0.069 in the seismic desgin, the overstrength factor is determined as $\Omega = 0.151/0.069 = 2.25$, and the period-based ductility is calculated as $\mu_T = 4.46/0.80 = 5.55$. The floor displacement profiles, on the other hand, illustrate the building deformation mechanisms with the progression of the roof displacement demand. As shown in Figure 5.24b, an intermediate story mechanism initiates at the lower three levels of building S-4 at a roof drift ratio of about 1.0%, which is consistent with the global pushover curve (Figure 5.24a).

Table 5.5 summarizes the pushover performance parameters of the steel prototype buildings. As shown in the table, the effective stiffness K^*_{eff} of each building is almost identical to the initial stiffness K^*_{init}, indicating that the building response remain essentially linear prior to effective yielding of the building. The presence of baseline stairs only significantly modifies the ultimate roof drift ratio $\delta_{r,u}$ and the ductility μ_T of the coupled systems, while its influence is minimal on other performance parameters. It is noted, however, that the deformation capacity of the coupled system is attributed to the extremely large value of IDR_{damage} (10%), which may not represent the behavior of the coupled systems in practice.

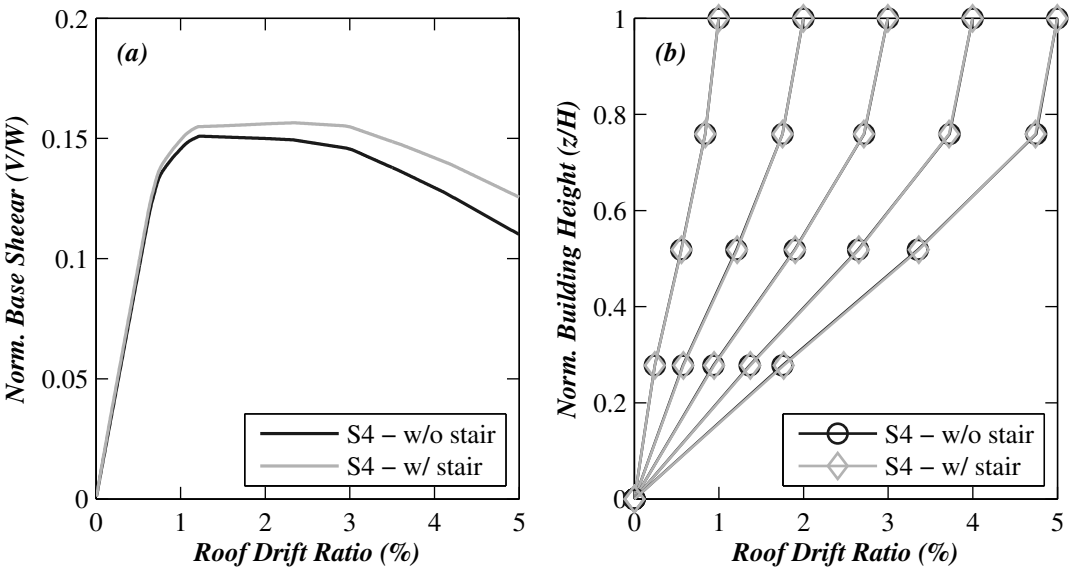

Figure 5.24. Pushover analysis results for S-4: (a) global pushover curve, and (b) floor displacement profile.

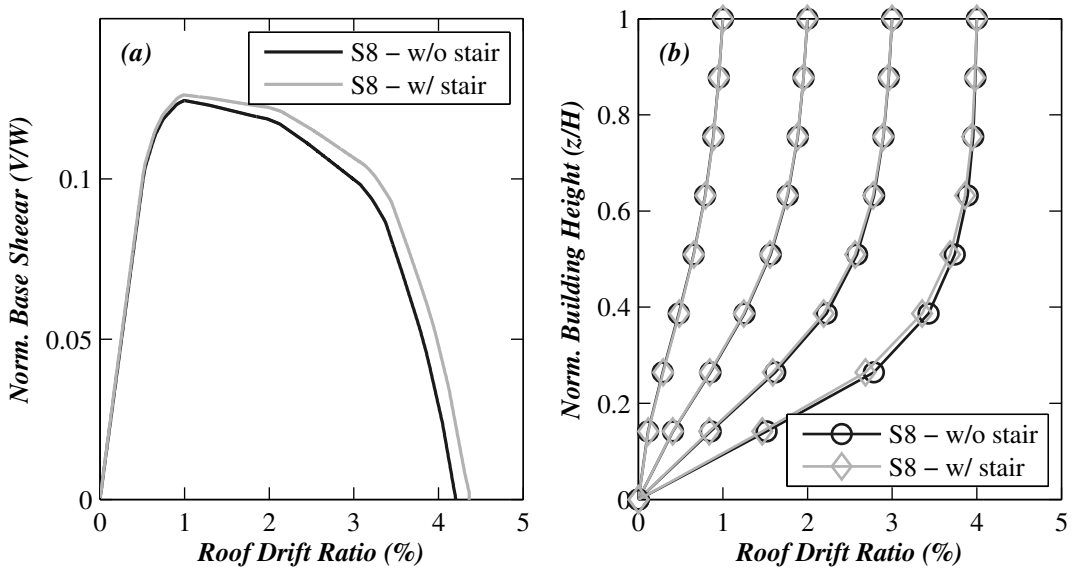

Figure 5.25. Pushover analysis results for S-8: (a) global pushover curve, and (b) floor displacement profile.

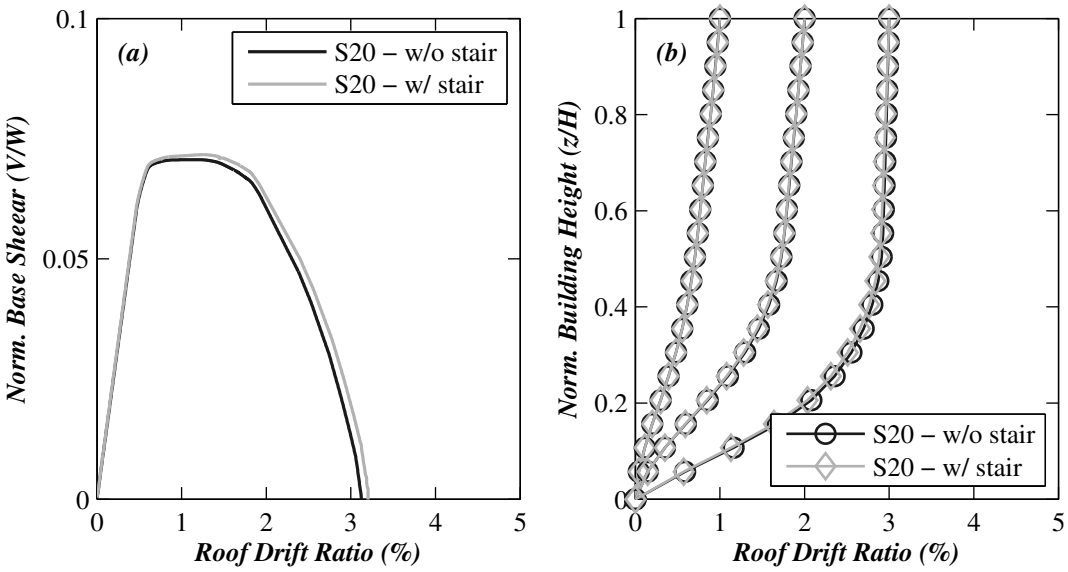

Figure 5.26. Pushover analysis results for S-20: (a) global pushover curve, and (b) floor displacement profile.

Table 5.5. Comparison of the pushover performance parameters of the steel prototype buildings

Prototype building		K^*_{init}	K^*_{eff}	V^*_{max}	$\delta_{r,y}$ (%)	$\delta_{r,u}$ (%)	Ω	μ_T
S-4	w/o stairs	0.189	0.188	0.151	0.80	4.46	2.25	5.55
	w/ stairs	0.197	0.195	0.157	0.82	5.01	2.34	6.13
S-8	w/o stairs	0.197	0.197	0.125	0.63	3.02	3.19	4.75
	w/ stairs	0.200	0.200	0.126	0.63	3.25	3.24	5.12
S-20	w/o stairs	0.126	0.126	0.071	0.55	2.12	1.91	3.86
	w/ stairs	0.128	0.127	0.072	0.55	2.17	1.94	3.95

Figures 5.27–5.29 present the pushover analysis results of the reinforced concrete bare structures and coupled systems with baseline stairs (with $\Omega_{stair} = 1$ and $IDR_{damage} =$ 10%). It is clearly shown in the figures that the pushover responses of the reinforced concrete buildings become nonlinear from the onset of lateral loading due to progressive concrete cracking. It is noted that the post-peak response of the reinforced concrete buildings is characterized by sudden drops of base shear forces. This is due to the fact that the beam and column elements of the reinforced concrete buildings are modeled using fiber beam elements, in which the reinforcing steel sustain the ultimate damage when the fiber achieves a strain of 0.15. Similar to the steel buildings, the floor displacement profiles of the reinforced concrete buildings indicate that inelastic deformation tends to concentrate at the lower levels. However, the formation of intermediate story mechanism of the reinforced concrete buildings initiate at a roof drift ratio much smaller than those of the steel buildings.

Table 5.6 summarizes the pushover performance parameters of the reinforced concrete buildings. Since the pushover response of the reinforced concrete buildings become nonlinear from the onset of loading, the effective stiffness K^*_{eff} are smaller than the initial stiffness K^*_{init} (about 50% of the K^*_{init}). It is noted that the initial stiffness K^*_{init} of the reinforced concrete buildings are about 2–3 times those of the steel building counterparts. Therefore, their effective yield roof drift ratios $\delta_{r,y}$ are also smaller than those their steel building counterparts. Even though the ultimate roof drift ratio of the reinforced concrete buildings $\delta_{r,u}$ are slightly smaller than those of the steel building, the period-based ductility μ_T of the reinforced buildings are larger as a result of smaller effective yield roof drift ratios $\delta_{r,y}$.

Effect of Stairs on Pushover Results

Figure 5.30 shows the effects of stair response modification factor Ω_{stair} on the initial stiffness K^*_{init} of the two sets of prototype buildings. As shown in the figure, the effects of stairs systems (with identical Ω_{stair}) are much more significant on the steel buildings due to the smaller stiffness of the building systems. For example, while the stiffness of building S-8 increases by about 20% with an Ω_{stair} of 8, the difference is less than 10%

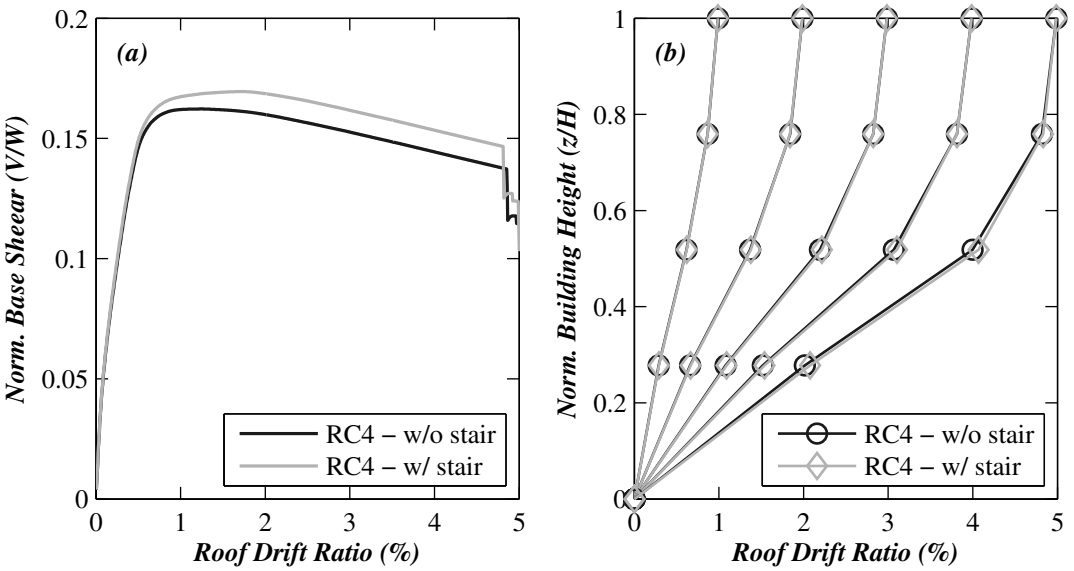

Figure 5.27. Pushover analysis results for RC-4: (a) global pushover curve, and (b) floor displacement profile.

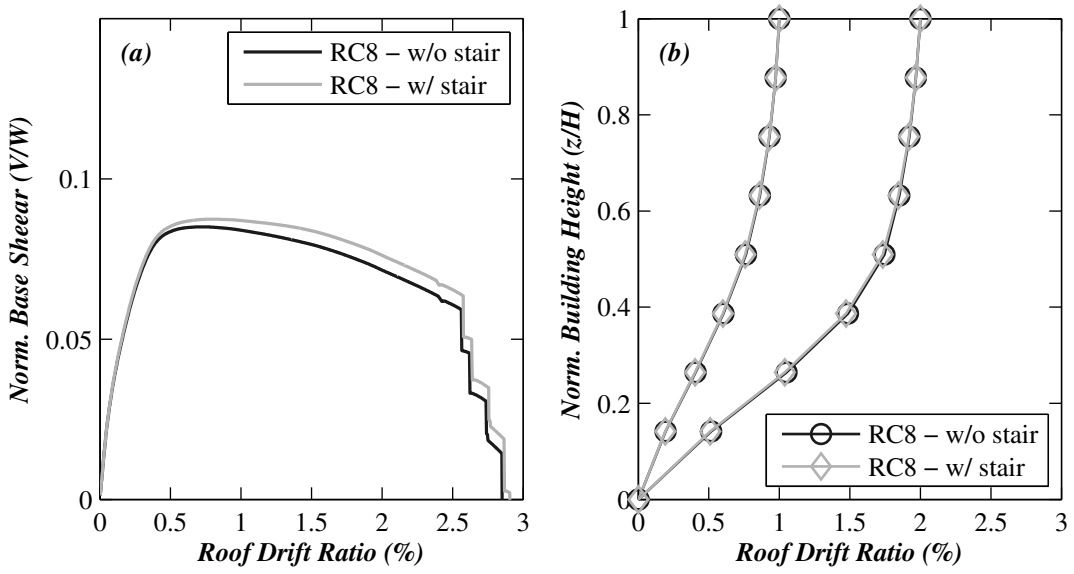

Figure 5.28. Pushover analysis results for RC-8: (a) global pushover curve, and (b) floor displacement profile.

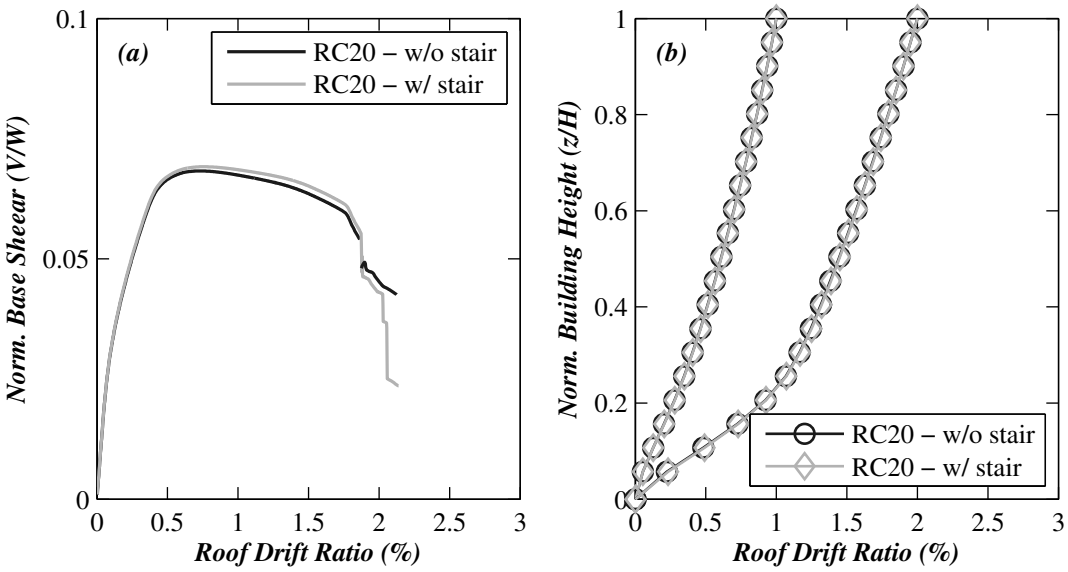

Figure 5.29. Pushover analysis results for RC-20: (a) global pushover curve, and (b) floor displacement profile.

Table 5.6. Comparison of the pushover performance parameters of the reinforced concrete prototype buildings

Prototype building		K^*_{init}	K^*_{eff}	V^*_{max}	$\delta_{r,y}$ (%)	$\delta_{r,u}$ (%)	Ω	μ_T
RC-4	w/o stairs	0.615	0.325	0.162	0.50	4.87	1.76	9.76
	w/ stairs	0.624	0.336	0.163	0.49	4.85	1.77	9.97
RC-8	w/o stairs	0.498	0.252	0.085	0.34	2.18	1.70	6.47
	w/ stairs	0.503	0.254	0.087	0.34	2.31	1.75	6.73
RC-20	w/o stairs	0.339	0.185	0.068	0.39	1.86	3.10	5.02
	w/ stairs	0.340	0.186	0.069	0.39	1.88	3.14	5.03

for building RC-8. In addition, the effects of stairs on building stiffness tend to attenuate as a result of the increase of story number. In the case of $\Omega_{stair} = 4$, the presence of stairs results in a stiffness increase of about 20% for building S-4 but less than 10% for buildings S-8 and S-20. These observations correlate well with the aforementioned modal period results, as the variation of stiffness and modal period are directly dictated by the stiffness contribution of the stair systems relative to their supporting structures.

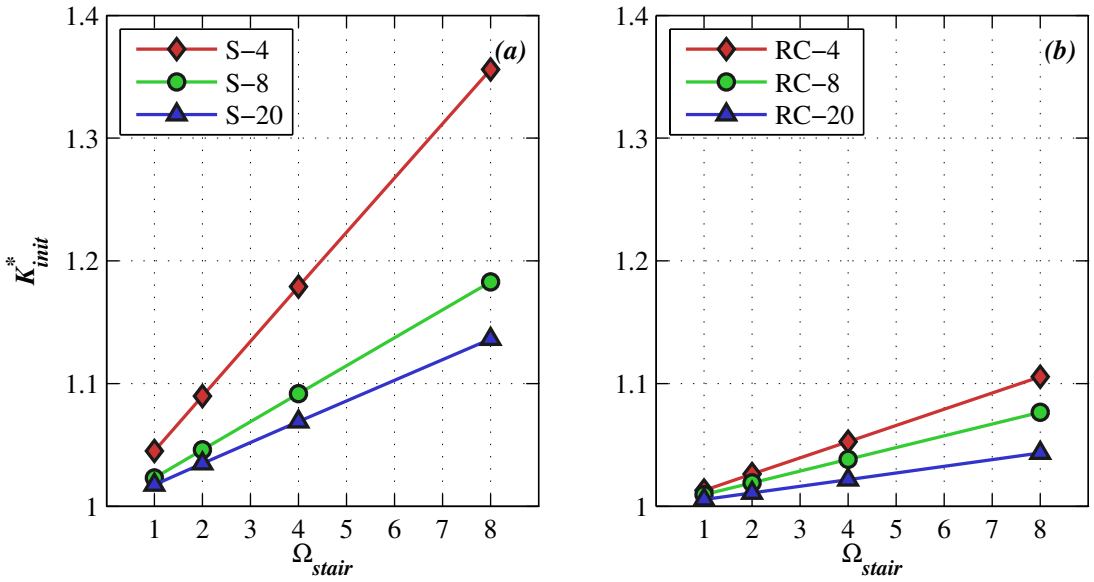

Figure 5.30. Effects of stair response modification factor Ω_{stair} on building initial stiffness: (a) steel buildings, and (b) reinforced concrete buildings.

As the responses of building S-4 appears most sensitive to the presence of stairs, it is selected to illustrate the effects of stair force-displacement response on the coupled building-stair systems. As shown in Figure 5.31a, three different values of stair response modification factor $\Omega_{stair} = 1, 4, 8$ are considered. A very large ultimate deformation capacity ($IDR_{damage} = 10\%$) is assumed for the stairs to isolate the effects of stair damage. It is shown that although the effective roof drift ratio $\delta_{r,y}$ remains similar for different Ω_{stair} values, larger Ω_{stair} values effectively postpones the occurrence of strength deterioration of the coupled systems. This is due to the fact that, if damage-free, the stair force increases monotonically until an interstory drift ratio of 2.5% is achieved. This consequently increases the ultimate roof drift ratio $\delta_{r,u}$, and a larger increase is associated

with a larger Ω_{stair} value. Figure 5.31b compares the pushover responses of the coupled systems with four different IDR_{damage} values (1.5%, 2.5%, 5%, and 10%), while the stair response modification factor Ω_{stair} is taken as 4 for all the cases. When IDR_{damage} of the stairs are relatively small (1.5% and 2.5%), damage to the stairs initiate prior to reaching the peak capacity of the coupled systems, which significantly reduces the ultimate roof drift ratio $\delta_{r,u}$ of the coupled systems due to sudden drops of the base shear caused by stair damage. In the case of IDR_{damage} = 5%, even though damage to the stairs initiates in the post-peak region, the ultimate roof drift ratio $\delta_{r,u}$ is also smaller than that of the bare building. This is because that the presence of stairs results in larger strength associated with the ultimate state of the coupled system, and therefore the building reaches the ultimate state immediately following the onset of stair damage.

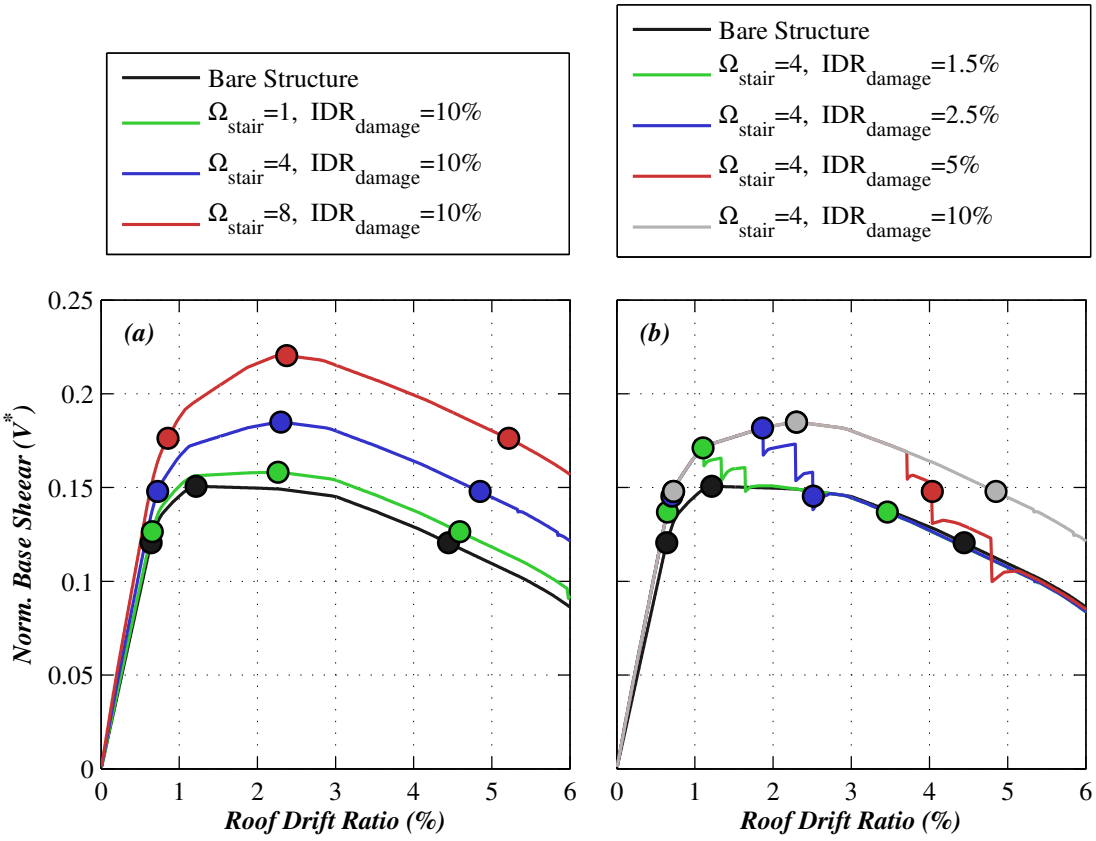

Figure 5.31. Building pushover response due to the effects of the stair system: (a) stair response modification factor Ω_{stair} and (b) stair ultimate deformation capacity IDR_{damage}.

Figures 5.32 and 5.33 present the overstrength factor Ω and the ultimate roof drift ratio $\delta_{r,u}$ of the coupled building-stair systems with variations of the structural systems as well as stair systems. The values presented in these figures are normalized by the corresponding values of their bare building counterparts. As shown in Figure 5.32, the overstrength factor Ω of the coupled systems increases with increasing Ω_{stair}. With a constant value of Ω_{stair}, increasing IDR_{damage} increases Ω when IDR_{damage} are relatively small (< 2.5%), but Ω remains constant when IDR_{damage} becomes larger. This is due to the fact that a large IDR_{damage} prevents stair damage from occurring prior to reaching the peak strength of the couple system. As shown in Figure 5.33, the presence of stairs reduces the ultimate roof drift ratio $\delta_{r,u}$ of the coupled building-stair systems in most cases. The largest reduction of $\delta_{r,u}$ occurs when the stairs have a large Ω_{stair} but a small IDR_{damage} (about 40% for the steel buildings and 30% for the reinforced concrete buildings). The only few exceptions that lead to increased building ultimate roof drift ratio $\delta_{r,u}$ is that the IDR_{damage} of the stairs are very high (e.g., 10% IDR), for which damage to stairs does not occur. However, as mentioned earlier, stairs in practice is very unlikely to sustain such high deformation without damage, and these results only intend to provide an upper bound limit for evaluating the effects of the stairs. Similar to the effects of stairs on the building overstrength factors, increasing the number of stories results in reduced effects of the stairs due to the increase of building stiffness and strength. Similar to the effects of stairs on the building stiffness and modal periods, increasing the number of story or use of a stiffer structural systems results in attenuated effects on the overstrength factor Ω and the ultimate roof drift ratio $\delta_{r,u}$ of the coupled systems as a result of the increasing contributions from the structural systems.

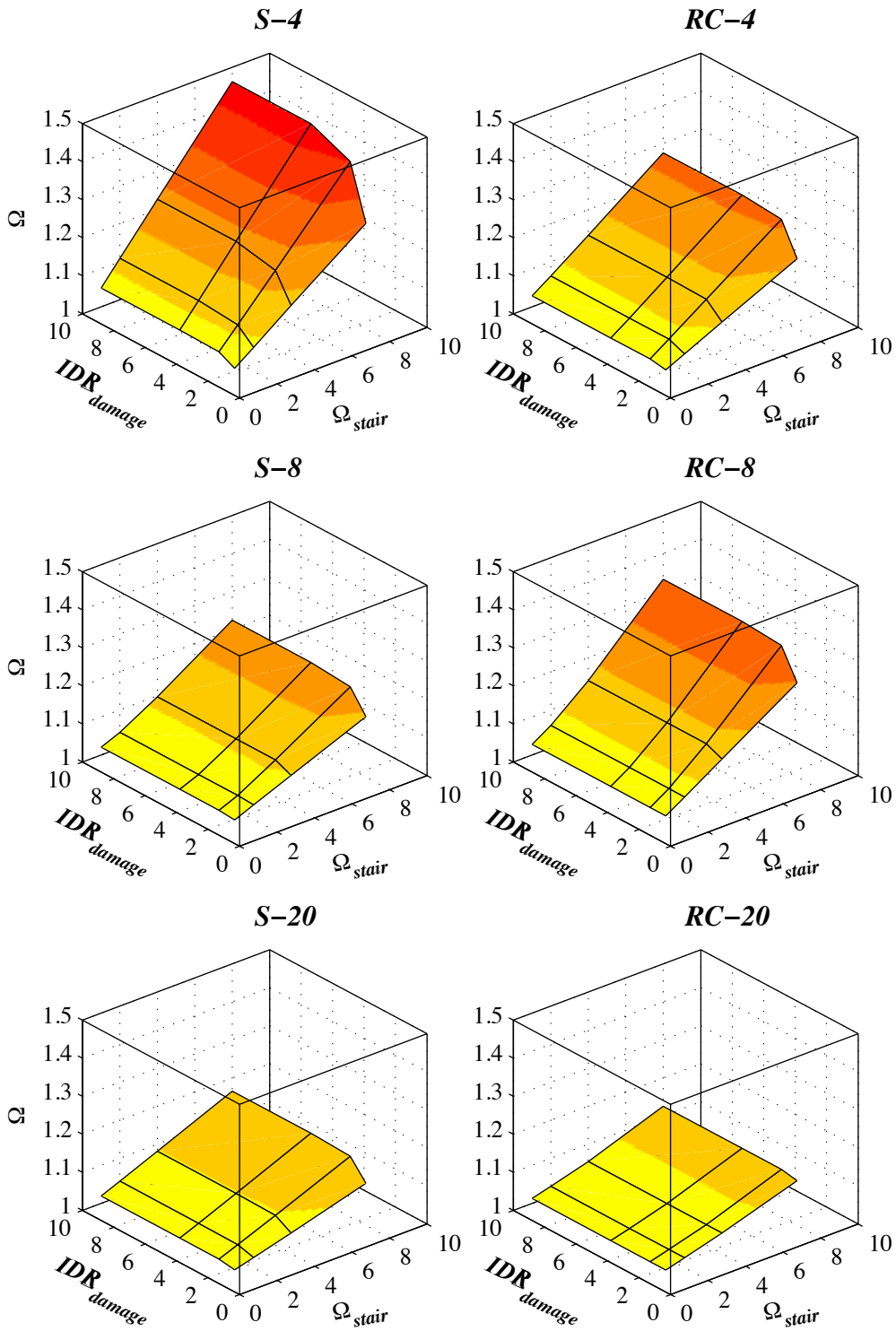

Figure 5.32. Effects of the stair response modification factor Ω_{stair} and ultimate deformation IDR_{damage} on the overstrength factor Ω of the coupled building-stair systems.

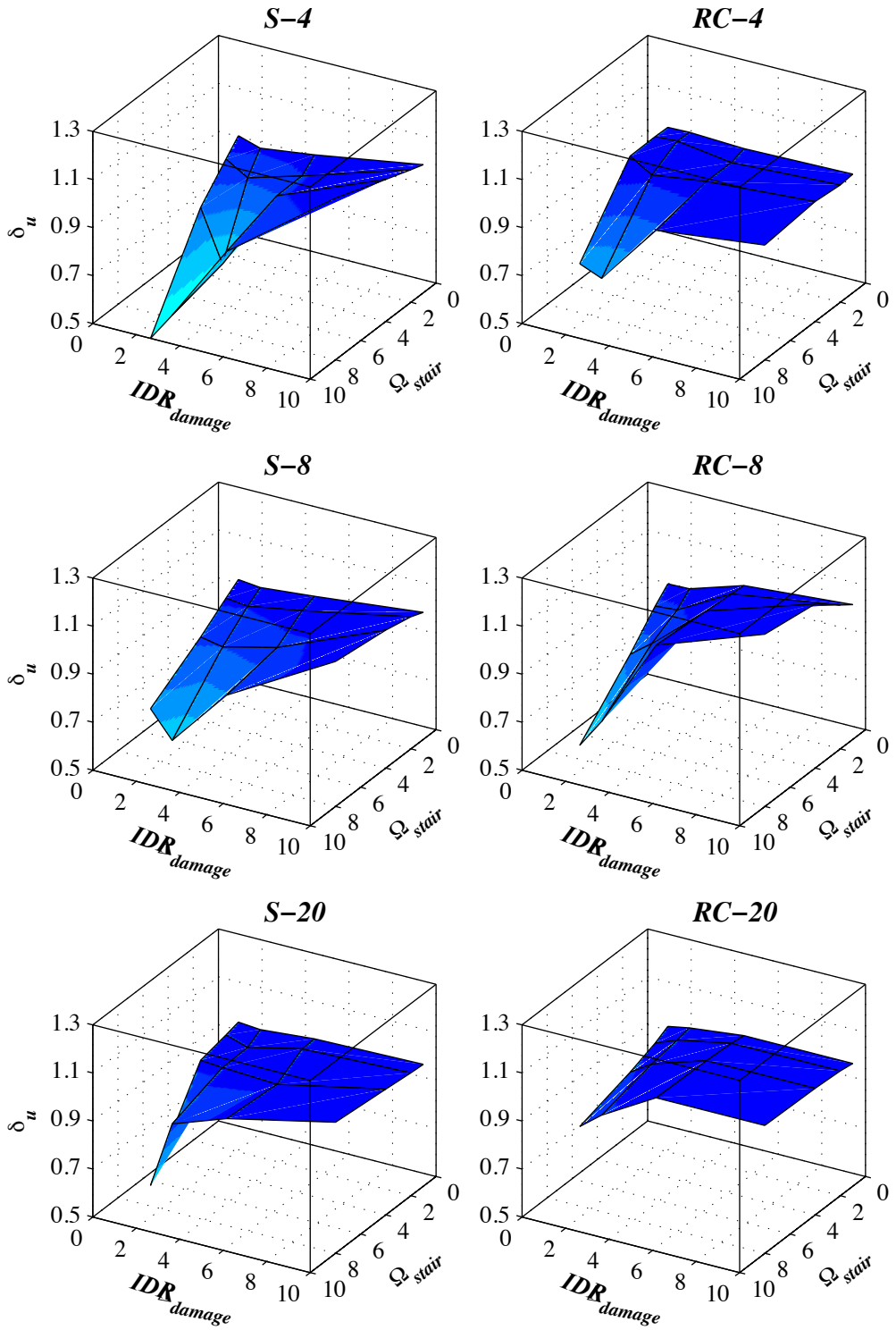

Figure 5.33. Effects of the stair response modification factor Ω_{stair} and ultimate deformation IDR_{damage} on the ultimate roof drift ratio $\delta_{r,u}$ of the coupled building-stair systems.

5.4.3 Nonlinear Dynamic Analysis

This section investigates the effects of stairs on the dynamic response of the coupled building-stair systems (e.g., floor accelerations, interstory drift ratios) during earthquake excitations. Dynamic analyses are conducted using Newmark-Beta method with a constant average acceleration rule ($\gamma = 0.5$ and $\beta = 0.25$), with a damping ratio of 2% corresponding to the first and third modes of the buildings. As discussed earlier, the cumulative effective modal weight of the first three modes of each prototype building accounts for over 95% of the total seismic weight of the building.

Input Motion

The input motion is a history earthquake record from the 1994 Northridge earthquake, with a moment magnitude M_w of 6.7 and a rupture distance R_{rup} of 15.8 km (referred to as CNP196 in the PEER Strong Motion Database). Figure 5.34 shows the acceleration time history and the 5% damped elastic pseudo-acceleration spectrum of the input motion. As shown in Figure 5.34b, the spectral shape of the input motion correlates well with that of the ASCE 7 design spectrum at the site of the prototype buildings (S_{DS}=1.0 g and S_{D1}=0.6 g) within the period range of 1–3 seconds. Despite of the oscillation over the design spectrum plateau($T_0 - T_s$), the averaged short period spectral value $S_{a,avg}(T_0 - T_s)$ is comparable to the design value S_{DS}. Table 5.7 compares the spectral accelerations of the input motion and those of ASCE 7-05 design spectrum at select periods. The comparison indicates that it is reasonable to consider the input motion as a design earthquake scenario for the buildings of interest. In addition,

To consider the building response under different seismic hazard levels, the input motion is amplitude scaled using three factors: 1) 25% scale for a 43-year serviceability level earthquake event (SLE-43), 2) 100% scale for a design earthquake event (DE), and (3) 150% scale for a maximum considered earthquake event (MCE). Since the spectral shape of the input motion are comparable to that of the ASCE 7-05 design spectrum within the period range of the prototype buildings, the input motion associated with a specific seismic hazard level is assumed to be identical for all the prototype buildings, thus providing motion-consistent comparisons for different prototype buildings.

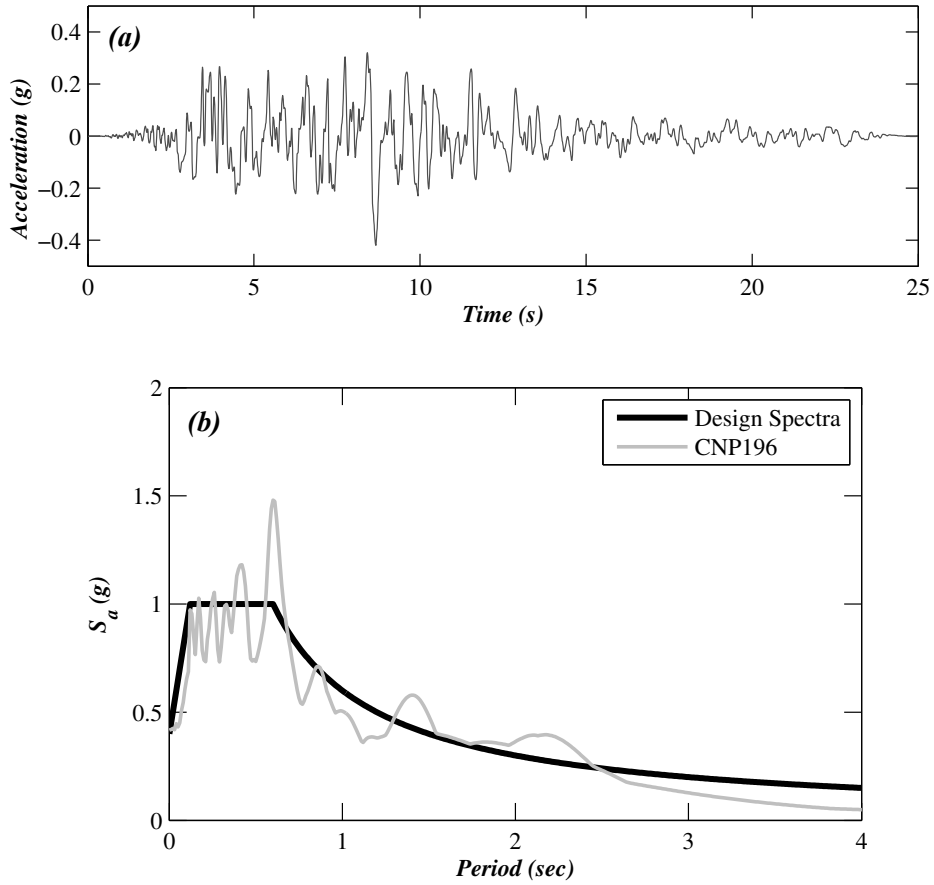

Figure 5.34. Earthquake input motion: (a) acceleration history, and (b) 5% damped elastic pseudo-acceleration spectrum and ASCE 7-10 spectrum.

Table 5.7. Spectral acceleration comparison of the input motion with ASCE 7-05 design spectrum (5% damped)

Spectral Acceleration	*PGA* (g)	$S_{a,avg}(T_0 - T_s)$ (g)	$S_a(T = 1.0)$ (g)	$S_a(T = 2.0)$ (g)
Input motion	0.42	0.95	0.51	0.3
ACSE-7	0.4	1.0	0.6	0.36

Building Dynamic Response

To demonstrate the effects of stair response modification factor on the floor responses of the coupled building-stair systems, Figure 5.35 shows the PFA and PIDR responses of building S-4 with different stair response modification factor Ω_{stair} (1, 4, and 8). The stair ultimate deformation capacity IDR_{damage} is taken as 5% such that the stairs in the building remain damage-free during all the dynamic analyses. In addition, floor acceleration and interstory drift ratio time histories of the building S-4 at select location and seismic hazard intensity level are presented in Figures 5.36.

As shown in Figures 5.35a–c, the presence of stairs results in larger or lower PFAs dependent on building height and seismic hazard level. This is due to the fact that the presence of stairs results in shortened building fundamental period, thus modifying the dynamic characteristics of the building. As can be seen in figure 5.36a, the roof accelerations differ distinctly from that of the bare building after 10 second and leads to considerably larger roof acceleration responses when Ω_{stair} are high (4 and 8). However, during the MCE motion (Figure 5.35c), the roof accelerations are not significantly influenced by Ω_{stair} due to the formation of story mechanism at the lower levels during the high intensity motion. While the presence of stairs slightly reduces the PFAs at level 3 during the DE motion, the PFAs at level 2 are reduced by as much as about 20% (Ω_{stair} = 4 and 8) during the MCE motion. As shown in Figure 5.36b, the floor accelerations at level 2 during the MCE motion are characterized by frequency contents associated with the higher modes. Since the higher modes are less sensitive to the presence of stairs, the acceleration responses for coupled building systems undergo no salient phase shift due to the variation of Ω_{stair}.

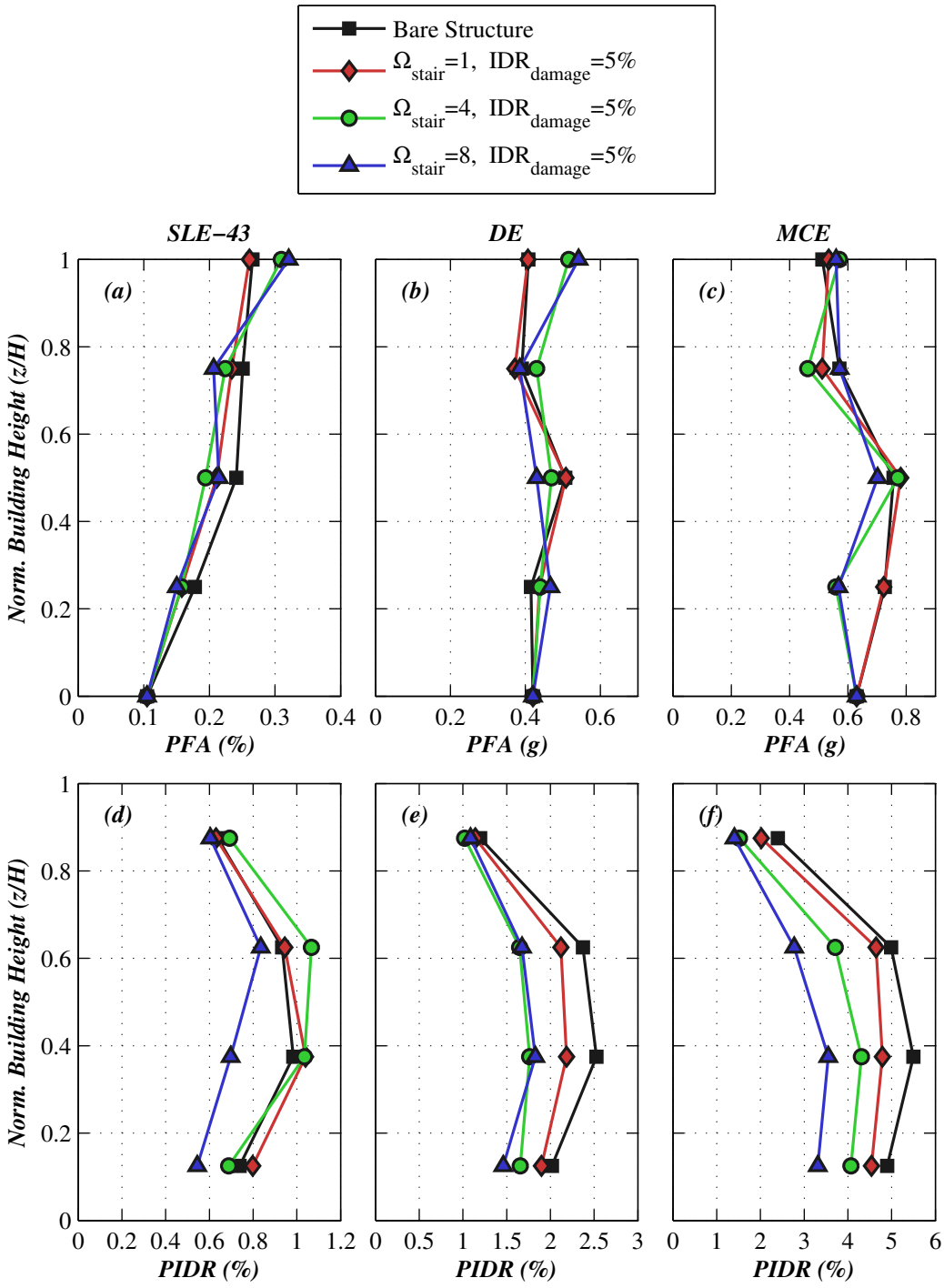

Figure 5.35. Effects of stair stair response modification factor Ω_{stair} on the peak responses of building S-4: (a) PFA – SLE-43 motion, (b) PFA – DE motion, (c) PFA – MCE motion, (d) PIDR – SLE-43 motion, (e) PIDR – DE motion, and (f) PIDR – MCE motion.

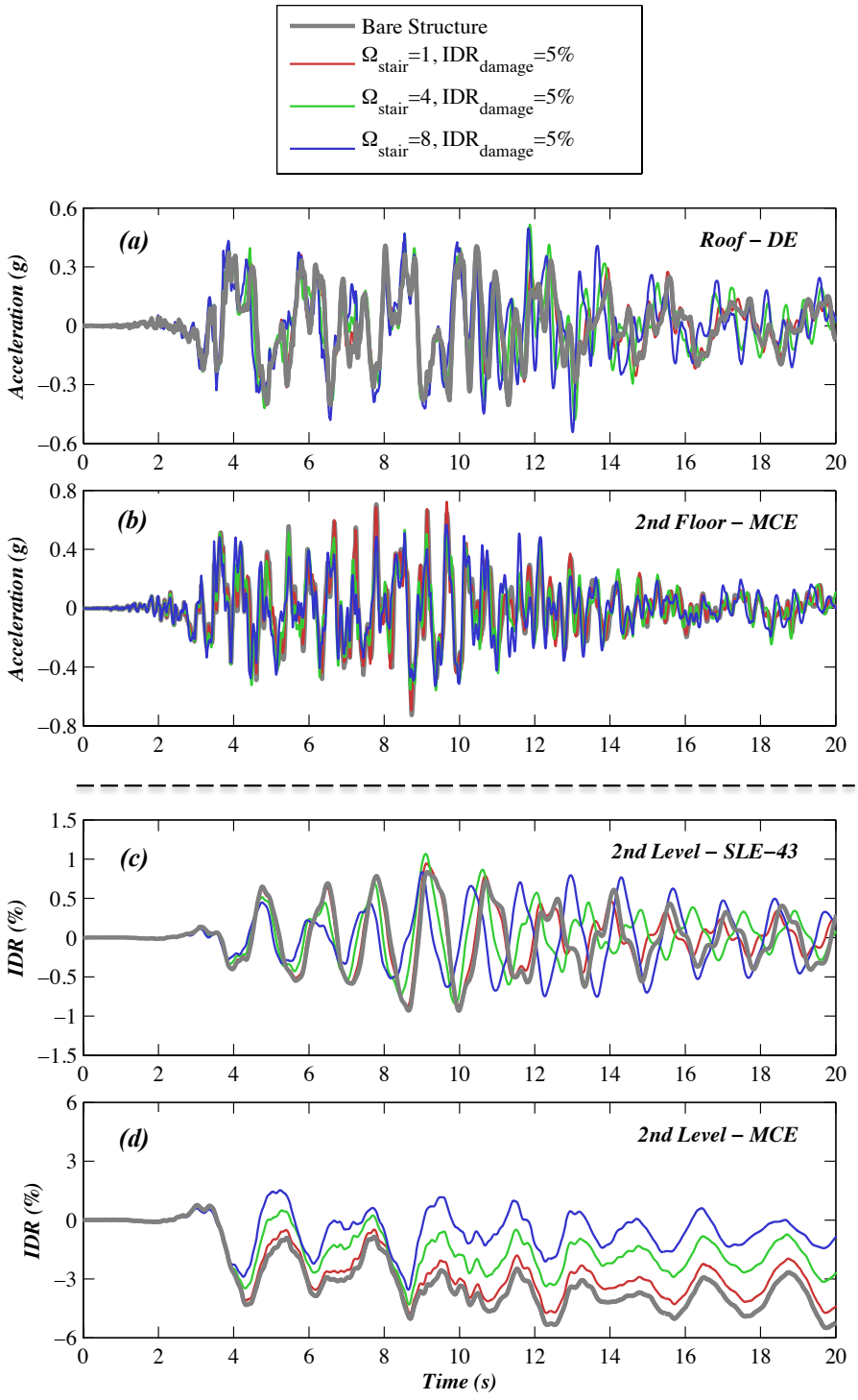

Figure 5.36. Effects of stair response amplification factor Ω_{stair} on time history responses of building S-4: (a) acceleration at the roof – DE motion, (b) acceleration at the 2nd floor – MCE motion, (c) interstory drift ratio at the 2nd level – SLE-43 motion, (d) interstory drift ratio at the 2nd level – MCE motion.

During the SLE-43 motion (Figure 5.35d), the PIDRs are slight higher than those of the bare building in the case of Ω_{stair} = 1 and 4, while the values are considerably lower in the case of Ω_{stair} = 8. This is due to the fact that while the presence of stairs leads to larger story stiffness, it also results in shortened fundamental building period and possibly larger dynamic load effects on the building systems. During the DE and MCE motions, however, the presence of stairs consistently reduces PIDRs of the coupled systems at all levels, and the reduction effects increases with larger building demands or larger Ω_{stair}. As shown in Figure 5.36c–d, while the interstory drift ratio at level 2 undergo pronounced phase shift during the SLE-43 motion for different values of Ω_{stair}, this effects is not significant during the MCE motions when the building systems sustain large inelastic deformation demands. In addition, it is shown in 5.36d that increasing Ω_{stair} effectively reduces residual interstory drifts of the building provided that the stairs are capable of sustaining large deformation without damage.

Figure 5.37 shows the PFA and PIDR responses of building S-4 with different stair ultimate deformability IDR_{damage} (1.5%, 2.5%, and 5%). The stair response modification factor Ω_{stair} is selected as 4 to emphasize the stair effects on the building response. It is noted that the achieved PIDRs of building S-4 during the SLE-43 motion are lower than 1.5% at all levels, indicating that the building responses of the coupled systems are independent of IDR_{damage} in absence of stair damage. For this reason, the result comparison during the SLE-43 motion includes only those of the bare building and the coupled system with IDR_{damage}=1.5%. Similarly, the building responses in the DE motion for IDR_{damage}=5% is not presented. As shown in Figures 5.37a–c, the effects of stairs on the building PFA are the most significant absent stair damage during the earthquake motions, such as in the case of IDR_{damage}=2.5% in the DE motion and IDR_{damage}=5% in the MCE motion. Once that stair damage initiates during the earthquake motions (e.g., IDR_{damage}=1.5% in the DE motion, IDR_{damage}=1.5% and 2.5%), the differences of the PFA responses between the coupled systems and their bare building counterpart reduced considerably and become comparable. Compared to those of the PFAs, the differences of the PIDR responses appear slightly larger, as shown in Figures 5.37d–f. Similarly, the differences appear to be the largest when the IDR_{damage} is large enough to prevent

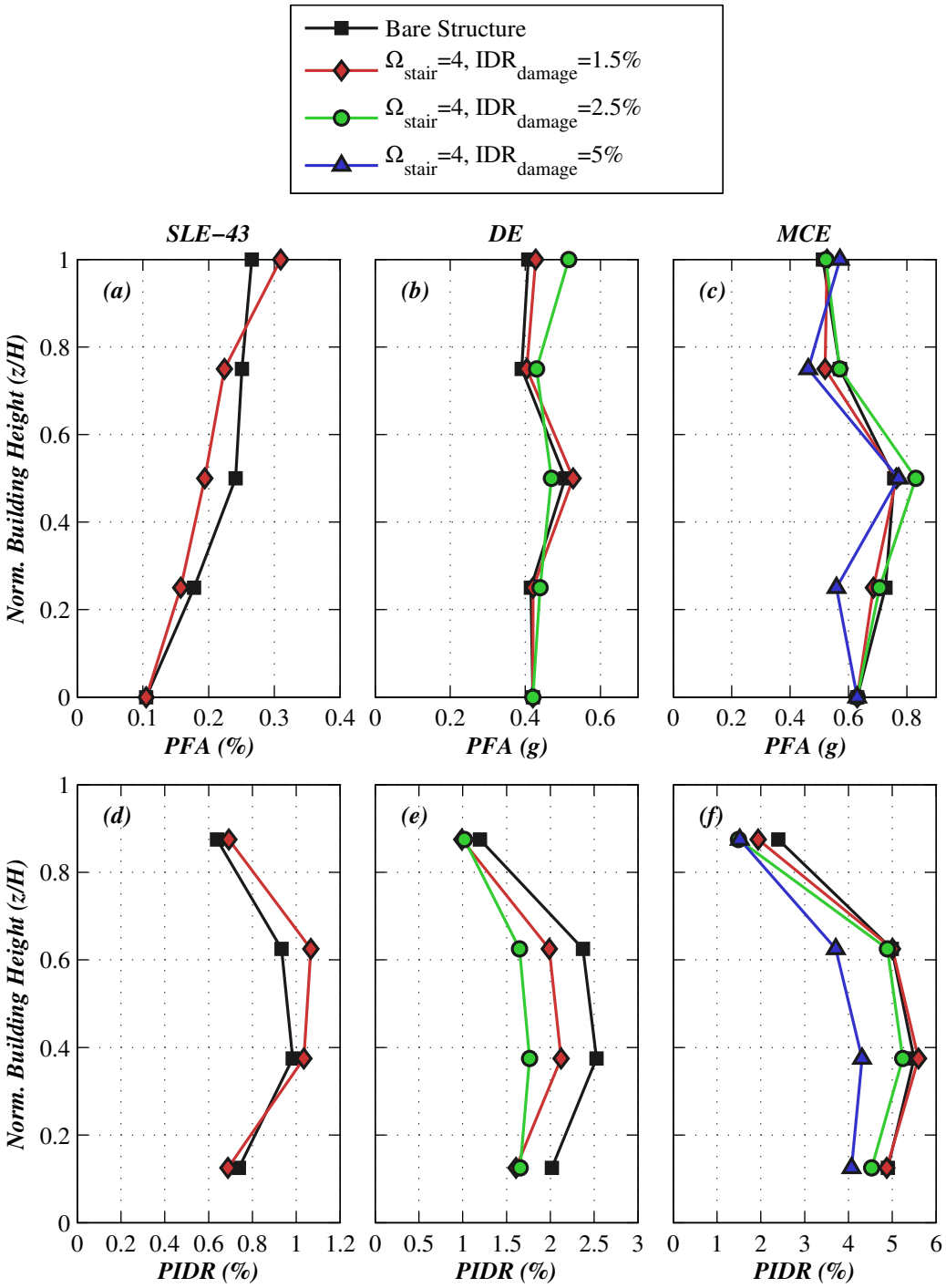

Figure 5.37. Effects of stair ultimate deformability IDR_{damage} on the peak responses of building S-4: (a) PFA – SLE-43 motion, (b) PFA – DE motion, (c) PFA – MCE motion, (d) PIDR – SLE-43 motion, (e) PIDR – DE motion, and (f) PIDR – MCE motion.

stair damage during the earthquakes.

Figures 5.38 and 5.39 present the normalized peak building responses of all six prototype buildings under the three motion intensity levels. The stairs incorporated into these buildings are characterized by identical force-deformation response ($\Omega_{stair} = 4$ and $IDR_{damage} = 5\%$). This indicates that no stair damage occur in the dynamic analyses, as the achieved PIDR of all coupled systems never exceed the IDR_{damage}. The normalized peak building responses of the coupled systems, denoted as PFA* and PIDR*, represent the ratio between the peak building responses (PFAs and PIDRs) of the coupled system and the corresponding responses of the bare building. As shown in the Figure 5.38, the presence of stairs may increase or decrease the building PFAs dependent on the location along the height of the building as well as the motion intensity level. Even though the roof often achieves the largest absolute PFA during an earthquake motion, in particular in the low-intensity motion, the largest PFA differences are observed at the intermediate floors for each prototype building. As shown in the Figure 5.39, the PIDR responses of the 4- and 8-story buildings are effectively reduced under the DE and MCE intensity levels, when these buildings sustain large inelastic deformations at the lower levels due to the presence of stairs, although PIDR responses may increase during the SLE-43 motion. For the 20-story buildings, however, the PIDR responses are not consistently lower than those of the bare buildings even during the DE and MCE motions. This is due to the fact that the PIDR demands of the two 20-story buildings are noticeably smaller than those with less stories during the DE and MCE motions, and that increasing the number of stories tend to render the buildings more sensitive to the higher-mode effects.

It is noted that the buildings with larger number of stories tend to attenuate the impact of stairs on building PFA responses, as the normalized PFAs of the 20-story buildings appear closer to unity than those of the 4- and 8-story buildings. Likewise, increasing the number of stories of the building also reduces the impact of stairs on the PIDR responses of the coupled building systems. This is because that the building stiffness and strength increases with increasing number of story, and therefore the effects of stairs on the building become less significant.

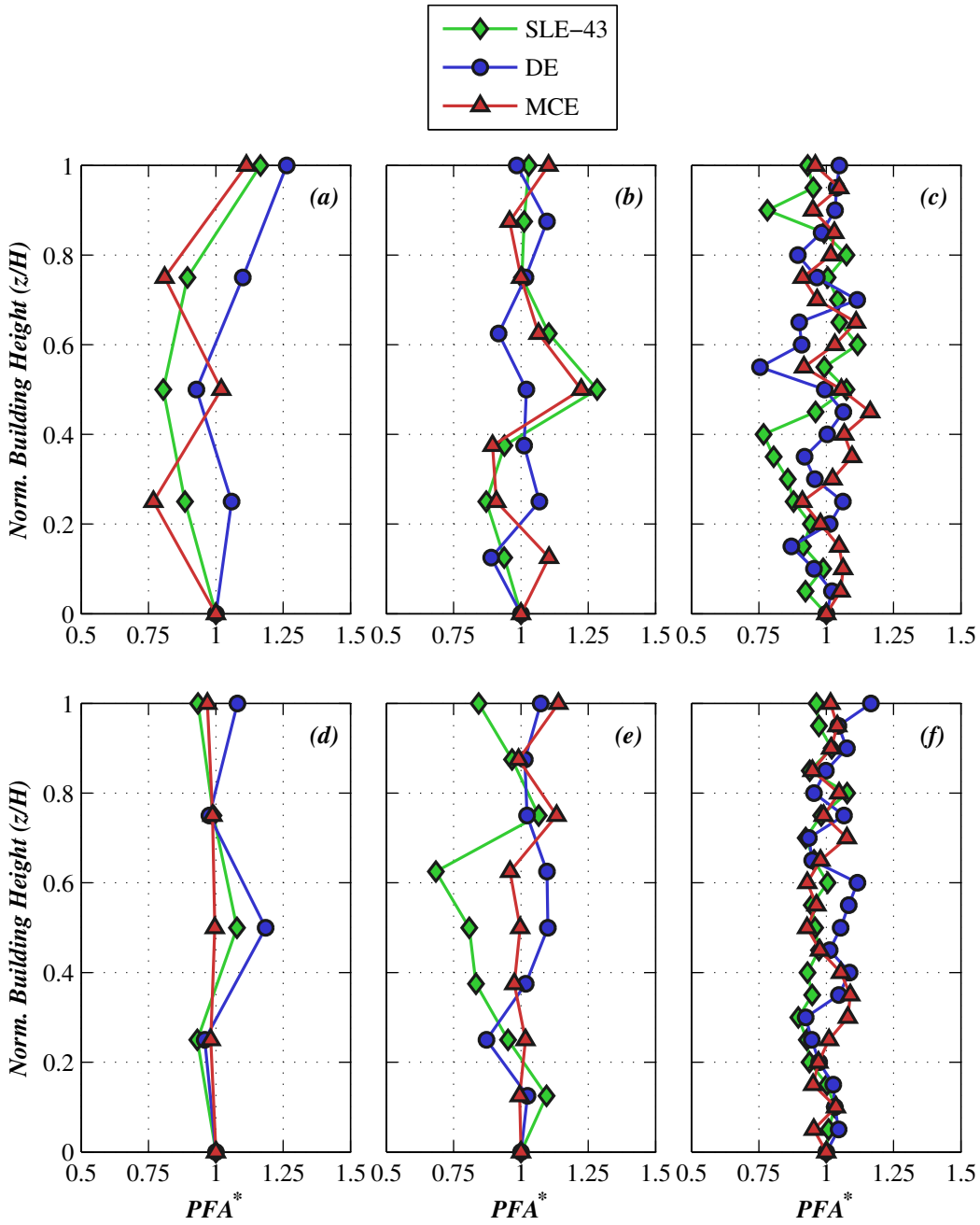

Figure 5.38. Normalized PFA responses of the prototype buildings with stairs incorporated (Ω_{stair}=4, IDR_{damage}=5%): (a) building S-4, (b) building S-8, (c) building S-20, (d) building RC-4, (e) building RC-8, and (f) building RC-20.

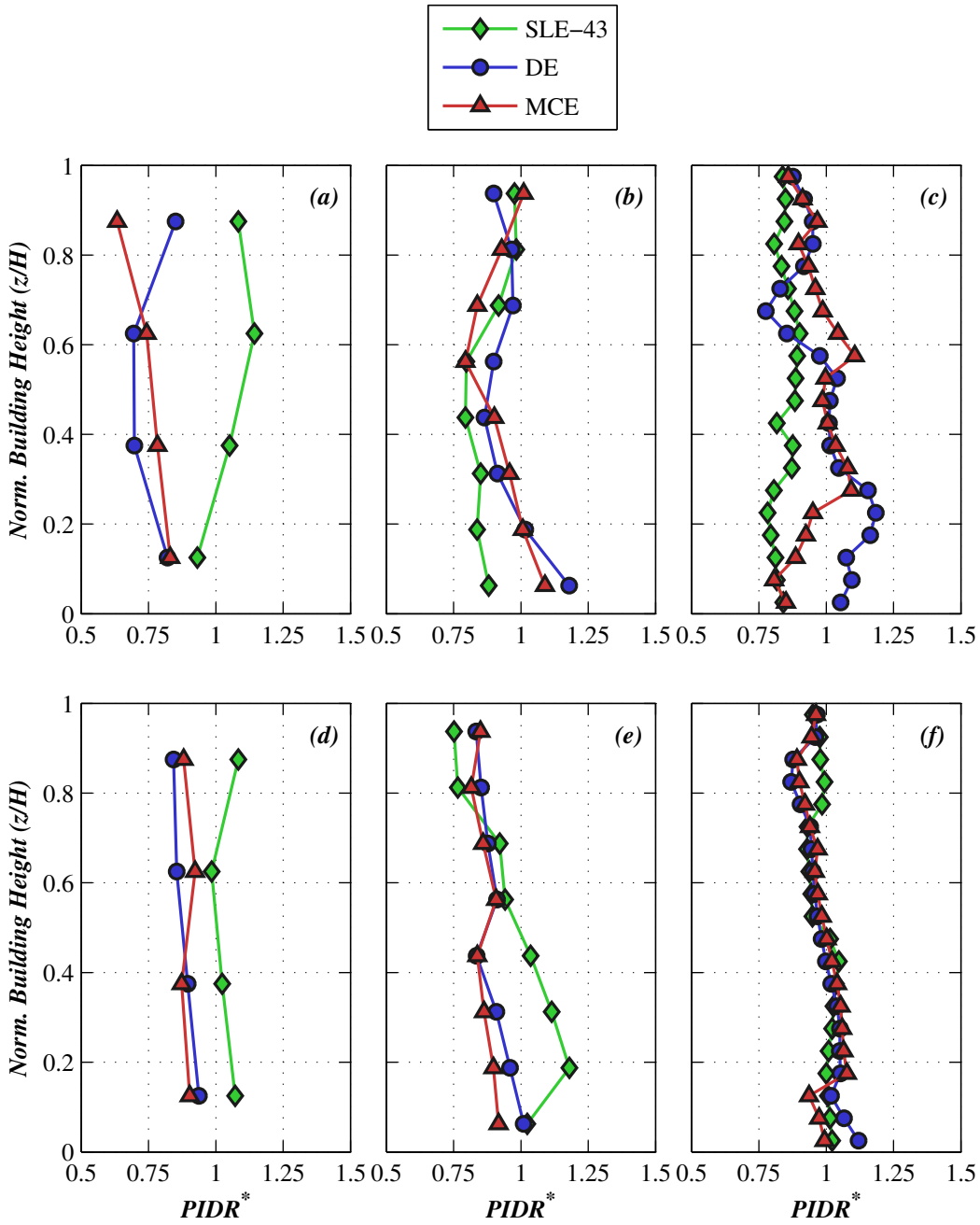

Figure 5.39. Normalized PIDR responses of the prototype buildings with stairs incorporated (Ω_{stair}=4, IDR_{damage}=5%): (a) building S-4, (b) building S-8, (c) building S-20, (d) building RC-4, (e) building RC-8, and (f) building RC-20.

5.5 Concluding Remarks

This chapter presents a system-level numerical parametric study to assess the interaction between buildings and stair systems on the seismic responses of the coupled systems. The coupled systems are modeled as design-oriented two-dimensional models in *OpenSees*. Parameters of interests include the variation of building type and the number of stories of the building as well as the force-displacement behavior of the stair systems. Key findings of the numerical parametric studies of the coupled building-stair systems are summarized as the following:

1. The effect of stairs on the seismic response characteristics of the coupled systems are dependent on the strength and stiffness contributions of the stair systems relative to those of the prototype building. The response of the steel buildings tends to be more sensitive to the presence of stairs than their reinforced concrete building counterparts, as they are often more flexible. Regardless of specific structural systems, the impact of stair systems on building responses tend attenuate as the building story number increases or the structural system becomes stiffer.

2. As indicated by eigenvalue analyses, the first-mode periods of the coupled systems appear more sensitive to the presence of stairs than those of the higher modes. However, the mode shapes of the coupled systems are almost identical to those of their bare building counterparts, as the calculated MAC values between the coupled systems and their bare building counterparts are nearly unity.

3. The presence of stairs in most cases reduces the ultimate roof drift ratio $\delta_{r,u}$ and the ductility μ_T of the coupled building-stair systems. This is due to the fact that the presence of stairs results in larger peak strength of the building-stair system, and therefore higher lateral force demands associated with its ultimate state (80% peak strength). In the case of low stair ultimate deformation capacity IDR_{damage} and large stair response modification factor Ω_{stair}, the coupled systems achieves ultimate state immediately following the onset of the stair damage, thus significantly reducing the ultimate deformation capacity and the ductility.

4. Irrespective of the specific building system or ground motion intensity, the PIDRs

of the low- and medium-rise (4- and 8-story) buildings tend to reduce when these buildings sustain large inelastic deformation demands at the lower levels, although these responses may increase during low-intensity motions. In contrast, the PIDR responses of the high-rise (20-story) buildings differ noticeably from those of the low- and medium-rise buildings due to the higher mode effects. Since their PIDR response are noticeably smaller during the moderate- or high-intensity motions, the PIDRs of the coupled systems does not consistently decreases and could be larger than those of the bare building along the height of the building.

The numerical parametric study presented in this chapter provides qualitative insights into understanding the seismic responses of buildings with interactions between the building and stair systems. It is noted that this study accounts only for stair participation in the form of strength and stiffness contributions of the stairs due to differential displacements imposed by the building. Therefore, further investigations are needed to include the dynamic effects of stair systems in particular in the case of heavier stairs. In addition, three-dimensional modeling of coupled building-stair systems are needed to investigate the coupling effects of stair systems under the two horizontal loading directions and the potential effects of stairs on building torsional responses.

Chapter 6

Probabilistic Seismic Response Analysis of Building-Stair Systems and Loss Estimation of Stair Systems

6.1 Introduction

This chapter extend the seismic analysis of the coupled building-stair systems into the seismic loss estimation of stairs using a probabilistic seismic performance assessment methodology. The objectives of this chapter are to: 1) evaluate the structural response characteristics of the coupled building-stair systems due to the interacting effects between buildings and stair systems, and 2) conduct a seismic loss assessment of stair systems in buildings. This study aims to provide insights into the seismic performance of the buildings-stair systems as well as the cost-efficiency of stair systems due to the interactions between the stairs and their supporting structure.

This chapter is organized into six sections. Section 6.2 introduces the general methodology of a probabilistic seismic performance assessment framework and the specific procedure for analyzing coupled building-stair systems. Section 6.3 discusses the site-specific seismic hazard analysis and ground motions used in the probabilistic seismic demand analysis. Section 6.4 presents the probabilistic seismic demand analysis results

of the coupled building-stair systems as well as building collapse performance. Section 6.5 discusses the detailed analysis procedure of seismic damage and loss analysis of stair systems. Subsequently the stair loss results and the influence of buildings and stair systems on the stair loss are presented. Lastly, Section 6.6 summarizes important findings regarding the probabilistic seismic response analysis and loss estimation of the coupled building-stair systems.

6.2 Probabilistic Seismic Analysis Methodology

Past few decades have repeatedly manifested severe economic consequences resulting from major earthquakes in the United States (e.g., the 1989 Loma Prieta earthquake, the 1994 Northridge earthquake) and other earthquake prone countries (e.g., 2010 Maule earthquake in Chile, 2011 Tohoku earthquake in Japan). In response to the potential consequences and the likelihood of occurrence of major earthquakes, probabilistic seismic analysis tools have been employed to assess the performance of new and existing structural systems (Cornell et al., 2002; Ellingwood et al., 2004). In particular, the Pacific Earthquake Engineering Research (PEER) Center has developed a probabilistic methodology for comprehensive seismic performance assessments of structural facilities (Deierlein et al., 2003; Porter, 2003). Research studies on estimating seismic losses of buildings and other civil infrastructures have appeared in numerous recent literature (e.g., Aslani and Miranda (2005); Goulet et al. (2007)).

6.2.1 General Framework

The PEER probabilistic seismic performance assessment framework consists of a four-stage analysis methodology, which includes seismic hazard analysis, structural demand analysis, damage analysis, and loss analysis. Seismic hazard analysis evaluates seismic Intensity measures *IM*s based on seismological and geotechnical data, which intends to characterize the seismic hazard in terms of mean annual probability of exceedance at a specific site location and design characteristics of a facility (McGuire, 2004). Structural demand analysis, as the second step of the framework, involves nonlinear structural analysis to evaluate Engineering Demand Parameters (*EDPs*). The struc-

tural demands of interest consist of story drifts, accelerations, forces, and other local structural responses (e.g., hinge rotations). Incremental Dynamic Analyses (IDA) are used to assess the probabilistic structural responses conditioned on seismic *IM*s, which involves a series of nonlinear dynamic analyses of a structural model subjected to multiple ground motion records, each scaled to different *IM* levels. Subsequently, seismic damage analysis relates the *EDP*s to Damage States (*DS*s), which describe the physical extent of structural and nonstructural damage. The output of seismic damage analysis is a fragility function that defines the probability of various damage levels conditioned on structural responses. Finally, loss analysis evaluates seismic performance, parameterized using different decision variables (*DV*s), conditioned on damage. *DV*s are often defined as quantifiable parameters related to the performance of a structural facility, such as repair and replacement costs, business downtime (loss of operability), and casualties. According to conditional probability and total probability theorem, the PEER probabilistic framework is implemented using a triple integral for seismic performance and loss assessment of a structural facility:

$$\lambda_{DV}(dv) = \iiint G_{DV|DS}(dv|ds)\, f_{DS|EDP}(ds|edp) \\ f_{EDP|IM}(edp|im) \left| \frac{\mathrm{d}\lambda_{IM}(im)}{\mathrm{d}im} \right| \mathrm{d}ds\, \mathrm{d}edp\, \mathrm{d}im \tag{6.1}$$

where $\lambda_{DV}(dv)$ is the mean annual rate (MAR) of DV exceeding a specified value dv. For example, $\lambda_{DV}(dv)$ can be the MAR of a total loss exceeding 50% of the total replacement cost of a structural facility. $G_{X|Y}(x|y)$ denotes Complimentary Cumulative Distribution Function (CCDF) of X conditioned on $Y = y$, and $f_{X|Y}(x|y)$ is the Probability Distribution Function (PDF) of X conditioned on $Y = y$. For example, $G_{EDP|IM}(edp|im)$ denotes the probability of an EDP exceeding a specified value edp (e.g., interstory drift) when subjected to ground motions with $IM = im$ (e.g., the first-mode spectral acceleration $S_a(T_1)$). The term $\mathrm{d}\lambda_{IM}(im)/\mathrm{d}im$ is the slope (first-order derivative) of the seismic hazard curve $\mathrm{d}\lambda_{IM}(im)$, which relates the ground motion IM to a MAR of exceedance.

The PEER PBEE framework assumes that all conditional distributions are Marko-

vian dependent such that previous conditioning information does not affect future distributions(Baker and Cornell, 2008). This assumption implies, for example, the distribution of a *DS* (damage state of a structural component) is conditioned only on *EDP* (structural response) but conditionally independent of the *IM* (spectra acceleration of the ground motion). Likewise, an *EDP* (structural response) is dependent only on the *IM* (spectra acceleration of the ground motion) but not further influenced by the magnitude or distance of the incident earthquake. These assumptions significantly simplify seismic loss calculations by dividing the triple integral into successive single integrals.

Uncertainties in probabilistic seismic analysis are often categorized into aleatory variability caused by inherent randomness and epistemic uncertainties due to lack of knowledge. Although epistemic uncertainties can be incorporated into the PEER PBEE framework, this study accounts only for uncertainties due to ground motion record-to-record (aleatory) randomness. The effects of epistemic uncertainties on the seismic performance and loss of coupled building-stair systems is not the scope of this study but can be addressed in future study.

6.2.2 Probabilistic Seismic Analysis of Building-Stair Systems

According to the PEER PBEE probabilistic framework, a three-stage analysis procedure is developed to investigate the effects of stairs on the seismic responses of the coupled building-stair systems as well as the seismic loss of stair systems in the buildings. Important aspects related to the seismic performance and loss estimation of the coupled systems are summarized as the following:

1. Three steel buildings (with 4, 8, and 20 stories) are considered as building variants in this study. This is due to the fact that the steel buildings appear more sensitive to the presence of stairs than their reinforced concrete building counterparts as a result of smaller stiffness contributions of the structural systems.

2. Stair systems incorporated in the coupled systems account for the variations of stair strength amplification effects (Ω_{stair}=1, 2, 4, and 8) and the stair ultimate deformability (IDR_{damage}=1.5%, 2.5%, and 5%).

3. The seismic Intensity Measure (IM) is defined as the 5% damped first-mode spectral acceleration $S_a(T_1, 5\%)$. It is noted that the first-mode period of the building T_1 is determined numerically using the bare building model instead of those calculated using the code-based equation.

4. A total of eleven IMs are considered in the seimsic demand analysis, corresponding to return periods T_R of 21, 43, 72, 140, 225, 475, 975, 2475, 4975, 9975, and 24975 years, respectively. It is noted that the highest IM (with a return period of 24975 years) is selected to ensure that a relatively high ratio (> 60%) of building collapse is achieved at this IM level.

5. The ground motions records used in the seismic demand analysis are the FEMA P695 far-field ground motion set (FEMA, 2009), which consists of 22 pairs of horizontal ground motion components with a total of 44 individual records. Details of this ground motion set is discussed later in the following section.

As shown in Figure 6.1, probabilistic assessment of stair loss in a building consists of seismic hazard analysis, seismic demand analysis, seismic damage analyze, and seismic loss analysis. Seismic hazard analysis aims to determine the seismic hazard curves at the site of interest using data generated by USGS Hazard Curve Application (http://geohazards.usgs.gov/hazardtool/). The hazard curve provides the mean annual rate (MAR) of seismic IM exceeding a specified value (Figure 6.1a). Subsequently, seismic demand analysis is conducted using incremental dynamic analyses (IDA) (Vamvatsikos and Cornell, 2002), which consists of nonlinear time-history simulations of the coupled building-stair models using an ensemble of earthquake motions with progressively increasing seismic IMs (Figure 6.1b). The IDA results are then utilized for quantifying the probabilistic characteristics of the EDPs (structural responses) as well as collapse hazard of the buildings at the given IMs. In seismic damage and loss analysis (Figure 6.1c), multi-layer Monte-Carlo simulations are conducted to estimate the seismic loss (overall damage) of stair systems conditioned on IM. These conditional loss metrics are subsequently integrated with the corresponding seismic hazard curve to obtained the overall seismic loss of stair systems. Details of each steps of the seismic loss analysis procedure are discussed in the following sections.

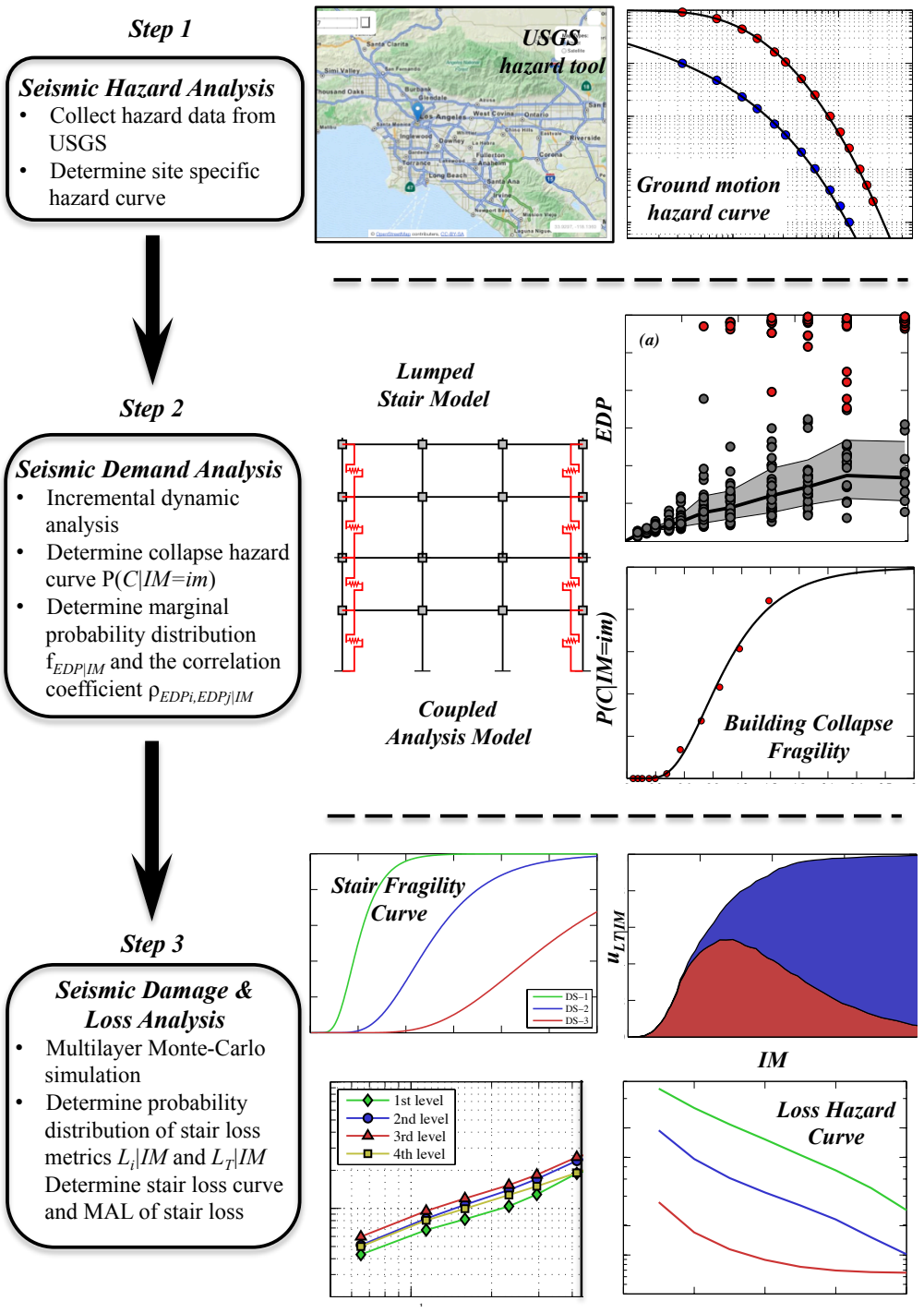

Figure 6.1. Probabilistic analysis procedure of coupled building-stair systems.

6.3 Seismic Hazard Analysis

6.3.1 Site-specific Seismic Hazard Analysis

The hypothetical site of the prototype buildings is located near downtown Los Angeles, California (33.996N, 118.162W) ($V_{s,30}$ = 285m/s). Using data generated by USGS Hazard Curve Application (http://geohazards.usgs.gov/hazardtool/) on the basis of the 2008 National Seismic Hazard Mapping Project (USGS, 2014), the uniform hazard spectra (UHS) of the hypothetical site is shown in Figure 6.2. The figure includes the UHS corresponding to return periods T_R of 43, 475, and 2475 years, respectively. The one-second spectral acceleration of the UHS is 0.17 g for a 43-year event (50% in 30 years), 0.55 g for a 475-year event (10% in 50 years), and 1.05 g for a 2475-year event (2% in 50 years). It is noted that the one-second spectral accelerations of the 475-year and the 2475-year events are consistent with the DE (S_{D1} = 0.6 g) and the MCE events (S_{M1} = 1.0 g) as prescribed in ASCE 7-05 (ASCE, 2005).

Since the spectral accelerations of the UHS are only available at discrete periods (dotted data points in Figure 6.2), the first-mode spectral acceleration of the building $S_a(T_1)$, which is employed as the *IM* in the seismic hazard analysis, is determined by interpolating the UHS at two adjacent periods in the linear-log space:

$$\ln(S_a(T)) = \frac{T - T_1}{T_2 - T_1}\ln(S_a(T_1)) + \frac{T_2 - T}{T_2 - T_1}\ln(S_a(T_2)) \quad (T_1 < T < T_2) \tag{6.2}$$

Figure 6.3 shows the seismic hazard curves of the three steel prototype buildings. The hazard curve $\lambda_{IM}(im)$ provides the mean annual rate (MAR) of the *IM* exceeding a specified *im*. The seismic hazard levels range from an MAR of 1×10^{-1} (T_R = 10 years) to 1×10^{-5} (T_R = 100,000 years). To achieve hazard-consistent result comparison among the three prototype buildings, Table 6.1 summarizes the *IM*s of the three buildings each associated with the return periods of 43, 475 and 2475 years, respectively. The three selected seismic hazard levels correspond to three code-specified earthquake scenarios: Serviceability Earthquake, Design Earthquake, and Maximum Considered Earthquake, respectively, which are hereafter referred to as IM_{43}, IM_{475}, and IM_{2475}.

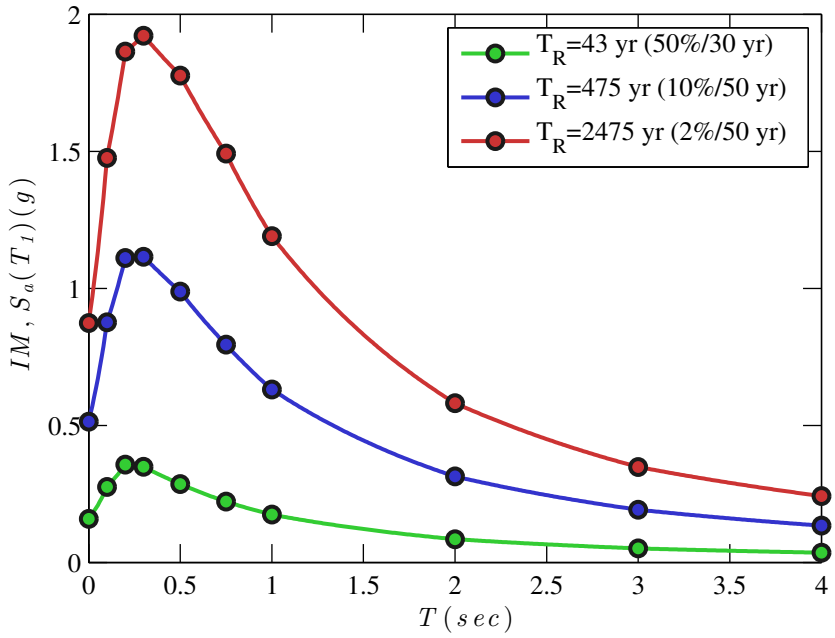

Figure 6.2. Uniform hazard spectra for the site of the prototype buildings (33.996N, 118.162W).

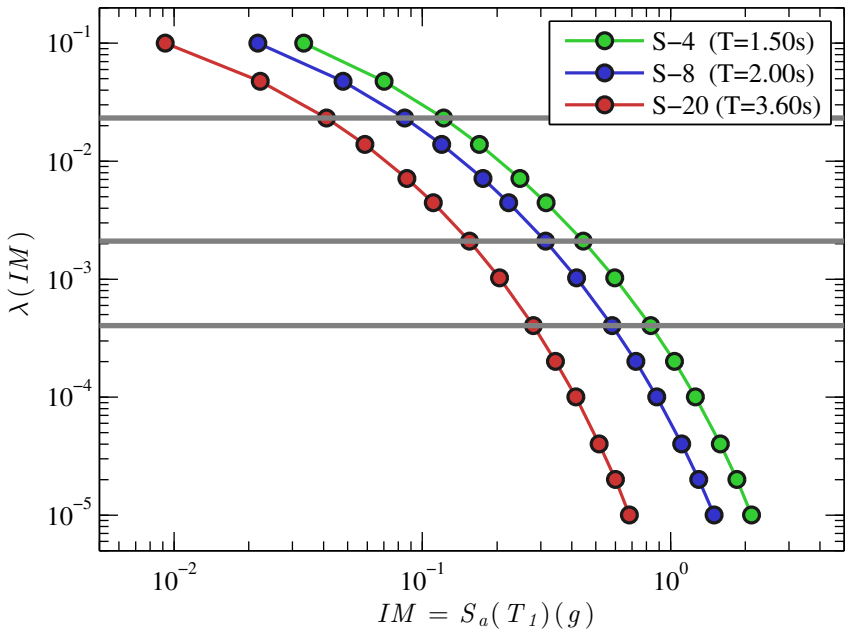

Figure 6.3. Site-specific hazard curves for the three steel buildings (33.996N, 118.162W).

Table 6.1. Seismic hazard for the three prototype buildings at three representative Intensity Measures

Seismic hazard level	T_R (year)	λ	IM		
			S-4 (g)	S-8 (g)	S-20 (g)
Serviceability Earthquake	43	4.76×10^{-2}	0.11	0.08	0.04
Design Earthquake	475	2.11×10^{-3}	0.42	0.31	0.16
Maximum Considered Earthquake	2475	4.04×10^{-4}	0.78	0.58	0.29

With the assumption that earthquakes with IM exceeding a value im within a given exposure time T follow a Poisson random occurrence model, the probability of exceedance (PE) $\mathrm{P}(IM > im)$ at a given exposure time T can be derived from the hazard curve $\lambda_{IM}(im)$ using the following equation:

$$\mathrm{P}(IM > im) = 1 - \mathrm{e}^{-\lambda_{IM}(im)T} \tag{6.3}$$

Assuming the probability of the earthquake IM follows lognormal distribution, the PE curve represents the Complementary Cumulative Density Function (CCDF) with median $\hat{\mu}_{\ln IM}$ and dispersion $\hat{\sigma}_{\ln IM}$:

$$\mathrm{P}(IM > im) = 1 - \mathrm{P}(IM \leq im) = 1 - \Phi\left(\frac{\ln(im) - \hat{\mu}_{\ln IM)}}{\hat{\sigma}_{\ln IM}}\right) \tag{6.4}$$

As shown in Figure 6.4, the discrete seismic hazard data points $\lambda_{IM}(im)$ (represented by blue circles) of building S-4 are first converted to the corresponding PE with an exposure time T of 50 years. The parameters $\hat{\mu}_{\ln IM}$ and $\hat{\sigma}_{\ln IM}$ of the lognormal distribution are subsequently identified by the least-square fit of the fourteen data points (represented by red circles). The lognormally-fitted seismic hazard curve $\lambda_{IM}(im)$ (Figure 6.4) and the slope (first derivative) of the hazard curve $\mathrm{d}\lambda_{IM}(im)/\mathrm{d}im$ (Figure 6.5) can be represented analytically as:

$$\lambda_{IM}(im) = -\frac{\ln(1 - \mathrm{P}(IM > im))}{T} = -\frac{1}{T}\ln\left[\Phi\left(\frac{\ln(im) - \hat{\mu}_{\ln IM)}}{\hat{\sigma}_{\ln IM}}\right)\right] \tag{6.5}$$

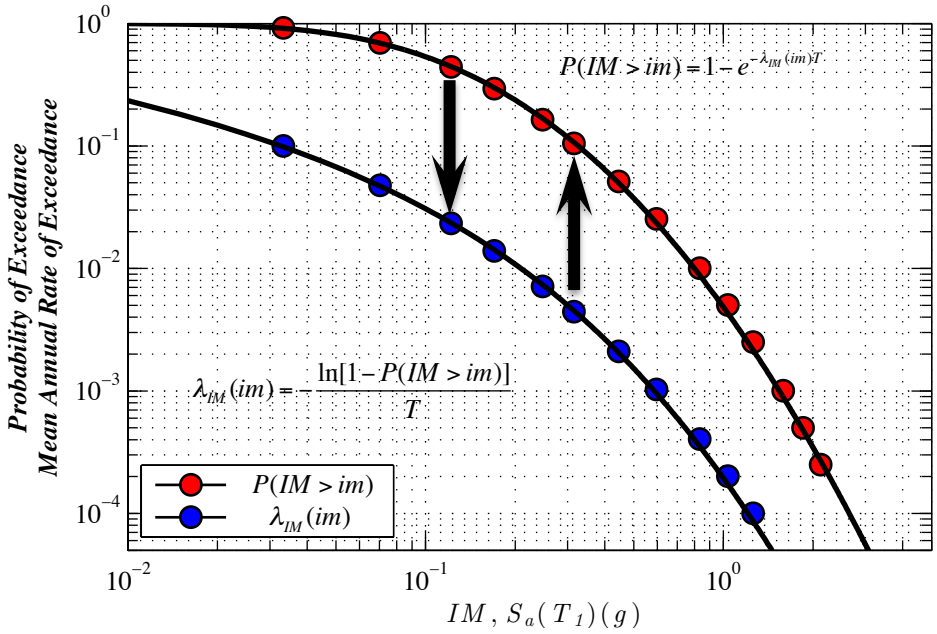

Figure 6.4. Lognormal fitting of seismic hazard exceeded in 50 years and corresponding seismic hazard curve of building S-4.

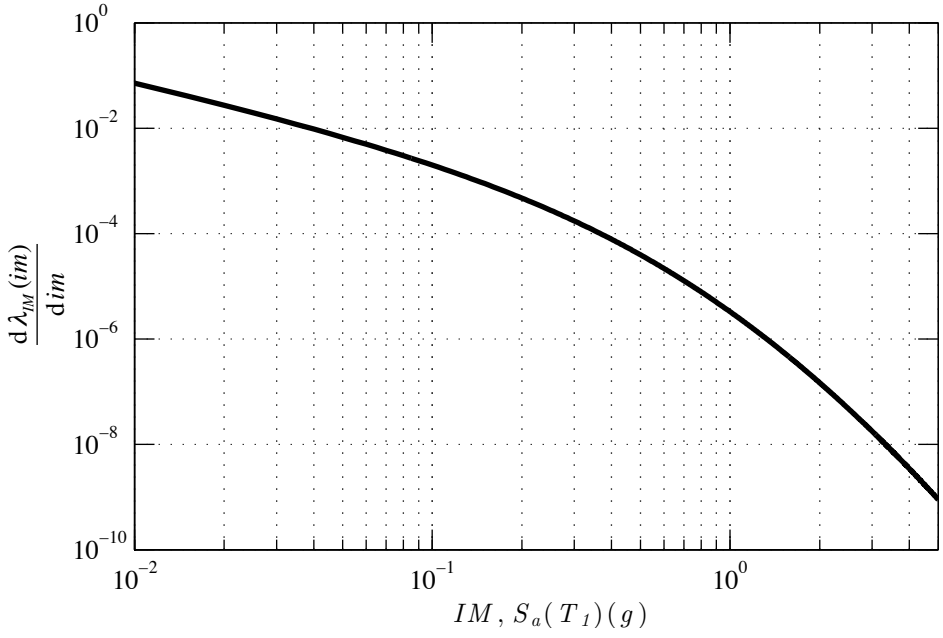

Figure 6.5. The fitted first-order derivative of the seismic hazard curves of building S-4.

$$\left|\frac{\mathrm{d}\lambda_{IM}(im)}{\mathrm{d}im}\right| = -\frac{1}{T}\left[\Phi\left(\frac{\ln(im)-\hat{\mu}_{\ln IM)}}{\hat{\sigma}_{\ln IM}}\right)\right]^{-1}\phi\left(\frac{\ln(im)-\hat{\mu}_{\ln IM)}}{\hat{\sigma}_{\ln IM}}\right)\frac{1}{\hat{\sigma}_{\ln IM}}\frac{1}{im} \tag{6.6}$$

where Φ and ϕ denotes the Cumulative Density Function (CDF) and Probability Density Function (PDF) of a standard normal distribution. The fitted seismic hazard curve $\lambda_{IM}(im)$ (Figure 6.4) and its slope (first derivative) $|\mathrm{d}\lambda_{IM}im/\mathrm{d}im|$ are subsequently employed for calculating the building collapse hazard and the loss hazard of the stair systems.

6.3.2 Ground Motion Set

Ground motions used in the seismic demand analysis employ the FEMA P695 far-field ground motion set (FEMA, 2009), which consists of 22 pairs of horizontal ground motion components (44 individual components). The ground motions were recorded from fourteen large-magnitude earthquake events with moment magnitude M_w in the range of 6.5 – 7.6 and epicentral distance R between 10 – 45 km. According to the NEHRP Site Class, sixteen sites are classified as Site Class D (stiff soil) and the remaining six sites as Site Class C (very stiff soil). It is noted that the FEMA P695 far-field ground motion set was selected with no account of spectral shapes of the ground motions or structure-specific properties. The earthquake source and site characteristics of the FEMA P695 far-field ground motion set are summarized in Table 6.2. It is noted that the original (unscaled) ground motions are normalized using the PGV_{PEER} value, which is determined as the geometric mean (square root of the product) of the peak ground velocities (PGV) for an individual horizontal component pair. Each pair of the ground motions is normalized such that their PGV_{PEER} value matches the median PGV_{PEER} value, which represents median PGV_{PEER} value of the ensemble of PEER ground motion database. The 5% damped pseudo-acceleration spectra $S_a(T)$ and displacement spectra $S_d(T)$ of the normalized ground motion records as well as the median and 16th/84th percentile spectra are presented in Figure 6.6. Additional information of the ground motion set is available in Appendix A of FEMA P695 (FEMA, 2009).

Table 6.2. Earthquake source and site characteristics for the FEMA P695 far-field ground motion set (FEMA, 2009)

Motion	Earthquake				Recording	NERHP
#	Event	Year	M_w	R (km)	Station	site class
1	Northridge	1994	6.7	17.2	Beverly Hills – Mulhol	D
2	Northridge	1994	6.7	12.4	Canyon Country – WLC	D
3	Duzce, Turkey	1999	7.1	12	Bolu	D
4	Hector Mine	1999	7.1	11.7	Hector	C
5	Imperial Valley	1979	6.5	22	Delta	D
6	Imperial Valley	1979	6.5	12.5	El Centro Array #11	D
7	Kobe, Japan	1995	6.9	7.1	Nishi-Akashi	C
8	Kobe, Japan	1995	6.9	19.2	Shin-Osaka	D
9	Kocaeli, Turkey	1999	7.5	15.4	Duzce	D
10	Kocaeli, Turkey	1999	7.5	13.5	Arcelik	C
11	Landers	1992	7.3	23.6	Yermo Fire Station	D
12	Landers	1992	7.3	19.7	Coolwater	D
13	Loma Prieta	1989	6.9	15.2	Capitola	D
14	Loma Prieta	1989	6.9	12.8	Gilroy Array #3	D
15	Manjil, Iran	1990	7.4	12.6	Abbar	C
16	Superstition Hills	1987	6.5	18.2	El Centro Imp. Co.	D
17	Superstition Hills	1987	6.5	11.2	Poe Road	D
18	Cape Mendocino	1992	7.0	14.3	Rio Dell Overpass	D
19	Chi-Chi, Taiwan	1999	7.6	10	CHY101	D
20	Chi-Chi, Taiwan	1999	7.6	26	TCU045	C
21	San Fernando	1971	6.6	22.8	LA - Hollywood Star	D
22	Friuli, Italy	1976	6.5	15.8	Tolmezzo	C

In seismic demand analysis, each ground motion component is amplitude-scaled incrementally to match the eleven *IM* levels. The *IM* is defined as the 5% damped elastic spectral accelerations associated with the building first (fundamental) mode $S_a(T_1, 5\%)$. To demonstrate the probabilistic characteristics of the ground motion set, the pseudo-acceleration response spectra of the amplitude-scaled ground motion components at three representative seismic hazard levels (corresponding to a return period T_R of 43, 475, and 2475 years, respective) are shown in Figure 6.7. As shown in the figure, while the spectral acceleration associated with the first-mode period $S_a(T_1)$ are all scaled to

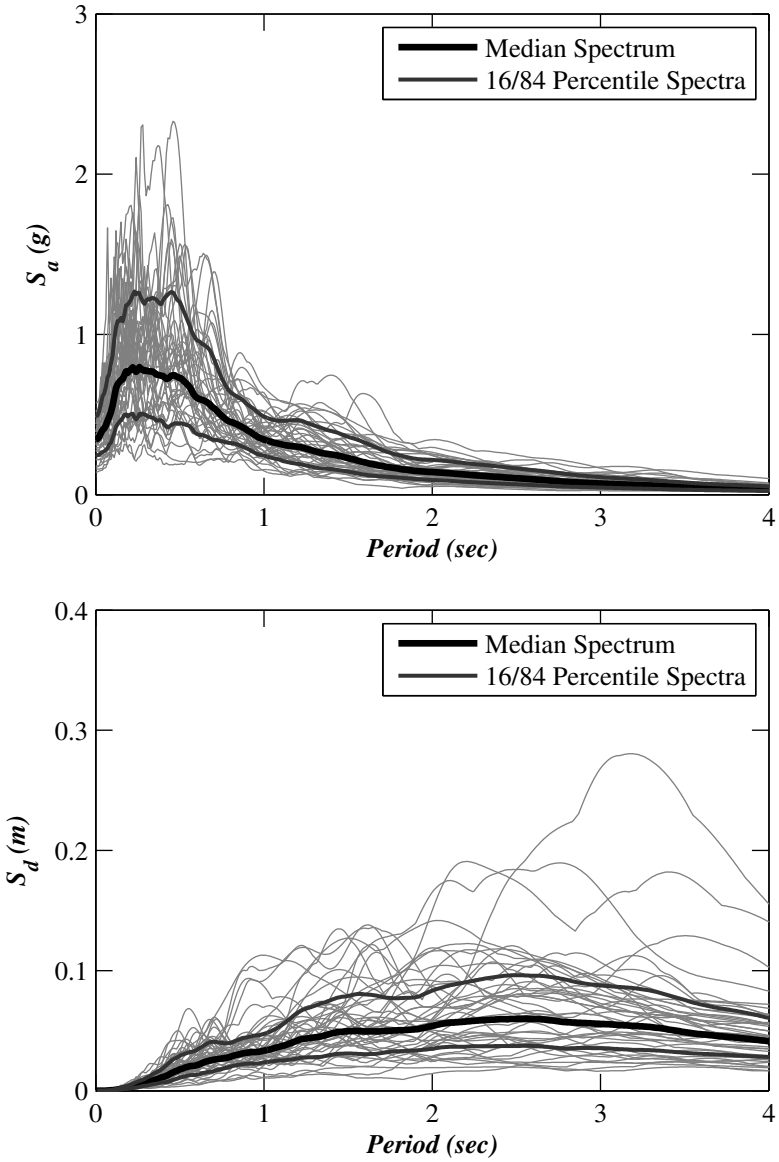

Figure 6.6. Response spectra of the FEMA P695 normalized far-field ground motion records (5% damped): (a) pseudo-acceleration spectra, and (b) displacement spectra.

match the target *IM* at a specific hazard level, the median spectra are much larger than the UHS when the period is shorter than the building fundamental period T_1, which often coincide with the higher modes of the buildings. The dispersion of the spectral accelerations of the scaled ground motions constitutes the dominant contributor to the variability of the *EDP*s conditional on a specific *IM* and the estimated stair loss.

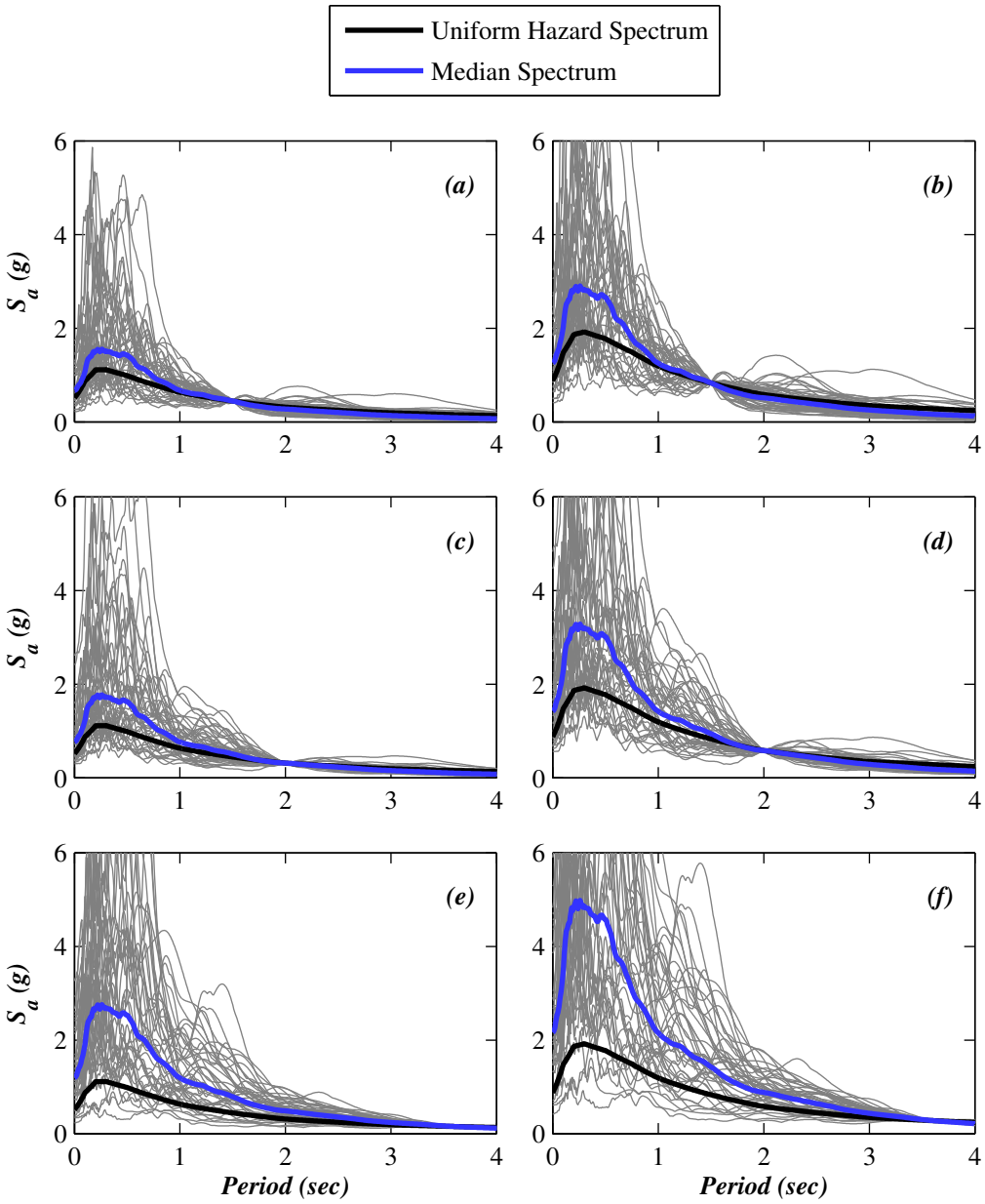

Figure 6.7. Pseudo acceleration spectra of ground motions scaled to different *IM* levels (5% damped): (a) S-4 – IM_{475}, (b) S-4 – IM_{2475}, (c) S-8 – IM_{475}, (d) S-8 – IM_{2475}, (e) S-20 – IM_{475}, and (f) S-20 – IM_{2475}.

6.4 Seismic Demand Analysis and Collapse Assessment

In seismic demand analysis, incremental dynamic analyses (IDA) (Vamvatsikos and Cornell, 2002) are conducted to investigate the probabilistic structural response of the coupled building-stair systems. IDA of each coupled system consists of an ensemble of nonlinear time-history analyses with 44 ground motion components scaled to the eleven *IM* levels. Due to the high computational demands, all numerical analysis and data post-processing were performed using the NEEShub high performance computational platform (NEES, 2015). Engineering Demand Parameters (*EDP*s) of interest (e.g., peak floor accelerations and peak interstory drift ratios) are then retrieved for further investigation. The objectives of the coupled system IDA are to quantify the building collapse fragility, and the statistics of *EDP*s conditioned on *IM*. These information are subsequently used in the seismic loss estimation of stair systems.

Figure 6.8 shows the PIDR responses of building S-4 (bare structure) at the eleven *IM* levels. Each data point represents the PIDR of an individual dynamic analysis using one of the 44 ground motions scaled to a specific *IM* level. In the present study, the building collapse is defined as the peak interstory drift ratio (PIDR) exceeds 10% at any story. Previous studies have concluded that a PIDR of 10% is a reasonable threshold to quantify building collapse hazards in a probabilistic analytical framework (Zareian and Krawinkler, 2007). Figure 6.8 presents the PIDR of building S-4 (bare building) from the IDA results (each discretized marker represents a PIDR for an individual nonlinear analysis – a red circle represents building collapse, and a grey diamond represents a building non-collapse case). Subsequently, the statistics of the PIDR responses in the case of building non-collapse are evaluated. The thick black line represents the median PIDR response for all the non-collapse simulation results, while the shaded area represents the range between 16th and 84th percentile PIDR values. It is noted that collapse of building S-4 initiates at an *IM* of 0.4 g (corresponding to a return period T_R of 475 years) with one occurrence of building collapse in all 44 ground motions at the given *IM* level. The occurrence of collapse increases significantly at the higher *IM* levels, attaining a ratio of more than 80% at the highest *IM* level (1.5 g).

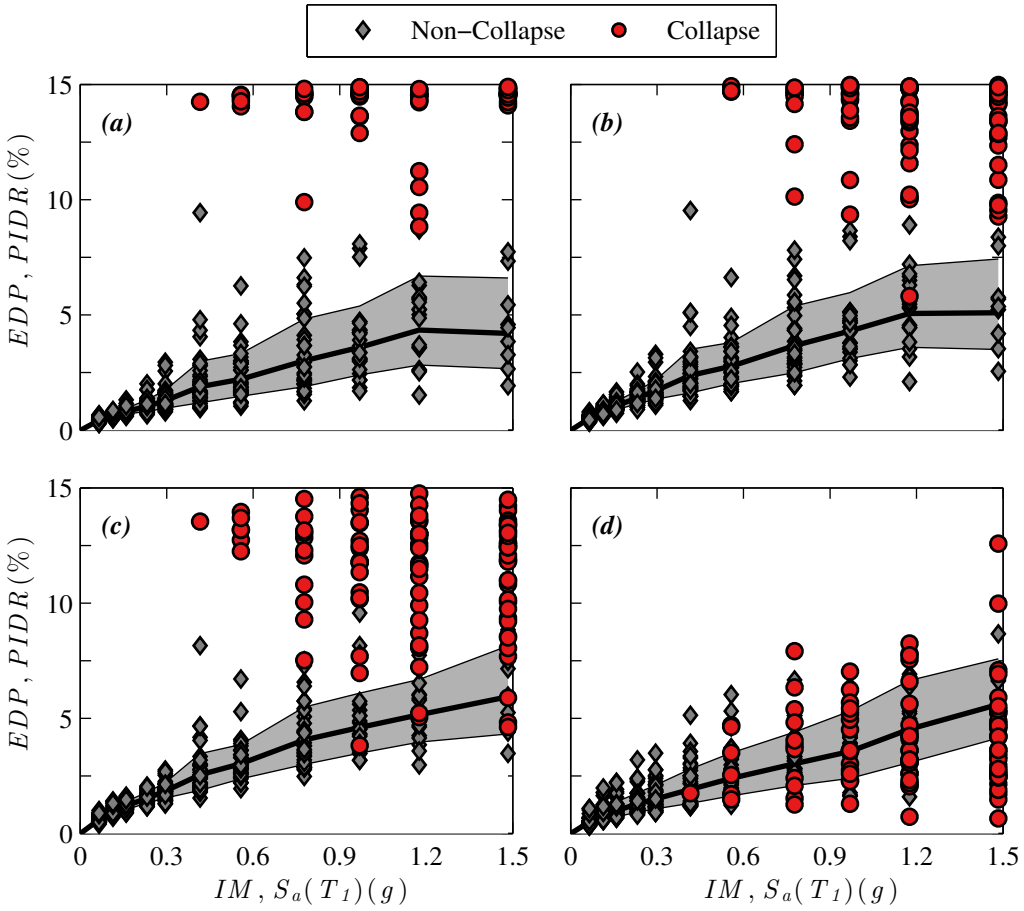

Figure 6.8. PIDR distributions of building S-4 (bare structure) at the eleven *IM* levels: (a) first story, (b) second story, (c) third story, and (d) fourth story.

6.4.1 Collapse Fragility Assessment

Collapse Fragility

In probabilistic seismic analysis, the collapse fragility function of a building is approximated using a lognormal cumulative distribution function (CDF), in which θ_{col} denotes the median of the fragility function (*IM* level with 50% probability of collapse) and β_{col} as the dispersion of collapse (the logarithmic standard deviation):

$$\mathrm{P}(C|IM = im) = \Phi\left(\frac{\ln im - \ln\theta_{col}}{\beta_{col}}\right) \tag{6.7}$$

where $\mathrm{P}(C|IM = im)$ is the conditional probability of building collapse at the given *IM*, and $\Phi(\,)$ is the standard normal CDF. The parameters of the collapse fragility function

θ_{col} and β_{col} are estimated using the maximum likelihood estimation (MLE) method (Baker, 2015; Lallemant et al., 2015). It is assumed that the observed occurrence of collapse or non-collapse from each ground motion is independent of observations from other ground motions, and therefore the probability of observing m collapses out of n ground motions at the given IM is assumed as a binomial distribution:

$$\mathrm{P}(m \text{ collapse in } n \text{ ground motions}) = \binom{n}{m} p_{im}^{m} (1 - p_{im})^{n-m} \tag{6.8}$$

where p_{im} is the simplified notation of $\mathrm{P}(C|IM = im)$. Since the IDA results consist the probability of building collapses at eleven $IM = im$ levels, the likelihood function for the entire IDA data set is defined as the product of the binomial probabilities at all IM levels:

$$\mathcal{L}(\theta_{col}, \beta_{col} \,|\, p_1, p_2, ...p_{n_{im}}) = \prod_{im=1}^{n_{im}} \binom{n}{m} p_{im}^{m} (1 - p_{im})^{n-m} \tag{6.9}$$

Figure 6.9 compares the fitted collapse fragility curve (solid line) of building S-4 (bare building) with the collapse probability empirically obtained using the simulated IDA data at the eleven IM levels (red circles). The figure indicates that the fitted fragility curve determined using the MLE technique agrees well with the empirical collapse observed from the IDA data. Since the maximum discrepancy between the fitted curve and the observed data points, which is used as test statistic for Kolmogorov-Smirnov (K–S) goodness-of-fit tests (Stephens, 1974), is less than 0.05. Therefore, the fitted fragility function passes the K–S test with a 5% significance level. This demonstrates the effectiveness of the lognormal distribution assumption in describing the collapse fragility of the prototype buildings.

Mean Annual Rate of Building Collapse

The mean annual rate (MAR) of building collapse λ_{col} is computed by integrating the fitted building collapse fragility curve over the corresponding seismic hazard curve:

$$\lambda_{col} = \int_0^{\infty} P(C|IM = im) \left| \frac{\mathrm{d}\lambda_{IM}(im)}{\mathrm{d}im} \right| \mathrm{d}im \tag{6.10}$$

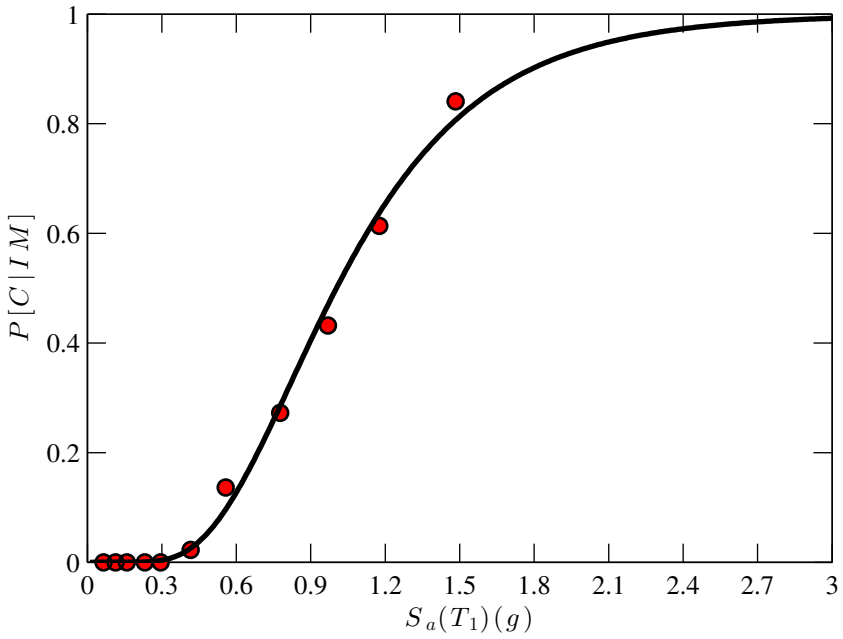

Figure 6.9. Collapse fragility curve for building S-4 (bare building).

The above integration is calculated using the Magnitude-oriented Adaptive Quadrature (MAQ) algorithm (Bradley et al., 2009). This algorithm is an extension of the Simpson's rule-base adaptive quadrature method developed specifically for evaluating integrals involved in the probabilistic seismic analysis. Without loss of generality, Equation 6.10 can be rewritten into a generic form:

$$I_1 = \int_0^{\infty} G(x)\, f(x) \mathrm{d}x \tag{6.11}$$

To handle the indefinite integral, the following mapping $t = 1/(x+1)$ is introduced to modify the above integral from the original domain $x \in [0, \infty)$ into a finite domain with $t \in (0, 1]$:

$$I_2 = \int_0^1 \frac{1}{t^2} G(\frac{1}{t} - 1)\, f(\frac{1}{t} - 1) \mathrm{d}t \tag{6.12}$$

The MAR of building collapse λ_{col} is then numerically evaluated in the t domain

using the MAQ algorithm. This algorithm integrates the sub-regions using three-point Simpson's rule with convergence checks at both the global and local levels. Additional details about the MAQ algorithm can be found in Bradley et al. (2009).

Figure 6.10 illustrates the steps of the MAQ algorithm for evaluating the MAR of collapse for building S-4 (bare building). Figures 6.10a–b show the building collapse fragility curve $P(C|IM = x)$ and the slope (first derivative) of the seismic hazard curve $|d\lambda_{IM}(x)/dx|$, respectively. The resultant integrand $P(C|IM = x)|d\lambda_{IM}(x)/dx|$ in the x (IM) domain is shown in Figure 6.10c. The integrand in the x domain is then transformed into the t domain prior to applying the MAQ algorithm (Figures 6.10d). It is clearly shown in Figure 6.10d that the integration points (red circle points) are distributed adaptively with a higher density in the regions of high curvature than in the regions of low curvature. It is noted that Figure 6.10c also represents the disaggregation of the building collapse MAR into the contributions of earthquakes with different seismic IM levels. As shown in the figure, the dominant contribution to building collapse is attributed to earthquakes with IM between 0.6 and 0.8 g, which correspond to a return period of 2475 years. This is due to the fact that earthquakes within this IM range, although less likely to cause building collapse than earthquakes with larger IMs, occur much more frequently than those high IM earthquakes.

Table 6.3 summarizes the building collapse MAR λ_{col} of the three prototype buildings (bare structures) and the corresponding probability of collapse within an exposure time of 50 years $P_{col,50}$. It is noted that $P_{col,50}$ is derived from λ_{col} by assuming that building collapse follows a Poisson's occurrence model. As shown in the table, although building S-4 appear most vulnerable to collapse due to its highest probability of collapse in 50 years (2.2%), this is only slightly higher as those of the other buildings S-8 (1.7%) and S-20 (1.8%). The estimated collapse hazards of the three prototype buildings are consistent with results presented in Elkady and Lignos (2014).

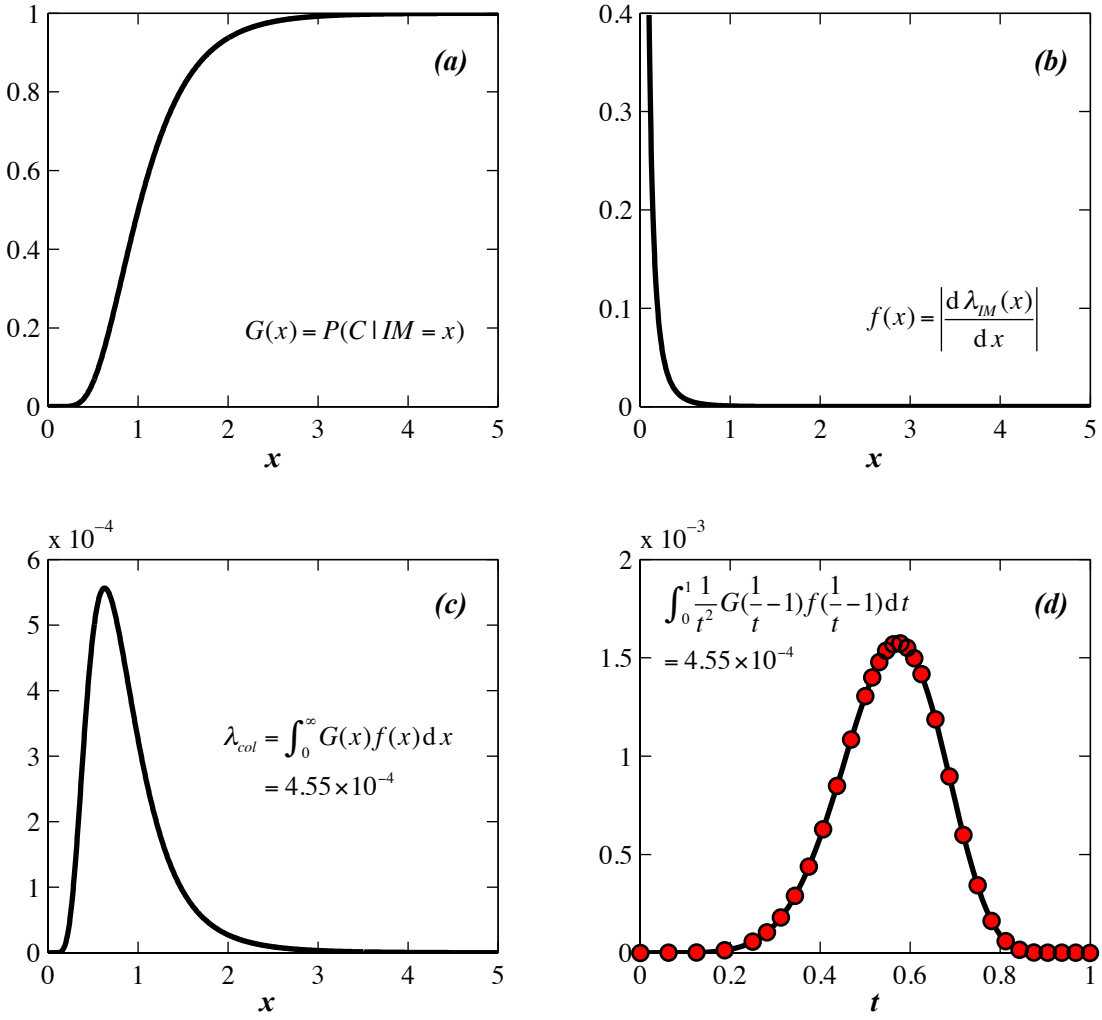

Figure 6.10. MAQ algorithm for calculating collapse MAR of building S-4 (bare building): (a) $G(x)$ in x domain (building collapse fragility curve), (b) $f(x)$ in x domain (slope of seismic hazard curve), (c) resultant integrand in x domain, and (d) resultant integrand in t domain and distribution of integration points.

Table 6.3. Collapse hazard for the steel prototype mabuildings (bare structure)

S-4		S-8		S-20	
λ_{col} ($\times 10^{-4}$)	$P_{col,50}$ (%)	λ_{col} ($\times 10^{-4}$)	$P_{col,50}$ (%)	λ_{col} ($\times 10^{-4}$)	$P_{col,50}$ (%)
4.45	2.2	3.35	1.7	3.55	1.8

Effect of Stairs on Building Collapse Hazard

To investigate the effects of stair systems on building collapse performance, Figure 6.11 compares the MAR of the coupled building-stair systems with those of their bare building counterparts. Variables of the stair systems include stair response modification factor (Ω_{stair} = 1, 4, and 8) and stair ultimate deformation capacity (IDR_{damage} = 1.5%, 2.5%, and 5%). The MAR results presented in the figures are normalized by those of their respective bare buildings, which is denoted as $\widehat{\lambda}_{col}$. As shown in the figure, the presence of stair systems results in a reduction of building collapse MAR of as much as 20% for building S-4, while its effects on the other two buildings are less significantly (< 10% reduction). These results are consistent with the aforementioned observations that the contribution of stair systems relative to the structural system increases as a result of the reduced stiffness and strength of the structural systems or the increased effects of the stairs.

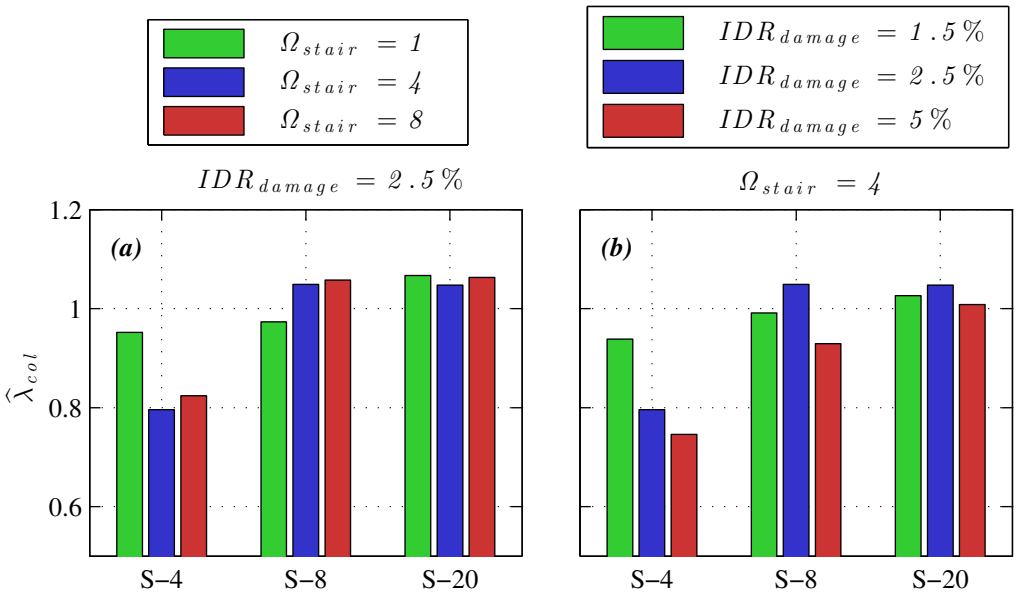

Figure 6.11. Effects of stairs on building collapse MAR: (a) effect of stair response modification factor Ω_{stair}, and (b) effect of stair ultimate deformation capacity IDR_{damage}.

6.4.2 Statistics of Structural Demands

For seismic loss analysis, the marginal probability distribution of an *EDP*(structural response) conditioned on *IM* is assumed to follow a lognormal distribution. Provided that building collapse does not occur, the marginal CDF of *EDP* conditioned on *IM* can be written as:

$$\mathrm{P}(EDP < edp|IM = im, NC) = \Phi\left(\frac{\ln(edp) - \ln\theta_{EDP|IM)}}{\beta_{EDP|IM}}\right) \tag{6.13}$$

where $\theta_{EDP|IM}$ is the median of *EDP* at a given *IM* level, $\beta_{EDP|IM}$ is the dispersion (logarithmic standard deviation) of *EDP* at a given *IM* level, and $\Phi(\ )$ represents the standard normal CDF. It is noted, however, that the PIDR threshold of 10% is used as the criteria to assess the building collapse, the PIDR distributions are slightly modified by using a truncated lognormal distribution with a upper limit of 10%. Similarly to the collapse fragility analysis, the distribution parameters of *EDP*s given *IM* are also identified using the MLE method (Baker, 2015).

Figure 6.12 compares the empirical (numerical) and fitted CDFs of the PIDR responses of building S-4 (bare structure) at three representative *IM* levels. It is shown in the figure that the fitted CDFs agree well with their respective empirical distributions at each of the three selected *IM* levels, although discrepancies become larger with a higher *IM* level. To further justify the effectiveness of lognormal assumption on the the PIDR distributions for all the prototype buildings, Kolmogorov-Smirnov (K-S) goodness-of-fit tests conducted. The test statistic D_n for K-S tests is defined as the absolute value of the maximum difference between the empirical and fitted CDFs. Figure 6.13 shows the test statistic D_n at a 5% significance level for the eleven *IM* levels. It can be seen from the figure that although the discrepancies introduced in estimating the PIDR distributions becomes larger at higher *IM* levels, the lognormal distribution remains a reasonable assumption for describing the PIDR distributions since the fitted lognormal CDFs pass the K-S test at all *IM* levels.

In seismic demand analysis, two assumptions are widely used to characterize the de-

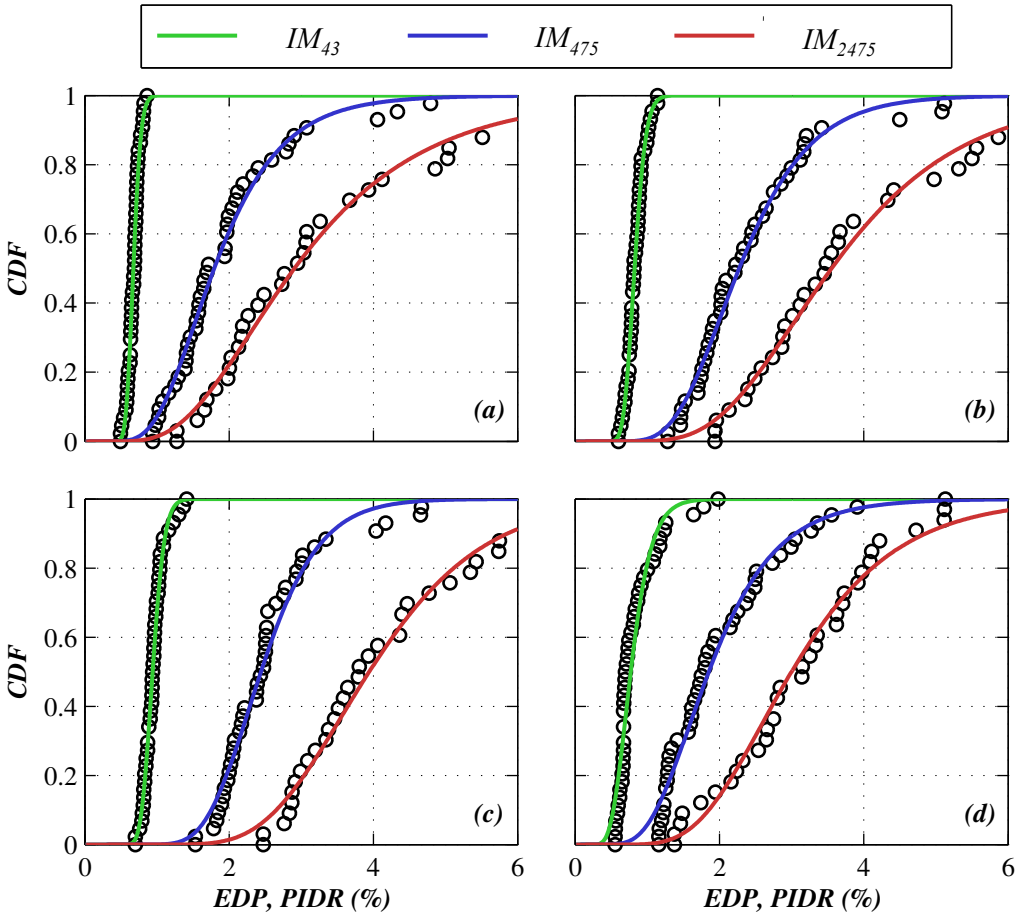

Figure 6.12. The empirical and fitted CDFs of the PIDR responses of building S-4 (bare structure) at three representative *IM* levels.

pendencies of *EDP* statistics as a function of *IM*: (1) the median $\theta_{EDP|IM}$ is assumed as a power function $\theta_{EDP|IM}(im) = aim^b$ of *IM* (power model assumption with parameters a and b), and (2) the dispersion $\beta_{EDP|IM}$ remains constant at all *IM* levels (constant dispersion assumption). Figure 6.14 shows the median $\theta_{EDP|IM}$ and the dispersion $\beta_{EDP|IM}$ curves of the building S-4 PIDR response (bare building). As shown in Figure 6.14a, the power model assumption provides a good approximation of the the median PIDR demands, since the relationship between *IM* and $\theta_{EDP|IM}$ appear essentially linear in the log-log space. In contrast, the constant dispersion assumption appears ineffective to represent the logarithmic standard deviations of the PIDR demands over the entire *IM* region (Figure 6.14b), as the PIDR dispersions $\beta_{EDP|IM}$ become notably larger at the higher *IM* levels (> 0.4 g) due to the building inelastic behavior at these *IM* levels.

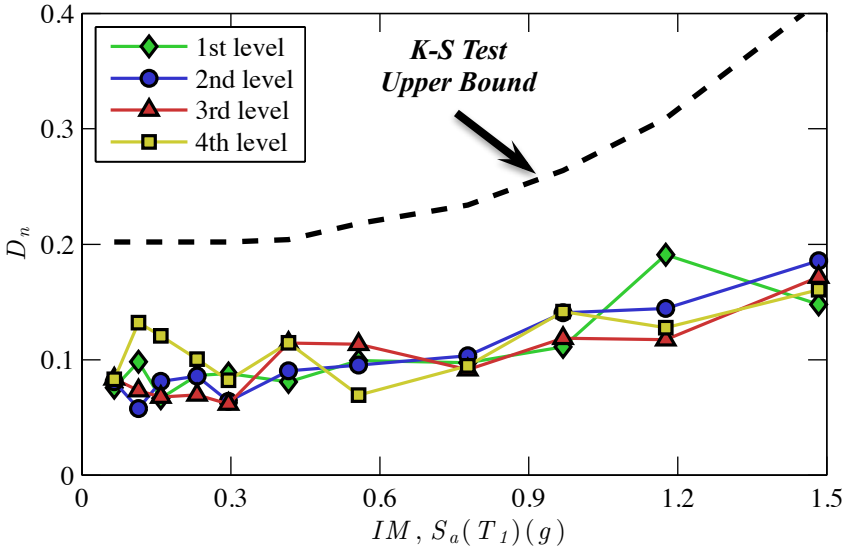

Figure 6.13. Kolmogorov-Smirnov goodness-of-fit tests of the PIDR distributions of building S-4 (bare building).

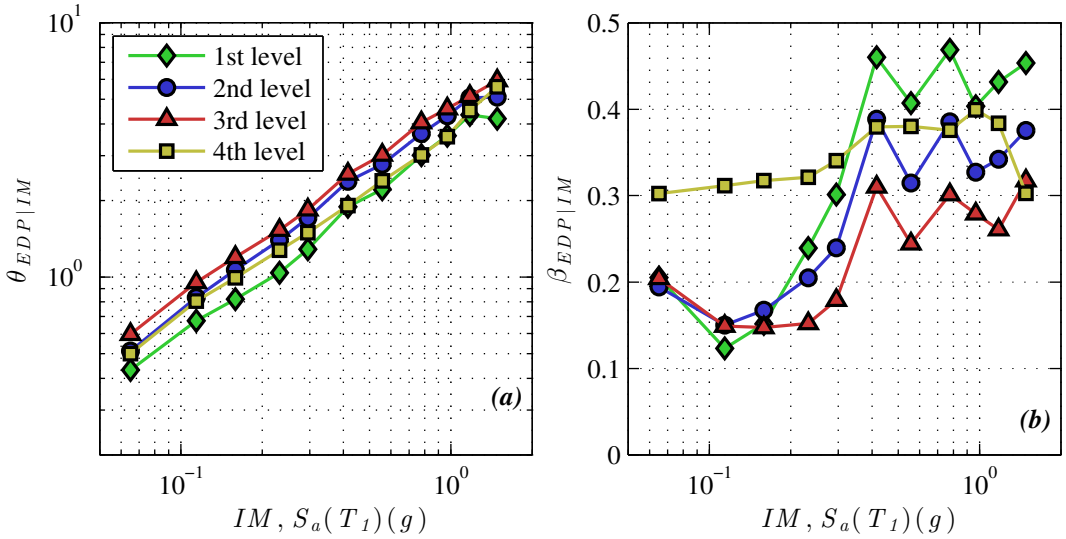

Figure 6.14. (a) Median $\theta_{EDP|IM}$, and (b) dispersion $\beta_{EDP|IM}$ curves of the building S-4 PIDR response (bare building).

Figure 6.15 presents the correlation coefficients $\rho_{EDP_i,EDP_j|IM}$ of the PIDR responses between the ith and jth story of the prototype buildings. For building S-4, it is noted that while the PIDRs at two different stories can be either positively or negatively correlated at the lowest IM level (corresponding to a T_R of 225 years), all the PIDRs become positively correlated at the two higher IM levels (corresponding to a T_R of 475 and 2475 years). In particular, the PIDR responses at the lower three stories become highly correlated ($\rho_{i,j|IM} > 0.8$) at the higher IM levels. This is likely attributed to the formation of story mechanism at the lower three stories of building S-4 during the high-intensity ground motions. For buildings S-8 and S-20, it is also observed that the correlation

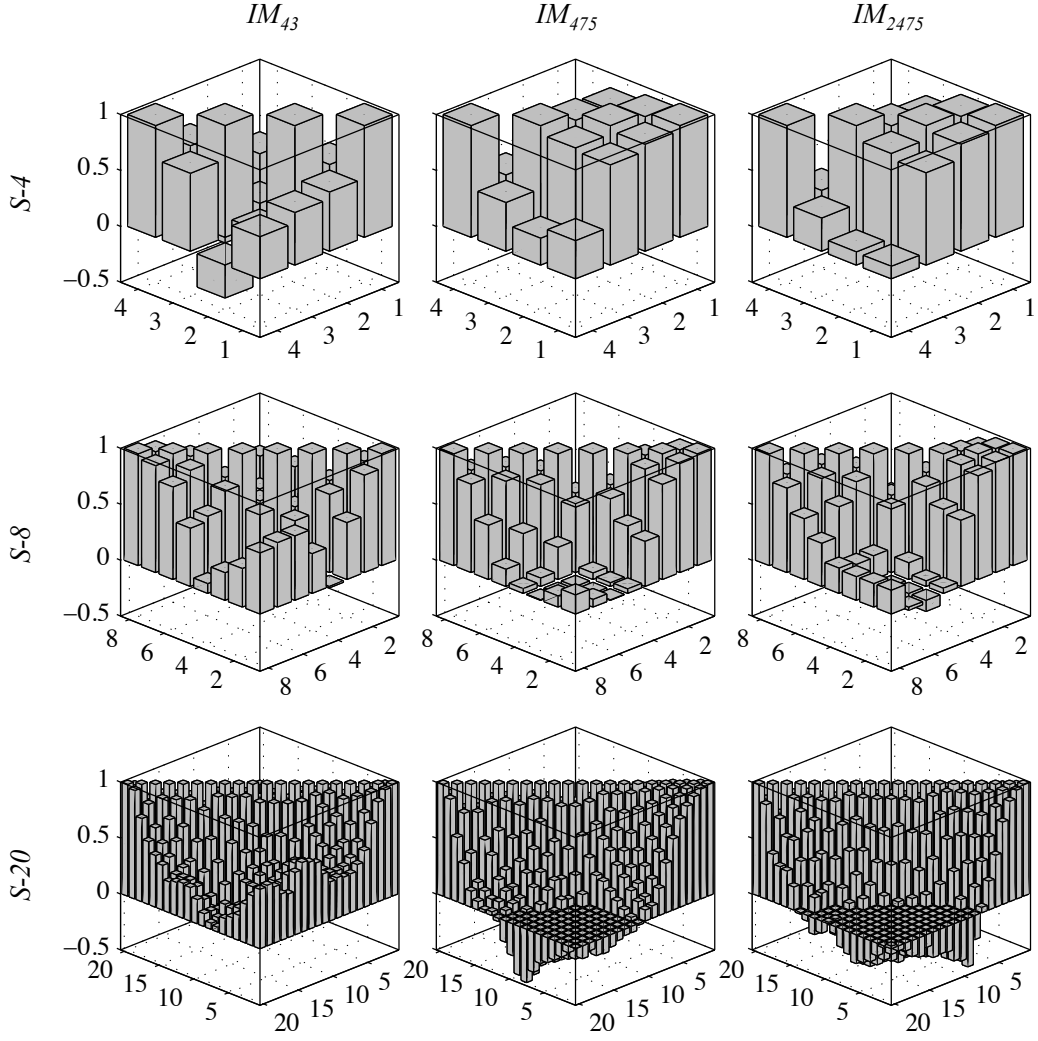

Figure 6.15. Correlation coefficients $\rho_{EDP_i,EDP_j|IM}$ of the PIDR responses of the three prototype buildings.

coefficients are more similar at the two higher *IM* levels but differ pronouncedly with those at the lowest *IM* level.

6.4.3 Probabilistic Structural Response

As discussed previously, lognormal distribution assumptions are suitable to describe the probabilistic characteristics of structural responses (i.e., PFAs and PIDRs) in the case of non-collapse. Figures 6.16 and 6.17 presents the probabilistic PFA and PIDR responses of the three prototype buildings (bare structures) at the three representative *IM* levels. The dotted black lines represent the median responses along the building height, while the shaded area represents the 16th and 84th percentile range of the corresponding response. When the building response remains essentially linear at the IM_{43} level, the median PFA responses of all the three buildings undergo substantial amplification at all floors and achieve the largest responses at the roof (Figure 6.16). In addition, the dispersions of the floor acceleration responses are comparable along the building height. As shown in Figure 6.17, the maximum median PIDR of building S-20 is achieved at the top stories as a result of higher mode effects but at the lower stories for buildings S-4 and S-8. At the IM_{475} and IM_{2475} levels when story mechanism are expected to occur at the lower stories of the buildings, building responses vary significantly from those at the IM_{43} level. The major differences are observed as the attenuated median PFAs as well as much larger median PIDRs at the lower stories as a result of concentration of inelastic deformation. In addition, the dispersions of both the PFAs and PIDRs at the lower floors are much larger than those at the upper floors at the two higher *IM* levels.

Figures 6.18 and 6.19 show the effects of stair response modification factor Ω_{stair} on the median PFA and PIDR responses of the three prototype buildings at the three representative *IM* levels. In Figures 6.18, stair systems incorporated into the buildings consider the variation of stair response modification factor Ω_{stair} (1, 4, and 8), while the IDR_{damage} is selected as 5% for all stairs. As shown in the figure, the median PFAs are affected by the stair effects with only minor differences (<5%) at the roof level, while their responses remain almost identical regardless of stair response modification factors. However, the effect of stairs on the median PIDR responses appears more significant,

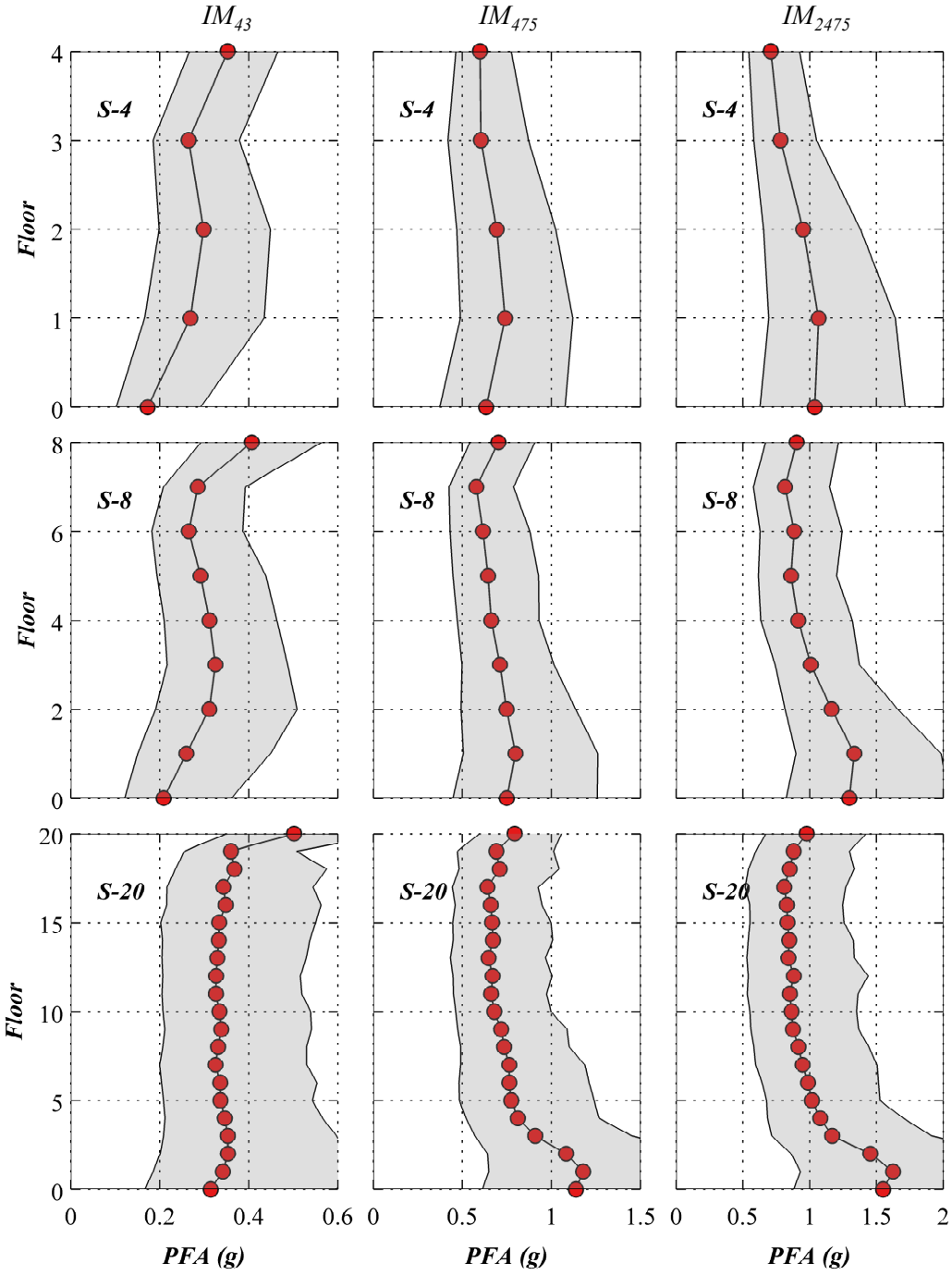

Figure 6.16. Probabilistic peak floor acceleration responses of the steel buildings at three presentative *IM* levels.

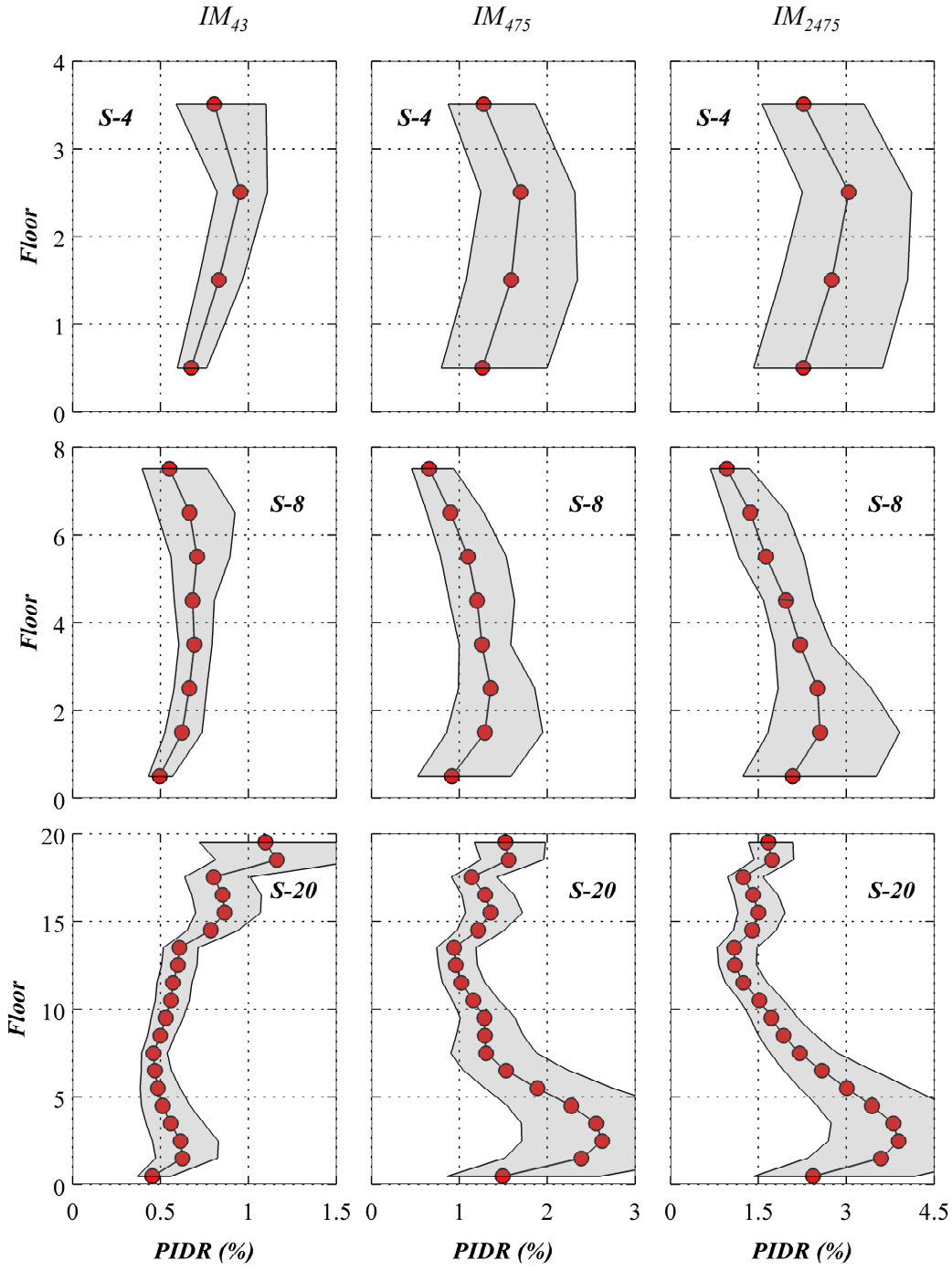

Figure 6.17. Probabilistic peak interstory drift responses of the steel building at three presentative *IM* levels.

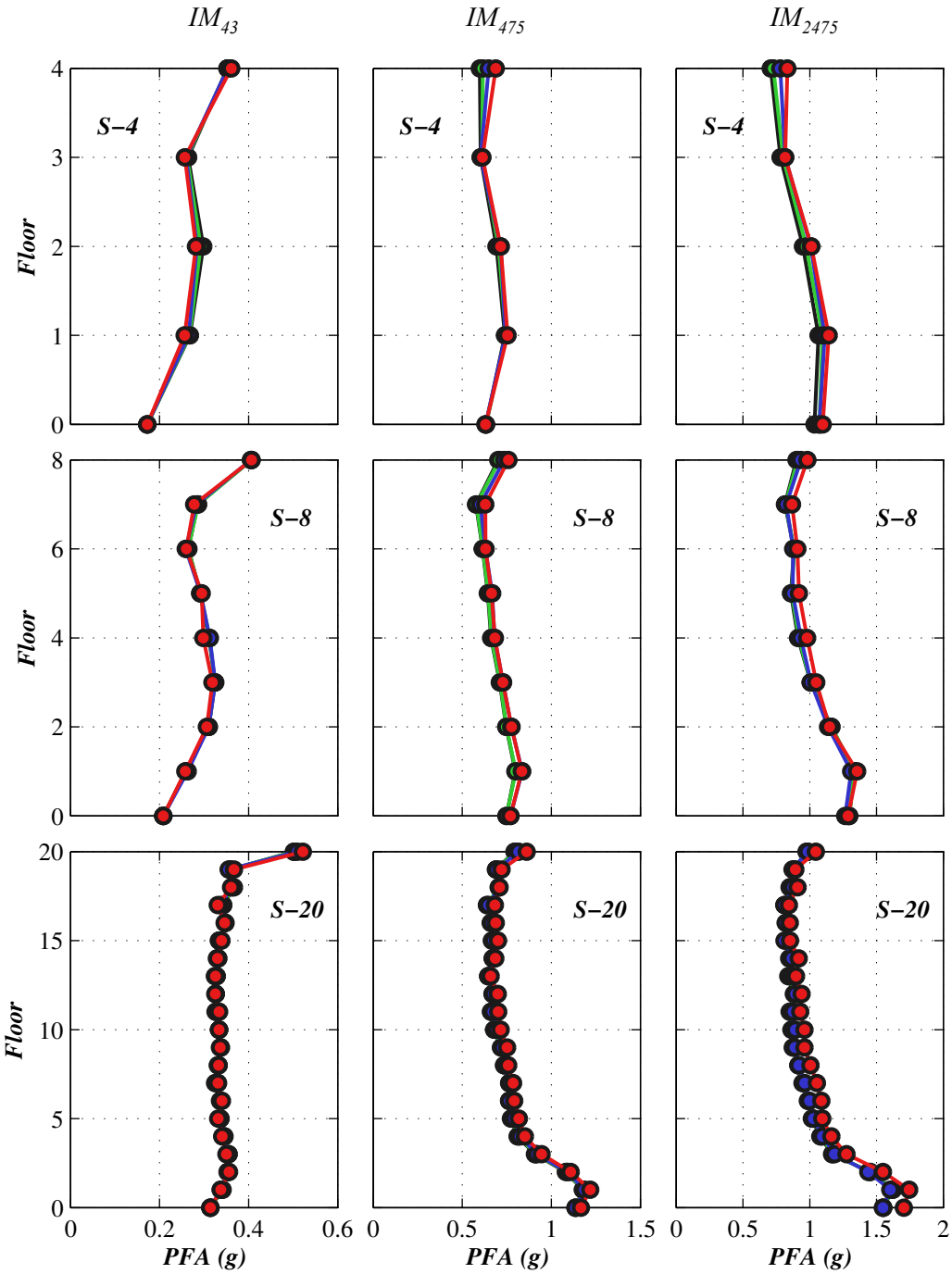

Figure 6.18. Effect of stair response modification factor Ω_{stair} on median peak floor acceleration responses of the steel buildings at three presentative *IM* levels.

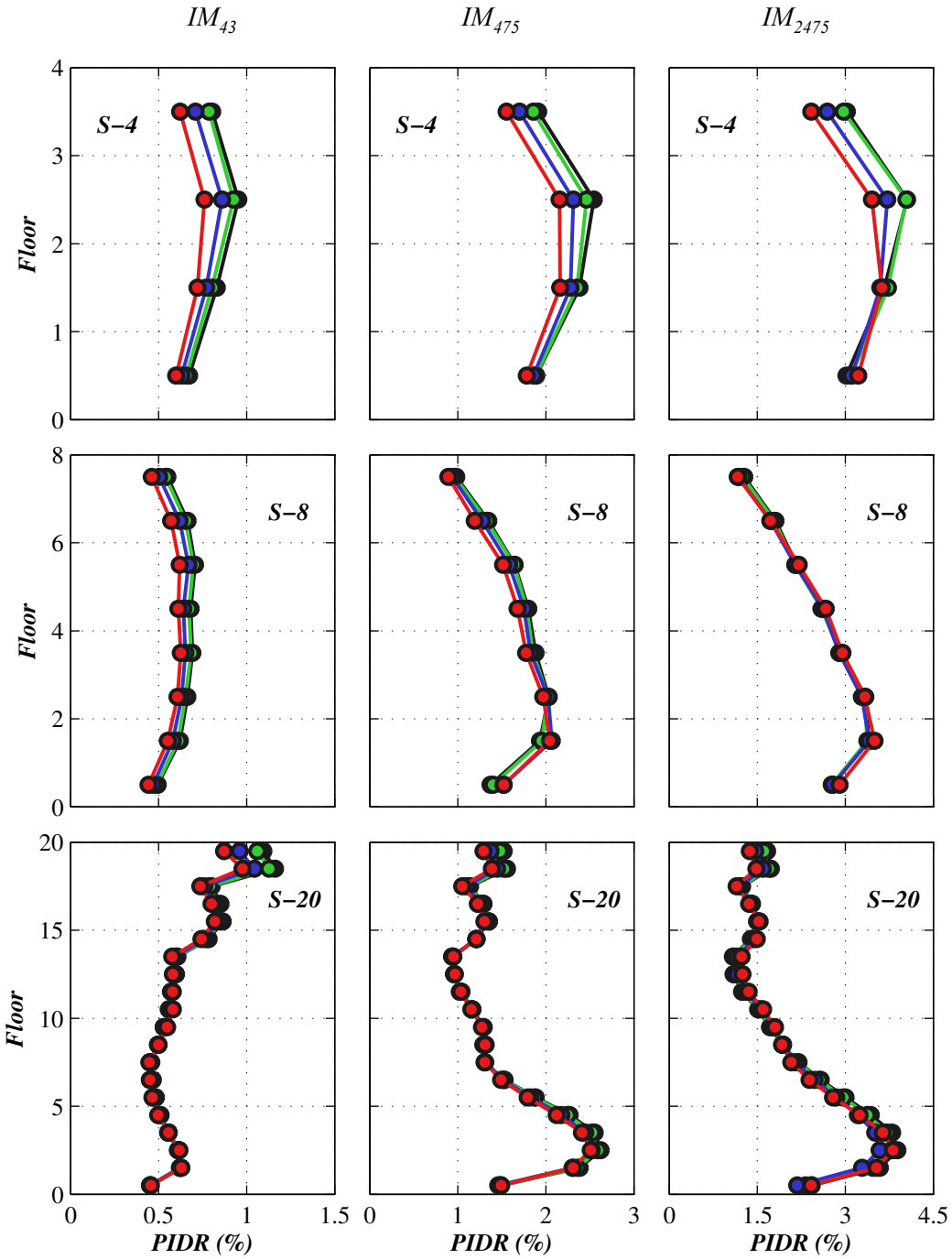

Figure 6.19. Effect of stair response modification factor Ω_{stair} on median peak interstory drift responses of the steel buildings at three presentative *IM* levels.

which result in a maximum PIDR of 10% for $\Omega_{stair} = 4$ and 20% for $\Omega_{stair} = 8$. Due to the increasing contribution of the buildings, the effect of stairs becomes less significant for buildings S-8 and S-20 (maximum difference < 5%). The comparisons of the probabilistic building responses demonstrate that the presence of stairs does not significantly modifies the building response. In addition, it is noted that the presence of stairs has more significant influence on PIDR responses than on the PFA responses. However, the effects of stairs tend to attenuate as the number of stories of the building becomes larger.

6.5 Probabilistic Seismic Damage and Loss Analysis

6.5.1 Seismic Fragility and Damage Analysis of Stairs

According to recent experimental studies (Higgins, 2011; Wang et al., 2015), physical damage to prefabricated steel stairs is categorized into three distinct Damage States (*DS*s) according to the implications of physical damage on stair functionality and repair actions. However, it is important to note that, the stair loss metric is defined as the quantity of stairs that lose their vertical loading capacity, and therefore the damage analysis of the stairs focuses only on the most severe damage state (DS_3).

In seismic damage analysis, the damage state function is generally expressed as:

$$Z = R - S \begin{cases} > 0, & \text{no failure (safe domain)} \\ = 0, & \text{damage limit state} \\ < 0, & \text{failure (unsafe domain} \end{cases} \tag{6.14}$$

where R and S are both random variables denoting the capacity and demand (load effect) related to a Damage State DS of interest (DS_3 in this study). In specific, S rerepsents the variability of EDPs, and R accounts for the inherent uncertainties in material, mechanical and geometric properties. The above sources of uncertainty are modeled through the probability of exceeding a given Damage State (DS_3 in this study) conditioned on the demand S (or EDP), $P(Z < 0|S = s)$ (or $P(DS|EDP = edp)$). This conditional probabil-

ity is often referred to as seismic fragility function (Porter et al., 2007) in probabilistic seismic analysis, which is idealized using lognormal distribution:

$$\mathrm{P}(DS \geq ds \,|\, EDP = edp) = \Phi\left(\frac{\ln(edp) - \ln\theta_{DS|EDP)}}{\beta_{DS|EDP}}\right) \tag{6.15}$$

where $\theta_{DS|EDP}$ and $\beta_{DS|EDP}$ denotes the median and dispersion (logarithmic standard deviation) of the lognormal distribution, and $\Phi(\,)$ represents the standard normal CDF.

According to the shake table test results of the prefabricated steel stairs as presented in Chapter 3, there are four data points associated with DS_3, with the PIDR demands of 0.74%, 1.41%, 2.08%, and 2.64%, respectively. As a result, the median $\theta_{DS|EDP}$ and the dispersion $\beta_{DS|EDP}$ are estimated as 1.5% and 0.6 using the FEMA P58 (2012) methodology. In the experimental studies of Higgins (2009), the two stair specimens constructed using similar structural systems but different connection details never achieved DS_3 throughout the entire cyclic static loading when they attained a maximum IDR of 2.5%. Therefore, a PIDR of 5% associated with DS_3 is assumed in the fragility analysis (Higgins, 2011). The tests results of the two recent experimental studies highlight the uncertainties for the seismic damage analysis of prefabricated steel stairs. As a result, this study considers three median $\theta_{DS|EDP}$ values, corresponding to 1.5%, 2.5%, and 5%, for considering the variability of stair deformability due to the connection details and other uncertainties related to material, welding quality, and etc., while the associated dispersion $\beta_{DS|EDP}$ are all taken as 0.6. The fragility curves for stairs with three different median $\theta_{DS|EDP}$ are shown in Figure 6.20.

6.5.2 Seismic Loss Analysis of Stair Systems

The loss metric of stairs in this study is defined as the quantity of stairs that sustain loss of the vertical load capacity (attainment of severe damage state DS_3) within a building. It is noted that the use of the quantity of damaged stairs as the loss metrics instead of direct monetary loss associated with stair damage is warranted by the following two considerations: 1) data correlating stair damage with their repair costs have been very

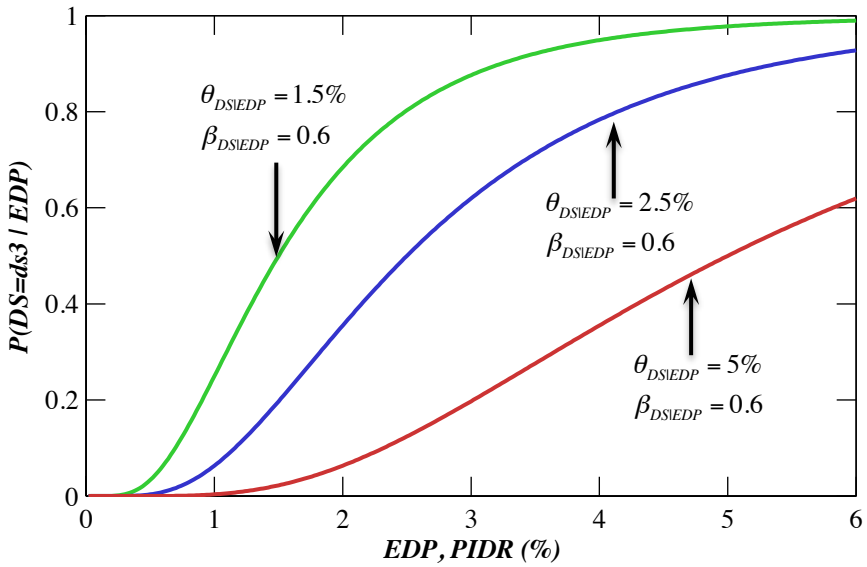

Figure 6.20. Fragility curves of stairs with three median $\theta_{DS|EDP}$ values.

limited in practice, and 2) the implications of stair damage is more related to the loss of building functionality rather than repair cost.

Stair total loss L_T within a building can be calculated as the sum of the stair story loss L_i over all stories:

$$L_T = \sum_{i=1}^{n_{story}} L_i \tag{6.16}$$

where n_{story} denotes the total number of stories of the building. In the presentation of stair loss results, normalized stair loss metrics $\widehat{L_i}$ and $\widehat{L_T}$ are often used, which represents the total stair loss relative to the total number of stairs in the building or the story stair loss relative to the number of stairs per story (2 stairs per story for all prototype buildings).

Analysis Procedure

Although direct numerical integration and first-order second-moment method are available to propagate uncertainties involved in the probabilistic seismic loss analysis framework, these methods are subject to limitations due to the high dimensionality or

potentially inaccurate predictions of the uncertainties. To assess the stair loss in a robust and accurate manner, this study employes a two-stage procedure combining Monte Carlo simulation method with direct numerical integration. The multi-layer Monte Carlo simulation (MCS) method (Conte, 2015) is employed in the first stage to estimate conditional stair loss metrics given IM. Loss metrics of interest include the conditional mean and standard deviation of stair total loss (e.g., $E[L_T|IM = im]$, $E[L_i|IM = im]$) as well as the conditional probability of stair total loss achieving or exceeding a specific value ($P(L_T \geq z|IM = im)$). In the second stage, the conditional loss metrics are numerically integrated with the corresponding seismic hazard curve to obtain the unconditional loss metrics (e.g., $E[L_T]$, $E[L_i]$, and $P(L_T \geq z)$).

According to total probability theorem, the conditional stair loss given IM can be attributed to two mutually exclusive and collectively exhaustive events, namely, building collapse (C) and non-collapse (NC). In the case of building collapse, it is assumed that damage of the entire building systems is beyond repair, and therefore the building including its contents needs demolition. The stair total loss L_T due to building collapse is consequently defined as the total number of stairs in the building, which is independent of IM. In the case of non-collapse, the stair total loss L_T is determined by conducting seismic damage analysis for each individual stairs within the building. In this regard, the conditional mean $E[L_T|IM = im]$ and and standard deviation $\sigma_{L_T|IM=im}$ are simply the sum of the collapse and non-collapse conditional mean or standard deviation weighted by their respective probabilities of occurrence:

$$\begin{aligned}\mathrm{E}[L_T|IM = im] = \mathrm{E}[L_T|NC \cap IM = im]\,\mathrm{P}(NC|IM = im) + \\ \mathrm{E}[L_T|C \cap IM = im]\,\mathrm{P}(C|IM = im)\end{aligned} \quad (6.17)$$

$$\sigma_{L_T|IM=im} = \sigma_{L_T|NC\cap IM=im}\,\mathrm{P}(NC|IM = im) + \sigma_{L_T|C\cap IM=im}\,\mathrm{P}(C|IM = im) \quad (6.18)$$

where $\mathrm{E}[L_T|NC \cap IM = im]$ and $\sigma_{L_T|NC\cap IM=im}$ denote the conditional mean and standard

deviation of the stair total loss provided that building collapse does not occur at the given IM, and $\mathrm{E}[L_T|C \cap IM = im]$ and $\sigma_{L_T|C\cap IM=im}$ denote the conditional mean and standard deviation of the stair total loss due to building collapse. As the stair total loss is defined as the total number of stairs in the building in the case of building collapse, $\mathrm{E}[L_T|C \cap IM = im] = \mathrm{E}[L_T|C] = n^t_{stair}$ and $\sigma_{L_T|C\cap IM=im} = \sigma_{L_T|C} = 0$. In the case of building non-collapse, $\sigma_{L_T|NC\cap IM=im}$ are determined using the "mean square" minus "squared mean" rule:

$$\sigma^2_{L_T|NC\cap IM=im} = \mathrm{E}[L^2_T|NC \cap IM = im] - (\mathrm{E}[L_T|NC \cap IM = im])^2 \tag{6.19}$$

Similarly, the conditional probability of stair total loss achieving or exceeding a given value z can be calculated as:

$$\begin{aligned}\mathrm{P}(L_T \geq z|IM = im) = \mathrm{P}(L_T \geq z|NC \cap IM = im)\,\mathrm{P}(NC|IM = im) + \\ \mathrm{P}(L_T \geq z|C \cap IM = im)\,\mathrm{P}(C|IM = im)\end{aligned} \tag{6.20}$$

where z is a percentile number that denotes the total stair loss relative to the total number of stairs in the building. Since the total stair loss is defined as the total number of stairs (n^t_{stair}) in the building in the case of building collapse, $\mathrm{P}(L_T \geq z|C \cap IM = im)$ is always equal to 1.

In the second stage, the conditional loss metrics obtained using the MCS method are numerically integrated with the corresponding seismic hazard curve to obtain the unconditional stair loss metrics. The mean annual loss (MAL) of stairs $\mathrm{E}[L_T]$ and the MAR of stair total loss achieving or exceeding a value $\lambda_{L_T}(z)$ (also referred to as loss hazard curve) can be calculated as:

$$\mathrm{E}[L_T] = \int_0^\infty \mathrm{E}[L_T|IM = im] \left|\frac{\mathrm{d}\lambda_{IM}(im)}{\mathrm{d}im}\right| \mathrm{d}im \tag{6.21}$$

$$\lambda_{L_T}(z) = \int_0^{\infty} P(L_T \geq z | IM = im) \left| \frac{\mathrm{d}\lambda_{IM}(im)}{\mathrm{d}im} \right| \mathrm{d}im \tag{6.22}$$

Assuming that the occurrence of earthquakes follows the Poisson's occurrence model, the MAR of stair total loss achieving or exceeding a value $\lambda_{L_T}(z)$ can be transformed to the probability $\mathrm{P}(L_T \geq z)$ at a given exposure time T. Therefore, the probability of no stair loss at the given exposure time T can be calculated as:

$$\mathrm{P}(L_T = 0) = 1 - P(L_T \geq 1) = 1 - (1 - e^{-\lambda_{L_T}(1)T}) = e^{-\lambda_{L_T}(1)T} \tag{6.23}$$

Multi-layer Monte Carlo Simulation

As discussed previously, multi-layer Monte Carlo simulation is employed to estimate the conditional stair loss metrics given *IM* (e.g., $\mathrm{E}[L_i|IM]$, $\mathrm{E}[L_T|IM]$, and $\mathrm{P}(L_T > z|IM = im)$) by "collapsing out" the intermediate conditional distributions (i.e., $f_{L|DM}$, $f_{DM|EDP}$, $f_{EDP|IM}$) involved in the probabilistic loss analysis. The objective of the Monte Carlo simulation is to sample the conditional distributions of L_T and L_T at a given sequence of *IM*s. The conditional loss metrics ($\mathrm{E}[L_i|IM]$, $\mathrm{E}[L_T|IM]$, and $\mathrm{P}(L_T > z|IM = im)$) are then statistically quantified using the samples generated using the Monte Carlo method. The step-by-step algorithm of the multi-layer Monte Carlo simulation is presented in Figure 6.21.

Loss Deaggregation Analysis

Since the aforementioned loss metrics are computed using integrations or summations as proposed in the loss analysis procedure, results contained in the intermediate steps can be used for efficient loss deaggregation analyses. These results is capable of identifying the dominant contributor for a specific loss metric and are therefore highly useful to support decision making. The stair loss metrics (e.g., the expected loss and the MAR of exceedance of stair loss), can be deaggregated into the contributions of building collapse and non-collapse, contributions of different stories, and the contributions of earthquake with different *IM* levels. These deaggregation results are presented in the following section.

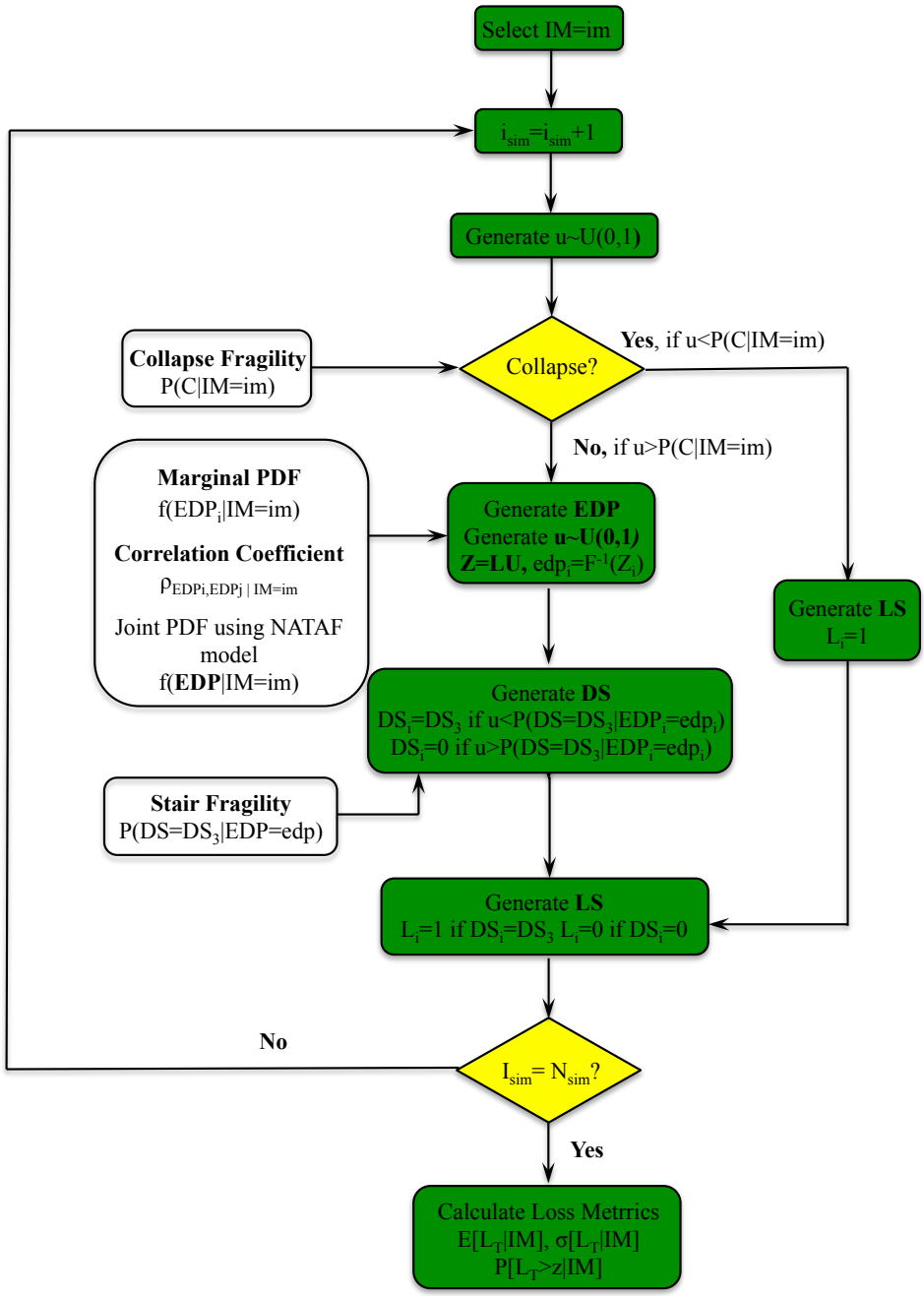

Figure 6.21. Multi-layer Monte Carlo simulation procedure for seismic loss analysis of stair systems.

6.5.3 Stair Loss Results

Stair Loss Metrics Conditioned on Intensity Measures

To illustrates the conditional stair loss metrics obtained using the MCS method, building S-4 (coupled system with $\Omega_{stair} = 1$ and $IDR_{damage} = 2.5\%$ – hereafter referred to as the baseline stair systems in this study). Figure 6.22 presents the normalized conditional mean of stair loss at each story $E[\widehat{L_i}|IM]$ of the baseline system, which represents the conditional mean of the stair loss per story relative to the number of stairs per story (2 stairs per story). Since the stair loss given IM is an accumulation of loss due to building collapse and non-collapse cases (Equation 6.17), deaggregation of $E[L_i|IM]$ into the contribution of building collapse and non-collapse cases are also presented in the fig-

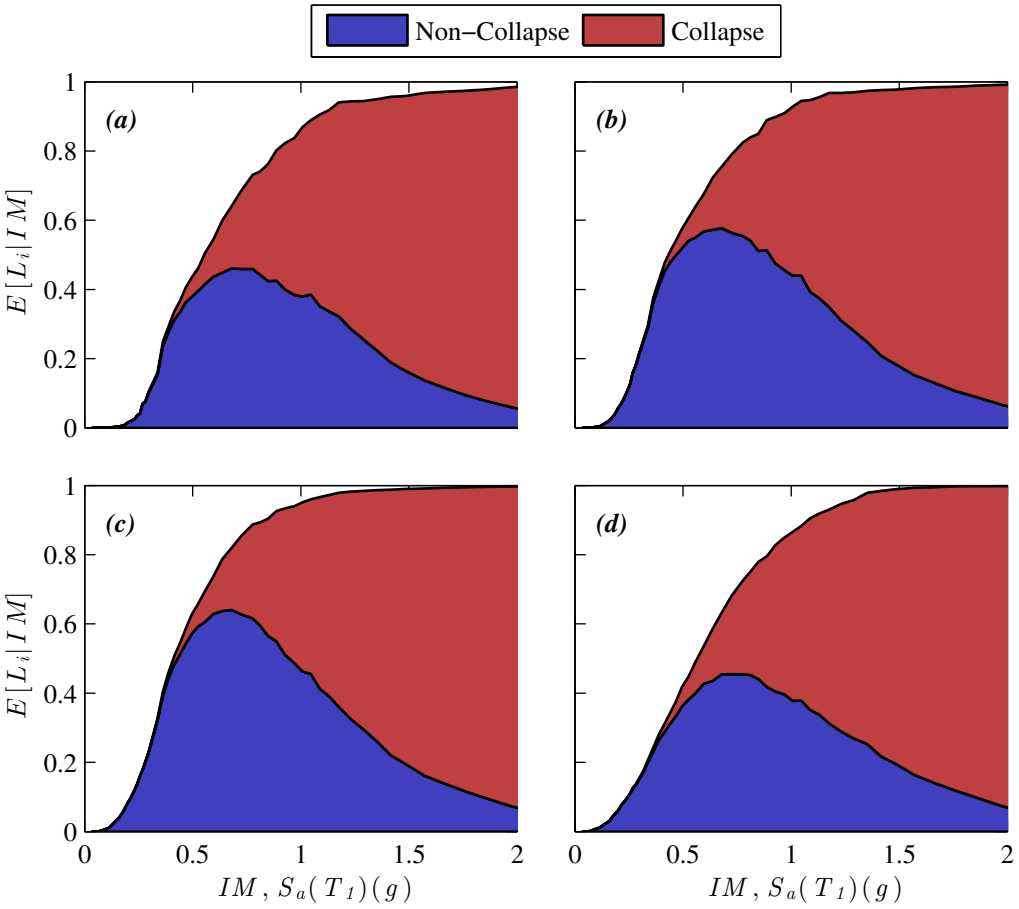

Figure 6.22. Conditional mean of the loss of stairs $E[L_i|IM]$ at each story of building S-4: (a) first story, (b) second story, (c) third story, and (d) fourth story.

ures. At low *IM* levels (*IM* < 0.4 g), the conditional mean values of the stair loss at each story is almost entirely the contribution of the stair damage in the absence of building collapse. The contribution due to building non-collapse to the stair loss continue to increase until the *IM* achieves around 0.8 g (corresponding to IM_{2475} level). As the *IM* exceeds 0.8 g, the contribution of the building collapse to the stair loss at each story increases rapidly and becomes the dominant factor for the stair loss as a result of the increase of the building collapse probability at the associated *IM* level.

Figure 6.23 shows the conditional mean of the total stair loss $E[L_T|IM]$ of building S-4 (with baseline stair systems), and the conditional standard deviation of total stair loss $\sigma_{L_T|IM}$ is shown in Figure 6.24. It is noted that $E[L_T|IM]$ and $\sigma_{L_T|IM}$ represent the conditional mean and standard deviation of the stair total loss relative to the total number of stairs within the building (8 stairs in building S-4). As shown in Figure 6.23, the deaggregation results of the conditional mean of the stair loss $E[L_T|IM]$ for building collapse and non-collapse cases is similar to those of the stair story loss $E[L_i|IM]$. At the *IM* value of about 0.4 g (corresponding to IM_{475} level), the conditional mean of the total stair loss achieves about 40% of the total number of stairs, which is almost exclusively attributed to damage of individual stairs in the case of building non-collapse. At the *IM* value of about 0.8 g (corresponding to IM_{2475} level), the conditional mean of the total stair loss achieves about 80% of the total number of stairs. The deaggregation of the conditional mean of the total stair loss indicates that 50% of the stair loss are due to stair damage in the case of building non-collapse and the remaining 30% due to building collapse. At very high *IM* level (>1.0 g), the contribution of building collapse to the total stair loss increases rapidly as a result of increasing building collapse probability and becomes the dominant effect that its contribution exceeds more 50% of the total number of stairs within the building. The conditional standard deviation of stair total loss $\sigma_{L_T|IM}$, as shown in Figure 6.24, increases monotonically until it achieves the largest value (30% of the total number of stairs in the building) at an *IM* value range of 0.4 g and 0.8 g. Subsequently, the conditional standard deviation decreases monotonically as the contribution of building collapse becomes more significant (*IM* >0.8 g). This is due to the fact that the stair loss in the case of building collapse is a constant (the total

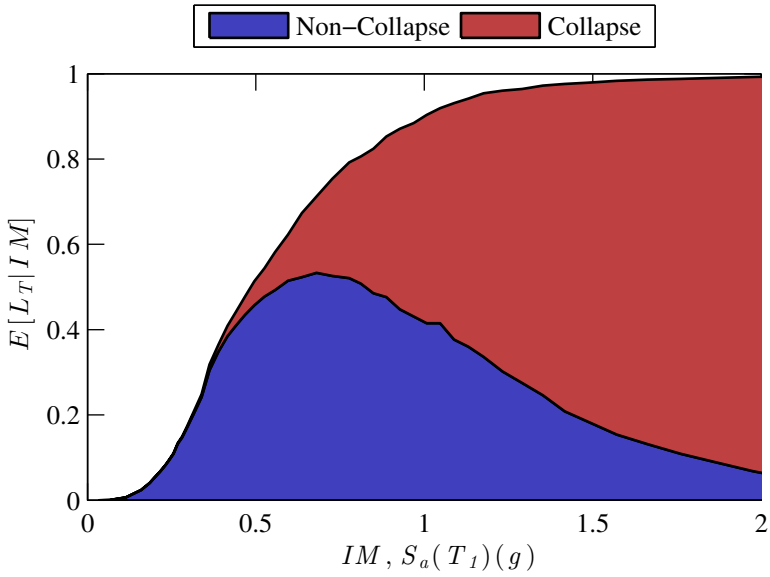

Figure 6.23. Conditional mean of the total stair loss $E[L_T|IM]$ of building S-4.

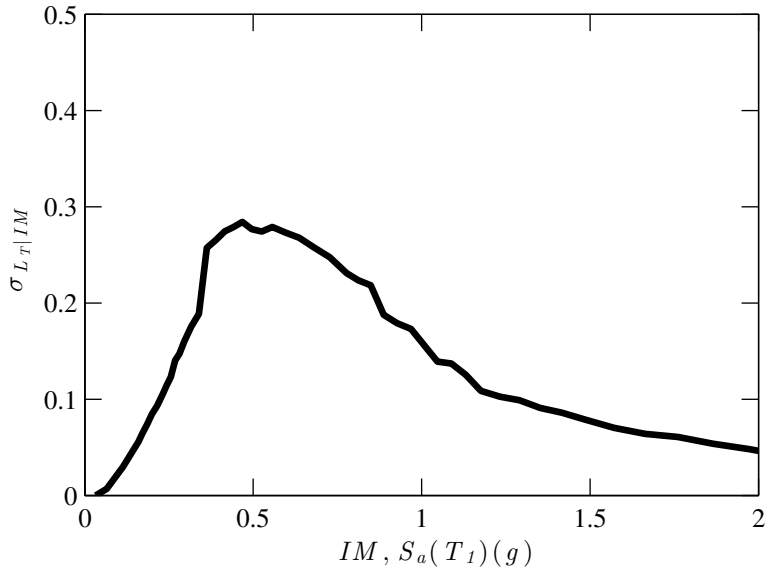

Figure 6.24. Conditional standard deviation of the total stair loss $\sigma_{L_T|IM}$ of building S-4.

number of stairs within the building), thereby reducing the variability of the stair loss at high *IM* levels.

In addition to the conditional mean and standard deviation of stair total loss, the conditional probability of the stair total loss achieving or exceeding a specific value z is a loss measure commonly used in seismic loss assessment. Figure 6.25 shows the conditional probability of $P(L_T \geq z|IM)$ of the total stair loss of building S-4 (with baseline stair systems) achieving or exceeding four different threshold values (25%, 50%, 75%, and 100%). As shown in the figure, the probability of no less than half of the stairs in the building fails at the *IM* of about 0.4 g (corresponding to IM_{475} level) is about 0.6, while the probability of loss of all stairs in the building is very low (less than 0.1). As the *IM* increases to about 0.8 g (corresponding to IM_{2475} level), the probability that stair loss is no less than half of the stairs in the building rises to a very high value of 0.9, and the probability of the failure of all stairs increases to 0.4.

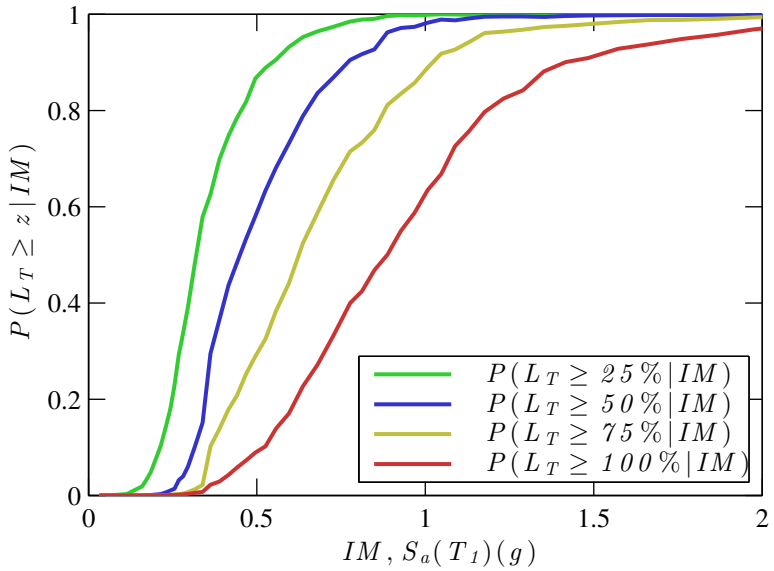

Figure 6.25. Conditional probability of the stair total loss achieving or exceeding a specific value for building S-4.

Deaggregation of Conditional Mean Stair Total Loss at Different Stories

Since the conditional mean of stair total loss $E[L_T|IM]$ of a building can be cal-

culated as the summation of $E[L_i|IM]$ over all stories of the building, $E[L_T|IM]$ can be deaggregated into the percentile contributions of stair loss at different stories. Figure 6.26 shows the deaggregation of the conditional mean of total stair loss $E[L_T|IM]$ of the three prototype buildings (with baseline stair systems) into story contributions. Regardless of specific prototype building, the building upper stories accounts for the majority of total stair loss at the low *IM* level (IM_{43}). This is due to the fact that while the mean of PIDRs at upper stories may be slightly lower than those of the lower stories, the PIDRs at upper stories are subjected to higher variability (larger dispersion) due to the higher mode effects (Figure 6.17). As the *IM* increases to a higher level (IM_{475}), the buildings undergo inelastic deformation at the lower stories of the buildings, which resulted in the formation of story mechanism. As a result, the higher contributions of the stair loss are associated with the lower stories instead of the higher stories. As the *IM* further increases to IM_{2475} level, the contributions of stair loss at different stories become more evenly distributed along the building height, although the contributions remain similar to those at the IM_{475} level. This is attributed to the fact that the stair loss achieves the maximum value at most of the stories due to larger PIDR demands of the buildings associated with this *IM* level, since the conditional mean of the total loss attains 60%–80% of the total stair number of the buildings.

Effect of Stair Variables on Conditional Stair Loss Metrics

Figure 6.27 illustrates the effects of the stair variables on the conditional mean of stair total loss $E[L_T|IM]$ of all prototype buildings. It is noted that the figures on the left column compare the effects of stair strength amplification factor (Ω_{stair}=1, 4, and 8) on the conditional mean of the total stair loss, while the figures on the right column compares those due to the stair ultimate deformability (IDR_{damage}=1.5%, 2.5%, and 5%). Likewise, Figure 6.28 illustrates the effects of these two sets of stair variables on the conditional standard deviation of the total stair loss $\sigma_{L_T|IM}$. As clearly shown in Figures 6.27–6.28, the variation of stair response amplification factor Ω_{stair} only slightly affects the total stair loss, since both the conditional mean and standard deviation of the total stair loss remain highly similar irrespective of Ω_{stair}. In contrast, the total stair loss differs pronouncedly with by varying the stair ultimate deformability (IDR_{damage}) val-

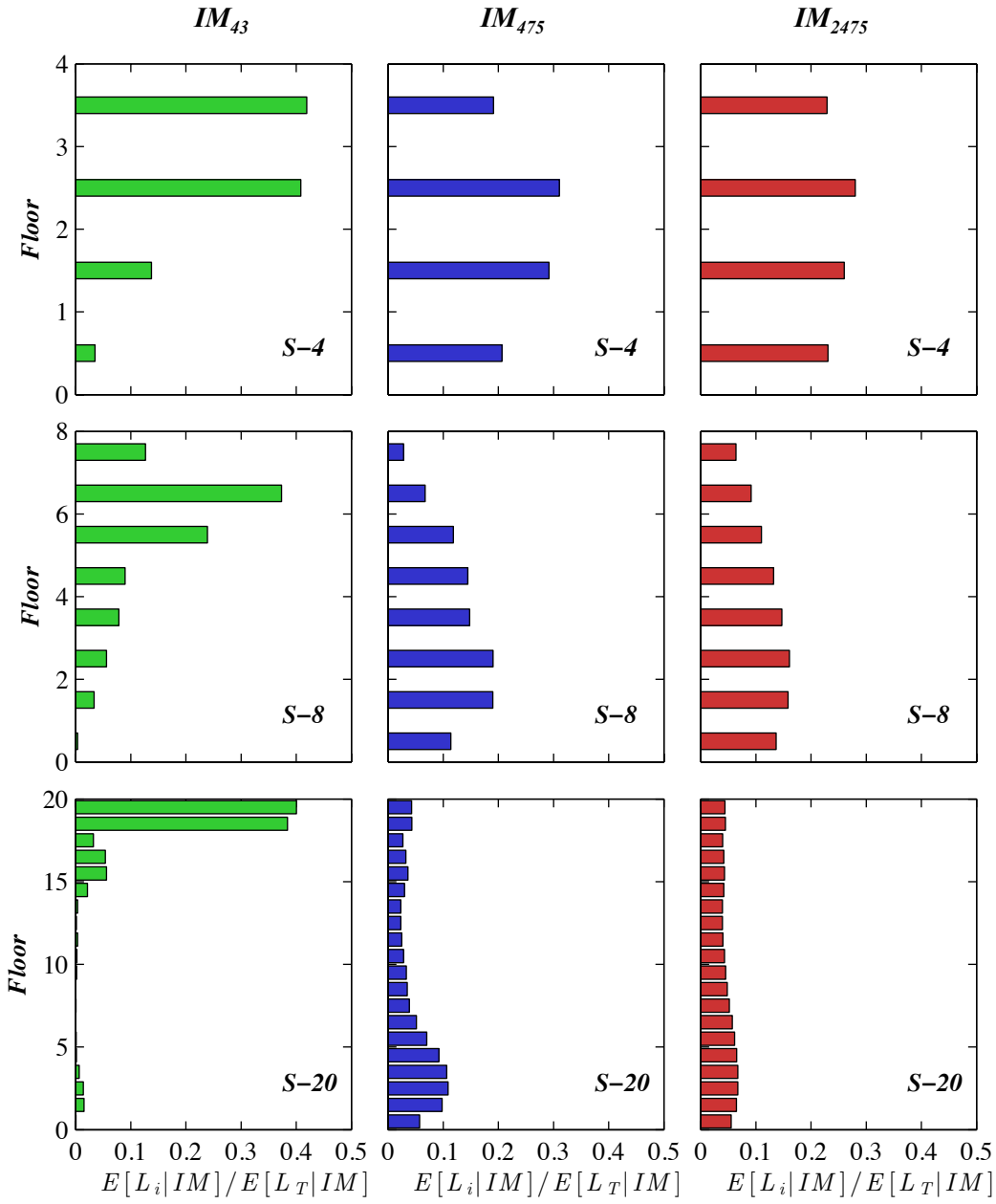

Figure 6.26. Deaggreation of conditional mean of the total stair loss $E[L_T|IM]$ into story contributions $E[L_i|IM]$ at the three representative *IM* levels.

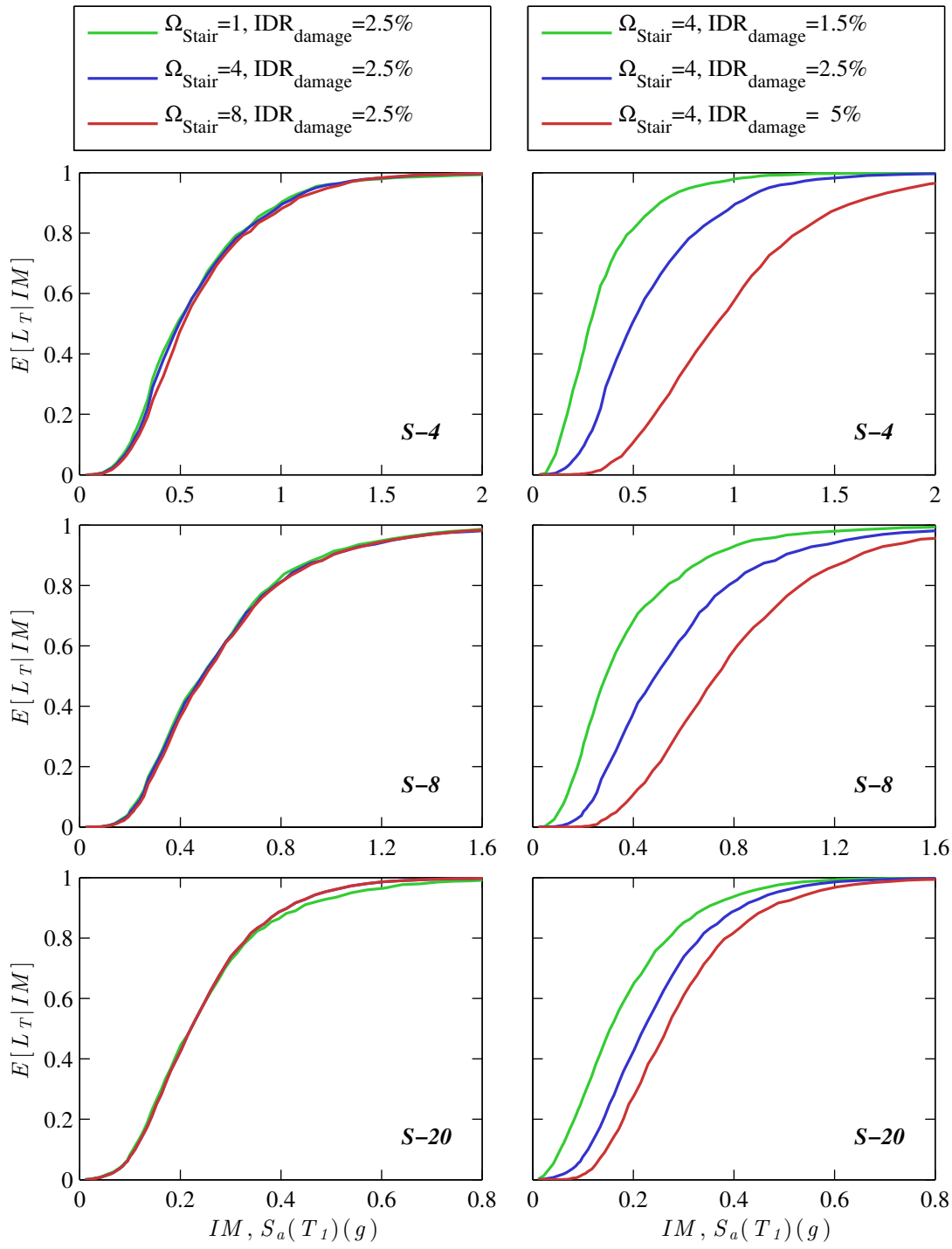

Figure 6.27. Variation of stair variables Ω_{stair} and IDR_{damage} on conditional mean of the total stair loss $E[L_T|IM]$.

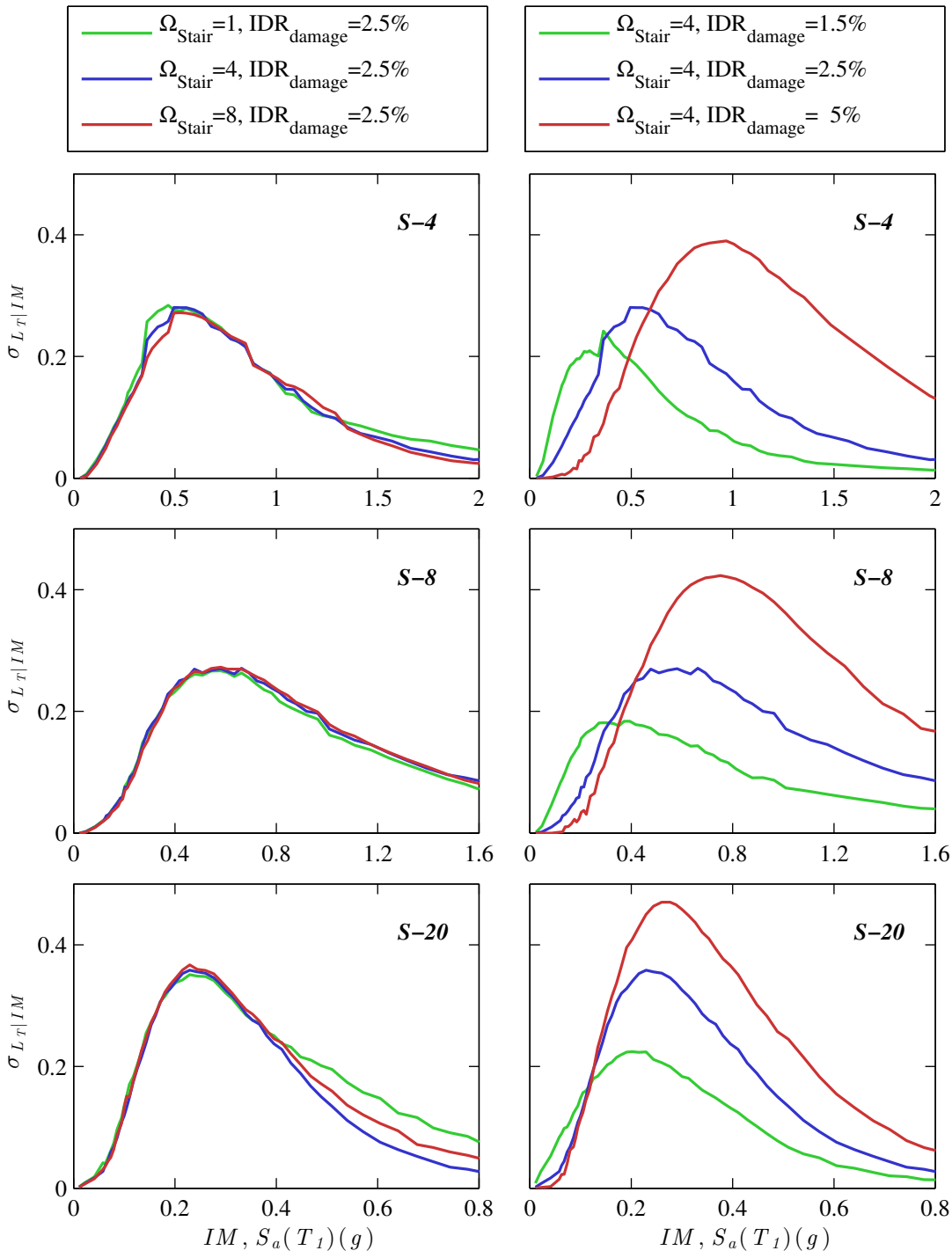

Figure 6.28. Variation of stair variables Ω_{stair} and IDR_{damage} on conditional standard deviation of the total stair loss $\sigma_{L_T|IM}$.

ues. It is shown in the figures that higher IDR_{damage} leads to smaller conditional mean values of the total stair loss at a specific *IM* (Figure 6.27) but larger conditional standard deviations (variability) (Figure 6.28).

Figure 6.29 compares the conditional mean of the stair total loss $E[L_T|IM]$ of the three prototype buildings at the three representative *IM* levels due to the stair effects. The results presented in each plot represent the conditional mean of the stair total loss $E[L_T|IM]$ of different prototype buildings with identical stair variables (Ω_{stair} and IDR_{damage}). Regardless of prototype buildings and *IM* levels, the variation of stair response amplification factor Ω_{stair} only slightly modifies the conditional mean of the total stair loss. For stairs with identical IDR_{damage} (2.5%) but different Ω_{stair} values (the second row of the figure), the conditional mean of the total stair loss of the three prototype buildings range between 20% and 40% at the IM_{475} level and between 60% and 80% at the IM_{2475} level. In contrast, the conditional mean differs significantly with varied stair ultimate deformability (IDR_{damage}) values. For stairs with identical Ω_{stair} of 1 but different IDR_{damage} values (the first column of the figure), the conditional mean at the IM_{475} level ranges between between 60% and 80% in the case of IDR_{damage}=1.5%, however the values drop to less than 10% in the case of IDR_{damage}=5%. This indicates that increasing IDR_{damage} value of the stair systems effectively reduces the seismic stair loss.

Unconditional Stair Loss Metric and Result Deaggregation

Similar to the building collapse MAR calculation, the unconditional stair loss metrics are obtained by integrating the conditional stair loss metrics with their respective seismic hazard curves. These loss performance indices are also calculated using the MAQ algorithm (Bradley et al., 2009). To identify the dominate contributing effects on stair loss, these results are then deaggregated into building story contributions or contributions for earthquake at different *IM* levels.

Figure 6.30 illustrates the steps for calculationg the stair MAL in building S-4 (with baseline stair systems). The conditional mean of total stair loss $\mathrm{E}[L_T|IM = im]$ and the slope (first derivative) of the seismic hazard curve $|\mathrm{d}\lambda_{IM}(x)/\mathrm{d}x|$ are shown separately

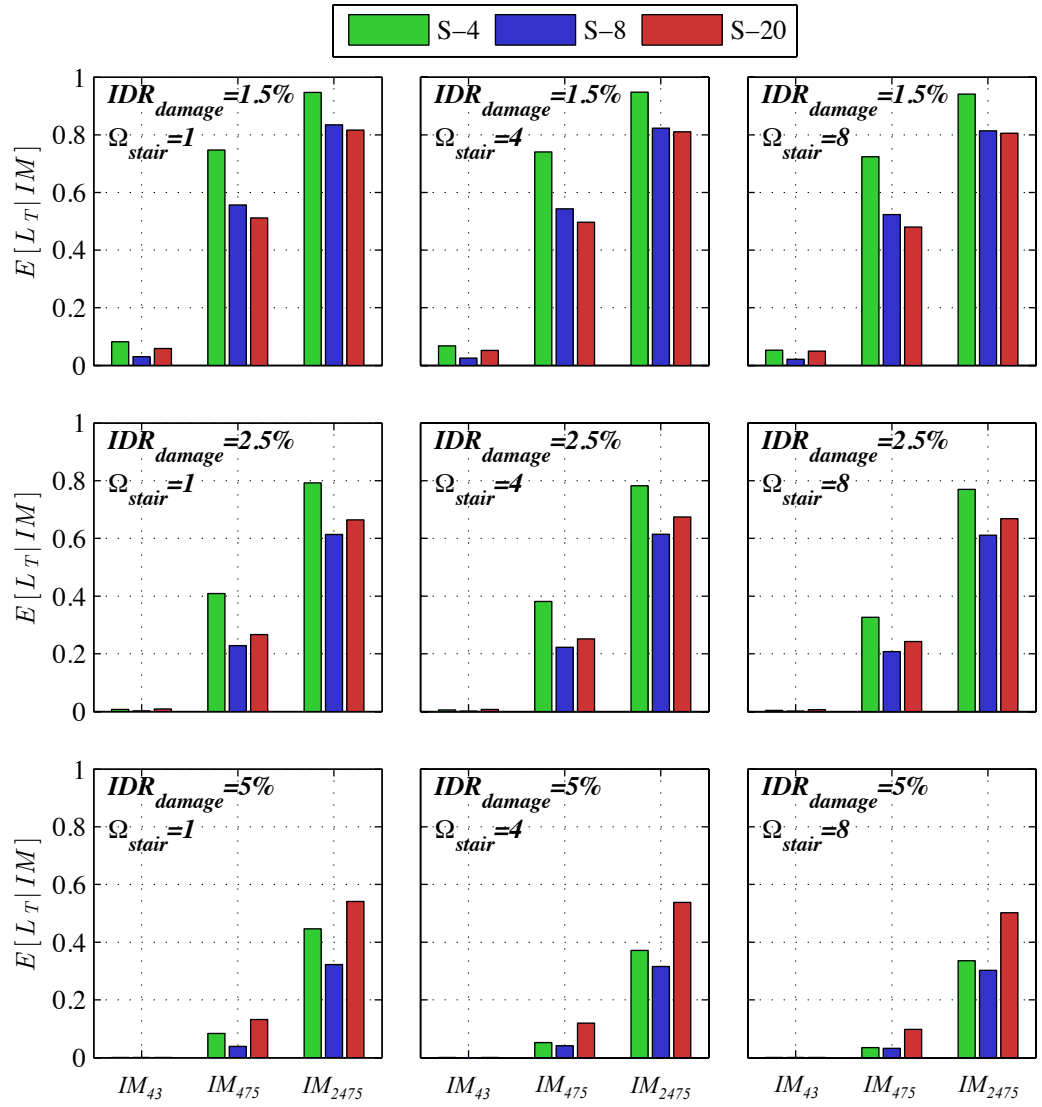

Figure 6.29. Comparison of conditional mean of the stair total loss $E[L_T|IM]$ of the three prototype buildings at the three representative *IM* levels.

in Figures 6.30a–b, respectively. The resultant integrand $\mathrm{P}(C|IM = x)|\mathrm{d}\lambda_{IM}(x)/\mathrm{d}x|$ is shown in Figure 6.30c. Following the transformation from x domain into t domain, the resultant integrand is numerically evaluated using the MAQ algorithm, and the integration point distribution is shown in Figures 6.30d. As shown in the figure, the total MAL of stairs is calculated as 0.0255, indicating that an average of 0.3% of stair loss in the building per annum. It is important to note that the curve as shown in Figures 6.30c represents the deaggregation of the stair MAL into the contributions of earthquakes with different seismic *IM* levels. As shown in the figure, the majority of MAL is attributed to earthquakes with *IM* between 0.3 and 0.5 g, which correspond to IM_{475} level. This is due to the fact that earthquakes within this *IM* range, although causing less significant stair loss than earthquakes with larger *IM*s, occur much more frequently than those high *IM* earthquakes.

Table 6.4 compares the unnormalized MAL $\mathrm{E}[L_T]$ and normalized MAL $\mathrm{E}[\widehat{L_T}]$ of the stairs in three prototype buildings with baseline stair systems. As shown in the table, building S-20 has the highest estimated value of unnormalized MAL among the three prototype buildings, which is about 3-4 times as much as those of buildings S-4 and S-8. When normalized by the total number of stairs in the buildings, building S-4 has the highest MAL (0.32%), which is about twice as high as those of buildings S-8 (0.16%) and S-20 (0.19%). This is possibly due to the fact that the story mechanism spans over the lower three stories of building S-4, while the effect of story mechanism becomes much more localized for buildings with more stories.

Since stair total MAL $E[L_T]$ can be calculated as the sum of $E[L_i]$ over every story of a building, $E[L_i]/E[L_T]$ represents the percentile contributions of stair MAL at different stories. Figure 6.31 shows the deaggregation of the stair total MAL $E[L_T]$ of building S-4 (with baseline stair systems) into the story contributions. As seen in this figures, the story contributions of stair loss for the buildings are highly correlated with their respective PIDR distributions (Figure 6.17). It is noted that building S-20 has the highest concentration of stair loss at the upper stories, while the majority of stair loss for buildings S-4 and S-8 are located at the lower stories. This is due to the fact that the

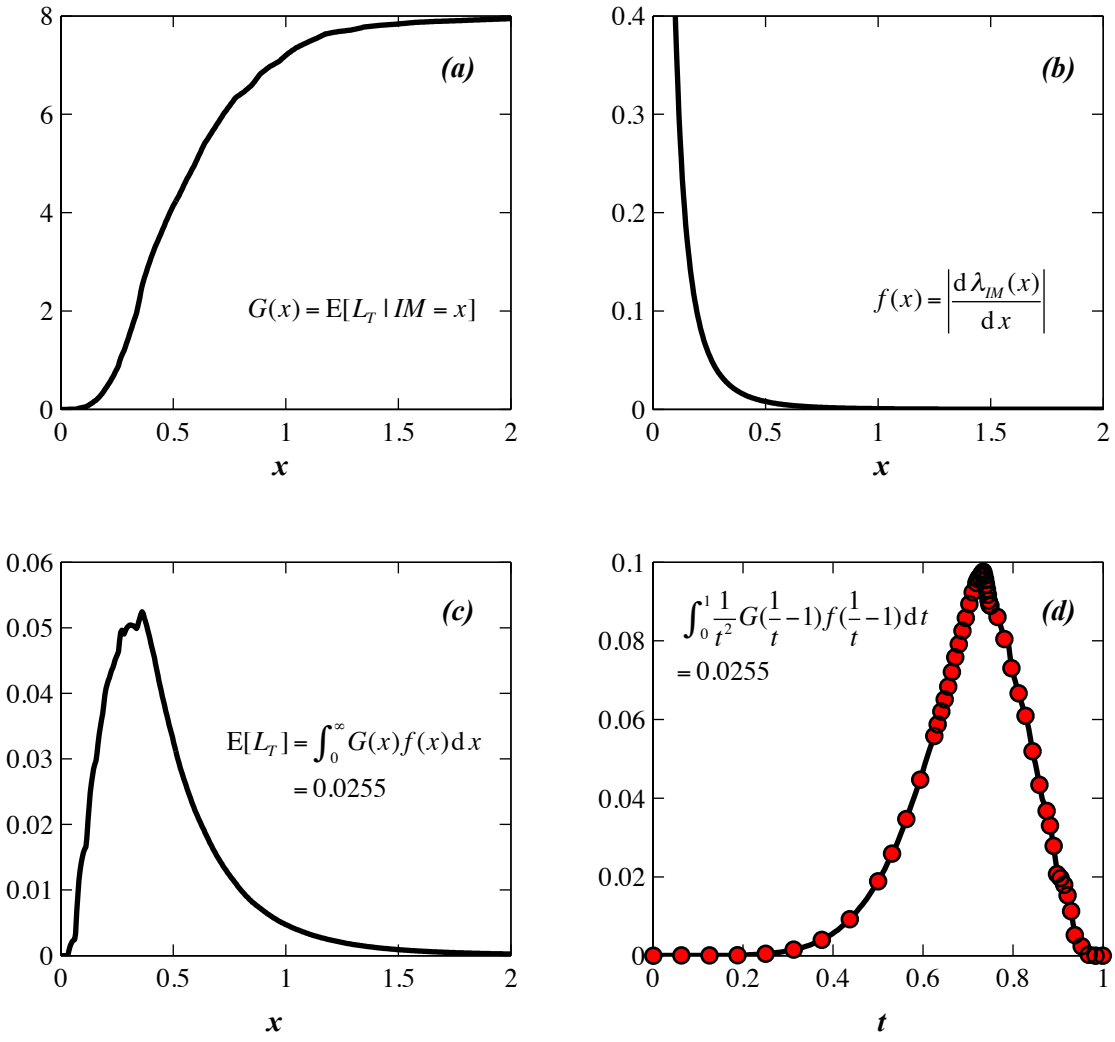

Figure 6.30. Evaluation the stair total MAL using the MAQ algorithm: (a) $G(x)$ in x domain (conditional mean of total stair loss $\mathrm{E}[L_T|IM = im]$), (b) $f(x)$ in x domain (slope of seismic hazard curve), (c) resultant integrand in x domain (Equation 6.21), and (d) resultant integrand in t domain and the integration point distribution.

Table 6.4. Mean stair loss in 50 years for the steel buildings

S-4		S-8		S-20	
$\mathrm{E}[L_T]$	$\mathrm{E}[\hat{L}_T]$ (%)	$\mathrm{E}[L_T]$	$\mathrm{E}[\hat{L}_T]$ (%)	$\mathrm{E}[L_T]$	$\mathrm{E}[\hat{L}_T]$ (%)
0.026	0.32	0.025	0.16	0.086	0.19

upper stories of building S-20 accounts for the majority of total stair loss at the low *IM* level (IM_{43} level), and therefore modifies the unconditional story loss distribution along the height of the building.

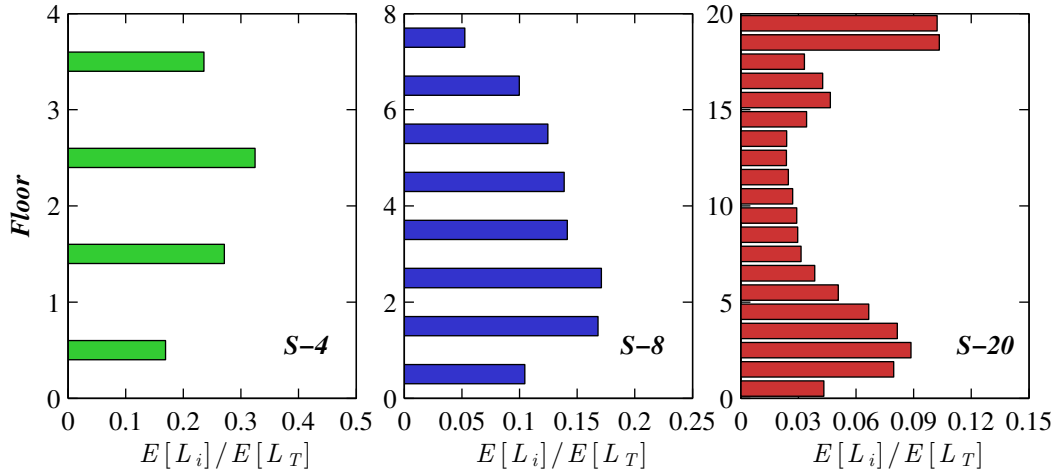

Figure 6.31. Deaggreation of stair MAL $E[L_T]$ into contributions at different stories $E[L_i]$.

In addition to MAL, seismic loss hazard curves are a useful loss performance measure. The loss hazard curve provides the MAR of seismic loss achieving or exceeding various specified loss levels. Figure 6.32 illustrates the loss hazard curve of the stairs in building S-4 (with baseline stair systems). It is noted that the specified loss level z in the figure represents the normalized stair loss relative to the total number of stairs in the building. Since the stair loss metric is defined as the number of damaged stairs in the building, the loss curves is a non-continuous function consisting of a set of discrete data points. As shown in the figure, the respective MARs of exceedance of the three data points (corresponds to a percentile stair loss of 25%, 50%, and 100%, respectively) is 5.0×10^{-3}, 2.0×10^{-3}, and 6.0×10^{-4}. Using the Possion's occurrence model assumption, the probability of stair loss achieving or exceeding the three selected loss values at a given exposure time of 50 years are 22%, 11%, and 3%, respectively. In addition, as the MAR of having one or more stair failure is approximately 0.01 as shown in the figure, the probability of no stair loss in 50 years can be computed as $\mathrm{P}(L_T = 0) \approx e^{(-0.01 \times 50)} \approx 60\%$ (Equation 6.23).

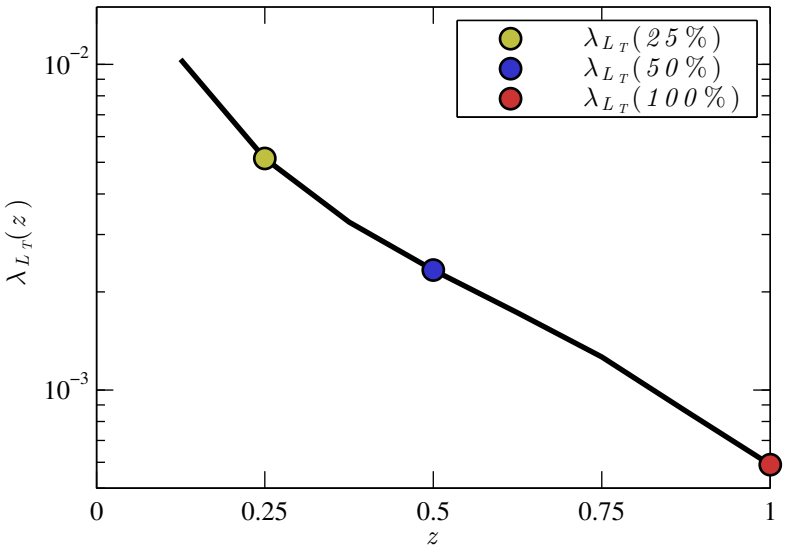

Figure 6.32. Stair loss hazard curve $\lambda_{L_T}(z)$ of building S-4.

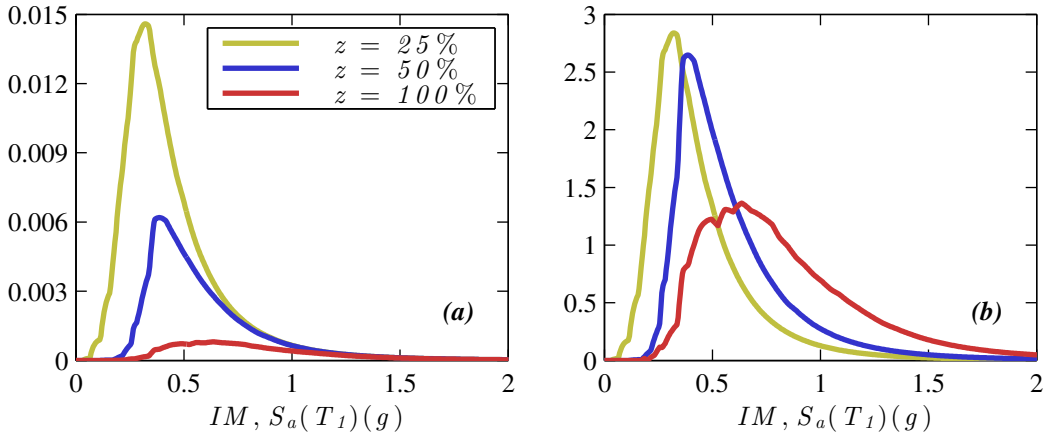

Figure 6.33. Deaggregation of MAR of stair total loss in building S-4 achieving or exceeding corresponding to the three specified values (25%, 50%, and 100%) into contributions associated with different *IM* levels: (a) original MAR of exceedance, and (b) normalized MAR of exceedance.

The MAR of stair total loss achieving or exceeding different specified loss levels can be deaggreated into contributions of earthquakes with different *IM*s. Figure 6.33 shows the deaggregation of the MAR of exceedance of stair loss of building S-4 at the three selected loss levels (corresponds to percentile stair loss of 25%, 50%, and 100%, respectively). While figure 6.33a shows the original MAR of exceedance with respect to *IM*, Figure 6.33b presents the relative contribution of MAR of exceedance by normal-

ized by the corresponding MAR value, indicating that the area underneath each curve is equal to unity. As can be seen in the Figure 6.33b, the dominant *IM* increases at a higher specified loss level. In addition, the peak becomes more flattened and its values becomes smaller at a higher specified loss level, indicating that a wider range of dominate *IM*s contributes similarly to the MAR of exceendance.

Effect of Stair Variables on Unconditional Stair Loss Metrics

Figure 6.34 illustrates the effects of the stair variables on stair loss hazard curves $\lambda_{L_T}(z)$ of all prototype buildings. It is noted that the three figures on the left column show the effects of stair response amplification factor (Ω_{stair} = 1, 4, and 8) on the loss hazard curves, while the three figures on the right column show the effects of stair ultimate deformability (IDR_{damage} =1.5%, 2.5%, and 5%). As clearly shown in the figures, the stair response amplification factor Ω_{stair} only minimally affects the total stair loss hazard curves, while the curves differ significantly with varying stair ultimate deformability IDR_{damage} for all these buildings.

Figure 6.35 compares the stair effects on the probability of the total stair loss achieving or exceeding three selected loss levels, P($L_T \geq 1$), P($\widehat{L_T} \geq 50\%$), and P($\widehat{L_T} \geq 100\%$), respectively, within a given exposure time of 50 years. It is noted that the probability of exceedance for a given loss level is computed from the corresponding MAR of stair loss using Poisson's model. The figures on the left column indicate that stair response amplification factors Ω_{stair} only slightly affect the probability of exceedance at any of the three selected loss levels, since increasing the Ω_{stair} leads to a probability reduction by a maximum of 20%. In contrast, the variation of IDR_{damage} drastically modifies the probability of exceedance at all loss levels. As shown in Figure 6.35d, the probability of stair loss of building S-4 achieving or exceeding 50% (4 stairs) in 50 years is about 0.3 when IDR_{damage} is equal to 1.5%, however the probability drops to 0.1 with a IDR_{damage} of 2.5%. If the IDR_{damage} further increase to 5%, the probability drops to about 0.02%, indicating that it is very unlikely that 4 or more stairs in building S-4 would fail in an exposure time of 50 years. However, as shown in Figure 6.35f, increasing the IDR_{damage} does not effectively reduce the probability of exceedance for the loss level of 100% for

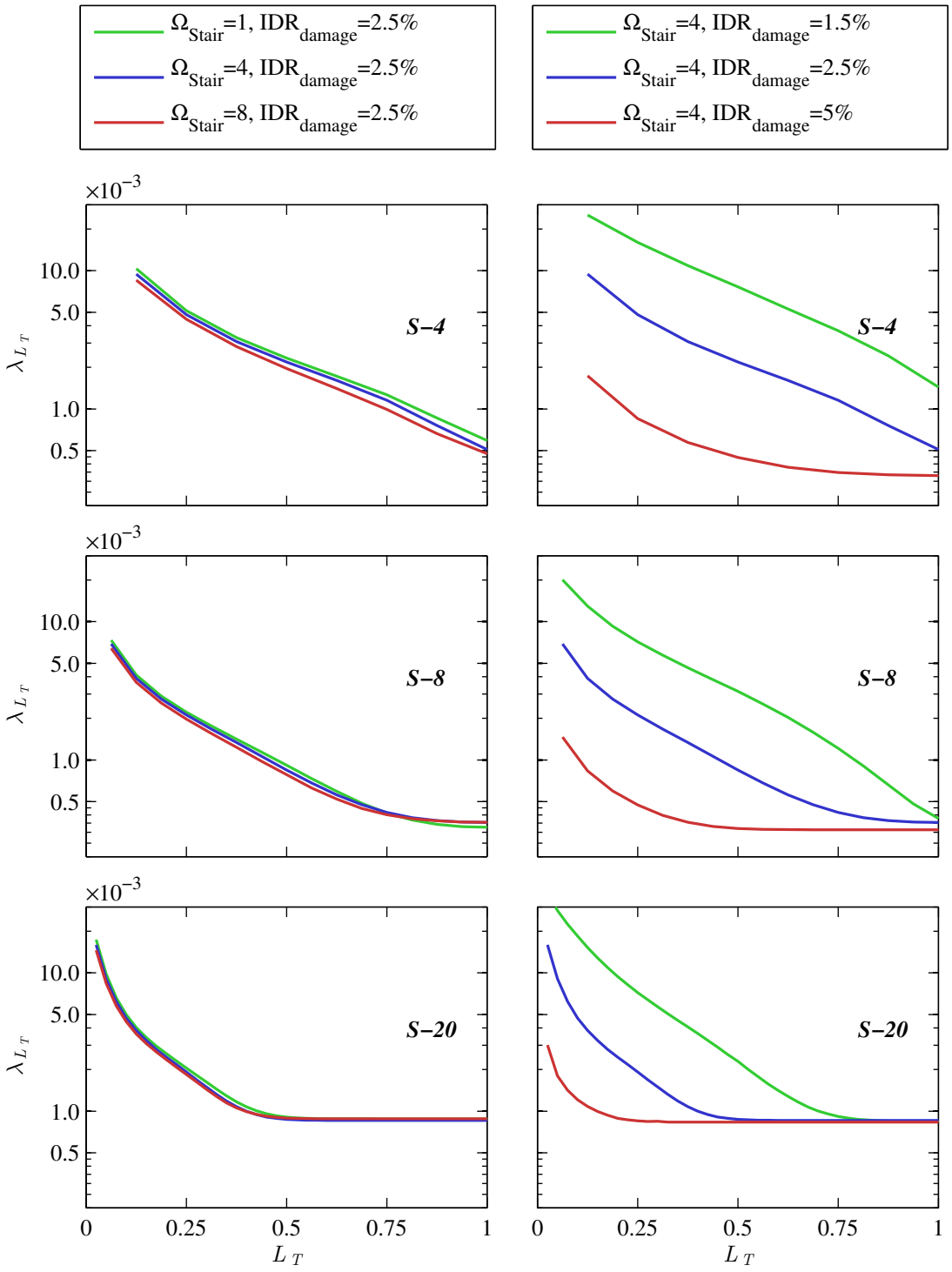

Figure 6.34. Effects of stair variables Ω_{stair} and IDR_{damage} on the total stair loss hazard curves $\lambda_{L_T}(z)$

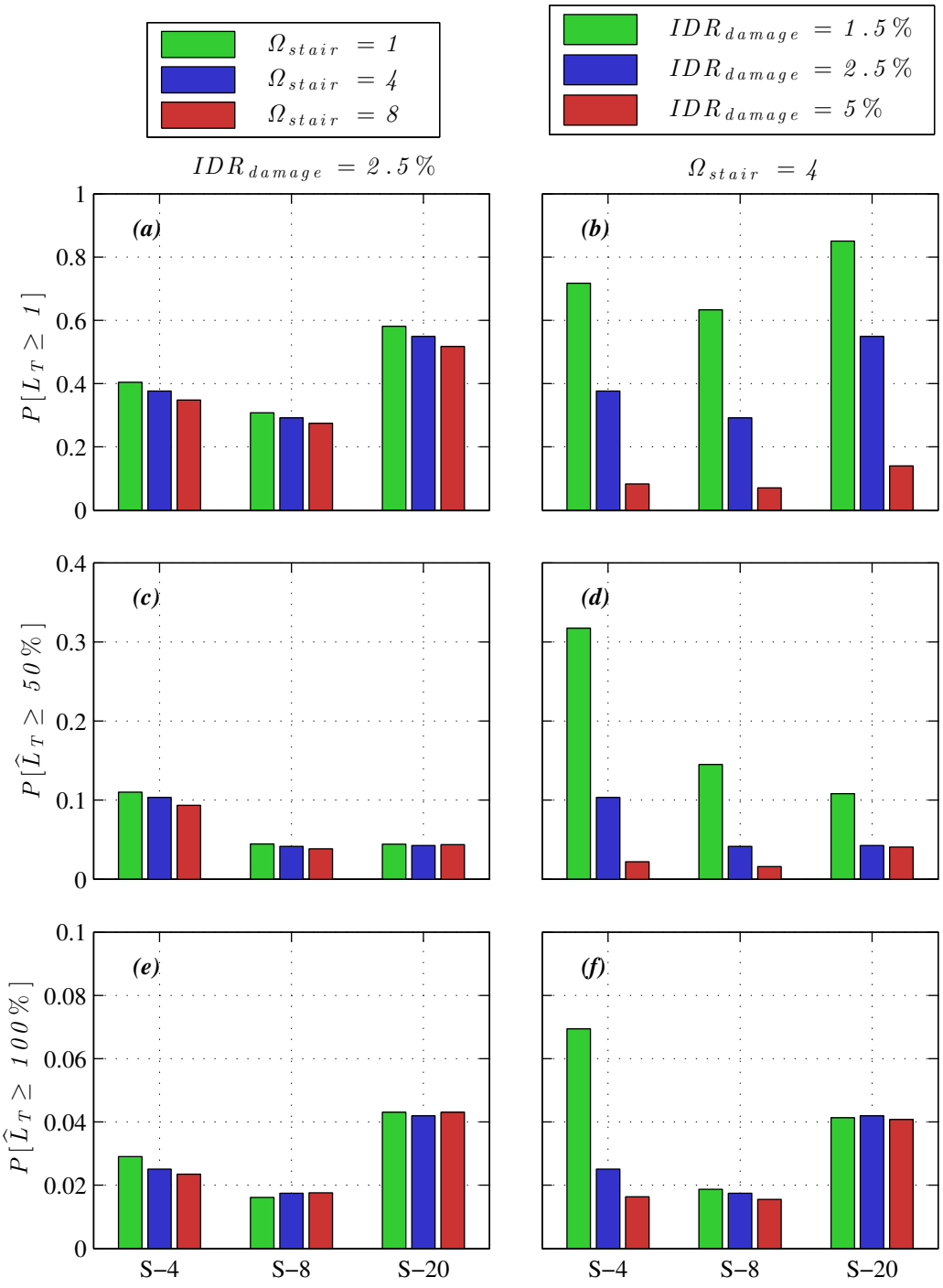

Figure 6.35. Effects of stairs on probability of exceedance of stair loss within a given exposure time of 50 years: (a) effect of Ω_{stair} on P($L_T \geq 1$), and (b) effect of IDR_{damage} on P($L_T \geq 1$), (c) effect of Ω_{stair} on P($\widehat{L}_T \geq 50\%$), and (d) effect of IDR_{damage} on P($\widehat{L}_T \geq 50\%$), (e) effect of Ω_{stair} on P($\widehat{L}_T \geq 100\%$), and (f) effect of IDR_{damage} on P($\widehat{L}_T \geq 100\%$).

buildings S-8 and S-20. This is due to the fact that it is very unlikely to cause 100% stair loss for these two buildings in the case of building non-collapse. Since increasing IDR_{damage} does not significantly reduces the building collapse MAR, the probability of stair loss reaching 100% remain similar regardless of IDR_{damage}.

Figure 6.36 compares the stair effects on the total stair MAL $E[L_T]$ of the three prototype buildings. Similarly, the variation of IDR_{damage} on MAL $E[L_T]$ is much more significant than those of Ω_{stair}. While increasing Ω_{stair} reduces the MAL by as maximum of 10% (Figure 6.36a), the increase of IDR_{damage} from 1.5% to 2.5% reduces the MAL by about 3 times and even more from 2.5% to 5% (Figure 6.36b). Although the effects may not appear significant, the effects of stairs on the MAL reduces when the building has more stories, as a result of increasing stiffness of the structural systems.

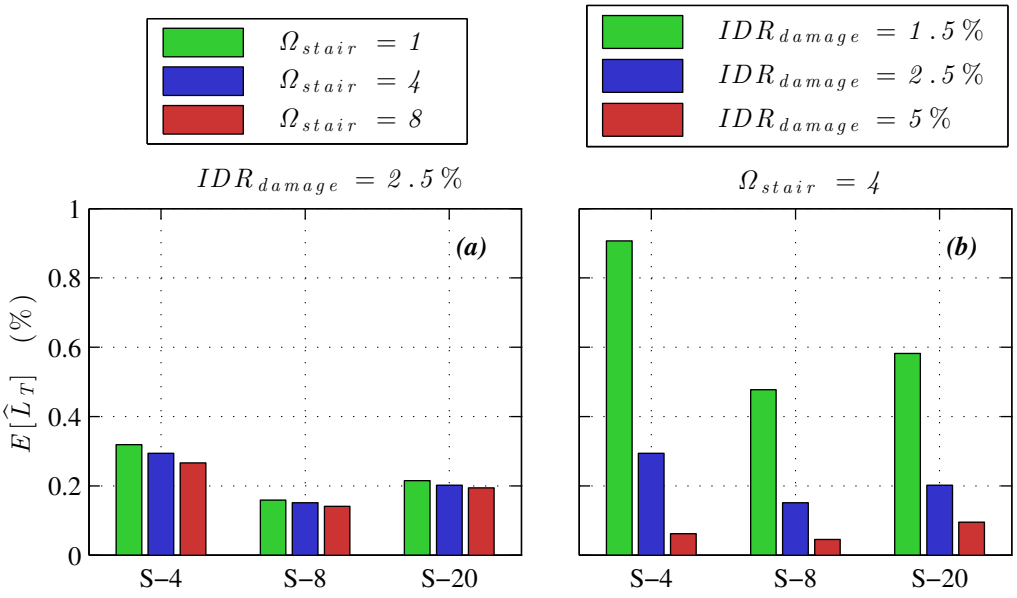

Figure 6.36. Effects of stairs on total stair MAL $E[L_T]$: (a) effect of stair response modification factor Ω_{stair}, and (b) effect of stair ultimate deformation capacity IDR_{damage}.

To demonstrate the dominate contributing effects due to the variation of stair effects, Figure 6.37 shows the deaggregation results of stair total MAL $E[L_T]$ of building S-4 with respect to *IM* levels. It is noted that the MAL deaggregation curves are all normalized such that the area underneath each curve is equal to unity. Since Ω_{stair} only have

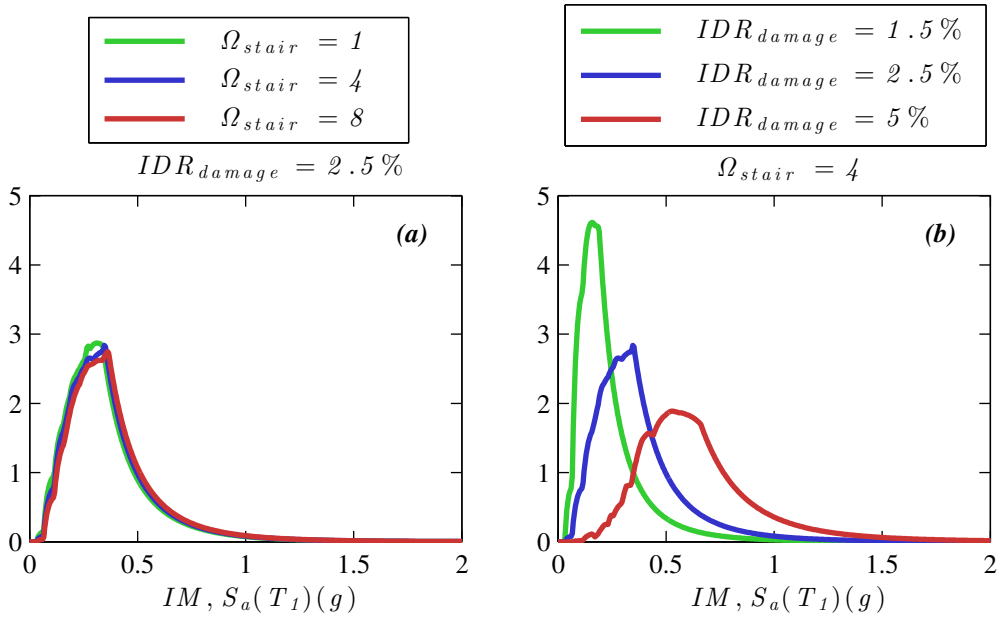

Figure 6.37. Deaggregation of stair total mean annual loss $E[L_T]$ of building S-4 into different *IM* levels (a) effect of stair response modification factor Ω_{stair}, and (b) effect of stair ultimate deformation capacity IDR_{damage}.

limited influence on the MAL $E[L_T]$, the MAR deaggregation curves remain similar to each other for different Ω_{stair} values (Figure 6.37a). In contrast, increasing IDR_{damage} significantly increases the dominant *IM* (associated with the peak) as well as the shape of the deaggregation curves (Figure 6.37b). As shown in the figure, the dominant *IM* is about 0.2 g for an IDR_{damage} = 1.5% but increases to 0.4 g when IDR_{damage} rises to 2.5%. Since earthquakes with an *IM* of 0.4 g (with associated return period of 475) occur much less frequently than a lower *IM* of 0.2 g (with associated return period about 100 years), the stair total MAL decreases significantly.

6.6 Concluding Remarks

This chapter conducts a probabilistic seismic demand analysis of coupled building-stair systems and loss estimation of stair systems using the performance-based earthquake engineering probabilistic seismic performance assessment methodology. The objectives of this study are to investigate the structural response characteristics of the coupled building-stair systems due to the interaction between buildings and stair sys-

tems as well as the seismic loss assessment of stair systems in buildings. Key findings of the probabilistic analysis of the coupled building-stair systems are summarized as the following:

1. The probabilistic seismic response analysis indicates that the presence of stair systems only moderately modifies the global building responses. It is shown in the probabilistic analysis that the median peak interstory ratios of the coupled systems differ from their bare building counterparts by only about 20%. The median peak floor acceleration responses appears even less sensitive to the presence of stair systems.

2. Regarding seismic loss of stair systems, the strength and stiffness contribution provided by the stairs moderately reduces the stair loss as a result of reduced structural interstory drift demands. The maximum reduction is observes as 20% for the estimated mean annual loss. In contrast, increasing the stair deformation capacity may significantly mitigate the estimated stair loss. The stair loss results demonstrate that increased stair deformation capacity effectively reduces the fragility of stair systems during low- to moderate-intensity earthquakes, allowing the stairs as a system to absorb large building interstory drift demands and thus reducing their loss potential.

It is important to note that although the study presented in this chapter focuses on the interaction of buildings and stair systems, a broader category of distributed nonstructural systems (e.g., cold-formed steel partition walls) can be readily incorporated into the system-level probabilistic seismic loss assessment framework. Research investigations of the effect of an inventory of nonstructural components on building performance characteristics and seismic loss of the entire building-nonstructural inventory can be performed using the analysis procedure presented in this chapter.

Acknowledgements

Portions of the following manuscript, for which the dissertation author was the primary investigator and author, are contained in this chapter:

- Wang, X., Hutchinson, T., and Conte, J. "Probabilistic Seismic Loss Assessment of Stair Systems in Buildings." In preparation for submission.

Chapter 7

Conclusions and Future Work

7.1 Motivation and Scope

Stair systems are critical nonstructural systems in buildings, providing a safe means of egress for building evacuation as well as much needed access for emergency responders. It is essential that stair systems remain operable in the aftermath of an earthquake and other extreme event to support immediate building accessibility and particularly during the assessment of safety and evacuation of occupants. To date, however, the state of knowledge regarding the seismic behavior of these critical nonstructural systems remains largely limited, despite the fact that past earthquakes repeatedly expose their vulnerability even in low- or moderate-intensity earthquakes.

To this end, a comprehensive experimental and numerical study of stair systems is conducted in this dissertation. The first portion of this dissertation presents a first-of-its-kind experimental investigation of a prefabricated steel stair system in a full-scale building shake table test program. In this work, the modal characteristics of the stair system identified using white noise base excitation tests as well as the physical observations of the stair system during earthquake tests of increasing intensities are summarized. The second portion of this dissertation involves a comprehensive computational study to capture at first the salient seismic response characteristics of steel stairs in an isolated configuration and subsequently the key response characteristics of buildings coupled with stair systems. Detailed three-dimensional finite element models of

a pair of prefabricated steel stairs are developed and their efficacy evaluated through extensive comparison with experimental data. The validated stair models are extended into a parametric study using a broader range of design variables commonly found in practice. Subsequently, a system-level numerical study is conducted to investigate the interaction between buildings and stair systems and the associated impacts on building response characteristics as well as estimated stair loss using a probabilistic seismic analysis framework.

7.2 Research Uniqueness

The shake table tests of a prefabricated steel stair system incorporated in a full-scale building shake table test program represent the first-of-its-kind system-level experimental study of these systems under realistic installation and dynamic loading conditions. These tests highlight the seismic vulnerability of modern designed stair systems and in particular identifies as a key research need the importance of improving the deformability of stair connections. In addition, a complete set of high-quality test data of the stairs and other nonstructural components and systems in these shake table tests were collected, which is publicly available within NEEShub database (Hutchinson et al., 2014; Pantoli et al., 2015a). These system-level test data provide unique opportunities for calibrating computational models in the future study.

To this end, the test data captured in the aforementioned study, as well as data from one other detailed test program, are used to develop high-fidelity finite element models of prefabricated steel stairs. The efficacy of the models are validated and subsequently employed in a parametric assessment of the seismic behavior of stairs with varied design variables. With minimal modeling simplicities, these detailed models are capable of predicting not only the global force-displacement response but as well the connection behavior and notably the deformation mechanisms of the stairs. To the author's knowledge, this study represents the first time that the seismic behavior of stair systems are studied using physics-based finite element models.

7.3 Major Findings

7.3.1 Full-scale Building Shake Table Testing

The experimental work in the dissertation presents the physical results and measured response of the prefabricated steel stairs in the shake table tests. In particular, emphasis of this system-level experimental study is focused on associating the seismic behavior of the stairs with the demands of the test building as well as their implications related to seismic design. Important findings regarding the dynamic characteristics and seismic behavior of the prefabricated steel stair systems in the shake table tests are summarized as follows:

1. The modal identification results indicate that the first modes of the stair corresponds to the global torsional vibration with a frequency of 8.9 Hz. As a result, the stairs observed considerable acceleration and displacement responses in the transverse-to-stair-run direction, even when loading was imposed entirely in the parallel-to-stair-run direction. The stair landing displacements were comparable in the two directions, and its accelerations in the transverse-to-stair-run direction was observed to be even larger than those in the parallel-to-stair-run (loading) direction.

2. During the seismic tests, severe damage to the stairs was detected at all levels except level 5. The most severe damage to the stairs consistently initiated in the form of vertical weld fracture of connection angles between the uppers flights and the slab embeds, with the associated peak interstory drift ratios (PIDRs) ranging from about 0.7% to 2.6%. Safe egress from the building was compromised even when the associated drift demands (PIDR as low as 0.7%) were much lower than the design performance target of the building (PIDR of 2.5%). As a result of predominantly torsional movement, the stair system observed considerable out-of-plane (transverse) forces and deformations of similar amplitudes to those imposed along the in-plane (longitudinal) direction, despite the uni-directional seismic input excitations to the test building.

3. The seismic behavior of stair systems is highly dependent on the deformability

of their connections to the building. For stairs in a scissor configuration (such as those presented herein), the torsional deformability of the system is particularly important. Prior to severe damage to the stairs in the seismic tests, the deformation of the upper flight-to-building connection accommodated more than 30% of the interstory drift demands, while the torsional deformation of the landing was about 50% of that of the interstory drift demands.

7.3.2 Detailed Finite Element Modeling

As an initial effort of the computational study, detailed finite element models of two steel stairs are developed and their efficacy subsequently validated through comparison with experimental data. The validated modeling approach is then used in a parametric study to assess the seismic behavior of stair systems using a broader range of design variables commonly found in practice. Based on the parametric results of a total of eight stair models with varied design details, key findings regarding the seismic behavior of the prefabricated steel stairs are summarized as follows:

1. The predominant frequencies of the stairs are 5–15 Hz for the transverse-to-stair-run (torsional) and 15–30 Hz for the parallel-to-stair-run vibrational modes, respectively. The frequency range of the two horizontal modes is likely to coincide with the higher modes of a typical multi-story frame building. The vertical vibration modes are less likely to be activated, as these frequencies are considered too high relative to those of the buildings during earthquake excitations.

2. The force-displacement responses of the stairs differ significantly for loading in the two horizontal directions. The stair is subjected to significantly larger force and relative landing displacement demands in the case of parallel-to-stair-run loading. This is due to the fact that the upper flight movement effectively improves the deformability of the stairs and reduces the force demands in the case of transverse-to-stair-run loading, while building drift demands impose large force and displacement demands on the landing and connections in the case of parallel-to-stair-run loading.

3. Among the four sets of design variables considered in this study (i.e., story height, connection and landing details, and geometric configuration), the modal characteristics and the seismic force-displacement response of the stairs are most sensitive to the variation of connection details and geometric configurations. These parameters significantly modify the deformation mechanisms of the stair systems. In particular, the connections are subjected to large stress and plastic strain demands under lateral loading.

7.3.3 Probabilistic Seismic Analysis of Coupled Building-Stair Systems

Subsequent to the component-level stair modeling study, coupled building-stair system analyses are conducted to evaluate the interaction effects on structural response. In addition, stair loss in the buildings are estimated within a probabilistic seismic analysis framework. Key findings of the building-stair system numerical study are summarized as follow:

1. The interactions between stair systems and their supporting structure are highly dependent on the strength and stiffness contribution of stair systems relative to the building structure. Increased contribution of stair systems (e.g., stairs with stiffer connections) or decreased contribution of the building structure (e.g., buildings with more flexible structural systems or less stories) leads to an increased effect of stair systems on the building response.

2. The presence of stair systems only moderately modifies the structural response and collapse potential of the building. The probabilistic seismic analysis results indicate that the median peak interstory ratios of the coupled systems differ from their bare building counterparts by only about 20%. The median peak floor acceleration responses appears even less sensitive to the presence of stair systems. In addition, the largest difference of the mean annual rate of collapse between the coupled systems and their bare building counterparts is also about 20%.

3. Regarding seismic loss of stair systems, the strength and stiffness contribution provided by the stairs moderately reduces the stair loss as a result of reduced

structural interstory drift demands. The maximum reduction is observes as 20% for the estimated mean annual loss. In contrast, increasing the stair deformation capacity may significantly mitigate the estimated stair loss. The stair loss results demonstrate that increased stair deformation capacity effectively reduces the fragility of stair systems during low- to moderate-intensity earthquakes, allowing the stairs as a system to absorb large building interstory drift demands and thus reducing their loss potential.

7.4 Recommendations for Future Work

Although the seismic performance of stair systems are studied in this and a few other research efforts, the state of knowledge regarding the behavior of these critical nonstructural systems remains largely inadequate. In this regard, the following experimental and computational investigations are recommended to advance the understanding of their seismic behavior:

1. The shake table test results highlight that stair connection failure may occur even when building drift demands remain significantly lower than that of the design recommendations. Further experimental studies are needed to understand the structural response and fracture potential of stair connections using different details, thus evaluating their efficiency for seismic design applications.

2. In addition to steel stairs, experimental studies are needed to characterize the force-displacement response and seismic performance of stairs constructed using other structural systems (e.g., precast concrete stairs, cast-in-place reinforced concrete stairs) or those configured with different geometric layouts (e.g., straight-run, multiple-run).

3. Since reinforced concrete stairs tend to be much heavier and stiffer than prefabricated steel stairs as studied in this dissertation, additional experimental or computational study are recommended to investigate such types of stairs and quantify their interactions with the supporting structure.

4. Previous studies of stair systems have been primarily focused on the seismic behavior of stairs under uniaxial loading conditions. However, the structural behavior of stairs, in particular those in a scissor configuration, is highly coupled in the two loading directions. As a result, further experimental and computational studies are recommended to understanding their response characteristics under complicated loading protocols.

5. Stair systems in conventional design practice are highly susceptible to differential displacements during earthquakes. This is primarily due to the fact that designers often attach both ends of the stair to the upper and lower floors of the supporting structure with very stiff connections. With an intent of mitigating the seismic vulnerability of these critical nonstructural systems, conceptual design strategies that aim at decoupling the multiple-support differential excitations are proposed:

   (a) **Landing Separation**. A simple yet practical solution, as shown in Figure 7.1, is to separate the stair at the middle of the landing platform. In this scenario, the stair is divided into two separate structural subassemblies. While the flight and landing posts of the lower part are attached to the lower floor, the upper part of the stair is connected to the upper floor with four "hang-down" landing posts and the flight-to-building connection. Physical separation of the upper and lower level of the stairs would allow each subassembly to respond independently to earthquake input excitations from the upper and lower floors of the building.

   (b) **Sliding Mechanism**. An alternatively solution of the seismic design strategy is to introduce a sliding mechanism to the stairs, which is similar to buildings with sliding isolation systems. Tentatively, the sliding mechanism can be implemented at the lower flight-to-building connection (or lower flight-to-building connection) to accommodate the differential displacement demands induced by multiple-support locations.

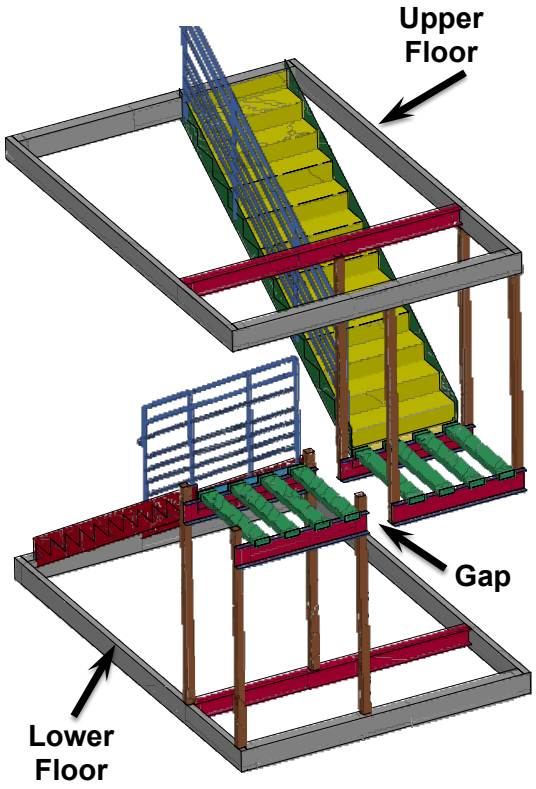

Figure 7.1. Innovative stair design strategy – landing separation.

These conceptual design strategies may effectively modify the kinematics of the stairs by eliminating the detrimental effect due to differential displacements imposed by the building. These *damage-free* design strategies are particularly worthwhile for structural facilities with high performance targets associated with a higher-than-design-event seismic hazard level. For instance, critical facilities such as hospitals and schools may be required to remain operable even in a maximum considered earthquake event. Applications of *damage-free* stairs within these critical facilities may substantially enhance the community seismic resilience.

Bibliography

Allemang, R. J. and Brown, D. L. (1982). "A correlation coefficient for modal vector analysis." *Proc., 1st International Modal Analysis Conference*, Orlando, FL, 110–116.

American Concrete Institute (ACI) (2005). *Building Code Requirements for Structural Concrete and Commentary*. American Concrete Institute, Farmington Hills, MI.

American Concrete Institute (ACI) (2008). *Building Code Requirements for Structural Concrete and Commentary*. American Concrete Institute, Farmington Hills, MI.

American Concrete Institute (ACI) (2014). *Building Code Requirements for Structural Concrete and Commentary*. American Concrete Institute, Farmington Hills, MI.

American Institute of Steel Construction (AISC) (2005a). *Prequalified Connections for Special and Intermediate Steel Moment Frames for Seismic Applications*. American Institute of Steel Construction, Chicago, IL.

American Institute of Steel Construction (AISC) (2005b). *Seismic Provisions for Structural Steel Buildings*. American Institute of Steel Construction, Chicago, IL.

American Institute of Steel Construction (AISC) (2005c). *Specification for Structural Steel Buildings*. American Institute of Steel Construction, Chicago, IL.

American Institute of Steel Construction (AISC) (2010). *Specification for Structural Steel Buildings*. American Institute of Steel Construction, Chicago, IL.

American Society of Civil Engineers (ASCE) (2006). *Minimum Design Loads for Buildings and Other Structures*. American Society of Civil Engineers, Reston, VA.

American Society of Civil Engineers (ASCE) (2010). *Minimum Design Loads for Buildings and Other Structures*. American Society of Civil Engineers, Reston, VA.

American Society of Mechanical Engineers (ASME) (2010). *Safety Code for Elevators and Escalators*. American Society of Mechanical Engineers, New york, NY.

Applied Technology Council (ATC) (2010). "Modeling and acceptance criteria for seismic design and analysis of tall buildings." *PEER/ATC 72-1*, Applied Technology

Council, Redwood City, CA.

Aslani, H. and Miranda, E. (2005). "Probability-based seismic response analysis." *Engineering Structures*, 27(8), 1151–1163.

Astroza, R., Ebrahimian, H., Conte, J., Restrepo, J., and Hutchinson, T. (2015). "System identification of a full-scale five-story reinforced concrete building tested on the nees-ucsd shake table." *Structural Control and Health Monitoring.* In press.

Ayres, J. and Sun, T. (1973). *Nonstructural Damage, the San Fernando Earthquake of Feb 9, 1971.* National Oceanic and Atmospheric Administration, Washington, DC.

Baker, J. W. (2015). "Efficient analytical fragility function fitting using dynamic structural analysis." *Earthquake Spectra*, 31(1), 579–599.

Baker, J. W. and Cornell, C. A. (2008). "Uncertainty propagation in probabilistic seismic loss estimation." *Structural Safety*, 30(3), 236–252.

Belleri, A., Moaveni, B., and Restrepo, J. I. (2014). "Damage assessment through structural identification of a three-story large-scale precast concrete structure." *Earthquake Engineering and Structural Dynamics*, 43(1), 61–76.

Bock, Y., Melgar, D., and Crowell, B. W. (2011). "Real-time strong-motion broadband displacements from collocated GPS and accelerometers." *Bulletin of the Seismological Society of America*, 101(6), 2904–2925.

Bradley, B. A., Lee, D. S., Broughton, R., and Price, C. (2009). "Efficient evaluation of performance-based earthquake engineering equations." *Structural Safety*, 31(1), 65–74.

Bull, D. K. (2011). "Stair and access ramps between floors in multi-storey buildings." *A report to the Canterbury Earthquakes Royal Commission*, Holmes Consulting Group, Christchurch, New Zealand.

Chang, B., Hutchinson, T., Wang, X., and Englekirk, R. (2013). "Experimental seismic performance of beam-column subassemblies using ductile embeds." *ASCE Journal of Structural Engineering*, 139(9), 1555–1566.

Chang, B., Hutchinson, T., Wang, X., and Englekirk, R. (2014). "Seismic performance of beam-column subassemblies with high strength steel reinforcement." *ACI Structural Journal*, 111(6), 1329–1338.

Chen, M., Pantoli, E., Wang, X., Astroza, R., Ebrahimian, H., Mintz, S., Hutchinson, T., Conte, J., Restrepo, J., Meacham, B., Kim, J., and Park, H. (2013). "BNCS Report #1: Full-scale structural and nonstructural building system performance during earthquakes and post-earthquake fire – Specimen design, construction, and test protocol."

SSRP-2013/09, Department of Structural Engineering, University of California, San Diego, La Jolla, CA.

Chen, M. C., Pantoli, E., Wang, X., Astroza, R., Ebrahimian, H., Hutchinson, T. C., Conte, J. P., Restrepo, J. I., Marin, C., and Walsh, K. D. (2015). "Full-scale structural and nonstructural building system performance during earthquakes: Part I – Specimen description, test protocol and structural response." *Earthquake Spectra.* In press.

Conte, J. P. (2015). *Personal Communications* (Jul 17, 2015).

Cornell, C. A., Jalayer, F., Hamburger, R. O., and Foutch, D. A. (2002). "Probabilistic basis for 2000 SAC federal emergency management agency steel moment frame guidelines." *ASCE Journal of Structural Engineering*, 128(4), 526–533.

Cosenza, E., Verderame, G. M., and Zambrano, A. (2008). "Seismic performance of stairs in the existing reinforced concrete building." *Proc., 14th World Conference on Earthquake Engineering*, Beijing, China.

Deierlein, G., Krawinkler, H., and Cornell, C. (2003). "A framework for performance-based earthquake engineering." *Pacific Conference on Earthquake Engineering*, Christchurch, New Zealand.

Downing, S. D. and Socie, D. (1982). "Simple rainflow counting algorithms." *International Journal of Fatigue*, 4(1), 31–40.

Ebrahimian, H., Astroza, R., Conte, J. P., Restrepo, J. I., and Hutchinson, T. C. (2013). "Pre-test nonlinear FE modeling and simulation of a full-scale five-story reinforced concrete building." *Topics in Dynamics of Civil Structures, Volume 4*, Springer, 503–511.

EERI (2014). "M 6.0 south Napa earthquake of August 24, 2014." *EERI Special Earthquake Report – October 2014*, Earthquake Engineering Research Institue, Oakland, CA.

El-Tawil, S., Mikesell, T., and Kunnath, S. K. (2000). "Effect of local details and yield ratio on behavior of FR steel connections." *ASCE Journal of Structural Engineering*, 126(1), 79–87.

Elkady, A. and Lignos, D. G. (2014). "Modeling of the composite action in fully restrained beam-to-column connections: Implications in the seismic design and collapse capacity of steel special moment frames." *Earthquake Engineering and Structural Dynamics*, 43(13), 1935–1954.

Ellingwood, B. R., Rosowsky, D. V., Li, Y., and Kim, J. H. (2004). "Fragility assessment of light-frame wood construction subjected to wind and earthquake hazards." *ASCE Journal of Structural Engineering*, 130(12), 1921–1930.

Federal Emergency Management Agency (FEMA) (2009). "Quantification of building seismic performance factors." *FEMA-P695*, Federal Emergency Management Agency, Washingtong, DC.

Federal Emergency Management Agency (FEMA) (2012). "Seismic performance assessment of buildings, Volume 1 – Methodology." *FEMA-P58*, Federal Emergency Management Agency, Washingtong, DC.

Federal Emergency Management Agency (FEMA) (2014). "Reducing the risks of nonstructural earthquake damage - a practical guide." *FEMA-E74*, Federal Emergency Management Agency, Washington, D.C. <http://www.fema.gov/earthquake-publications/fema-e-74-reducing-risks-nonstructural-earthquake-damage>. (Feb 20, 2014).

Filippou, F., Popov, E., and Bertero, V. (1983). "Effects of bond deterioration on hysteretic behavior of reinforced concrete joints." *EERC 83-19*, Earthquake Engineering Research Center, University of California, Berkeley, Berkeley, CA.

Goulet, C. A., Haselton, C. B., Mitrani-Reiser, J., Beck, J. L., Deierlein, G. G., Porter, K. A., and Stewart, J. P. (2007). "Evaluation of the seismic performance of a code-conforming reinforced-concrete frame building – from seismic hazard to collapse safety and economic losses." *Earthquake Engineering and Structural Dynamics*, 36(13), 1973–1997.

Gupta, A. and Krawinkler, H. (2000). "Dynamic P-delta effects for flexible inelastic steel structures." *ASCE Journal of Structural Engineering*, 126(1), 145–154.

Haselton, C. and Deierlein, G. (2007). "Assessing seismic collapse safety of modern reinforced concrete frame." *PEER 2007/08*, Pacific Engineering Research Center, University of California, Berkeley, Berkeley, CA.

Haselton, C. B., Liel, A. B., Deierlein, G. G., Dean, B. S., and Chou, J. H. (2010). "Seismic collapse safety of reinforced concrete buildings. I: Assessment of ductile moment frames." *ASCE Journal of Structural Engineering*, 137(4), 481–491.

Higgins, C. (2009). "Prefabricated steel stair performance under combined seismic and gravity loads." *ASCE Journal of Structural Engineering*, 135(2), 122–129.

Hutchinson, T., Restrepo, J., Conte, J., Pantoli, E., Chen, M., Wang, X., Astroza, R., and Ebrahimian, H. (2014). *Shake Table Testing of a Five Story Building Outfitted with NCSs (BNCS Project)* DOI: 10.4231/D38W38349.

Ibarra, L. F., Medina, R. A., and Krawinkler, H. (2005). "Hysteretic models that incorporate strength and stiffness deterioration." *Earthquake Engineering and Structural Dynamics*, 34(12), 1489–1512.

Imregun, M. and Ewins, D. (1993). "Realisation of complex mode shapes." *Proc., 11th International Modal Analysis Conference*, Kissimmee, FL, 1303–1309.

International Code Council (ICC) (2003). *International Building Code*. International Code Council, Falls Church, VA.

International Code Council (ICC) (2012). *International Building Code*. International Code Council, Falls Church, VA.

Jia, L. J. and Kuwamura, H. (2013). "Prediction of cyclic behaviors of mild steel at large plastic strain using coupon test results." *ASCE Journal of Structural Engineering*, 140(2), 04013056.

Jones, S. L., Fry, G. T., and Engelhardt, M. D. (2002). "Experimental evaluation of cyclically loaded reduced beam section moment connections." *ASCE Journal of Structural Engineering*, 128(4), 441–451.

Kam, W. Y. and Pampanin, S. (2011). "The seismic performance of RC buildings in the 22 February 2011 Christchurch earthquake." *Structural Concrete*, 12(4), 223–233.

Kanvinde, A. and Deierlein, G. (2007). "Cyclic void growth model to assess ductile fracture initiation in structural steels due to ultra low cycle fatigue." *Journal of Engineering Mechanics*, 133(6), 701–712.

Krawinkler, H. and Seneviratna, G. (1998). "Pros and cons of a pushover analysis of seismic performance evaluation." *Engineering Structures*, 20(4), 452–464.

Kuntz, G. L. and Browning, J. (2003). "Reduction of column yielding during earthquakes for reinforced concrete frames." *ACI Structural Journal*, 100(5), 573–580.

Lallemant, D., Kiremidjian, A., and Burton, H. (2015). "Statistical procedures for developing earthquake damage fragility curves." *Earthquake Engineering and Structural Dynamics*, 44(9), 1373–1389.

Li, B. and Mosalam, K. M. (2013). "Seismic performance of reinforced-concrete stairways during the 2008 Wenchuan earthquake." *ASCE Journal of Performance of Constructed Facilities*, 27(6), 721–730.

Lignos, D. G. and Krawinkler, H. (2010). "Deterioration modeling of steel components in support of collapse prediction of steel moment frames under earthquake loading." *ASCE Journal of Structural Engineering*, 137(11), 1291–1302.

Lignos, D. G. and Krawinkler, H. (2012). "Development and utilization of structural component databases for performance-based earthquake engineering." *ASCE Journal of Structural Engineering*, 139(8), 1382–1394.

Livermore Software Technology Corporation (LSTC) (2013a). *LS-DYNA Keyword*

User's Manual – Volume 1 (Version 971). Livermore Software Technology Corporation, Livermore, CA.

Livermore Software Technology Corporation (LSTC) (2013b). *LS-DYNA Keyword User's Manual – Volume 2 (Version 971)*. Livermore Software Technology Corporation, Livermore, CA.

Lowes, L. N., Moehle, J. P., and Govindjee, S. (2004). "Concrete-steel bond model for use in finite element modeling of reinforced concrete structures." *ACI Structural Journal*, 101(4), 501–511.

Lu, L. W., Ricles, J. M., Mao, C., and Fisher, J. W. (2000). "Critical issues in achieving ductile behaviour of welded moment connections." *Journal of Constructional Steel Research*, 55(1), 325–341.

Mander, J. B., Priestley, M. J., and Park, R. (1988). "Theoretical stress-strain model for confined concrete." *ASCE Journal of Structural Engineering*, 114(8), 1804–1826.

Mao, C., Ricles, J., Lu, L. W., and Fisher, J. (2001). "Effect of local details on ductility of welded moment connections." *ASCE Journal of Structural Engineering*, 127(9), 1036–1044.

Mazzoni, S., McKenna, F., Scott, M. H., and Fenves, G. L. (2014). *Open System for Engineering Simulation User-Command-Language Manual (Version 2.4.0)*. Pacific Earthquake Engineering Research Center, University of California, Berkeley, Berkeley, CA <http://www.opensees.berkely.edu/>.

McGuire, R. K. (2004). *Seismic Hazard and Risk Analysis*. Earthquake Engineering Research Institute, Oakland, CA.

Miranda, E., Mosqueda, G., Retamales, R., and Pekcan, G. (2012). "Performance of nonstructural components during the 27 February 2010 Chile earthquake." *Earthquake Spectra*, 28(S1), 453–471.

Mitra, N. and Lowes, L. N. (2007). "Evaluation, calibration, and verification of a reinforced concrete beam-column joint model." *ASCE Journal of Structural Engineering*, 133(1), 105–120.

Moaveni, B., He, X., Conte, J. P., Restrepo, J. I., and Panagiotou, M. (2010). "System identification study of a 7-story full-scale building slice tested on the UCSD-NEES shake table." *ASCE Journal of Structural Engineering*, 137(6), 705–717.

Moehle, J. P., Hooper, J. D., and Lubke, C. D. (2008). "Seismic design of reinforced concrete special moment frames: a guide for practicing engineers." *NIST GCR 8-917-1*, National Institute of Standards and Technology, Gaithersburg, MD.

National Institute of Standards and Technology (NIST) (2010). "Evaluation of the FEMA P-695 methodology for quantification of building seismic performance factors." *NIST GCR 10-917-8*, NEHRP Consultants Joint Venture, Washingtong, DC.

Network for Earthquake Engineering Simulation (NEES) (2015). *NEEShub Website*. Network for Earthquake Engineering Simulation <https://nees.org/>. (accessed Jun 20, 2015).

Ozcelik, O., Luco, J., Conte, J., Trombetti, T., and Restrepo, J. (2008). "Experimental characterization, modeling and identification of the NEES-UCSD shake table mechanical system." *Earthquake Engineering and Structural Dynamics*, 37(2), 243–264.

Panagiotakos, T. B. and Fardis, M. N. (2001). "Deformations of reinforced concrete members at yielding and ultimate." *ACI Structural Journal*, 98(2), 135–148.

Pantoli, E., Chen, M., Wang, X., Astroza, R., Ebrahimian, H., Mintz, S., Hutchinson, T., Conte, J., Restrepo, J., Meacham, B., Kim, J., and Park, H. (2013a). "BNCS Report #2: Full-scale structural and nonstructural building system performance during earthquakes and post-earthquake fire – Test results." *SSRP-2013/10*, Department of Structural Engineering, University of California, San Diego, La Jolla, CA.

Pantoli, E., Chen, M. C., Hutchinson, T., and Restrepo, J. (2013b). "BNCS Report #3: Full-scale structural and nonstructural building system performance during earthquakes and post-earthquake fire – Camera and analog sensor details." *SSRP-2013/11*, Department of Structural Engineering, University of California, San Diego, La Jolla, CA.

Pantoli, E., Chen, M. C., Hutchinson, T. C., Astroza, R., Conte, J., Ebrahimian, H., Restrepo, J., and Wang, X. (2015a). "Landmark dataset from the building nonstructural components and systems (BNCS) project." *Earthquake Spectra.* In press.

Pantoli, E., Chen, M. C., Wang, X., Astroza, R., Ebrahimian, H., Hutchinson, T. C., Conte, J. P., Restrepo, J. I., Marin, C., Walsh, K. D., et al. (2015b). "Full-scale structural and nonstructural building system performance during earthquakes: Part II – NCS damage states." *Earthquake Spectra.* In press.

Peeters, B. and De Roeck, G. (2001). "Stochastic system identification for operational modal analysis: a review." *Journal of Dynamic Systems, Measurement, and Control*, 123(4), 659–667.

Porter, K., Kennedy, R., and Bachman, R. (2007). "Creating fragility functions for performance-based earthquake engineering." *Earthquake Spectra*, 23(2), 471–489.

Porter, K. A. (2003). "An overview of PEER's performance-based earthquake engineering methodology." *Proc., 9th International Conference on Applications of Statistics and Probability in Civil Engineering*, San Francisco, CA.

Roha, C., Axley, J. W., and Bertero, V. V. (1982). "The performance of stairways in earthquakes." *UCB/EERC-82/15*, Earthquake Engineering Research Center, University of California, Berkeley, Berkeley, CA.

Scott, B., Park, R., and Priestley, M. (1982). "Stress-strain behavior of concrete confined by overlapping hoops at low and high strain rates." *ACI Structural Journal*, 79(1), 13–27.

Simmons, P. W. and Bull, D. K. (2000). "The safety of single storey straight stairflights with mid-height landings under simulated seismic displacements." *Report 2000-09*, Department of Civil Engineering, University of Cantebury, Christchurch, New Zealand.

Stephens, M. A. (1974). "EDF statistics for goodness of fit and some comparisons." *Journal of the American statistical Association*, 69(347), 730–737.

Suárez, L. E. and Singh, M. P. (2000). "Review of earthquake performance, seismic codes, and dynamic analysis of elevators." *Earthquake spectra*, 16(4), 853–878.

Tegos, I. A., Panoskaltsis, V. P., and Tegou, S. D. (2013). "Analysis and design of staircases against seismic loadings." *Proc., 4th ECCOMAS Thematic Conference on Computational Methods in Structural Dynamics and Earthquake Engineering*, Kos Island, Greece.

US Geological Survery (USGS) (2014). *USGS Hazard Curve Application*. US Geological Survery <http://geohazards.usgs.gov/hazardtool>. (accessed Sep 20, 2014).

Vamvatsikos, D. and Cornell, C. A. (2002). "Incremental dynamic analysis." *Earthquake Engineering and Structural Dynamics*, 31(3), 491–514.

Van Den Einde, L., Restrepo, J. I., Conte, J., Luco, E., Seible, F., Filiatrault, A., Clark, A., Johnson, A., Gram, M., Kusner, D., and Thoen, B. (2004). "Development of the George E. Brown Jr. network for earthquake engineering simulation (NEES) large high performance outdoor shake table at the University of California, San Diego." *Proc., 13th World Conference on Earthquake Engineering*, Vancouver, Canada.

Van Overschee, P. and De Moor, B. (1996). *Subspace Identification for Linear Systems: Theory, Implementation, Applications*. Kluwer Academic Publishers, Boston, MA.

Wang, X., Ebrahimian, H., Astroza, R., Conte, J., Restrepo, J., and Hutchinson, T. (2013). "Shake table testing of a full-scale five-story building: pre-test simulation of the test building and development of an NCS design criteria." *Proc., 2013 ASCE Structures Congress*, ASCE, Pittsburg, PA.

Wang, X., Pantoli, E., Hutchinson, C., Restrepo, J., Wood, R., Hoehler, M., Grzesik, P., and Sesma, F. (2015). "Seismic performance of cold-formed steel wall systems in a

full-scale building." *ASCE Journal of Structural Engineering*, 141(10), 04015014.

Yoshida, F., Uemori, T., and Fujiwara, K. (2002). "Elastic-plastic behavior of steel sheets under in-plane cyclic tension-compression at large strain." *International Journal of Plasticity*, 18(5), 633–659.

Zareian, F. and Krawinkler, H. (2007). "Assessment of probability of collapse and design for collapse safety." *Earthquake Engineering and Structural Dynamics*, 36(13), 1901–1914.

Zareian, F., Lignos, D., and Krawinkler, H. (2010). "Evaluation of seismic collapse performance of steel special moment resisting frames using FEMA P695 (ATC-63) methodology." *Proc., 2010 ASCE Structures Congress*, Orlando, FL, 1275–1286.

Zareian, F. and Medina, R. A. (2010). "A practical method for proper modeling of structural damping in inelastic plane structural systems." *Computers and Structures*, 88(1), 45–53.

Appendix A

Construction Drawings of the Stair System

This appendix provides the construction shop drawings of the prefabricated steel stairs. The original drawing set, provided by the Pacific Stairs Company, consists of a total of seven drawing files in PDF format. In this appendix, it is noted that three original drawings (i.e., Erection Layout, Rail Layout, Rough Ppening / Embed Layout) are divided into halves (left and right parts) and resized to improve their readability.

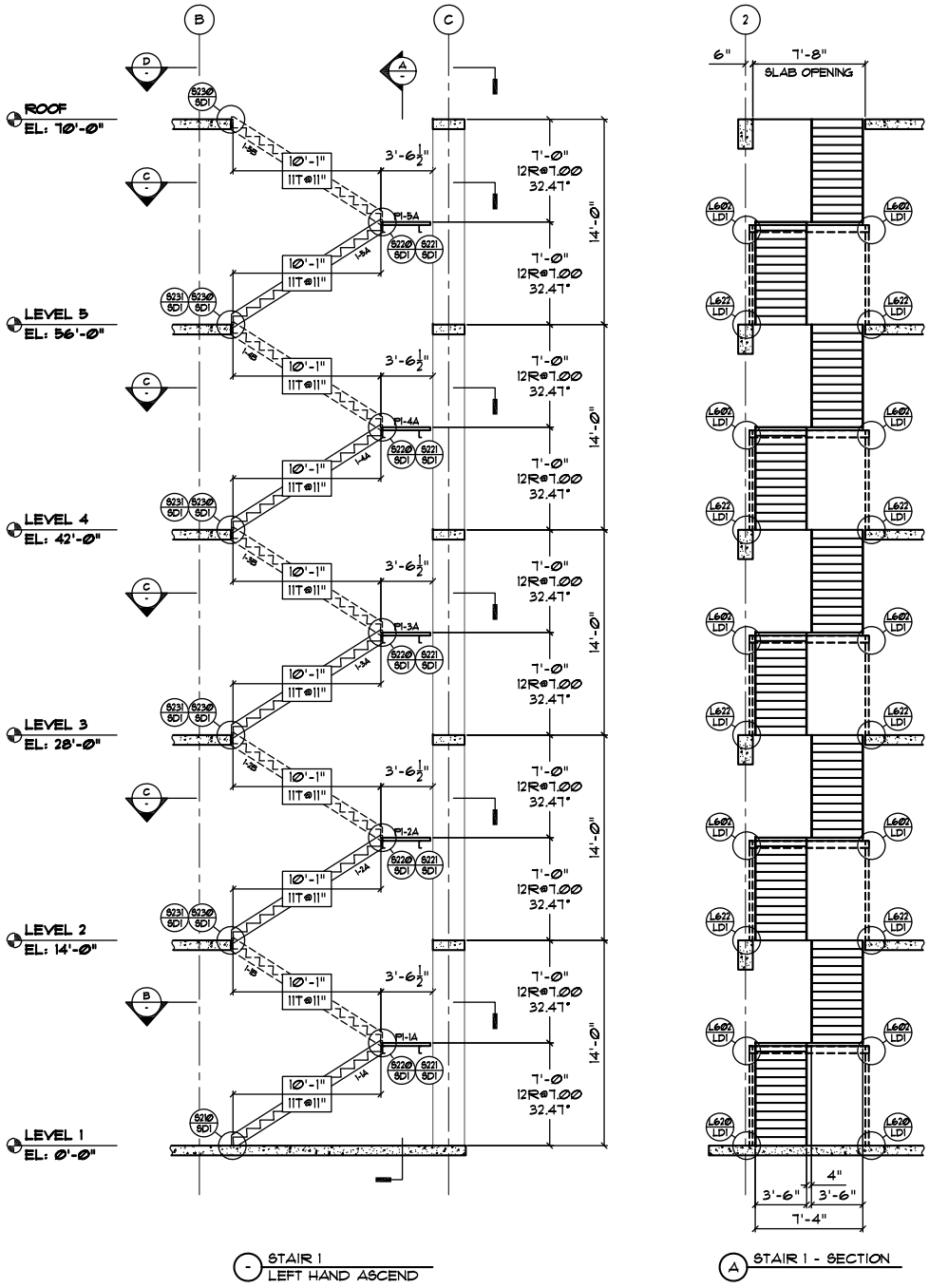

Erection Layout (left part)

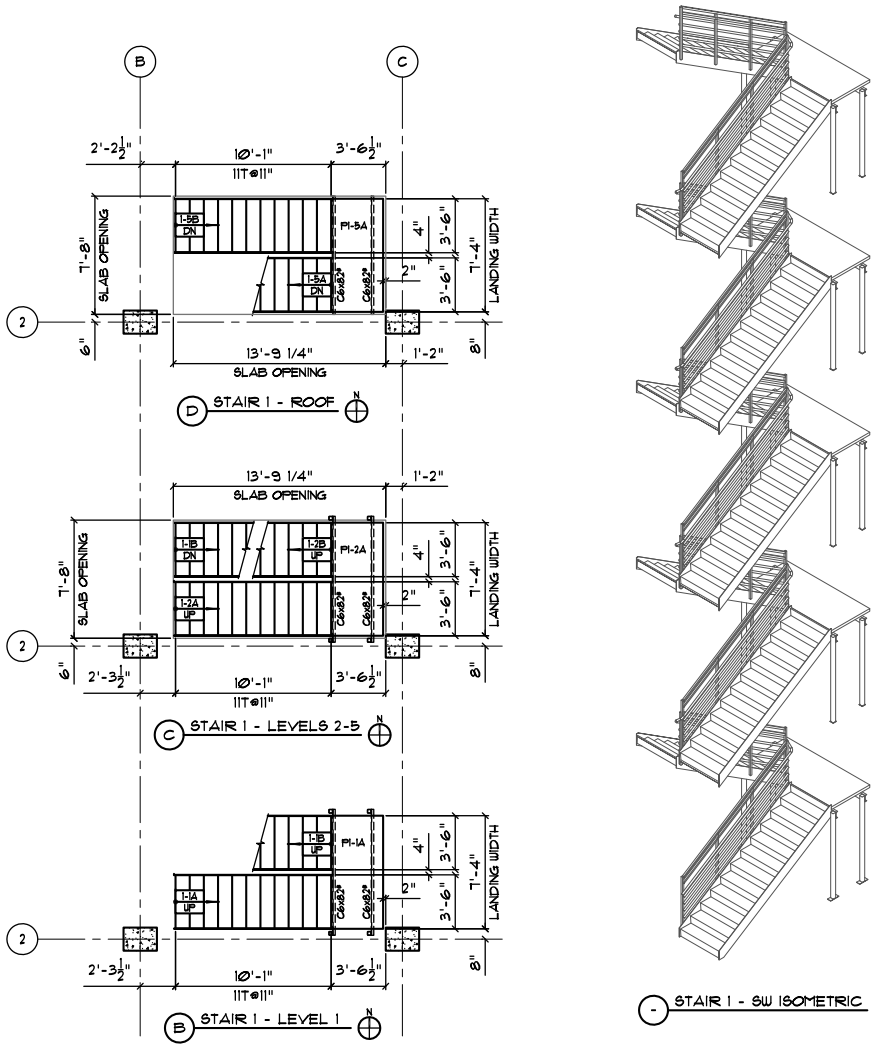

NOTE:
DIMENSIONS ARE TO FACE OF FINISH, NOSING, GRID LINE, OR OUTSIDE OF STRINGER. SEE RO DWGS. FOR SLAB EDGE DIMENSIONS.

SEAL / SIGNATURE

Project: UCSD TEST SPECIMEN SAN DIEGO, CA		
Scale: NONE	Customer:	Drawn by: BRIAN H.
Date: Ø2/Ø1/2Ø11	N/A	Checked by: TG
Description: STAIR 1 - ERECTION LAYOUT		
PACIFIC STAIR CORPORATION 8690 STAIR WAY NE SALEM, OR 97305 (503) 390-8305		Drawing no: 784-E1.Ø

Erection Layout (right part)

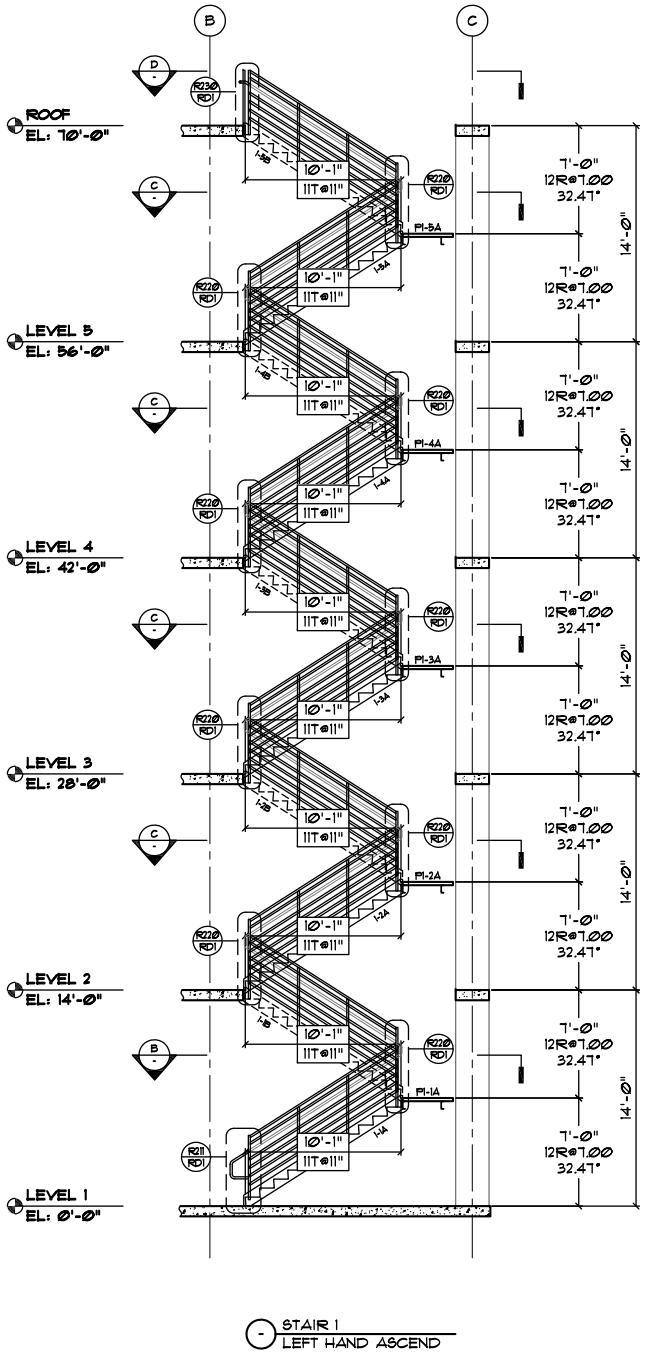

Rail Layout (left part)

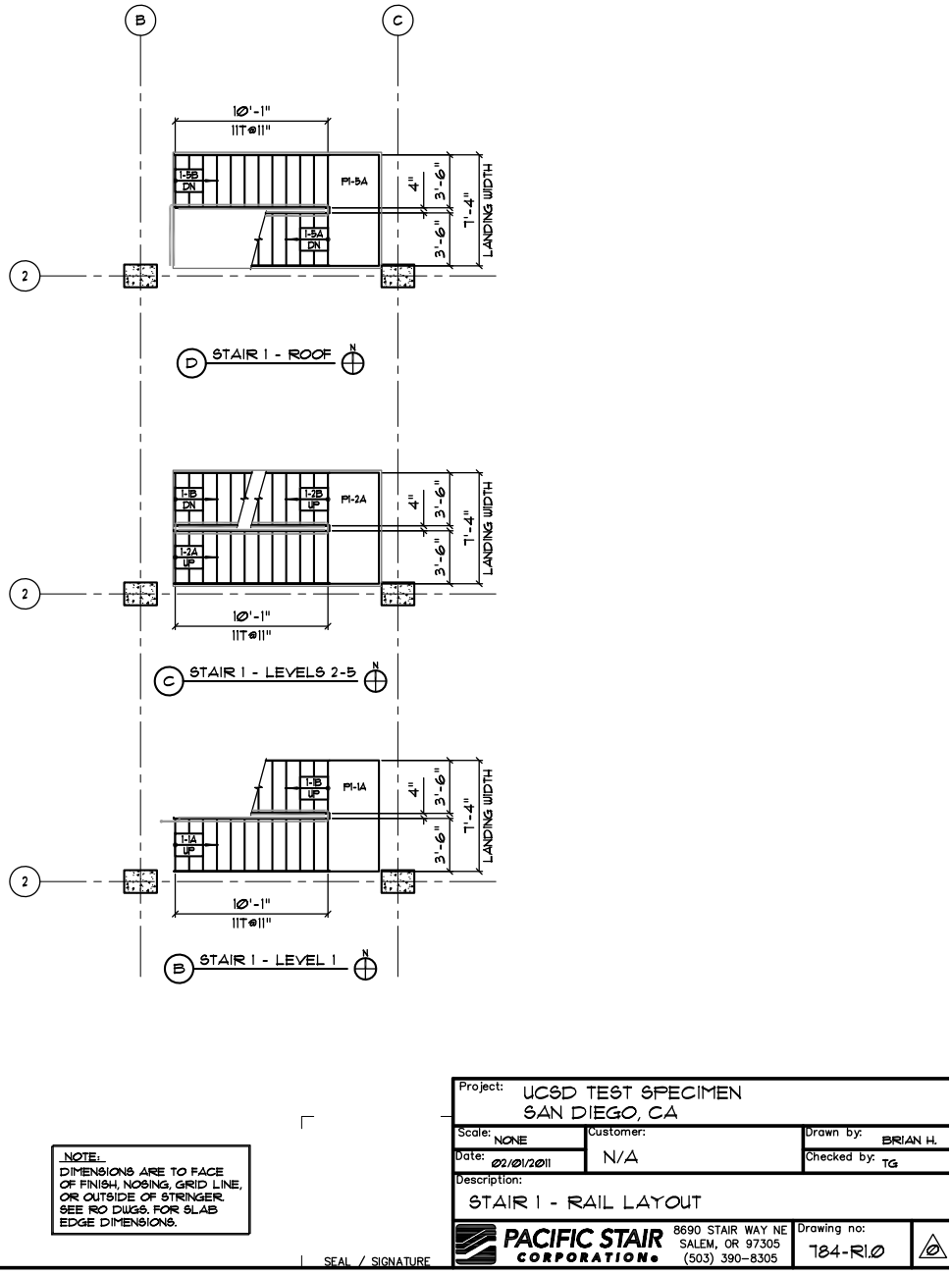

Rail Layout (right part)

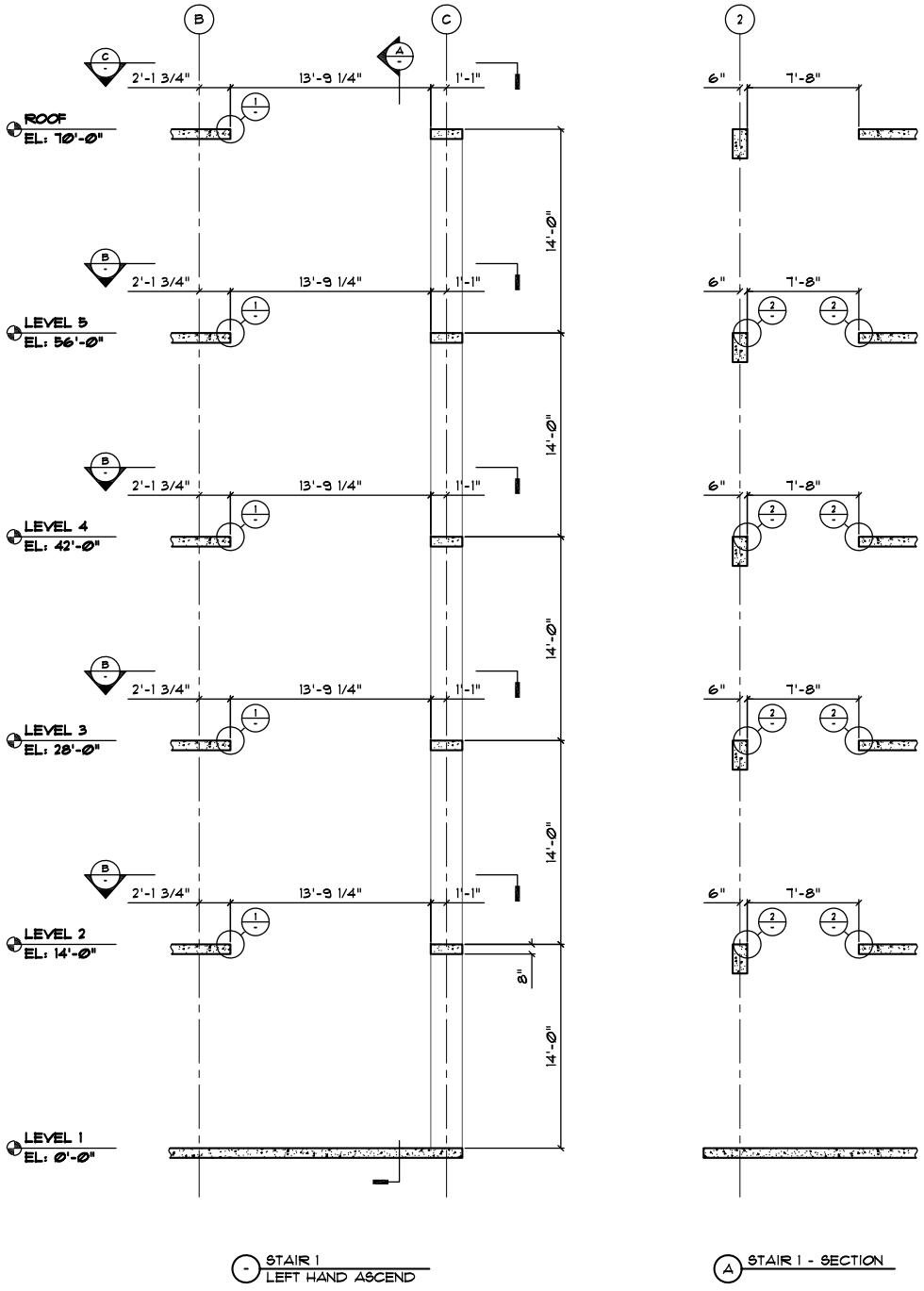

Rough Opening / Embed Layout (left part)

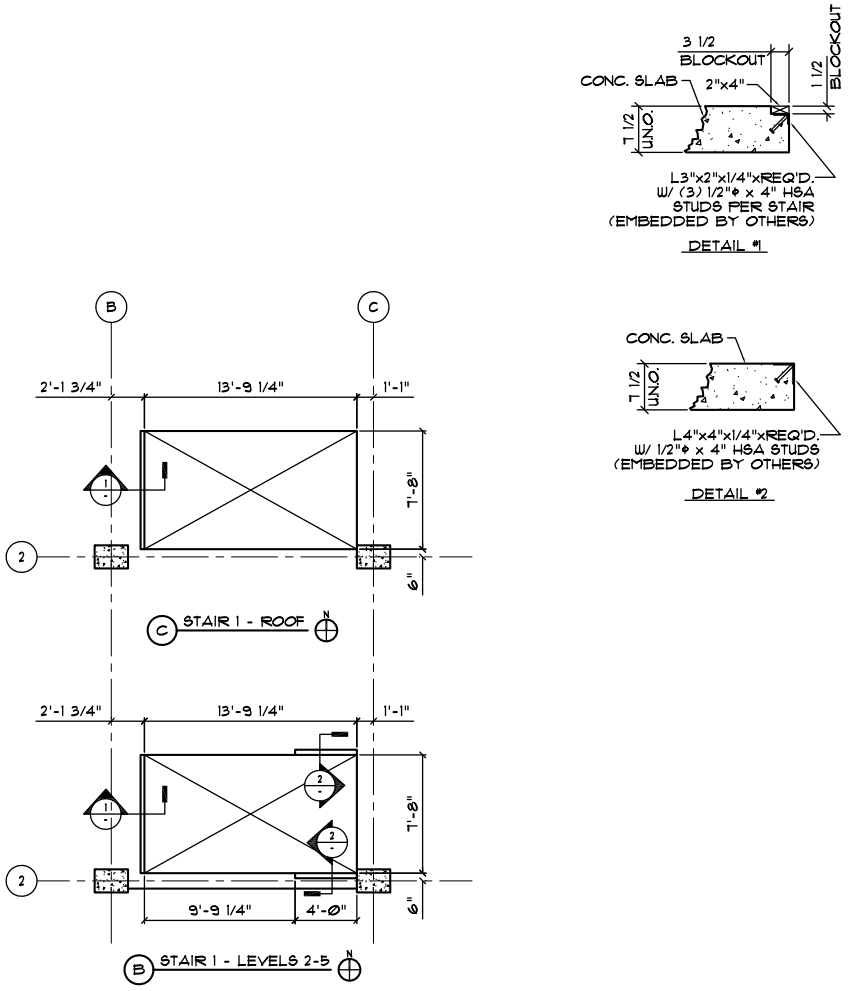

Rough Opening / Embed Layout (right part)

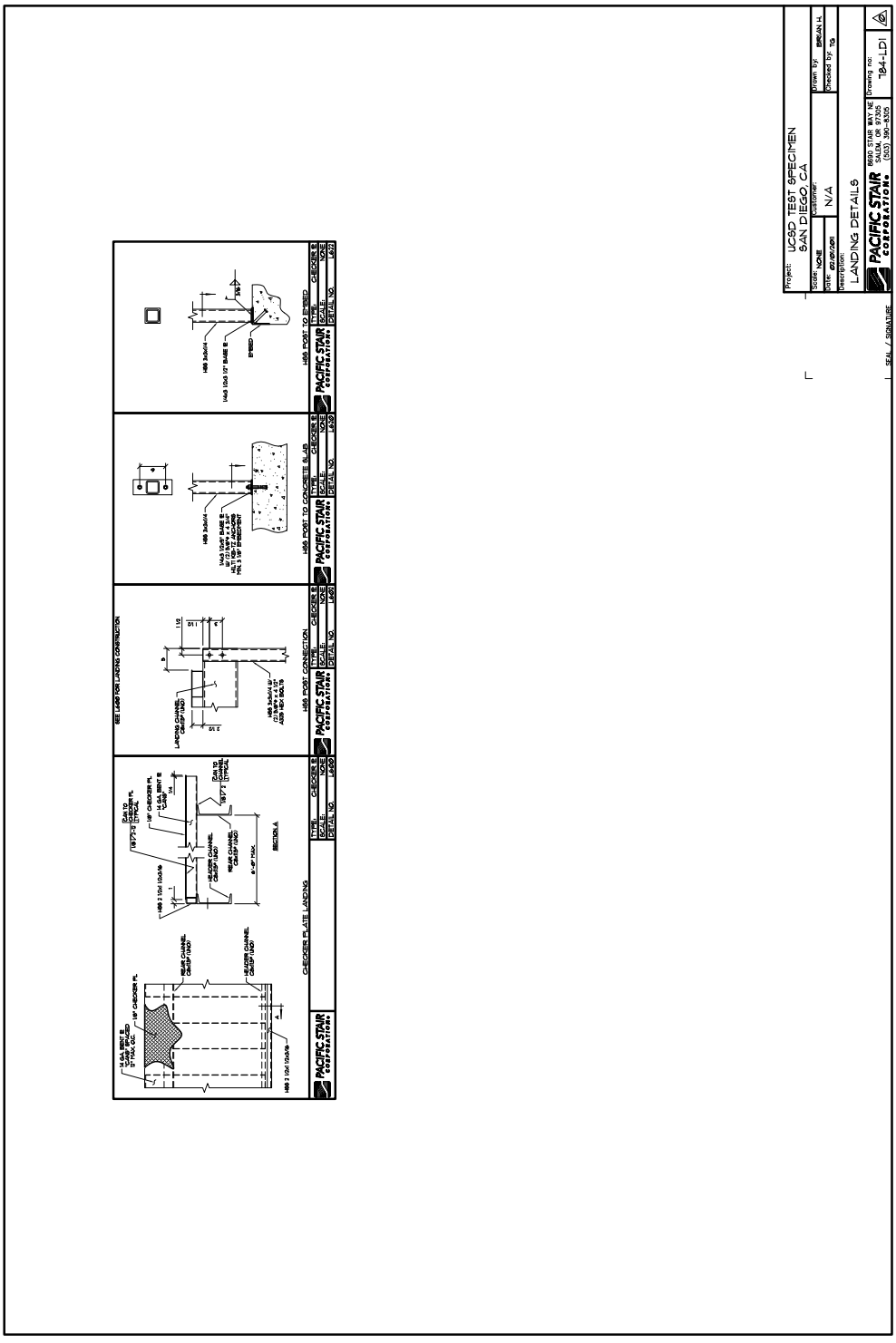

Landing Details (original)

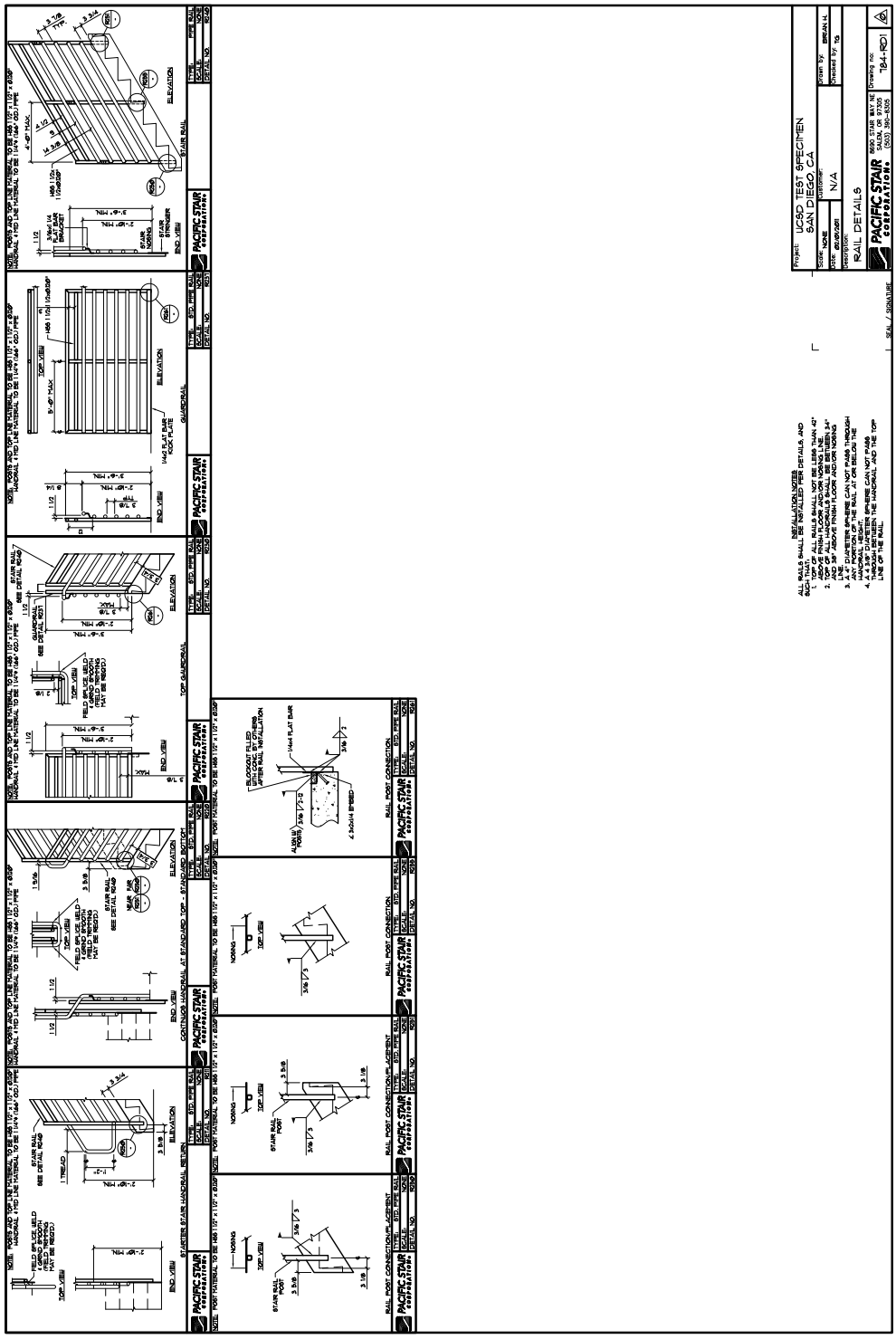

Rail Details (original)

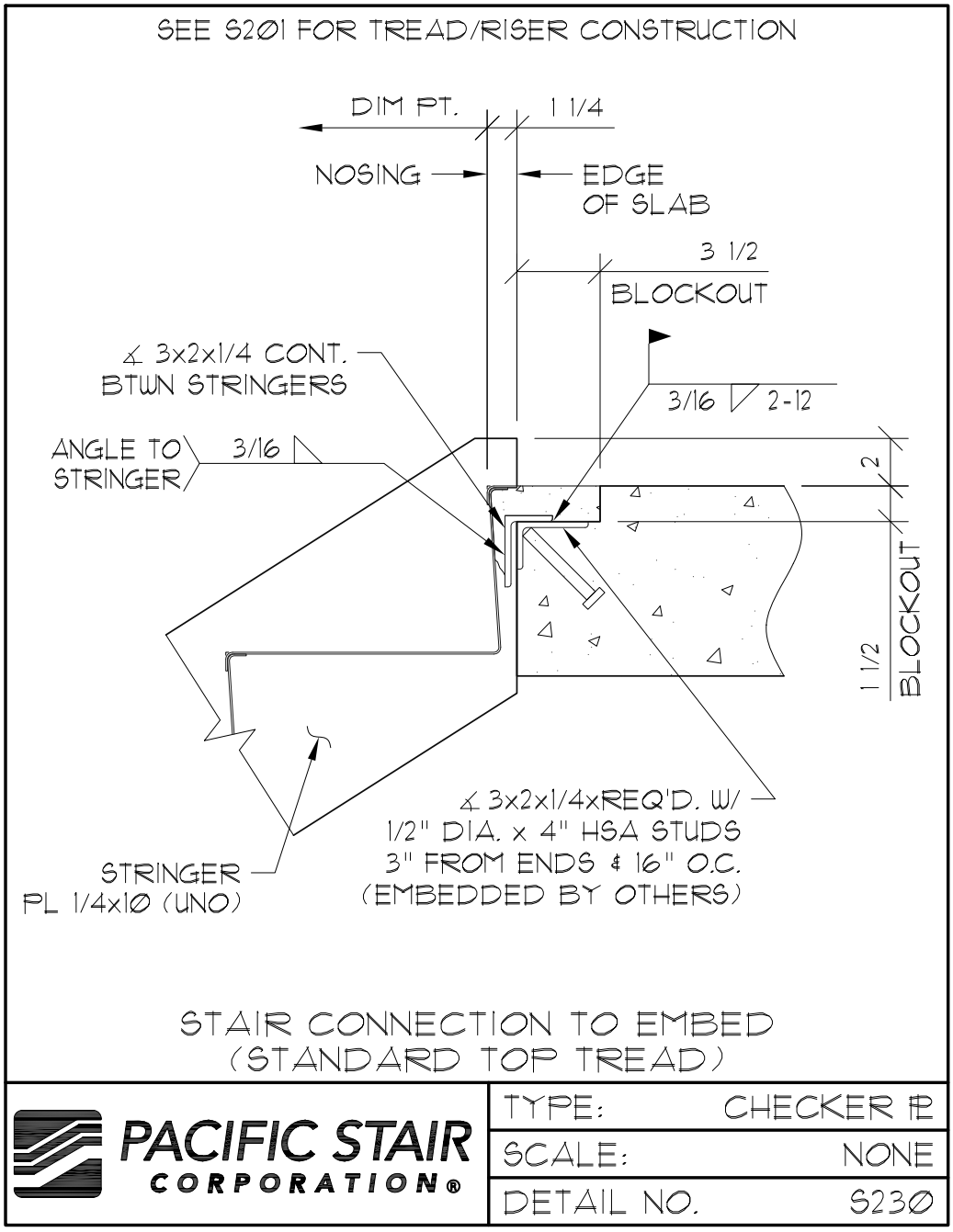

Stair Connection to Embed – Standard Top Tread (original)

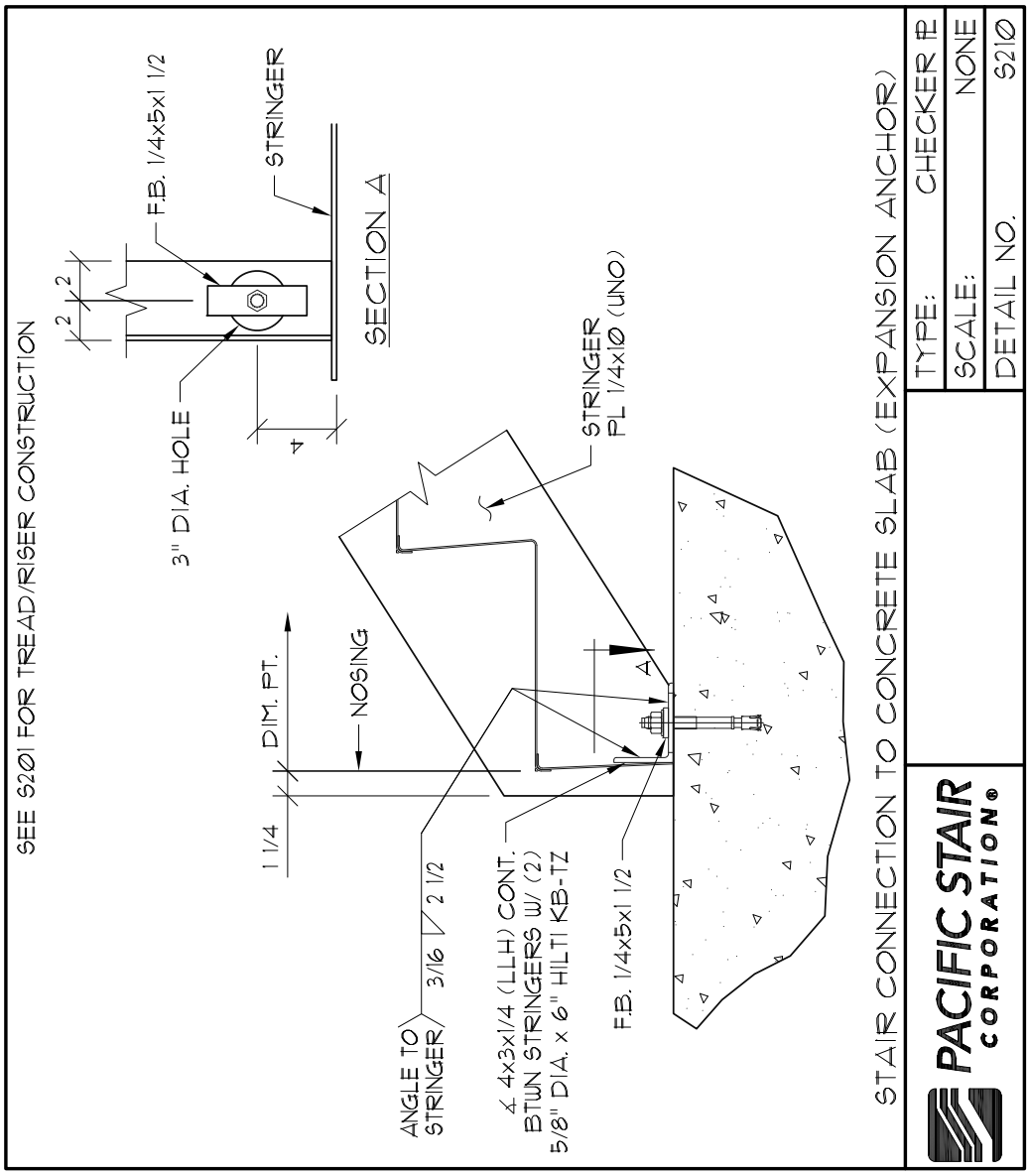

Stair Connection to Concrete Slab – Expansion Anchor (original)

Appendix B

Measured Stair Acceleration Response

This appendix presents the measured acceleration response of the stair at level 2 during each of the thirteen earthquake tests of the shake table test program. A total of eighteen accelerometers were installed on the steel stair at level 2, six each on the two (upper and lower) flights and the landing (Figure B.1) during these earthquake tests. The acceleration time histories of the stair are presented in Figures B.2 through B.40.

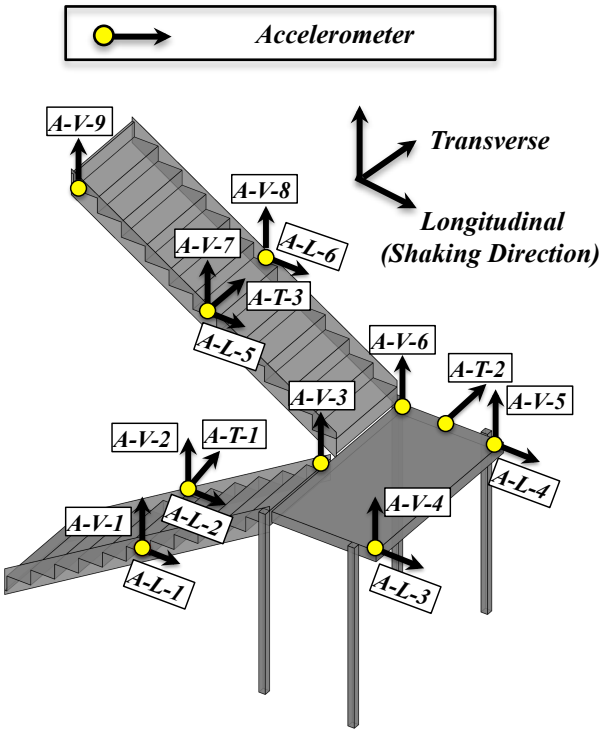

Figure B.1. Accelerometer layout of the steel stair at level 2.

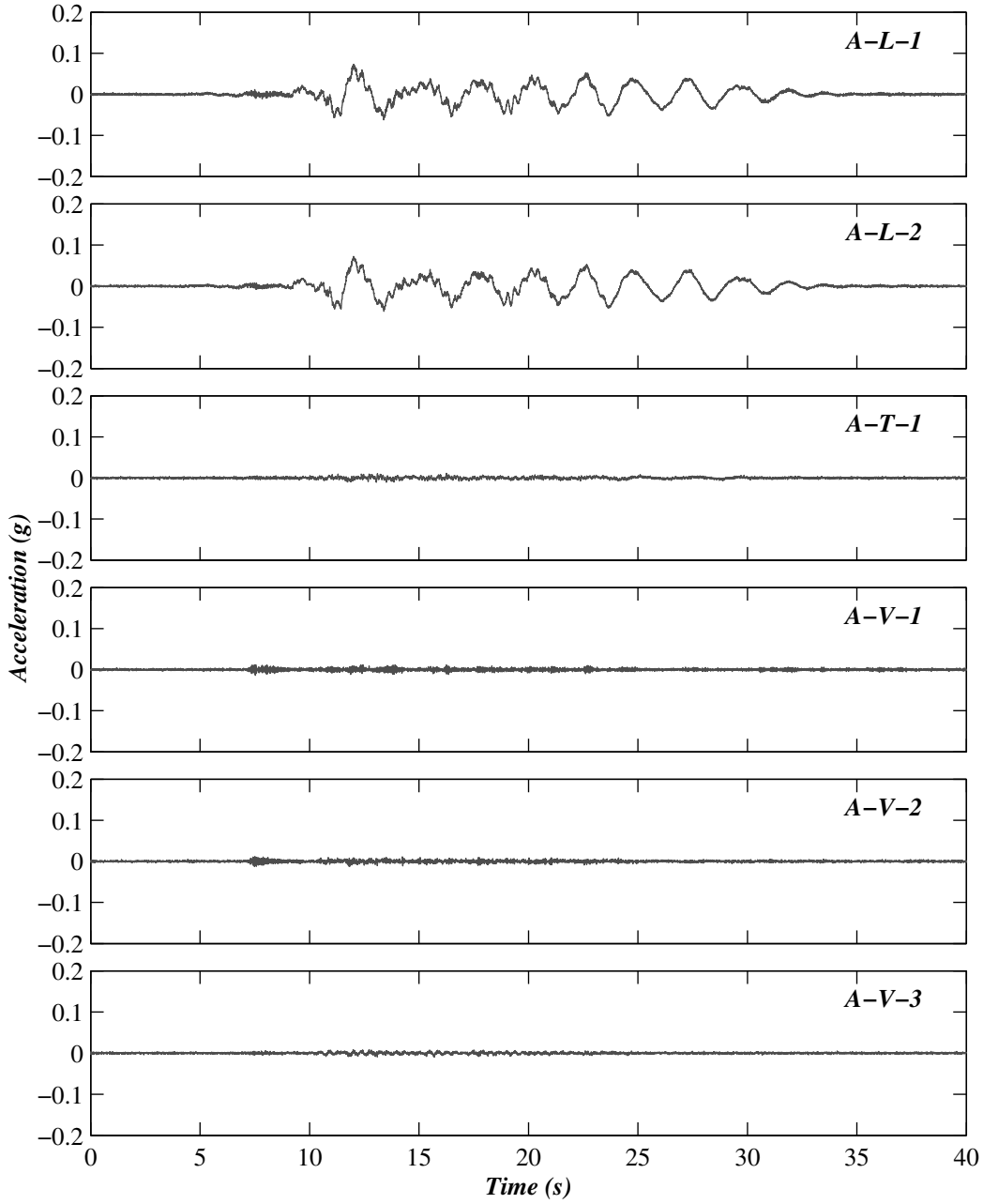

Figure B.2. Acceleration time history responses of the lower flight at level 2 during test BI-1.

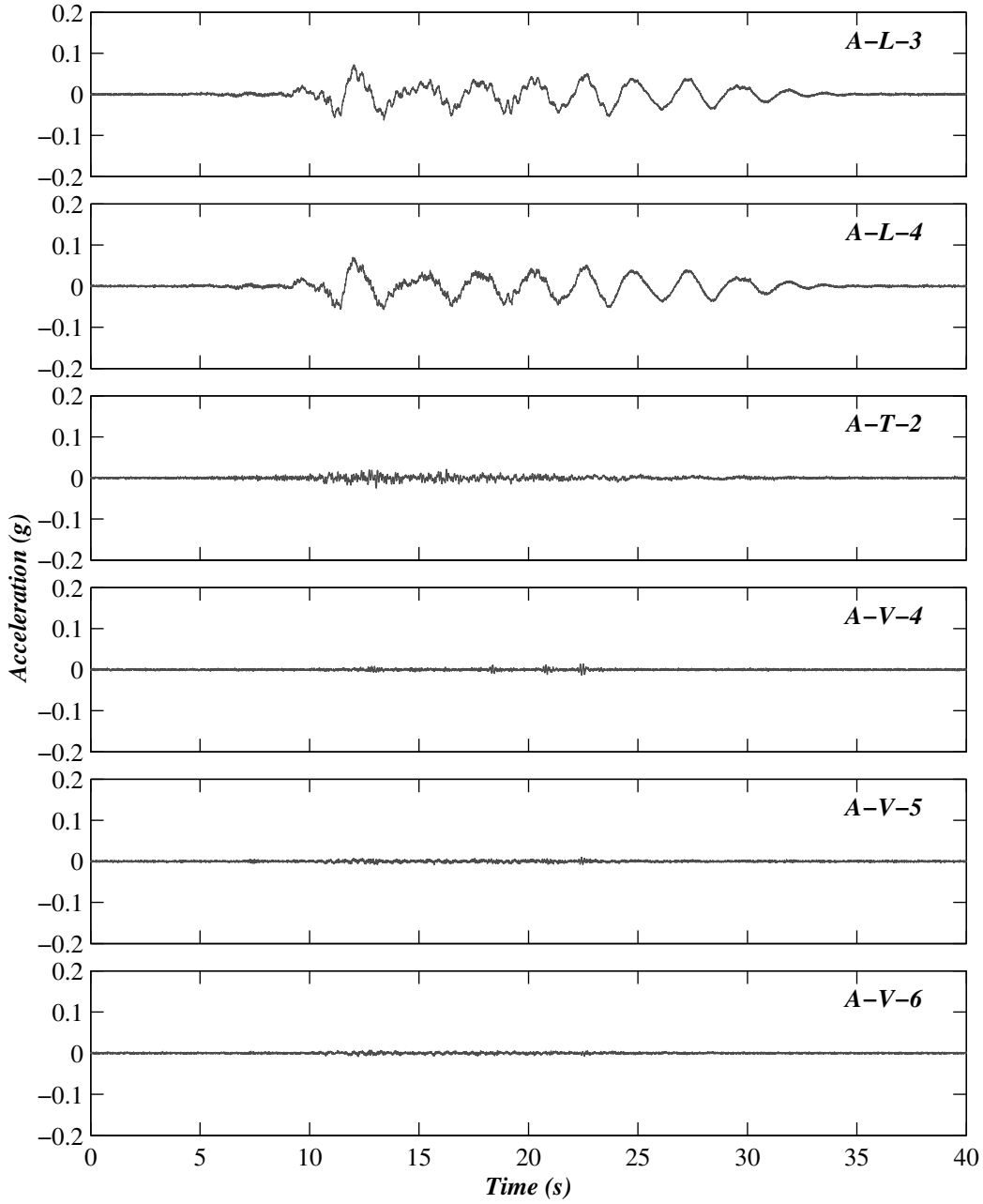

Figure B.3. Acceleration time history responses of the landing at level 2 during test BI-1.

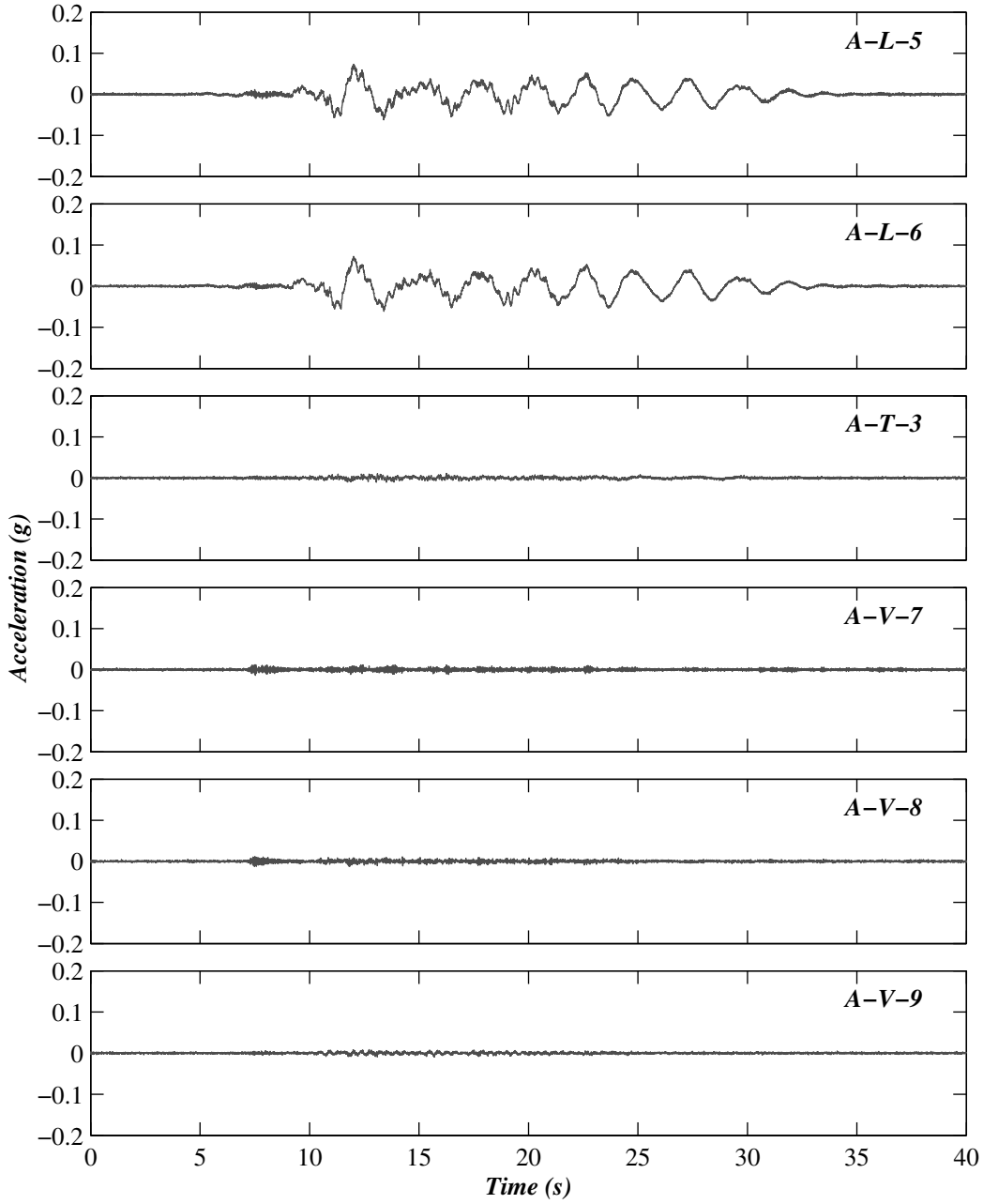

Figure B.4. Acceleration time history responses of the upper flight at level 2 during test BI-1.

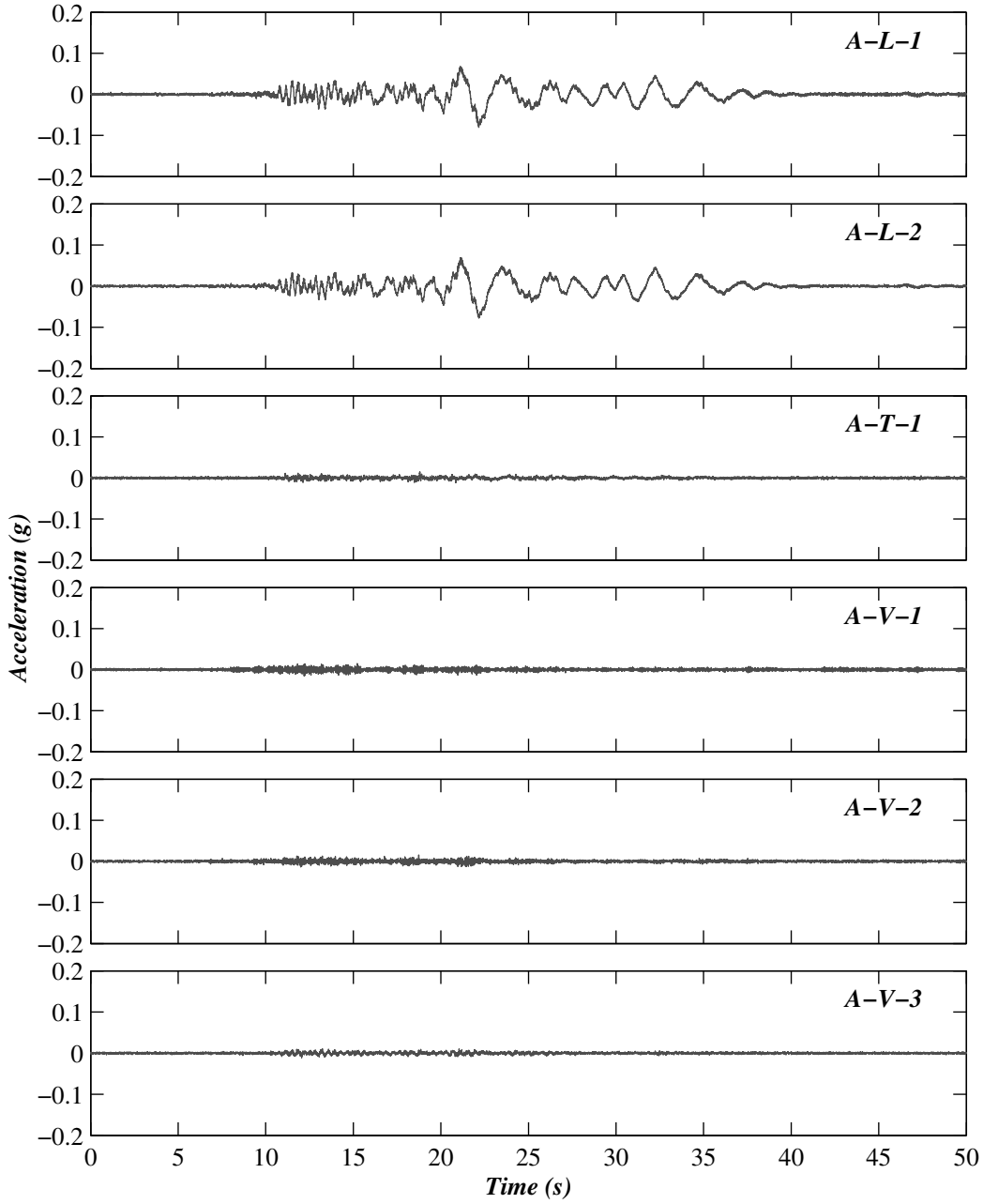

Figure B.5. Acceleration time history responses of the lower flight at level 2 during test BI-2.

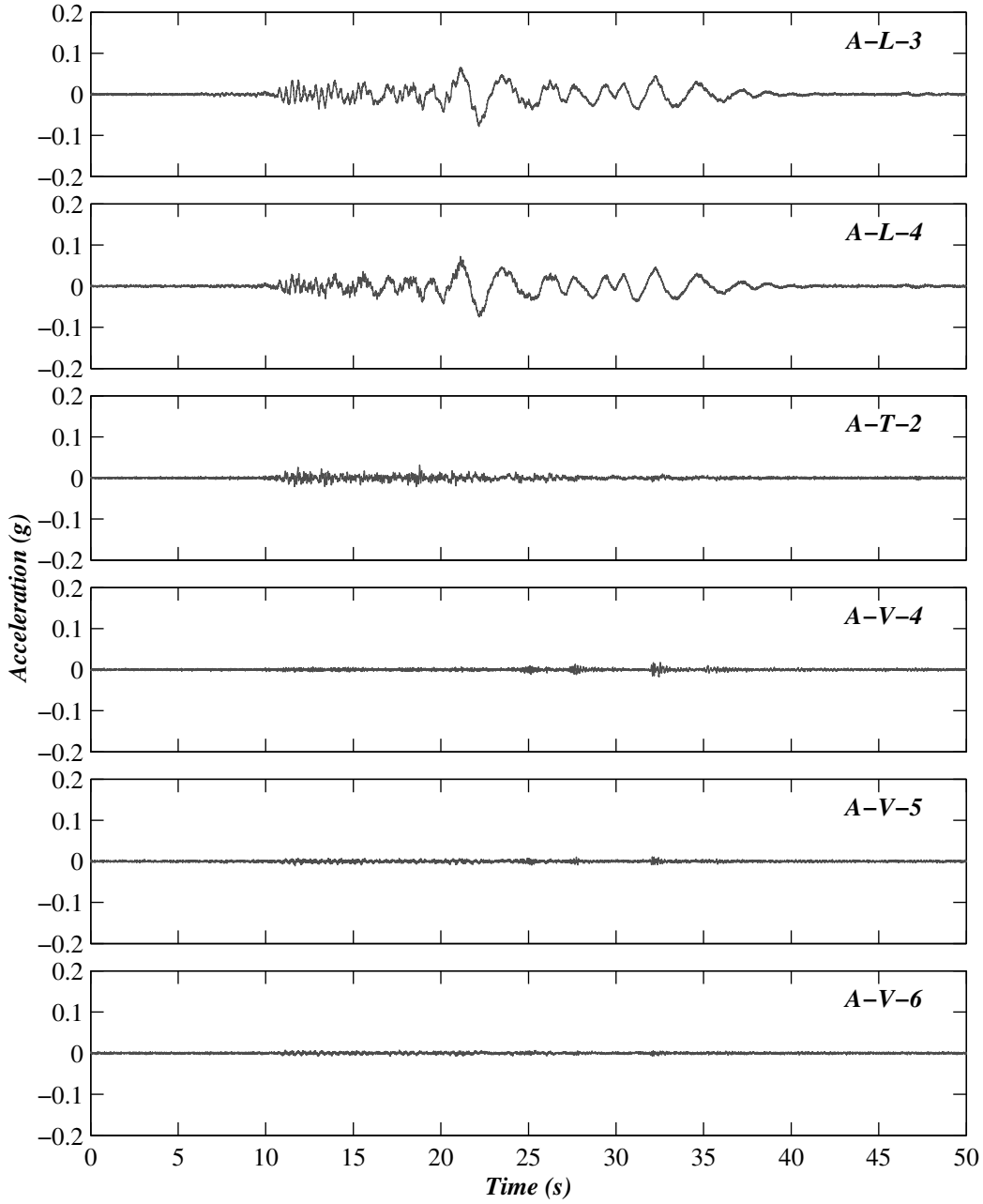

Figure B.6. Acceleration time history responses of stair landing at level 2 during test BI-2.

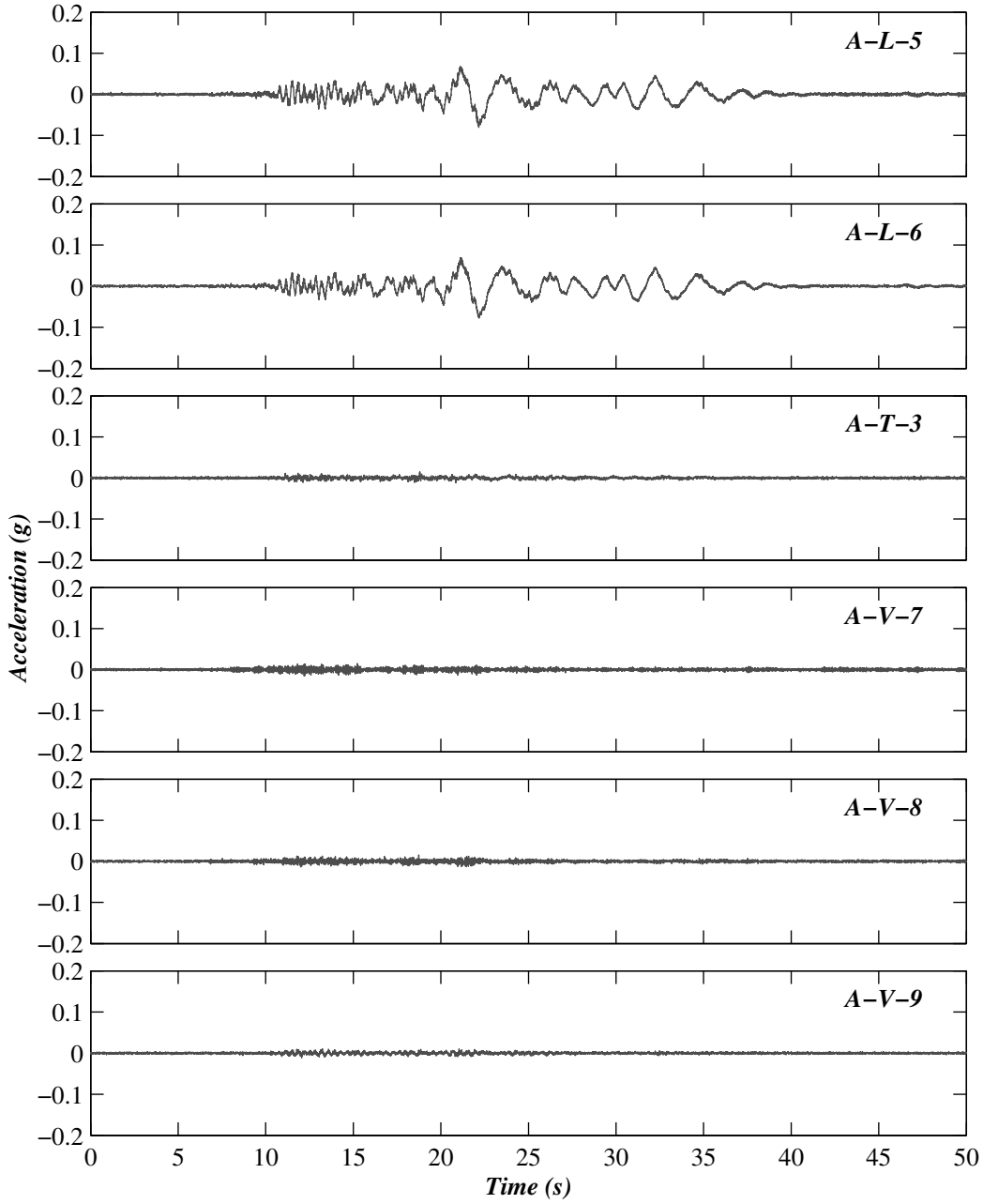

Figure B.7. Acceleration time history responses of the stair upper flight at level 2 during test BI-2.

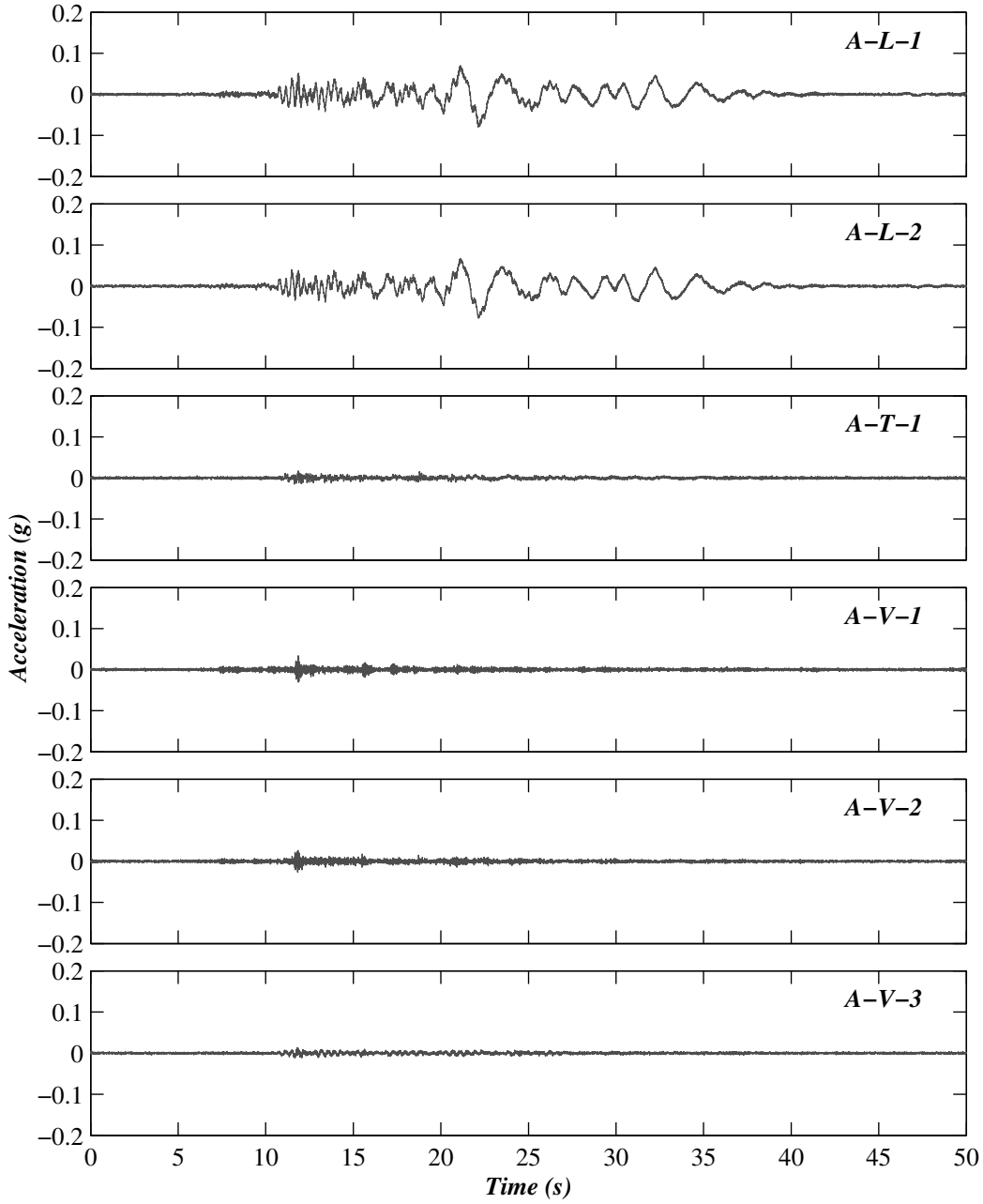

Figure B.8. Acceleration time history responses of the lower flight at level 2 during test BI-3.

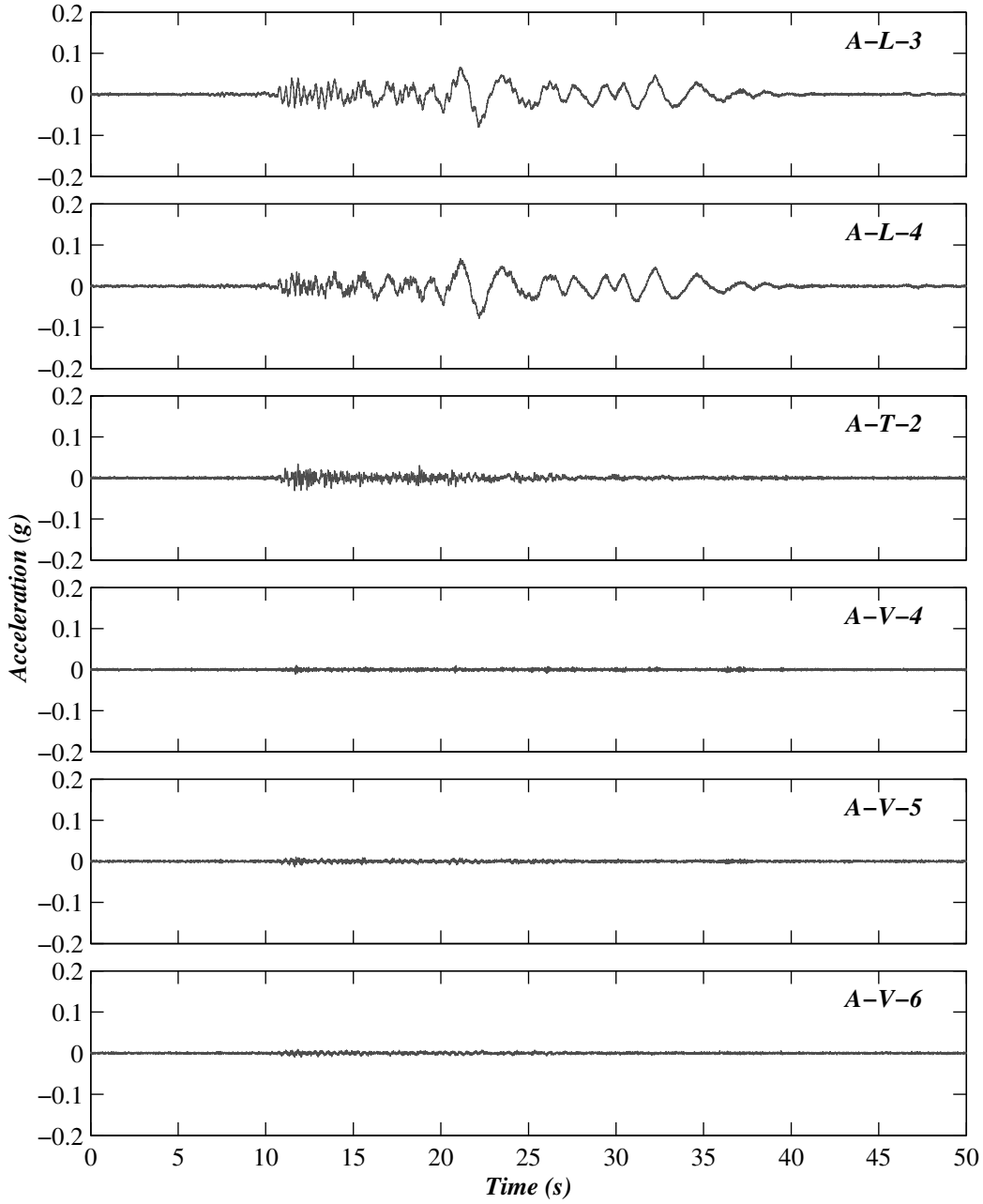

Figure B.9. Acceleration time history responses of stair landing at level 2 during test BI-3.

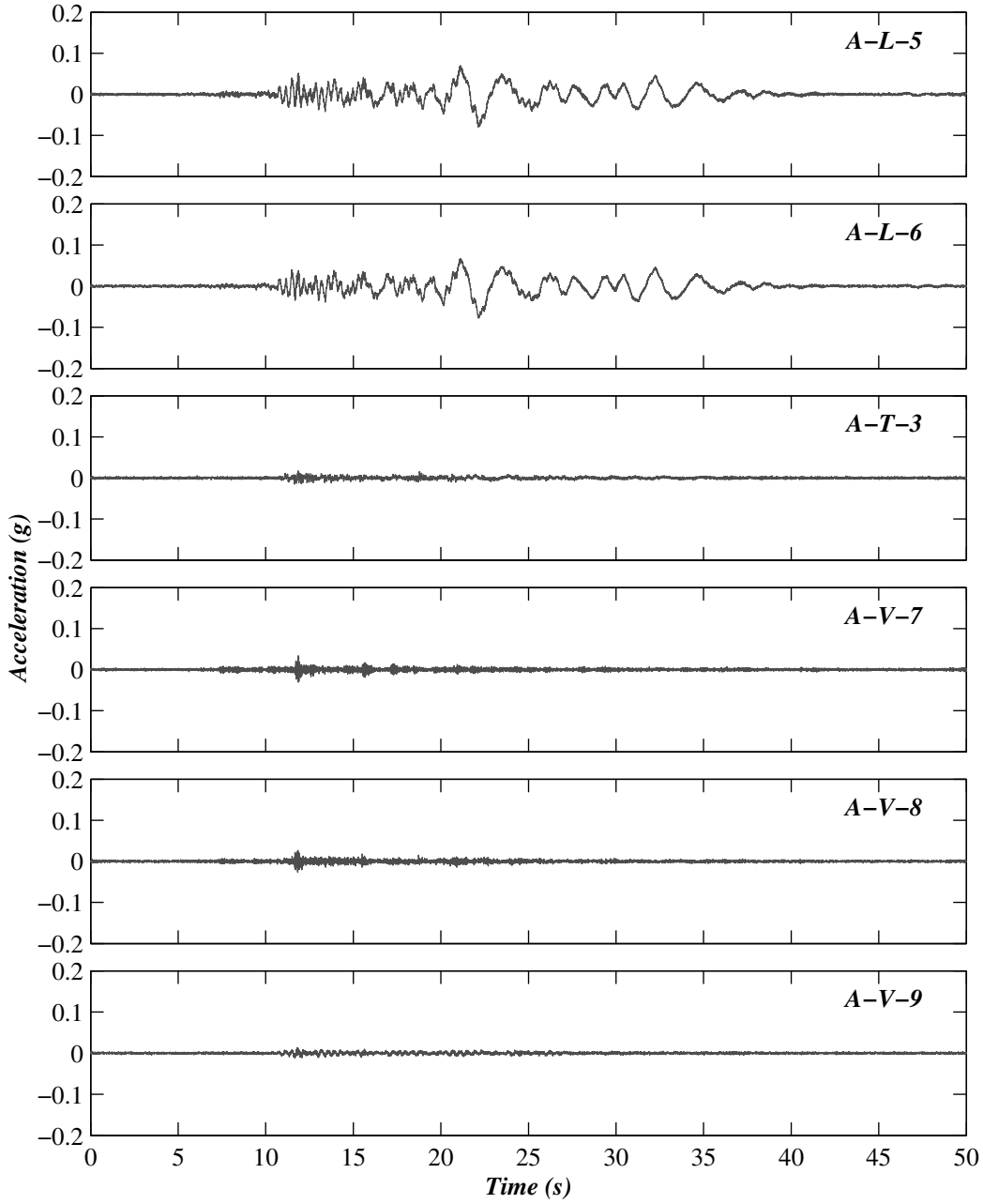

Figure B.10. Acceleration time history responses of the stair upper flight at level 2 during test BI-3.

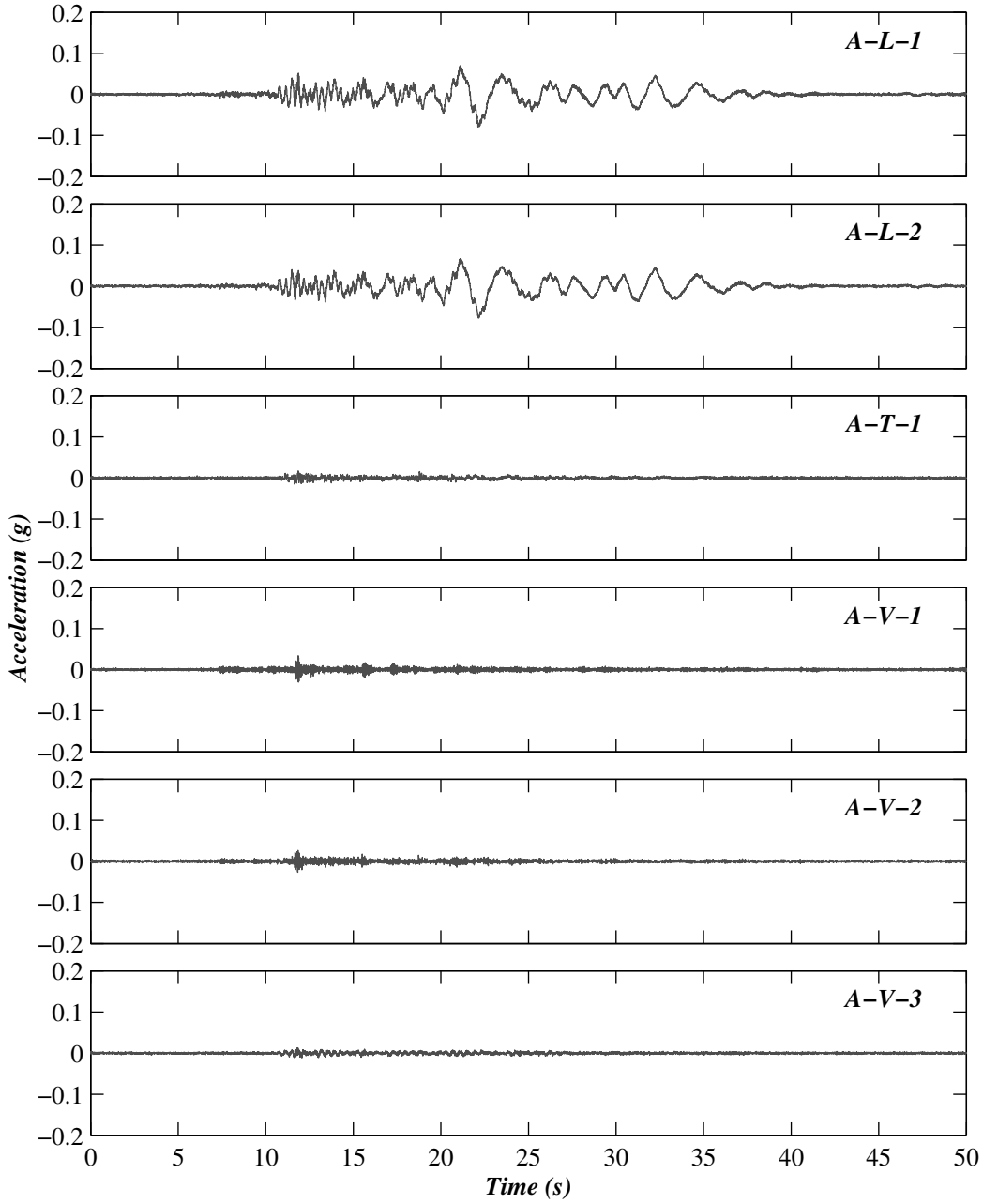

Figure B.11. Acceleration time history responses of the lower flight at level 2 during test BI-4.

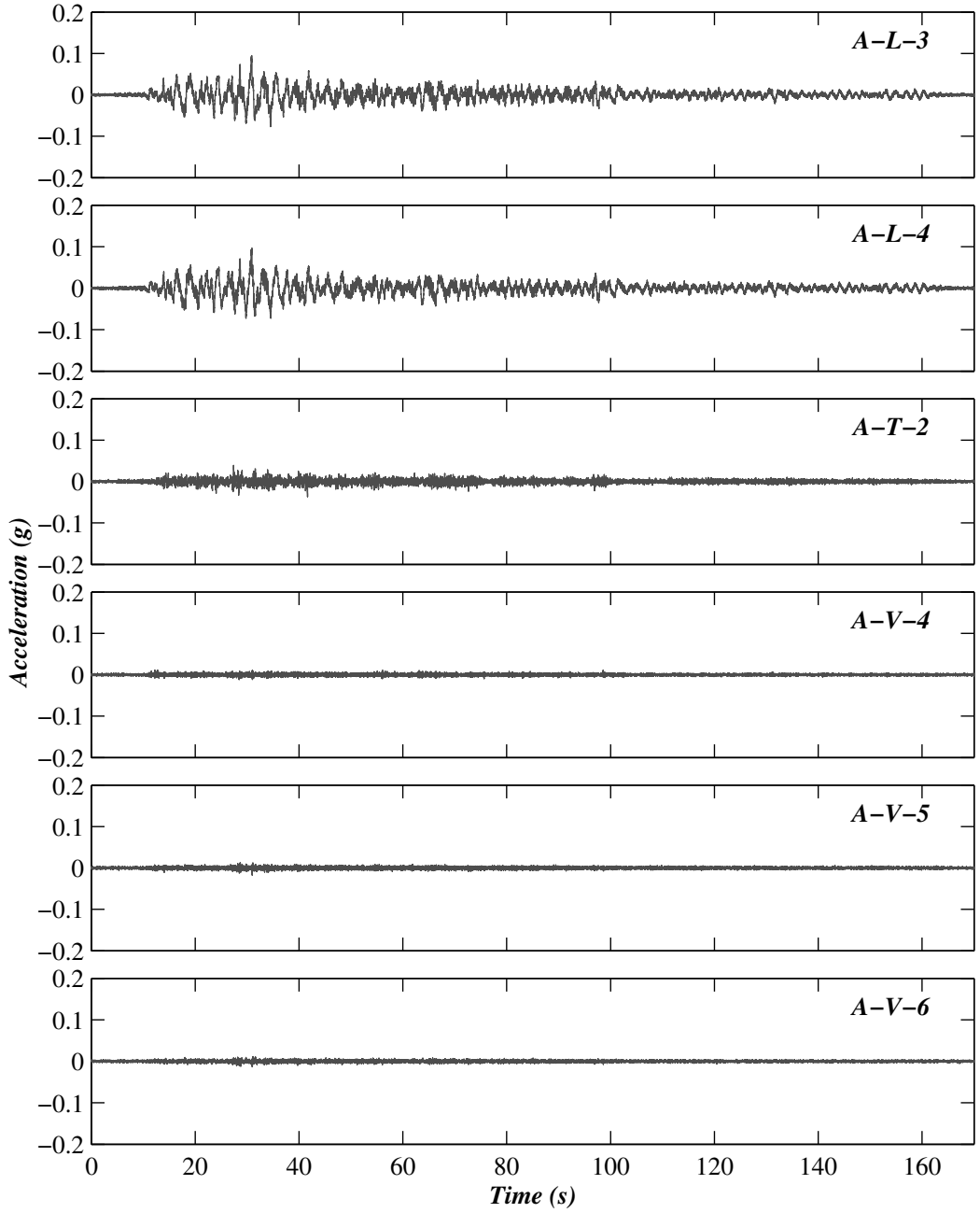

Figure B.12. Acceleration time history responses of stair landing at level 2 during test BI-4.

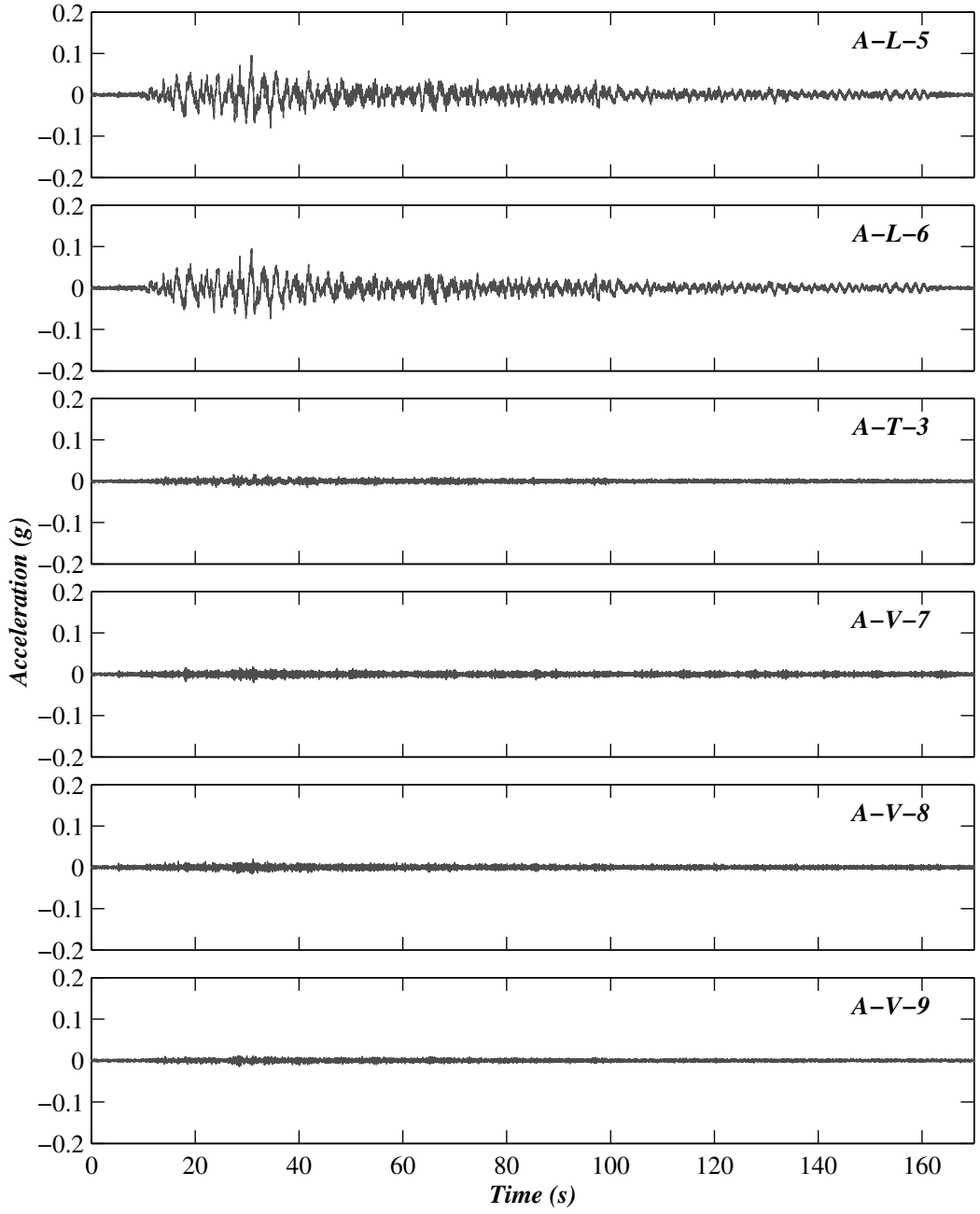

Figure B.13. Acceleration time history responses of the stair upper flight at level 2 during test BI-4.

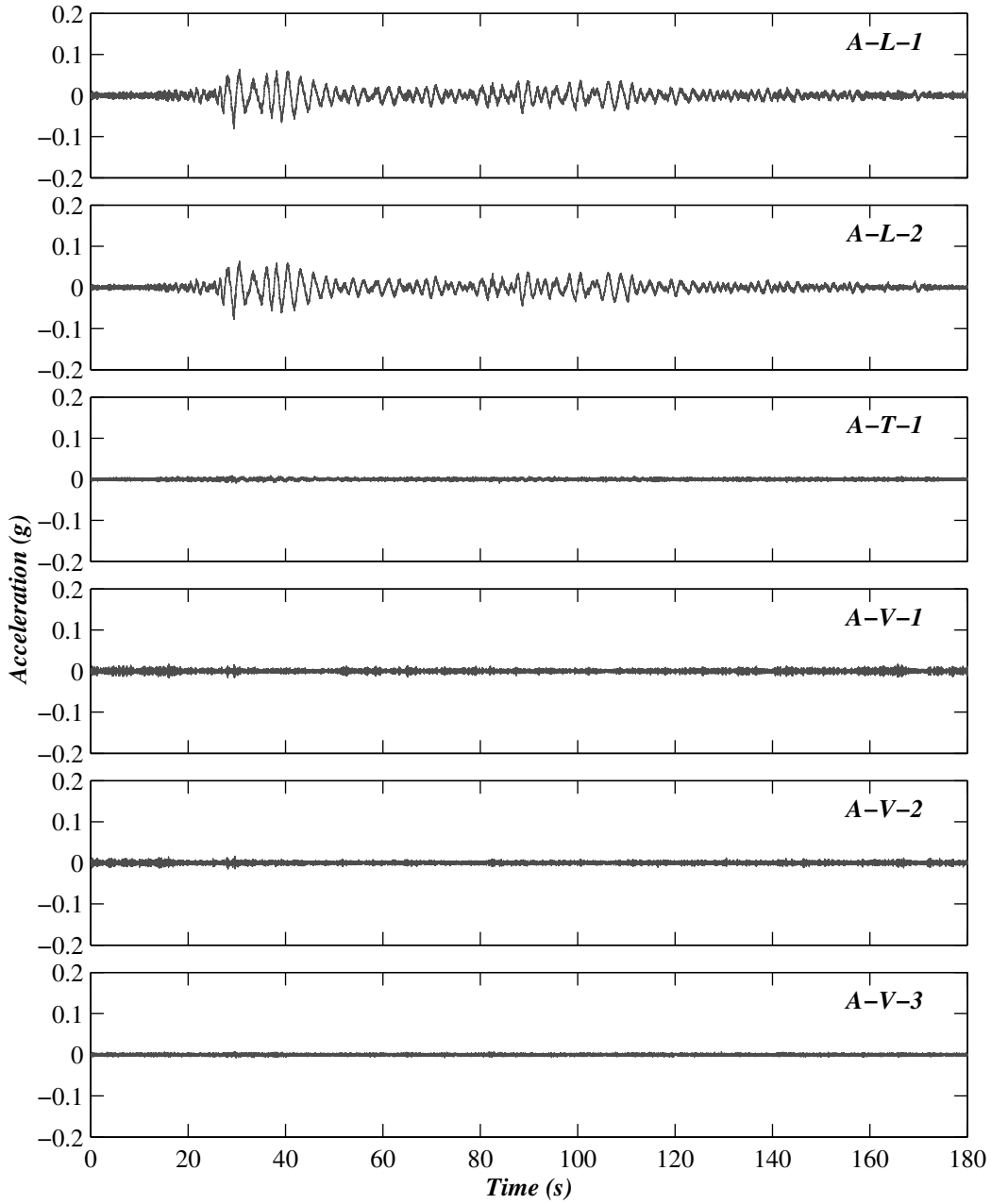

Figure B.14. Acceleration time history responses of the lower flight at level 2 during test BI-5.

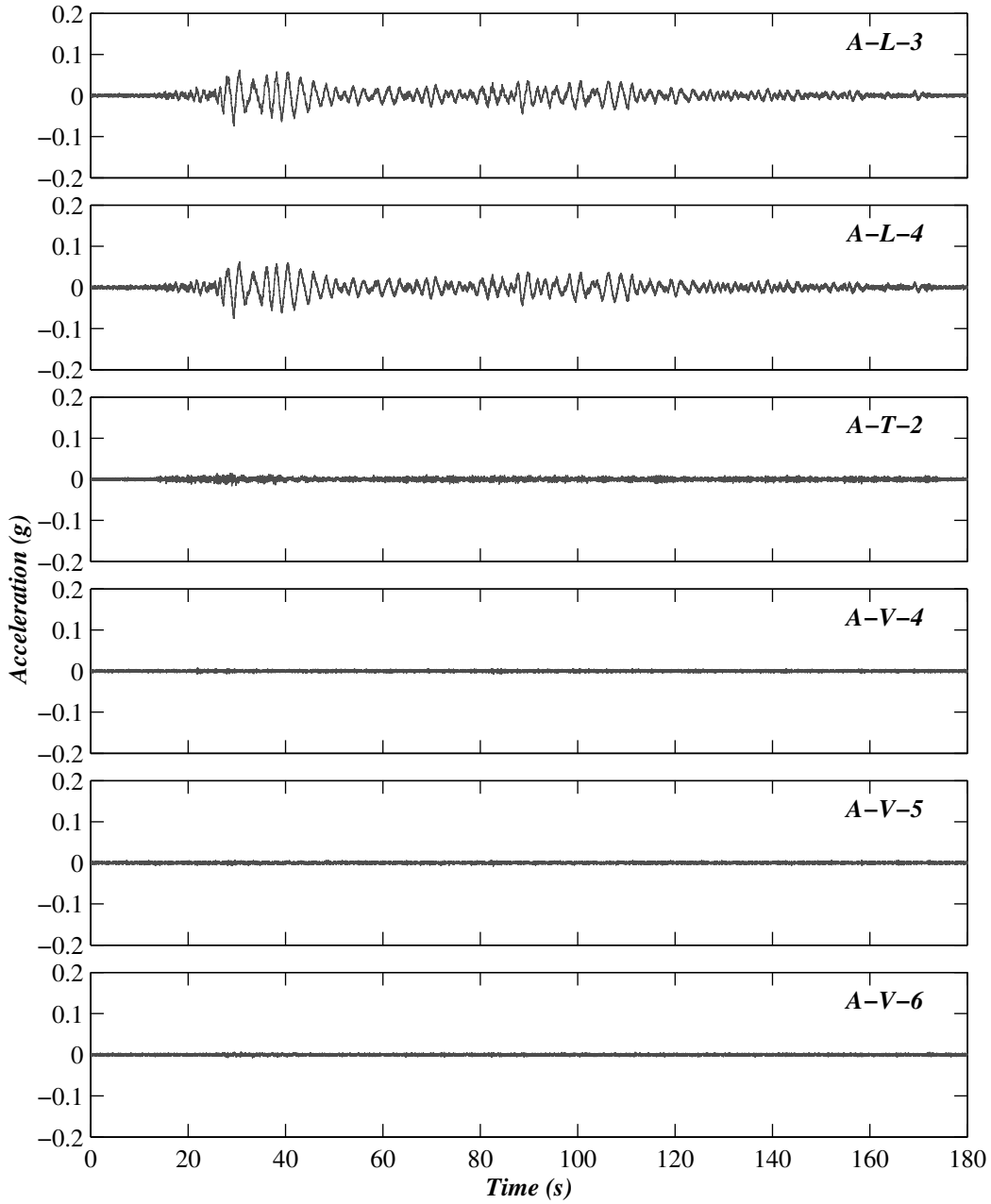

Figure B.15. Acceleration time history responses of stair landing at level 2 during test BI-5.

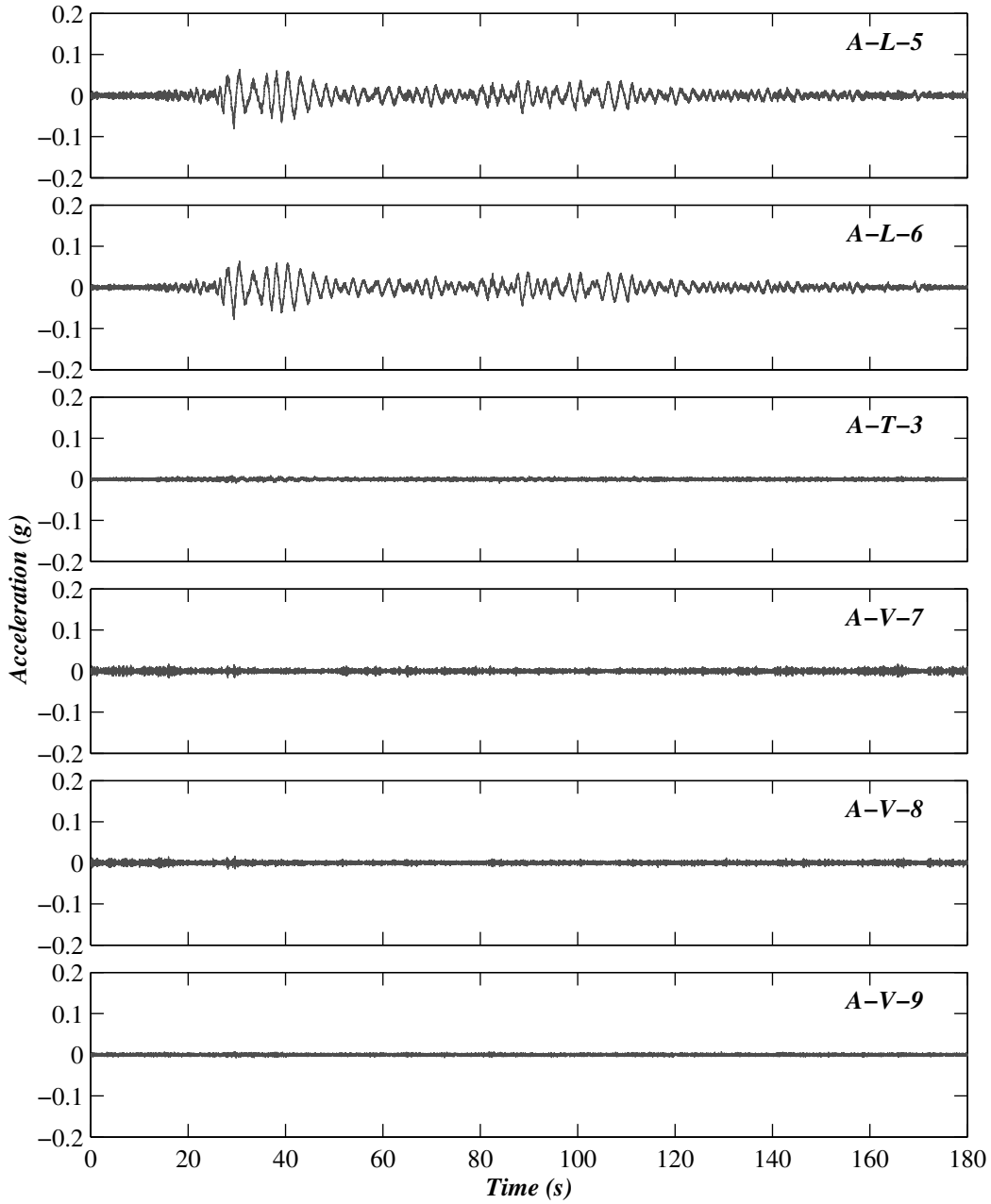

Figure B.16. Acceleration time history responses of the stair upper flight at level 2 during test BI-5.

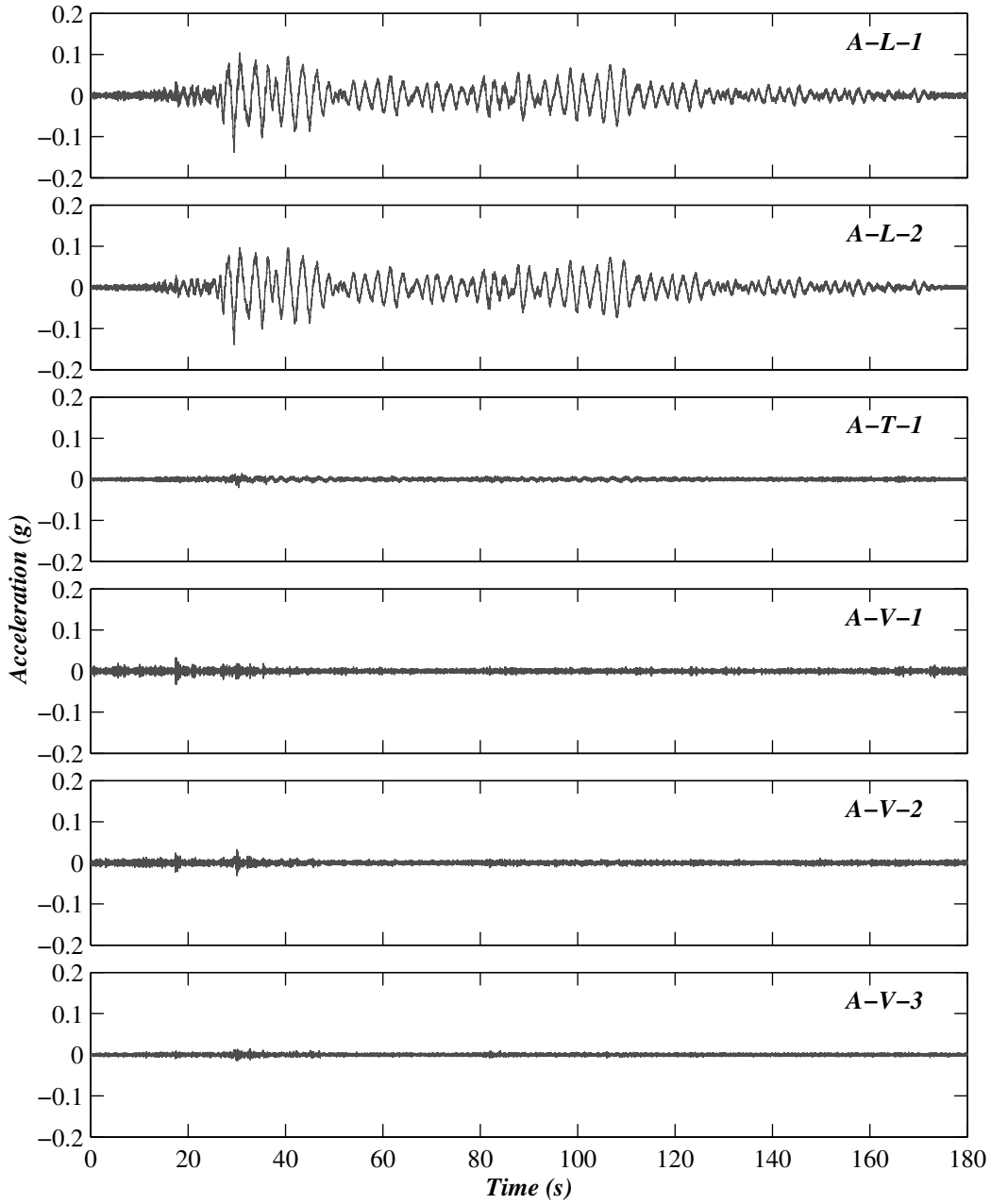

Figure B.17. Acceleration time history responses of the lower flight at level 2 during test BI-6.

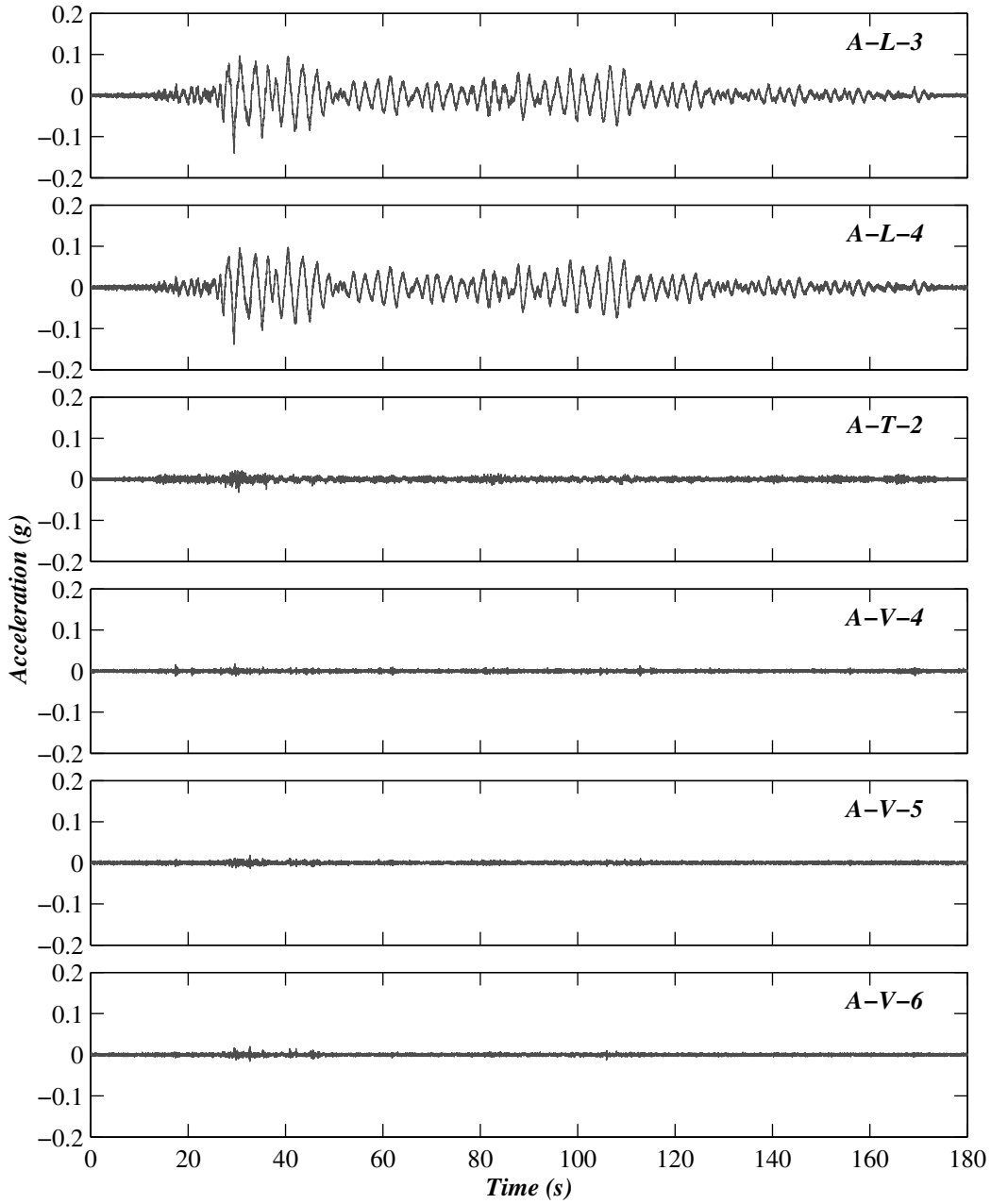

Figure B.18. Acceleration time history responses of stair landing at level 2 during test BI-6.

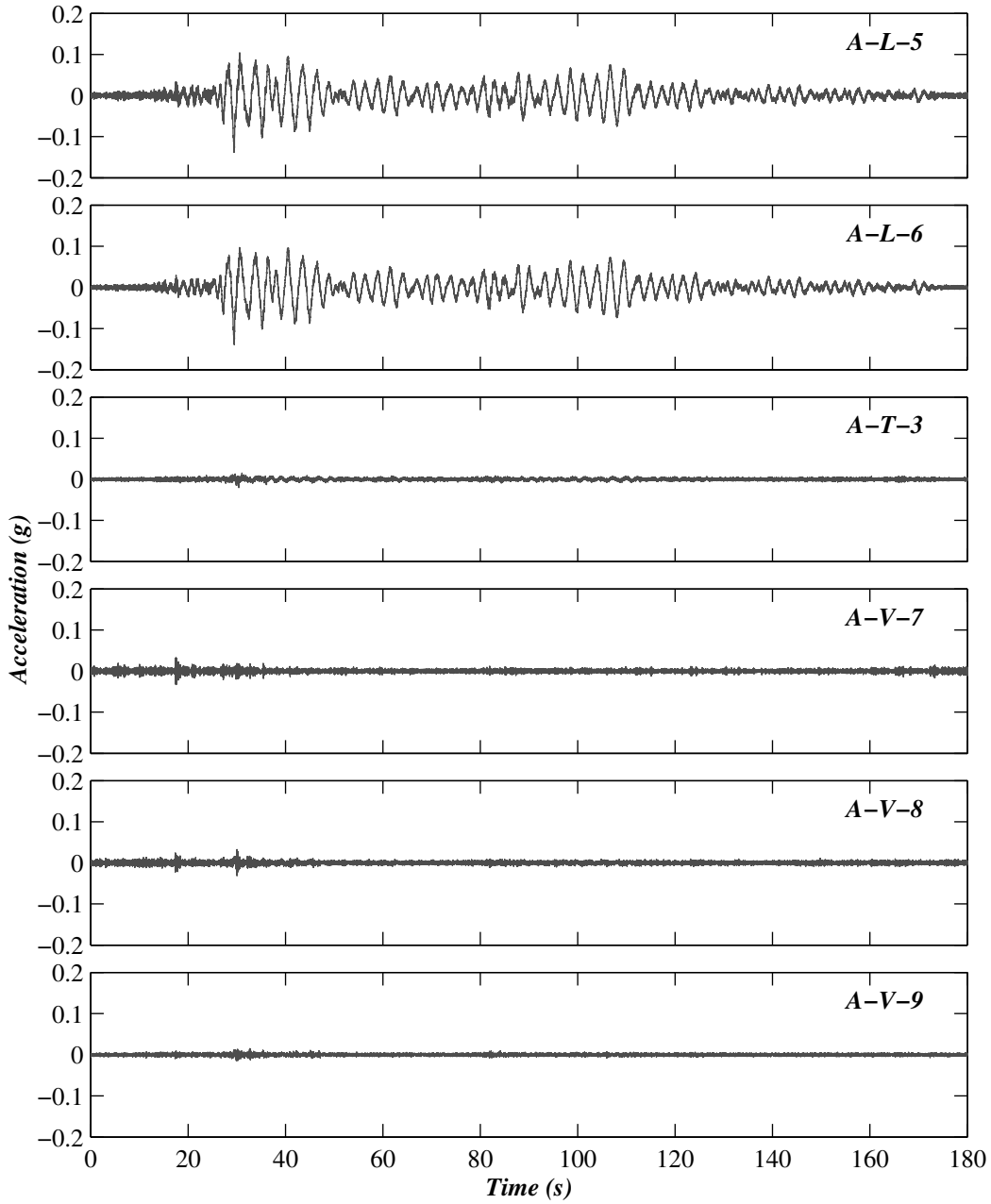

Figure B.19. Acceleration time history responses of the stair upper flight at level 2 during test BI-6.

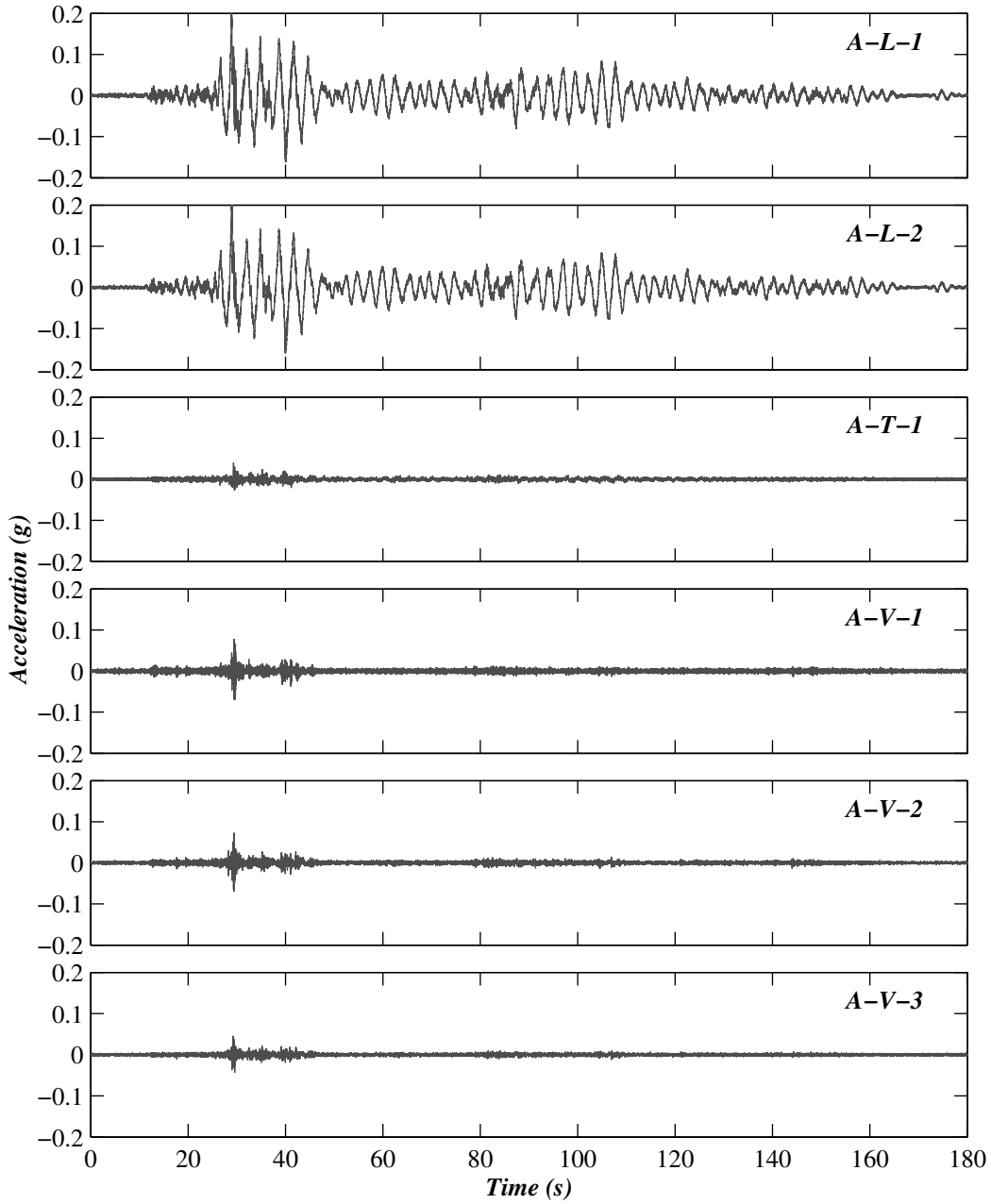

Figure B.20. Acceleration time history responses of the lower flight at level 2 during test BI-7.

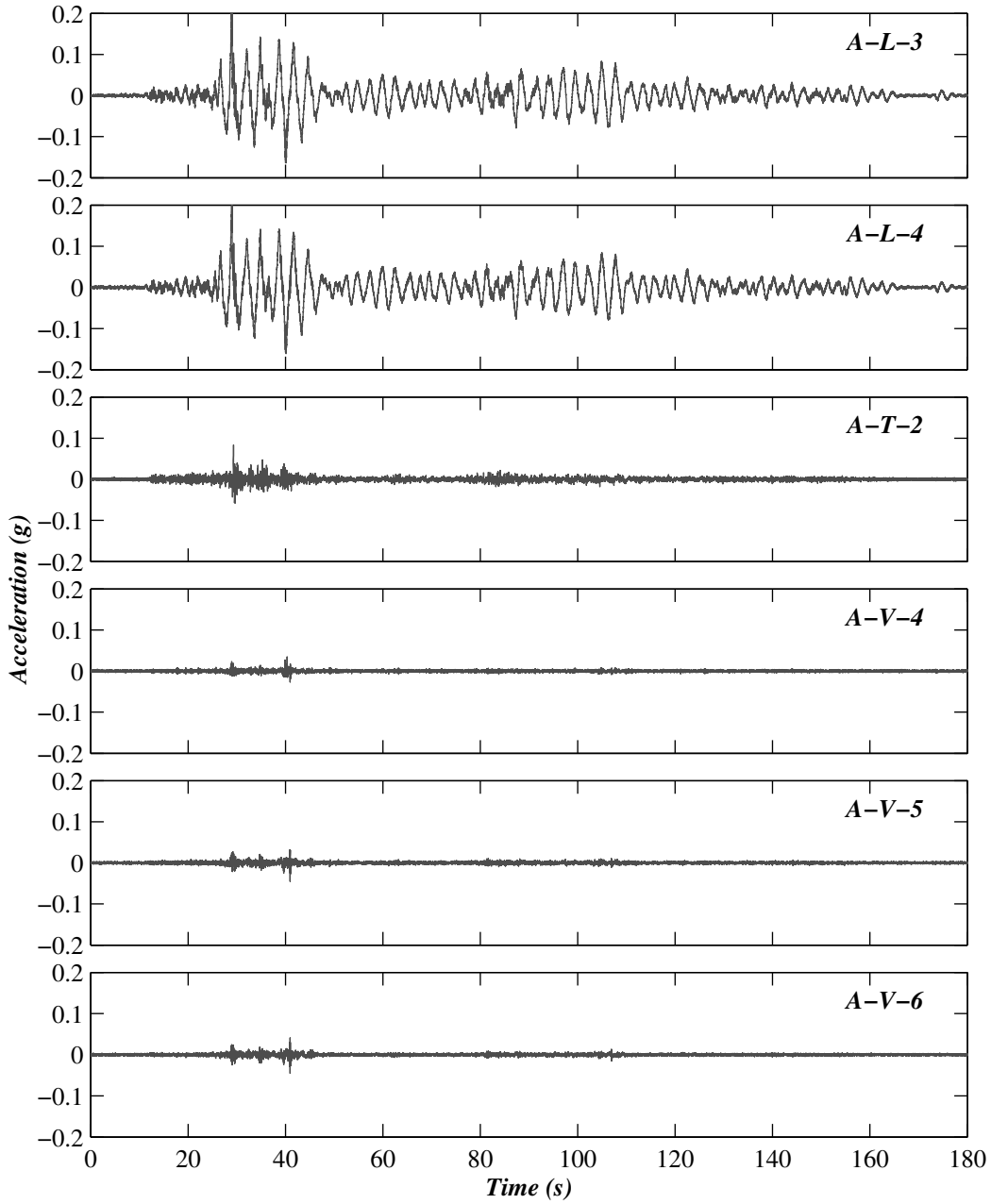

Figure B.21. Acceleration time history responses of stair landing at level 2 during test BI-7.

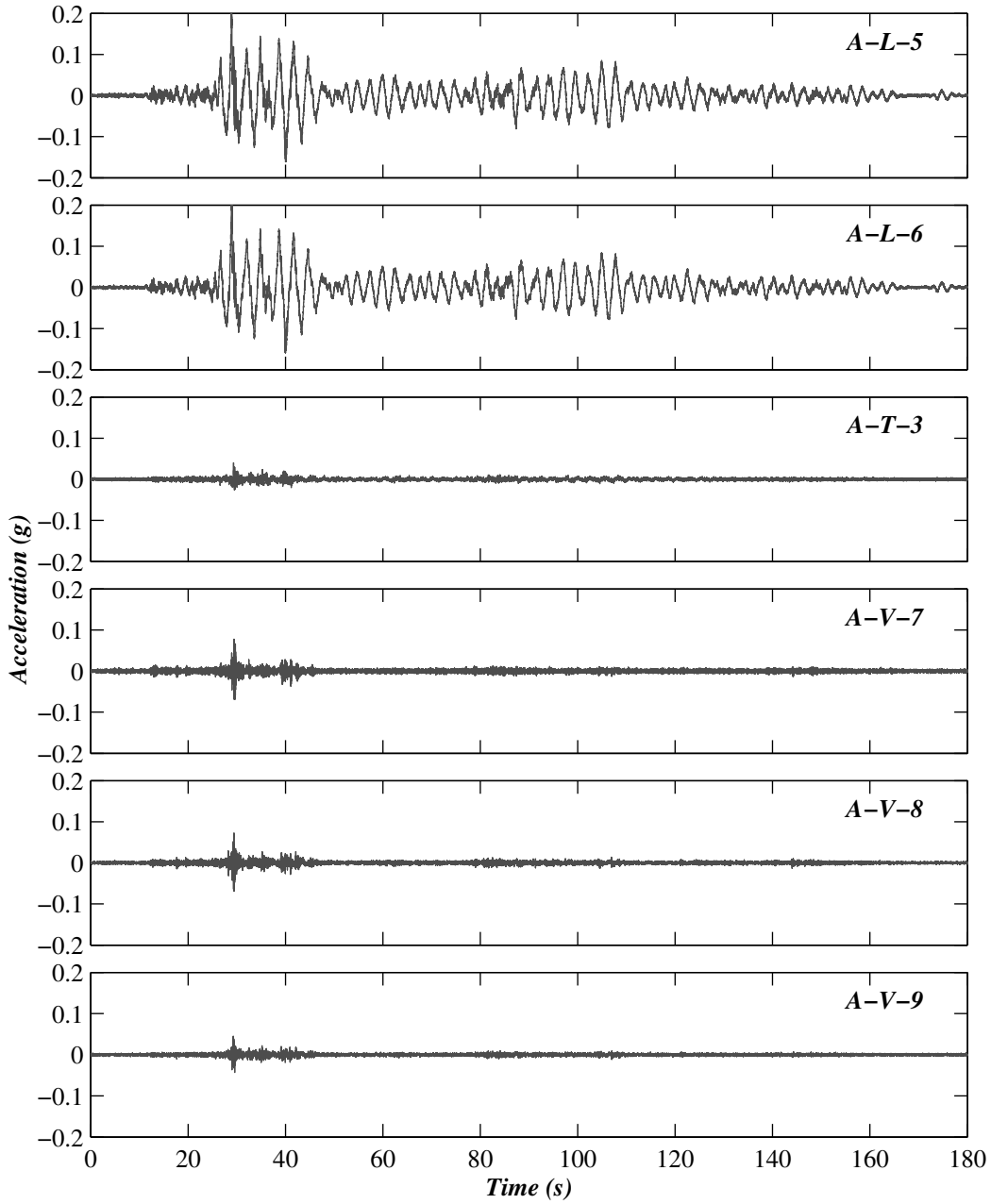

Figure B.22. Acceleration time history responses of the stair upper flight at level 2 during test BI-7.

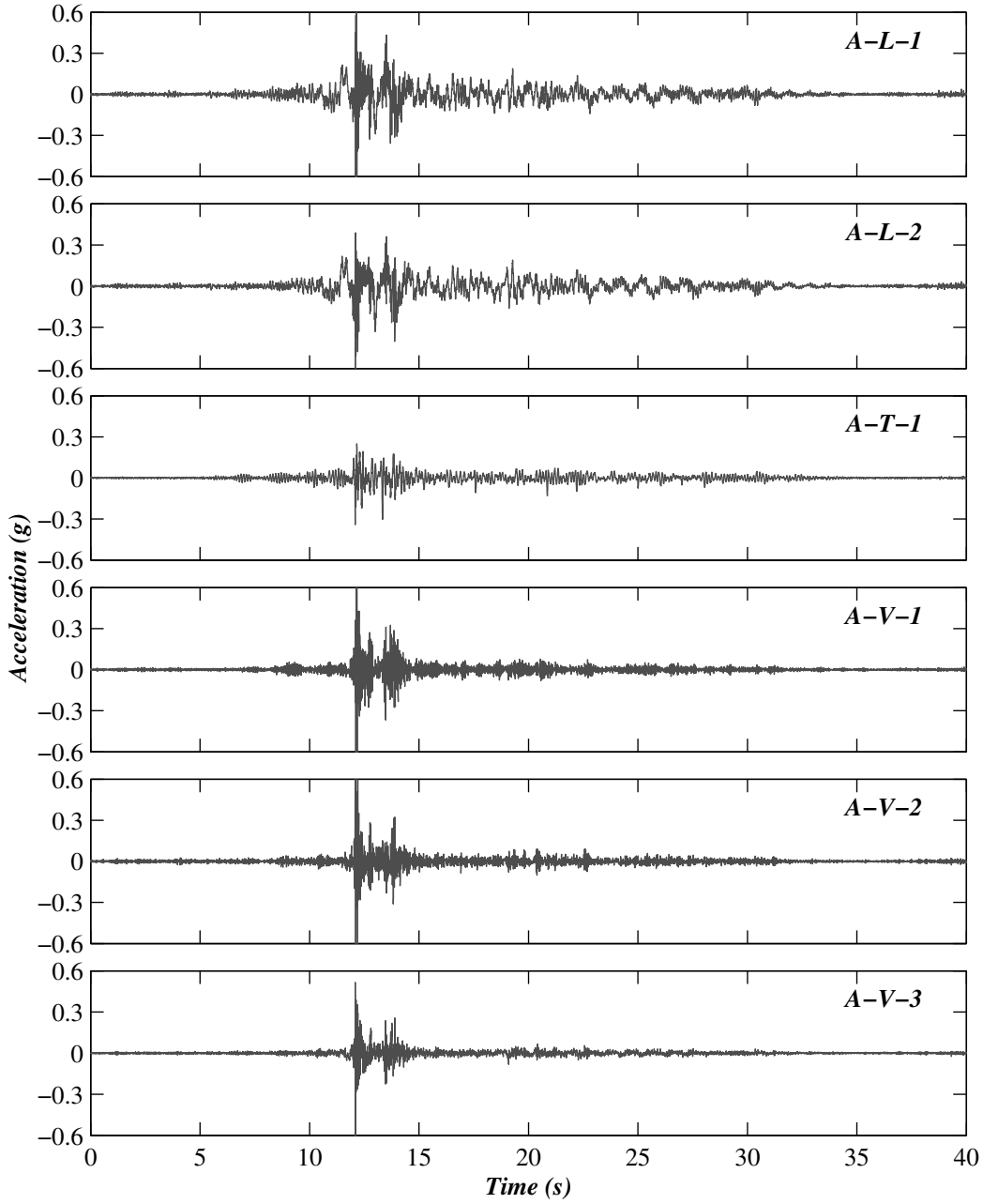

Figure B.23. Acceleration time history responses of the lower flight at level 2 during test FB-1.

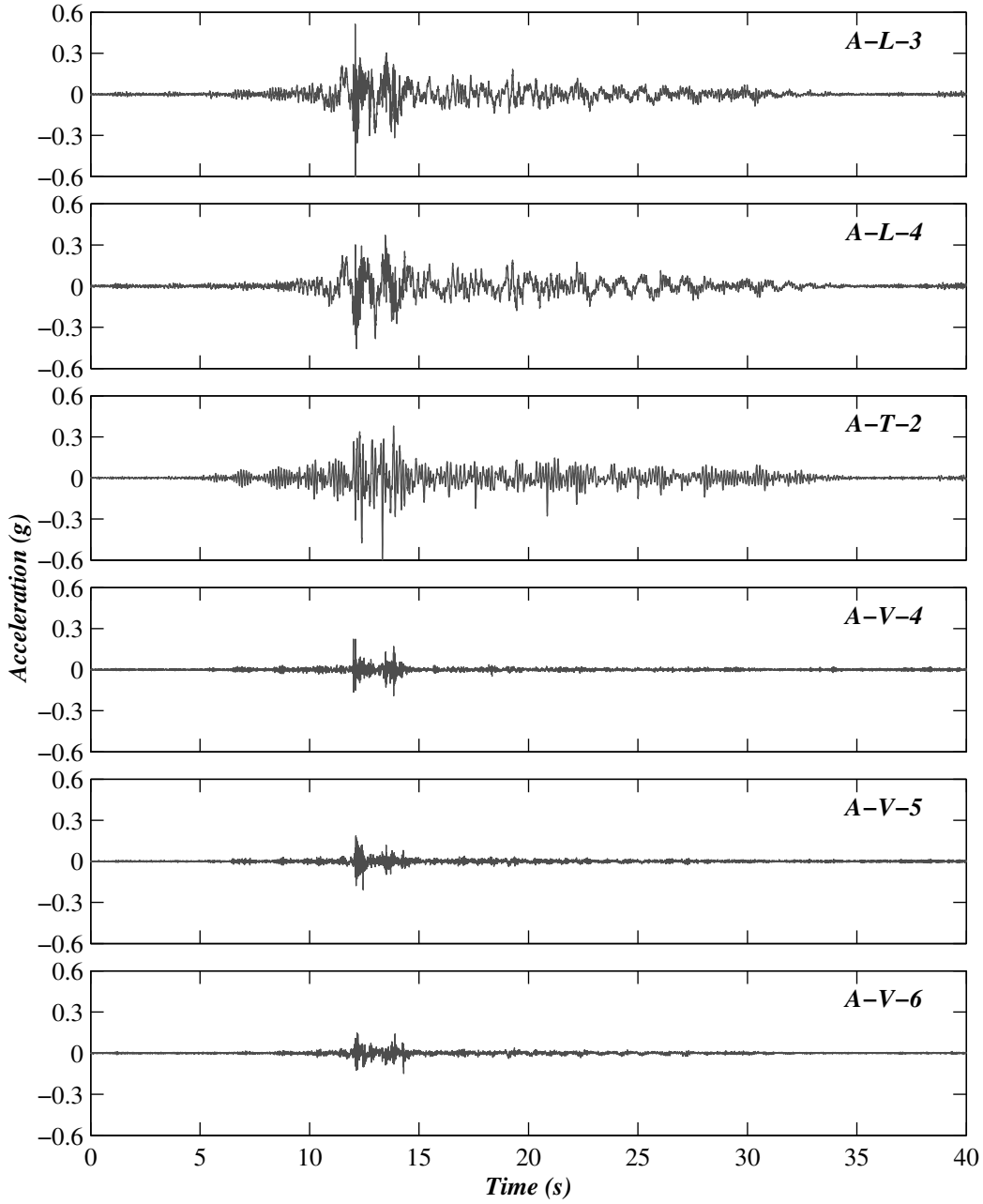

Figure B.24. Acceleration time history responses of the landing at level 2 during test FB-1.

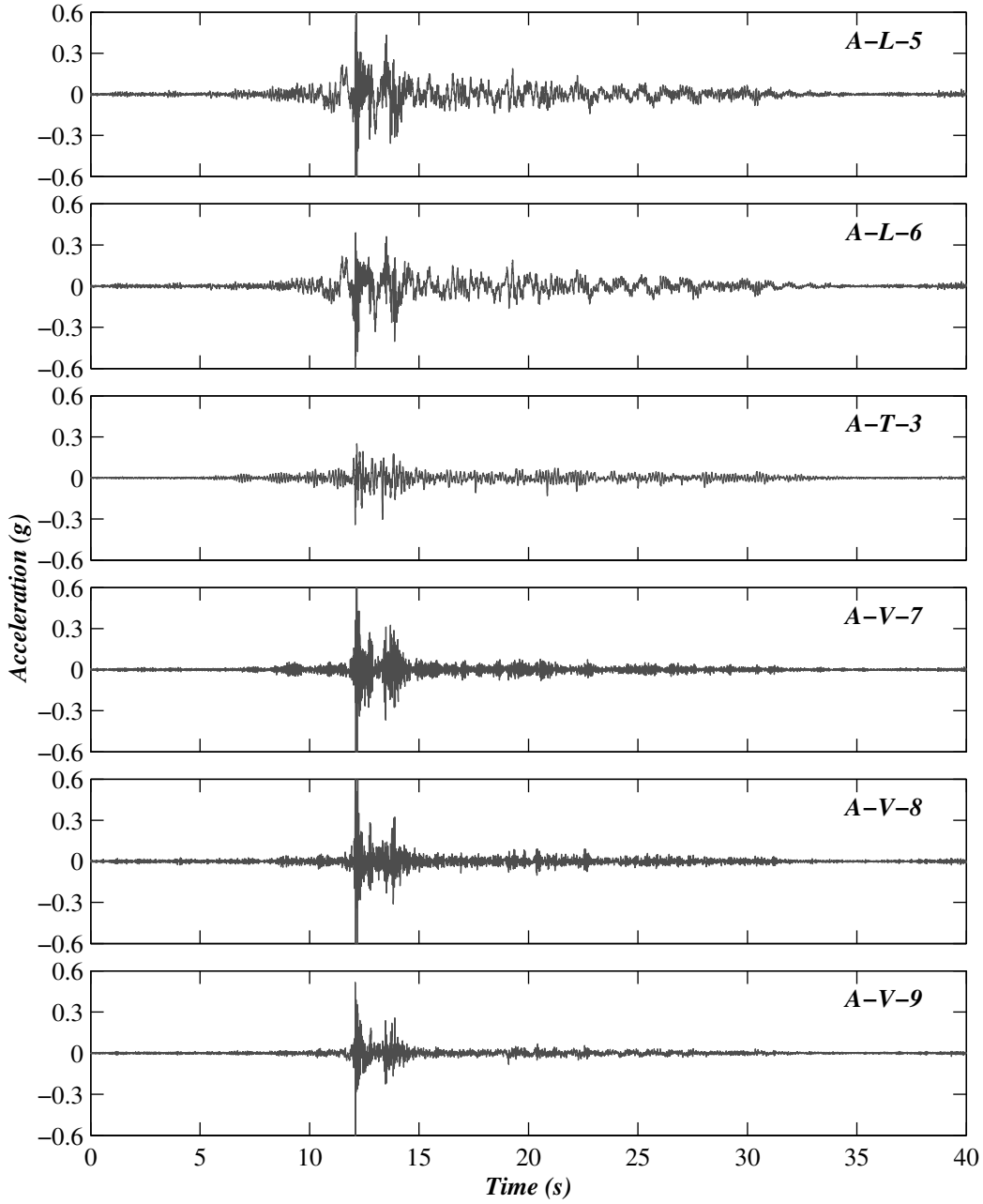

Figure B.25. Acceleration time history responses of the upper flight at level 2 during test FB-1.

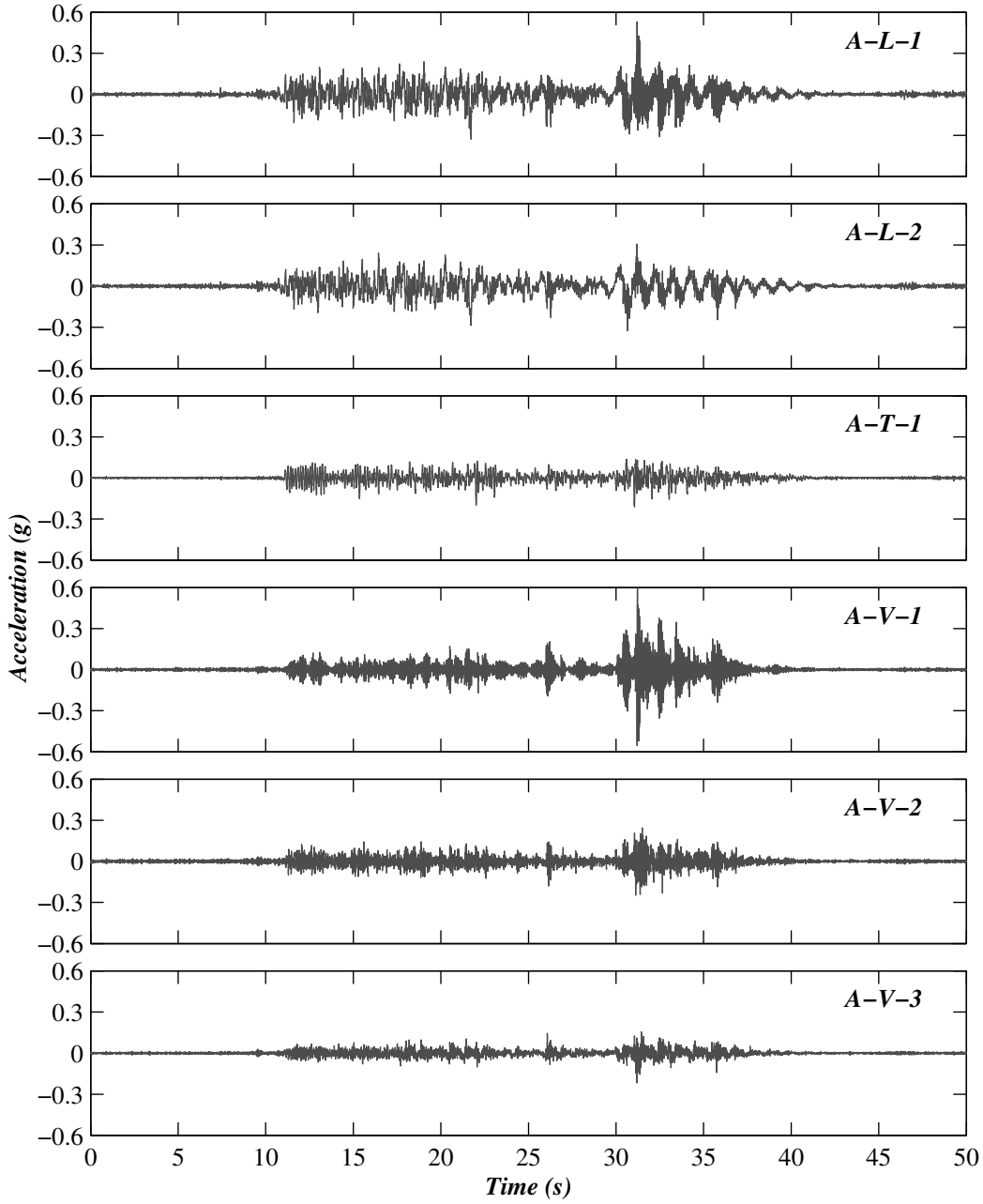

Figure B.26. Acceleration time history responses of the lower flight at level 2 during test FB-2.

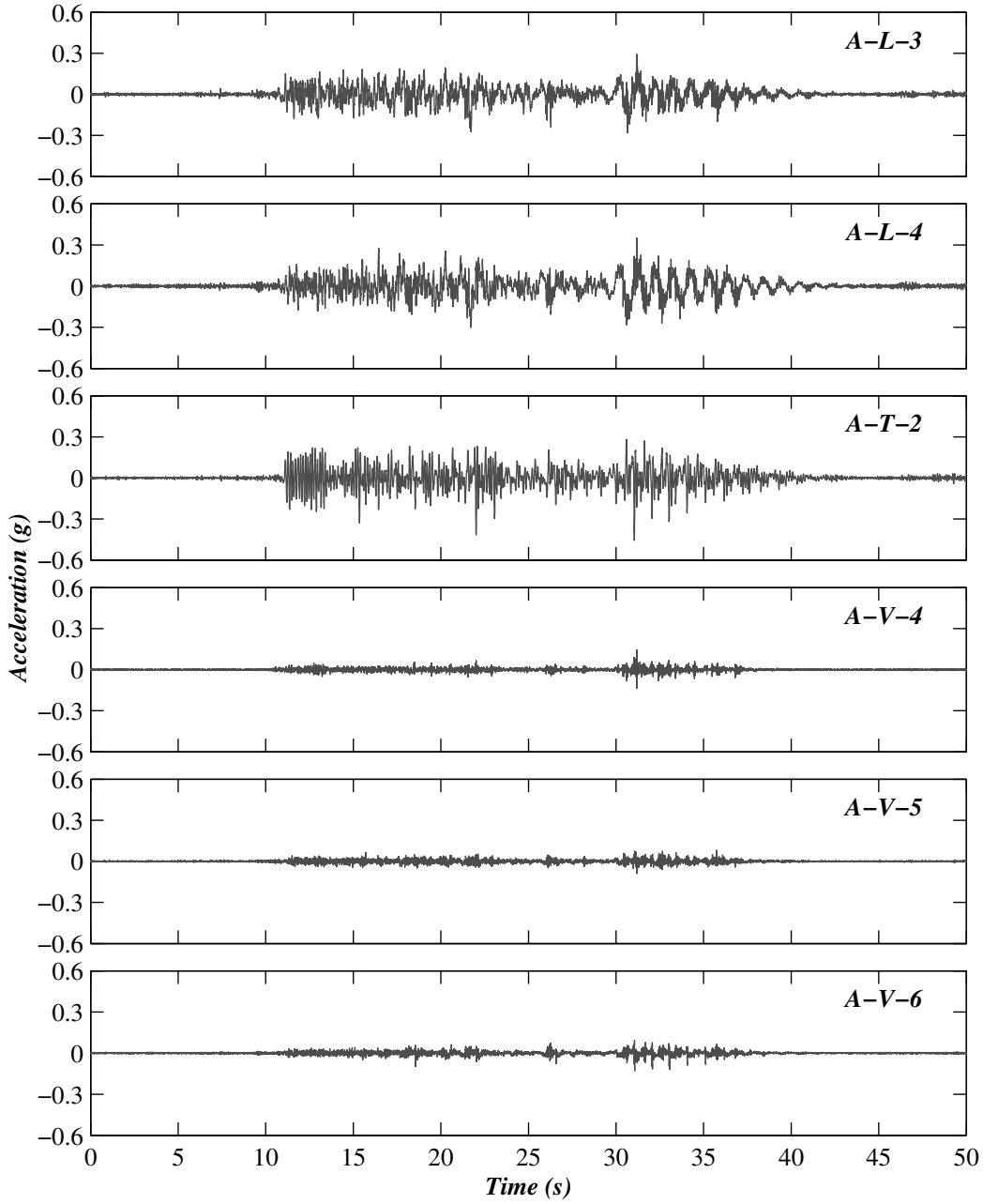

Figure B.27. Acceleration time history responses of stair landing at level 2 during test FB-2.

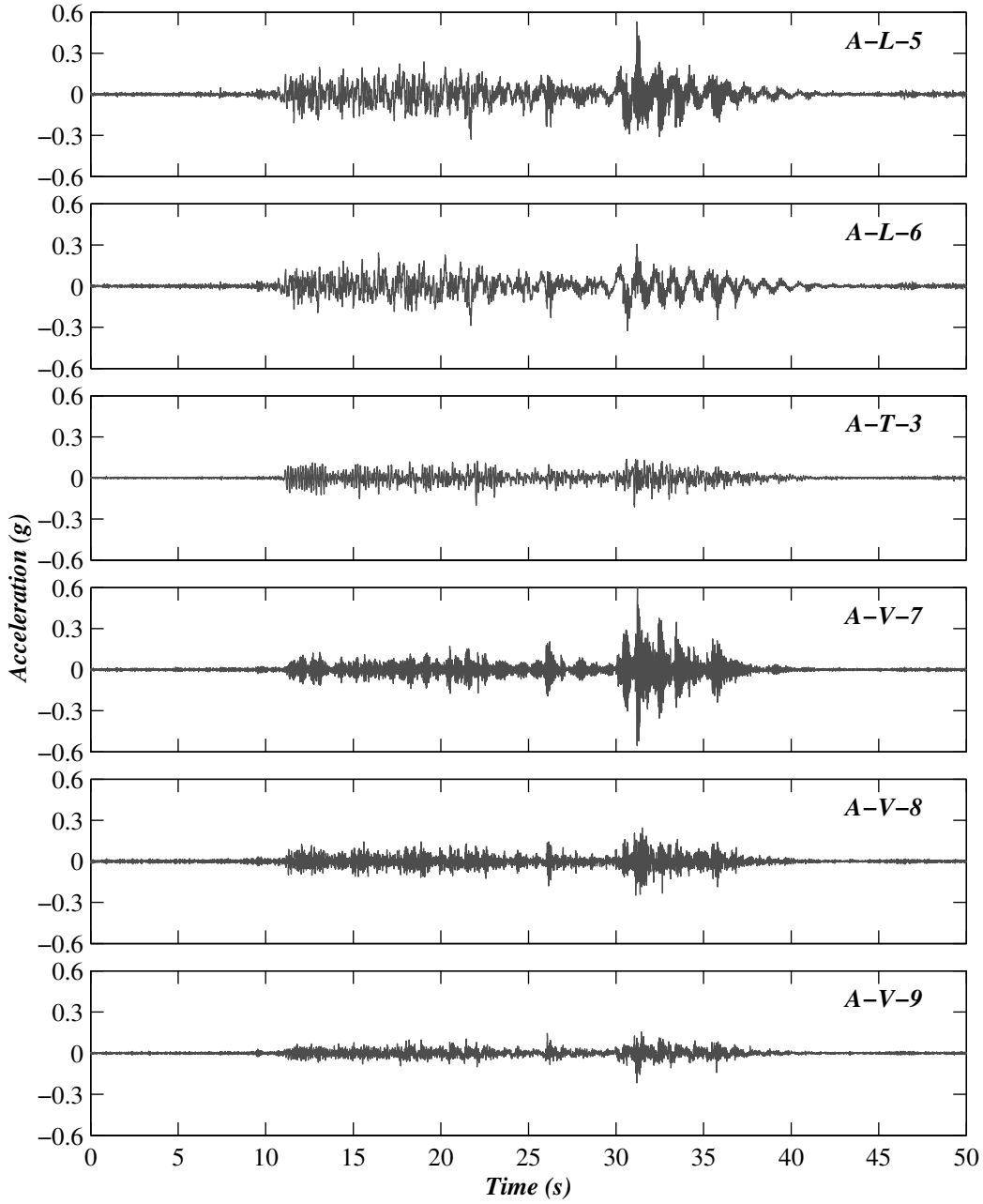

Figure B.28. Acceleration time history responses of the stair upper flight at level 2 during test FB-2.

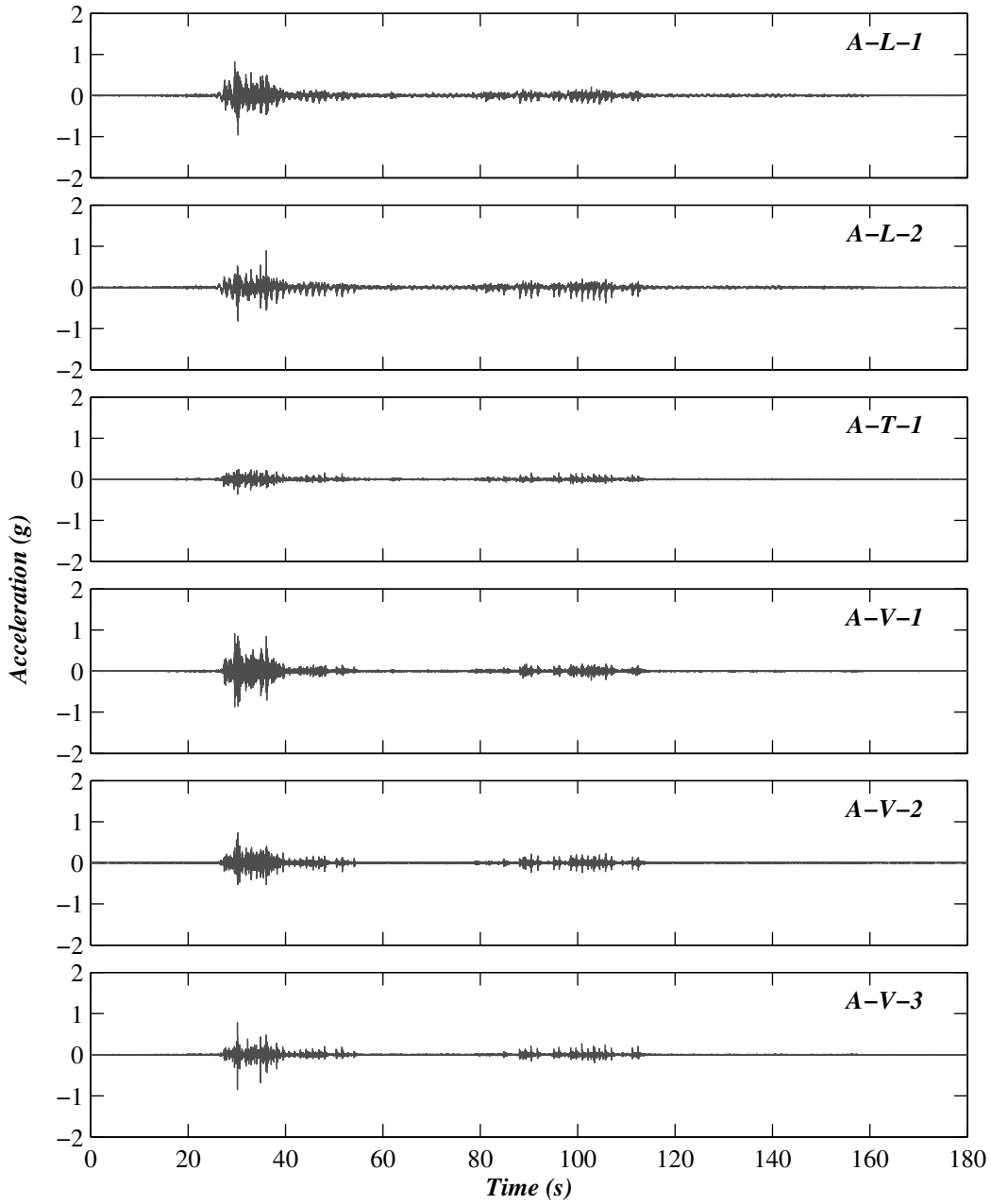

Figure B.29. Acceleration time history responses of the lower flight at level 2 during test FB-3.

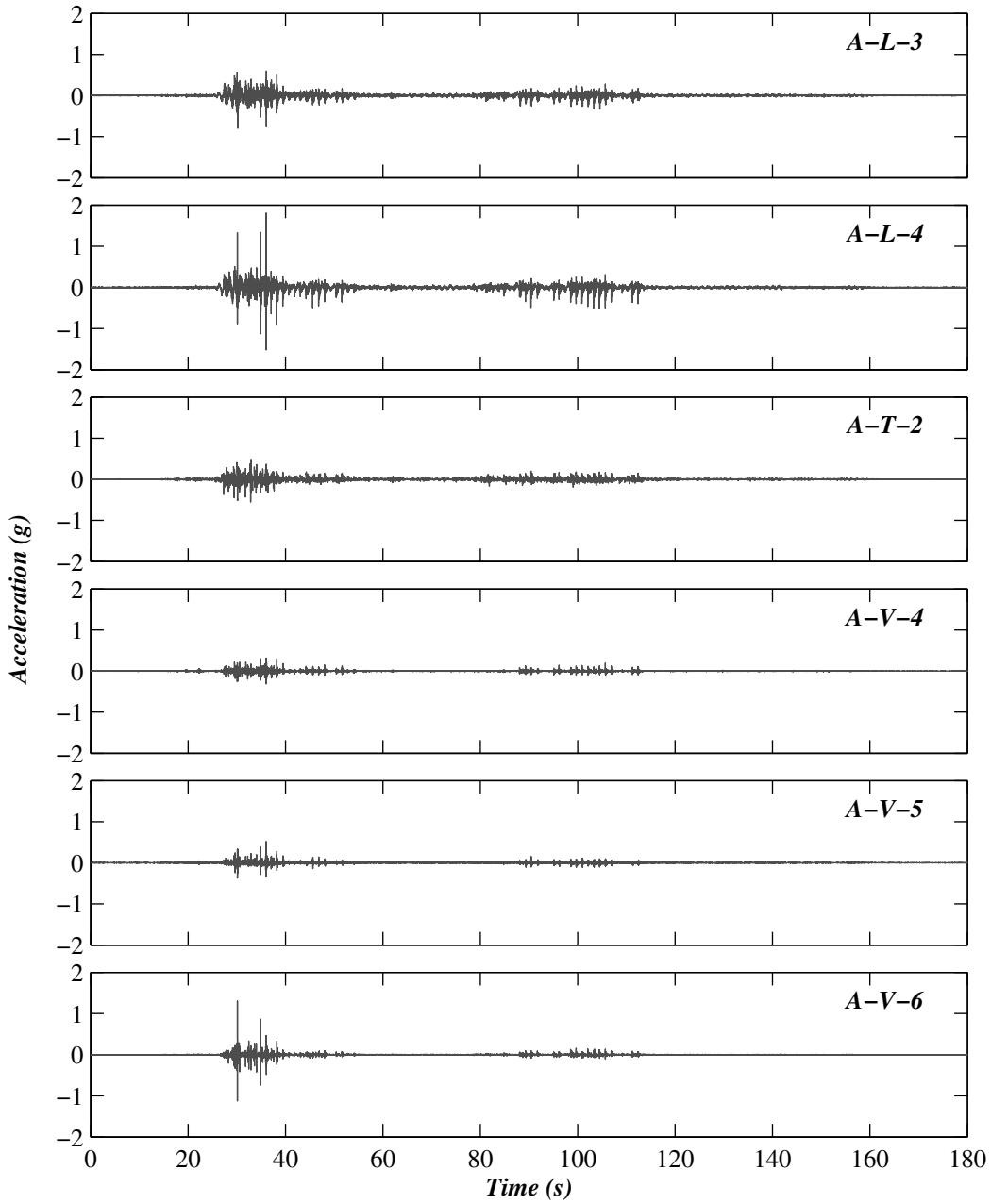

Figure B.30. Acceleration time history responses of stair landing at level 2 during test FB-3.

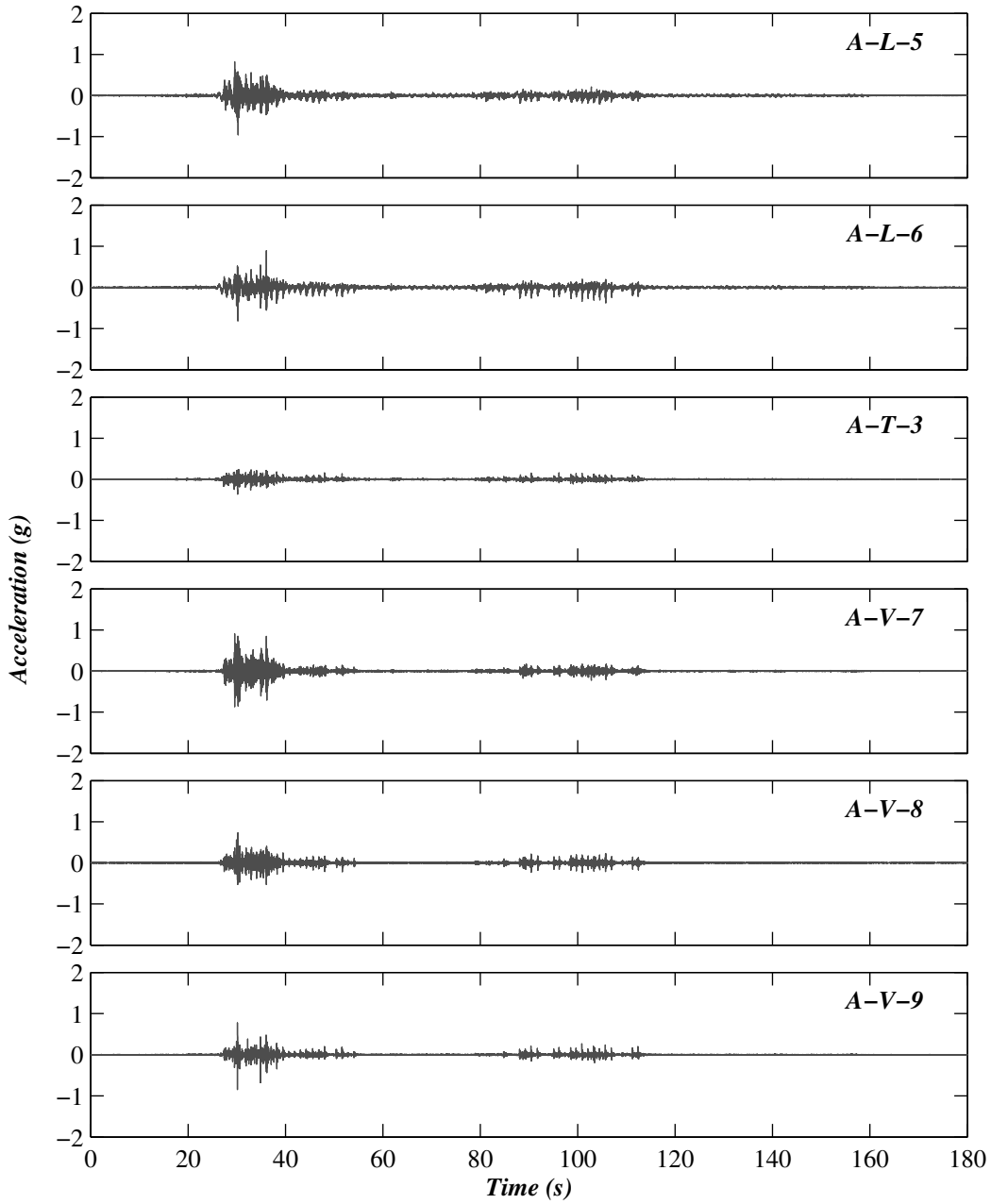

Figure B.31. Acceleration time history responses of the stair upper flight at level 2 during test FB-3.

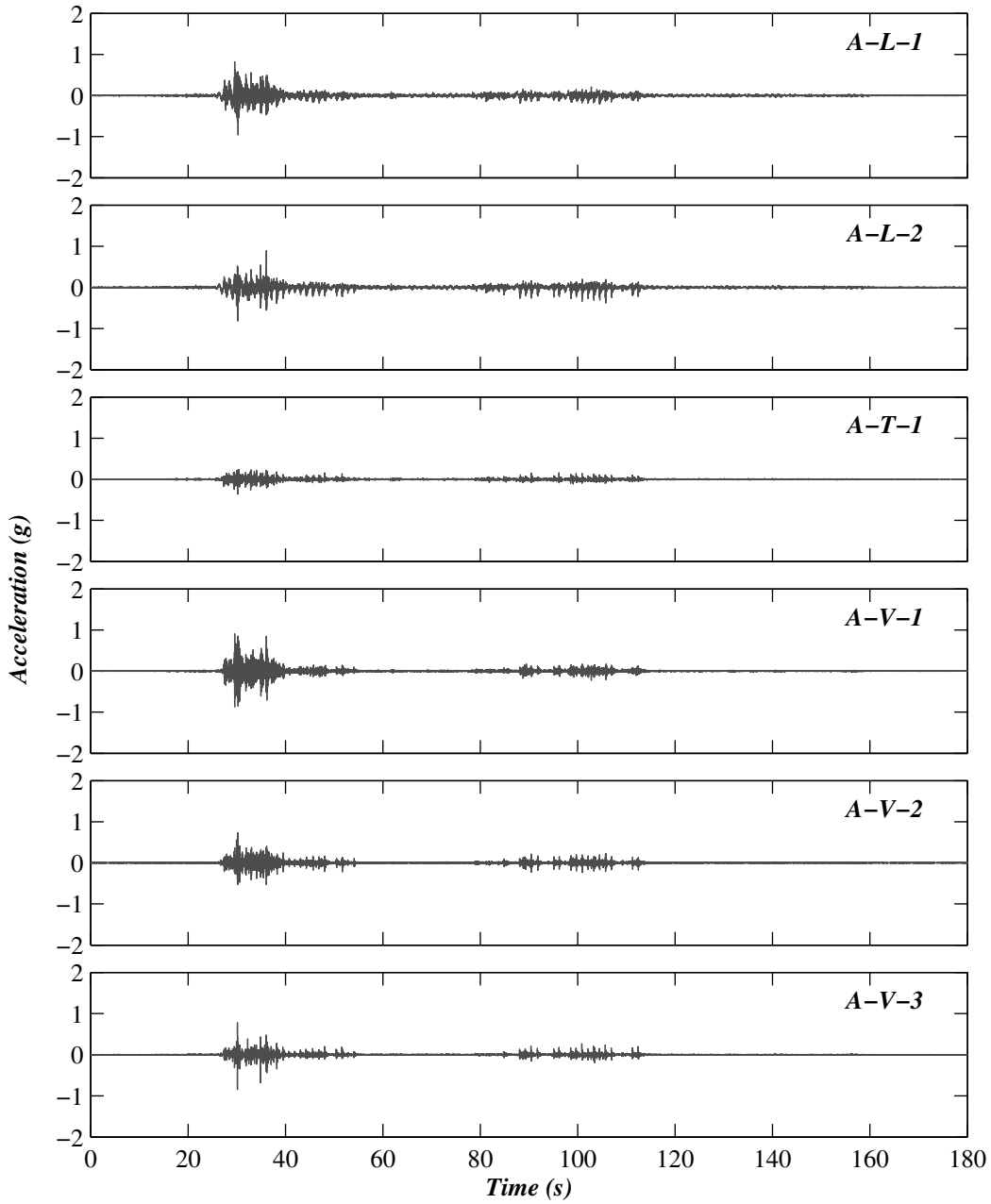

Figure B.32. Acceleration time history responses of the lower flight at level 2 during test FB-4.

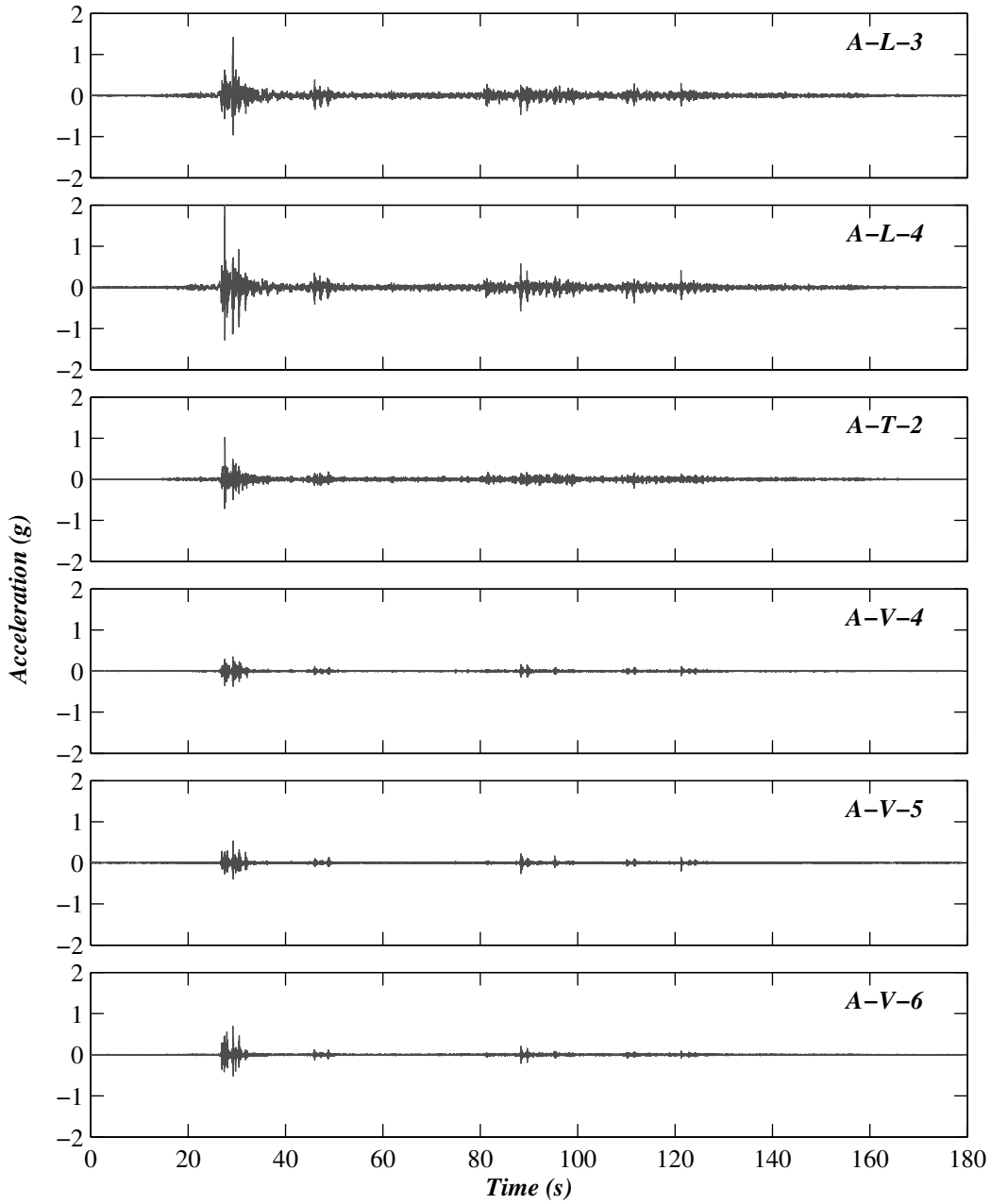

Figure B.33. Acceleration time history responses of stair landing at level 2 during test FB-4.

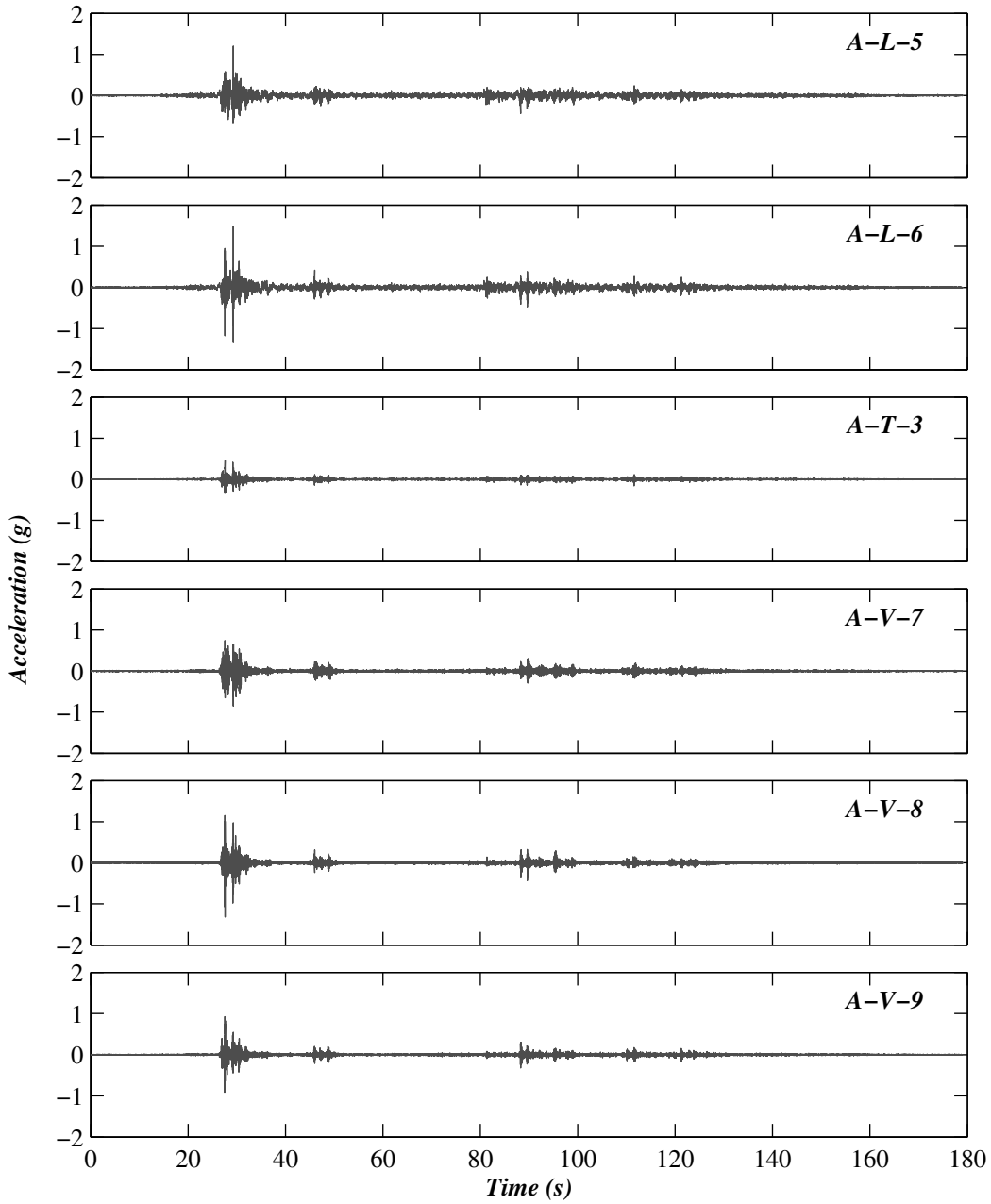

Figure B.34. Acceleration time history responses of the stair upper flight at level 2 during test FB-4.

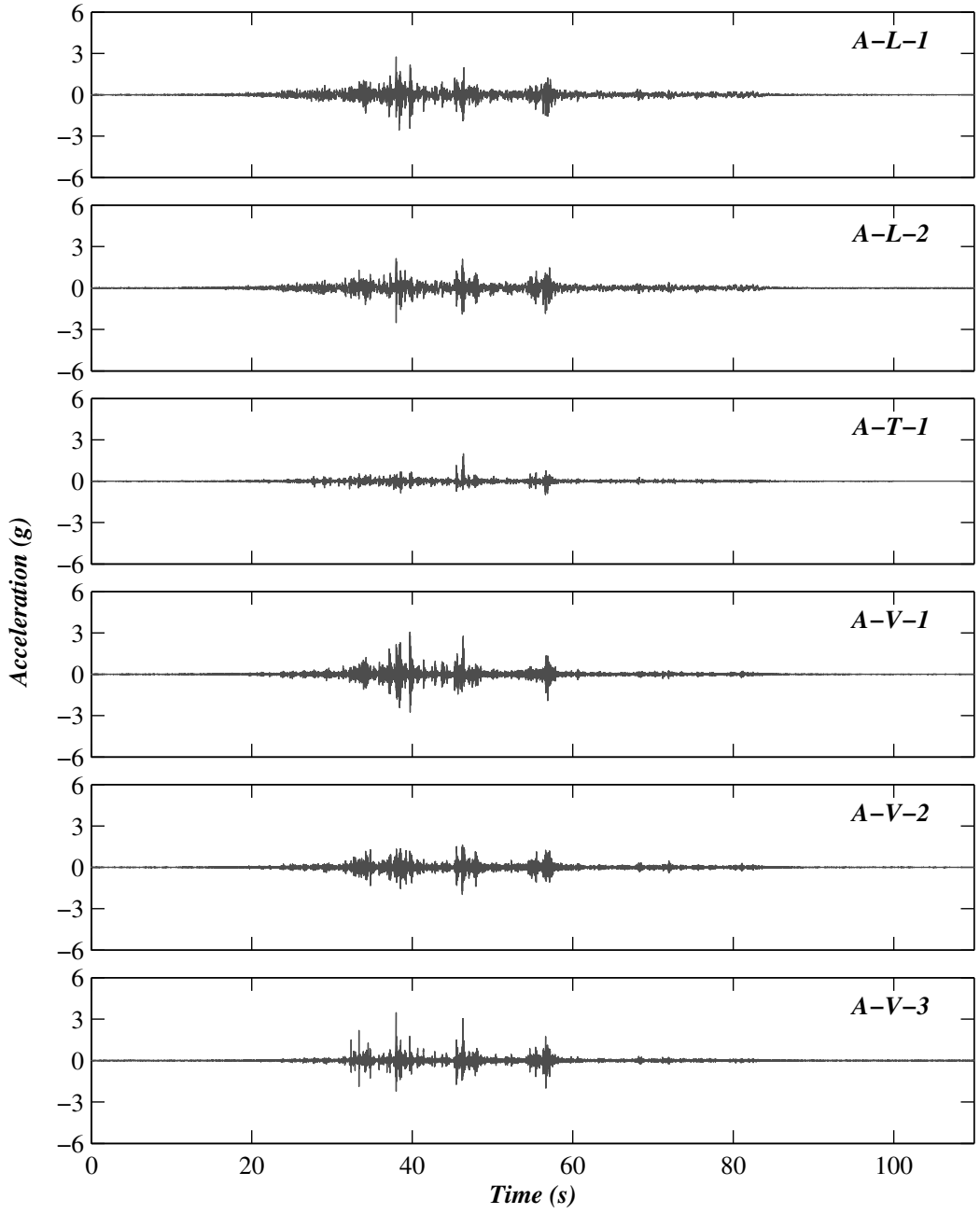

Figure B.35. Acceleration time history responses of the lower flight at level 2 during test FB-5.

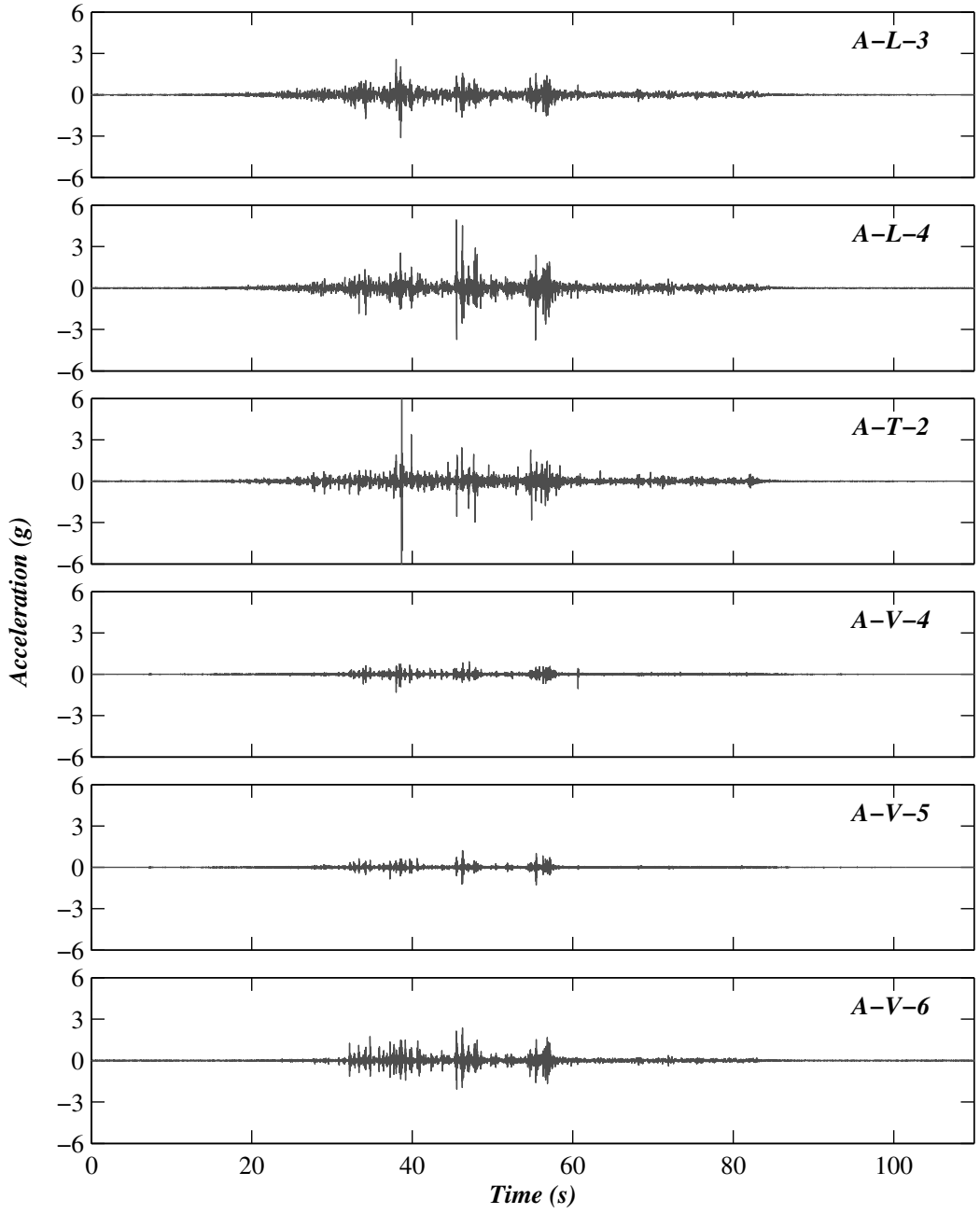

Figure B.36. Acceleration time history responses of stair landing at level 2 during test FB-5.

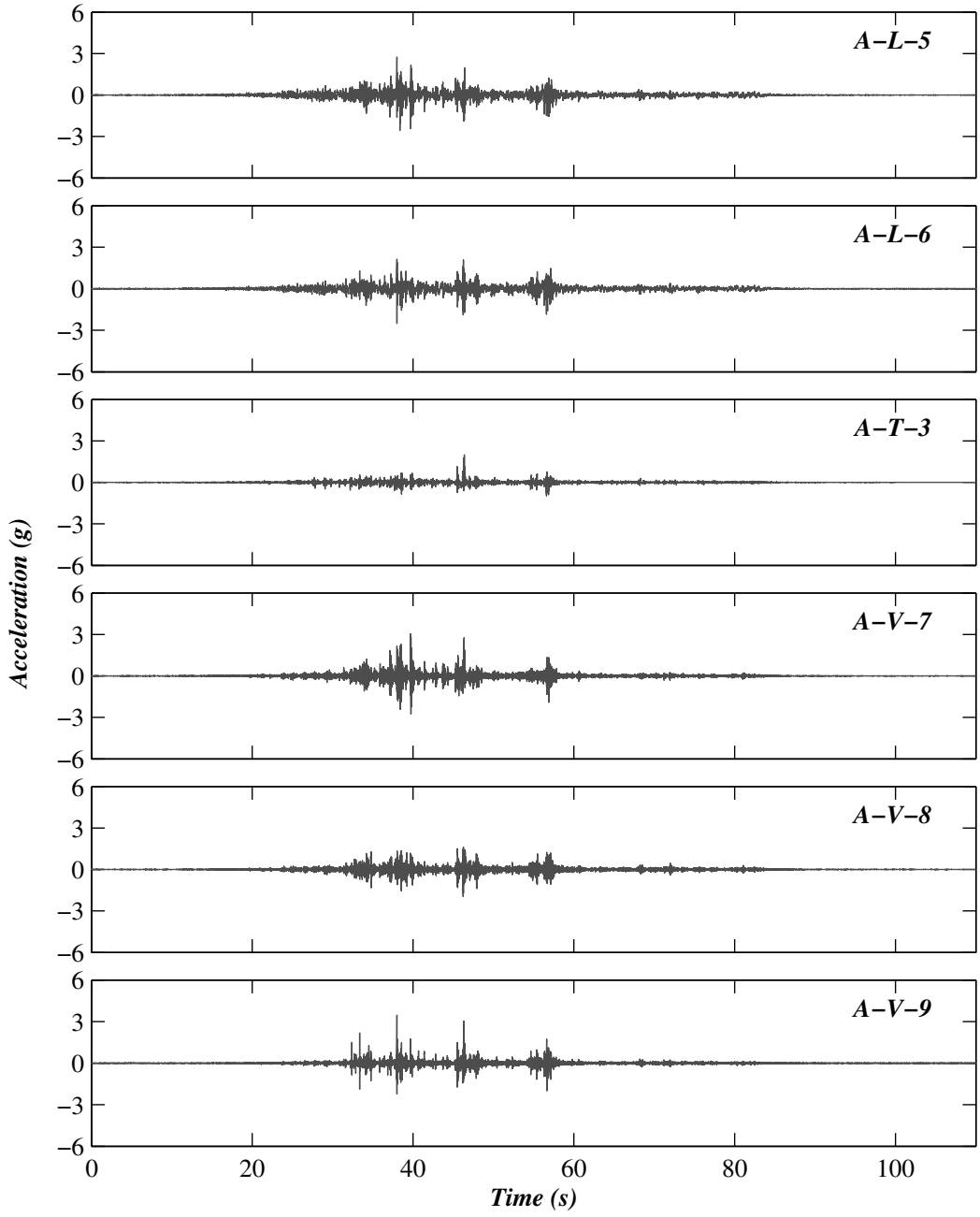

Figure B.37. Acceleration time history responses of the stair upper flight at level 2 during test FB-5.

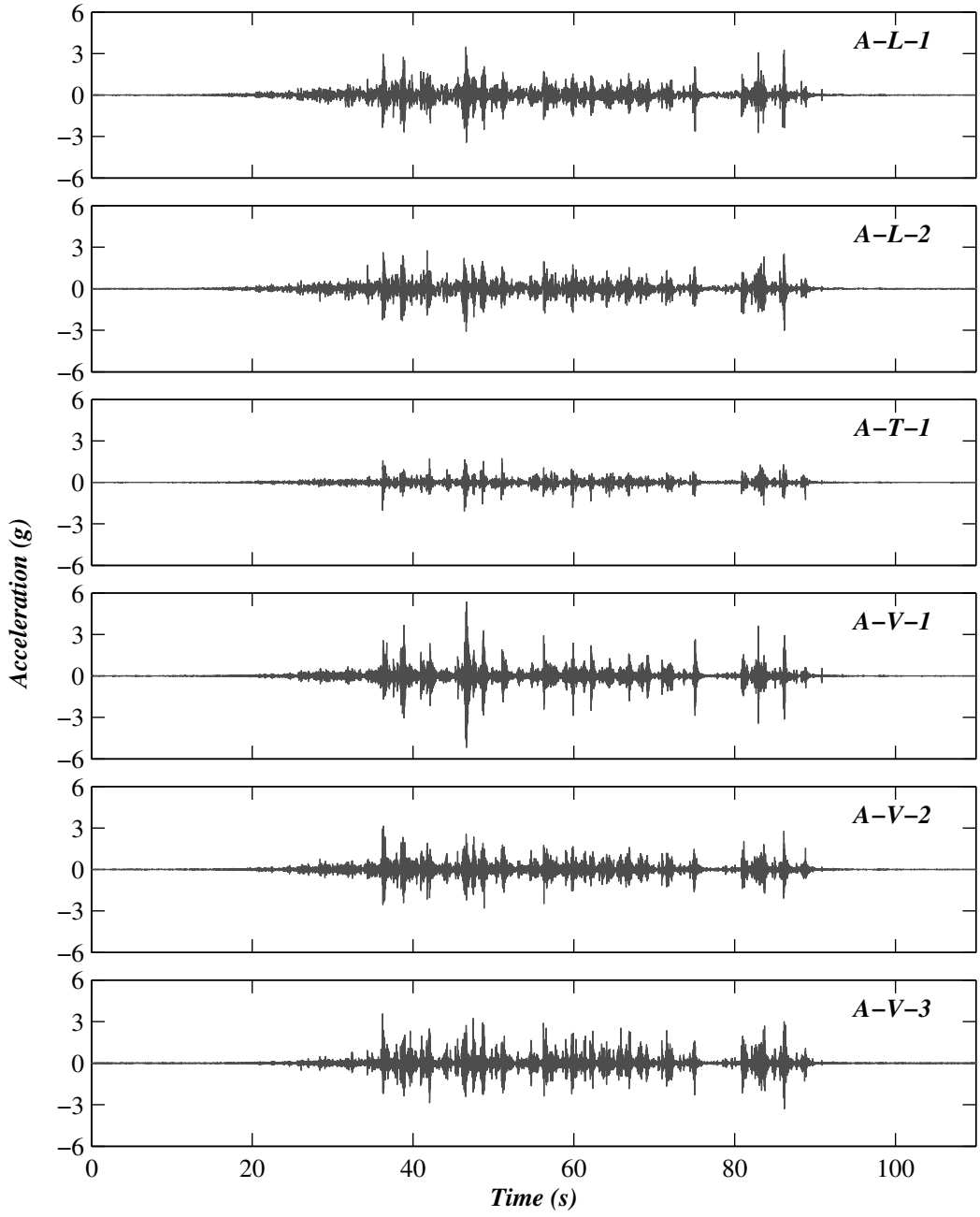

Figure B.38. Acceleration time history responses of the lower flight at level 2 during test FB-6.

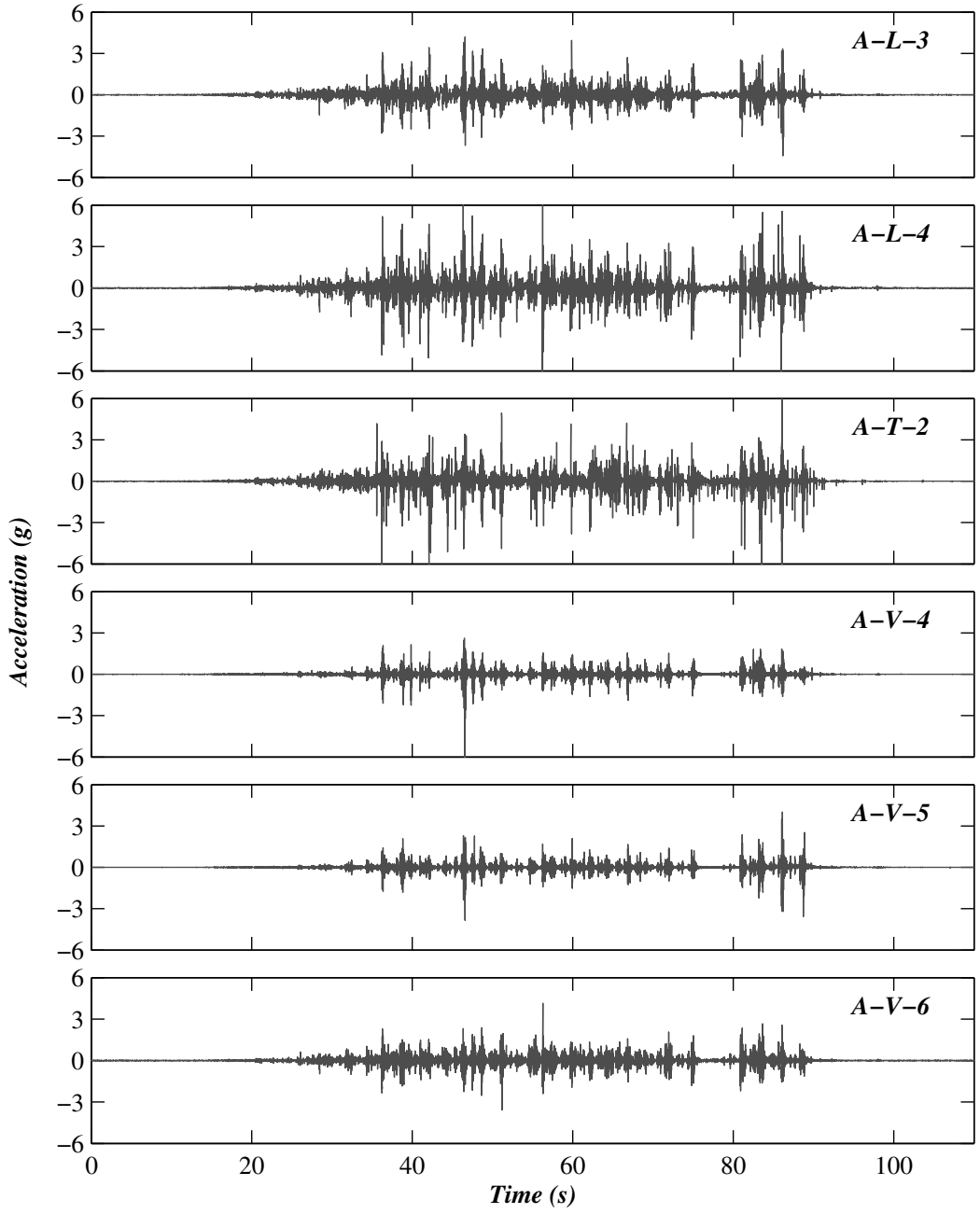

Figure B.39. Acceleration time history responses of stair landing at level 2 during test FB-6.

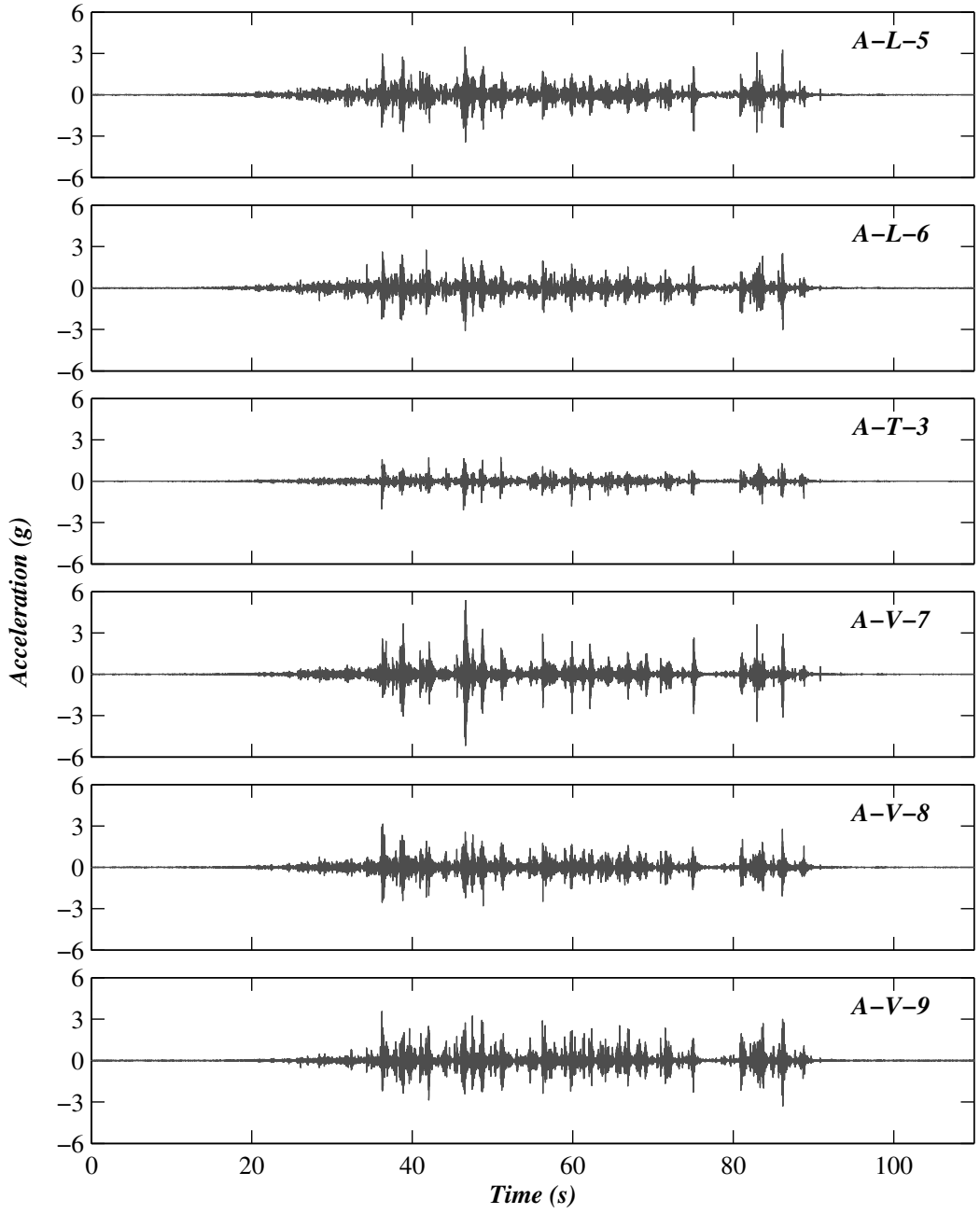

Figure B.40. Acceleration time history responses of the stair upper flight at level 2 during test FB-6.

Appendix C

Shake Table Test Results of Elevator System

C.1 Introduction

Within the full-scale building shake table test program (see Chapter 2), two operable egress systems were installed and tested with the building at full-scale, allowing investigation of the system-level interaction of these systems with the test building. To complement the experimental study of the stair system discussed in Chapter 3, this appendix presents important findings regarding the seismic behavior of the fully functional passenger elevator tested with the full-scale building. To the author's knowledge, this study represents the first-of-its kind system-level experimental research on the seismic behavior of elevator systems.

This appendix is organized into five sections. Section C.2 provide a description of the elevator system, including the seismic design criteria, instrumentation plan, and test configurations during the shake table test sequence. White noise test results with elevator configured under different test locations are presented in Section C.3. Section C.4 discusses the physical and measured responses of the elevator system during the seismic tests. Lastly, Section C.5 summarizes the important findings regarding the seismic behavior of the elevator system during the shake table test program as well as their

implications related to design practice.

C.2 Description of Elevator System

A fully functional traction elevator was installed to access all levels of the test building at the northwest side of the test building (Figure 2.2a). As shown in Figures C.1a and C.1b, the shaft had a dimension of 2.6 × 2.1 m and was enclosed by reinforced concrete shear walls on the east and west faces and cold-formed steel partition walls on the south and north faces. The cabin was located in the middle of the hoistway, while the counterweight was located on the east side. The brackets on the east wall (Omega brackets) provided support for three guide-rails (one for the cabin and two for the counterweight), while the brackets on the west wall (Z bracket) supported the single cabin guide-rail. The drive machine and the sheave were located on top of the guide-rails on the east side of the shaft. The elevator entrance doors were placed on the partition walls at the south side of the shaft, with an opening of 1.1 × 2.1 m . Additional details of the important elevator components are described as the following:

- Cabin: the interior dimensions of the cabin were 2.1 × 1.7 × 2.4 m and the weight was ~9.4 kN. Sand bags weighting 6.2 kN (40% of the elevator's rated capacity) were placed inside of the cabin during all seismic tests and white-noise excitation tests to simulate a passenger load, resulting in a total weight of ~15.6 kN (see Figure C.1c).

- Counterweight: the dimensions of the counterweight frame were 2.7 × 1.2 m and its total weight (including the steel plates) was ~16.0 kN (see Figure C.1d).

- Guide-rails: 18.0 kg/m guide-rails were used for the cabin, whereas the counterweight utilized 12.3 kg/m guide-rails.

- Brackets and anchorage: the brackets (Omega brackets on the east wall and Z bracket on west walls) were evenly spaced along the vertical direction of the shaft walls at an interval of ~2.1 m (half the story height). With the exception of the brackets at floor 4 that employed M16 T-headed bolts attaching to cast-in anchor channels, all brackets were attached to the shaft walls with two M16×120 mm

concrete wedge anchors on each bracket. All wedge anchors were pre-tensioned by applying 81 N-m of torque to the anchor bolts, although the pretension applied on the instrumented wedge anchors was subsequently removed to allow for measurement of the anchor forces during the seismic tests. The M16 T-headed bolts in the anchor channels (at level 4 only) were all instrumented, and an installation torque of 200 N-m was applied on each anchor bolt. The locations of the instrumented anchors are discussed later.

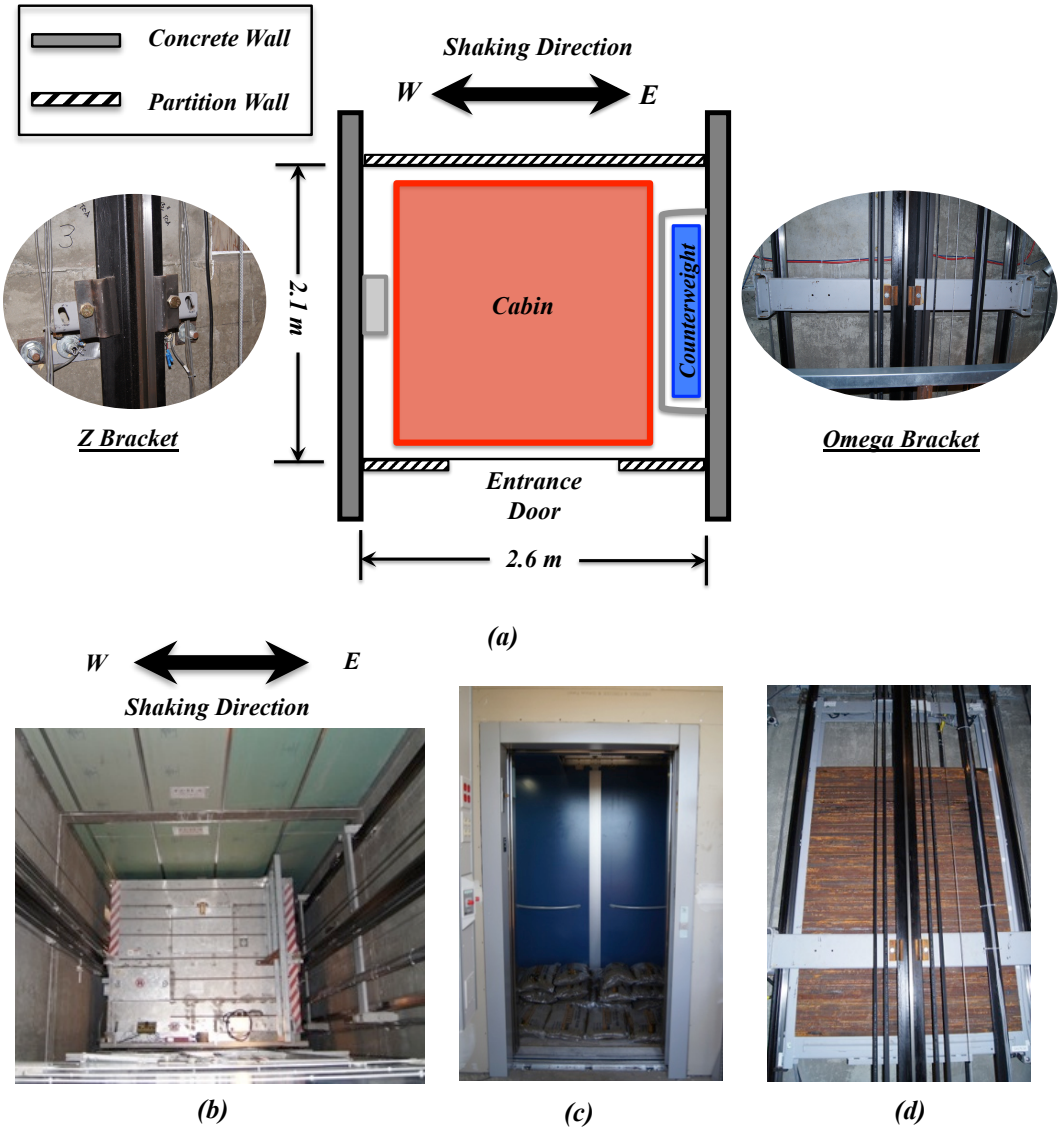

Figure C.1. Elevator hoistway: (a) plan layout, (b) photograph (view down from level 3), (c) cabin with sand bags, and (d) counterweight.

C.2.1 Elevator Design

The elevator in the test building was designed in accordance with ASME A17.1 provisions (ASME, 2010). The required deflection of the bracket support (attachment point of bracket anchors on the shaft walls) was limited to 2.5 mm, and the total deflection of the rail support (including the bracket and the building support deflection) was limited to 6 mm. Two lateral load cases – non-seismic (normal operation) and seismic – were considered in the strength design of the guide-rail systems. For non-seismic applications, the horizontal loads were the maximum static loads based on the cabin and counterweight guide shoes reaction loads during its normal operation as recommended by the manufacturer. For the seismic design, however, horizontal forces applied on the guide-rail system were determined as the seismic impact loads of the cabin and counterweight in addition to the inertial forces induced by the machine drive and its support on top of the guide-rails. Horizontal accelerations of 0.5 g for the cabin and counterweight and 1.0 g for the machine drive and its support were considered in the seismic design.

C.2.2 Instrumentation

The elevator and its attachments to the building were instrumented with an array of uni-axial accelerometers and strain gauges connected to a multi-node distributed data acquisition system, which collected data at a sampling frequency of 240 Hz. As shown in Figures C.2a and C.2b, six uni-axial accelerometers were installed on each of the cabin (CAB-X-X) and counterweight (CWT-X-X). In addition, all bracket anchors at floor 1 and from floor 4 to the mid-height of level 5 were instrumented with uni-axial strain gages (SG-X-X) installed concentrically in the anchor shaft between the nut and the anchor expansion cone. Each instrumented anchor was calibrated prior to installation to establish the relation between the axial strain and applied axial load. Shear forces in the anchors were not measured because the primary loading direction was parallel to the anchor longitudinal axis. Each bracket consisted of a pair of anchors attached to it (distinguished by SG-X-XS and SG-X-XN), and thus resulting in a total of twenty instrumented anchors (Figure C.2c). The instrumented wedge anchors were initially installed with the required installation torque of 81 N-m to set the anchor expansion

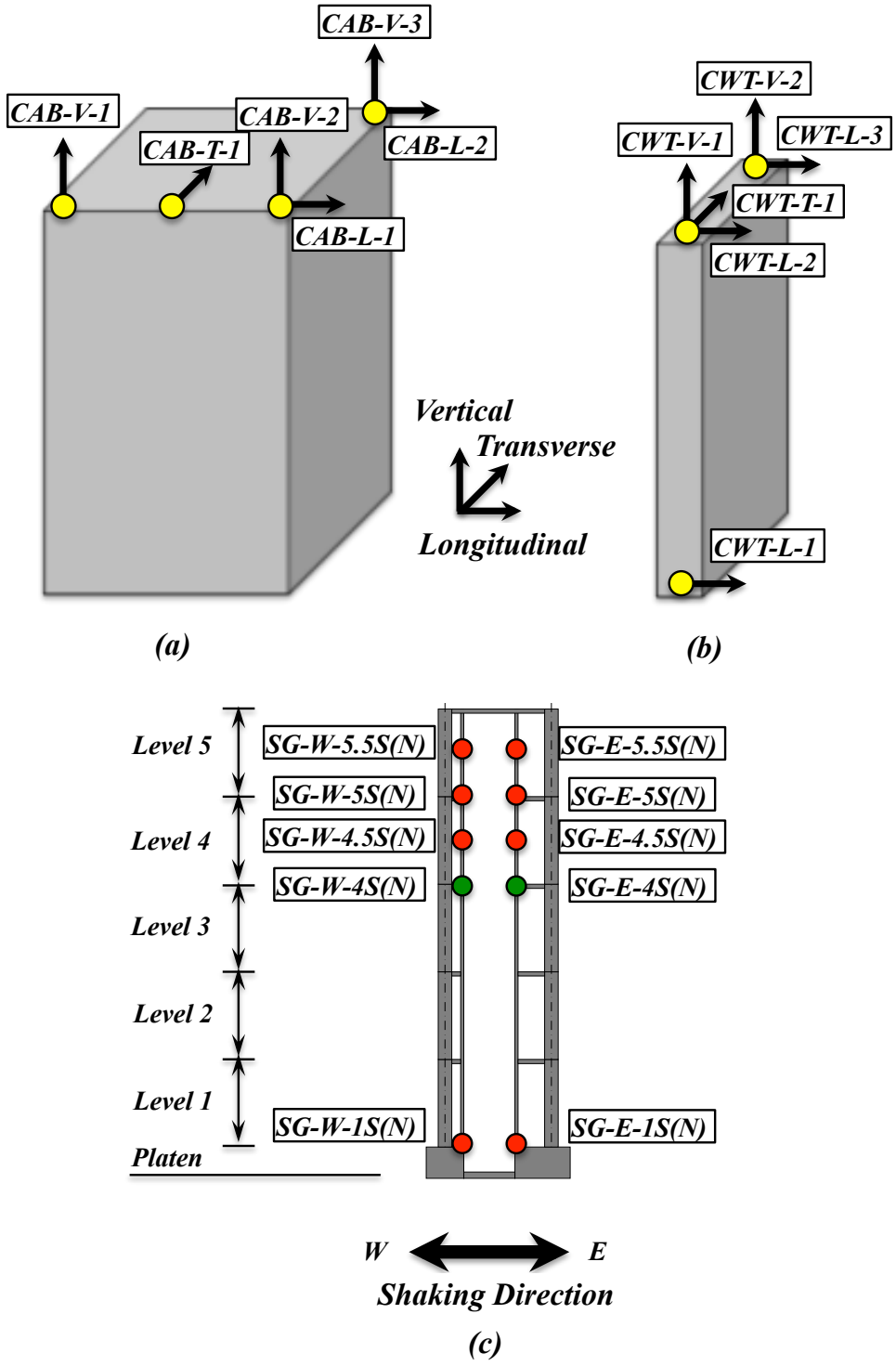

Figure C.2. Elevator instrumentation: (a) accelerometers on the cabin, (b) accelerometers on the counterweight, and (c) strain gauges of the bracket anchors (SG-X-XS and SG-X-XN denote the anchors on the north and south sides attaching the same bracket).

elements in concrete and clamp the guide-rail brackets in position. The pretension was subsequently removed and set to 5 N-m to effectively eliminate the clamping force, thus allowing the strain gauges to measure the seismically induced anchor tension forces. The cast-in anchor channel T-headed bolts were installed with the required installation torque of 200 N-m, which was retained during the earthquake tests to assure proper function of these anchors. Therefore, the force measurements in these bolts are expected to be insignificantly small (<< 1kN) unless the clamping force is exceeded by earthquake induced tension forces in these bolts. Additional details of the instrumentation of the elevator and the test building can be found in Pantoli et al. (2013b).

C.2.3 Test Configurations

As schematically shown in Figure C.3, three test configurations were considered by varying the location of the cabin and the counterweight in the white noise (WN) tests: a) Configuration I (C-I) – the cabin at level 1 and the counterweight at level 5; b) Configuration II (C-II) – both the cabin and the counterweight at the building mid-height (level 3); and c) Configuration III (C-III) – the cabin at level 5 and the counterweight at the level 1. It is noted that an elevator is expected to expend the majority of its life cycle in Configuration I, and, therefore, this configuration was adopted as the primary configuration in the seismic tests. For C-I, the acceleration responses at floor 1 may be considered as input to the cabin and those at floor 5 may be considered as input to the counterweight; likewise, the acceleration responses at floor 5 may be considered as input to the cabin and those at floor 1 may be considered as input to the counterweight for C-III. When the cabin and the counterweight are concentrated at level 3 (C-II), the acceleration responses at floor 3 impose the predominant demand on these components.

Table C.1 compares the mass of the cabin and counterweight with those of the corresponding floors in the three different configurations. As shown in the table, the mass of the elevator components was significantly smaller than that of the corresponding floor of the building. The largest weight concentration (C-II) resulted in the mass of the elevator cabin and counterweight combined still less than 5% of the mass of the corresponding floor. It is noted, however, that the elevator-building mass ratio may be even smaller

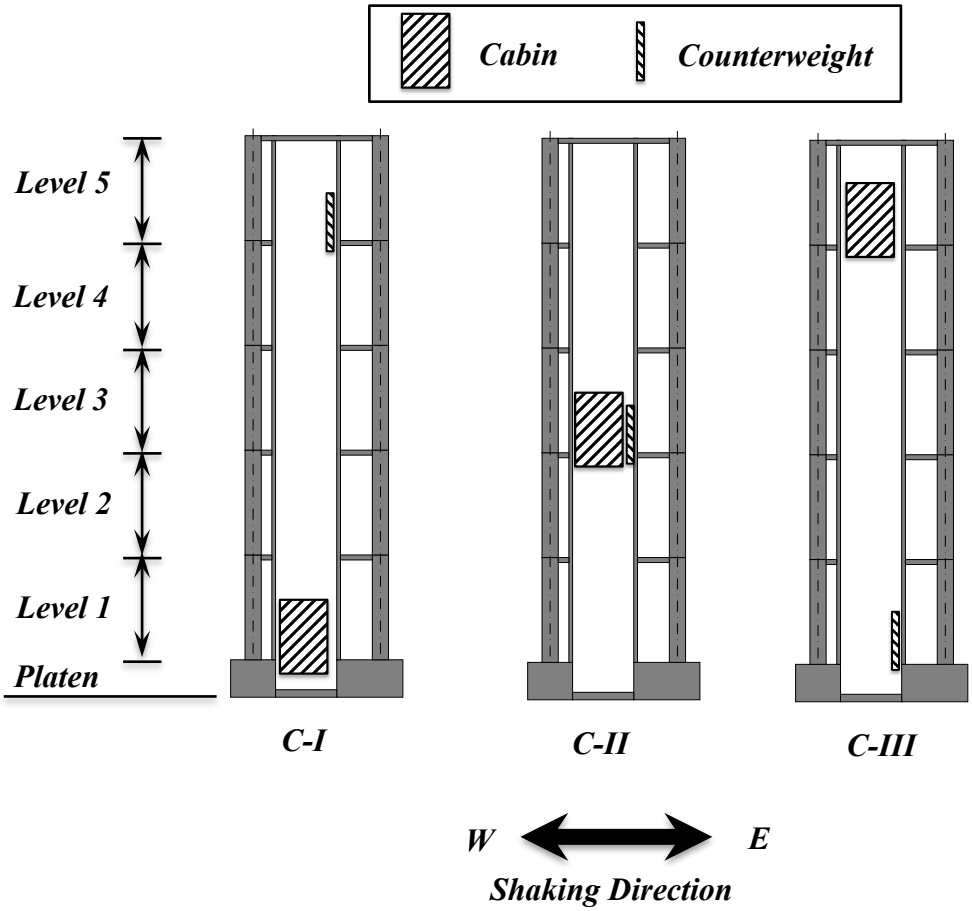

Figure C.3. Test configurations for the elevator system (west bay of the building).

Table C.1. Comparison of the elevator component mass and floor mass in different test configurations.

Elevator test configuration	M_{cab}/M_{floor}	M_{cwt}/M_{floor}	$(M_{cab}+M_{cwt})/M_{floor}$
C-I	0.8%	1.5%	N/A
C-II	2.1%	2.1%	4.2%
C-III	1.5%	0.8%	N/A

Notes: M_{cab} = cabin mass (1.59 metric ton); M_{cwt} = counterweight mass (1.63 metric ton); M_{floor} = floor mass (211.7 metric ton at floor 1, 77.2 metric ton at floor 3, and 108.5 metric ton at floor 5).

for typical buildings, as the test building had a small footprint compared with buildings used in practice.

C.3 White Noise Test Results

Three low-amplitude white noise (WN) base excitation tests, while the elevator was placed in each of the three test configurations, were conducted prior to the seismic test stage. During these WN tests, the building was fixed at its base. The purpose of these tests was to study the dynamic amplification characteristics of the elevator components under different configurations as well as its effects on the modal properties of the test building. It is noted that the elevator was operational and the installation was complete at the time of these tests. In addition, the installation of nonstructural components within the test building was nearly complete and therefore the mass distribution of the building and its nonstructural components did not vary significantly compared with that of the seismic test stage. Each of the three WN tests consisted of input excitations of two distinct amplitude levels with nominal (target) root-mean-square (RMS) accelerations of: 1.0% g, and 1.5% g. However, the amplitude of the achieved excitation in the first RMS 1.0% g WN test was twice as large as the other two WN tests of the identical amplitude level, and therefore the results from this test are not considered in the study.

Table C.2. Acceleration responses of the cabin and counterweight in the white noise tests.

Test configuration	RMS amplitude		Cabin			Counterweight		
	Target	Achieved	PFA	PCA^{cab}_{long}	Ω^{cab}_{long}	PFA	PCA^{cwt}_{long}	Ω^{cwt}_{long}
	(g)	(g)	(g)	(g)		(g)	(g)	
C-I	1.5%	0.93%	0.068	0.076	1.13	0.091	0.448	4.92
C-II	1.0%	0.62%	0.022	0.031	1.42	0.022	0.149	6.90
	1.5%	0.85%	0.058	0.104	1.80	0.058	0.298	5.13
C-III	1.0%	0.56%	0.031	0.172	5.56	0.022	0.042	1.94
	1.5%	0.84%	0.087	0.306	3.51	0.064	0.165	2.59

Notes: PFA = peak floor acceleration associated with either the cabin and or counterweight (as relevant); PCA^{cab}_{long}, PCA^{cwt}_{long} = peak component accelerations of the cabin and counterweight in the longitudinal direction; Ω^{cab}_{long}, Ω^{cwt}_{long} = acceleration amplification factor of the cabin and counterweight in the longitudinal direction.

Table C.2 summarizes the peak component accelerations (PCAs) of the cabin and counterweight and the associated peak floor accelerations (PFAs) measured during the WN tests. The acceleration amplification ratios of the elevator components Ω, defined as

the ratio between the PCA of individual components (cabin and counterweight) and the PFA of the associated floor, are also presented in the table. The measured acceleration responses were filtered with a fourth-order Butterworth filter with band-pass frequencies between 0.25 and 100 Hz to preserve the high-amplitude impulse-like acceleration responses. As shown in the table, the amplification effects of the counterweight were notably larger compared with those of the cabin at similar locations. The acceleration amplification effects of the cabin were significant ($\Omega > 3.5$) only when the cabin was located at the top (C-III) but remained moderate in the other two configurations ($\Omega < 2$). In contrast, the amplification ratio Ω exceeded 4 when the counterweight was at the top of the building (C-I) and reached as much as 7 when the counterweight was located at the mid-height of the building (C-II). Since the masses of the cabin and counterweight were comparable in these tests, the differences in the acceleration amplification effects between the cabin and the counterweight may be attributed to the detailing and varied flexibility of the guide-rails (e.g., guide-rail sections, attachment details, gap provisions).

Figure C.4 presents the natural frequencies of the first three vibrational modes of the test building under the RMS 1.5% g WN tests – the first longitudinal (1-L) mode, the

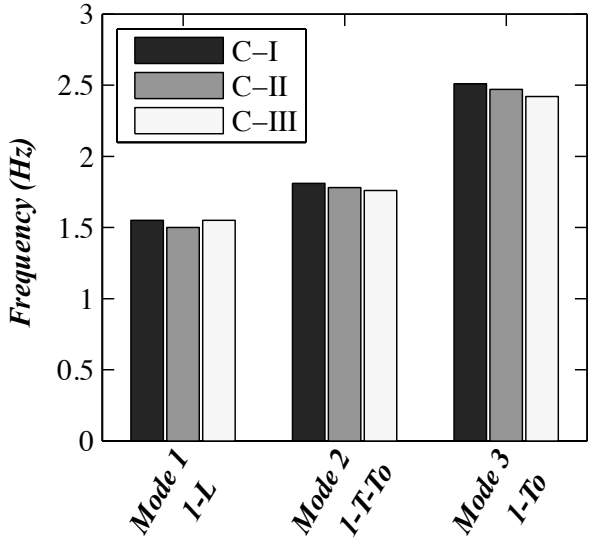

Figure C.4. The first three natural frequencies of the test building (in the fixed base configuration) with elevator components placed in configurations C-I to C-III (Figure C.3).

first transverse and torsional (1-T+To) mode, and the first torsional (1-To) mode. The natural frequencies of the test building are identified using the deterministic-stochastic identification (DSI) method Van Overschee and De Moor (1996). These results indicate that the natural frequencies of the building remained nearly identical regardless of the location of the cabin and counterweight, as the identified frequencies varied less than 5% among the different test configurations. For smaller elevator to building mass ratios, which may be encountered in practice, one may conclude that the impact of the elevator on the fundamental frequencies of the building would be even less. Additional details of modal identification results of the test building can be found in Astroza et al. (2015).

C.4 Earthquake Test Results

C.4.1 Physical Observation

Post-shaking inspection of the elevator was conducted at each inspection phase immediately following the seismic test to characterize the physical damage of individual components and to evaluate its functionality. The inspections were conducted by operating the elevator along the full height of the building and performing stops at each floor. The elevator remained fully operational and no damage to the elevator was observed up through test FB-4. The onset of damage was first observed following test FB-5 (design event earthquake with a PIDR of 2.5% at level 2) in the form of incipient door gaps (<25 mm) and minor crushing of the door with the surrounding cold-formed steel partition walls at levels 2 and 3 of the building (see Figure C.5a). The elevator remained functional in spite of the presence of these gaps. During test FB-6, however, the doors at the lower three levels sustained severe damage when averaged PIDR demands were extremely large (~6% at the lower two levels and ~3.5% at level 3). The gaps between the doors at levels 2 and 3 reached a maximum residual of 200 mm at their base (see Figure C.5b), and corner crushing of the elevator doors progressed as a result of severe interaction between the doors and the partition walls C.5c). These eventually resulted in the inoperability of the elevator following test FB-6. However, inspection conducted during the demolition stage revealed no visible damage to the cabin, the counterweight, the guide-rail and anchorage system, or other components within the elevator shaft.

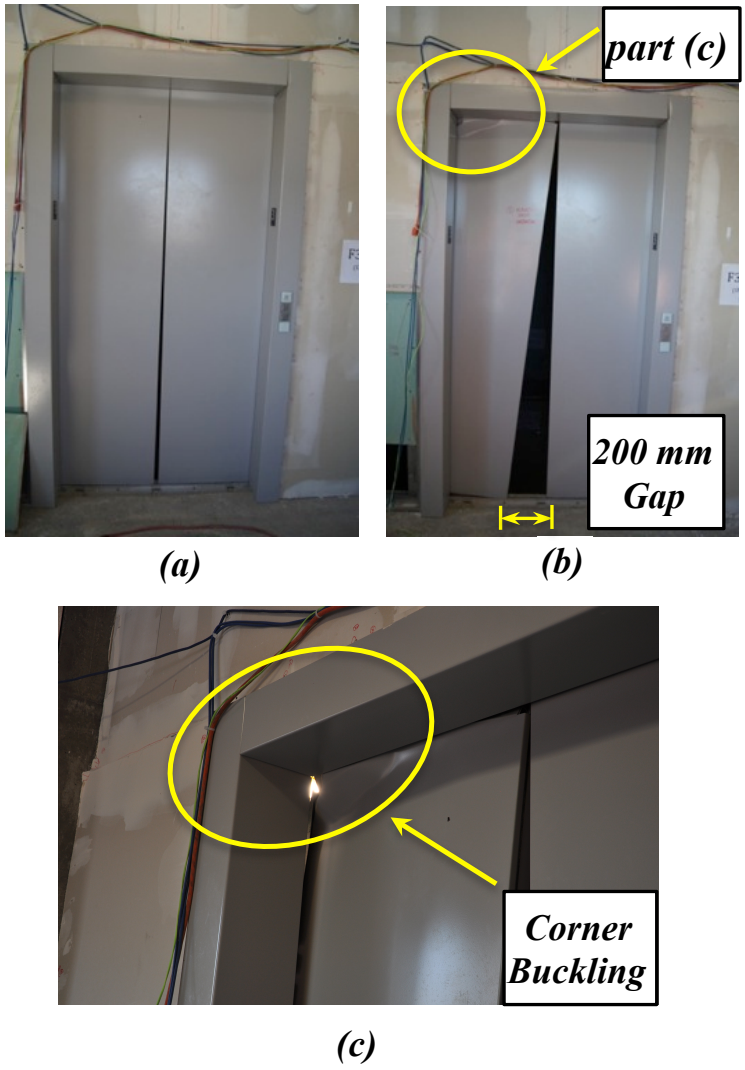

Figure C.5. Damage to the elevator: (a) incipient gapping of the door at level 3 following test FB-5, (b) door distortion at level 3 following test FB-6, and (c) corner crushing of the door at level 3 following test FB-6.

Elastic flexing of the guide rails in the vertical direction was detected, possibly due to the residual drifts of the building at the end of the tests.

C.4.2 Measured Response

Accelerations

The absolute acceleration time histories of the cabin and counterweight (elevator in configuration C-I) and the associated Fourier amplitude spectra (FAS) during tests FB-1 and FB-5 are presented in Figures C.6 and C.7. The longitudinal accelerations of the cabin (CAB-L-1 and CAB-L-2) and counterweight (CWT-L-2 and CWT-L-3) were comparable at the two corners of each component, however the counterweight accelerations contained much more high-amplitude impulse-like contents in their responses. Since no transverse excitation was imposed on the test building, the transverse floor excitations and the transverse accelerations of the cabin and counterweight (CAB-T-1 and CWT-T-1) were much smaller than their longitudinal counterparts, and the individual peaks of the transverse acceleration responses coincided with the impulse-like responses in the longitudinal direction. The Fourier amplitude spectra (FAS) of the acceleration responses indicate that the longitudinal accelerations of the cabin and counterweight were dominated by responses with frequencies less than 10 Hz, and the peaks consistently occurred around 1 Hz, which corresponds to the first longitudinal vibration mode of the test building. In contrast, the transverse accelerations contained frequency contents primarily higher than 10 Hz, possibly associated with their individual natural frequencies excited by the impact loading.

Table C.3 summarizes the peak component accelerations (PCAs) of the cabin and counterweight and their associated longitudinal peak floor accelerations (PFAs) during all seismic tests. It is noted that two band-pass Butterworth filters with different high frequency cutoff values were applied on the measured acceleration histories. The first filter, with a high frequency cutoff of 100 Hz (Nyquist frequency of the measured data), is intended to preserve high-amplitude impulse-like responses recorded on individual components due to impact loading, as these responses may damage the electronic

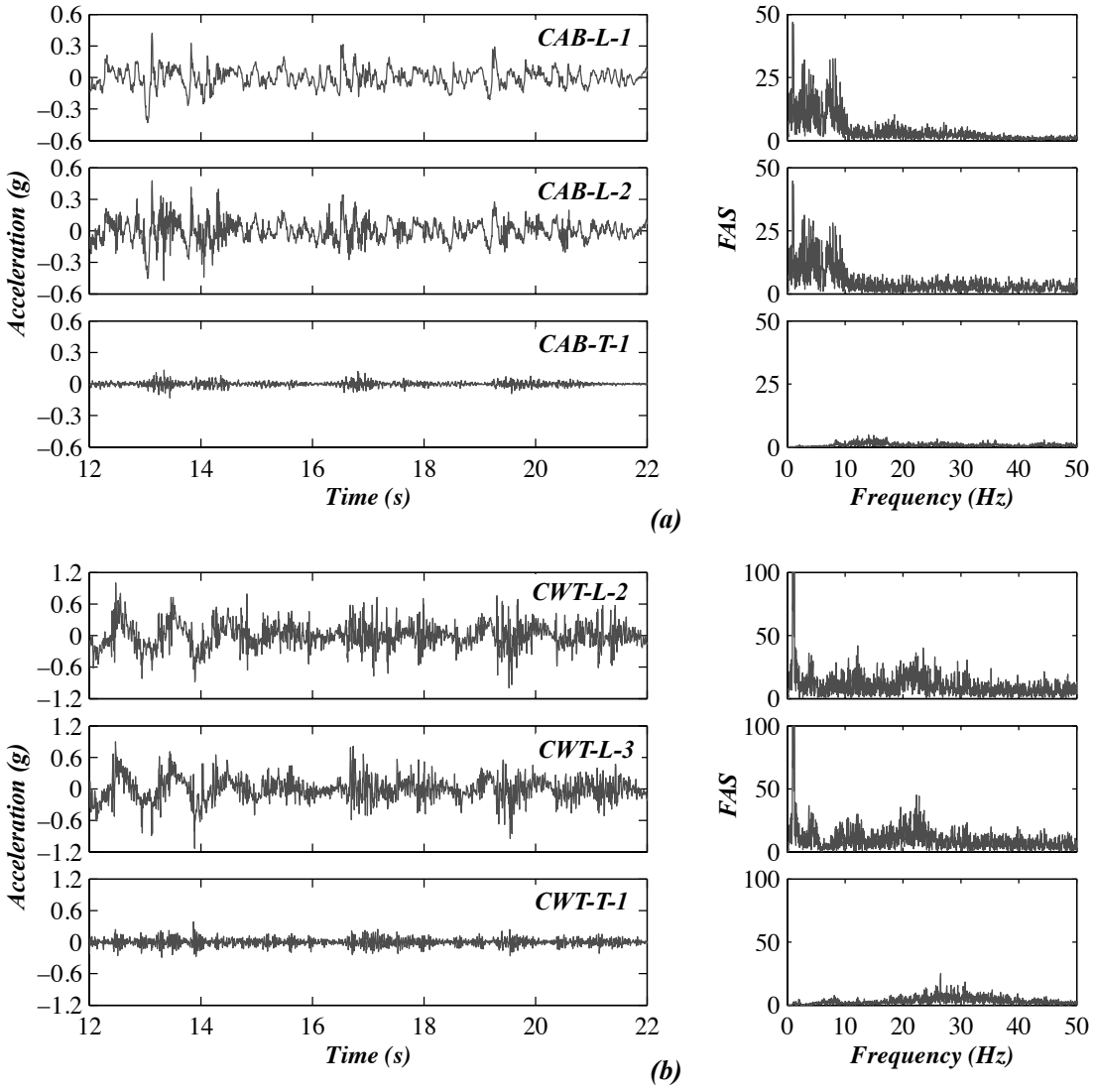

Figure C.6. Acceleration time histories and associated Fourier amplitude spectrum of: (a) cabin, and (b) counterweight during test FB-1.

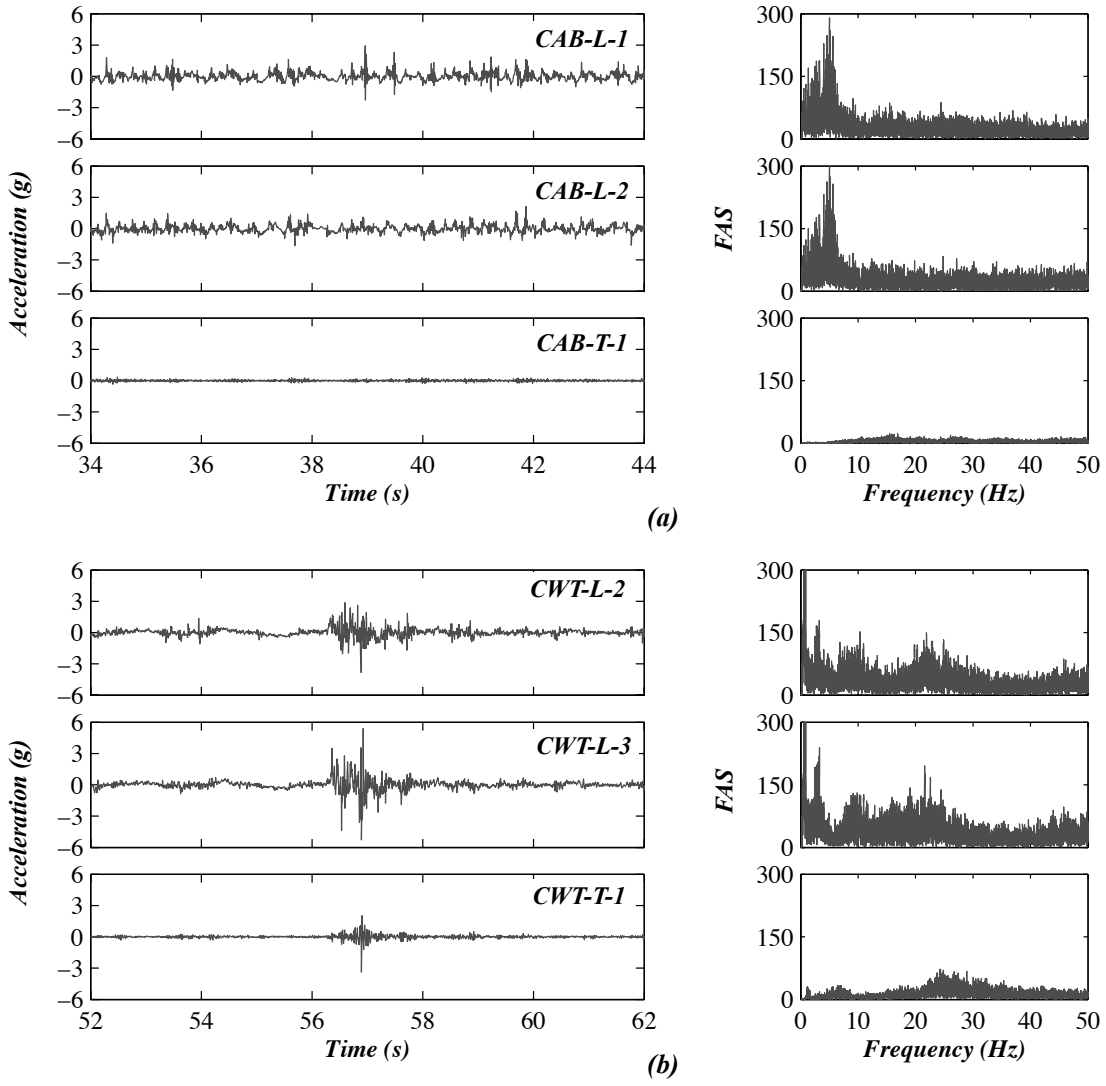

Figure C.7. Acceleration time histories and associated Fourier amplitude spectrum of: (a) cabin, and (b) counterweight during test FB-5.

Table C.3. Peak component acceleration responses of the cabin and counterweight during the seismic tests.

Test name	Cabin							Counterweight						
	PFA	CAB-L-1		CAB-L-2		CAB-T-1		*PFA*	CWT-L-2		CWT-L-3		CWT-T-1	
		100 Hz	25 Hz	100 Hz	25 Hz	100 Hz	25 Hz		100 Hz	25 Hz	100 Hz	25 Hz	100 Hz	25 Hz
	(g)	(g)	(g)	(g)	(g)	(g)	(g)	(g)	(g)	(g)	(g)	(g)	(g)	(g)
BI-1	0.082	0.087	0.087	0.109	0.082	0.011	0.006	0.084	0.273	0.158	0.206	0.134	0.065	0.029
BI-2	0.090	0.097	0.095	0.100	0.094	0.010	0.008	0.092	0.340	0.166	0.250	0.196	0.071	0.033
BI-3*	0.096	0.103	0.101	0.104	0.102	0.011	0.010	0.094	0.202	0.157	0.149	0.124	0.070	0.025
BI-4*	0.105	0.120	0.116	0.115	0.113	0.018	0.015	0.096	0.272	0.217	0.233	0.181	0.129	0.042
BI-5	0.073	0.082	0.080	0.077	0.076	0.014	0.005	0.075	0.235	0.146	0.186	0.145	0.052	0.026
BI-6	0.135	0.152	0.147	0.147	0.143	0.012	0.010	0.154	0.268	0.192	0.260	0.219	0.068	0.039
BI-7	0.184	0.233	0.214	0.214	0.201	0.018	0.011	0.237	0.435	0.283	0.414	0.296	0.129	0.054
FB-1	0.205	0.430	0.413	0.477	0.436	0.133	0.075	0.350	1.001	0.751	1.128	0.818	0.384	0.161
FB-2	0.180	0.389	0.350	0.542	0.430	0.121	0.064	0.347	1.103	0.746	1.004	0.696	0.327	0.147
FB-3	0.211	0.282	0.272	0.499	0.249	0.068	0.040	0.466	1.712	1.008	1.466	1.252	0.767	0.225
FB-4	0.251	0.466	0.439	0.623	0.427	0.102	0.061	0.565	1.456	1.097	1.763	1.382	0.710	0.304
FB-5	0.638	2.933	1.505	2.644	1.239	0.345	0.150	0.685	3.819	2.596	6.113	3.227	3.375	1.044
FB-6	0.798	5.828	3.239	2.939	1.530	0.540	0.207	0.654	3.126	2.330	5.409	3.777	1.694	0.678

Notes: * denotes that the elevator was tested under C-III and was otherwise tested under C-I; *PFA* – peak floor acceleration associated with the cabin and counterweight.

components of the elevator. However, these impulse-like responses may involve high-frequency local vibration as opposed to global acceleration responses of the elevator components, and therefore a second filter with a high frequency cutoff of 25 Hz was applied to remove these high frequency impulses. For each application, the low frequency cutoff was selected as 0.25 Hz. During the BI tests, the longitudinal PCAs of the cabin and the counterweight were relatively low (0.25 g for the cabin and 0.4 g for the counterweight) in the presence of impulse-like responses and even lower (0.2 g for the cabin and 0.3 g for the counterweight) when the impulse-like responses were filtered. As the associated PFAs became slightly larger during the first four FB tests, the observed PCAs of the cabin increased moderately (to about 0.6 g), and those of the counterweight increased sharply (as large as 1.8 g). During the last two FB tests (FB-5 and FB-6), extremely large impulse-like accelerations (>6 g) were measured on both the cabin and counterweight as a result of the pronounced increase of the input excitations. By applying the filter with the 25 Hz high frequency cutoff these acceleration responses remained larger than 3 g for the cabin and counterweight. The transverse PCAs of the cabin were significantly lower than their longitudinal counterparts in both the FB and BI tests (<0.6 g). However, while the transverse PCAs of the counterweight were also much lower than their longitudinal counterparts in the BI tests and the first four FB tests, the peak accelerations became very large in the last two FB tests, with amplitudes as large as 1/3 of those in the longitudinal direction. Provided the fact that no input excitation was applied in the transverse direction and the building torsional response was not significant, these large transverse accelerations were possibly due to the oblique impact between the counterweight and the guide-rails.

Figure C.8 presents the acceleration amplification ratios Ω of the cabin and counterweight compared with the associated PFAs in the seismic tests. The acceleration amplification ratios Ω are determined as the ratio between the PCA of individual components and the PFAs of the associated floor. As the PFAs of the cabin and counterweight were comparable during the BI tests, the cabin observed only slight acceleration amplification effects ($\Omega < 1.5$), but the amplification effects were larger for the counterweight ($\Omega = 1.5 - 3$) (Figures C.8a and C.8b). The amplification effects continued to increase

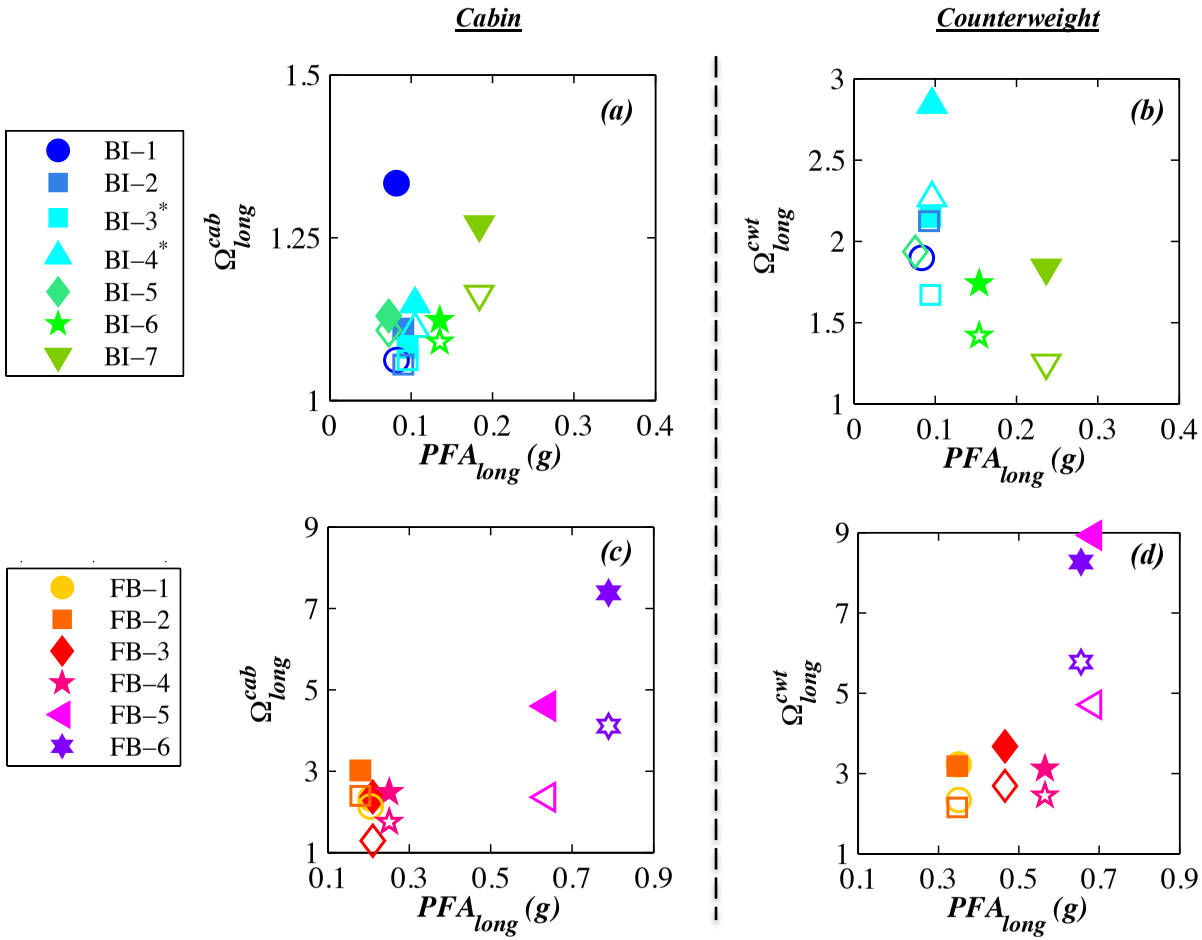

Figure C.8. Acceleration amplification ratios: (a) cabin in the BI tests, (b) counterweight in the BI tests, (c) cabin in the FB tests, and (d) counterweight in the FB tests (solid markers denote the high frequency cutoff of 100 Hz, while hollow markers denote the high frequency cutoff of 25 Hz; * denotes that the elevator was tested in configuration C-III, otherwise the test was conducted with the elevator placed in configuration C-I).

during the first four FB tests as the associated PFAs became higher; Ω values were as large as 3 for the cabin and 4 for the counterweight while the impulse-like acceleration responses were preserved (Figure C.8c and C.8d). As both the cabin and counterweight sustained significant impacts during the last two FB tests, Ω increased sharply and attained values as large as 9 for both components when the high cutoff frequency is selected as 100 Hz and about 5 when it is selected as 25 Hz. It is noted that the observed acceleration amplification ratios of both the cabin and counterweight during the FB tests were much larger than those prescribed in Table 13.6-1 of ASCE 7-10 (ASCE, 2010), in which the acceleration amplification factor (denoted as a_p) is defined as 1.0 for elevator components, assuming them as rigid nonstructural components. Although no observable damage to the elevator components was directly attributed to these high acceleration amplification effects, it is recommended that future investigation be conducted to provide design guidelines regarding expected peak accelerations of elevator components during earthquakes.

Anchor forces

Figures C.9 and C.10 provide the force time histories of the bracket anchors at floor 5 (SG-E-5N/S and SG-W-5N/S) during test FB-1 and FB-5, respectively. To obtain the anchor forces, the strains measured from the instrumented anchors were filtered with a low-pass fourth-order Butterworth filter with a corner frequency of 15 Hz and subsequently converted to anchor forces using the calibration factors determined prior to the tests. It is noted that test FB-5 represents an earthquake scenario that achieved the design performance objectives of the building (PIDR of 2.5% and PFA of 1.0 g). The figures demonstrate that the response characteristics of the anchor forces on the two sides of the walls were distinctly different. The peak forces were more than 7 kN on the east wall but less than 1.5 kN on the west wall, and the occurrences of these peaks at the two sides of the walls appeared to be uncorrelated. The reason for this was that the peak anchor forces of the east wall were dominated by pounding of the counterweight with its guide rails, while those of the west wall were induced by multiple-support differential displacements of the cabin guide-rail supports, as the cabin was located at level 1 during the FB tests.

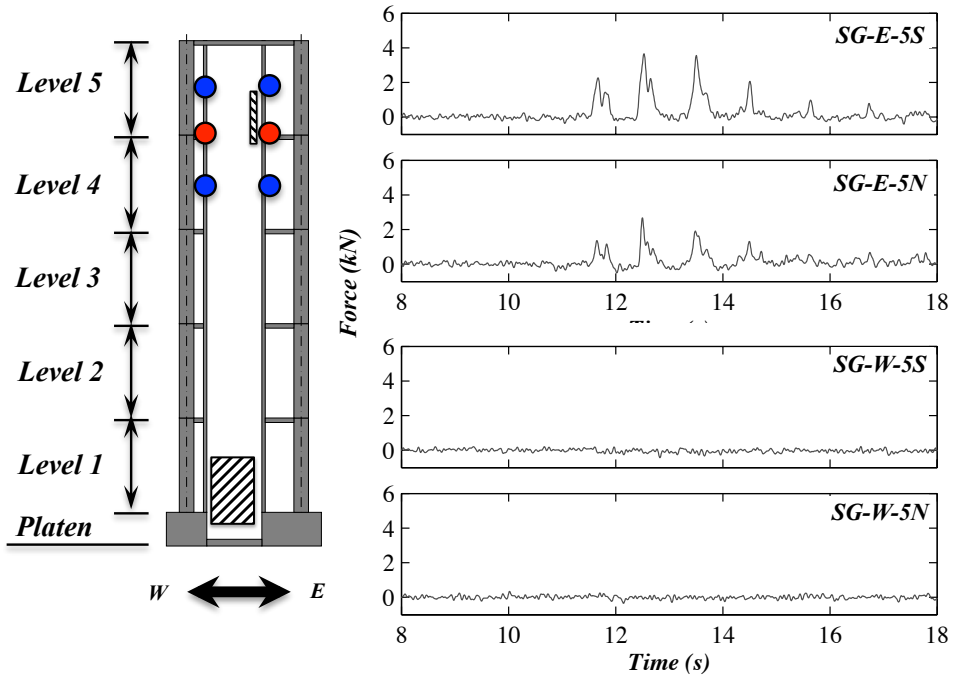

Figure C.9. Time histories of the bracket anchor forces at floor 5 during test FB-1.

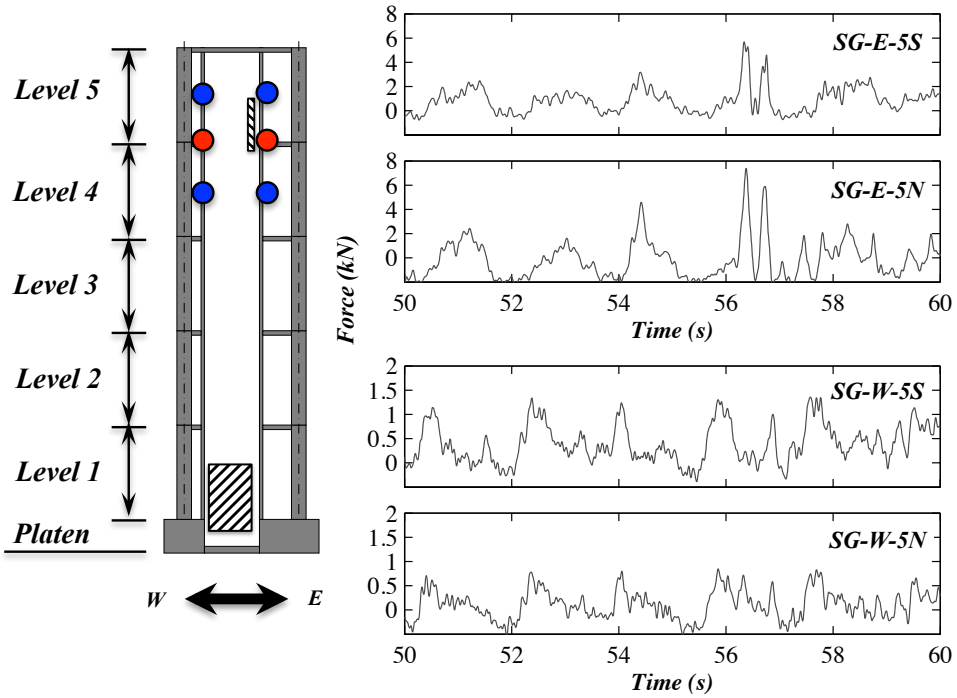

Figure C.10. Time histories of the bracket anchor forces at floor 5 during test FB-5.

Table C.4 presents the peak forces in the wedge anchors from the mid-height level of 4 to the mid-height of level 5 (Figures C.9 and C.10) in the FB test phase. It is noted that the forces measured on the instrumented T-headed anchor channel bolts in these tests appeared much larger than the excepted values, since these bolts should have registered only insignificantly small forces (<< 1kN) if the pretension of the bolts were properly applied. Due to the uncertainties of the pretension on these bolts during the seismic tests and the associated influences on the validity of these force measurements, the measured forces of these bolts are not presented. As the anchor forces on the west wall at these locations were attributed to multiple-support differential displacements of the cabin guide-rail, the peak forces were larger at the lower level as a result of larger PIDR demands, and the peak forces of the two anchors on the bracket appeared less

Table C.4. Peak anchor forces of the brackets from the mid-height of level 4 to the mid-height of level 5 during the FB tests.

Test	Anchor Location	PFA [1]	$PIDR$ [2]	West Wall		East Wall	
				South	North	South	North
		(g)	(%)	(kN)	(kN)	(kN)	(kN)
FB-1	5.5	–	0.13	– [3]	0.93	1.18	2.46
	5	0.35	–	0.43	0.44	3.66	2.67
	4.5	–	0.24	0.59	0.71	1.07	0.77
FB-2	5.5	–	0.14	–	1.13	0.86	3.13
	5	0.39	–	0.45	0.43	3.01	1.49
	4.5	–	0.26	0.70	0.81	1.18	0.56
FB-3	5.5	–	0.23	–	1.18	1.61	4.56
	5	0.58	–	0.51	0.47	4.54	3.38
	4.5	–	0.43	1.10	1.33	1.57	1.37
FB-4	5.5	–	0.36	–	1.60	2.32	4.34
	5	0.64	–	0.92	0.92	4.86	4.57
	4.5	–	0.74	0.95	0.97	3.90	3.18
FB-5	5.5	–	0.54	–	2.14	5.03	9.44
	5	0.99	–	1.37	1.02	5.70	7.38
	4.5	–	1.09	2.84	3.11	6.21	5.86
FB-6	5.5	–	0.66	–	2.30	6.49	10.06
	5	0.90	–	1.40	1.10	4.87	8.42
	4.5	–	1.29	6.37	7.71	6.78	7.67

[1] PFA = peak floor acceleration at floors 5 and 4 (corresponding to anchor locations 5 and 4); [2] $PIDR$ = peak interstory drift at levels 5 and 4 mid-height (corresponding to anchor locations 5.5 and 4.5); [3] the embedded strain gage in the anchor was damaged prior to the seismic tests

scattered than those on the east wall. In contrast, since the anchor forces of the east wall were dominated by seismic impact loading at these locations (in particular at floor 5 and mid-height level 5), the peak forces were larger than those at the same height of the west wall and also differed significantly on the two ends (south and north) of the brackets. The peak anchor forces at the two ends of the bracket at mid-height level 4 were less scattered than those at the above levels, indicating that they were less subjected to impact loading since they were about one span away from the closest location of impact loading. It is noted that the controlling nominal tensile strength of the wedge anchors was 31.8 kN per ACI 318-14 (ACI, 2014), and the pretension induced by the 81 N-m installation torque is estimated to be about 18.8 kN. As the maximum seismic forces of the wedge anchors attained during the earthquake tests were only about 10 kN, these anchors would be sufficiently safe with a factor of about 5 and the pretension would not have been unloaded, if the anchor pretension were not eliminated.

C.5 Summary and Conclusions

A fully functional elevator was installed within a full-scale five-story reinforced concrete building and was subsequently tested with the building under a range of earthquake motions with increasing intensity. In addition, low-amplitude white noise base excitation tests were conducted to study the dynamic response of the elevator while the locations of the cabin and counterweight were varied. Important findings regarding the dynamic characteristics and seismic behavior of the elevator system in these shake table tests as well as their implications related to seismic design of elevator systems are summarized as follows:

1. Low-amplitude white noise base excitation tests indicate that the acceleration amplification of the counterweight were larger than those of the cabin when their vertical locations were comparable. This may be attributed to their varying attachment details, flexibility, and gap provisions related to the guide-rails. Since the mass of the elevator components was much smaller than the building floor mass, varying the location of the cabin and counterweight caused no significant modification of the modal properties of the building.

2. The elevator remained functioning up to and including the design event earthquake. Major damage to the elevator system was restricted to the entrance doors when the inter-story drift demands were more than twice as large as the design recommended values (2.5% interstory drift). The extremely large interstory drift demands at the lower three levels of the test building caused significant interaction between the elevator doors and their surrounding cold-formed steel partition walls, eventually resulting in severe distortion and corner crushing of the elevator doors.

3. Seismic impact between the elevator components (cabin and counterweight) and the guide-rails produced high-amplitude impulse-like accelerations on these components, with peak accelerations as large as 6 g on both the cabin and the counterweight. Although no observable damage to the elevator components was attributed to these impact loads, these high-amplitude accelerations may potentially damage the electronic components of the elevator system.

4. Application of a low pass filter to the measured cabin and counterweight accelerations, which was intended to remove impact-induced acceleration spikes, indicates that the peak accelerations of these components were between 1.5 and 3 g. These values remain well above the ASME A17.1 design recommendation of 0.5 g.

5. As the cabin and counterweight sustained significant impacts during the design and above-design events, the observed acceleration amplification ratio of these components (attaining as large as 9) are much larger than that suggested by ASCE 7 provisions. Elevator components in ASCE 7 are assumed as rigid components with component amplification factors of 1.0. Future investigations are needed to provide design guidelines regarding expected peak accelerations of elevator components during service, design, and maximum considered earthquakes.

6. Differential displacements of the bracket supports may also impose considerable forces on the guide-rails and may result in plastic yielding of guide-rails. Therefore, it is recommended that the effects of differential displacements be accounted for in the design of elevator guide-rails.

These tests allowed investigation of the seismic behavior of an elevator system as installed within a full-scale building when subjected to realistic dynamic loading. Importantly, these tests indicate that the interaction of elevator doors with their surrounding components must be explicitly addressed in future design to improve the seismic resilience of elevator systems. In addition, the use of well-restrained guide shoes with air gaps is recommended as it demonstrated the potential of effectively reducing the derailment hazard of cabins and counterweights during high-intensity earthquakes.

Acknowledgements

Portions of the following submitted publication, for which the dissertation author was the primary investigator and author, are contained in this appendix:

- Wang, X., Hutchinson, T., Astroza, R., Conte, J., and Restrepo, J. "Shake Table Testing of an Elevator System in Full-Scale Five-Story Building Shake Table Tests." Submitted to *Earthq. Eng. Struct. Dyn.*

Appendix D

Pre-test Simulation – OpenSees Model

D.1 Introduction

As part of the full-scale building shake table test program (see Chapter 2), pre-test predictions of the seismic response of the test building are essential for the development of the earthquake test protocol and design of the nonstructural systems in the test building. In this regard, two nonlinear finite element models of the test building, namely, 1) a design-oriented model implemented in the *OpenSees* platform, and 2) a detailed finite element model prepared using the general finite element software *DIANA*, are developed independently in an effort to predict the nonlinear dynamic response of the test building during the earthquake tests (Wang et al., 2013). These pre-test simulation results provided useful insight for the overall test execution as a result of earthquake motion selection and scaling as well as the seismic design of the nonstructural components to be installed on the test building. While the results of the *DIANA* model are described in Ebrahimian et al. (2013), this appendix focuses on the pre-test simulation study of the test building using the *OpenSees* model.

D.2 Model Description

In the *OpenSees* model (Figure D.1), the columns and walls of the test building are modeled using force-based beam-column elements. Rigid-link constraints are imple-

mented for wall-slab connections to ensure the compatibility of deformations between the floor slabs and walls. The material model for the reinforcement in these components uses the Uniaxial material *Steel02* (modified Menegotto-Pinto constitutive model), which has been shown to be computationally capable of capturing both kinematic and isotropic hardening as well as the Bauschinger effect (Filippou et al., 1983). Uniaxial material *Concrete02* is utilized for unconfined and confined concrete (Scott et al., 1982), with a multi-linear unloading/reloading rule that takes into account the effects of stiffness degradation and energy dissipation under cyclic loading. To address the issue of localization in force-based beam elements for strain-softening behavior, the material stress-strain relation is regularized based on the fracture energy of the concrete.

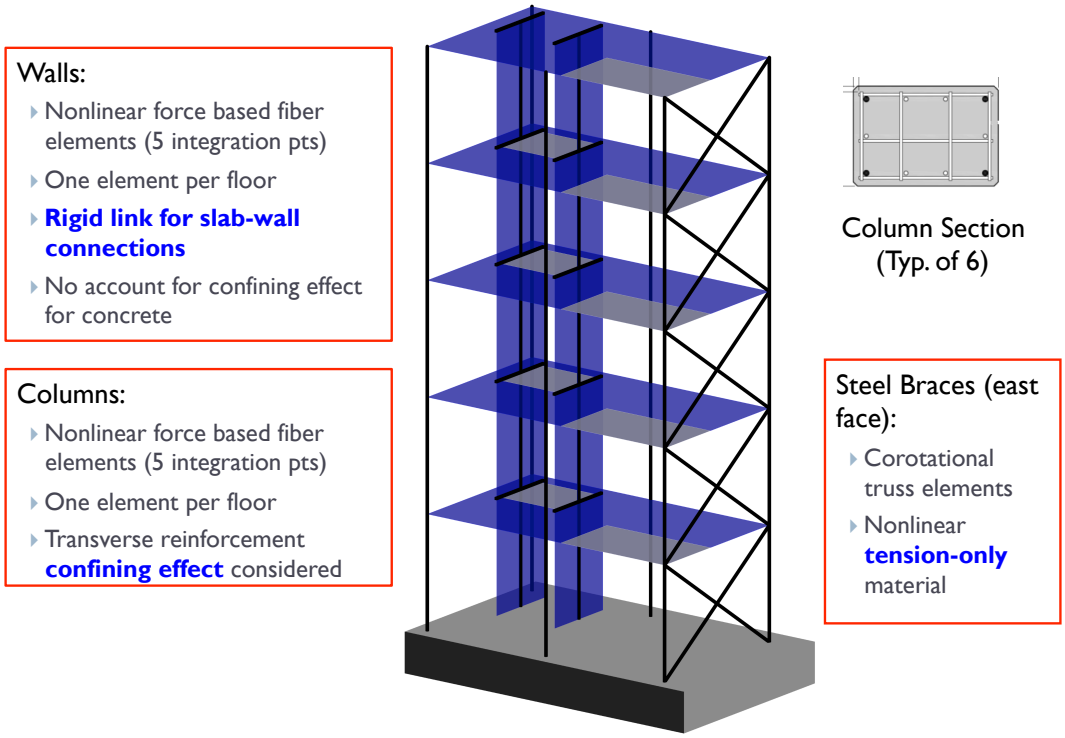

Figure D.1. Pre-test building model and modeling details of the shear walls and columns.

For modeling the moment frame beams of the test building, a zero-length section element is introduced at the interface that connects the joint and beam. It is assumed that the overall nonlinear response of the beam-column joint is lumped at the connect-

ing interface, and the remaining portion of the joint is modeled as rigid body elements for simplicity. This method aims at modeling the strain penetration effect of reinforced concrete columns, with the plane section assumption that associates rigid-body rotation at the zero-length section with the fiber deformation. In the current model, the zero-length section element has identical geometry as the adjacent beam fiber section; however, different material constitutive models are adopted within the fibers. In the zero-length section, deformation of the ductile rod fiber represents the total bond-slip integrated along the anchored length in the beam-column joint. Similarly, deformation of the concrete fiber is taken as the sum of the concrete strain over the half width of the beam-column joint.

Due to the lumped nature of the fiber section at the beam-column joint, the accuracy of the numerical results depend significantly on the ability of the fiber section to capture the interface behavior characteristics (e.g. stiffness degradation, bond deterioration pinching effect, and contact/detachment between the joint and the beam) of the test subassemblies. For this section, the uniaxial *Hysteretic* material is adopted since it allows for a compromise between simplicity and versatility, supports implementation of multi-linear segments, and allows an analyst to take into account a wide range of component hysteretic behaviors. Within this model, the slip-bar stress relation of the rod at the interface is required to define the envelope of the hysteretic material model. The model also includes parameters that control the nonlinear hysteretic response under cyclic loading, which are calibrated using experimental data of the beam-column subassemblies tests (Chang et al., 2013, 2014).

Figure D.2 illustrates the modeling details of a typical floor system. The perimeter slab beams at the north and south edges of the west bays and the one at the west edge of the test building are also modeled using force-based beam-column elements. The effective width of the slab beams are taken to be the same as that of the adjacent column joints since additional hoops were provided at the perimeter region of the slab at a width equal to that of the column. The selected concrete and reinforcement material models for slab beams are identical to the ones used for the columns. In addition, the

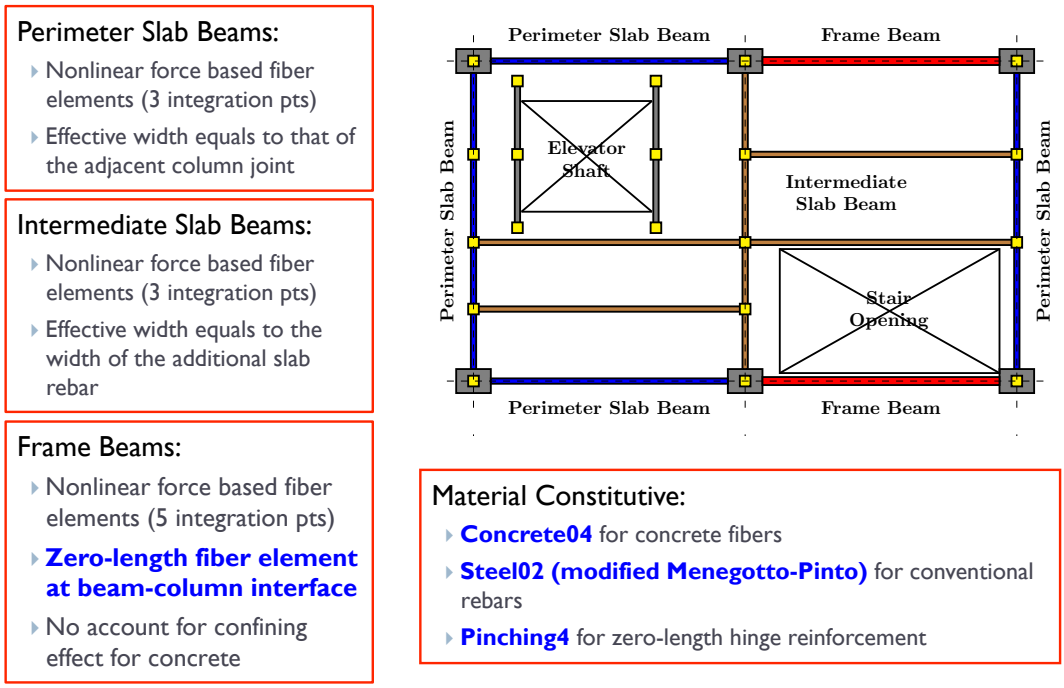

Figure D.2. Modeling details of beams and slabs of a typical floor.

diagonal steel braces at the east side of the test building are modeled using corotational truss elements that are capable of considering the large deformation of the elements. Since the braces in the test building were only designed to be effective when they were subjected to tensile forces, the material constitutive for the steel braces is assumed as nonlinear-elastic with no compression.

Rayleigh damping is incorporated into the model to account for the energy dissipation of the test building and its NCSs in nonlinear dynamic analysis. During the pre-test simulations, a damping ratio of 2% is assigned to the first and the second vibration modes in the longitudinal direction (the shaking direction). The modal frequencies of the building are determined by conducting eigenvalue analysis assuming the initial properties of the building. These eigenvalue analysis results are presented later in this appendix.

D.3 Estimated Pre-test Weight of the Building

The building weight used in the pre-test simulations was estimated using hand calculations. In specific, the construction drawings were used for calculating the weight of the structural skeleton and those of the NCSs were determined by summing the weights of all the components. Table D.1 summarizes the floor-by-floor weight distribution of the test building and the nonstructural components and systems (NCSs). The total weight of the test building including its NCSs was estimated as about 6256 kN, which closely matches the readings from the jacks obtained later during the building lifting stage. It is important to note that the test building is considered fixed at the base of the columns and walls in the pre-test simulations, and therefore the weight of the foundation is excluded from the that of the entire building, resulting in a total weight of 4483 kN. Subsequently, the weight of each structural frame member (e.g., columns, beams, and walls) is distributed to the corresponding elements at their end nodes. In addition, the weight of the exterior facade is distributed to the perimeter nodes based on the tributary length, while those of the remaining NCSs and the structural slabs are distributed proportionally into their tributary nodes.

Table D.1. Estimated pre-test weight of the building and its nonstructural components (units in kN).

Floor #	Structure	NCSs	Total per floor
Roof	466.6	133.0	599.6
Floor 5	577.4	429.2	1022.8
Floor 4	577.8	438.6	1016.0
Floor 3	581.0	167.3	745.1
Floor 2	581.0	157.9	738.9
Floor 1	1906.0	240.6	2146.6
Total	4689.8	1566.6	6256.4

D.4 Pre-test Simulation Results

D.4.1 Eigen Analysis

The modal characteristics of the test building are evaluated by conducting eigenvalue analysis using the initial stiffness and the total mass of the building including the masses of the NCSs. Figure D.3 presents the mode shapes and the corresponding periods of the first four vibration modes of the test building. As shown in the figures, the fundamental mode corresponds to building longitudinal vibration with a period of 0.71 second (Figure D.3a). Figures D.3b–c indicate that the second and third modes are both coupled in the torsional and transverse directions as a result of an asymmetric layout of the framing members (e.g., transverse shear wall offsets). The fourth mode of the building corresponds to the second longitudinal mode with a period of 0.20 second (Figure D.3d). These estimated dynamic characteristics of the test building are consistent with the system identification results obtained using the white noise test data at the completion of the building construction (Astroza et al., 2015).

D.4.2 Nonlinear Dynamic Analysis

In addition to eigenvalue analysis, nonlinear time history analysis are conducted to predict the nonlinear building response under the earthquake motions of varied amplitude. It is noted that the earthquake motions used in the pre-test simulations are the target motions for the earthquake tests, which differs from the achieved input motions (those measured on the shake table platen) during the tests. Figures D.4 and D.5 compare the predicted (numerical) and measured (experimental) peak building responses in the direction of motion (east-west direction) during tests FB-1 (serviceability level earthquake) and FB-5 (design level earthquake), respectively. The peak responses shown in the figures include the peak floor accelerations (PFAs) and peak interstory drift ratios (PIDRs), which are calculated as the averaged response of those at the four corners of the test building.

Despite the discrepancies at the certain locations, the predicted largest PIDRs and the PIDR distributions along the vertical direction appear to agree in overall with the

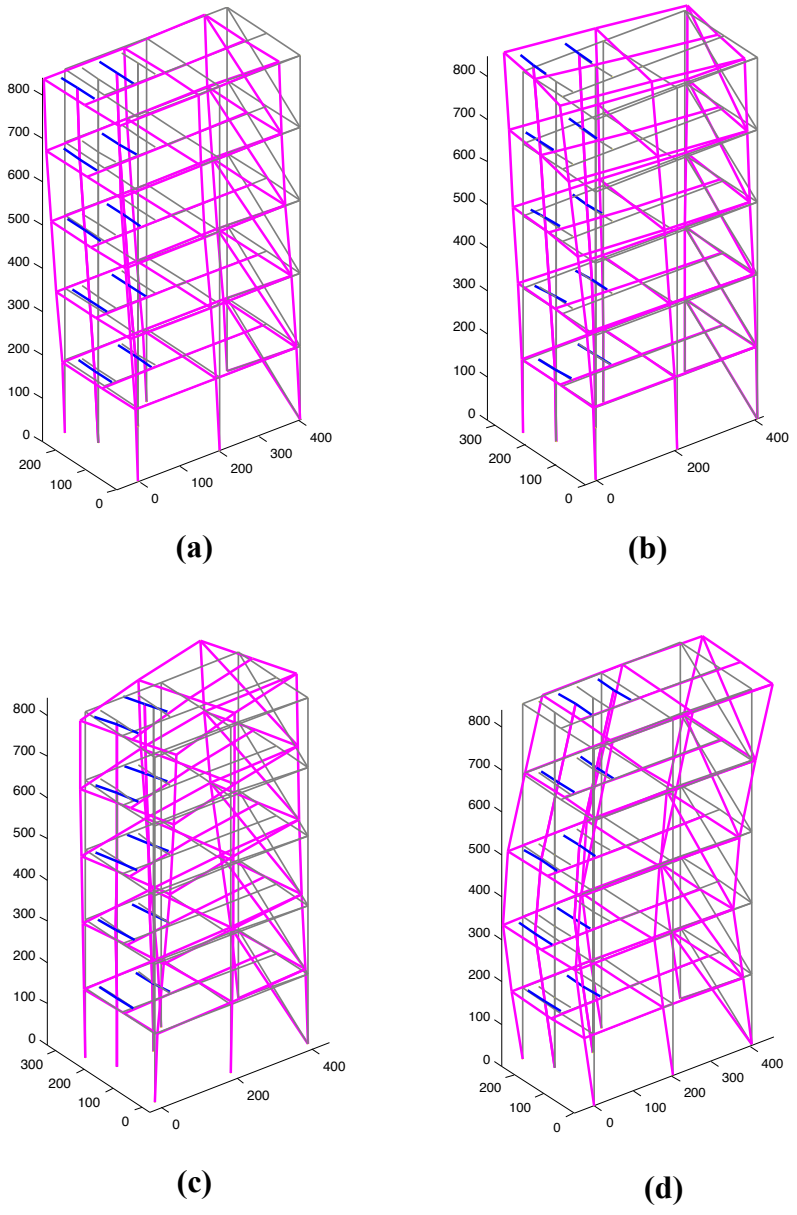

Figure D.3. Estimated modal shapes and the associated modal periods: (a) first mode (T=0.71 sec), (b) second mode (T=0.68 sec), (c) third mode (T=0.47 sec), and (d) fourth mode (T=0.20 sec).

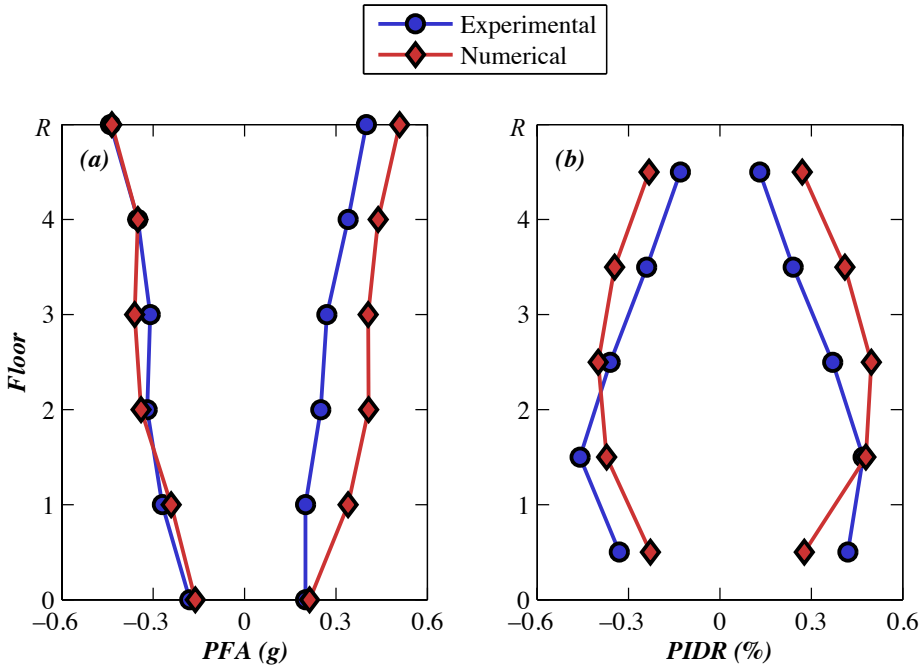

Figure D.4. Predicted and measured building responses during FB-1: (a) peak floor accelerations, and (b) peak interstory drift ratios.

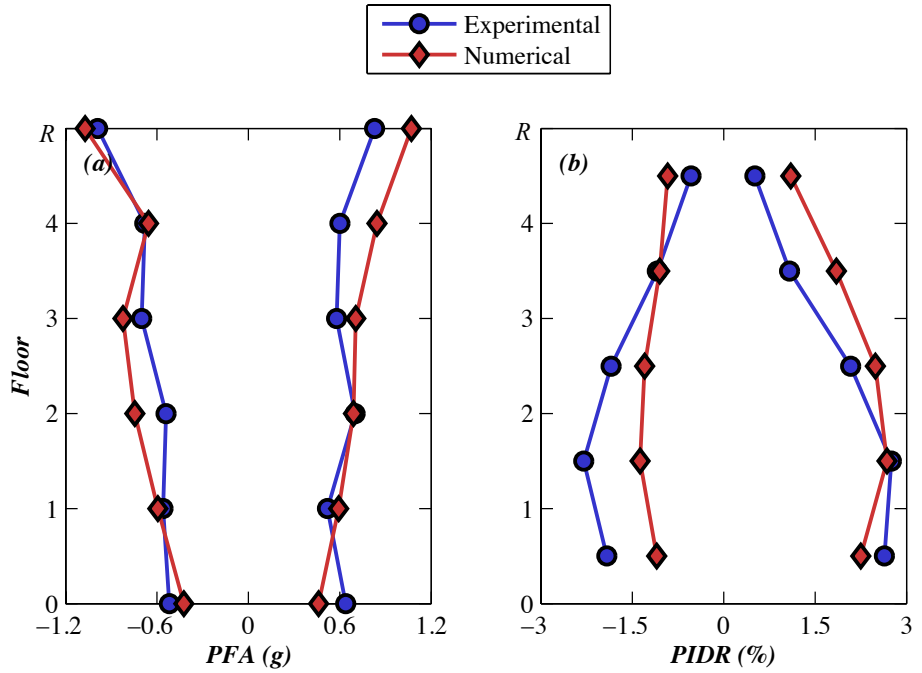

Figure D.5. Predicted and measured building responses during FB-5: (a) peak floor accelerations, and (b) peak interstory drift ratios.

experimental results under both low- (FB-1) and high-amplitude (FB-5) earthquake scenarios. In addition, the model is shown to be capable of capturing the most salient nonlinear behavior of the test building under high-amplitude earthquake. As indicated by Figure D.5b, the predicted building PIDRs at the lower levels are much larger than those at the upper levels during the design event FB-5.

D.5 Summary

This appendix presents a pre-test numerical modeling work of the full-scale test building. The appendix first summarizes the modeling techniques of the building implemented in *OpenSees* and subsequently presents the pre-test simulation results of the test building. Comparison of the peak floor responses of the numerical and experimental results indicates that the model of the test building reasonably reflects the dynamic characteristics as well as the most salient nonlinear behavior of the building (concentration of displacement demands over the lower floors) under large-amplitude earthquakes, thus providing useful guidance for earthquake test motion selection and design of the nonstructural systems installed on the test building.